

DIGEST

**1998
IEEE/LEOS
Summer
Topical
Meetings**

Broadband
Optical
Networks and
Technologies:
*An Emerging
Reality*

Optical MEMS
Technically
Co-Sponsored by
the Optical Society
of America

Smart Pixels

Organic
Optics and
Optoelectronics

**20 - 24 July
1998**

**Monterey
Plaza Hotel
Monterey, CA**



IEEE
Networking the World™



19990315 017

1998 IEEE/LEOS
Summer Topical Meeting

20 – 24 July 1998

Broadband Optical Networks and Technologies:
An Emerging Reality

Optical MEMS

Smart Pixels

Organic Optics and Optoelectronics

Monterey Plaza Hotel
Monterey, CA

IEEE Catalog Number: 98TH8369
ISBN: 0-7803-4953-9

REPORT DOCUMENTATION PAGE			Form Approved OMB No. 0704-0188	
Public reporting burden for this collection of information is estimated to average 1 hour per response, including the time for reviewing instructions, searching existing data sources, gathering and maintaining the data needed, and completing and reviewing the collection of information. Send comments regarding this burden estimate or any other aspect of this collection of information, including suggestions for reducing this burden, to Washington Headquarters Services, Directorate for Information Operations and Reports, 1215 Jefferson Davis Highway, Suite 1204, Arlington, VA 22202-4302, and to the Office of Management and Budget, Paperwork Reduction Project (0704-0188), Washington, DC 20503.				
1. AGENCY USE ONLY (Leave Blank)	2. REPORT DATE July 1998	3. REPORT TYPE AND DATES COVERED Final Technical		
4. TITLE AND SUBTITLE Technical Digest of the 1998 Summer Topical Meeting on Organic Optics and Optoelectronics		5. FUNDING NUMBERS G N00014-98-1-0806		
6. AUTHORS Multiple				
7. PERFORMING ORGANIZATION NAME(S) AND ADDRESS(ES) Institute of Electrical and Electronics Engineers, Inc. 445 Hoes Lane, P.O. Box 1331 Piscataway, NJ 08855-1331		8. PERFORMING ORGANIZATION REPORT NUMBER		
9. SPONSORING / MONITORING AGENCY NAME(S) AND ADDRESS(ES) Office of Naval Research Ballston Centre Tower One 800 North Quincy Street Arlington, VA 22217-5660		10. SPONSORING / MONITORING AGENCY REPORT NUMBER		
11. SUPPLEMENTARY NOTES				
12a. DISTRIBUTION / AVAILABILITY STATEMENT APPROVED FOR PUBLIC RELEASE		12b. DISTRIBUTION CODE		
13. ABSTRACT (Maximum 200 words)				
14. SUBJECT TERMS polymer devices; polymer-based devices, fabrication, testing; passive polymeric waveguide devices and fibers, electro-optic polymers and ultra-fast modulators; organic electroluminescent devices; photorefractive polymers			15. NUMBER OF PAGES 254	
			16. PRICE CODE	
17. SECURITY CLASSIFICATION OF REPORT Unclassified	18. SECURITY CLASSIFICATION OF THIS PAGE Unclassified	19. SECURITY CLASSIFICATION OF ABSTRACT Unclassified	20. LIMITATION OF ABSTRACT UL	

1998 IEEE/LEOS
Summer Topical Meeting

20 – 22 July 1998

Broadband Optical Networks and
Technologies:
An Emerging Reality

Monterey Plaza Hotel
Monterey, CA

IEEE Catalog Number: 98TH8369
ISBN: 0-7803-4953-9

The papers in this book make up the digest of the 1998 IEEE/LEOS Summer Topical Meetings. They reflect the author's opinions and are published as presented and without change in the interest of timely dissemination. Their inclusion in this publication does not necessarily constitute endorsement by the editors, the Institute of Electrical and Electronics Engineerings, Inc.

Copyright and Reprint Permission: Abstracting is permitted with credit to the source. Libraries are permitted to photocopy beyond the limit of U.S. copyright law for private use of patrons those articles in this volume that carry a code at the bottom of the first page, provided per-copy fee indicated in the code is paid through Copyright Clearance Center, 222 Rosewood Drive, Danvers, MA 01923. For other copying, reprint or republication permission, write to IEEE Copyrights Manager, IEEE Operations Center, 445 Hoes Lane, PO Box 1331, Piscataway, NJ 08855-1331.

© 1998 by the Institute of Electrical and Electronics Engineers, Inc. All rights reserved.

IEEE Catalog Number: 98TH8369

ISBN: 0-7803-4953-9 Softbound Edition
0-7803-4954-7 Microfiche Edition

ISSN: 1099-4742

Library of Congress:

Additional copies can be ordered from:

IEEE Service Center
445 Hoes Lane
P.O. Box 1331
Piscataway, NJ 08855-1331
Tel: (732) 981-1393
Fax: (732) 981-9667

Broadband Optical Networks and Technologies: *An Emerging Reality*

Co-Chairs:

Ray McFarland, *Department of Defense, Ft. Meade, MD*
Alan Willner, *University of Southern California, Los Angeles, CA*

Program Committee:

Rod Alferness, *Lucent Technologies Bell Laboratories, Holmdel, NJ*
Polina Bayvel, *University College London, London, UK*
Josep Berthold, *CIENA, Linthicum, MD*
G.K. Chang, *Bellcore, Red Bank, NJ*
Chongcheng Fan, *Tsinghua University, Beijing, CHINA*
Nick Frigo, *AT&T Labs-Research, Red Bank, NJ*
Sarry Habiby, *Tellium, Red Bank, NJ*
Robert Leheny, *DARPA, Arlington, VA*
T.P. Lee, *National Science Foundation, Arlington, VA*
Julian Lucek, *British Telecom, UK*
Rama Nune, *MCI Telecommunications, Richardson, TX*
Kenji Okada, *NTT, JAPAN*
Rajiv Ramaswami, *Tellabs, Hawthorne, NY*
Kristin Rauschenbauch, *MIT Lincoln Laboratories, Lexington, MA*
Ira Richer, *CNRI, Reston, VA*

TABLE OF CONTENTS

Monday, 20 July 1998

Session MA: Keynote Session

MA1	Predicting the Unpredictable – The Impact of All Optical Networking	N/A
MA2	DARPA's Plan for the Future Internet	N/A

Session MB: Optical Networking: From Access to Backbone

MB1	Development of Optical Network Elements.....	N/A
MB2	Extending WDM into the Access Network.....	N/A
MB3	A WDM-PON Using Fabry-Perot Lasers as Upstream Transmitters	3
MB4	Two Way DWDM Optical Network for Analog and Digital Transmission.....	5

Session MC: Optical Network Enabling Technologies

MC1	Wafer Fused Optoelectronics for Switching	7
MC2	Dynamic Spectral Equalization Using Micro-Opto-Mechanics	9
MC3	WDM Routers Based on Hierarchic Optical Discrete Fourier Transform Matrices.....	11
MC4	Simple Dynamic Model and Experiments on Laser Gain-Clamped EDFA	13
MC5	MEMS for Future-Deployable Switching Elements	N/A

Tuesday, 21 July 1998

Session TuA: Optical Networking Around the World

TuA1	Tackling the Bear: International Standards for Optical Networking.....	N/A
TuA2	Planning of Optical Networks in China.....	17
TuA3	Application of Photonic Network Technologies in Japan.....	19

Session TuB: Technologies for Ultra High Performance Optical Networks

TuB1	Asynchronous Digital Optical Networks	21
TuB2	Optical Fiber Ring 150 Gbps Data Storage Loop and Spontaneous Variable-Length Pattern Generation	23
TuB3	100 GBIT/S Parallel-to-Serial and Serial-to-Parallel Conversion Using Electroabsorption Modulators.....	25
TuB4	40 Gb/s Digital Logic Level Receiver	27
TuB5	Impact of Dispersion Compensation Gratings on OC-192 Systems	29

Session TuC: Optical Networking Applications

TuC1	Optical Network Management.....	N/A
TuC2	Restoration Capacity for Resilient Wavelength-Routed Optical Transport Networks.....	31
TuC3	Dynamic Sub-second Restoration in WDM Optical Transport Networks.....	33
TuC4	Optical Network Management and Control	N/A

TABLE OF CONTENTS

Wednesday, 22 July 1998

Session WA: Evolution of Optical Networks

WA1: WDM: An Emerged Reality	N/A
WA2: Optical Networks in the Real World	37
WA3: Islands of Transparency – An Emerging Reality in Multiwavelength Optical Networking.....	N/A

Broadband Optical Networks and Technologies: *An Emerging Reality*

Monday, 20 July 1998

MA: Keynote Session

MB: Optical Networking: From Access to
Backbone

MC: Optical Network Enabling Technologies

Monday Papers Not Available

- MA1 Predicting the Undpredictable – The Impact of ALL Optical Networking, *David Farber, University of Pennsylvania, Philadelphia, PA*
- MA2 DARPA's Plan for the Future Internet, *Bertram Hui, DARPA, Arlington, VA*
- MB1 Development of Optical Network Elements, *N. V. Srinivasan, Lucent Technologies, Bell Laboratories, Holmdel, NJ*
- MB2 Extending WDM into the Access Network, *Eric Swanson, MIT Lincoln Laboratories, Lexington, MA*
- MC5 MEMS for Future Field-Deployable Switching Elements, *Ming Wu, UCLA, Los Angeles, CA*

A WDM-PON using Fabry-Perot Lasers as Upstream Transmitters

S. L. Woodward, P. P. Iannone, K. C. Reichmann, and N. J. Frigo

AT&T Labs-Research
Newman Springs Laboratory
Red Bank, NJ 07701-7033

Introduction

In order to reduce the initial cost of deploying a wavelength-division-multiplexed passive-optical network (WDM-PON) it has been proposed that broadband optical sources be used in the optical network unit (ONU). A wavelength-grating router (WGR) at the remote node would "spectrally slice" the broadband light, so that light from each ONU would reach the Central Office (CO). [1],[2]. Previous work on spectral slicing has focussed on the use of LED's as broadband sources [1]-[3]. Although LED's are commercially available, their output power is low (typically less than -10 dBm). We demonstrate that Fabry-Perot lasers can be used as sources in a spectrally-sliced PON.

Uncooled, unisolated lasers are less expensive than LED's and typically have over ten times the output power, which increases the potential transmission distance of a PON. However, a Fabry-Perot laser does not inherently have a broad optical spectrum, and there are other shortcomings that must be dealt with if they are to be used as sources in a spectrally-sliced PON. We demonstrate that these shortcomings are not insurmountable, and that a spectrally-sliced PON employing Fabry-Perot lasers is capable of transmitting 10 Mbps through each port of a WGR followed by 18 km of fiber.

To broaden the optical spectrum of the Fabry-Perot laser, we drive the laser into clipping (the modulation depth is increased, so that the laser is driven below threshold). Simply broadening the spectrum does not insure that light will be transmitted through each port of the router, the mode spacing of the router and the laser must be compatible. Since we are using uncooled lasers, the wavelengths of the lasing modes will vary with time, therefore the mode spacing of the Fabry-Perot lasers should be less than the channel spacing of the router. This insures that at least one mode (or fractions of two modes) will be aligned with each channel of

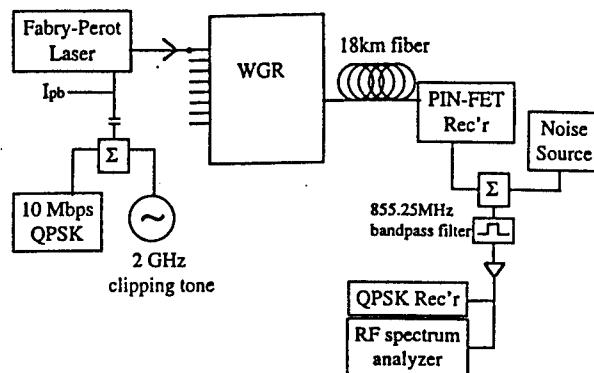


Figure 1: The experiment.

the router. In our experiments we used a laser with a mode spacing of 0.76 nm, and a router with a channel spacing of 1.3 nm at 1.3 μm (the router was designed to have 100 GHz (0.8 nm) spacing at 1.55 μm).

The most significant drawback to using a Fabry-Perot laser, rather than an LED, is the high relative intensity noise (RIN). Transmitting the laser through a WGR (or any narrow optical band-pass filter) will convert mode-fluctuations into RIN [4]. Without the WGR present the laser's RIN was -135 dB/Hz, but with the WGR present the RIN rose by 40 dB to approximately -95 dB/Hz. This was the dominant noise source in our experiments.

In our experiments we chose to use sub-carrier transmission, rather than baseband transmission. The RIN was lower at RF frequencies, and using an RF subcarrier to transmit the data allows multiple users to access the system, either by assigning each a different subcarrier frequency (subcarrier-multiplexing (SCM)) or by sharing a single RF channel via time-division-multiple access (TDMA).

The Experiment

Figure 1 shows our experiment. We used a quadrature-phase-shift-keyed (QPSK) sig-

nal to transmit 10 Mbps. The laser was pre-biased to 1 mW output power (measured at the fiber pigtail). A $2^{23} - 1$ pseudo-random bit-stream was transmitted on a subcarrier centered at 855.25 MHz with a 50% optical modulation depth (OMD). A clipping tone (OMD=100%) at 2 GHz was also present. With the clipping tone present, the transmission loss through the WGR varied from 15 dB to 22 dB, without the clipping tone present the loss varied from 13 dB to 31 dB. The presence of upstream signals from additional users was simulated by adding white gaussian noise after the receiver. Received signals were sent to a QPSK receiver, and also monitored using an RF spectrum analyzer. Our QPSK modem was equipped with Reed-Solomon forward-error-correction (FEC). Use of FEC reduces the data bit-rate from 10 Mbps to 9.17 Mbps. We measured the bit-error rate (BER) both before and after FEC.

Measurements were made using each input port of the WGR. The BER was below 10^{-9} (without FEC) regardless of which input port was used. However, the electrical signal strength varied by almost 15 dB, so that if multiple lasers were simultaneously transmitting signals upstream, the RIN from one could easily cause errors in another ONU's channel.

This variation in the signal level implies that for signals from multiple ONU's to be sub-carrier multiplexed together, power equalization must be performed. This was achieved by adjusting the laser's pre-bias current so that the QPSK signal's power equaled a constant value, regardless of which input port was being used.

In a subcarrier-multiplexed PON limited by RIN, the BER is limited by the amount of noise introduced by additional optical carriers, rather than by the receiver's noise. Figure 2 shows the BER versus the amount of additional noise supplied by the noise source shown in Figure 1. If signals from each ONU are subcarrier multiplexed, then the total noise one expects at the receiver is the sum of the measured noise from each input port: -57 dBm. With FEC employed, all eight input ports had $\text{BER} < 10^{-9}$ when that amount of noise (-57 dBm) was added to the received signal.

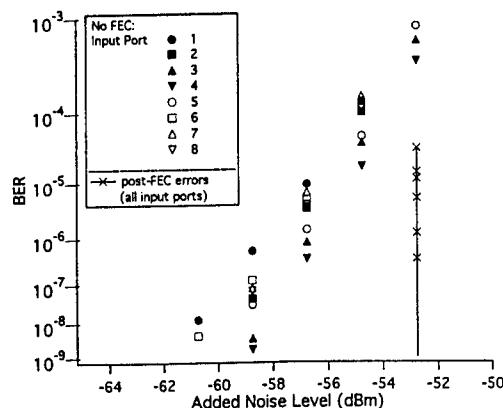


Figure 2: The BER versus added white gaussian noise. The sum of the RIN transmitted through all eight ports of the WGR corresponds to -57 dBm added noise.

Conclusions

We have demonstrated that Fabry-Perot lasers can be used in spectrally-sliced PON's, though their performance is limited due to mode fluctuations being converted to intensity noise. 10 Mbps transmission was demonstrated through a WGR followed by 18 km of fiber. No alignment of the modes of the laser and the passbands of the WGR were required. If FEC is employed, then up to eight ONU's can be subcarrier-multiplexed together, giving each a dedicated channel with an effective bit-rate of 9.17 Mbps. If the QPSK channels are shared, then the noise-margin, and the number of ONU's served could be increased.

References

- [1] S. S. Wagner and T. E. Chapuran, "Broadband High-Density WDM Transmission Using Superluminescent Diodes," *Electronics Letters*, vol. 26, no. 11, pp. 696-697, May 24, 1990.
- [2] M. Zirngibl, C. H. Joyner, L. W. Stulz, C. Dragone, H. M. Presby, and I. P. Kaminow, "LARNet, a Local Access Router Network," *IEEE Photonics Technology Letters*, vol. 7, no. 2, pp. 215-217, February, 1995.
- [3] P. P. Iannone, N. J. Frigo, and T. E. Darcie, "WDM passive-optical-network architecture with bidirectional optical spectral slicing," *Optical Fiber Conference '95 Technical Digest*, Tu K2, pp. 51-53, February 1995.
- [4] K. Petermann, *Laser Diode Modulation and Noise*, Kluwer Academic Publishers, The Netherlands, pp. 186-194, 1988. (ISBN 90-277-2672-8).

Two way DWDM optical network for analog and digital transmission

Xingyu Zou, David Piehler, Israel Levi, Chuan Xie, and Jeng-Rong Yeh

Harmonic Lightwaves, Inc.

549 Baltic Way

Sunnyvale, California 94089

phone: 408-542-2798, FAX: 408-542-2512

e-mail: xingyu.zou@harmonic-lightwaves.com

Cable modems have seen rapid deployment in the past year due to demand for high-speed internet services. Cable modems communicate with frequency division multiplexed data conforming to the MCNS (multimedia cable network system) standard. Upstream data is QPSK modulated onto RF subcarriers in the 5-40 MHz band, and downstream data is QAM-64 modulated onto RF subcarriers that might otherwise be assigned to analog television channels. Widespread implementation of dense wavelength-division-multiplexing in digital network provides the commercially available WDM components. In this paper, we describe a simple, scaleable two way WDM analog system that is easy to upgrade in the existing HFC infrastructure.

At first glance WDM may seem to be a poor choice for analog transmission. In the world of analog CATV, nonlinear fiber optic effects will cause excessive crosstalk between the same TV channels launched into fibers at different wavelengths[1]. Although complex cancellation techniques[2] can mitigate this effect, the only effective use of DWDM in analog CATV has been to use different non-overlapping sets of the RF spectrum on different wavelengths. Additionally the gain tilt in the EDFA and the dispersion in the fiber[3] cause significant second order distortions due to their interaction with the chirp of a directly modulated DFB lasers. Our downstream and upstream system design minimize these effects.

Our downstream system (shown in Fig.1) uses an externally modulated, optically amplified transmitter operating at 1547.7 nm for the broadcast of 80 analog channels in the 50-550 MHz band. Downstream digital information is QAM modulated onto RF subcarriers above 550 MHz which directly modulate four DFB transmitters operating at: 1550.9, 1552.5, 1554.1, 1555.7 nm. In principle the number of QAM optical channels can be greater. At the hub site, the digital optical channels are separated by one WDM while the broadcast optical signal is split. Another WDM multiplexer is used to combined the broadcast and narrowcast digital optical channels, sending the optical signals to specific nodes where both wavelengths are detected by a single receiver. Figure 2 shows the operation window with broadcast optical power at 3 dBm. Due to the fact that QAM signals tolerate lower CNR (carrier to noise ratio) and higher distortion, digital subcarriers are 6~10 dB lower than analog signals. The broadcast CNR degradation caused only by the insertion of digital optical signal is less than 1 dB. Depending on QAM channel plan, intermodulation distortion caused by 7 QAM channels can add 2 dB more CNR penalty at certain analog channels. To minimize the impact of added digital signal, the modulation index and optical power of digital signal can be adjusted.

Our upstream configuration is shown in Figure 3. Return path signal is regenerated at hub site with four nodes sharing one WDM lasers. They are optically combined at hub site and demultiplexed at headend. We use "noise-in-the-slot" measurement[4] to characterize the system performance in the 5-40 MHz band. We have measured that the dynamic range for $S/(N+I) > 40$ dB is more than 15 dB for return signals.

In conclusion, we have demonstrated a robust two way WDM network within a conventional HFC plant. The broadcast analog signal maintains $CNR > 50$ dB with narrowcast signal $CNR > 40$ dB. The return path achieves $S/(N+I) > 40$ dB with 15 dB dynamic range. Both exceeds the bit-error-free requirement for digital signals.

Acknowledgment: The authors would like to thank Oleh Snieszko and Butch Robertson of TCI for fruitful discussions and suggestions.

References

- [1] Koji Kikushima, Hisao Yoshinaga, and Makoto Yamada, "Signal crosstalk due to fiber nonlinearity in wavelength multiplexed SCM-AM-TV transmission systems", in OFC '95, paper PD24, San Diego, CA, 1995.
- [2] F.S. Yang, L.G. Kazovsky, M.E. Marhic and X.Y. Zou, "Cancellation of SRS crosstalk in an analog WDM optical communication system by a parallel technique", in OFC '98, paper TuO4, San Jose, CA, 1998.
- [3] E.E. Bergmann, C.Y. Kuo, and S. Y. Huang, "Dispersion-Induced composite second-order distortion at 1.5 μ m", IEEE Photon. Tech. Lett., vol.3, 59 (1991).
- [4] Oleh J. Snieszko and Tony Werner, "Return path active components test method and performance comparison", 1997 Conference on Emerging Technologies Proceedings Manual, 263 (1997).

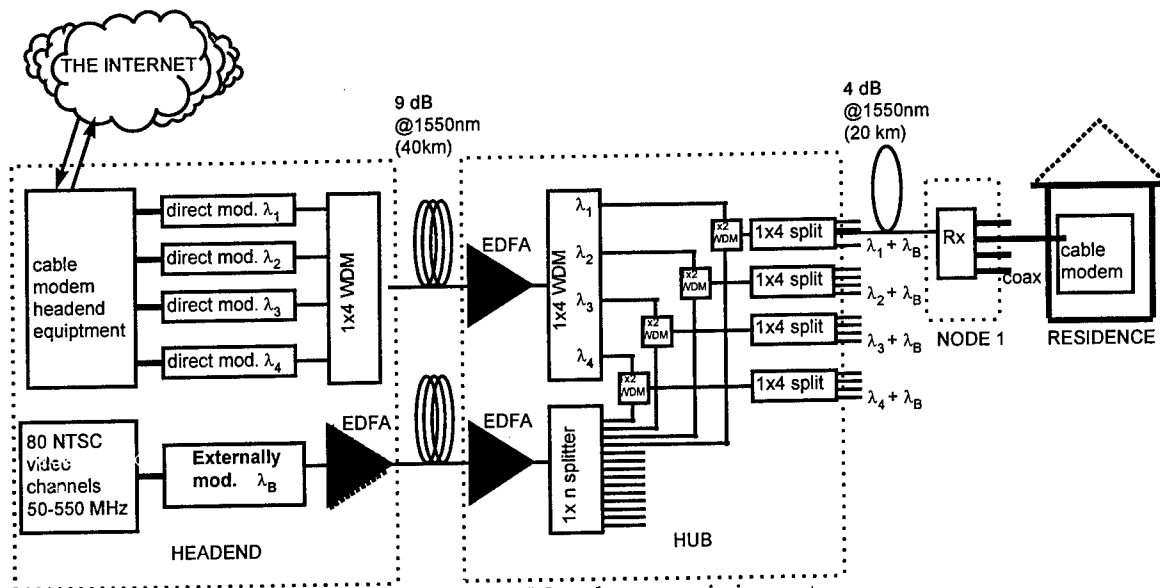


Figure1. Experimental setup of downstream WDM analog transmission system.

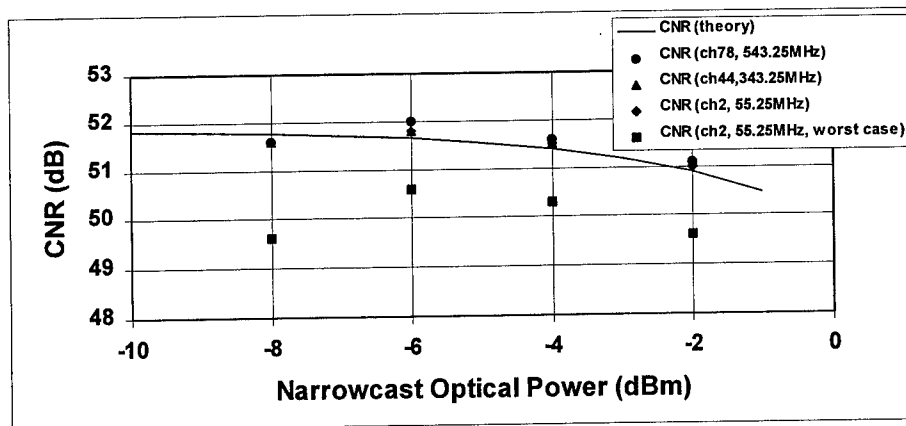


Figure2. Broadcast analog CNR degradation due to insertion of narrowcast digital signals. Modulation index of the QAM channels is adjusted to keep digital RF 10 dB down from analog RF. QAM channel plan is adjusted for optimum or worst case CNR penalty at channel 2.

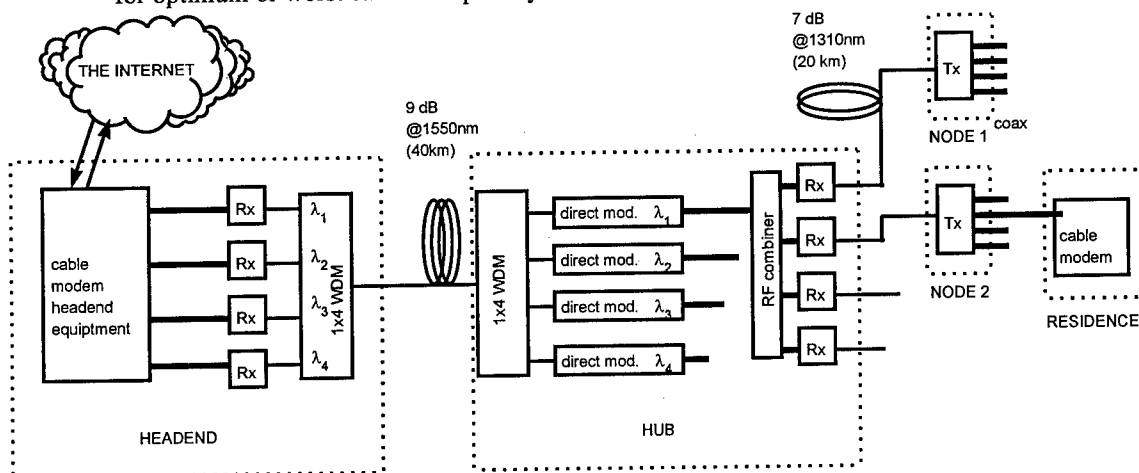


Figure3. Experimental setup of upstream WDM HFC system.

Wafer Fused Optoelectronics for Switching

Ali Shakouri, Bin Liu, Patrick Abraham, and John E. Bowers

Multidisciplinary Optical Switching Technology Center
Department of Electrical and Computer Engineering
University of California, Santa Barbara, CA 93106
ali@opto.ucsb.edu

Major requirements for photonic switching elements are scalability, low loss and low crosstalk. In high speed packet switched networks, there is a need for large size waveguide switches that incorporate fiber loop memories and integrated semiconductor optical amplifiers. Wafer fusion techniques can be used to combine planar waveguides fabricated on two different substrates into a 3D structure in which there is vertical coupling between arrays of single mode waveguides through the fused regions (Figs. 1,2) [1]. In addition, application of a bias at fused regions will allow a change of gain or index for switching purposes.

The Fused Vertically Coupled (FVC) waveguide structure shown in Fig. 2, was analyzed by 3D finite difference Beam Propagation Method (BPM). A single-mode ridge-loaded waveguide structure based on InP substrate, with 0.5 μm InGaAsP ($\lambda=1.3 \mu\text{m}$) core region, 0.1 μm cladding and 0.1 μm ridge height, is vertically coupled through a fused gap layer to an identical waveguide. The gap layer thickness is varied from 0.1 to 0.6 micron with its index ranging from InP to InGaAsP ($\lambda=1.4 \mu\text{m}$). Fig. 3 displays the calculated coupling length for different parameters of the gap layer. Ultra short couplers with 40-220 μm coupling length and 20-32 dB extinction ratio can be realized. A passive vertical coupler with 0.4 μm InP gap layer was fabricated by fusing two $8 \times 10 \text{mm}^2$ samples under pressure and at a temperature of 630 $^{\circ}\text{C}$ in a hydrogen atmosphere for 30 minutes. Fig. 2 shows the stain etched SEM picture of a finished FVC. The fused interface is not visible, which is an indication of the high quality of the fusion process. The near field pattern at the output of a FVC, 5.5 mm long, is recorded by an IR camera and it is shown in Fig. 5. It can be seen that by changing the input wavelength, light is switched from the upper to the lower waveguide. Since the shapes of the two waveguide modes are very similar, one can get a high extinction ratio. Our measurement shows the extinction ratio is about 15 dB. Fig.4 shows the intensities of the upper and lower waveguides as a function of wavelength. From the oscillation period (about 12 nm) and considering material and waveguide dispersions, coupling length is calculated to be 62 μm at 1.55 μm which is very close to BPM result of 58 μm .

The optical loss at the fused interface is an important factor in the design of coupler and switch structures. This was investigated using single mode InGaAsP-based fused waveguide structures. Comparison of the transmission loss in ridge-loaded waveguide structures with and without a fused layer near the core region, reveals an excess loss of 1.1 dB/cm at 1.55 μm wavelength. Finally a PIN FVC was fabricated and characterized. It can be seen in Fig. 6 that with a bias of 2.3V the light is switched from the top to the bottom waveguide. In conclusion, fused couplers and switches can give the added advantage of vertical integration by separating the input and output waveguides and create compact and scalable 3D photonic integrated circuits.

This work is supported by the DARPA center MOST.

References:

[1] B. Liu, A. Shakouri, P. Abraham, B.-G. Kim, and J. E. Bowers, submitted to Appl. Phys. Lett..

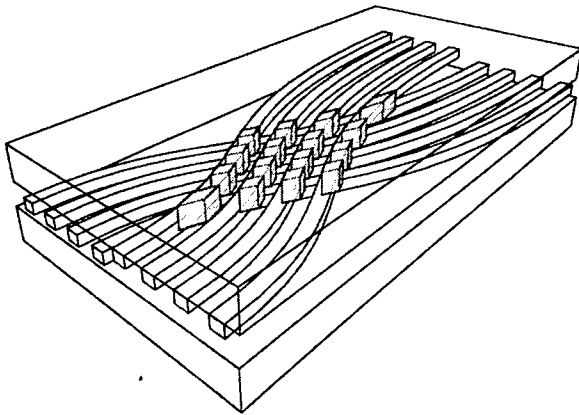


Fig. 1 InP Crossbar switch based on coupling between independent arrays of waveguides on each substrate.

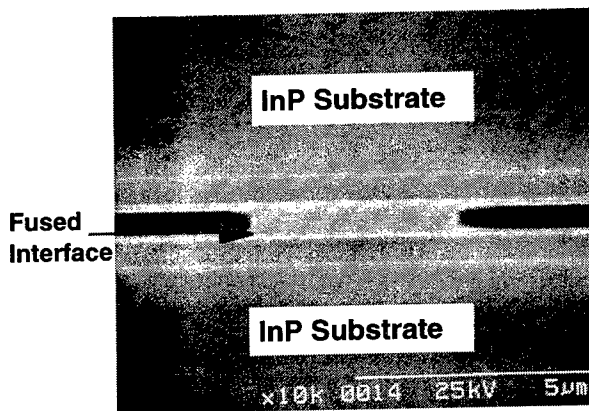


Fig. 2 Stain etched SEM picture of a fused vertical coupler

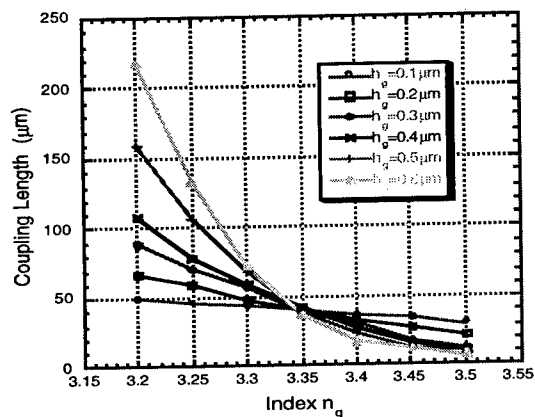


Fig. 3 Coupling length as a function of gap layer index for different thicknesses of the gap layer.

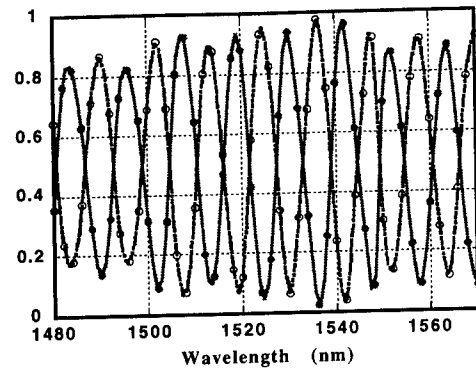


Fig. 4 Measured intensity of the upper and lower waveguides as a function of wavelength.

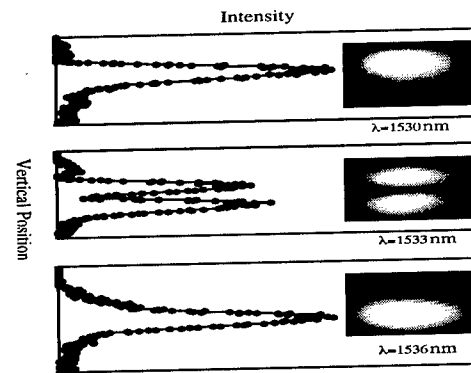


Fig. 5 Photograph of the near field pattern at the coupler output at 1530, 1533 and 1536nm wavelengths.

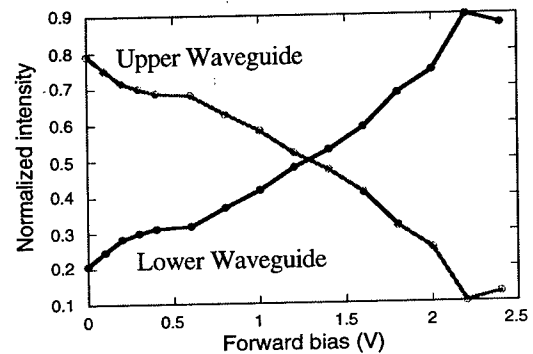


Fig. 6 Measured bias dependence of the output intensity for a 3.5mm fused vertical switch.

MC2

4:00pm - 4:15pm

Dynamic Spectral Equalization Using Micro-Opto-Mechanics

J. E. Ford and J. A. Walker

Bell Laboratories, Lucent Technologies, 101 Crawfords Corner Road, Holmdel NJ 07733

Power equalization in WDM systems can be achieved by a variety of means including signal pre-emphasis, fixed fiber gratings, and individual attenuators placed between two wavelength routers. Each of these approaches represents a tradeoff in network operator flexibility. In this paper, we demonstrate a dynamic WDM equalizer using a voltage-controlled variable reflectivity strip mirror and free-space wavelength mux to provide dynamic control over wavelength power levels across a continuous transmission spectrum.

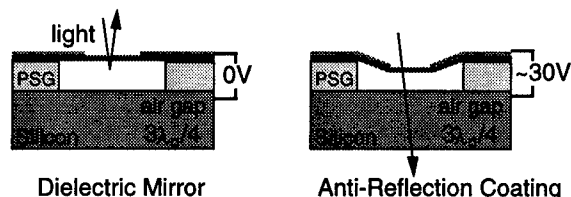


Figure 1: MARS micromechanical modulator

The MARS (for mechanical anti-reflection switch) modulator [1] shown in Figure 1 is basically a dielectric coating on a silicon substrate. A silicon nitride $\frac{1}{4}\lambda$ layer separated from the silicon substrate by a fixed $\frac{3}{4}\lambda$ spacer acts as a dielectric mirror with about 72% reflectivity. Voltage applied to electrodes on top of the membrane creates an electrostatic force and pulls the membrane closer to the substrate. When the membrane gap is reduced to $\lambda/2$, the layer becomes an anti-reflection coating with close to zero reflectivity. This 0.4 micron vertical deflection is small compared to the 200 to 500 micron wide membrane. Electrically the device behaves as a tiny capacitor, with zero static power dissipation.

MARS modulators are used in a WDM equalizer by placing a row of modulators at the (wavelength-dispersed) focal plane of a fiber-optic spectrometer and collecting the reflected light into an output fiber.

The first MARS WDM equalizer tested [2] used segmented devices, where the silicon nitride membrane was cut between adjacent electrodes to make each modulator mechanically independent. These devices were ultimately found to have curled at the edges, creating nonuniform attenuation across the width of each device and unacceptably narrow wavelength passbands.

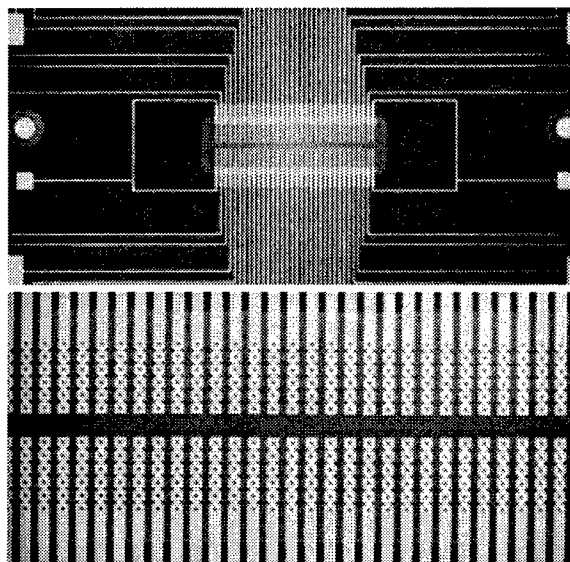


Figure 2: MARS Variable-Reflectivity Strip Mirror

Figure 2 shows our new approach, which uses a continuous unbroken modulator strip with electrodes applying force at discrete steps along a continuous narrow membrane. The membrane deflects like a rubber sheet, with smooth, shallow depressions (of up to 0.4 microns across a 290 micron suspended width) created wherever voltage is applied. This increases mechanical coupling between channels, but creates the best possible optical surface. The optically active region was a strip 40 microns wide by approximately 1 mm long, with 32 electrodes spaced at a 28 micron pitch (0.8 nm in wavelength).

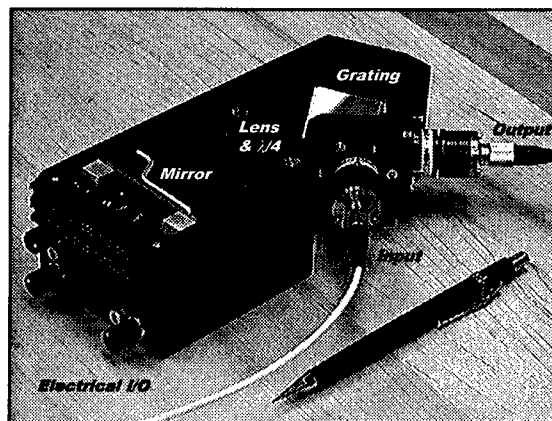


Figure 3: Free-space WDM optics and package.

This array is placed into a free-space optics wavelength multiplexing package (Figure 3) which uses refractive optics to image an input fiber through a planar diffraction grating to disperse the input light by wavelength across the array, then directs the reflected light back through the grating into an output fiber. A quarter wave plate flips the polarization of the light for the second pass through the grating to cancel polarization dependent diffraction losses. With a gold mirror at the device plane this package has 4 dB total insertion loss and 0.2 dB polarization dependent loss.

The results with the packaged device is that applying 0 to 60 V to one electrode creates a 3 nm wide Gaussian-shaped feature with 22 dB dynamic range. Intermediate regions between two nearby features are somewhat attenuated. For example, the midpoint between two 15 dB depressions separated by 7 nm has about 5 dB loss. In other words, the equalizer can create an arbitrary smooth variation in transmission.

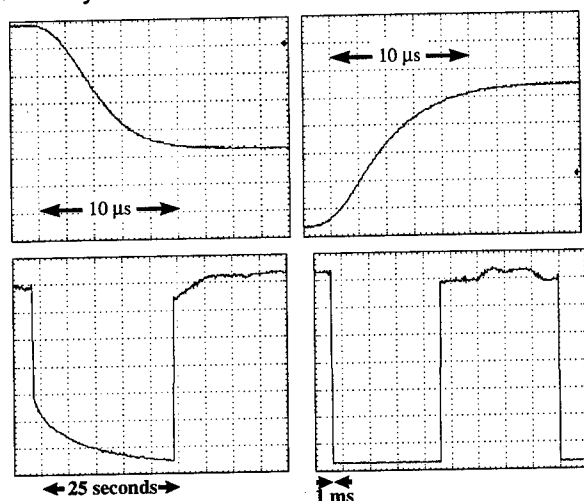


Figure 4: Dynamic response.

Figure 4 shows the equalizer time dynamics. The rise and fall time is less than 10 microseconds (top two traces) but there is a slow relaxation effect (bottom left trace) possibly due to static charge buildup on the dielectric membrane. Closed-loop feedback can suppress this effect and achieve fast response over a range limited by the total static charging (sacrificing 1-2 dB of the original 22 dB dynamic range). The bottom right trace shows fast, high-contrast equalizer response to an increased voltage step.

The equalizer's electronic control for the following experiments was 32 manually-adjusted trim-pots acting as voltage dividers for a common voltage supply provided by seven 9V batteries in series.

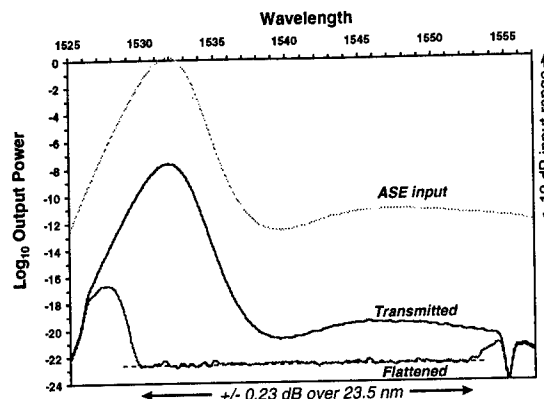


Figure 5: Equalized Erbium fiber amplifier ASE.

Figure 5 shows how the equalizer can flatten non-uniform amplifier gain. The upper curve is the original amplified spontaneous emission (ASE) output of an Erbium fiber amplifier with > 12 dB dynamic range. When this signal is transmitted through the packaged equalizer (with zero applied voltage) the excess loss varies smoothly from 8 to 9 dB across the 24 nm operating range. With an appropriate voltage setting, the ASE signal (in effect, the amplifier gain) was flattened to < 0.5 dB over a 23.5 nm bandwidth. Small ripples in loss (with less than 0.5 dB total excursion) are apparently due to scatter off the gold electrodes. Increasing the optical window width by 50% should eliminate these features.

The equalizer has also been used to demonstrate flattening of multiple laser inputs. 8 laser signals at 200 GHz pitch with signal levels that varied by an order of magnitude were equalized to within 0.4 dB variation, then re-amplified to compensate for excess loss. The final output was uniform to within a 0.65 dB range.

These results demonstrate how the WDM equalizer might be used in conjunction with an amplifier and a WDM detector to create a self-contained component capable of finding and correcting any problem with signal levels in a transmission system.

The authors would like to express appreciation to Lucent colleagues Keith Goossen and Martin Nuss for extremely helpful discussions, Cheng-Chun Chang for his lab expertise, Chris Doerr for the multi-frequency laser, and Fred Beisser for machining and the voltage control electronics.

- /1/ K. Goossen, J. Walker, and S. Arney, IEEE Phot. Tech. Lett. 6, p.1119, 1994.
- /2/ J. Ford, J. Walker, M. Nuss and D. Miller, Digest IEEE/LEOS 1996 Summer Topical Meetings on Broadband Optical Networks, p.26, 1996.

WDM Routers Based on Hierarchic Optical Discrete Fourier Transform Matrices

M. E. Marhic

Department of Electrical and Computer Engineering
Northwestern University
2145 N. Sheridan Rd., Evanston, IL 60208

F. S. Yang and L. G. Kazovsky,

Department of Electrical Engineering
202 Durand Bldg., Stanford University
Stanford, CA 94305

$N \times N$ WDM routers are currently based on two star couplers using diffraction [1] or multimode interference [2], connected by an array of waveguides. The diffraction-based star couplers each perform an approximate spatial discrete Fourier transform (DFT) [3], which leads to the well-known periodic router interconnection pattern. Here we study the use of another family of star couplers to implement the DFT: they are made by a hierarchic combination of 2×2 couplers [4]. In such networks, a number of phase shifts must be introduced; if they are implemented by means of path length differences, they are wavelength-dependent. We show that this has a relatively small effect on the performance of an otherwise ideal router, in that crosstalk for wavelengths away from the design wavelength exhibit relatively low crosstalk into undesired outputs.

Following the hierarchic synthesis introduced in Ref. [4], we find that the required structure for an 8-point DFT is as shown in Fig.1. The unit-magnitude complex number written next to a segment corresponds to its amplitude transmission coefficient, t , at the design frequency ν_d (the default is 1). Each hatched square represents a 2X2 coupler, with scattering matrix, $S = \frac{1}{\sqrt{2}} \begin{pmatrix} 1 & i \\ i & 1 \end{pmatrix}$ which is assumed to be independent of wavelength.

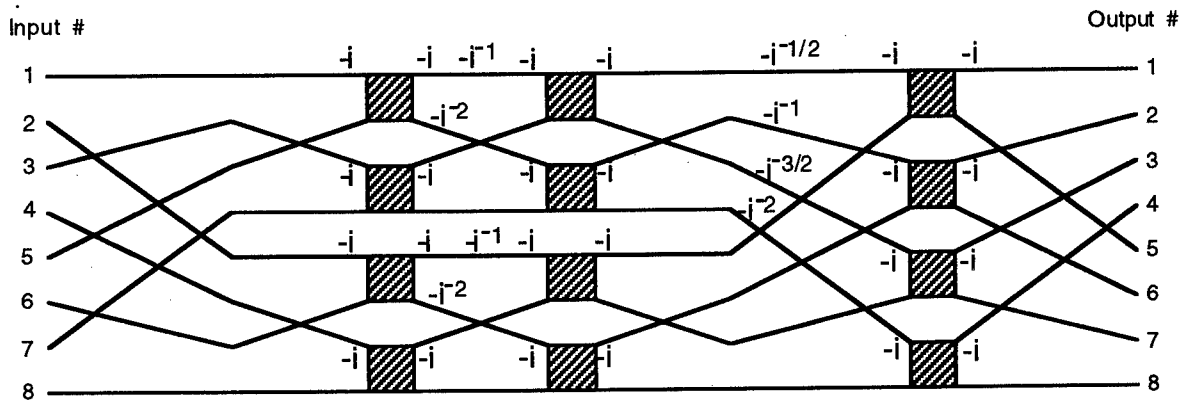


Figure 1: Schematic for 8-point DFT hierarchic star coupler

In contrast to the diffraction-based stars, hierarchic stars can implement an inverse DFT (IDFT). To do this, Fig. 1 should be modified as follows: 1) all the $-i$ terms next to the corners of the squares should not change; 2) in all other terms, i should be replaced by $-i$.

We have studied crosstalk due to the frequency dependence of the t 's: at a frequency $\nu \neq \nu_d$, t is replaced by t^{ν/ν_d} , due to the frequency-dependence of the phases. We considered two star networks, respectively performing an ideal DFT and an ideal IDFT at ν_d , connected by an array of N waveguides, with lengths increasing linearly with guide number $k = 1, \dots, N$. We considered a comb of N frequencies, spaced by $\Delta\nu$: the l th frequency is $\nu_l = \nu_1 + (l-1)\Delta\nu$ ($l = 1, \dots, N$). The phase shift experienced by ν_l in the k th guide of the array is given by $\frac{2\pi}{N}k(l-1)$.

We chose ν_d near the center of the spectrum, i.e. $\nu_d = \nu_{(N/2)}$; we then expect the largest crosstalk to occur for ν near the extreme frequencies, ν_1 and ν_N . The frequency dependence of a DFT star coupler with a representation such as in Fig.1 can be introduced by replacing $-i$ everywhere in the figure by

$-i \cdot \exp[-i \frac{2\pi}{N}(l - \frac{N}{2})\Delta\nu/\nu_d]$; the same substitution should be made for an IDFT network. (This assumes that each phase shift at ν_d is implemented by the shortest possible path difference.)

We have implemented an iterative program to simulate the corresponding matrix operations, and obtained crosstalk values for representative parameters. We use $m = 1, \dots, N$ to denote the number of the input fiber. For $\lambda_d = 1550$ nm, $\Delta\nu = 125$ GHz (about 1 nm), $N = 32$, $m = 1$, we found that the worst crosstalk occurred for $l = 2$, but did not exceed -37 dB; this is excellent performance for a router covering a 32 nm range. Doubling $\Delta\nu$ to 250 GHz, for a total range of 64 nm (which could be of interest for broadband optical amplifiers), did not increase crosstalk above -31 dB.

These numbers indicate that the inevitable frequency dependence of the DFT star couplers is actually moderate, and under otherwise ideal conditions leads to crosstalk which is at a level of interest for practical applications. It should also be noted that, instead of choosing the shortest possible path difference to implement a particular phase at ν_d , other choices can be made; these however, will exhibit different frequency dependences. Hence, there are in fact many different ways to implement a DFT star coupler at ν_d , and each implementation will lead to a different frequency dependence for the WDM router. Thus it is likely that some other choices will lead to performance exceeding that of the simple approach studied so far, which we have no reason to believe to be optimum.

Integrated optic implementation of the DFT star couplers envisioned in [4] can in principle be obtained by using silica technology, which is now mature. As a relevant example, an 8X8 thermo-optic switch has recently been implemented by this technology [5]: it incorporates 256 2X2 couplers, i.e. more than the 192 couplers that would be required for making a 64-point DFT matrix. The insertion loss, due to light propagating through 16 consecutive couplers, and 29 cm of waveguide, was only of the order of 5 dB. Individually-controlled thermo-optic heaters are used throughout the structure to control phases. It exhibits uniform performance over a 30 nm range. Permanent phase adjustment can also be made by other means [6]. All these features indicate that integrated $N \times N$ DFT networks should also be feasible, with good characteristics, for values of N of interest in practical applications (e.g. $N=16$ or 32).

A potential advantage of the hierarchic star coupler approach is that, if it is implemented as discussed above by means of silica waveguide technology, then by changing the phases internal to the star couplers, as well as the lengths of the waveguides connecting them, it may be possible to implement a variety of routing functions besides the one discussed here. Then this approach would provide means for changing the interconnection pattern in WDM networks, with less complexity than for an optical cross-connect capable of implementing arbitrary interconnection patterns. (As an example, if the IDFT star coupler is changed into a second DFT coupler, this is equivalent to a permutation of the output guides of the original router.)

In summary, we have introduced the possibility of synthesizing WDM routers based on $N \times N$ hierarchic star couplers. We have examined how the required phase shifts can be introduced by means of path length differences, and studied in detail the crosstalk introduced by the frequency dependence of these phases. We have found that crosstalk levels are moderate, even in units designed for a wavelength range as large as 64 nm. Additional opportunities exist for improving performance further, by implementing the phases by different path differences. The many degrees of freedom of hierarchic star couplers could also be used for making versatile reconfigurable routers

- [1] C. Dragone, IEEE Photon. Technol. Lett., 3, p. 812 (1991).
- [2] L. O. Lierstuen and A. Sudbø, IEEE Photon. Technol. Lett., 7, p. 1034 (1995).
- [3] C. Dragone, J. Lightwave Technol., 7, p. 479 (1989).
- [4] M. E. Marhic, Opt. Lett., 12, p. 63 (1987).
- [5] T. Goh, A. Himeno, M. Okuno, H. Takahashi, and K. Hattori, IEEE Photon. Technol. Lett., 10, p. 358 (1998).
- [6] H. Yamada, K. Takada, and S. Mitachi, J. Lightwave Technol., 16, p. 364 (1998).

Simple Dynamic Model and Experiments on Laser Gain-Clamped EDFA

Qian Yu and Chong-cheng Fan

Department of Electronic Engineering, Tsinghua University, Beijing 100084, CHINA

The laser gain-clamped erbium-doped fiber amplifier (EDFA) is quite attractive for applications in WDM optical networks for its simple and reliable gain stabilization and equalization [1-3]. A simple model describing transient dynamics of laser gain-clamped EDFA is presented in this paper. Factors governing the power excursion due to relaxation oscillations after abrupt channel dropping are examined. Specifically, it is found that this dynamic excursion (in dB) is roughly inversely proportional to the relaxation oscillation frequency, and explicit expression of this frequency was derived. Experimental results are shown and compared with theoretical predictions.

Let $y(t)$ be the co-propagating lasing signal power at the erbium-doped fiber (EDF) input point of a laser gain-clamped EDFA, then we have

$$y(t) = y(t - \tau_n) \cdot G_l^n(t) + y_{sp} + y_{ex}(t) \quad (1)$$

or

$$\tau_n \frac{dy(t)}{dt} = \ln[G_l^n(t)] \cdot [y(t) - \frac{y_{sp} + y_{ex}(t)}{1 - G_l^n(t)}] \quad (2)$$

where t is time, τ_n is the round-trip time in laser cavity, $G_l^n(t)$ is the round-trip gain of lasing signal, y_{sp} is an equivalent input power of ASE noise within laser bandwidth, and $y_{ex}(t)$ is the external input optical power at lasing wavelength λ_l (for instance, laser power leaked from the previous-stage EDFA). The transient dynamics of a piece of EDF can be modeled based on its average inversion level [4]. The physical meaning is that, in a unit time interval, the net loss of photons in the EDF should equal to the increase of excited-state Er^{3+} population. For improved simulation accuracy, our model includes ASE effect by using additional ASE beams with appropriate input power levels and center wavelengths. The dynamic model for a m -stage gain-clamped EDFA consists of $m+1$ coupled differential equations: one for the lasing signal power as given by (2) and m others for the average inversion of corresponding EDF sections.

Using a perturbation analysis, the relaxation oscillation frequency of a m -stage laser gain-clamped EDFA is found to be

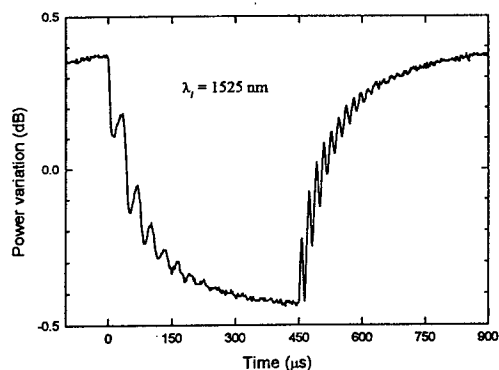
$$f_{relax} \approx \frac{1}{2\pi} \sqrt{\frac{q}{P_l^{IS} \tau_0 \tau_n} \sum_{j=1}^m (P_l^{out,j} - P_l^{in,j})} \quad (3)$$

where $q = 1$ (for ring-laser structure) or $q = 2$ (for Fabry-Perot laser structure), P_l^{IS} is the intrinsic saturation power at λ_l , τ_0 ($\approx 10.5\text{ms}$) is the meta-stable state Er^{3+} life time, $P_l^{in,j}$ or $P_l^{out,j}$ is the input or output laser power of the j -th EDF stage. Given EDFA gain and pump power levels, lower total input power of amplified signals corresponds to higher lasing power and hence higher f_{relax} . On the other hand, it will reach maximum value at $\lambda_l \sim 1.53\mu\text{m}$ where P_l^{IS} is minimum.

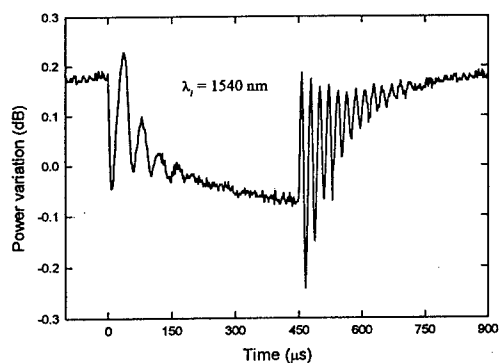
In our experiment (setup similar to [5]), the feedback loop of the lasing signal is formed by a 980-nm pumped EDFA, two wavelength-insensitive couplers, a tunable bandpass filter and a variable attenuator. At -17dBm input power, the EDFA gain is 33dB and 1dB-gain bandwidth is 15nm. A 1549.9-nm signal with -18.3dBm input power represents seven out of eight channels to be added or dropped abruptly. The surviving channel locates at 1560.6nm with -27dBm input power. While λ_l is changed, the cavity loss is adjusted so that the EDFA gain at 1549.9nm is always 33dB. Fig. 1 shows the transient response of the 1560.6-nm signal output power to the on/off modulation of the 1549.9-nm signal under $\lambda_l = 1525\text{nm}$ and 1540nm , respectively. Here the modulation period is 0.9ms. The spikes in these curves are caused by laser relaxation oscillations, while the difference between the steady-state surviving-signal output power levels arises from fiber inhomogeneity [5]. Fig. 2 shows the corresponding simulation result for $\lambda_l = 1540\text{nm}$, while fiber inhomogeneity is not included in the modeling. Fig. 3 shows the comparison between experimental and simulated results on f_{relax} and the height of the first overshooting peak (ΔP_{over} , see Fig. 2) after abrupt dropping of the 1549.9-nm signal. A reasonable agreement can readily be found. Factors influencing ΔP_{over} can be shown from a rough theoretical estimation given by

$$\Delta P_{over} [\text{dB}] \approx \frac{10}{\ln 10} \times \frac{1}{4 f_{relax} \tau_0} \times \sum_{j=1}^m \frac{P_d^{out,j} - P_d^{in,j}}{P_s^{IS}} \quad (4)$$

Here subscripts "d" and "s" denote drop and surviving signals, respectively. From (3) and (4), the dynamic excursion arising from relaxation oscillations is roughly inversely proportional to f_{relax} , and can be reduced by appropriate lasing wavelength ($\sim 1.53\mu\text{m}$), shorter laser cavity length, or higher lasing signal power. Fig. 4 shows good



(a)



(b)

Fig.1 Measured surviving signal power transients. The lasing wavelength λ_l is (a) 1525nm, (b) 1540nm.

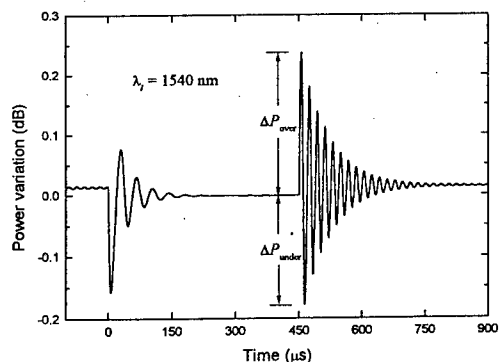


Fig. 2 Simulated 1550.6-nm signal power transients under same condition of Fig. 1.

agreement between simulated and measured total power excursion ($\Delta P_{over} + \Delta P_{under}$) of 1560.6-nm signal output power versus 1549.9-nm signal input power, while the amplifier gain is clamped at 33dB.

More detailed simulation and measured results, especially those for gain stabilized EDFA chains, will be presented at the meeting.

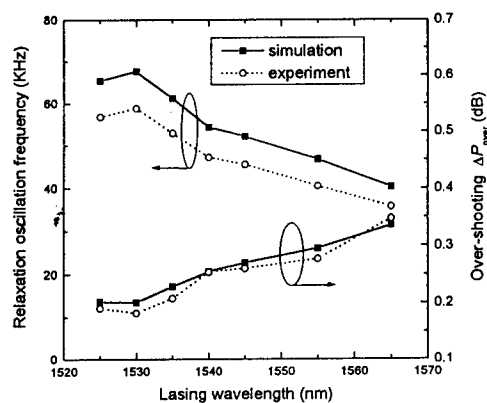


Fig. 3 Laser relaxation oscillation frequency and the height of the first overshooting peak after dropping of the 1549.9-nm signal for a group of lasing wavelengths.

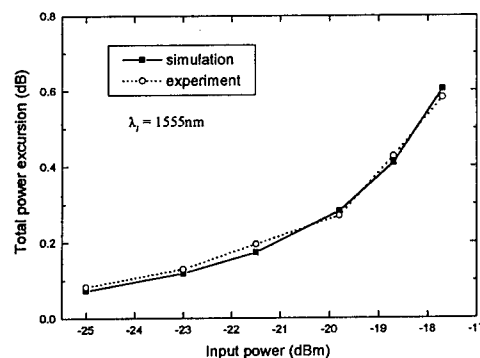


Fig. 4 Total dynamic power excursion versus drop signal input power.

Reference

- [1] M. Zimgibl, *Electron. Lett.*, vol. 27, No. 7, pp. 560-561, 1991.
- [2] E. Delevaque, *et al.*, *Electron. Lett.*, vol. 29, No. 12, pp. 1112-1113, 1993.
- [3] B. Landousies, *et al.*, *Electron. Lett.*, vol. 32, No. 20, pp. 1912-1913, 1996.
- [4] Y. Sun, *et al.*, *IEEE J. Selected Topics in Quantum Electron.*, vol. 3, No. 4, pp. 991-1012, 1997.
- [5] G. Luo, *et al.*, *IEEE Photon. Technol. Lett.*, vol. 9, No. 10, pp. 1346-1348, 1997.

Broadband Optical Networks and Technologies: *An Emerging Reality*

Tuesday, 21 July 1998

- TuA: Optical Networking Around the World
- TuB: Technologies for Ultra High Performance
Optical Networks
- TuC: Optical Networking Applications

Tuesday Papers Not Available

- TuA1 Tackling the Bear: International Standards for Optical Networking, *John Eaves, AT&T, Holmdel, NJ*
- TuC1 Optical Network Management, *Yukun Tsai, Bellcore, Red Bank, NJ*
- TuC4 Optical Network Management and Control, *Mari Maeda, DARPA, Arlington, VA*

Planning of Optical Networks in China

Wanyi Gu, IEEE member, Yunfeng Shen
Beijing University of Posts and Telecommunications
Beijing 100876, China

SUMMARY

Introduction

As the basic part of China's National Information Infrastructure, telecommunication has been developed quickly since the 1980's. A more forwarding leap emerged in China's telecommunication network construction after 1990 and the network has become the second largest in the world by 1997. In August 1997, for example, the capacity of public telephone exchanges reached 100 million lines, 99.7 percent of which are digital exchanges; the telephone subscribers reached 74.32 million, including 64.05 million local telephone subscribers and 10.26 million mobile telephones. Optical cables are also widely used in China, and the total length of cables (including trunk, local and access networks) has reached 820 thousand kilometers. Based on optical fiber cables, digital microwave and satellite subsidiary, a transport network with fully coverage, large capacity and high rate has been basically formed. New technologies such as SDH, EDFA, and WDM has been or will be used soon in it. However, the development of the transport network is still slower than needed. Accompanied by the development of telephone, data communications and multimedia communications, more and more capacity is needed. In order to meet the needs of economic development and social progress, the development of optical networks in China is imperative.

Research and development trend of WDM all-optical networks in China

WDM technique has been used in China's local and trunk optical networks, and it makes very effective utilization of fiber bandwidth and can offer flexible cross-connecting based on wavelength routing. So, although research projects such as optical ATM switching and OTDM networks are also going on, the major researches on optical networks in China are WDM all-optical networks which have the advantages of broadband, enormous capacity, transparency and reconfiguration ability. The project of WDM all-optical experimental networks which we are working on is supported by the National (863) High Technique Development Program. The National Natural Science Found is also going to launch a major project about WDM all-optical networks, including both networking and material technologies.

Our research group in BUPT (Beijing University of Posts and Telecommunications) cooperating with Peking University and Tsinghua University is developing an WDM all-optical experimental network with OXC (optical cross-connecting) and OADM (optical add and drop multiplexing) nodes. The structure of OXC node developed in BUPT is shown in Fig.1.

In Fig.1, four 2x2 optical switches cross-connect two WDM links, each of which consists of four different wavelengths in 1.55 μm range. The switch matrix is controlled by the network management center which can provide dynamic routing selection and network reconstruction signals, and can survey the performances and faults of optical layer by detecting the signals of surveying wavelength at 1.3 μm using HDLC protocol.

Fig.2 shows the WDM optical experimental network being developed by Peking Univ., Tsinghua Univ. and BUPT. The network consists of two OXC's, one of which cross-connects the signals of different links of trunk networks while the other one cross-connects the signals between local and trunk networks. The second OXC drops some signals to the local network which consists of two OADM nodes. The experimental network will be completed in this year, and virtual wavelength routing networks will be studied continuously.

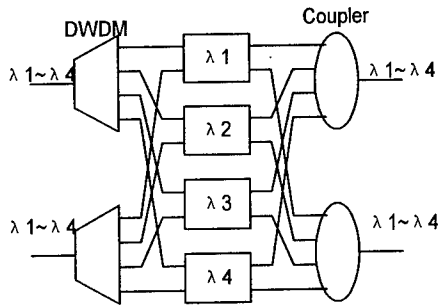


Fig.1 The structure of our OXC

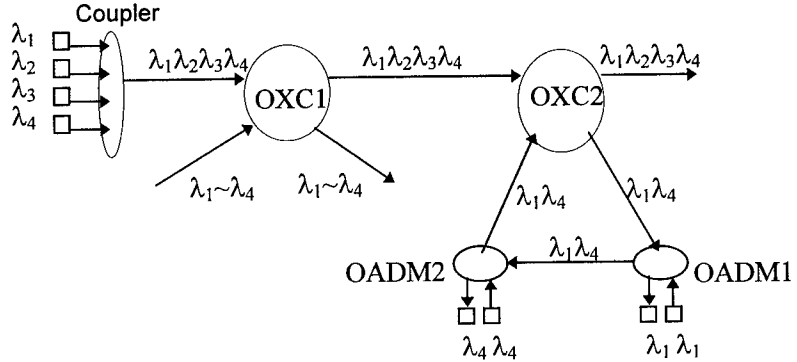


Fig.2 Diagram of the WDM optical experimental network

We have studied the layered structure, node structure and control and management scheme of WDM all-optical networks. Transmission limits such as interferometric crosstalk, transient response of EDFA, chromatic dispersion and nonlinearity in WDM all-optical networks are also studied based on this experimental network.

The control and management of optical networks are very important. We take the optical network as an independent layer of transport networks based on the concept of TMN (telecommunications management network), and manage it independently from SDH networks. We are going to use supervisory wavelength (at 1.51 or 1.31 μ m) to carry management signals and perform the management of performances, faults, configurations and securities.

The experimental network we currently developed is based on fixed wavelength routing without wavelength converters. Wavelength converters, especially the converters based on SOA, are being researched in China for avoiding wavelength blocking and increasing the flexibility and capacity of the networks. Virtual wavelength routing is our next research project.

As the development trend is mentioned, we think that WDM all-optical networks technology would be firstly used in local and metropolitan networks, and then trunk networks. High capacity local or metropolitan networks would use WDM technology and OADM to improve their transmission capacity, flexibility and survivability. OXC would then be used to interconnect such WDM optical networks and construct larger and larger WDM all-optical networks. Having the link and wavelength modularity, WDM all-optical networks can easily develop in node, link and wavelength dimensions. Finally, it would expand to access networks when the needed components are cheap and reliable enough.

Conclusion

The development of optical networks in China is imperative in order to meet the demand of communication capacity. WDM all-optical networks are very promising to meet this demand. Various aspects of them are researched widely and deeply to accelerate their applications in China.

TuA3 (Invited)
9:30am - 10:00am

Application of Photonic Network Technologies in Japan

Masafumi Koga
NTT Optical Network Systems Laboratories
e-mail; koga@exa.onlab.ntt.co.jp
tel. +81-468-59-2443
fax. +81-468-55-1282

Abstract;

The recent traffic explosion, triggered by the Internet, is reflected in the succession of announcements in the US market of larger capacity WDM point-to-point transmission systems. Not only has the traffic volume of data communication increased, but also requirements for new high speed services are becoming more tangible. In the near future, high-speed services will spread rapidly, and when the service price falls under some threshold, the second traffic explosion will occur.

To cope with the first and second traffic explosions, network designers must create bandwidth abundant multimedia networks that offer large-capacity at reasonable price. In order to offer large bandwidth at reasonable price, cost reductions are needed in nodes as well as transmission lines. The node cost can be reduced by simplifying the node architecture with wavelength routing technologies. Since through optical paths are not terminated at the electrical level, they simply pass through the node by way of routing switches. As a result, the electrical cross-connect system or the electrical router will become slimmer and overall photonic transport network cost can be reduced. Thus, wavelength routing is a cost-effective technology.

We have already developed a photonic trans-router designed to achieve 320-Gbit/s throughput. The remaining issues in hardware development are system supervision and optical layer performance monitoring for network operation. Our recent activities have developed several technologies for system supervision and optical layer performance monitoring.

Graceful network introduction is an important issue to be considered. Therefore, the maximum commonality with already established SDH networks should be retained, i.e. some SDH technologies should be applied. Optical paths, for example, should employ the STM-N frame structure, and accommodate Virtual Containers (VC-4-16c etc.), ATM cell, and IP packet. These technologies enable non-intrusive QoS monitoring of the optical layer by utilizing the overhead processing LSIs already developed for SDH, and can offer robust networks that permit fault management.

Photonic network technologies will enable us to offer bandwidth abundant and ubiquitous multimedia networks. Toward this goal, NTT is now planning testbeds for the field trial to be conducted from late 1998 to 2001. These technologies will be first introduced in our network for the provision of large bandwidth and cost-effective ATM leased line services.

TuB1 (Invited)
1:30pm - 2:00pm

Asynchronous Digital Optical Networks

David Cotter

BT Laboratories, B55/131, Martlesham Heath, Ipswich, Suffolk IP5 3RE, UK
david.cotter@bt-sys.bt.co.uk

An 'emerging reality' in broadband optical networks is that the existing approaches to photonic networking have significant and fundamental limitations. This paper will explore these limitations, and will describe how they could be overcome by using a radically different approach based on asynchronous digital optical processing.

The device technologies needed for photonic networking based on WDM (wavelength-division multiplexing) are becoming well established, and several network trials are in progress. In contrast, photonic networking based on OTDM (optical time-division multiplexing) requires special devices and sub-systems that are available currently only in a few research laboratories. Whilst there have been several demonstrations of OTDM point-to-point transmission, so far there have been only a very few experiments to demonstrate the feasibility of OTDM networking [1-4].

The WDM approach to photonic networking has some very attractive advantages: in addition to the relative simplicity and commercial availability of the devices needed, WDM networks can be created in a wide variety of architectures with great flexibility (the obvious main restriction being merely that any pair of photonic transmission paths cannot use the same wavelength on a shared fibre link). However the much-vaunted advantage of WDM networks that they could, in principle, support 'transparency' (i.e. data signals could be carried in any modulation format) has become discredited. Transparency implies 'analogue' optical transmission, which does not allow synchronous digital techniques, such as 3R regeneration in the optical domain, to be used. The inability to perform full optical regeneration of analogue signals leads to practical scaling limitations due to noise accumulation from optical amplifiers, crosstalk and nonlinearity, all of which severely restrict the number of network switching nodes through which signals can pass without fatal degradation. This causes a significant limitation in architecture and scalability. A feasible, though costly, solution currently being advocated by some equipment vendors is to sacrifice transparency, standardise the transmission format, and regenerate each wavelength channel individually at the outputs of WDM cross-connects. In effect, this is a hybrid arrangement using analogue switching together with channel-by-channel digital regeneration.

Although the limitations of WDM photonic networking are becoming more widely realised, less well known are corresponding limitations in the OTDM approach to photonic networking. The main attraction of OTDM is that the inherent 'digital' format allows optical signal processing techniques such as 3R regeneration [5] or soliton-control techniques [2]. These techniques can maintain the integrity of the signals as they pass through a very large number of network nodes (at least as many as 690 [2]). Despite this impressive potential for scalability, however, the OTDM approach to photonic networking suffers from severe restrictions in the network architecture that can be used. This comes

from the need to maintain proper bit-level synchronism between all nodes and sub-systems throughout the network.

In a sense, therefore, the advantages and disadvantages of the existing approaches to photonic networking are complementary. The analogue WDM approach to networking is asynchronous (the cross-connects do not require synchronism between different channels) making for network flexibility, but appears not to be readily scaleable. On the other hand the bit-synchronous nature of OTDM is both its greatest virtue (allowing digital signal regeneration in the optical domain and almost infinite network scalability) and drawback (the difficulty of maintaining adequate synchronism in any but the most simple of network architectures). A further limitation suffered by both WDM and OTDM circuit-switched networks is the limited address space arising from physical addressing (i.e. there is a finite number of accessible wavelength or time channels).

In response to this, some of our longer-range research at BT Labs is currently focused on a radically different approach based on asynchronous digital optical processing. We aim to combine the advantages of high-speed digital optical processing (almost infinite extendibility of the physical network —such as in OTDM) with the architectural flexibility of asynchronous networks (as in analogue WDM). In the approach being followed, information is carried as fixed-length packets in ultra-high-speed digital optical format, encoded with payload data and control information. The use of logical, rather than physical, addressing allows massive scalability. In the time domain the network is divided into regular time slots with global synchronism at the packet level. However, a crucial advantage of our approach is that synchronism between packets at the (picosecond) bit-level is not required. This produces great simplification in network control and synchronisation.

Recent progress in developing techniques for high-speed asynchronous signal processing and regeneration will be described.

- [1] Ellis A D, Widdowson T, Shan X and Moodie D G, "Three node 40 Gbit/s OTDM network experiment using electro-optic switches", *Electronics Letters*, **30**, 1333-1334 (1994)
- [2] Ellis A D and Widdowson T, "690 node global OTDM network demonstration", *Electronics Letters*, **31**, 1171-72 (1995)
- [3] Cotter D, Lucek J K and Marcenac D, "Ultra-high Bit Rate Networking: From the Trans-Continental Backbone to the Desktop", *IEEE Communications Magazine*, **35** (4), 90-95 (1997)
- [4] Lucek J K, Gunning P, Moodie D G, Smith K and Pitcher D, "SynchroLan: A 40 Gbit/s optical-TDMA LAN", *Electronics Letters*, **33**, 887-888 (1997)
- [5] Lucek J K and Smith K, "All-optical signal regenerator", *Optics Letters*, **18**, 1226-28 (1993)

TuB2
2:00pm - 2:15pm

Optical Fiber Ring 150 Gbps Data Storage Loop and Spontaneous Variable-Length-Pattern Generator

*J.D. Moores, Lincoln Laboratory, Massachusetts Institute of Technology,
244 Wood Street, Lexington, MA 02173-9108*

In future ultra-high-speed optical networks, there will be a need for ultra-high-speed packet buffers [1]. The highest-data-rate stored packets reported to date were 80 Gbps [2], discounting the 200 GHz pulsed laser [3]. Here we report spontaneous generation and storage of 150 Gbps packets in a fiber ring, depicted in Fig. 1, using 9:1 rational-harmonic modulation [4] (see also [5]), so that the packet roundtrip time is 1616 $1/9$ RF periods. The loop stores up to 14545 bits at 150.01713 Gbps.

For the first time, the loop is modulated to generate different packet envelopes. An example is shown in Fig. 2, which is a 50 GHz digital sampling scope trace using a 45 GHz bandwidth detector. However, the temporal window corresponds to one period, or 96.95 ns, so individual pulses are not resolved. Here, the ~16.7 GHz CW was mixed with a simple periodic digital pattern, giving rise to a 10.2 ns packet.

Compared with previous storage loop designs, loop stability and ONEs density are improved using a lower-loss, non-bulk-component cavity, and using higher power, lower RF CW. Higher orders of rational-harmonic modulation are utilized. Figure 3 shows an RF spectrum, DC to cavity fundamental. The subharmonics are a clear signature of 9:1 rational-harmonic modulation. Figure 4 is a 150 Gbps optical spectrum with 2.6 nm, or 320 GHz full width at half maximum. Figure 5 is an autocorrelation of a 10.2 ns 150 Gbps packet, and the main peak FWHM is 1.7 ps. The ratio of the central peak to the side peaks is roughly 4:1, with even side peaks, which is the expected autocorrelation of a random pattern.

References

- [1] K. Rauschenbach, K. Hall, J. Moores, E. Swanson, M. Haner, H. Haus, and W. Wong, IEEE LEOS Annual Meeting, UO4.1 (31 Oct. - 3 Nov., 1994).
- [2] J.D. Moores, OFC '97, TuQ3 (Feb. 1997).
- [3] E. Yoshida and M. Nakazawa, *Electron. Lett.*, **32** 1370 (23 June 1996).
- [4] J.D. Moores, W.S. Wong, and K.L. Hall, *Optics Lett.*, **20**, 2547 (15 Dec. 1995).
- [5] Onodera, N., Lowery, A.J., Zhai, L., Ahmed, Z., and Tucker, R.S., *Applied Physics Letters*, **62**, 1329 (22 March 1993).

Acknowledgments

Many sincere thanks to K.L. Hall, M. L. Stevens, J. Korn, K.A. Rauschenbach, and C. I. Fennelly.

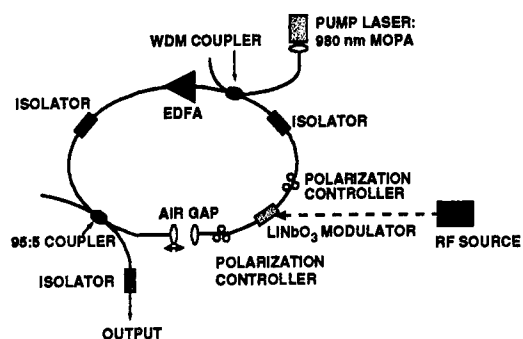


Figure 1. Schematic of storage loop. EDFA = erbium doped fiber amplifier. MOPA = master oscillator power amplifier.

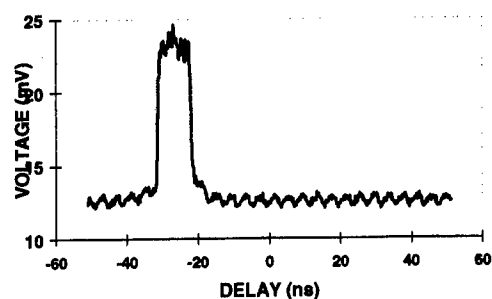


Figure 2. Digital sampling oscilloscope trace showing an intentionally shortened 10.2 ns packet at 150 Gbps. Loop roundtrip is 96.95 ns.

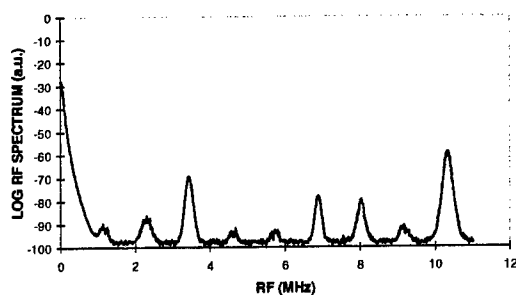


Figure 3. RF spectrum for 150 Gbps packet. Fundamental frequency is 10.314 MHz. Subharmonics reveal 9:1 rational harmonic modulation.

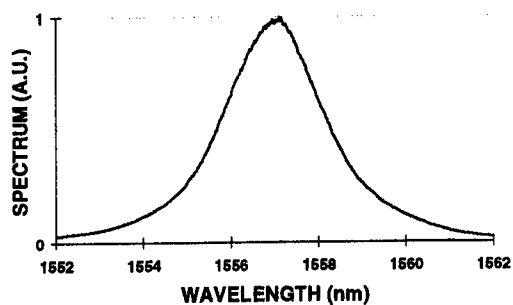


Figure 4. Optical spectrum of 150 Gbps packet, linear scale.

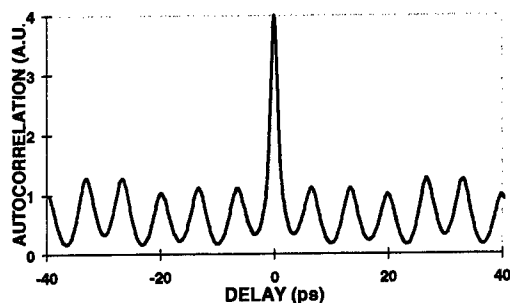


Figure 5. Autocorrelation of 150 Gbps spontaneously generated and stored packet. Main peak FWHM is 1.7 ps.

TuB3
2:15pm - 2:30pm

100 GBIT/S PARALLEL-TO-SERIAL AND SERIAL-TO-PARALLEL CONVERSION USING ELECTROABSORPTION MODULATORS

J.K.Lucek, A.D.Ellis, D.G.Moodie, D.Pitcher, P.Gunning and D.Cotter

BT Laboratories, Martlesham Heath, IPSWICH, IP5 7RE, UK.

It is predicted that CPU speed will reach 10 GHz by 2011¹. Given that even today the backplane capacity of a PC is 1-2 Gbit/s and that of a workstation is about 8 Gbit/s, it is not unreasonable to expect a future i/o requirement for high-end hosts of several tens of gigabits per second, especially as there are moves towards removing the existing bottlenecks that exist between host backplanes and the network interface. An issue to be addressed is how to support these data rates over the wide area. Striping the data across multiple fibres or wavelengths is a possibility. However, inverse multiplexing at the receiving end would be difficult due to the skew resulting from differing path lengths or dispersion respectively - at a particular receiver, the skew will depend on the point of origin of the data within the network. An alternative approach is to carry the data from each host as a serial bitstream. This fits in with present trends, for example the change of HIPPI from parallel transmission to serial. Methods are required to convert data from the parallel form used within the host backplane to a serial form at the transmitter, and to reconvert the data from serial to parallel form at the receiver.

In this paper we show that electroabsorption modulators (EAMs) can be used as the basis of serial-to-parallel and parallel-to-serial convertors, the latter by demonstrating the use of an EAM to extract a 10 Gbit/s channel from a 100 Gbit/s serial bit-stream. We envisage that a further stage of serialisation or parallelisation would be carried out in the electrical domain at the transmitter and receiver respectively to fit in with the requirements of the backplane. Figure 1 shows the layout of the experiment. The output of a 10 GHz optical pulse source was split ten ways and passed through ten EAMs. Each EAM has 10 Gbit/s drive electronics, which allow each to be driven by a separate 10 Gbit/s data line. In the current experiment, the EAMs were driven by 10 Gbit/s data derived from a single pattern generator. The optical data-stream from each modulator was combined in bit-interleaved fashion with sufficient delay ($n \times (10\text{ns} + 10\text{ps})$, $n=0$ to 9) to ensure decorrelation of the data channels. The 100 Gbit/s serial stream thus created is shown in figure 2(a). In order to extract one of the 10 Gbit/s channels from the aggregated data, the data was passed into an EAM having a 13.5 dB/V absorption slope. A 10 GHz electrical clock was passed through a frequency doubler. The output of this contained 10 and 20 GHz components and was amplified and applied to the EAM so as to create an 8 ps transmission window. This easily allowed a 10 Gbit/s channel to be separated from the other nine channels (figure 2(b)) regardless of input polarisation. The bit-error ratio plots in figure 3 show almost no penalty.

In conclusion, we have used an EAM to extract a 10 Gbit/s channel from a 100 Gbit/s data stream. A bank of these devices could form the basis of a serial-to-parallel convertor for high-speed data streams. EAMs are ideal for this application because of their compactness and polarisation insensitivity², and because they lend themselves to integration.

¹ J Hyde (Intel), ECS50 Symposium, University of Southampton, July 1997

² D.G.Moodie et al Electronics Letters, vol. 33, pp. 2068-2070, 1997

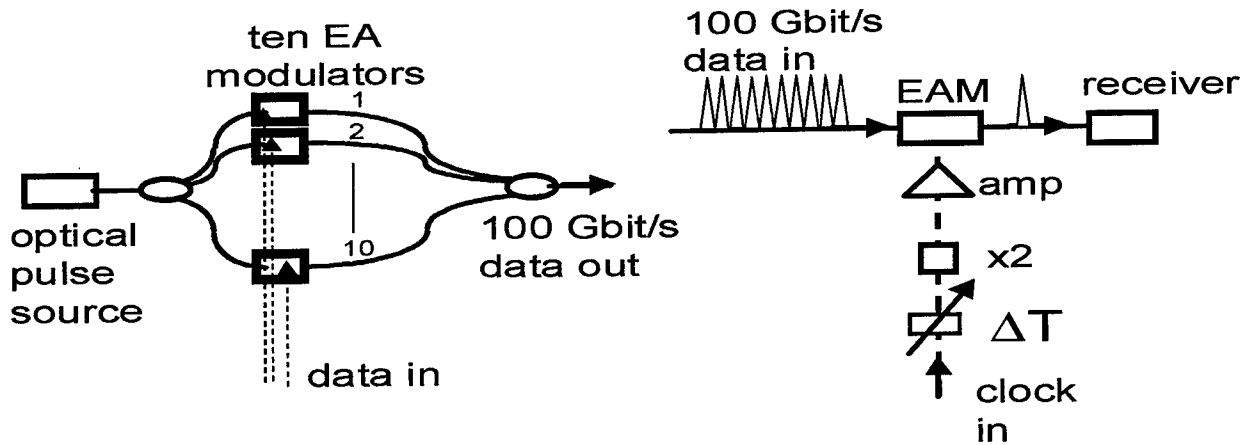


Figure 1: LHS: parallel to serial convertor at transmitter. RHS: electroabsorption modulator (EAM) based channel selector at receiver

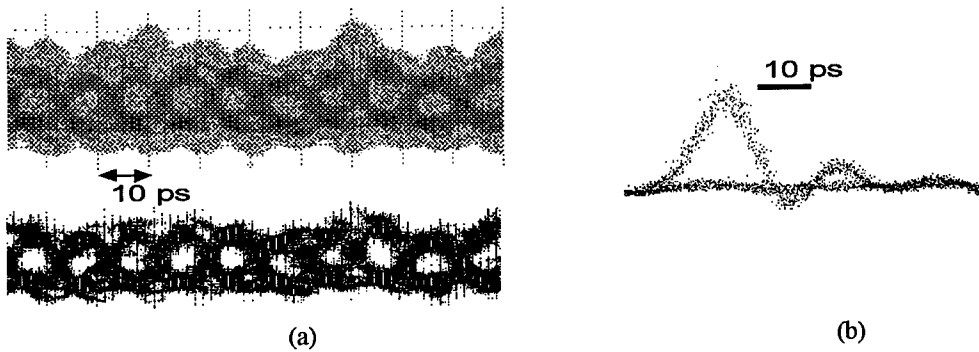


Figure 2: (a) sampling oscilloscope trace of 100 Gbit/s data stream: upper trace: raw trace (grey scale), lower trace: same trace post-processed by thresholding function
(b) sampling oscilloscope trace showing extracted 10 Gbit/s channel

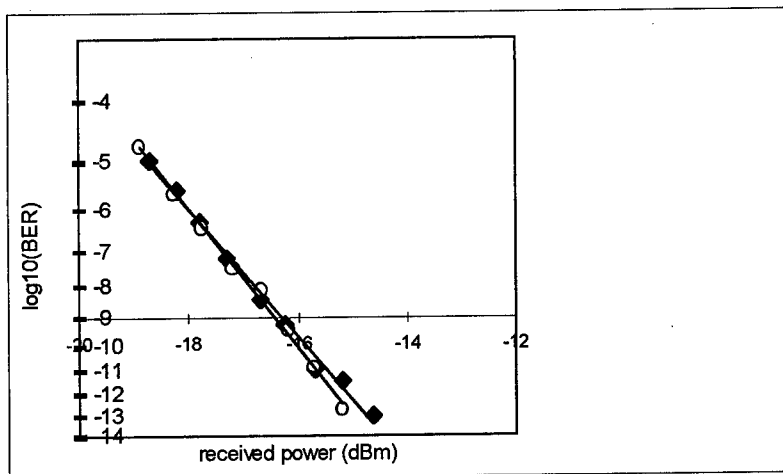


Figure 3: bit error ratio plots: circles=back-to-back, diamonds=channel selector

40 Gb/s Digital Logic Level Receiver

Michael L. Dennis, Keith J. Williams, and Irl N. Duling, III

Naval Research Laboratory, Code 5670, Washington, DC 20375

Phone: (202)767-9352 Fax: (202)404-1576 dennis2@nrlfs1.nrl.navy.mil

Abstract

We demonstrate a simple 40 Gb/s receiver generating output voltages directly from the photodiode sufficient to directly drive high speed logic devices (>0.5 V). The receiver consists of a commercially available *p-i-n* photodiode and a multi-stage erbium fiber preamplifier with gain control for equalizing the output signal.

Introduction—In order to reach signal levels sufficient for driving decision circuitry, traditional receiver designs have used either avalanche photodiodes or standard high speed *p-i-n* photodiodes followed by electronic amplification. As time division multiplexed data rates continue to climb well beyond 10 Gb/s, the bandwidth requirements for electronic and avalanche amplification are increasingly difficult to achieve. These bottlenecks are eliminated by using high current detectors (familiar in the microwave photonics field) as we have previously demonstrated to speeds of 24 Gb/s [1].

In this paper we demonstrate a photoreceiver based on a standard *p-i-n* photodiode, generating an output voltage of >1.0 V peak-to-peak at a data rate of 40 Gb/s. The output is sufficient to drive high speed logic devices directly without further amplification, simplifying the overall receiver design. While a 40 Gb/s 1 V_{p-p} receiver has been reported previously [2], our device uses a commercially available higher quantum efficiency photodiode (0.74 vs. 0.26 A/W), easing preamplifier requirements.

Experiment—The receiver follows our previous design [1], consisting of a two stage erbium fiber optical preamplifier with a 3 nm bandpass filter for suppressing out-of-band amplified spontaneous emission (the filter bandwidth was chosen to match the optical bandwidth of our mode locked fiber laser

source), followed by a high current photodiode. The pump power of the second stage of the preamp is controlled to yield a constant photocurrent. The photodiode (Picometrix DGM-20) is internally impedance matched ($50\ \Omega$), so that only 1/2 of the photocurrent is available. We have also used unterminated photodiodes (Picometrix DM-15ir) which yield substantially larger voltages ($\sim 2\times$), however, signal distortion and inter-symbol interference due to multiple RF reflections limit their applicability. The detectors are standard commercially available devices, though the pigtailling has been optimized to fill the active area of the detector. While the detectors are specified to currents up to 2.0 mA, these optimized devices are capable of currents in excess of 10 mA, as determined from compression current

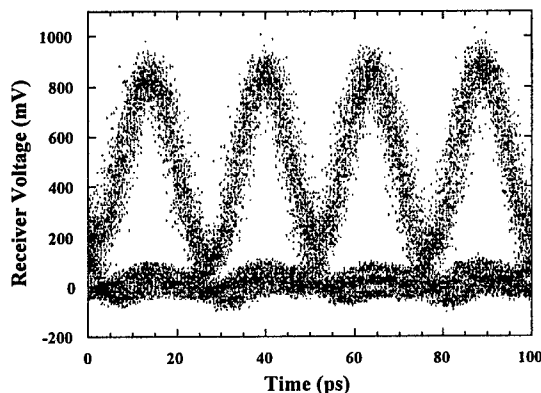


Figure 1. 40 Gb/s return-to-zero eye pattern. Photocurrent: 10.0 mA; base-to-peak voltage: 0.80 V; data pattern: $2^{31}-1$ bit word, 1/2 mark ratio, 4 \times multiplexing of 9.953 Gb/s data; $Q=8.0$.

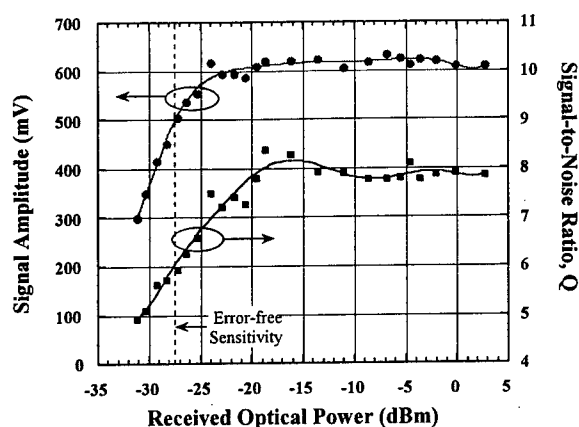


Figure 2. Peak-to-peak receiver voltage and Q vs. received optical power. The photodetector current is held constant (7.5 mA) for $ROP > -26$ dBm. The output voltage exceeds 0.5 V for all powers with $Q > 6$ (error-free). The fits are intended only as a guide to the eye.

measurements [3].

For test purposes, we encode the output of a mode locked fiber laser (~ 1.5 ps pulsewidth) [4] with a 10 Gb/s pseudo-random pattern, which is then bit-interleaved to 40 Gb/s via birefringence walkoff in two sections of polarization maintaining fiber spliced at 45° [5]. A typical eye pattern is illustrated in figure 1, demonstrating output of 0.8 V peak-to-peak. With an unterminated detector, signals in excess of 1.5 V p-p have been obtained.

As we lack equipment capable of directly measuring the bit-error ratio at 40 Gb/s, or of electronically demultiplexing the data to lower rates, we have quantified the receiver performance by calculating the signal-to-noise ratio Q from voltage histogram data [6]. The results are illustrated in figure 2, along with a plot of the output peak-to-peak voltage as a function of received optical power (ROP). Our measurements are limited to $Q < 8$ due to amplitude noise in the source laser and timing jitter in the oscilloscope triggering. As figure 2 illustrates, signal levels of > 0.5 V are obtained for all received optical powers greater than the error-free ($Q = 6.0$,

corresponding to a bit error ratio of 10^{-9}) sensitivity of -27.5 dBm. The rolloff in signal amplitude below -25 dBm is due to a combination of ASE saturation of the preamplifier and the limit of available pump power to its second stage.

Conclusion—We have demonstrated a simple high speed receiver design capable of generating digital logic-level signals. Our approach constitutes an enabling technology for future high speed TDM transmission systems and networks in that it obviates the need for broadband digital amplifiers and is readily constructed from commercially available components. Further improvements in receiver sensitivity can be made over the current design by optimizing the filter bandwidth and the gain and saturation output power of the preamplifier.

Acknowledgments—This research was supported by the Office of the Chief of Naval Research.

References

1. K.J. Williams, M.L. Dennis, I.N. Duling, C.A. Villarruel and R.D. Esman, *Optical Fiber Communications Conference*, Vol. 2, 1998 OSA Technical Digest Series (OSA, Washington, DC, 1998), p. 52; —, *Photon. Technol. Lett.* **10**, 588.
2. Y. Miyamoto, M. Yoneyama, K. Hagimoto, T. Ishibashi, and H. Shimizu, CLEO/Pacific Rim '97, post-deadline paper PD2.11.
3. K.J. Williams and R.D. Esman, *Photon. Technol. Lett.* **8**, 148 (1996); K.J. Williams, R.D. Esman and M. Dagenais, *Photon. Technol. Lett.* **6**, 639 (1994).
4. T.F. Carruthers and I.N. Duling, *Opt. Lett.* **27**, 1927 (1996).
5. M.L. Dennis, T.F. Carruthers, M.F. Arend, and I.N. Duling, in *Conference on Lasers and Electro-Optics*, Vol. 11, 1997 OSA Technical Digest Series (OSA, Washington, DC, 1997), p. 416.
6. N.S. Bergano, F.W. Kerfoot and C.R. Davidson, *Photon. Technol. Lett.* **5**, 304 (1993).

Impact of Dispersion Compensation Gratings on OC-192 Systems

Y. Li, D. Way, N. Robinson and S. Liu

Abstract: This paper analyzes the system impact of Dispersion Compensation Gratings (DCG) with regards to its group delay ripple amplitude, frequency, as well as dispersion deviation. Computer simulations in terms of power penalty and Bit Error Rate (BER) tests on OC-192 systems are correlated and presented. Requirements on DCG delay ripple are derived.

Introduction: OC-192 DWDM requires dispersion compensation as well as dispersion slope compensation. Dispersion Compensation Grating (DCG) is now competing with Dispersion Compensation Fiber (DCF) owing to its compactness, low loss, low nonlinear effects and low Polarization Mode Dispersion (PMD). Recently, there has been increasing demand for commercialization of DCG. However, its performance has not yet been able to support OC-192 system deployment due to the presence of group delay ripple^[1]. Delay ripple results in distortions to the pulse shape and introduces unacceptable Bit Error Rate (BER) power penalty in transmission systems.

We characterize delay ripple by ripple amplitude (local delay), ripple frequency (local dispersion) and dispersion deviation in the modulation bandwidth. Many measurement techniques to characterize the reflectivity and dispersion of DCG have been reported^[2-3], tradeoffs in wavelength resolution and accuracy of the delay have been studied. However, due to the randomness of the dispersion ripple, there is no direct association of ripple to BER. Therefore, it becomes a necessary but formidable task to fully characterize DCG over system operation bandwidth in terms of BER and power penalty. One alternative to a full-length BER test is to use computer simulation to predict power penalty. A proper characterization of Differential Group Delay (DGD) is essential to a good correlation between the BER test and simulations.

Characterization: The test setup consists of an HP8168 tunable laser source sweeping at 1pm step, a network analyzer (HP8753) which biases an external modulator and reads the phase delay

and amplitude from DCG in relative to its internal reference. The modulation frequency is tunable from 300MHz to 2GHz. An external wavelength meter is used to record the actual wavelength. Fig.1 shows the delay measurement of a DCG using 300MHz, 1GHz and 2.5GHz modulation frequency.

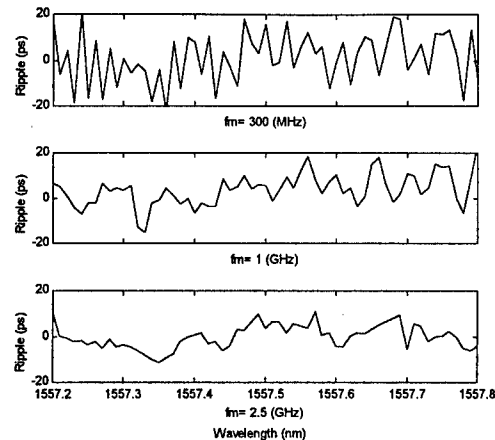


Fig.1 Delay measurement at various f_m

Although most of the recent publications suggest using modulation frequency in GHz range to suppress noise in measurement^[2-3], we found poor correlation between simulation based on DGD measurement using higher than 1GHz modulation frequency and BER tests. This leads us to believe that high modulation frequency not only suppressed the noise, but the ripple itself as well. The error in delay measurement is contributed by two factors: one is the phase resolution in network analyzer, the other is the phase distortion introduced by the beating of two side bands that are inherent in AM modulation. First, phase resolution and delay accuracy is related by

$$\Delta\tau = \frac{\Delta\phi / 360}{f_m}$$

where $\Delta\phi$ is the phase resolution in degree and f_m is the modulation frequency in GHz. $\Delta\phi$ in the HP8753 network analyzer is typically 0.1 degree, the time delay resolution is 0.92ps for $f_m=300\text{MHz}$. Second, the beating of two side bands in AM signal results in a slow varying cosine term on top of the modulation frequency^[4]

$$E = E_0 \cos\left(\frac{4\pi^2 \cdot 10^{-6}}{2} \beta^2 L \cdot f_m^2\right) \cos(2\pi f_m t) e^{-ikL}$$

where $\beta^2 L$ is typically equal to 1700ps² (as in 80km of SMF-28 fiber). We can derive from the equation above that, by reducing modulation frequency from 1GHz to 300MHz, we can reduce the error in the slow varying term by 2

orders of magnitude. We can conclude that, with ample time resolution to spare, lower modulation warrants more accurate results. However, its impact to the overall accuracy cannot be quantified at this time due to lack of information on the network analyzer.

Simulation: In the simulation, impulse response function of DCG is reconstructed from DGD measurement and then multiplied to the Fourier spectrum of a 128 bits pseudo-random bit sequence. Before inverse FFT, we added a 5th order Bessel filter with 3dB cutoff frequency at 6.4GHz, typical for OC-192 receivers. Power penalty is measured at the center of the eye. The BER test result on the DCG we characterized using OC-192 system is plotted in Fig.2. The power penalties are 0.2dB at 1557.38nm and 5~7dB at 1557.31nm, respectively.

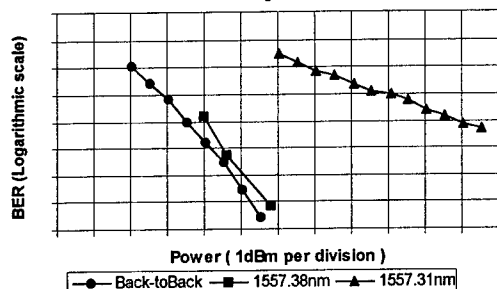


Fig.2 BER Tests results on OC-192 system

Then we ran simulations with DGD measurements taken at various modulation frequencies. We found good correlation for the DGD measurement taken at 300MHz-modulation frequency. The eye-diagram plotted in Fig.3 indicates power penalty of 0.8 dB and 5.2 dB at these two wavelengths respectively.

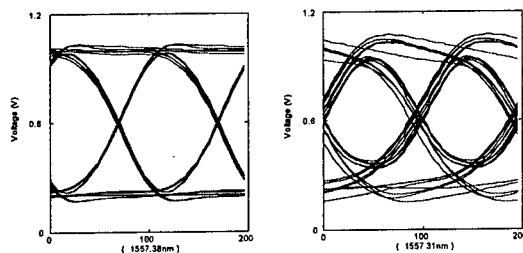


Fig. 3 Eye-diagrams by simulations

Analysis of delay ripple: Using the software that has been calibrated by the BER test, we analyzed the impact of the ripple amplitude and frequency. We modeled ripple as sinusoidal function with ripple amplitude varying from ± 10 ps to ± 60 ps and frequency varying from 25

cycles/nm to 5 cycles/nm. The power penalty is shown in Fig.4.

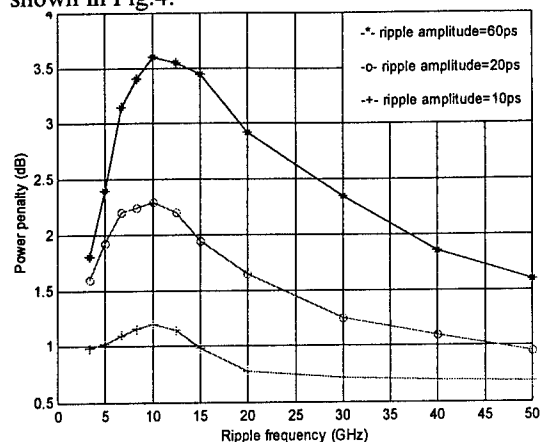


Fig. 4 Power penalty due to sinusoidal ripple

The maximum power penalty occurs at the ripple frequency that is in the vicinity of line rate (NRZ coding). The power penalty decreases at both ends of the spectrum. The gentle slope at the high-end is due to the low-pass filter we used. At the lower end, the ripple will eventually become residual dispersion. The analysis shown here allows one to derive maximum ripple amplitude at given acceptable power penalty. One can also derive from here the required wavelength step (at least $2 \times$ Nyquist-rate sampling of the frequency that contributes to power penalty).

Conclusion: We presented the BER test result of a DCG on OC-192 system. Simulations of DCG power penalty have been well correlated to system tests. We analyzed the power penalty due to ripple amplitude and ripple frequency. We conclude the following: 1. To ensure less than 1 dB power penalty on OC-192 system, DCG ripple amplitude shall not exceed ± 10 ps. 2. The modulation frequency that is used to characterize DCG shall be 300MHz and the wavelength step shall be 2pm to ensure the accuracy of the measurement.

References:

- [1] K.O. Hill, F. Bilodeau, B. Malo, T. Kitagawa, S. Theriault, D.C. Johnson, and J. Albert. *Opt. Lett.* **19**, 1314-6, 1994.
- [2] L. Davidson and T. Stephens, "Measurement of Group Delay Characteristics of Chirped Fiber Bragg Gratings", ACOFT '95.
- [3] J.E. Roman, M.Y. Frankel, R.D. Esman, OFC '98 Technical Digest, 6-7 (1998).
- [4] B. Christensen, J. Mark, G. Jacobsen and E. Bodtker, *Electron. Lett.* **29**, 132-134 (1993).

Restoration capacity for resilient wavelength-routed optical transport networks

Stefano Baroni[†], Polina Bayvel[†], and Richard J. Gibbens[‡]

[†] Electronic Engineering Dept., University College London, Torrington Place, London WC1E 7JE, England

[‡] Statistical Laboratory, University of Cambridge, 16 Mill Lane, Cambridge CB2 1SB, England

Introduction

The design of resilient wavelength-routed optical network (WRON) architectures is key for telecom operators to deploy the WDM optical transport layer [1]. Link failures due to cable cuts have been widely recognised to have the most significant impact on the network performance. For optical restoration [2], the utilised strategy is crucial in determining the spare capacity requirement. Different survivability techniques have recently been analysed [3], and results reported [4]-[5]. However, the influence of the physical topology on the restoration capacity has not been identified, particularly in comparison to the strategies available at the higher network layers, such as SONET/SDH [2].

In this work, we analyse several different network topologies which provide full traffic restoration for single link failures. The results show that restoration capacity requirements are critically affected by the physical connectivity.

Network model

The analysed network architecture consists of N nodes arbitrarily connected by L links (physical connectivity $\alpha = 2L/(N(N-1))$ as in [5]). Each node consists of a terminal directly connected to an optical cross-connect (OXC). Both the OXC configurations without (WSXC) and with (WIXC) wavelength interchange functionality are analysed. For the WSXC case, the transmitters/receivers in the terminals can be fixed-tuned (WSXC-F: restoration lightpaths maintain the same wavelengths) or agile (WSXC-A: restoration wavelength can be changed). Each link consists of a bundle with (CI) at least one fibre ($f_j \geq 1$, for all links j), with each fibre carrying up to W wavelengths (referred to as *wavelength multiplicity*). A single-hop logical topology is assumed, with a *uniform* traffic demand.

An integer linear (ILP) formulation for the exact solution of the routing and wavelength allocation (RWA) problem was developed (not shown here). However, for large topologies this approach is computationally inefficient, and a heuristic algorithm was designed for the analysis of these. The aim is to assign the minimum total number of fibres, $F_T = \sum_j f_j$, subject a requirement of (i) without restoration, $F_{T_{w/o}}(W)$, an *active* lightpath for each node-pair, and (ii) with restoration, $F_{T_{w/r}}(W)$, an active lightpath for each node-pair and a *restoration* lightpath for every active lightpath interrupted by any link failure. In this work, end-to-end path restoration is assumed, since it is most efficient in reducing the restoration capacity requirement [3][4].

Results and discussion

Several mesh networks with different size and connectivity [5] were analysed for different values of W .

Fig. 1(left) shows the total number of fibres $F_T(W)$ required for the NSFNet topology ($N = 14$, $L = 21$, $\alpha = 0.23$) to carry the uniform traffic without and with link failure restoration versus W . Consider the curves without restoration. As expected, the total number of fibres decreases with W , and for $W = 16$ one fibre per link suffices ($F_{T_{w/o}}(W) = L$). Given the condition (CI), a further increase in W does not reduce $F_{T_{w/o}}(W)$. As shown, the difference between the WIXC and WSXC cases is negligible, implying that no improvements are achievable by the introduction of wavelength interchange in the OXCs, as already reported in [5]. A larger number of fibres is required to make the network resilient to single link failure. $F_{T_{w/r}}(W)$ also decreases with W and reaches the value 21 for $W = 32$. However, a different behaviour is shown for the two WSXC cases. If wavelength agility is provided within the terminals (WSXC-A case), the benefit achievable with wavelength interchange in the OXCs is very small, even with restoration. Conversely, a larger capacity is needed if the same wavelengths are to be maintained in both the active and restoration lightpaths, that is when fixed-tuned transmitters/receivers are provided in the end-nodes (WSXC-F case). This is illustrated in Fig. 1(right), where the extra capacity required for restoration is defined as $E_C(W) = F_{T_{w/r}}(W)/F_{T_{w/o}}(W) - 1$. In the WIXC case, for $W \leq 8$, about 40% extra capacity is necessary. However, as W increases, the *excess* capacity deployed while allocating the active lightpaths becomes larger and can be used for restoration. Therefore $E_C(W)$ decreases tending to zero for $W = 32$ (for which the capacity allocated is sufficient for both active and restoration lightpaths). As previously described, the WSXC-A case resulted in a similar behaviour. For the WSXC-F case, the extra capacity initially increases with W and approaches values as large as

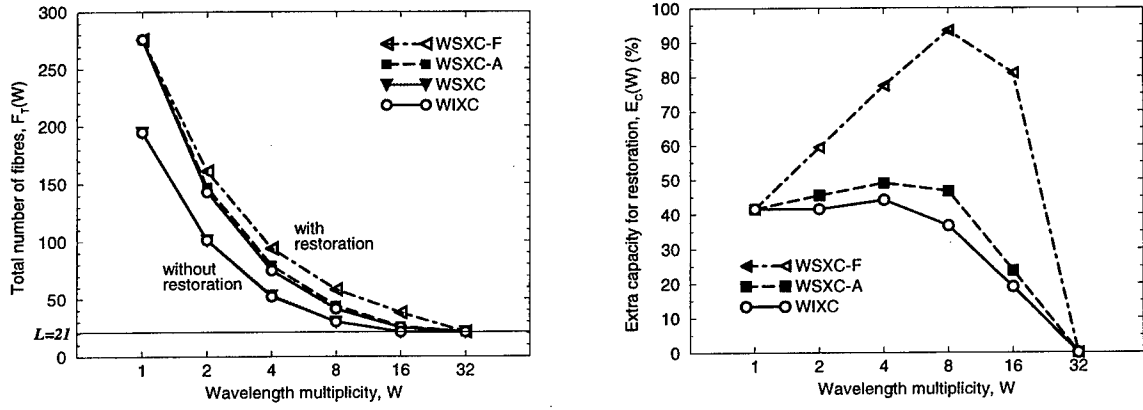


Figure 1: Results for the NSFNet: (left) $F_T(W)$ and (right) $E_C(W)$ versus W .

95% for $W = 8$. Again, for $W > 8$, $E_C(W)$ decreases to zero for $W = 32$. These results highlight the trade-off between wavelength agility in the terminals to minimise the extra capacity for restoration and increased complexity for network-wide wavelength control.

The extra capacity required for all the analysed topologies is shown, as an example, for the WIXC case (Fig. 2). As expected, a ring network requires about 100% extra capacity for restoration. However, as the physical connectivity α increases, $E_C(W)$ decreases, since the restoration capacity allocated within the network links can be shared more efficiently by the network light-paths. For example for the ARPANet, EON, and NSFNet (whose α is close to 0.2), $E_C(W)$ is about 50 – 60%. As shown, if the physical connectivity is increased even further, $E_C(W)$ can become as small as 40%. It is worth noting that, as expected, the value of W after which $E_C(W)$ starts decreasing also decreases with an increase of α .

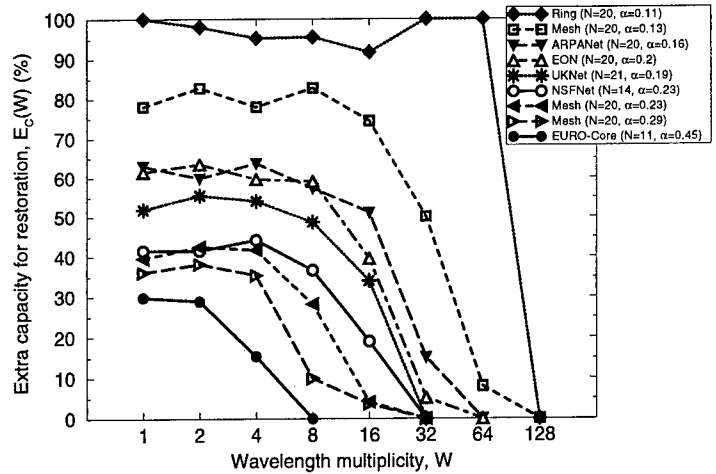


Figure 2: Results for all the analysed topologies: $E_C(W)$ versus W for the WIXC case.

Conclusions

The capacity required to build resilient wavelength-routed optical networks was analysed. The results demonstrate the importance of wavelength agility in the terminals and the key role played by the physical connectivity.

1. R. K. Butler, D. R. Polson, "Wave-Division Multiplexing in the Sprint Long Distance Network", *IEEE Communications Magazine*, Feb. 1998, pp.52-55.
2. O. Gerstel, "Opportunities for optical protection and restoration", *Proc. OFC'98*, pp.269-270.
3. L. Nederlof, M. Garnot, F. Masetti, "A Comparison of Survivability Methods for Optical Networks", *Proc. NOC'97*, pp.103-110.
4. B. Van Caenegem, N. Wauters, P. Demeester, "Spare Capacity Assignment for Different Restoration Strategies in Mesh Survivable Networks", *Proc. ICC'97*, pp.288-292.
5. S. Baroni, S. K. Korotky, P. Bayvel, "Wavelength interchange in multi-wavelength optical transport networks", *Proc. ECOC'97*, pp.164-167.

TuC3

4:15pm - 4:30pm

Dynamic sub-second restoration in WDM optical transport networks

R. Jagannathan, S. Alagar, M. Garnot, F. Masetti

Alcatel Corporate Research Center

1225, N.Alma Road,

Richardson, TX- 75081-2206

The deployment of WDM networks [1] enables a fiber to provide a huge bandwidth several factors above the current levels. Considering the enormous amount of information carried by a fiber in WDM networks, restoring traffic disrupted by a fiber/cable cut is even more critical than the SONET network [2]. This paper provides a summary of results of our spare capacity planning and distributed restoration schemes on two networks. The restoration scheme is a distributed path restoration algorithm [3]. The spare capacity planning was efficient and the distributed restoration algorithm restored 100% within a second for single link failures. *The results show that sub-second distributed restoration is possible in WDM networks.*

The two networks considered are the Pan-American network [4] Figure 1, and the Pan-European network [5] Figure 2, with some of their key attributes shown in Table 1.

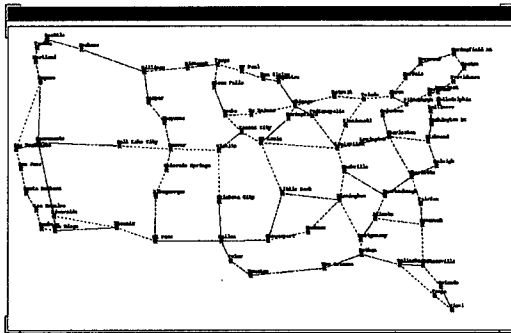


Figure 1 : Pan-American Optical Network

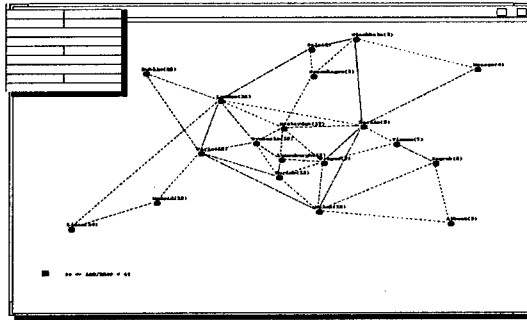


Figure 2 : Pan-European Optical Network

Attribute	Pan-American Network	Pan-European Network
Nodes	79	19
Links	102	39
Origin-Destination pairs	155	171
End-end DS-3 channels	1064	1962

Table 1

The network topology and the optical traffic matrix at OC-192, are the inputs to the Planning Tool [6]. It then performs efficient routing of the traffic [6] and dimensioning of the network using wavelength assignment algorithms [7]. The tool also allocates spare capacity for path restoration, which could be shared effectively [4] by multiple non-contending channels under the scenario of a single link failure. It was assumed that wavelength conversion is possible at every cross-connect [8]. Wavelength conversion at every node provides more possibilities for distributed restoration to re-route failed paths since the contention for a wavelength in a fiber can be resolved [9] by converting any of the wavelengths. Wavelength conversion also helps in reducing the number of spare fibers required for restoration and in the physical 2R regeneration when using all-optical wavelength converters. The results of the planning tool are shown in Table 2.

The output of the Planning Tool (traffic paths, spare capacity on each link) is given as input to the restoration algorithm, which considers only single link failure at a time. The simulator selects each link (one after another), fails all fibers in the selected link and uses a distributed algorithm to restore paths that are disrupted. The algorithm does not use any pre-planning and proceeds with no prior knowledge of either the topology or the existing spare capacities for restoration provided by the Planning Tool. The parameters used by the Simulator are shown below. The simulation was run on an Ultra Sparc workstation.

Propagation delay: 8 microseconds (at 40% speed of light)

Transmission Speed: 1.5 Mbs
 Crossconnection time: 0.01/0.02 seconds per connection
 Minimum message processing delay: 0.001 seconds

Planning Tool Output	Pan-American Network	Pan-European Network
End-end OC-192 channels	155	342
Total fiber length for working channels	52,044	83,980
Total fiber length for spare channels	35,282	64,950
Total number of fibers for working channels	252	142
Total number of fibers for spare channels	158	84

Table 2

The results of the distributed restoration algorithm are shown in figures below. The graphs show the restoration time for each link failure. The average times required for 100% restoration in the Pan-American and the Pan-European networks (for a cross-connection time of 0.02 seconds) are 0.38 seconds and 0.42 seconds respectively.

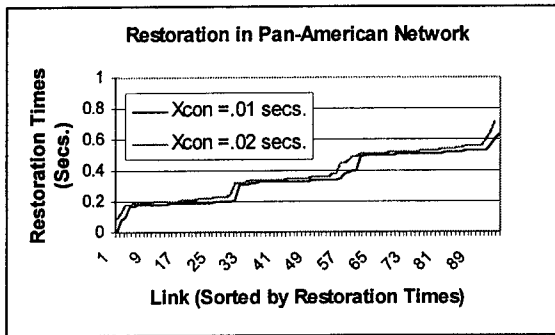


Figure 3

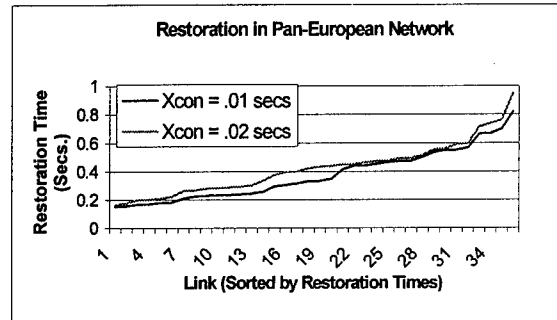


Figure 4

The graphs also show that reduction in cross-connection time (from 0.02 seconds to 0.01 seconds) in these networks does not result in a significant reduction in restoration time. The reason is the number of cross-connections (at OC-192 level) that needs to be made in WDM networks is low, in sharp contrast to the number cross-connections (at STS-1 level) that needs to be made in SONET based networks. Thus WDM reduces the number of connections and enables sub-second distributed restoration.

References

- [1] C. A. Brackett, "Dense wavelength division multiplexing networks: principles and applications", IEEE J. on Sel. Areas in Comm., vol. 8, no. 6, pp. 948-964, Aug. 1990.
- [2] Wayne D. Grover, "Survivable Broadband Transport Networks", Prentice-Hall/IEEE Press, 1997.
- [3] S. Venkatesan, "An Efficient On-line Restoration Algorithm", Alcatel Technical Report, February 1994.
- [4] M. Garnot et al., "Dimensioning and design of the WDM optical layer in transport network", SPIE conference on All-Optical Communication: Architecture, Control, and Network Issues III, November 2-3, 1997, pp. 244-252.
- [5] M. J. O'Mahony, et al., "Ultra high capacity optical transmission network European research project COST239", Conference on Telecom, CONTEL'93, Zagreb, July, 1993.
- [6] M. Garnot et al., "Routing strategies for optical paths in the WDM networks", ICC'97, Montreal, June 1997.
- [7] I. Chlamtac, A. Ganz, G. Karmi, "Lighpath Communication: An Approach to High Bandwidth Optical WAN's", IEEE Transactions on Communications, vol. 40, no. 7, July 1992, pp. 1171-1182.
- [8] A. Jourdan et al., "Design and Implementation of a Fully Reconfigurable All-Optical Crossconnect for High Capacity Multiwavelength Transport Network", IEEE Journal of Lightwave Technology, vol. 14, no. 6, June 1996, pp. 1198-1206.
- [9] M. Garnot et al., "Dimensioning and Optimization of the Wavelength-Division-Multiplexed Optical Layer of Future Transport Networks", to be published to IEEE ICC'98, Atlanta, June 7-11, 1998.

Broadband Optical Networks and Technologies:
An Emerging Reality

Wednesday, 22 July 1998

WA: Evolution of Optical Networks

Wednesday Papers Not Available

- WA1 WDM: An Emerged Reality, *Steve Alexander, CIENA Corporation, Linthicum, MD*
- WA3 Islands of Transparency – An Emerging Reality
In Multiwavelength Optical Networking,
Adel Saleh, AT&T Labs – Research, Red Bank, NJ

WA2 (Invited)
9:00am - 9:30am

Optical Networks in the Real World

Thomas C. McDermott
Alcatel Network Systems, Inc.
MS 408-200
P.O. Box 833802
Richardson, TX. 75083-3802

With rapid advances in optical component technology, new equipment and architectures can be proposed to provide faster, higher-capacity, more flexible, and more reliable communications systems. It is now possible to consider optical-networking (the switching or routing of signals directly in the optical format) without the need to convert to the electronic domain. Constraints arise however, when optical networks are deployed by commercial telecom operators. These constraints are related to the need of the operator to provide a reliable service for the signals being carried by these networks.

Current optical transmission systems (currently based on the SONET or SDH standards in particular) provide many features that aid an operator in determining system performance, system status, and help to isolate faults. As the need for data transmission is growing rapidly in the network, the desire to transport Internet-Protocol (IP) frames over optical systems arises, in addition to traditional time division multiplexed (TDM) telephony voice and data signals.

Layering - In most networks, a layered approach is used in building up the various pieces of equipment and the various formats used in building a network. The idea is that each layer provides a service, hopefully in a service-independent way to the layers above it. In this manner, it is thought that maximum flexibility to introduce new formats is maintained, while preserving the installed base of existing equipment. For example, the physical layer of SONET is based on optical fiber, but can also be based on coaxial cable or microwave radio. The interface between the physical layer and the link layer (SONET) is such that SONET does not change with different physical layers. The physical layer provides for transmission of information, while the link layer provides some type of assurance that information is actually conveyed.

In data communications, the link layer provides for retransmission upon detection of error. However

given the low expected error rates in optical systems, SONET only provides for detection of errors. Some systems (such as microwave radio, and likely high-speed optical systems) provide for Forward Error Correction (FEC) rather than retransmission.

The networking layer provides for formatting of the information to be transmitted. In the case of Time Division Multiplex (TDM) data, there is no information as to the destination. In the case of Internet Protocol (IP) each IP packet contains the destination address of the packet. Thus, traditionally the network layer provides for routing a signal within a network. ATM can provide such a layer of virtual circuits over which IP packets can travel. This assumes a connection-oriented paradigm for the network. IP without ATM assumes a connectionless paradigm for the network. Both approaches are being used.

A drawback of using these layers is that there is a cascade of inefficiencies built-up when each is separately engineered from the others. This is the price paid for layering a system. These inefficiencies are usually excessive overhead data bits, thus reducing the capacity of the system to deliver actual information.

It has been proposed that some of the layers be eliminated, specifically the SONET layer due to its limitations. IP over optics (as opposed to IP over SONET over Optics) has been proposed. SONET was designed at a time when only point-to-point optical links were contemplated, and thus it is not completely suited to dynamically switched or multi-point service. However, one of the fundamental things provided by the SONET/SDH layer is a number of features needed by network operators in the real world. The elimination of the SONET layer will require that many of these same features be invented and utilized in whatever format ends up being deployed for optical networks.

SONET Features - The features provided the SONET layer are: 1) line coding (one's density,

transition density), 2) Fault localization and sectionalization, 3) Equipment fault isolation, 4) Link fault isolation, and 5) Link performance monitoring. Line coding provides a balanced, scrambled signal that maintains average power at 50%, and encodes sufficient transitions to assure adequate clock recovery. The basic fault locating mechanism in SONET is to separately identify a PATH, a LINE, and a SECTION. Each route between two end points is a PATH. A path is composed of switched transmission entities, and each entity is a LINE. Finally, a line is composed of several concatenated SECTIONS. At the end points, path information is placed in the payload overhead, and remains unaltered until it reaches the destination end-point. This allows verification of circuit integrity between the end points, isolation of one-way faults, and measurement of the bit error rate for the path. Similarly, Optical terminals (Line Terminating Elements, LTEs) multiplex several SONET signals together, and append LINE overhead. The purpose of the LINE overhead is to allow isolation of faults between two peered LTE's. Thus faults that result from the mis-route of one line can be traced exactly to the offending line, independent of the path information. Finally, each electronic regenerating or terminating equipment injects SECTION information, and terminates SECTION information. Thus a section fault is uniquely identified, even in a cascade of sections (i.e.: regenerators) independently of line or path faults.

Cascaded Sections - Consider the case of an fiber cut in a cascade of regenerator devices. The regenerator downstream of a failure will detect a loss-of-signal. If, however it did not modify its output, then all downstream regenerators would detect errors. In order to prevent this the detecting regenerator inserts a dummy signal, AIS (Alarm Identification Signal) that quiets the alarms of the downstream regenerators. Thus the only alarms will be from the regenerators on either side of the cable cut. This results in fault isolation to the affected section. There are numerous other types of faults that can occur, and the path/line/section paradigm provides robust and accurate localization of the fault.

Additionally, each regenerator measures the bit error rate (BER) of the signal, by computing the Bit-Interleaved-Parity (BIP) signal. The section BIP allows isolating a BER problem to the offending section so that it can be repaired. Line BIP allows computation of the effective error rate for the line.

In order to run a network in the real world, it is mandatory to be able to detect and isolate problems quickly and accurately before dispatching staff with replacement equipment to repair the problem. The use of standardized equipment and formats facilitates this greatly. Similarly, SONET provides equipment and route protection restoration mechanisms. These are provided by the so-called K-bytes that control the switching of multiplex (line) equipment. In the simplest case, a working and a redundant protection line are provided (optical transmitter, receiver, fibers in the cable). In the event of a failure on the working channel, all traffic is switched to the protection channel within 50 msec. This is done in a manner that appears well encapsulated by the line - equipment outside the affected line are not switched erroneously. The protection channel can be routed diversely, or even around the other direction of a ring, providing protection against cable cuts.

Optical Network - In an optical network, the line switching elements do not necessarily have to contain electronics. In this case, isolating a line fault requires some higher level of intelligence. At this time, most proposals for optical networking envision that it will be most useful for restoration, and for management and leasing of wavelengths to customers. Thus, a network management system will have to keep track of the configuration and topology of the network, and identify route errors. Some have proposed totally transparent switching nodes, which are rate and format independent. These would allow a customer to introduce any format whatsoever to the operator's network, and thus are desirable. However, careful control of such a network to prevent problems such as accumulated chromatic dispersion, PMD, loss accumulation, etc. along a route (or along a different failure-restored route) would be exceptionally challenging. The allowed values for the optical parameters are dependent on the route, the protection route, and both the rate and possibly the format of the (unknown) payload.

We may choose in the future to build new optical networks that employ dynamic routing. Such a network for example could optically route IP packets. There are some drawbacks to SONET in such an all-optical system. However, in the real world whatever format may be chosen will have to provide for fault and performance management and isolation, or else it will not be practical or cost effective for the network operator to supply a high-quality service.

AUTHOR INDEX

Abraham, P.	MC1	Reichmann, K. C.	MB3
Alagar, S.	TuC3	Robinson, N.	TuB5
Alexander, S.	WA1	Saleh, A. A. M.	WA3
Baroni, S.	TuC2	Shakouri, A.	MC1
Bayvel, P.	TuC2	Shen, Y.	TuA2
Bowers, J. E.	MC1	Srinivasan, N. V.	MB1
Cotter, D.	TuB1	Swanson, E.	MB2
Cotter, D.	TuB3	Tsai, Y.	TuC1
Dennis, M. L.	TuB4	Walker, J. A.	MC2
Duling, III, I. N.	TuB4	Way, D.	TuB5
Eaves, J.	TuA1	Williams, K. L.	TuB4
Ellis, A. D.	TuB3	Woodward, S. L.	MB3
Fan, C.-C.	MC4	Wu, M.	MC5
Ford, J. E.	MC2	Xie, C.	MB4
Frigo, N. J.	MB3	Yang, F. S.	MC3
Garnot, M.	TuC3	Yeh, J.-R.	MB4
Gibbens, R.	TuC2	Yu, Q.	MC4
Gu, W.	TuA2	Zou, X.	MB4
Gunning, P.	TuB3		
Iannone, P. P.	MB3		
Jagannathan, R.	TuC3		
Kazovsky, L. G.	MC3		
Koga, M.	TuA3		
Levi, I.	MB4		
Li, Y.	TuB5		
Liu, B.	MC1		
Liu, S.	TuB5		
Lucek, J. K.	TuB3		
Maeda, M.	TuC4		
Marhic, M. E.	MC3		
Masetti, F.	TuC3		
McDermott, T.	WA2		
Moodie, D. G.	TuB3		
Moore, J. D.	TuB2		
Piehler, D.	MB4		
Pitcher, D.	TuB3		

IEEE/LEOS
Summer Topical Meeting

20 – 22 July 1998

Optical MEMS

Monterey Plaza Hotel
Monterey, CA

IEEE Catalog Number: 98TH8369
ISBN: 0-7803-4953-9

The papers in this book make up the digest of the 1998 IEEE/LEOS Summer Topical Meetings. They reflect the author's opinions and are published as presented and without change in the interest of timely dissemination. Their inclusion in this publication does not necessarily constitute endorsement by the editors, the Institute of Electrical and Electronics Engineerings, Inc.

Copyright and Reprint Permission: Abstracting is permitted with credit to the source. Libraries are permitted to photocopy beyond the limit of U.S. copyright law for private use of patrons those articles in this volume that carry a code at the bottom of the first page, provided per-copy fee indicated in the code is paid through Copyright Clearance Center, 222 Rosewood Drive, Danvers, MA 01923. For other copying, reprint or republication permission, write to IEEE Copyrights Manager, IEEE Operations Center, 445 Hoes Lane, PO Box 1331, Piscataway, NJ 08855-1331.

© 1998 by the Institute of Electrical and Electronics Engineers, Inc. All rights reserved.

IEEE Catalog Number: 98TH8369

ISBN: 0-7803-4953-9 Softbound Edition
0-7803-4954-8 Microfiche Edition

ISSN: 1099-4742

Library of Congress:

Additional copies can be ordered from:

IEEE Service Center
445 Hoes Lane
P.O. Box 1331
Piscataway, NJ 08855-1331
Tel: (732) 981-1393
Fax: (732) 981-9667

Optical MEMS

General Co-Chairs:

James Walker, *Lucent Technologies Bell Laboratories, Holmdel, NJ*
Ming Wu, *University of California, Los Angeles, CA*

Program Chair:

Kaigham J. Gabriel, *Carnegie Mellon University, Pittsburgh, PA*

Program Committee:

Robert Boudreau, *AMP Inc., Harrisburg, PA*
Young-Ho Cho, *Kaist, Taejon, SOUTH KOREA*
Phil Congdon, *Texas Instruments, Dallas, TX*
Nico F. de Rooij, *University of Neuchatel, Neuchatel, SWITZERLAND*
Masayoshi Esashi, *Tohoku University, Sendai, JAPAN*
Sadik C. Esener, *University of California San Diego, La Jolla, CA*
Joseph Ford, *Lucent Technologies Bell Laboratories, Holmdel, NJ*
Hiroyuki Fujita, *University of Tokyo, Tokyo, JAPAN*
Hiroshi Goto, *OMRON Corporation, Ibaraki, JAPAN*
Klas Hjort, *Uppsala University, Uppsala, SWEDEN*
Lih Y. Lin, *AT&T Labs-Research, Red Bank, NJ*
Karen Markus, *MCNC, Research Triangle Park, NC*
S. Middelhoek, *Delft University of Technology, Delft, The Netherlands*
Richard S. Muller, *University of California, Berkeley, CA*
Albert P. Pisano, *DARPA, Arlington, VA*
Renshi Sawada, *NTT Opto-electronics Labs, JAPAN*
James Smith, *Sandia National Laboratories, Albuquerque, NM*
Yu-Chong Tai, *California Institute of Technology, Pasadena, CA*
Elias Towe, *DARPA, Arlington, VA*
Hans van den Vlekkert, *CSEM, Neuchatel, SWITZERLAND*

TABLE OF CONTENTS

Monday, 20 July 1998

Session MA: Applications

MA1	The Intergration of Surface Micromachined Devices with Optoelectronics: Technology and Application.....	3
MA2	Optical MEMS Potentials in Optical Storage.....	5
MA3	MEMS-Technology – A Route to Bring the Optical Fibre to the end User?.....	7

Session MB: Metrology & Fabrication

MB1	Using Video Microscopy to Characterize Microelectromechanical Systems	9
MB2	The Effects of Internal Stresses on the Precision of Moveable Structure for Optical MEMS	11
MB3	Design and Fabrication of a Polysilicon Micro Mirror with a Flat Surface by Gold Metallization.....	13
MB4	Array of High Quality Surface Micromirrors by Chemical Mechanical Polishing of Dielectric And Metal	15
MB5	Deep Proton Lithographic CAD-CAM for the Fabrication of Monolithic Micro-optical Elements.....	17

Session MC: Fiber Optic Switching I

MC1	Micromachined Optical Switches for Free-Space Beam Steering.....	19
MC2	MEM Mirrors Application in Optical Cross-Connects	21
MC3	Micromechanical Fiber Optic Switches Based on Electromagnetic Torsion Mirrors.....	23
MC4	Surface Micro-Machined Polarization Beam Splitting System	25

Session MD: Fiber Switching II

MD1	Reflective Modulators and By-Pass-Switches: Two MEMS Components for Fiber Optic Communication	27
MD2	Micro Optics for Micromachined Fiber Optic Switches.....	29
MD3	Bistable Micromechanical Fiber-Optic Switches on Silicon.....	31
MD4	An-Out-of-Plane Polysilicon Actuator with A Smooth Vertical Mirror for Optical Fiber Switch Application	33

Tuesday, 21 July 1998

Session TuA: Optical Technology

TuA1	Replicated Plastic Optical Components for Optical Micro Systems	37
TuA2	Optical Coatings & Microstructures.....	N/A
TuA3	Micro-optical Components for Parallel Optical Networks	39

TABLE OF CONTENTS

Session TuB: Sensors

TuB1	A Micromachined Scanning Confocal Microscope.....	N/A
TuB2	A Fiber-optic Tactile Microsensor for Detection of Tip of A Fiberscope	41
TuB3	High Temperature Operation of Optically Resonant Microbeams.....	43
TuB4	Integrated Micro-displacement Sensor That can be Incorporated into Mini 3-Dimensional Actuator Stage.....	47
TuB5	Micro-Mechanical Optoelectronic Switch and Amplifier (MIMOSA)	49

Session TuC: Fiber & Integration Optic Packaging

TuC1	Integrated Optics for WDM	51
TuC2	Microsystems for Three Axis Active Fiber Alignment.....	53
TuC3	A Micro Optical Bench for Alignment-Free Optical Coupling.....	57
TuC4	Full Duplex 1.31/1.55 μ m Wavelength Division Multiplexing Optical Module Using A Planar Lightwave Circuit Platform	59
TuC5	OptoElectronic Multichip Modules Using MEMS Fabrication Techniques.....	61

Session TuD: Spectral Components

TuD1	Tunable Microcavity Based on III-V Semiconductor Micro-Opto-Electro-Mechanical Structures (MOEMS) with Strong Optical Confinement	63
TuD2	Electrostatically Operated Micromirrors for A Hadamard Transform Spectrometer.....	65
TuD3	Optical Modulator with Independent Control of Attenuation and Spectral Tilt	73
TuD4	Miniaturized Piezo Electric Chopper For Fiber Optical Multimode Applications Realized Using LIGA-Technology.....	75

Session TuE: Poster Session

TuE1	Diamond Microstructures for Optical MEMS.....	77
TuE2	Technique to Improve Flatness of MEM Backplane.....	79
TuE3	Laser Opto-Microactuators Rotated by Molecular Gas Dynamics Effects.....	81
TuE4	Deflectable Micro-Mirror Arrays for Implementation of A Recirculating Folded Perfect Shuffle Processor	83
TuE5	Erbium-Doped Waveguide Devices for WDM Application.....	85
TuE6	Optical Design of Micro-Optical-Electro-Mechanical Systems	87
TuE7	Proposal of Human Eye's Crystalline Lens-Like Variable Focusing Lens	89
TuE8	A Novel Approach to Corner Compensation of Multistep Si(100) Terraced Structure for Microlens	91

TABLE OF CONTENTS

Wednesday, 22 July 1998

Session WA: Adaptive Optics/SLMs

WA1: MOEMS for Adaptive Optics	95
WA2: Technology and Applications of Micromachined Membrane Deformable Mirrors	97
WA3: Design and Fabrication of 10 x 10 Micro SLM Array for Phase and Amplitude Modulators	99
WA4: A Proposal of Vertical Spring as A Mechanical Element for MEMS and Fabrication of Vertical Spring Using Simple Shadow Evaporation Process.....	101

Session WB: Displays & Scanners

WB1: Surface-Micromachined Micro-Scanning Display	N/A
WB2: CMOS Friendly MEMS Manufacturing Process	103
WB3: Thin-Film Actuated Mirror Spatial Light Valve for High-Brightness Projection Displays	105
WB4: Two-Dimensional Optical Scanner With Large Angular Rotation Realized by Self-Assembled Micro-Elevator.....	107
WB5: Micromachined Mirrors in A Raster Scanning Display System	109

Optical MEMS

Monday, 20 July 1998

MA: Applications

MB: Metrology & Fabrication

MC: Fiber Optic Switching I

MD: Fiber Switching II

The Integration of Surface Micromachined Devices with Optoelectronics: Technology and Applications

M.E. Warren, O. Blum, C.T. Sullivan, R.J. Shul, M.S. Rodgers and J.J. Sniegowski
Sandia National Laboratories, MS0603, Albuquerque, NM 87185

Sandia National Laboratories has a substantial effort in development of microelectromechanical system (MEMS) technologies. This miniaturization capability can lead to low-cost, small, high-performance "systems-on-a-chip", and have many applications ranging from advanced military systems to large-volume commercial markets like automobiles, rf or land-based communications networks and equipment, or commercial electronics. One of the key challenges in realization of the microsystem is integration of several technologies including digital electronics; analog and rf electronics, optoelectronics, sensors and actuators, and advanced packaging technologies. In this work we describe efforts in integrating MEMS and optoelectronic or photonic functions and the fabrication constraints on both system components. The MEMS technology used in this work are silicon surface-machined systems fabricated using the SUMMiT (Sandia Ultraplanar Multilevel MEMS Technology) process developed at Sandia. This process includes chemical-mechanical polishing as an intermediate planarization step to allow the use of 4 or 5 levels of polysilicon.¹

Use of photonic components to activate and power MEMS structures is of interest, because it allows for remote operation of the device. Furthermore, this scheme provides for optical isolation, preventing inadvertent activation of a component and increasing the safety of the system. We have demonstrated powering of electrostatic comb drives using series-connected photo-voltaic (PV) cells to provide the 75 volts needed. The control signals for the drive was provided by the open circuit voltage of the PV cells modulated by a fiber-coupled 850 nm laser diode. The operation of this device demonstrates feasibility of optically isolating MEMS components and providing drive signals by transmission of optical power.

A second demonstration consisted of a micromachined shutter, interrupting the beam from a Vertical-Cavity Surface-Emitting Laser (VCSEL). The VCSEL was designed to emit at a wavelength of 1.06 microns,² since at that long wavelength the silicon in the MEMS device is more transparent than at shorter wavelengths. Figure 1 shows the VCSEL beam transmitted through the shutter aperture. VCSELs allow for surface-mounting techniques, such as flip-chip bonding, to be used for precision placement of the devices relative to the MEMS parts and the surface-normal emission allows the MEMS components to operate in-plane, not requiring erection of standing structures. The shutter wheel in figure 1 was coated with evaporated gold to increase its opacity with the VCSEL source. This was done after release by a low-temperature shadow-mask deposition that did not induce strain on the polysilicon wheel. A special hybrid package was assembled that allowed the VCSEL to be located close to the MEMS device and enabled the entire optical beam to pass through the shutter aperture without auxiliary optics. By thus blocking or passing a laser beam, the MEMS shutter can be used to enable transfer of signals or power by optical means.

Continuing work in this area includes improving our post-processing capabilities on MEMS with the addition of metallization prior to release. This will facilitate more advanced packaging options for MEMS components, such as flip-chip bonding as well as adding to the optical performance of mirrors and shutters. This however requires a metallization scheme which will survive the release process or requires protection during the release process. Another approach to allow light transmission through the MEMS uses through-vias in the silicon substrate. This would allow the use of shorter wavelength VCSELs, including visible wavelengths. Figure 2 shows a via etched through the full thickness of a MEMS die. The edge of a hinged polysilicon mirror is visible through the via. This combination of bulk-micromachining processes with surface-micromachined structures has great potential for integrated microsystems. We are also developing high efficiency diffractive optical elements in polysilicon for incorporation in MEMS-based micro-optical systems.

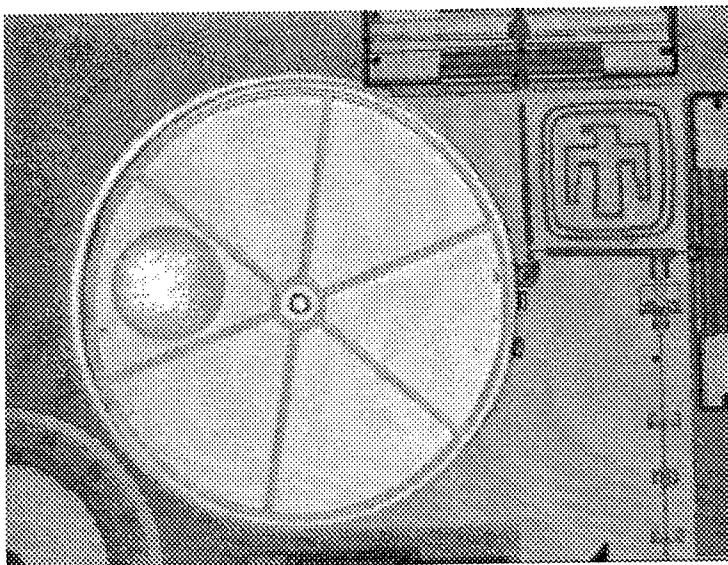


Figure 1. Top view of the metallized shutter and a VCSEL beam visible through a hole in that shutter.

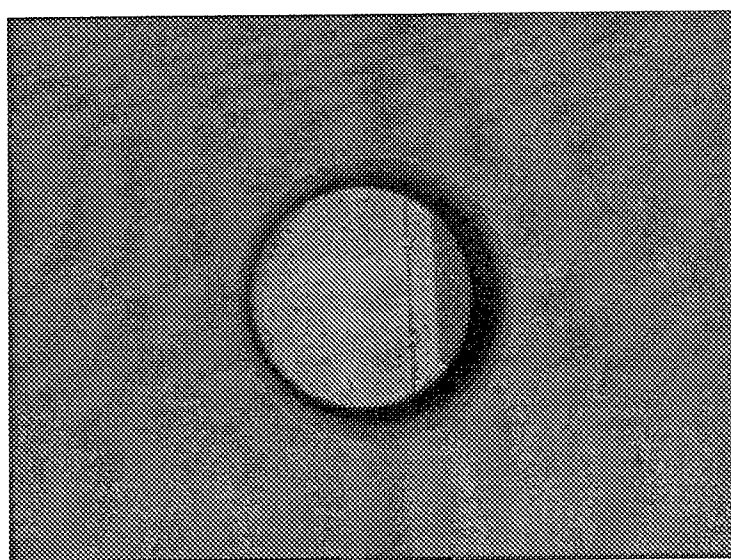


Figure 2. A via hole in the substrate of a MEMS device viewed from the bottom of the substrate. The via whole is through the entire 635-micron thickness of the substrate, stopping on a dielectric layer beneath the polysilicon MEMS structures. A part of a tilting polysilicon mirror that has not yet been released or erected is visible through the hole.

The authors would like to acknowledge K.D. Choquette and H.Q. Hou for providing the 1.06 nm VCSEL, R.F. Carson for packaging development, J. Banas and C.G. Willison for processing support. Sandia is a multiprogram laboratory operated by Sandia Corporation, a Lockheed Martin Company, for the United States Department of Energy under contract DE-AC04-94AL85000.

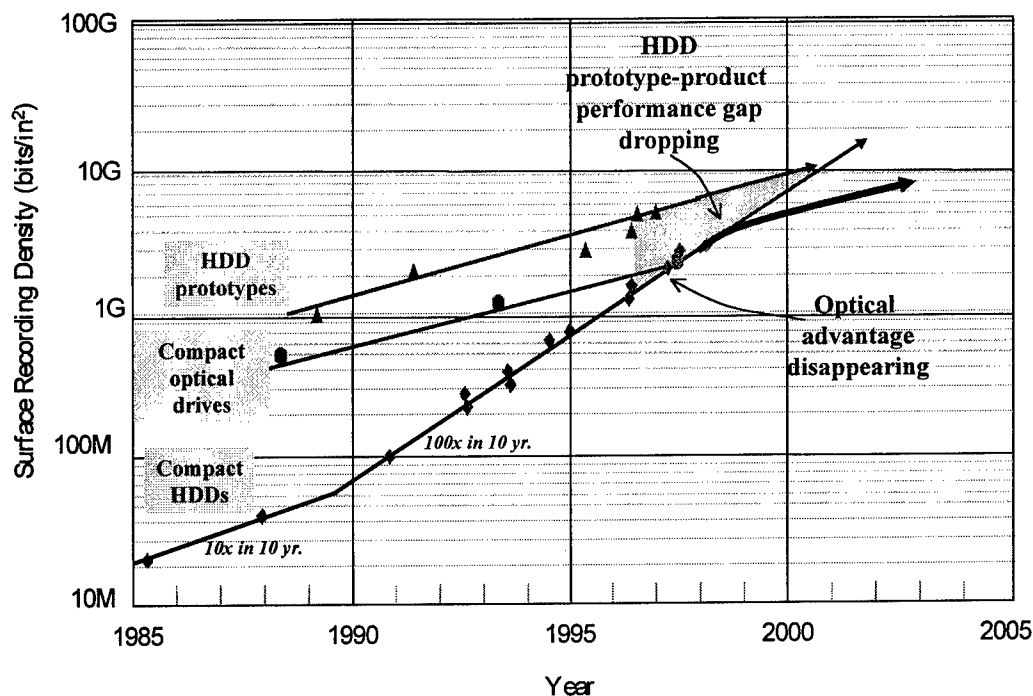
1. C.C. Barron, B.R. Davies, J.J. Sniegowski, M.S. Rodgers, J.H. Comtois and M.A. Michalick, Proc. SPIE, **3223**, pp. 10-16, 1997
2. H.Q. Hou, K.D. Choquette, K.M. Geib, B.E. Hammons, IEEE Photon. Technol. Lett., **9**, pp. 1057-1059, 1997.

Optical MEMS Potentials in Optical Storage

F. B. McCormick

Call/Recall, Inc.
6160 Lusk Blvd.
San Diego, CA 92121
fmac@call-recall.com

Optical storage may be experiencing a rebirth with the advent of DVD ROM disks, but magnetic disk storage continues to dominate the storage market, and is even encroaching on applications previously dominated by optical storage (e.g.- removable storage, near-line libraries, etc.). While optical data storage initially offered greater areal densities than magnetic data storage, the last few years has seen magnetic hard disk drive densities overtaking those of optical storage products, due to the 60% cumulative annual growth rate of areal density in magnetic disk storage products. In addition, most magnetic drive systems take advantage of the small size of the



Source: IBM

Figure 1. Areal density trends for magnetic and optical disk data storage.

flying head to stack multiple platters (typically 4-10) within a single drive, using multiple heads, but increasing the overall drive capacity dramatically.

To compete with this steady increase in capacity and performance at relatively fixed cost, new approaches are being pursued to increase the capacity and performance of optical disk storage products. Micromachining technologies will play an important role in these new systems. For example, massively parallel page-oriented techniques such as holographic optical storage may use MEMS based display technology as data page composers. Texas Instrument's DMD

system has already been used in this capacity in several holographic optical storage demonstrations.¹ MEMS-based beam deflectors are also being explored for holographic systems as addressing actuators.

Perhaps the first commercial application of optical MEMS for optical storage will be as tracking actuators, as in, for example, Quinta's ultra-compact magneto-optical storage heads for their "optically assisted Winchester" approach.² This storage system applies fiber optics, microoptics, and optical MEMS to realize a compact head, which should enable several closely spaced platters per drive with multiple heads, as in magnetic Winchester systems. At Call/Recall, Inc., a monolithic disk with hundreds of data layers is being explored to provide the increased capacity of multiple platters without requiring duplication of the optical head assembly. In this approach, MEMS micro-mirror arrays may enable increased performance and reliability via rapid adaptive compensation of tracking, focus, and optical aberration errors caused by disk fabrication tolerances, operational shock and temperature exposure, and disk and system aging effects.

Magnetic system head assemblies benefit from the batch fabrication economies of modern thin film lithography for fabricating and integrating the heads and sliders. The application of MEMS components and micromachined optical bench packaging techniques³ to optical storage may offer similar cost advantages for the integration of optical sources, detectors, and modulators and deflectors. While much remains to be demonstrated, the potential performance and cost benefits offered by these applications are strong drivers for the eventual introduction of optical MEMS technologies into future optical storage systems.

References

¹ S. Campbell, K. Curtis, A. Hill, T. Richardson, M. Tackitt, and W. Wilson, "Digital holographic memory using a digital micromirror device SLM and a CMOS active pixel camera," in *Optical Data Storage*, Vol. 8, OSA Technical Digest Series (Optical society of America, Washington, DC, 1998), pp. 168-170.

² A technical overview is available at www.quinta.com.

³ M. C. Wu, "Micromachining for optical and optoelectronic systems," *Proc. IEEE* 85 (IEEE Press, Piscataway, NJ, 1997), pp. 1833-1856.

MEMS-technology – A route to bring the optical fibre to the end user?

by Gunnar Edwall, Ericsson Components, S-100 44 Stockholm, Sweden

The telecom-network is the worlds largest machine - for speech

The telephony network is often characterised as the world's largest machine. Today it provides the opportunity for man, wherever he is, to get in touch with other people located anywhere all over the world. The network offers full real-time interactivity (without time-delay). Given these properties it is, however, today restricted to speech only. The driving force for the evolution of telecom and information technology at large, is the fundamental human wish for freedom and mobility. Man wants to be able to access information and communication immediately, wherever he is, without previously planning for contact. Moreover, he wants always to feel present, meaning that information like pictures and sound transmitted to him shall have full resolution, equal to the resolution of the human senses, even if he is on the move. In a somewhat longer time perspective, many of the things we see around us might exchange information with each other in order to support us with even more data to serve as background for our decisions. In this vision we talk about things (and not only people) that communicate with different types of information in a full multimedia fashion.

The need is real-time interactive multimedia services at the same cost as today's telephony

New types of mixed information services within the real time interactive multimedia area, like e.g. video conferencing, interactive video services, picture telephony and data communication, will pose new demands for increased capacity in the telecommunications network.

Technically, two-way communications with unnoticeable delay and lip synchronism is required. The up- and down-stream traffic shall be symmetric. Moreover, to gain wide acceptance, the cost of the required improvements must be marginal compared to that of the telecommunication systems today.

Optics and radio are the fundamental technologies for broadband networks

Two fundamental technologies are required to implement the vision given. Mobility calls for radio, whereas capacity calls for opto. The dominant requirements for future capacity comes from picture based services like improved truly interactive Internet, multimedia and cable TV. The capacity on each subscriber line needs to be improved by a factor of 30-1000 (depending on to what extent real-time signal coding can be employed) from today's capacity of 64 kbit/s (in Europe), if the vision shall be fulfilled.

Since the available frequency spectrum for cellular radio is limited, any increase in the bandwidth needed for new types of services, over that of speech, in practice means that the information needs to be coupled into the fixed network closer to its point of origin. Already today the transmission capacity on fixed copper lines have several constraints and optical fibres, with their inherently large bandwidth, are rapidly spreading into the fixed network. Thus, deployment of optical transmission all the way to, or at least very close to the end subscriber, would greatly help to fulfil the vision.

Low cost opto-electrical modules are key components

If optical fibres are installed to locations close to the end subscriber this leads to mass volume deployment. The crucial obstacle to overcome is to produce, install and maintain the fibre optic link more cost effectively than its copper alternative. As a rough estimate, the cable and its installation account for half of the investment required whereas the systems part stands for the rest. The cost for the cable and its installation is mainly costs for civil work, which are similar for all transmission media. Of the systems parts, the cost for the opto-electric modules, i.e. the transmitters and receivers at both ends of the subscriber line, are the dominating costs which must be drastically reduced.

To meet the capacity requirements outlined, single mode (SM) technology is needed. In the opto-electrical modules of today, packaging is the major contributor to cost. The packaging process is highly manual and involves a large proportion of labour to achieve precision alignment, down to the micrometer level, to couple light between the different light producing, light detecting and light guiding structures in the module. Moreover, the active light emitting and detecting semiconductors are delicate structures that need to be protected from mechanical and

chemical damage. This is valid both during packaging and at use, meaning e.g. that they cannot be exposed at the module interfaces.

The conclusion must be that opto-electrical modules, which can be produced at low cost in high volumes, are key components.

Is MicroMechanics the key to the information society?

With respect to light coupling in single mode structures a comparison can be made to the connection of two ordinary garden water hoses. If the alignment is not perfect a substantial amount of the light will leak. In the SM opto case, however, the mechanical alignment precision needed is of the order of a tenth of a micrometer, which is obviously quite delicate and time consuming.

If we try to define some pertinent areas of interest to bring down the cost of opto-electrical modules the following research topics might be distinguished.

- to reduce the cost of individual components in the modules
- to reduce the labour needed for mechanical alignment and assembly of the optical parts
- to increase the optical coupling by expanding the light coupling regions, (i.e. to relax the requirements on mechanical alignment)
- to improve the semiconductor laser towards a "dream laser" with negligible threshold current, high quantum efficiency also at increased temperatures (to produce more light at a given thermal heat dissipation, again in

order to relax the requirements on mechanical alignment)

- to introduce simple but robust light guiding structures to bring the light to the optical interface of the opto modules
- to package the modules in a robust but inexpensive way
- to reduce the need for testing and handling of individual components and modules
- to achieve a high production yield

The optimal design of the opto modules is a trade off between the above mentioned and additional "events". In order to make the trade off; deep insight in the underlying technology for the different events is needed. The situation resembles the effort to win a penthalon sports event.

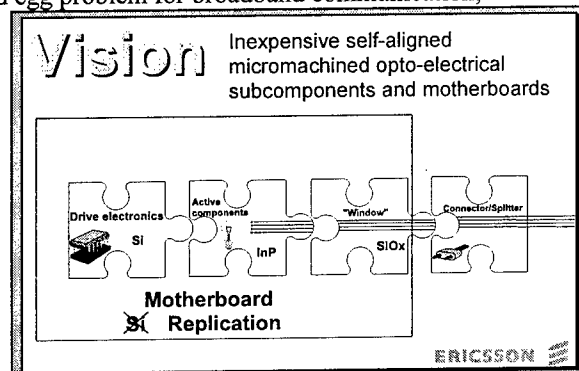
It is envisaged that micromechanics will be used to overcome several of the obstacles. However, when new technology is developed, there are several constraints for it to be industrially acceptable. Since, at high volume the production cost must be low, this means that:

- minimum manual labour is involved
- low cost materials are used
- high yield is achieved
- high reliability is a prerequisite

- temperature and environmental stability is granted
- good thermal transportation properties exists
- minimal testing is required
- process compatibility exists between steps

In order to provoke new ideas from the research community the following areas are mentioned, where micromechanics can be envisaged to overcome the chicken and egg problem for broadband communication,

- Electro-optical active components with micromechanical (passive?) alignment principles
- Passive components with mating micromechanical alignment principles
- Micromachined substrates with (passive?) alignment facilities
- Micro-replication of substrates (including microfabrication of tools and moulds)
- Inexpensive packaging



Keep it small, yet simple!!!

USING VIDEO MICROSCOPY TO CHARACTERIZE MICROMECHANICAL SYSTEMS

Dennis M. Freeman (freeman@mit.edu)
Research Laboratory of Electronics
Massachusetts Institute of Technology
Cambridge, Massachusetts 02139

C. Quentin Davis (qdavis@igen.com)
IGEN International, Inc.
16020 Industrial Drive
Gaithersburg, MD 20877

ABSTRACT

Because MEMS combine electrical and mechanical components, testing MEMS includes measuring a variety of types of signals, including both electrical and mechanical signals, at the very least. By comparison to the large number of powerful tools that have been developed to test electrical behaviors of microfabricated systems, relatively few tools are currently available for measuring mechanical properties. We have developed tools for in situ measurement of mechanical properties of MEMS based on light microscopy, video imaging, and machine vision. In this paper, we demonstrate that the system can measure motions of MEMS with nanometer resolution.

METHODS

Test structures are placed on the stage of a light microscope and driven with a periodic stimulus (Figure 1). Stroboscopic illumination is used to take stop-action images. Sequences of images are acquired at multiple planes of focus to obtain 3D information. Computer vision algorithms are used to determine motions directly from the sequence of 3D images.

Video microscopy. The microscope (Zeiss Axioplan, Oberkochen, Germany) uses a long (9.8 mm) working-distance objective (Zeiss LD-Epiplan 20X, numerical aperture 0.4), which accommodates the use of electrical probes. The magnified image is projected onto a scientific grade, 12-bit CCD camera (Photometrics 200 series with a Thompson 7883 CCD, Tucson, AZ) with 576×384 pixels spaced on a $23 \mu\text{m}$ grid.

Stroboscopic illumination. The maximum frame rate of a scientific-grade video imager is typically on the order of tens of Hz. To image faster motions, we use stroboscopic illumination. In early experiments, we used a gas discharge strobe lamp (Chadwick-Helmuth Co. Inc., El Monte, CA). Pulse-to-pulse variations in light from a gas discharge strobe can cause motion artifacts. Therefore, light is coupled to the microscope through a fiber optic scrambler (Technical Video Ltd., Woods Hole, MA). The duration of the strobe pulse ($8 \mu\text{s}$) limits the maximum frequency of motion that our system can measure. To relax this constraint, we have recently developed a stroboscopic light source using a green LED (Nichia NSPG500S, Tokushima 774, Japan), which is orders of magnitude faster.

Motion estimates from video images. Eight images of the target are acquired at evenly-spaced phases of the sinusoidal stimulus. Displacements between images acquired at successive phases are estimated directly from the video images. Although image resolution is limited by the optics [3] to distances

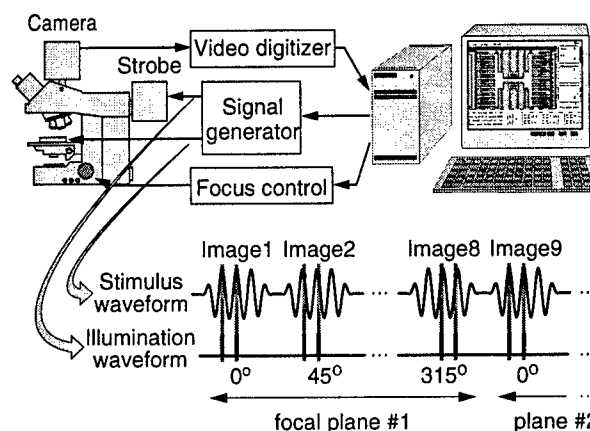


Figure 1. Computer microvision measurement system. The computer controls the signal generator, which provides a stimulus waveform for the test structure as well as an illumination waveform that determines the phase of motion illuminated by the stroboscopic light source. By controlling the focus of the microscope, the computer can take images at multiple planes of focus.

on the order of the wavelength of light (typically 550 nm), displacements between two such images as small as nanometers can be reliably measured [2]. Displacement estimates at successive phases are used to reconstruct time waveforms of motion. The magnitude and phase of the fundamental component of that waveform were computed with an FFT. Further details are provided elsewhere [1].

3D measurements. Silicon is opaque to green light, and only the top surfaces of structures can be viewed with a light microscope. Nevertheless, sequences of images obtained from multiple planes of focus contain information about out-of-plane position. Images are acquired at different focal planes by turning the fine-focus control of the microscope with a stepper motor. Images from above the best plane of focus appear blurred. When the multiple planes are assembled into a 3D image, 2D surfaces appear to have thickness because of this blurring. Out-of-plane motions of the target generate out-of-plane motions of the blurred 3D images, which can be tracked by the same algorithms used to track in-plane motions.

RESULTS

We applied computer microvision to measure motions of a microfabricated accelerometer (Figure 2) fabricated using surface micromachining techniques at MCNC (Research Triangle Park, NC). A shuttle and associated combs are suspended above the substrate via a folded-beam cantilever spring system.

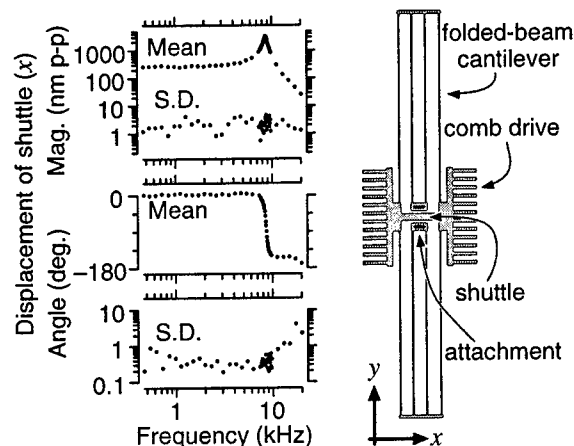


Figure 2. Frequency response of a microfabricated accelerometer. The drawing shows the central shuttle and associated comb drives of the accelerometer as well as its attachment to the substrate through folded-beam cantilevers. The plots show the mean and standard deviations (S.D.) of 5 repeated measurements of the x component of the shuttle's motion as a function of frequency. The two comb drives were excited with opposite phases of a sinusoidal (2 V peak-to-peak) stimulus added to a common 62 V DC bias.

Accelerations of the substrate cause relative motions that can be sensed as a change in capacitance between the interdigitated teeth of combs attached to the shuttle and substrate. The shuttle can also be moved by applying an electrical potential across the interdigitated teeth.

We have applied computer microvision to measure the frequency response of the accelerometer (Figure 2). Results are well approximated by a second-order system with a resonant frequency of 8.86 kHz and a quality of tuning of 13.6. The standard deviation of repeated measurements is <5 nm in magnitude and the signal to noise ratio is nearly 60 dB at resonance. The standard deviation of repeated phase measurements is less than 1° except when the magnitude is less than 50 nm.

The computer microvision system can also measure motions of the accelerometer that are orthogonal to the plane of focus. In this device, out-of-plane motions represent failure modes that limit performance. By examining a tooth on opposing combs and a small section at the center of the shuttle (Figure 3), we see that the shuttle is rocking about a point near its center. Repeatability of this measurement is within 4 nm in magnitude and a few degrees in phase.

DISCUSSION

Video microscopy has long been recognized as a powerful tool for qualitative inspections of MEMS. In this paper, we have shown that by analyzing images from a light microscope with algorithms from computer vision, it can be a powerful quantitative measurement tool as well. Because it is based on light microscopy, the system is inexpensive and easily integrated into research and fabrication facilities. The principal disadvantage of light microscopy is that image resolution is limited to optical wavelengths, which are typically a fraction of a micrometer. However, image blur does not limit the resolution with which multiple images can be aligned. Thus

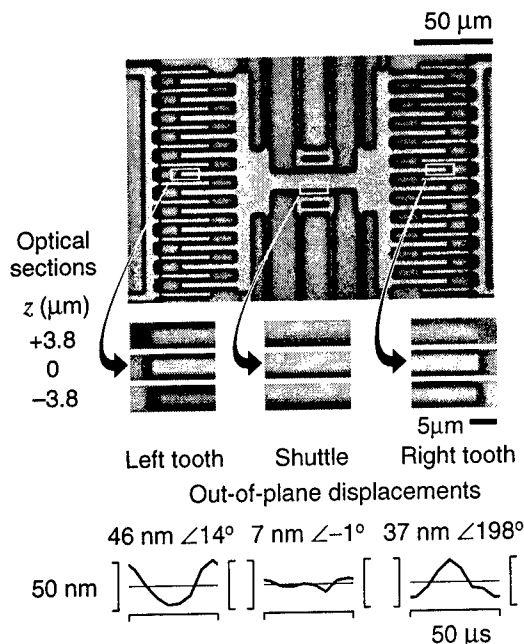


Figure 3. Out-of-plane motions of a microfabricated accelerometer. Regions of interest (white boxes) in the top image are magnified in the center panels and displayed with corresponding portions of images taken at focal planes above (3.8 μm) and below (-3.8 μm) the in-focus plane. Similar portions of images from 30 focal planes (separated by 0.545 μm) and at 8 evenly spaced phases during the stimulus cycle were analyzed to determine out-of-plane motion (plots). The two comb drives were excited with opposite phases of a 20 kHz sinusoidal (60 V peak-to-peak) stimulus added to a common 62 V DC bias.

light microscopy can be used to measure motions as small as nanometers.

ACKNOWLEDGMENTS

The computer microvision system was originally conceived and constructed to characterize micromechanics of the inner ear, supported by the NIH (2 R01 DC00238). Application of computer microvision to MEMS is supported by DARPA (F30602-97-2-0106). D. M. Freeman was supported in part by the W. M. Keck Career Development professorship.

REFERENCES

1. C. Q. Davis and D. M. Freeman. Statistics of subpixel registration algorithms based on spatio-temporal gradients or block matching. *Optical Engineering*, pages 1290-1298, 1998.
2. C. Q. Davis and D. M. Freeman. Using a light microscope to measure motions with nanometer accuracy. *Optical Engineering*, pages 1299-1304, 1998.
3. H. H. Hopkins and P. M. Barham. The influence of the condenser on microscopic resolution. *Proc. Phys. Soc.*, 63:737-744, 1950.

The effects of internal stresses on the precision of moveable structures for optical MEMS

Staffan Greek and Klas Hjort

Uppsala University, Dept. of Materials Science

Box 534, SE 751 21 Uppsala, Sweden

To perform optimally moveable micromachined structures for optical MEMS have high demands on planarity and stability in positioning. By combining Finite Element Analysis (FEA) with measurements on micromachined structures, we investigate how the average internal stress and the internal stress gradients of a moveable microstructure affects the precision in positioning the microstructure, with examples taken from a tuneable Fabry-Perot filter micromachined in InP, Figure 1.

A film from which a moveable microstructure is made contains normally an internal stress originating from the processes used to manufacture the film. The internal stress will affect the behaviour of the microstructure. A homogeneous stress causes a released microstructure to expand (compressive stress) or contract (tensile stress). In precision MEMS a compressive stress should be avoided since the structure may buckle under the compressive force. A tensile stress in the film gives rise to a tensile force in the structure that acts to stiffen the structure against movement. We present FEA of the moveable mirror of a tuneable Fabry-Perot filter where the stress stiffening resistance against actuation is investigated. The internal stress of the InP film is evaluated with indicator structures, Figure 2.

The internal stress in a film varies often along the thickness of the film. The stress gradient thus induced in the film causes the released structures to bend, Figure 3. In the case of the Fabry-Perot filter, SIMS (Secondary Ion Mass Spectroscopy) profiles indicated that the InP film contained As located to a thin layer at the bottom of the film. Due to the As contents, the thin layer has a compressive internal stress stronger than the stress in the rest of the film and thus the whole InP film contains an internal stress gradient. The InP film was modelled as a bimorph with one thin layer, representing the layer containing As, and one thick layer, representing the rest of the film. From the deflection of indicator structures, Figure 2, and the curvature of released beams, Figure 3, the stresses in the layers were calculated. The movement of a Fabry-Perot filter mirror with an internal stress gradient was investigated with FEA. A possible method to compensate the bending due to the As content at the bottom of the film is to deposit an identical layer at the top of the film so that the film has a symmetric stress distribution. To maintain the overall tensile stress state of the film, the necessary tensile stress of the centre portion of the film was calculated. The actuation response of a Fabry-Perot filter mirror thus compensated was investigated with FEA to compare the model including a bimorph stress gradient to the previous model of homogeneous internal stress.

A moveable microstructure is fixed to the substrate at base points at the fixture plate. If the plate is on top of a sacrificial layer, these fastening points may be undercut when the structure is released. An internal stress gradient in the film will induce a bending moment at the fastening points and this moment depends on the length of the undercut. The length of the undercut also governs the forces within a microstructure since a long undercut allows the microstructure to relax more than a short undercut does. Hence the stress stiffening forces will be larger in the microstructure with a short undercut and that structure will therefore resist actuation to a greater extent. The deflection of the moveable Fabry-Perot filter mirror with an internal stress gradient was investigated with FEA at

varied lengths of undercut. The mirror's resistance to actuation due to stress stiffening was also investigated at different lengths of undercut.

The internal stress effects we studied were mainly concerned with InP. However, micromachined structures for optical MEMS often include a bimorph system with different internal stresses, either intentionally as reflective coatings of different materials or unintentionally as in microstructures from CMOS foundries.

We conclude that it is vital for the performance of optical MEMS that the bimorph systems are investigated and that the effects of the internal stresses are modelled in the design work. The presented work contains a method which can be applied to many material systems in the design work of micromachined structures.

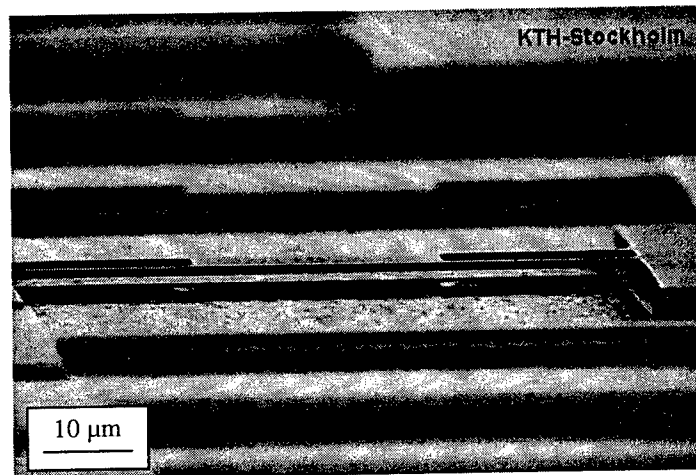


Figure 1. The moveable mirror of a Fabry-Perot filter micromachined in InP. SEM image courtesy Juergen Daleiden and Nicolae Chitica, KTH Stockholm.

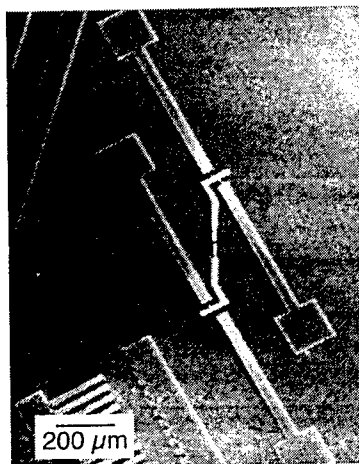


Figure 2. An indicator structure deflected due to an internal stress in the film.

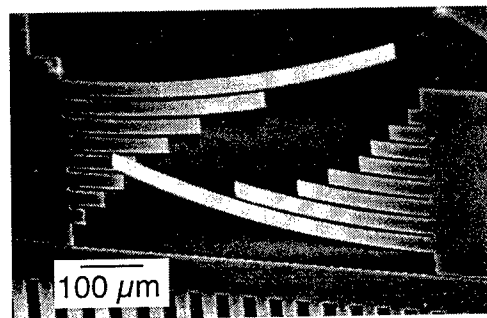


Figure 3. Released beams of InP bending upwards due to an internal stress gradient.

Design and fabrication of a polysilicon micro mirror with a flat surface by gold metallization

Young-Hoon Min and Yong-Kweon Kim

School of Electrical Engineering, Seoul National University
#301-1104, San 56-1, Shillim-dong, Kwanak-gu, Seoul, 151-742, Korea
Tel: +82-2-888-5017 Fax: +82-2-873-9953 Email: yhmin@plaza1.snu.ac.kr

A silicon based micro mirror array is a highly efficient component for use in optical applications as adaptive optical systems and optical correlators. Many types of micro mirror or micro mirror array have been studied and proposed in order to obtain the optimal performance according to their own purpose. In this kind of micro mirror, it is important to fabricate a micro mirror with a flat surface because the initial curvature of mirror influences a great deal of optical performance. The surface curvature of the mirror reduces both the initial separation of the mirror electrode and the stable mirror deflection distance in electrostatically actuated model. An optical distortion is also caused by the curvature and various methods are proposed in order to obtain the flat surface in micro mirror. Based on a design strategy developed in collaboration with MCNC, acceptably planar polysilicon mirror was obtained when all cuts in polysilicon and oxide layers were restricted to widths no longer than $1.5\ \mu\text{m}$ ^{[1][2]}. In MUMPs process, a top layer of gold is used for low resistance wiring or as a reflective surface of micro mirror for optical use and a concave curvature is obtained ^[3]. This curvature is due to residual tensile stress in the gold metallization and to compressive stress in the polysilicon structure. As a method of minimizing the curvature, "trapped oxide" method was proposed ^[4] and the minimal curvature was accomplished by using both polysilicon layers to trap the second oxide layer. More recent mirror is being designed under the concept to reduce curvature of mirror surface.

A micro mirror array designed, fabricated and tested in this paper is consisted of 5×5 single layer polysilicon, electrostatically driven actuators (Fig. 1). The micro mirror array for the optical phase modulation is made by using only two masks and can be driven independently by 25 channel circuits. About 6π phase modulation is obtained in He-Ne laser ($\lambda=633\text{nm}$) with 67% fill-factor. Initial deflections of mirror and spring due to stress gradient of structure element are about $0.535\ \mu\text{m}$ by modeling and $0.522\ \mu\text{m}$ by measurement respectively (Fig. 2) and have an influence on the deflection characteristics and pull-in behavior of the actuators.

In this paper, a new method to obtain the flat surface in spite of the stress unbalance of the structure is proposed. The curvature of mirror surface is due to the stress unbalance of the structure. The polysilicon structure which has largely used as micro mirror has a compressive residual stress and a negative stress gradient in general. Therefore, the surface of the micro mirror which is consisted of polysilicon has a convex curvature. The net bending moment with respect to neutral surface by stress distribution determines the curvature eventually and can be removed by optimal deposition of the mirror metal which has slightly tensile stress. The concept to obtain a flat surface is shown in Fig. 3. Gold is used as a mirror metal with tensile stress and titanium is used as an adhesive metal with residual stress free. The adhesion strength of chrome is higher than that of titanium but chrome has very large tensile stress and cannot be afforded to adjust the net bending moment of the structure by increasing the thickness of gold. The flat surface of the mirror is obtained by about 500\AA of gold metallization using the proposed concept (Fig. 4) and the nearly flat spring is obtained by given structure when the gold metallization on mirror reaches about 2000\AA (Fig. 5). The thickness of adhesion metal between mirror metal and polysilicon is 100\AA of titanium.

The experimental results show that the flat surface of the polysilicon micro mirror can be obtained by the optimal metallization and it will be expected to acquire a micro mirror with better performance in optical use.

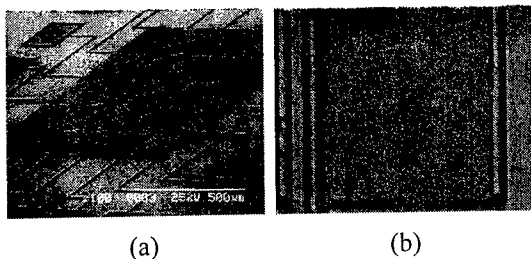


Fig. 1 Fabricated mirror array
(a): 5 x 5 mirror (b): mirror pixel

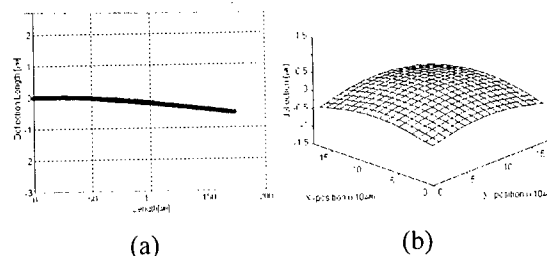
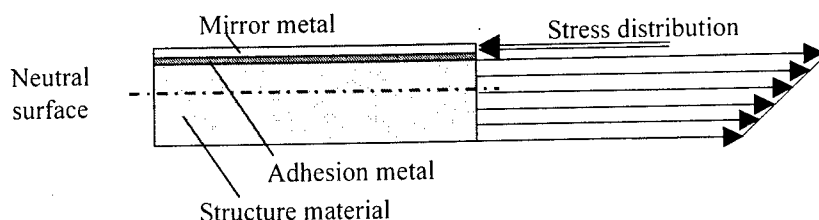


Fig. 2 Initial curvature
(a): spring (b): mirror



$$M_h = (M_h)_{Structure} + (M_h)_{Adhesion} + (M_h)_{Mirror}, \text{ w.r.t. neutral surface}$$

$$\rho = \frac{E(I_z)_{equivalent}}{(M_h)_{net}},$$

$$\delta_{spring} = \rho \left(1 - \cos\left(\frac{L}{\rho}\right)\right), \quad \delta_{mirror} (p-p) = 2\rho \left(1 - \cos\left(\frac{L}{2\rho}\right)\right)$$

Fig. 3 A new concept to obtain flat surface

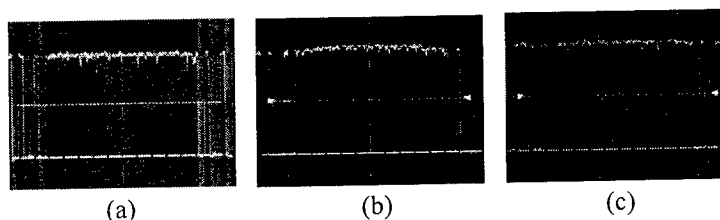


Fig. 4 Curvature of mirror
(a): Before release (b): After release (c): Gold 500 Å

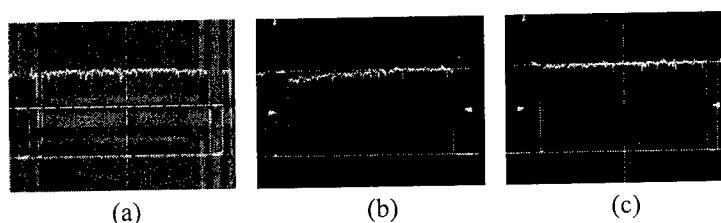


Fig. 5 Curvature of spring
(a): Before release (b): After release (c): Gold 2000 Å

References

- [1] T.Bifano, R.Krishnamoorthy, "Surface Micromachined Deformable Mirrors", *SPIE*, Vol.2641, 1995
- [2] T.Bifano et. al, "Continuous-membrane surface-micromachined silicon deformable mirror", *Opt. Eng.*, Vol.35, No.5, 1997
- [3] M.C.Roggeman, "Use of micro-electro-mechanical deformable mirrors to control in aberrations in optical systems : theoretical and experimental results", *Opt. Eng.*, Vol.36, No.5, 1997
- [4] David M. Burns and Victor M. Bright, "Non linear flexure for stable deflection of an electrostatically actuated micromirror", *SPIE*, Vol.3226, 1997

MB4

11:30am - 11:45am

Array of high quality surface micromirrors by chemical mechanical polishing of dielectric and metal

**I. Underwood, J.T.M. Stevenson, D.W. Calton,
A.M. Gundlach and D.G. Vass***

The University of Edinburgh Department of Electronics and Electrical Engineering
(* Department of Physics and Astronomy)

The Kings Buildings Mayfield Road Edinburgh EH9 3JL UK
Tel +44 131 650 5652 fax +44 131 650 6554 email i.underwood@ee.ed.ac.uk

Introduction

The reflective Spatial Light Modulator (SLM) technology of Ferroelectric Liquid Crystal (FLC) on a CMOS VLSI substrate is now relatively mature [1]. In order to optimize the optical performance of such a SLM, the silicon backplane should exhibit the following properties

- the backplane should be optically flat, both
 - globally (across the backplane) in order to minimize distortion introduced by reflection from its surface and
 - locally (within a pixel) in order to minimize scattering
- the pixel mirrors should occupy as much of the pixel area as possible, with minimal gaps between mirrors, in order to maximize the amount of reflected light
- the SLM surface should be microscopically smooth in order to promote good alignment of the FLC molecules

While the above goals are in principle achievable in CMOS or similar technology, they are incompatible with a typical modern process in which the top metal layer has the following properties

- thick layer
- large grain size
- coarse feature size

In order to resolve the above incompatibility we have developed micromachining techniques which are applied (in various combinations) as a post-processing sequence to "fully" processed wafers from a silicon foundry (such as Alcatel-Mietec or Austria Mikro Systeme).

The post processing techniques involve the deposition, polishing and patterning of both dielectric and metal layers on top of the "fully" processed wafer.

Chemical mechanical polishing

Planarization of a dielectric layer on a wafer surface can be accomplished by the use of spin-on materials or by the use of Chemical Mechanical Polishing (CMP) of a deposited layer. Both techniques have been used successfully for SLMs [2,3]. We have investigated both and have recently concentrated on CMP as it offers a greater degree of planarization which is important for an optical device. The CMP step is followed via etching and then by deposition and patterning of an unsintered aluminium layer. This technique has been extremely successful; using it we have achieved pixel fill factors in excess of 90%.

The residual undesirable properties of SLMs produced using the above technique are

- light scattering from the step-like edges of the pixel mirrors (see Figures 1b and 2a)
- disruption of FLC flow during cell filling (and consequent disruption to FLC alignment alignment) caused by the topography at the edges of the pixel mirrors (see Figures 1b and 2a)

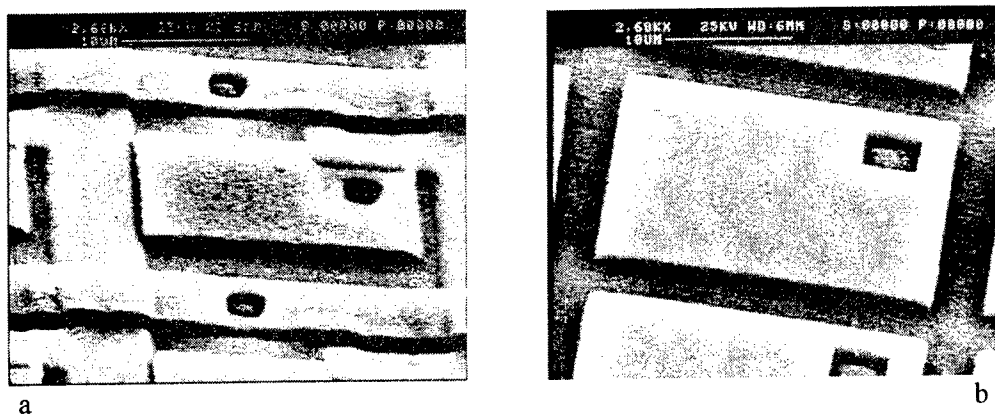


Figure 1 One pixel of backplane surface (a) before and (b) after planarization

Damascene process

The damascene planarization process [5] also starts with deposition and CMP of a dielectric layer. Next mirror shaped holes are etched into the dielectric and a blanket metal deposition carried out. The "Damascene" step involves polishing back the metal until the dielectric is exposed in the gaps between the mirrors thus electrically isolating neighbouring mirrors. The final profile has the mirror surface coplanar with the intervening dielectric as shown in Figure 1b.

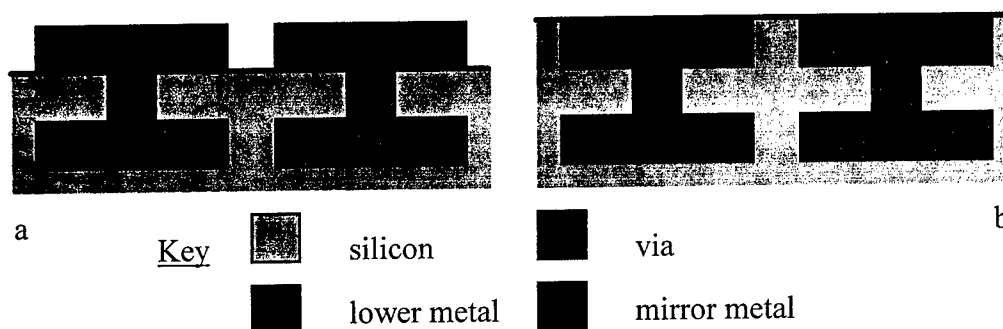


Figure 1. Wafer cross sections (a) conventional planarization (b) Damascene planarization

We have produced Damascene test structures and have characterized the Damascene process. Overall, the results indicate a likelihood of improved backplane characteristics over those obtained with conventional (dielectric CMP) planarization. We are currently carrying out Damascene planarization of a SLM product wafer.

Acknowledgments

The work described in this paper has been funded by the UK EPSRC under the SCIOS program.

References

- [1] I. Underwood "Liquid crystal over silicon spatial light modulators - principles, practice and prospects", OSA TOPS Vol. 14, pp76-88, 1997
- [2] A. O'Hara et al, "Post processing using microfabrication techniques to improve the optical performance of liquid crystal over silicon backplane SLMs", Proc. SPIE 2641, pp129-39, 1995
- [3] M.H. Schuck et al, "Planarization of LCoS microdisplays using benzocyclobutene polymeric resins" Digest of OSA annual Meeting, 1995
- [4] A. O'Hara et al, "Investigation of novel structures on silicon backplane SLMs to improve the device performance", OSA TOPS Vol 14, pp111-7, 1997

Deep Proton Lithographic CAD-CAM for the fabrication of Monolithic Micro-optical Elements

*P. Tuteleers, P. Vynck, H. Ottevaere, V. Baukens, G. Verschaffelt,
S. Kufner, M. Kufner, A. Hermanne*, I. Veretennicoff and H. Thienpont*

*Vrije Universiteit Brussel, Department of Applied Physics and Photonics (TW-TONA),
Pleinlaan 2, 1050 Brussel, Belgium*

tel.: ++ 32 2 629 3613, fax: ++ 32 2 629 3450, e-mail: Patrik.Tuteleers@vub.ac.be

**Eenheid Cyclotron, Laarbeeklaan 103, 1090 Brussel, Belgium*

1. Introduction

The technology of deep proton lithography in PMMA (poly methyl methacrylate) is a fabrication method for monolithic integrated refractive micro-optical elements and micro-mechanical holder structures, which allows structural depths in the order of several hundred microns[1,2]. Different optical functions can be fabricated in one block and form monolithic integrated optical systems. In addition mechanical support structures and alignment features can be integrated with these optical systems. This paper will focus on the technological requirements of the irradiation, the development and diffusion procedures and of the Computer Aided Design – Computer Aided Manufacturing (CAD-CAM) approach, which are necessary to achieve reproducible micro-optical components.

2. Basic Processes

The fabrication process consists of three basic procedures: an irradiation of a PMMA substrate followed by either a development of the irradiated regions or a swelling of the irradiated regions by organic vapour. If required both processes can be applied to different regions within one sample.

The idea of the process is based on the fact that proton irradiation of linear PMMA with high molecular weight splits the polymer chains and thus changes the chemical properties of the material. In front of the PMMA sample a metal mask is placed which is either fully transparent or fully opaque for the proton beam. The shape of the mask is directly projected onto the PMMA sample where the impinging high energy protons create well defined domains with reduced molecular weight. More complex structures can be created by moving the sample, done by the CAD-CAM software, during irradiation behind a mask with only one aperture (eg. a circular hole).

The irradiated domains can be dissolved in a special developer, because they show higher solubility than the non-irradiated domains. This process allows the fabrication of structures with optical quality, which can be used as deflection surfaces. Moreover alignment features and mechanical support structures can be integrated on the same sample during the same irradiation session. Alternatively to the development a completely different process can be applied to the irradiated PMMA: a swelling of the irradiated domains. This process makes use of the fact that the irradiation of PMMA changes also the swelling behaviour of PMMA when it is exposed to organic vapour, eg. styrene vapour. For the fabrication of microlenses the circular aperture of the mask is directly projected to the PMMA. During diffusion a considerable volume expansion can be observed which forms surface microlenses. Finally these lenses can be stabilized by thermal- or photopolymerization.

3. Practical Setup

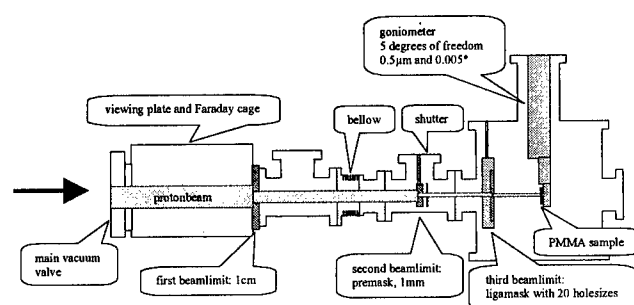


Fig 1. General overview of the setup and cross-section

To accomplish the fabrication, the software has to control the the setup shown in figure 1:

High energy protons coming from the cyclotron enter the beam line as indicated by the arrow at the left side of figure 1. At this place the beam has a diameter of several centimeters. From here the beam is reduced by three apertures. The first one reduces a large part of the beam and is water-cooled to compensate for the heat-production. The second aperture acts as a premask: by moving it up or down one aperture of the final mask can be selected.

The final mask is a 300 μm thick nickel plate which contains holes different sizes in a range from 20 μm up to 1 mm and has been structured by the so-called LIGA technique [3]. This type of mask has been chosen, because it has to be thick enough to fully absorb the protons. Furthermore the shape of the holes has to be perfectly cylindrical, since any tilt or lateral imperfection in the holes would affect the resulting PMMA structure.

A shutter is installed between the premask and the final mask to enable a fast and easy interrupt of the beam, in case that the sample is moving without the need to irradiate that part of the sample.

During the radiation, the computer uses only the Z and Y axis of the goniometer, to move the sample around, and the shutter to interrupt the beam. To make the process easy for the user we have implemented the process in a CAD-CAM system. After simulating the optical system, its design is drawn with a CAD program and saved as a plotter file. This file is then loaded in the CAM software that controls the setup for the deep proton lithography. This way of manufacturing makes it possible to go from an idea to a practical component in a matter of hours.

The dose, which is locally deposited onto the PMMA, is the most critical parameter in the irradiation process, and has therefore to be controlled exactly. This measurement is performed at the sample holder. If the protons have enough energy to pass through the PMMA sample, they reach the backplate of the sample holder, where they induce a current. This current is a measure for the deposited dose and is read out with a pico-amperemeter. For many applications a constant dose deposition over a whole structure is required. This would be straightforward, if a constant current and a constant speed of the motor drive could be assumed. However the intensity of the proton beam is not sufficiently constant. These instabilities can be compensated by a step by step irradiation. This means that the motors will only move to the next position if enough dose is received at that very position. The computer takes about 26000 current samples per second for the integration process. After the pointdose has been reached, the sample is moved to the following radiation point. When an optical line is being cut, a typical steptime is about 100 ms, with a step of 500 nm. With this method an exact control of the dose is now possible.

4. Conclusions and Perspectives

The characterisation of the individual optical elements shows that all the necessary elementary optical components for integrated refractive micro-optical components for optical interconnects can be provided with the technology of deep proton lithography such as micromirrors, fiber holes, lenslet arrays and positioning features. The surfaces of micromirrors or – prisms have been measured with a WYKO profilometer. The flatness of these elements can be better than 1 μm over a length of several millimeter and the roughness is in the range of about 20 nm. Experiments are underway to design and fabricate micro-optical systems which take advantage of the monolithic integration potential of this technology. In fig. 2 we show examples of components and structures that have been fabricated with this technique. At the conference we will highlight the fundamental mechanisms behind this type of lithography and the latest experimental characteristics of different components, illustrating the benefits of the new CAD-CAM approach.

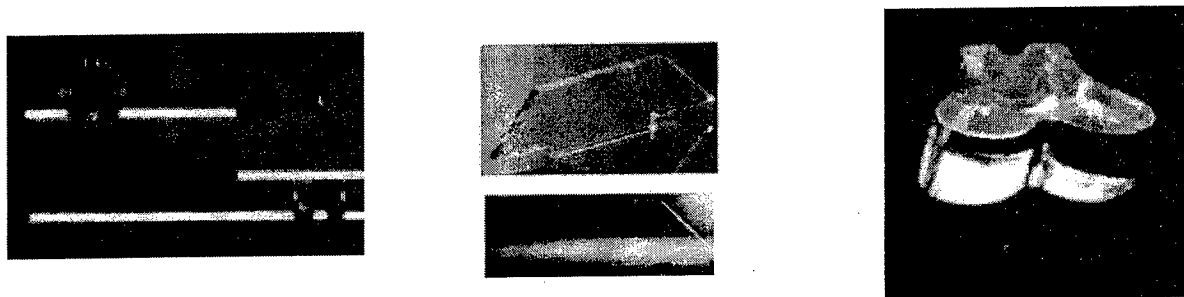


Fig. 2 Mechanical features as clips, micro mirrors and cylindrical lenses.

5. References

- [1] M. Kufner and S. Kufner: "Micro-optics and Lithography", VUB Press, Brussels, 1997.
- [2] M. Kufner, S. Kufner: "Fabrication of monolithic integrated fiber-lens connector arrays by deep proton irradiation", *Microsystems Technology*, Vol. 2, p. 114 - 118, 1996.
- [3] K.-H. Brenner, M. Kufner, S. Kufner, J. Moisel, A. Müller, S. Sinzinger, M. Testorf, J. Göttert, J. Mohr: "Application of three-dimensional micro-optical components formed by lithography, electroforming, and plastic molding", *Appl. Optics* 32 (32), 6464-6469, 1993.

MC1 (Invited)
1:30pm - 2:00pm

Micromachined Optical Switches for Free-Space Beam Steering

Hiroyuki Fujita, Hiroshi Toshiyoshi

Institute of Industrial Science, The University of Tokyo
7-22-1 Roppongi, Minato-ku, Tokyo 106 Japan

The optical application of microelectromechanical system, MEMS, has achieved a remarkable progress since Petersen, et al [1] successfully deflected light beams with small cantilevers driven by electrostatic force in 1977. One of the most promising market of optical MEMS today, is in fiber communication networks such as an FTTH (fiber to the home) project by NTT to be completed in 2010. Micro optomechanical switches [2] is expected to play a critical role because they are cost-effective for improving the reliability and the flexibility of the network.

There are two major types of micro optomechanical switches; one is based on movable optical fibers or optical waveguides and the other is based on movable micromirrors inserted in the light path in free space. In the latter type, the light beam that travels in the free space between fibers or optical waveguides goes either straight or is reflected by the mirror. Thus the beam is coupled to one of output fibers. Advantages of the type are as follows:

- (1) The size of switch is very small because the beam can be directed to an arbitrary angle.
- (2) Multiple switching is possible in a device because beams do not interfere with each other in free space.
- (3) Small driving force is required because it is easier to drive mirrors than fibers and waveguides.

Researchers have devoted their effort to reduce the insertion loss and achieved a typical value of ~2 dB. The sources of loss are coupling loss across the free space and reflection loss at the mirror. The coupling loss can be decreased by making the distance between ends of fibers/waveguides small, by collimating the beam, and with better alignment. Smoother mirror surface covered with metals of high reflectance reduces the reflection loss.

Marxer, et al. [3] fabricated a 2x2 micro optomechanical switch with comb-driven mirror by using deep RIE (reactive ion etching) technology. The distance between fibers with conical ends is approximately 50 micrometers. The RIE conditions were finely tuned so that the etched mirror had smooth and vertical surfaces and was thin. Grooves to accommodate fibers were etched at the same time as the mirror in order to assure good alignment. They packaged the device in a 30 mmx30 mmx8 mm steel housing and obtained the switching time of 0.2 ms at the driving voltage of 50 V, loss below 1 dB in the bar state and below 2 dB in the cross state. They also showed that antireflection coating at the end of the fiber reduced the backreflection.

Miyauchi, et al. [4] used the surface of the silicon substrate as the mirror. We coated gold on the mirror surface to improve the reflectance. The mirror was either electrostatically or magnetically rotated in 90 degrees out of plane and inserted in the light path. We defined the mirror and V-grooves for fibers with the same mask to have good alignment. We used TEC (thermally expanded core) fibers to reduce the coupling loss because we had rather long light path of 500 micrometers. The device is a single-mirror version of our previous matrix switch [5]. Optical performance of the device is presented in this meeting [6].

Anisotropic etching of a $\langle 110 \rangle$ silicon substrate by wet etchants such as KOH and TMAH produces $\langle 111 \rangle$ vertical wall that is suitable for a mirror. Miller, et al.[7] used a $\langle 111 \rangle$ mirror attached to a cantilever in their 2x2 switch. When the cantilever was electromagnetically driven, the mirror was vertically inserted to the light path. Polysilicon film deposited in a groove with $\langle 111 \rangle$ walls can also serve as a good mirror. Mita, et al.[8] etched a thin vertical groove in $\langle 110 \rangle$ substrate, deposited a SiO₂ sacrificial layer and a polysilicon layer and fabricated a polysilicon replica of the groove. A cantilever was patterned out of a polysilicon layer, released, and raised out of plane of the substrate permanently by reshaping technology[9]. Thus, we obtained a cantilever actuator with the vertical mirror for a 2x2 switch. The detail of the switch is presented in this meeting[8].

Using hinge structures, Lee, et al. [10] made the polysilicon vertical mirror that was raised 90 degrees out of the substrate. The mirror was driven by an SDA (scratch drive actuator[11]) array for a 2x2 switch. Self-assembly and adjustment of three-dimensional hinged structures was performed by the SDA array.

Electroplated metal in micromolds patterned by X-ray lithography(LIGA process) or made of special photo resist can provide a vertical mirror of good optical quality. Mohr[12] used a LIGA process to make a vertical mirror and a comb-drive for a bypass switch. Fibers and spherical lenses for collimation were positioned precisely in optical loss was 5dB for reflection mode; the loss is attributed to the low reflectivity of nickel (1.5dB) and the roughness of the sidewall ($R_a=50$ nm, ~ 1.5 dB). Reflectance of nickel that is most commonly used for electroplating was measured to be 78 % at the wavelength of 1.55 micrometers by Uenishi, et al.[13]. The reflectance reached 98 % when gold film was deposited on the surface.

Yasseen, et al.[14] constructed a 1x8 switch composed of a rotational mirror on top of an electrostatic micromotor and fibers with GRIN(grating index) lenses for collimation. The motor rotates in repeatable steps; fibers are aligned to those angles. They achieved the loss of 2.3 dB for single mode fibers and the switching time of 18 ms.

REFERENCES

- [1] K. Petersen, "Silicon as a Mechanical Material" Proc. IEEE, **70** (1982) 420.
- [2] H. Fujita, H. Toshiyoshi, Chap. 8 in SPIE Handbk on Microlithography and Microfabrication, vol. 2 (1997) 435-515
- [3] C.Marxer, C.Thio and N.F.de Rooij, O.Anthamattam, R.Battig, B.Valk, P.Vohel, IEEEConf. on Optical MEMS and Applications(MOEMS97) Nara, Jpn, Nov. (1997) 233
- [4] D.Miyauchi, H.Toshiyoshi, H.Fujita, IEEEConf. on Optical MEMS and Applications(MOEMS97) Nara, Jpn, Nov. (1997) 253
- [5] H. Toshiyoshi, H. Fujita, IEEE/ASME J. of Microelectromechanical Syst., **5** (1996) 231-237.
- [6] M. Miyauchi, H. Toshiyoshi, H. Fujita, IEEE/LEOS Topical Meeting of Optical MEMS, Monterey, CA, July (1998)
- [7] R.A.Miller, Y-C Tai, G.Xu, J.Bartha, F. Lin, Internatnl Conf. on Solidstate Sensors & Actuators(Transducers97) Chicago, Il, 16-19 June (1997) vol. **1**, 89-92.
- [8] M. Mita, H. Toshiyoshi, H. Fujita, IEEE/LEOS Topical Meeting of Optical MEMS, Monterey, CA, July (1998)
- [9] Y. Fukuta, T. Akiyama, H. Fujita, Trans. IEE Japan, **117-E** (1997) 20-26.
- [10] S-S Lee, E.Motamedi, M-C Wu, Internatnl Conf. on Solidstate Sensors & Actuators(Transducers97) Chicago, Il, 16-19 June (1997) vol. **1**, 85-88
- [11] T. Akiyama, D. Collard, H.Fujita, IEEE/ASME J. of Microelectromechanical Syst., **6** (1997) 10-17
- [12] J.Mohr, IEEEConf. on Optical MEMS and Applications(MOEMS97) Nara, Jpn, Nov. (1997) 221
- [13] Y.Uenishi, E.hashimoto, K.Honma, S.Nagaoka, IEEEConf. on Optical MEMS and Applications(MOEMS97) Nara, Jpn, Nov. (1997) 249
- [14] A.A. Yaseen, J. Mitchell, T.Streit, D.A. Smith, M. Mehregany, IEEE Workshop on Micro Electro Mechanical Systems(MEMS98), Heidelberg, Germany, Jan (1998) 116-120

MC2 (Invited)
2:00pm - 2:30pm

MEM Mirrors Application in Optical Cross-Connects

Herzel Laor
Agile Fiber LLC

2050 Hillsdale Circle, Boulder, CO 80303-5618
Tel: 303-641-0514. herzel@netbox.com

Summary

Optical Cross-Connects (OXC) will play a critical role in providing telecommunications companies the much needed management of OC-48 (2.5 Gbps) and larger trunks which the explosion in bandwidth demand has created. Just as the advance from 3.4 KHz to 1.5 Mbps created a market for Digital Cross-Connects (DXCs) of over \$1 Billion a year, a similar or larger market size is expected to develop for OXCs.

Today, the largest available OXC is a 72x72 matrix, which uses Multi-Mode fibers and Piezo-electric actuators. These are deployed in live traffic environments since the end of 1996. Not only are much larger OXC's a requirement but they must also use Single-Mode fiber. Telecommunications companies today are requesting sizes starting at 256x256 and projecting their requirements to scale up to 2,048x2,048 in the next 3-5 years.

One way to achieve a large OXC would be to cluster a network of smaller OXC's. However, insertion loss and crosstalk issues using this approach would limit the size of an OXC to less than 100x100. The best way to construct a large size OXC is to use directable beams in a plane or in a volume (See fig 1). Directable beams in a volume will enable construction of one switching stage OXC's scalable up to 10,000x10,000. In addition, since light beams do not interact when crossing over each other, the transmission media can be air resulting in extremely low crosstalk. With each beam passing through only two units – one directable transmitter and one directable receiver – low insertion loss is also achievable.

To create a directable beam transmitter or receiver unit, a MEM mirror with two degrees of freedom is required. Due to the diameter of a collimated beam a relatively large mirror area will be required. A beam diameter of 2 to 3 mm is required for an OXC sized at 1,024x1,024. A symmetrical design will also be important to handle brightness theorem considerations.

In a 1,024x1,024 OXC the transmit and receive array size would be 32x32. Each dimension of the mirror movement should allow for at least 32 resolution points and the mirror should be controllable in a linear fashion in both degrees of freedom.

Beam alignment and accuracy become the final challenges because even the smallest deviation of the mirror angle would deflect the directed beam off target. Traditional mechanical methods of beam alignment are not capable of achieving the level of accuracy required for a large scale OXC. The solution is a closed loop servo control mechanism, which has been very successful in the existing OXCs. The 72x72 OXCs discussed above use an added light sources to create auxiliary beams monitored by detectors that continually ensure the data beams accuracy. Similar mechanisms will be employed by MEM actuated OXCs.

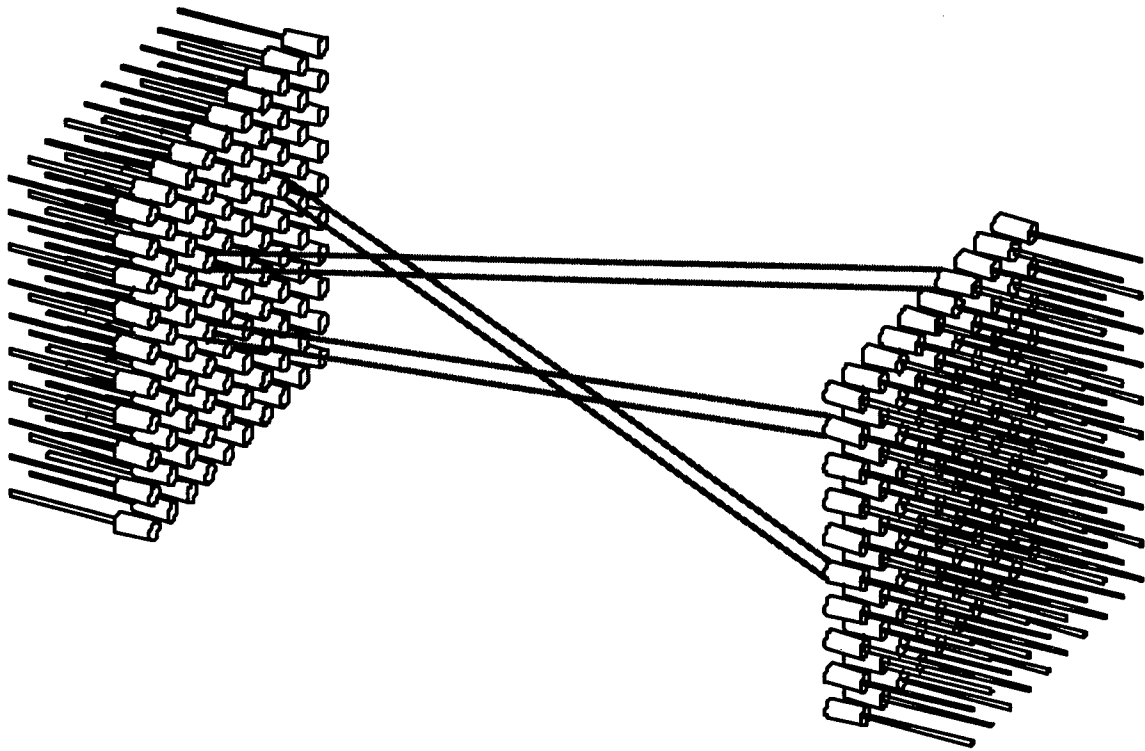


Figure 1. Directable beams connect directable transmitters and receivers.

Micromechanical Fiber Optic Switches based on Electromagnetic Torsion Mirrors

H. Toshiyoshi, D. Miyauchi*, and H. Fujita

Institute of Industrial Science, University of Tokyo, 7-22-1 Roppongi Minato-ku, Tokyo 106-8558, Japan

TEL: +81-3-3402-6231 ext.2384 FAX: +81-3-3402-6337

E-mail : hiro@iis.u-tokyo.ac.jp

*Address: R&D center, TDK Corporation, 15-7 Higashi Owada 2, Ichikawa, Chiba 272, Japan

Introduction Micromachined optical switches are under intensive study for data communication networks and measurement instruments. We have demonstrated electrostatic micro torsion mirrors for fiber optic switches [1, 2]. However, the electrostatic operation required large operation voltage. On the other hand the magnetic operation is expected to realize self-latching optical switches, which hold on/off-state without power consumption. In this report, we study the magnetic operation of NiFeCo sputtered torsion mirrors.

Concept The mirror design (Figure.1) is similar to that of our previous device reported in ref.[2]. A mirror supported by two beams is arranged in a 45 degree inclination to the four optical fibers. The mirror is coated with a magnetic film and can be attracted inward by 90 degrees (mirror is on) by applying a magnetic field perpendicular to the chip. At the on-state, the light beam from the input fiber is reflected by the mirror into the output fiber. Single mode TEC (Thermally Expanded Core, from $6\mu\text{m}$ to $20\mu\text{m}$) fibers are used to extend the coupling distance up to 1 mm in a free-space. Fig.2 (a) shows the device during the fabrication process (after patterning magnetic film, top view), and Fig.2(b) is the SEM view of the completed device. The mirror is $150\mu\text{m} \times 500\mu\text{m}$, and the torsion beams are thin and long ($20\mu\text{m}$ wide, $620\mu\text{m}$ long, and $0.3\mu\text{m}$). Optical fibers are placed in V-grooves, which were made by TMAH anisotropic etching of the silicon substrate.

Process Fig.2 shows the fabrication sequence. (1) Silicon oxide ($3\mu\text{m}$) and polysilicon ($0.25\mu\text{m}$) are deposited by LPCVD on a (100) silicon substrate of $300\mu\text{m}$ thick and patterned by RIE and BHF. (2) LPCVD silicon nitride ($0.05\mu\text{m}$) is deposited and patterned by RIE. Note that the mirror and the V-grooves are defined at this step, and thus the optical fibers are self-aligned to the mirror later. (3) Silicon oxide ($2\mu\text{m}$) is deposited by LPCVD and patterned by buffered HF. (4) The front side of the silicon substrate is anisotropically etched by TMAH to make V-grooves; the silicon nitride patterned in step (2) defines the edge of the V-grooves, and the upper silicon oxide protects the polysilicon. (5) Magnetic film of Ni₆₆Fe₁₆Co₁₈ ($1.1\mu\text{m}$) is ion-beam-sputtered and patterned by wet etching. The film was found to be "soft magnetic" because of the small coercive force (3.3 Oe), and the saturation magnetization was measured 1.0 T. (6) A masking layer of Cr ($0.3\mu\text{m}$) is deposited by vacuum evaporation on the back side. After patterning the chromium by wet etching, the back side of the substrate is slightly etched ($30\mu\text{m}$) by RIE. The remaining silicon made by the step-etch holds the flat surface of the mirror. (7) After partially removing the chromium, the backside is etched again until the silicon oxide. (8) The silicon oxide is removed in BHF to release the mirror. Finally, Cr/Au films of $0.01 / 0.05\mu\text{m}$ are deposited by vacuum evaporation to finish the mirror surface.

Operation Figure.4 shows the magnetic field dependence of the torsion mirror angle. The strength of the field is controlled by the gap between the mirror and a permanent magnet. Magnetic field larger than 400 Oe is needed to attract the mirror by 90 degrees. Figure.5 shows the photograph of the torsion mirror under operation at 600 Oe. The torsion mirror rotates 90 degrees and the visible light ($\lambda = 633\text{nm}$) from the incident fiber is reflected by the mirror into the output fiber. The insertion loss through the optical path (between the input and output fibers) was -6.0 dB at the wavelength of $1.55\mu\text{m}$; the value includes the coupling loss of the fibers (-3.3 dB) and the reflection loss of the mirror (-0.5 dB). Figure.6 shows the switching curve of the device driven by a coil. The measured switching time is 0.2 s (off-state to on-state), which can be improved by reducing the mass of the torsion mirror. We are going to develop a "hard magnetic" film on the mirror to realize the full-latching mechanism based on the combination of an electromagnetic coil with a core of permanent magnet; the toggle motion of the mirror is controlled by flipping the magnetization in the core (by switching current into the external coil), and no power is consumed to keep the switching state since the remaining magnetization of the core holds the mirror at either on- or off-state.

[1] H.Toshiyoshi, and H.Fujita, "Electrostatic Micro Torsion Mirrors for an Optical Switch Matrix", IEEE J.Micromechanical systems 5(4), (1996), pp.231-237.

[2] D.Miyauchi, H.Toshiyoshi, and H.Fujita, "Optical Cross-Connect Switch by Silicon Micromachining", Proc.MOEMS97, Nara, 1997, pp253-258.

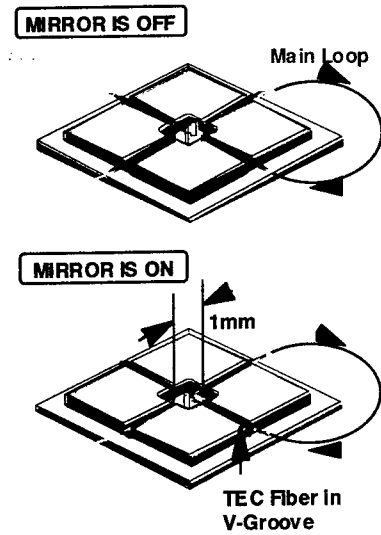


Fig.1 Configuration of the optical switch.

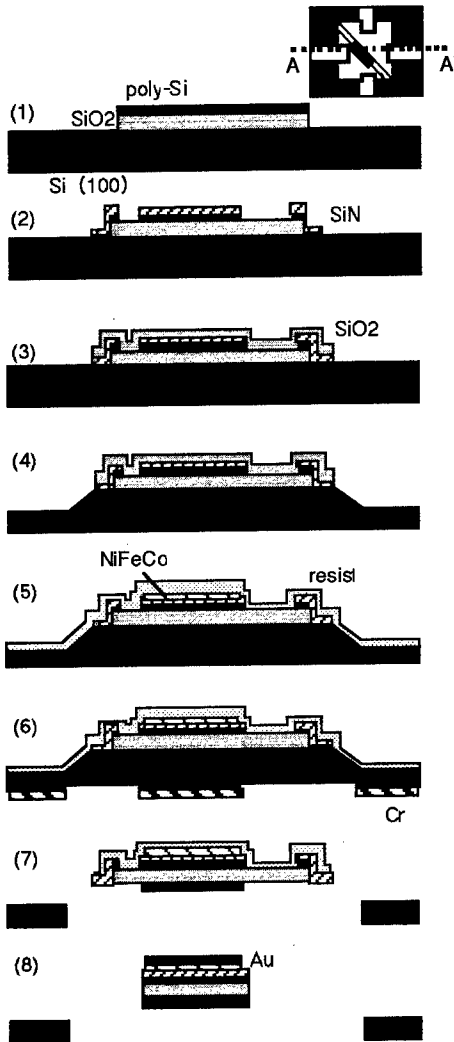


Fig.3 Fabrication sequence.

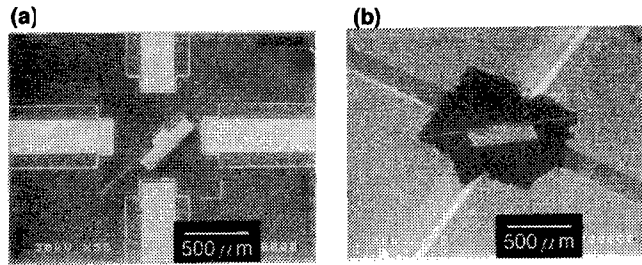


Fig.2 SEM view of the torsion mirror. (a) after patterning of NiFeCo film, (b) after releasing of the mirror.

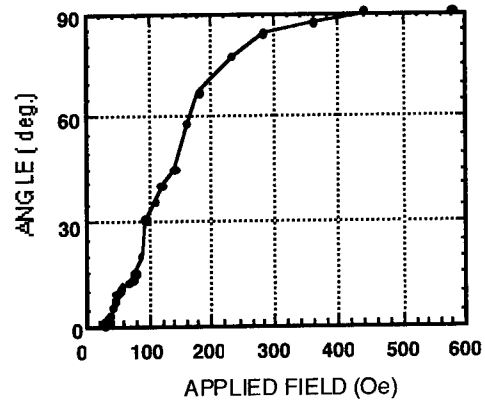


Fig.4 Mirror angle under applied field.

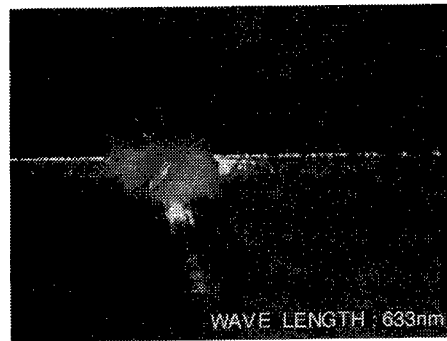


Fig.5 Operation of the torsion mirror using permanent magnet.

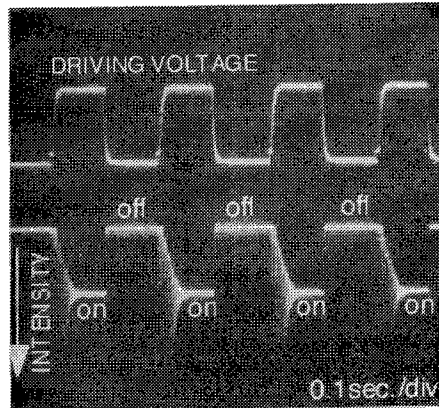


Fig.6 Wave trace of the optical switching.

Surface Micro-Machined Polarization Beam Splitting System

Chuan Pu*, Zuhua Zhu#, Yu-Hwa Lo#

* School of Applied and Engineering Physics, # School of Electrical Engineering
329 Phillips Hall, Cornell University, Ithaca, NY 14853

Summary

Polarization beam splitter(PBS) is of great importance in optical applications nowadays, such as sensing, data storage, communication, imaging, and signal processing, where polarization states of the light are concerned. Conventionally, PBS is made of birefringent crystals, and is quite bulky and not easy for integration. Using MUMPS (Multi-User Mems ProcesS) design offered by MCNC (Mems Center at North Carolina), which is a commercial foundry providing three layer polysilicon surface micro-machining process, we have successfully realized an integrated polarization beam splitting system on a single Si chip. Fig. 1 shows a schematic diagram and a SEM picture of the fabricated system, which is composed of one binary phase Fresnel lens[1][2] to collimate a 1.3 μ m laser beam out of a single mode fiber and a 3.5 μ m thick polysilicon thin film serving as the PBS, utilizing the polarization sensitive nature of a dielectric film to split an oblique incident optical beam into two orthogonally polarized beams.

It is well known in optics that when a beam of light is incident on a thin film at its brewster angle (determined by $\tan^{(-1)}(n_f/n_i)$, where n_f is the refractive index of the thin film and n_i for the ambience from the incident side[3]), the TM mode (Transverse Magnetic, where the magnetic field is perpendicular to the incident plane) will be totally transmitted, leaving the reflected light to be pure TE mode (Transverse Electric). The transmitted light is still a mixture of TE and TM mode, yet by choosing a high index material such as Si, and a proper thickness for the thin film[3], the reflectivity for TE mode could be easily tuned higher than 90%, leaving the transmitted light mostly TM polarized. Fig. 2(a) shows the simulation plot of Si thin film reflectivity and transmissivity as a periodical function of the film thickness at Brewster incident angle. Clearly, the TM wave is totally transmitted, leaving the reflected light to be purely TE wave. In addition, the transmittivity for TE wave could be as low as 3% under optimal conditions with precise control of the polysilicon film thickness, yielding a high polarization extinction ratio for the transmitted light. In our fabricated device, an incident angle (70°) slightly different from the Brewster angle was used. A similar simulation plot for the fabricated PBS is shown in Fig. 2(b). With a thickness of 3.5 μ m for our PBS, we are expecting polarization extinction ratios of 9.2dB for the transmitted light and 17.6dB for the reflected light.

After the polysilicon surface micromachining process at MCNC, the devices were sent back to us and the Fresnel zones of the lens were formed by selectively etching down a certain depth of polysilicon[2] on the lens surface using Reactive Ion Etching (RIE). The devices were then released in 49% hydrofluoric acid for 15 minutes. The long etch time was needed as there were no release holes in most part of our devices in order to improve the optical quality. The devices were then lifted up perpendicular to the substrate with vacuum tweezers and micro-probes and fixed to the substrate by micro-hinges and micro-spring latches [4].

The binary-phase Fresnel lens we fabricated has successfully collimated the laser light with a FWHM divergence angle of 0.41°, reduced from 5.7° without collimation. The diffraction efficiency of the lens is 25%, including the reflection loss of the lens itself. The collimated 1.3 μ m laser beam was then separated into two linearly (TE and TM) polarized beams by the PBS, which has an insertion loss of around 50% because of surface scattering and light attenuation by polycrystalline silicon. The insertion loss could be reduced in the future by surface planarization, and employing a thinner polysilicon film. As summarized in Table 1, the polarization extinction ratios are 10 dB for the transmitted beam and 21 dB for the reflected beam, which are in good agreement with our prediction. The polarization extinction ratio for the transmitted beam can be enhanced substantially by employing multilayer coating on the polysilicon surface, or by cascading multiple polarization beam splitters in the optical path. Our polarization beam splitting system is compact (less than 1mm² each) and easy to fabricate. It can be integrated into other free-space and fiber optic systems to fulfill more sophisticated functions.

References

- [1] L. Y. Lin, S. S. Lee, K. S. J. Pister, and M. C. Wu, "Micro-machined three-dimensional micro-optics for integrated free-space optical system," *IEEE Photon. Technol. Lett.*, vol. 6, pp. 1445-1447, 1994.

- [2] K. Rastani, A. Marrakchi, S. F. Habiby, W. M. Hubbard, H. Gilchrist, and R. E. Nahory, "Binary phase Fresnel lenses for generation of two-dimensional beam arrays," *Appl. Opt.*, vol. 30, no. 11, pp. 1347-1354, 1991.
- [3] M. Born, E. Wolf, *Principles of Optics*, Pergamon Press, 1980.
- [4] K. S. J. Pister, M. W. Judy, S. R. Burgett, and R. S. Fearing, "Microfabricated hinges," *Sensors and Actuators A*, vol. 33, pp. 249-256, 1992.

Table I: Characteristics of Polarization Splitting System with a 70° incident angle

	TE	TM	Extinction Ratio (dB)
Reflectivity	$R_{TE} = 38.4\%$	$R_{TM} = 0.29\%$	$10 \cdot \log(R_{TE}/R_{TM}) = 21$
Transmissivity	$T_{TE} = 4.9\%$	$T_{TM} = 49\%$	$10 \cdot \log(T_{TM}/T_{TE}) = 10$

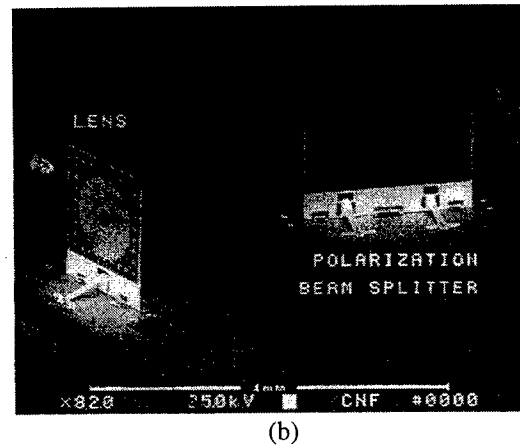
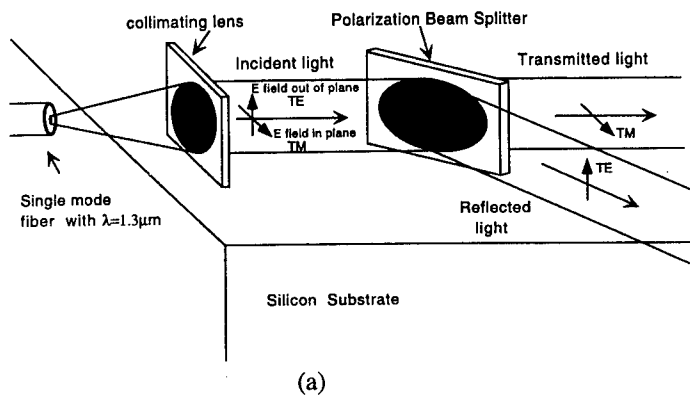


Fig. 1. Schematic diagram (a) and SEM photograph (b) of a surface micromachined polarization beam splitting system.

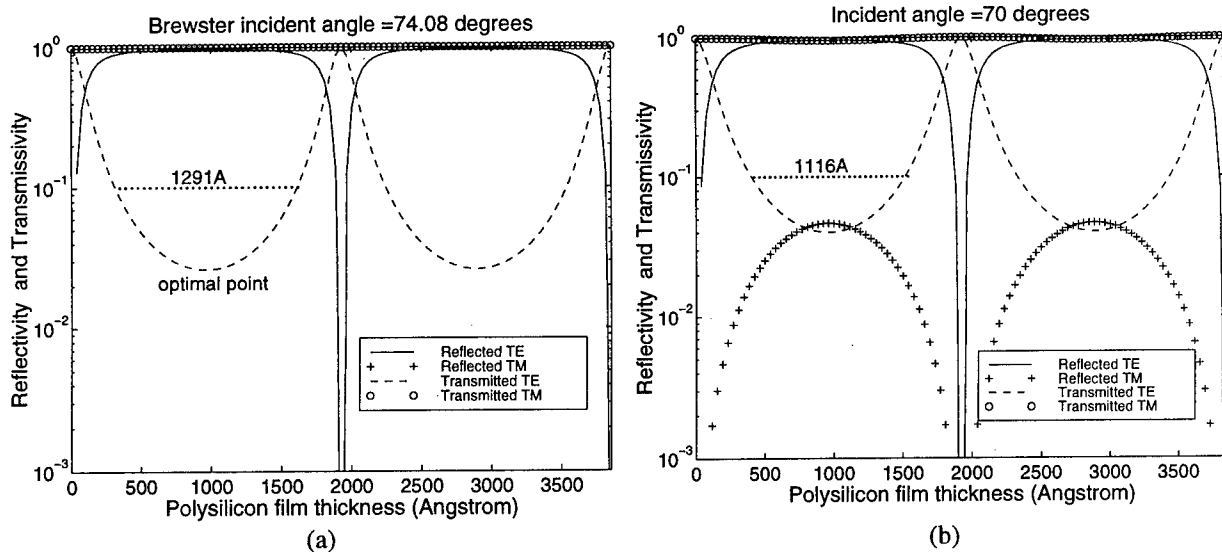


Fig. 2. Simulation results of the PBS at (a) Brewster incident angle, and (b) a 70° incident angle, which is the incident angle for our device.

Reflective Modulators and By-Pass-Switches: Two MEMS Components for Fiber Optic Communication

C. Marxer and N.F. de Rooij

Institute of Microtechnology
University of Neuchâtel, Jaquet-Droz 1, 2007 Neuchâtel, Switzerland
Tel.: +41 32 720 5121; Fax.: 41 32 720 5711; E-mail: cornel.marxer@imt.unine.ch

INTRODUCTION

Opto-mechanical devices are well suited for miniaturisation. For modulation or redirection of light principally only a moving surface is needed, which can move faster if it's smaller. In addition the beam diameter, especially of guided optics, matches well with the scale of micromechanics. At the imt developments on integrated actuators have early been focused on optical applications [1]. For applications in fiber optic communication these works have resulted in two components: The first component is a reflective modulator used for bi-directional single fiber data links. The second component is a 2x2 fiber optic switch intended for by-pass switching.

REFLECTIVE MODULATOR

Today's full duplex, bi-directional single fiber optical links operate with active light sources at both ends of the communication link. In contrast to conventional fiber optic communication links with separate fibers for each direction, bidirectional links can be realised with only one fiber using so called "BiDi" modules at both link terminals [2]. An alternative to this 'active-active' solution relies on reflective modulation, where part of the incoming light is used for the return channel. Based on silicon micromechanics such modulators have the potential of low fabrication costs and can be produced in large quantities.

Figure 1 illustrates the device architecture. The duplexer is composed of a single mode fiber carrying the in- and outgoing light, the micromechanical silicon modulator and the InGaAs-phodiode chip for the downstream data detection. Fabricated by surface micromachining the modulator is based on the Fabry-Perot principle and uses a electrostatically actuated polysilicon membrane to modulate light. The modulator is illuminated across the silicon substrate from a backside hole to achieve a low insertion loss. Additionally the sidewalls of the hole passively align the single mode fiber to the modulator on the topside of the chip.

The characteristics are summarised in Table 1.

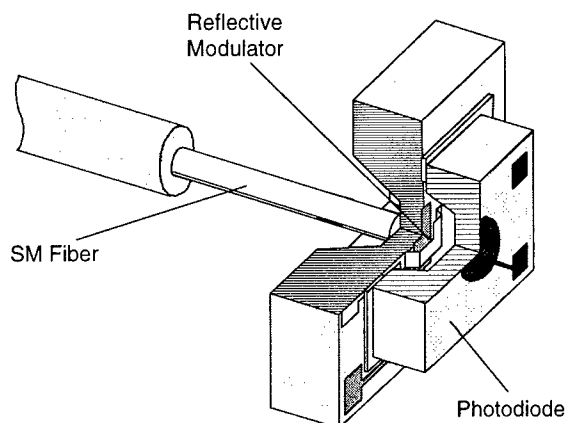


Figure 1: Cross section of reflective duplexer.

Table 1: Measured Modulator Characteristics:

λ [nm]	insertion loss	On-Off ratio	DC-bias	AC V_{pp}	rise time
1260		9 dB	90 V	5 V	
1310	< 3 dB	10 dB	84 V	7 V	< 200 ns
1360		15 dB	69 V	17 V	

The modulator is inherently not sensitive to polarisation. The insertion loss is typically 1-3 dB. For a modulator with a bandwidth of 2 - 3 Mbit/s a wavelength dependent DC voltage of 69 - 90 V has to be applied. A modulation voltage of 5 - 17 V is superimposed to get On-Off ratios of typically 10 dB.

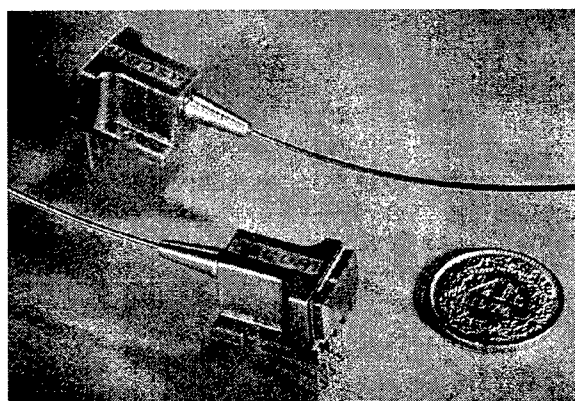


Figure 2: Packaged reflective duplexer.

FIBER OPTIC 2X2 SWITCH

For the more complex structure of today's fiber optic networks there is a increasing need for low loss and low crosstalk fiber optic switches. Since the low crosstalk requirements are difficult to achieve with waveguide based devices till now mainly mechanical switches are used in practice. Conventional mechanical switches, although they achieve low loss and high isolation, tend to be bulky and slow and their reliability is not certain. Especially the speed and size limitations could be overcome using the MEMS technology and several groups have demonstrated MEMS based switches [3,4]. Nevertheless it pointed out that it was very challenging to achieve losses below 1 dB. Our switch comes already quite close to these very stringent loss requirements. The switch is of the moving mirror type, i.e. between two pairs of fibers at 90° a mirror can be inserted to switch light. The vertical mirror is fabricated by deep reactive ion etching (DRIE) [5] and metal coated to increase its reflectivity. The use of tapered fibers allows to avoid any imaging optics. Basically to build the switch only the MEMS chip and the fibers with a conical shaped end are necessary. This results in a very simple design which is well suited for a large scale production. Figure 1 shows a top detail view of the 2x2 micromechanical switch. In the bar state the light from the two pairs of fibers goes in a straight path, in the cross state the vertical mirror reflects the two light beams by 90° in order to couple the light into the output fibers normal to the input fibers. The quality of the vertical mirror is of primary importance in order to keep the light loss minimal also in the cross state. The mirror should be as flat, vertical and thin as possible. The light loss is below 1 dB in the bar state, whereas in the cross state the loss was asymmetrical: 2 dB in one

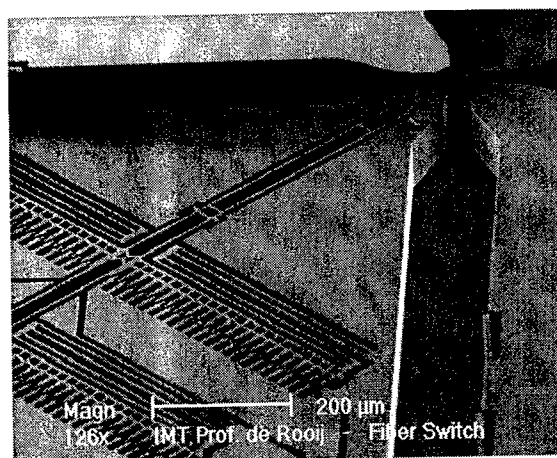


Figure 3: SEM-micrograph of micro-mechanical fiber switch including electrostatic comb drive actuator, micro-mirror and fiber alignment grooves.

path and about 3.8 dB in the other one. This asymmetry was willingly introduced by a small lateral offset of the mirror to improve the coupling for one path to the detriment of the other. The characteristics are summarised in Table 2.

Table 2: Characteristics MEMS-mirror based switch:

Insertion Loss (bar state)	0.5 - 1 dB
Insertion Loss (cross state)	2 - 3 dB
crosstalk attenuation	> 50 dB
backreflection attenuation	> 40 dB
switching speed	< 1 ms
driving voltage	5 V CMOS
supply voltage (power)	5 V (70 mW)

The switching mirror is actuated by an electrostatic comb drive actuator. At rest the mirror is in the reflecting state and is pulled out of the optical path when a sufficiently high voltage is applied. Thus when power is turned off the switch returns into the cross state. To get a switching time below 1 ms a voltage in the order of 50 V is necessary. Using a charge pump circuit this voltage is generated out of a IC compatible 5 V supply voltage.

Conclusions

We have reported on two MEMS based components for fiber optic communication: a reflective modulator and a fiber optic switch. Both devices take advantage of the silicon micromechanics technology not only for their functionality but also to allow self aligned positioning of the single mode fibers. Therefore they have the potential of low fabrication costs and can be produced in large quantities

REFERENCES

- [1] V. P. Jaeklin, et al., "Optical microshutters and torsional micromirrors for light modulator arrays", *Tech. Dig. IEEE MEMS. Workshop*, Fort Lauderdale, FL, USA, February 1993, pp. 124-127
- [2] H. L. Althaus et al., "Microsystems and Waferprocesses for Volumeproduction of Highly Reliable Fiber Optic Components for Telecom- and Datacom- Application", *Proceedings of 47th Electronic components and Technology Conference*, May 18-21, 1997, San Jose, Ca, pp. 7-15
- [3] S. S. Lee, et al., "Surface-Micromachined Free-Space Fiber Optic Switches with Integrated Microactuators for Optical Fiber Communication Systems", *Dig. of techn. Transducers '97*, Chicago, pp. 85 - 88.
- [4] E. Ollier et al., "Micro-Opto Mechanical Switch Integrated On Silicon", *Electron. Lett.* 31 (23), pp 2003-2005 (1995)
- [5] C. Marxer et al., "Vertical Mirrors Fabricated By Deep Reactive ion Etching for Fiber Optic Switching Applications", *IEEE J. of MEMS*, vol. 6, no. 3, September 1997, pp. 277 - 285

Micro-optics for micromachined fiber optic switches

H. P. Herzig and Y.-A. Peter

Institute of Microtechnology, University of Neuchâtel, Switzerland

Modern micromachining enables the fabrication of passive and active optical components, such as lenses, gratings and fan-out elements. These components are ideal for building compact micro-optical systems [1]. We will summarize the potential and limitations of these elements, as well as their integration into systems for the case of fiber optic interconnects and switches.

Micro-optical elements: The typical procedure to fabricate micro-optical elements is to realize a surface-relief pattern into photoresist by multiple mask projection or by direct writing methods (e-beam, laser beam) [1]. The surface-relief is then transferred into quartz by etching, or into plastic by replication. Different types of elements are available. Diffractive elements (DOE's) can perform various optical functions, such as deflection, focusing, multiple beam-splitting (Fig. 1) and wavelength demultiplexing. Refractive lenses can be manufactured by melting resist technology (Fig. 2). The lenses have a diameter of a few μm up to a few mm and an f-number below $f/5$. Highly interesting for building compact systems, are hybrid (refractive/diffractive) elements. They can perform multiple functions at once and they can compensate for aberrations. Figure 3 shows an example of a hybrid element which can be used for wavelength demultiplexing. The element has been fabricated by interference on top of a microlens [3]. Limitations of micro-optical elements are the diffraction efficiency, stray-light and the resolution of the fabrication process.

Systems: Our goal is to realize a 3-D system for fiber optic switches, as shown in Fig. 4. The system connects one input fiber to 6 or 8 output fibers. An advantage of the system is that the distances between input fiber and output fibers are equal. In addition, the configuration can be extended to switch which connects 8 input fibers to 8 output fibers. A key problem in such systems is the alignment of the different components. We have built a first test system (Fig. 5) to study the alignment of refractive microlenses with respect to a fiber array. A high lateral precision is required for single mode fiber injection, typically better than $1\ \mu\text{m}$. The alignment along the optical axis is less critical. Our system consists of a microlens placed between one input fiber and one output fiber. The fibers are held in V-grooves and the microlens is mounted on an XY-stage. The lens is fabricated by the melting resist technology. The mechanical parts are realized by wire electro-discharge machining (wire-EDM) at AGIE Losone. Two piezo-electrical actuators make the flexible bearings of the stage move in X and Y direction (Fig. 6). A feedback loop allows an accurate lateral adjustment in order to optimize the fiber injection. We will present the results obtained with this system and the progress made in the final 3-D switching system.

- [1] H. P. Herzig, ed., *Micro-Optics: Elements, Systems, and Applications*, (Taylor & Francis, London, 1997), ISBN: 0 7484 0481 3 HB.
- [2] Ph. Nussbaum, R. Völkel, H. P. Herzig, M. Eisner, S. Haselbeck. "Design, fabrication and testing of microlens arrays for sensors and microsystems", *Pure Appl. Opt.* **6**, 1-20 (1997).
- [3] P. Ehbets, H. P. Herzig, P. Nussbaum, P. Blattner, R. Dändliker, "Interferometric fabrication of modulated submicron gratings in photoresist", *Appl. Opt.* **34**, 2540-2547 (1995).
- [4] S. Traut, I. Philipoussis, Ph. Nussbaum, H. P. Herzig, "Holographically recorded gratings on microlens arrays", *Topical Meetings Digest Series (European Optical Society, 1998)*, Vol. 16, pp. 32-33.

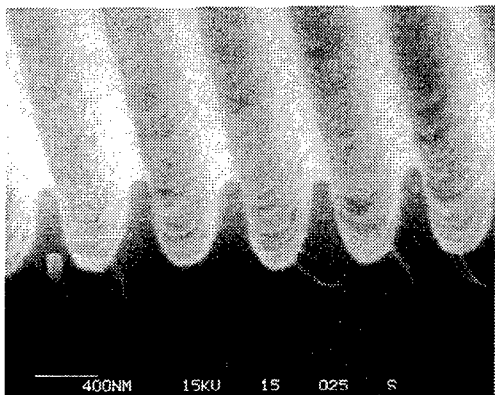


Fig. 1 Scanning electron microscopy picture of a grating structure. This element is an off-axis fan-out element that generates 9 equal spots in the first diffraction order [3]. The grating period is $577\text{ }\mu\text{m}$.

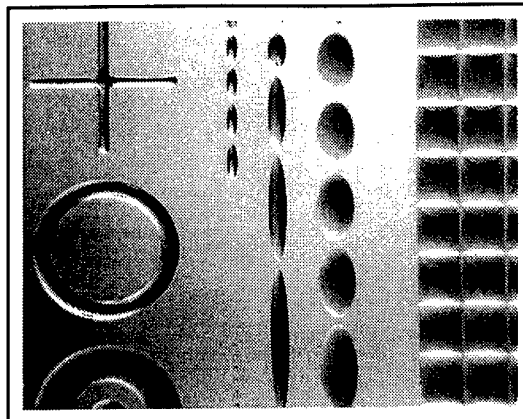


Fig. 2 Microlenses fabricated by reflow technique: elliptic, rectangular and ring lenses [2].

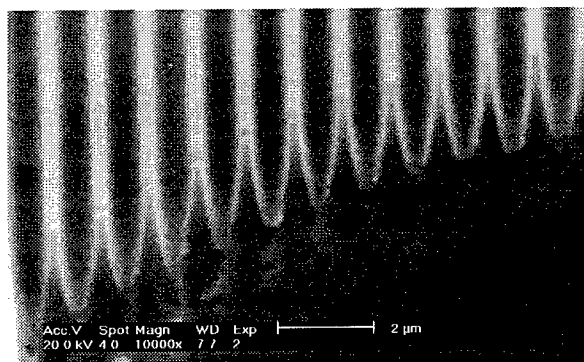


Fig. 3 Cross section of a grating on top of a microlens [4].

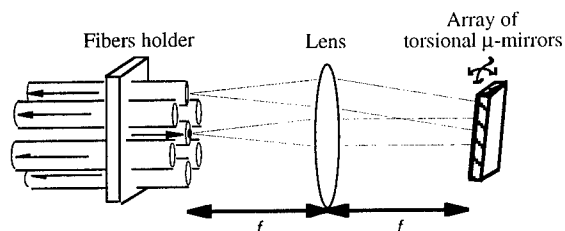


Fig. 4 Schematic drawing of a 3D optical switch with a fiber bundle (one input fiber and six output fibers).

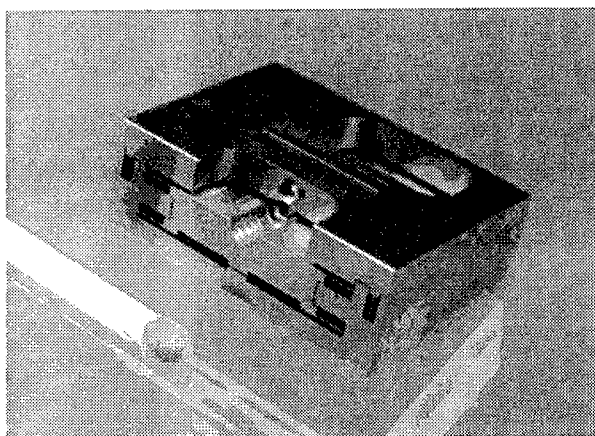


Fig. 5 Miniaturized X-Y stage: electro-eroded translation stage for fiber alignment, fabricated at AGIE, Losone by S. Bottinelli, EPFL.

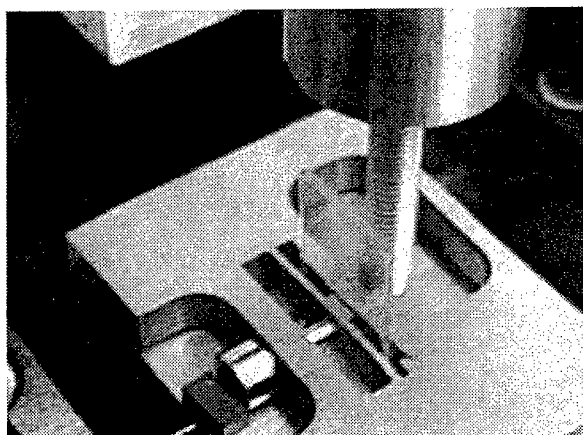


Fig. 6. Setup of the AGIE XY-table.

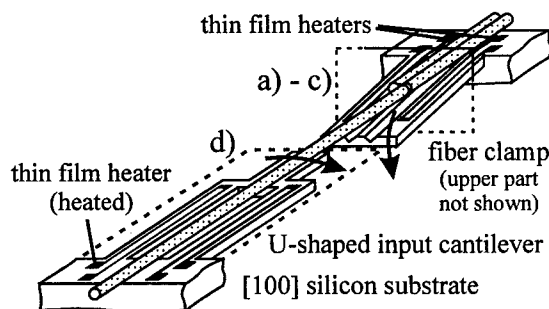
Bistable Micromechanical Fiber-Optic Switches on Silicon

Martin Hoffmann, Peter Kopka, Edgar Voges

Universität Dortmund, Lehrstuhl für Hochfrequenztechnik, Otto-Hahn-Str. 6, D-44227 Dortmund, Germany
Tel. +49-231-755-4619 – Fax: +49-231-755-4631 – WWW: <http://www-hft.e-technik.uni-dortmund.de>

Introduction

While optical communications started with point-to-point connections, complex network structures become more and more important. Due to the high data rates and the importance of a reliable information transmission network concepts taking reconfiguration in case of fiber breaks into account are under investigation. Within the ACTS project COBNET (Corporate Optical Backbone NETWORK) both a WDM- and a SDM double ring network are developed [1]. After a fiber break is detected, the receivers in the High End – and Low End Nodes behind the failure are switched e.g. from the clockwise operating ring to the counter-clockwise ring.



Protection switches have to meet typical requirements: Both insertion loss and cross talk have to be very low. They have to be long term stable, preferentially with a bistable switching characteristic. On the other hand no high switching speed is required. Well known solutions are precision mechanic switches using microoptics. Also integrated optical devices are well known such as Mach-Zehnder switches and digital (thermo-)optical switches [2]. Also integrated optical / micromechanical solutions [3, 4] have been proposed.

Fig. 1: Micromechanical Fiber Switch
{Bistable operation a)-d): see Fig. 2}

The fiber-optical switch described here is based on silicon micromachining and standard single- or multimode fibers (Fig. 1) [5]. It combines the low cross talk level (< -60 dB) of fiber-optical switches with the easy-to-handle fabrication techniques of silicon micromachining. The basic concept is the movement of an input fiber between two V-grooves containing the output fibers. A bistable operation is achieved by a fiber clamp. The actuators are based on thermal effects. While the fiber clamp is driven by the bimaterial effect (Fig. 2a-c)), the linear expansion is used for the lateral fiber movement (Fig. 2d)). In contrast to other concepts [4] the silicon cantilevers itself are part of the actuator resulting in easy fabrication and high efficiency. For the complete switch only 3 mask levels are needed (2 for wet etching (front / back side), 1 for the thin film heaters). No additional microoptic elements (except the fibers) have to be mounted for this device. The only part that has to be additionally mounted is the upper part of the fiber clamp. To avoid back reflections, the fiber end faces should be coated with an antireflective coating.

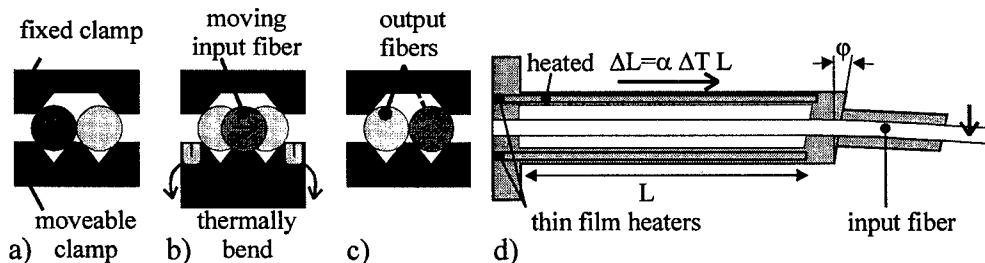


Fig. 2: a)-c) Bistable operation of the fibre clamp; d) U-shaped cantilever for lateral fiber movement

Fabrication

For a precise alignment of optical fibers in integrated-optical and micro-optical applications V-grooves in (100)-silicon are well known structures. They can be easily fabricated by anisotropic wet etching in alkaline solutions (e.g. KOH, potassium hydroxide). Etching stops at (111)-planes. The V-groove depth is well defined by the width of the mask. But konvex corners have to be protected by corner compensation structures [6].

To produce cantilevers in (100)-silicon as they are used for this switch the wafer has to be structured from both sides (Fig. 3). All rectangular areas which are exposed to KOH are at first etched like V-grooves. If front and back side grooves meet each other, fast etching (110)-planes are exposed to the KOH (etch rate ratio: $(110)/(100) \cong 3/2$). Time controlling this etching step results in vertical side walls. As this structuring requires fast etching at high temperatures, silicon nitride (Si_3N_4) is preferred as masking material.

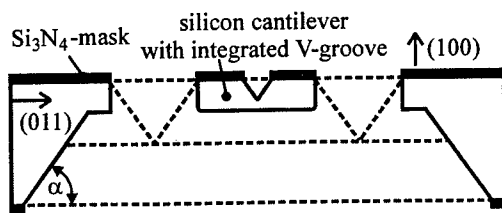


Fig. 3: Full wafer micromachining
dashed lines: intermediate etching plains

found that the thin film heaters are neither detached nor etched in the following etching process in KOH which is time limited to adjust the cantilever thickness. This process is not critical because the etch rate can be carefully controlled by the temperature of the etch solution ($\pm 0.1\text{K}$). Cantilevers with a thickness of about $80\text{ }\mu\text{m}$ show high mechanical stability and high yield. The switch fabrication is completed by gluing the fibers into the V-grooves using UV-curing resin. The upper part of the V-groove clamp, also fabricated by wet etching, is put upside-down onto the output cantilevers. This cover defines the vertical position of the fibers. The upper clamp has to be aligned and to be fixed carefully with respect to insertion loss. It can be extended to allow a hermetical sealing of the active fiber switch.

A single switch has a width of 3 mm and a length of 50 mm . The layout also allows the fabrication of arrays. Our test array contains ten switches with different cantilever layouts and grooves for fiber positioning and has overall dimensions of $39\text{ mm} \times 50\text{ mm}$. A fabrication on (110)-silicon substrates is also possible with slight modifications in the layout.

Results

First 1×2 bistable micromechanical fiber switches have been fabricated (Fig. 4). They show an excellent mechanical operation of the actuators. The power for the horizontal shift is below 200 mW . Changing the material of the thin film heaters from chromium to nickel reduces the power needed for opening the fiber clamp to 700 mW . Switching without releasing the fiber clamp is possible if the switching power for the horizontal shift is increased. Optical measurements show insertion losses below 3 dB , for some switches below 1.1 dB .

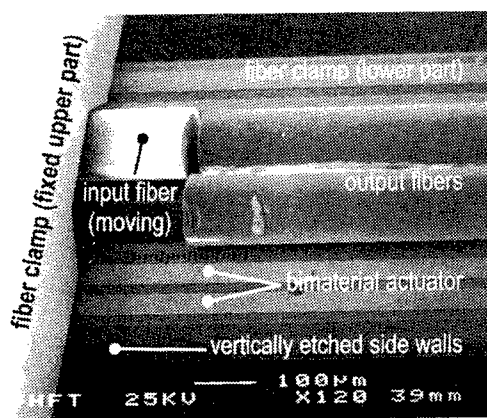


Fig. 4: Close-up view of the fibre coupling region

These varying results are due to tolerances during positioning of the upper fiber clamp. The crosstalk is below the limits of our measurement equipment (-70 dB). The switching time is estimated to be several 10 milliseconds, exact times have to be confirmed. As the fiber switch is bistable, the switching power is needed for a very short period of time. For the fiber clamp the switching power can further be reduced by removing the silicon nitride and by using a layout as it is used for the U-shaped input cantilevers (less material to be bend).

A realization on $[110]$ silicon is under development using a piezoelectric actuator for the fiber clamp. This switch concept can easily be extended to 1×3 and 1×4 switches or adapted for micromechanical attenuators which are also investigated.

- [1] W. Denzel, B. Meekers, "Photonics in the backbone of corporated networks – the ACTS COBNET Project", Proc. of NOC'97, Part 3, IOS Press, Antwerp, Belgium, p. 25-32, (1997)
- [2] M. Hoffmann, P. Kopka, E. Voges, "Thermo-optical digital switch arrays in silica-on-silicon with defined zero-voltage state", J. of Lightwave Technology, Vol. 16, No. 3, p. 395ff, (1998)
- [3] E. Ollier, P. Labeye, F. Revol, "Micro-opto mechanical switch integrated on silicon", Electron. Lett., p. 2003-2005, (1995)
- [4] L.A. Field, D.L. Burriesci, P.R. Robrish, R.C. Ruby, "Micromechanical 1×2 optical fiber switch", Sens. Actuators A53, p. 311-315, (1996)
- [5] M. Hoffmann, P. Kopka, T. Groß, E. Voges, "All-silicon bistable micro-mechanical fibre switches", Electron. Lett. Vol. 34, No. 2, p. 207-208, (1998)
- [6] M. Bao, C. Burrer, J. Esteve, J. Bausells, S. Marco, "Etching front control of $\langle 110 \rangle$ strips for corner compensation", Sens. Actuators A37-38, p. 727-732, (1993)

An Out-of-Plane Polysilicon Actuator with a Smooth Vertical Mirror for Optical Fiber Switch Application

Makoto Mita, Daisuke Miyauchi*, Hiroshi Toshiyoshi and Hiroyuki Fujita

Institute of Industrial Science, The University of Tokyo

7-22-1 Roppongi, Minatoku, Tokyo 106-8558 Japan

* Address: R&D center, TDK Corporation.

15-7 Higashi Owada 2, Ichikawa, Chiba 272, Japan

INTRODUCTION

Micromachined optical switches are under intensive study for optical communication networks. Some of them require special high-aspect-ratio technologies such as LIGA[1] and deep RIE[2]. Some are a few millimeters in size[3,4]. We have designed a 2x2 micro optical switch which is micro-meters in size, fully micromachined except one step, and has a simple mechanism because of electrostatic actuation.

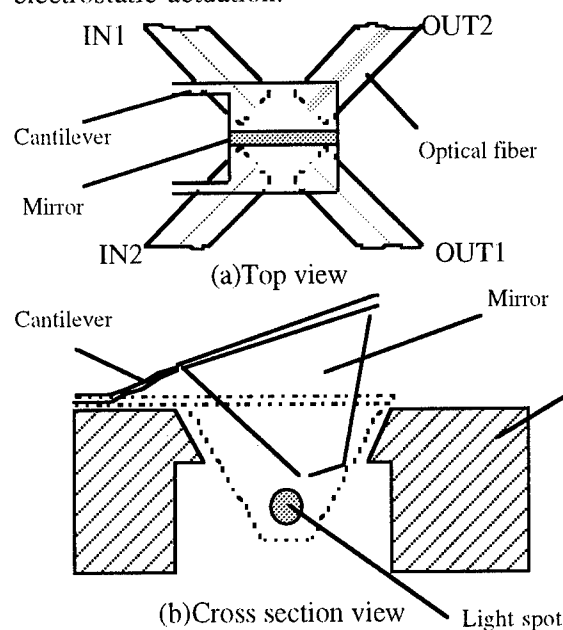


Fig.1 Device schematics

Fig.1 shows the schematic representation of the switch. It is composed of a plate supported by curled cantilevers, a smooth mirror attached vertically to the plate, driving electrodes, and a trench and grooves in a substrate. When the plate is attracted electrostatically to the driving electrodes, the mirror moves perpendicular to the substrate and reflects the light beams from an input optical fiber(IN1) into an output fiber (OUT2); optical fibers are placed in grooves etched in the backside of the substrate. By

removing the electrostatic force, the plate and the mirror move up and the light beam is directly introduced to a fiber(OUT1).

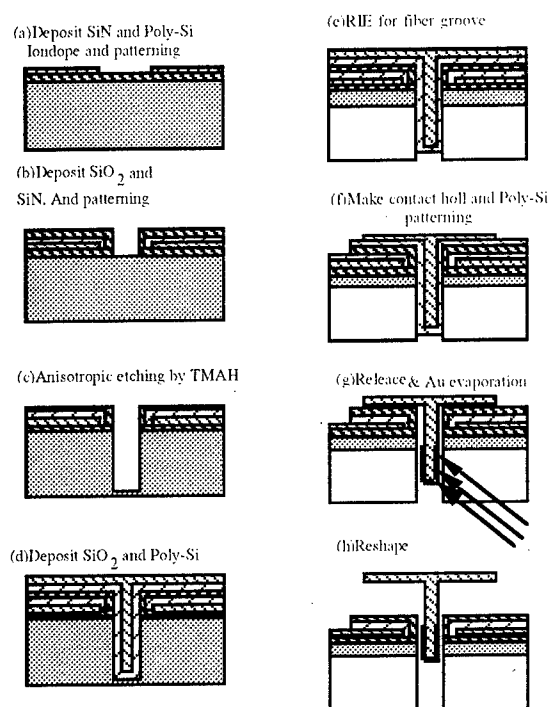


Fig.2 Proposed process flow of optical switch

Fig.2 depicts a possible fabrication process. First driving electrodes are patterned and insulated. The trench was formed by anisotropic wet etching in a (110) substrate and covered by sacrificial oxide. Poly-Si is deposited and patterned in the actuator and mirror. Four grooves are dry etched from the backside. After sacrificial etching, The mirror is metalized by evaporation. Finally, the actuator is raised out-of-plane and held there by plastic deformation caused by Joule heating (reshaping process[5]).

The switch has following advantages:

- (1) The distance between fibers can be as close as a few tens of micrometers,
- (2) fiber alignment is assured by grooves,
- (3) the mirror can be as large as a few

hundreds of microns,
(4) the mirror surface is smooth because it is the replica of a wet-etched (111) plane, and
(5) fabrication can be batch processed except the final reshaping step.

TEST DEVICE

In order to confirm the concept, we have fabricated a test device.

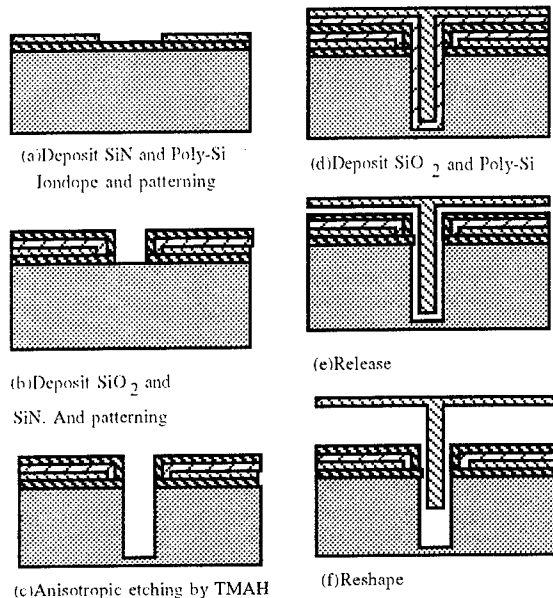
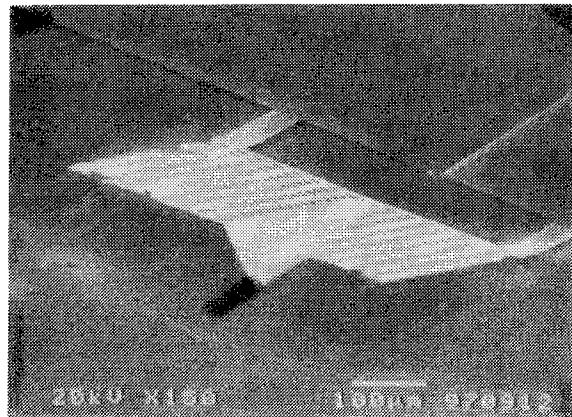


Fig.3 Process flow of the test device

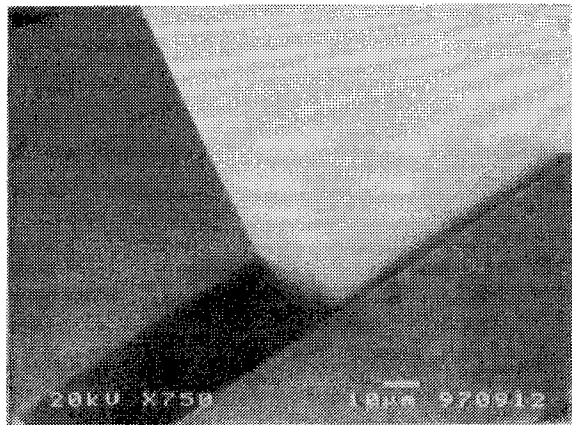
The fabrication process is shown in Fig. 3. First driving electrodes is made by LPCVD of silicon nitride (0.1 μm) and Poly-Si (1 μm) on Si(110) substrate (300 μm). Then patterning the nitride and Poly-Si by RIE. After the electrode is covered by silicon oxide(1 μm) and silicon nitride(0.1 μm),the trench is formed by anistropic etching in TMAH solution. It is 30 μm wide, 500 micrometers long and 170 μm deep. Sacrificial silicon oxide (4 μm) and poly-Si(1 μm) are deposited by LPCVD. Then, the poly-Si is P-ion doped and patterned by RIE to form the plate and cantilevers. After etching the sacrificial oxide by HF, the plate and mirror are raised out-of plane and held there by plastic deformation. The reshaping is done with a current of 20 mA and current duration of 1 minutes.

SEM pictures are shown in Fig. 4. The plate is 500 μm square and 1 μm in thickness. Cantilevers are 400 μm in length and 50 μm in width. The height of the plate edge is 100 μm from the substrate. The characterization of the actuator is under way and will be given in the presentation. Using a simple cantilever which was reshaped, the life-time test was

carried out. We did not observe any failure even after one million cycles of bending operation with electrostatic force.



(a) Reshaped cantilever with mirror



(b) Close up view of mirror and trench
Fig.4 SEM micrograph of the test device

References

- [1] J.Mohr, et al. "Micro Optical Switching by Electrostatic Linear Actuators with Large Displacements" Proc. Transducers-93, pp.120-123
- [2] C.Marxer, et al. "Vertical Mirrors Fabricated By Reactive Ion Etching For Fiber Optical Switching Applications" Proc. MEMS-97, pp.49-54
- [3] R. A. Miller, et al. "An Electromagnetic MEMS 2x2 Fiber Optic Bypass Switch" Proc. Transducers-97, pp.89-92
- [4] Shi-Sheng Lee, et al. "Surface-Micromachined Free-Space Fiber Optic Switches With Integrated Microactuators for Optical Fiber Communication System" Proc. Transducers-97, pp.85-88
- [5] Fukuta, et al. "A RESHAPING TECHNOLOGY WITH JOULE HEAT FOR THREE DIMENSIONAL SILICON STRUCTURES" Proc. Transducers-95, pp.174-177

Optical MEMS

Tuesday, 21 July 1998

TuA: Optical Technology

TuB: Sensors

TuC: Fiber & Integrated Optic Packaging

TuD: Spectral Components

TuE: Poster Session

Tuesday Papers Not Available

- TuA2 Optical Coatings & Microstructures,
*Brian Sullivan, National Research Council of
Canada, Ottawa, Ontario, Canada*
- TuB1 A Micromachined Scanning Confocal
Microscope, *G. S. Kino, Stanford University,
Stanford, CA*

Replicated Plastic Optical Components for Optical Micro Systems

J. Söchtig, M. Rossi and S. Westenhöfer

CSEM Centre Suisse d'Electronique et de Microtechnique SA; Badenerstrasse 569, CH-8048 Zurich, Switzerland; (phone +41 1 492 6350, FAX + 41 1 491 0007, juergen.soechtig@csemne.ch)

H. Schiff

Paul Scherrer Institute Villigen; CH-5232 Villigen, Switzerland

Micro-optical Benches

Micro-optical systems will play an increasingly important role in the fields of communications, optical interconnects, sensing and actuation due to their small size and potential low cost. For free-space micro-optical devices, the concept of miniaturized optical benches has attracted much interest in the last few years. Silicon micromachining technologies have been employed for the fabrication of passive optical components (such as lenses, gratings, beamsplitters and filters) as well as micropositioners (such as translation or rotation stages), often combined with lasers, LEDs or photodetectors as active components [1]. For guided wave micro-optical devices, hybrid assembly of lasers and detectors with photonic lightwave circuits on silicon optical motherboards/benches having etched V- or U-grooves for fiber placement, is also a common approach [2]. In addition to silicon processing technologies, polymers and replication technologies have also been used for the realization of plastic optical platforms [3].

Our approach for passively aligned and low loss coupling of fiber-to-fiber, fiber array-to-array, or lasers / detectors to (single-mode) fibers is schematically shown in Figure 1. A silicon or polymeric platform with built-in alignment features, such as V-grooves, alignment posts or rails, is used for the placement of fibers (or fiber ribbons). Replicated plastic optical components such as diffractive optical elements (DOEs) are used for imaging and inserted into the platform. Specific to the solution is the fabrication of the imaging components as replicated plastic elements with built-in mechanical alignment structures to fit into the complementary features of the micro-optical bench.

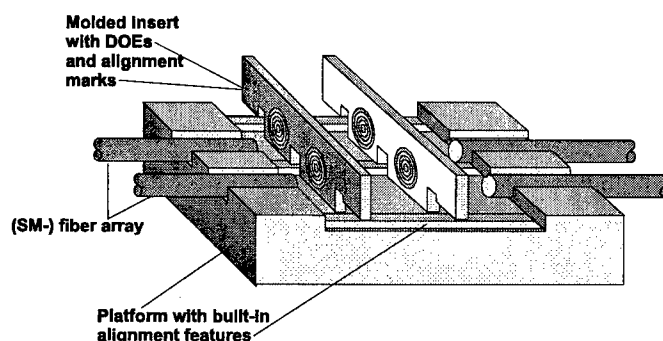


Fig. 1. Optical bench concept.

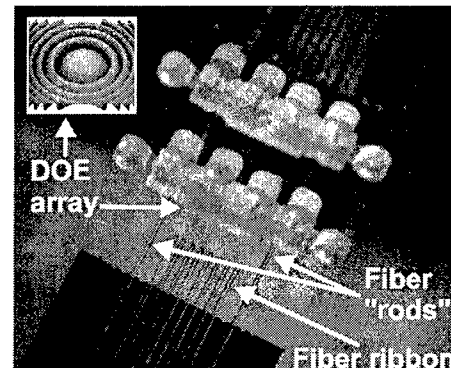


Fig. 2. Photograph of a micro-optical bench arrangement for two opposite fiber array collimators. Fibers are used as guiding "rods".

A fabrication process is presented for polymer inserts in micro-optical benches, which combine the mechanical precision of the LIGA-process with the wide variety of optical functions offered by diffractive optical elements. For this purpose metal masters with laser written continuous surface relief lens elements [4] (see also AFM image of such a lens in the upper left part of Figure 2) and LIGA-structures (metal frames with smooth and vertical sidewalls of 0.5 mm thickness) were used in a combined molding tool. Precision micro-optical elements were replicated with this tool by injection molding (see the two plastic inserts in the bench arrangement of Figure 2). Various positioning schemes and bench arrangements are under development [5]. As an example, Figure 2 shows a micro-optical bench using silicon V-groove arrays for the alignment of fibers, two of them serving as guiding "rods", while the light of the fiber ribbon is imaged by the lenses of the inserts in a collimation arrangement.

Microsystem for Biochemical Analysis

Another important area in which we use replicated plastic optical components is chemical and biochemical sensing. Optical sensor chips based on planar waveguides with coupling gratings are used as miniaturized platforms for measuring and monitoring the values of chemical and physical quantities. Protein sensing layers immobilized at the surface of waveguiding films can bind antibodies with high selectivity from an analyte medium such as blood. The monolayer formation is monitored e.g. by fluorescence detection or registration of effective refractive index changes. Wavelength and refractive index selective waveguide grating couplers transduces these parameter changes into e.g. lateral or angular deflections [6]. Very low-cost processes such as replication and thin film deposition for the fabrication of these optical chips are essential for the large quantities of disposable sensors needed.

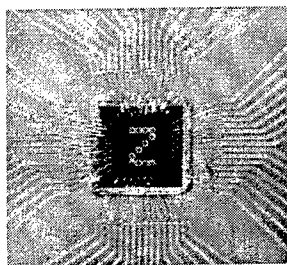


Fig. 3. 8*8 VCSEL array in alphanumeric display mode.

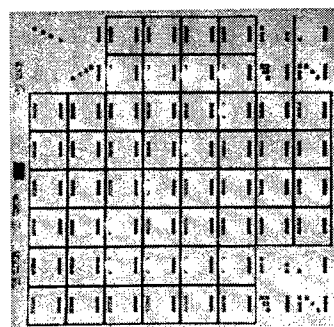


Fig. 4. VCSEL array emission coupled to a sensor pad array with input and output gratings.

We are currently developing hybrid microsystems with individually addressable lasers of 8*8 VCSEL (Vertical Cavity Surface Emitting Laser) arrays (see Figure 3) and replicated waveguide sensors for biochemical analysis arrays. The VCSEL array light sources [7] as well as the replicated waveguide grating coupler sensor arrays are being fabricated and packaged at CSEM. Figure 4 shows 12 out of 64 lasers of the VCSEL array on matrix positions forming the letter "z" imaged to the input coupler gratings of such a sensor pad array.

ACKNOWLEDGEMENTS

The work of K.H. Gulden, R. Lenarcic, M. Moser, and H.P. Schweizer is gratefully acknowledged for developing the VCSEL arrays at CSEM Zurich. Part of this work was supported by the European Union in the framework of the HCM II program and funded by the Swiss Bundesamt für Bildung und Wissenschaft (BBW). Additionally, funding was provided by the Swiss Priority Program MINAST. The authors wish to express their special thanks to Prof. W. Ehrfeld and his team at the Institute of Microtechnology, Mainz (Germany) for support of LIGA related and injection molding work.

REFERENCES

- [1] M.E. Motamedi, M.C. Wu and K.S.J. Pister, "Micro-opto-electro-mechanical devices and on-chip optical processing", *Opt. Eng.*, **36**, 128-1297 (1997)
- [2] T. Hashimoto, Y. Nakasuga, Y. Yamada, H. Terui, M. Yanagisawa, K. Moriwaki, Y. Suzuki, Y. Tohmori, Y. Sakai, and H. Okamoto, "Hybrid integration of spot-size converted laser diode on planar lightwave circuit platform by passive alignment technique", *IEEE Photon. Technol. Lett.*, **8**, 1504-1506 (1996)
- [3] A. Neyer, T. Knoche, L. Müller, R. Klein, D. Fischer and V.A. Yunkin, "Low cost fabrication technology for low loss passive polymer waveguides at 1300 nm and 1550 nm", *Proc. ECOC '93, Montreux 1993*, 337-340
- [4] H.-P. Herzig (ed.) "MICRO-OPTICS: Elements, systems and applications", Taylor & Francis, London, Bristol (1997). Chapter 4: "Direct writing of continuous-relief micro-optics" by M.T. Gale
- [5] J. Söchtig, H. Schiff, B.D. Patterson and S. Westenhöfer, "Replicated diffractive optical lens components for laser diode to fiber coupling in optical bench arrangements", *Proc. SPIE 3226*, 44-55 (1997)
- [6] R.E. Kunz, G. Duveneck and M. Ehrat, "Sensing pads for hybrid and monolithic integrated optical immunosensors", *Proc. SPIE 2331*, 2-17 (1994)
- [7] K.H. Gulden, M. Moser and S. Lüscher, "High performance deep red AlAs/AlGaAs VCSELs for applications in sensing", *Proc. SPIE 2682*, 125-135 (1996)

Micro-optical components for parallel optical networks

Jens Hossfeld, Wolfgang Ehrfeld, Michel Neumeier, Jens Schulze, Lutz Weber, Antoni Picard
Institut fuer Mikrotechnik Mainz GmbH, Carl-Zeiss-Strasse 18-20, D-55129 Mainz, Germany

ABSTRACT

Key components for parallel optical links are fabricated cost-effectively using LIGA technology. Multifiber ferrules and mechanical splices, 1x2 and 4x4 singlemode matrix switches and micro lens arrays with passive alignment structures are presented.

FABRICATION TECHNOLOGIES

Since the assembly is often the most costly part of the manufacture of a micro-optical system, passive alignment methods play the key role in cost reduction. The LIGA technology¹ allows the low cost replication of high precision structures for a large choice of materials. Its first steps lithography and electro-plating can be used to produce inserts for its last step the mass replication, e.g. in polymers. The parts of the tool with lower dimensional accuracy can be manufactured using precision mechanical methods (e.g. micro electro discharge machining² (EDM)).

CONNECTIONS

A central task in parallel optical networks is the coupling of fiber arrays. The mechanical accuracy required in the coupling devices ranges from a few micron in the case of standard multimode fibers to one micron and below for singlemode fibers. The mechanical splice developed at IMM basically consists of an array of rectangular grooves (130 μ m wide and deep) in a PMMA substrate with small PMMA bumps at the groove walls for passive alignment (fig. 1). They are manufactured by hot embossing using a LIGA shim. The snapped in fibers are fixed using adhesive, which works as immersion liquid and fixes a protective cover plate simultaneously. These splices show an excellent insertion loss of 0.06 ± 0.03 dB for standard singlemode fibers.



Figure 1: Mechanical splice structures for singlemode fiber coupling embossed in PMMA.

For push-pull multifiber connections the IMM has designed and built a multifiber ferrule for twelve-fiber-wide ribbon connectors^{3,4} (fig. 2). Fiber positioning inside this ferrule is performed using pairs of elastic V-

grooves, which compensate slight differences in fiber diameters without losing accuracy. With these ribbon fiber connectors insertion loss is kept to only 0.35 ± 0.20 dB for 50 μ m core fibers. They are produced by injection molding. The molding tool contains LIGA inserts for the highest precision front part of the ferrule and wire eroded inserts for the less precise parts of the ferrule body.

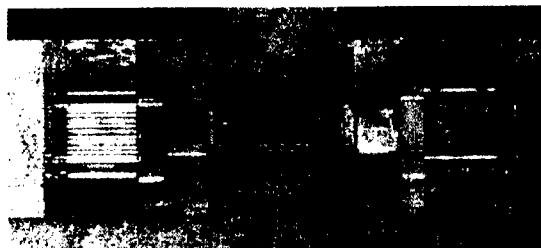


Figure 2: Mold insert for ferrule production consisting of LIGA parts and parts made by EDM.

SWITCHES

For the automatic reconfiguration of transparent networks optical switches are required. Of special interest are 1x2 switches e.g. to bypass a damaged fiber line or NxM matrix switches for rerouting or reshuffling of data lines. Based on a soft magnetic nickel-iron frame a 1x2 fiber moving switch has been realized (fig. 3). The 300 μ m thick main frame was obtained using LIGA technology by a specially adapted electroplating process to yield high fatigue strength under pulsating bending stress. All fibers are guided by exactly positioned polymer auxiliary structures fixed to the central or outer part of the frame respectively.

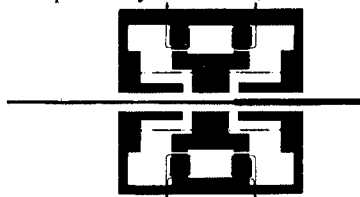


Figure 3: Electromagnetically driven fiber switch.

A very different approach has been realized in the case of the NxM matrix switch⁵ (fig. 4). It consists of a transparent polymer block containing prismatic air cavities. An incident light beam gets deflected at the polymer-air boundary due to total reflection. To switch, an index matched switching body is electromagnetically moved to fill the cavity and the light can pass the cavity without deviation. A liquid film provides optical contact and supports the gliding of the body. This system offers the important benefits that no active optical area needs to be

moved and that switching cells can be combined to compact matrix switches.

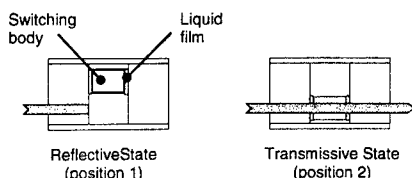


Figure 4: One switching cell of the 4x4 matrix switch

1x2 and 2x2 matrices based on a PMMA matrix and glycerin as immersion liquid have been realized. The outer dimensions of the 2x2 switch are 15x15x7 mm³. The insertion loss is 1.9 dB @ 1310 nm for both the reflective and the transmissive state. Cross talk is below -40 dB and the switching time is about 100ms.

MICRO LENS ARRAYS

Many different fabrication processes for refractive microlens arrays have been developed^{6,7}. Most of them are capable of a cost-effective mass production, but suffer from a lack of cheap passive alignment concepts. Combining the LIGA technology with contactless embossing of microlenses (CEM) the IMM has developed a cost-effective technique for the manufacture of microlens arrays with external alignment structures⁸. In this technique a mounting frame of metal or high melting polymer is fabricated using LIGA technology. It contains the external alignment structures and a set of holes defining the positions for the lenses.

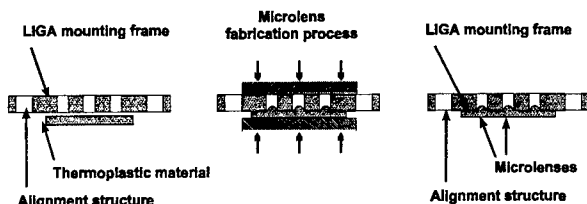


Figure 5: Fabrication process for CEM microlens arrays with external alignment structures.

In the embossing step the thermoplastic lens material is pressed onto the mounting frame forming spherical lenses in the holes due to surface tension without touching the tool (fig. 5). Microlenses of various shape have been produced with diameters from 30 to 700µm and numerical apertures of up to N.A.=0.25. Astigmatic lenses can be obtained if elliptical holes are used. The integration of such a lens array becomes straight forward using the external alignment structure at the LIGA frame for a passive alignment e.g. onto a structured silicon substrate (fig. 6).

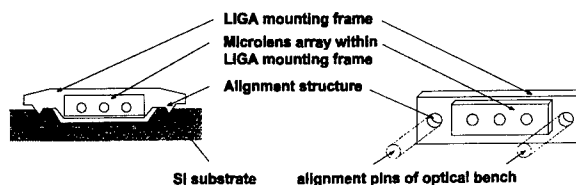


Figure 6: alignment of a microlens array onto a Si-substrate (left) or onto a micro-optical bench (right).

SUMMARY AND CONCLUSION

It was shown that LIGA technology is a powerful tool for the cost-effective manufacture of components for transparent optical networks. It combines the use of mass replication techniques (injection molding and hot embossing) and the ability to produce high dimensional accuracy in the range of one micron for passive alignment concepts. For the presented high performance components - multifiber splice and ferrule, 1x2 and 4x4 switch and the microlens array - different materials had to be structured, e.g. optical and engineering polymers, metals and magnetic alloys. Not at least this flexibility and the fact that the required X-ray-sources become more and more accessible lead to the conclusion that LIGA technology will further speed up the evolution of optical data communication.

ACKNOWLEDGEMENT

This work was financially supported by the German Government within the research project OPTOHYBRID (No. 16SV202/2) and by the European Commission within the ACTS project PLATO (AC041). Furthermore we would like to thank our industry partners for the excellent co-operation.

REFERENCES

- 1: W. Ehrfeld, H. Lehr, Rad. Phys. and Chem. 45(3), 1995, pp. 349-365.
- 2: A. Wolf, W. Ehrfeld, H. Lehr, F. Michel, M. Nienhaus, H.P. Gruber, Proc. of 9-IPES/UME4 97, 26.-30.05.97, Braunschweig, Vol. 2, pp. 657-660
- 3: H.-D. Bauer, W. Ehrfeld, M. Gerner, T. Paatzsch, A. Picard, H. Schiff, L. Weber, Proc. Int. Symp. on Microsystems, Intelligent Materials and Robots (MIMR), Sendai, Japan, 1995, pp. 33-36.
- 4: L. Weber, H.-D. Bauer, F. Michel, A. Picard, W. Ehrfeld, Proc. EUPAC, Essen, Germany, 1994, pp. 104-106.
- 5: M. Neumeier, W. Ehrfeld, J. Jäger, A. Picard, J. Schulze, Proc. SPIE Photonics West 1998, to be published
- 6: Z. D. Popovic, R. A. Sprague, G. A. N. Connell, Appl. Opt. 27, 1988, pp. 1281-1284.
- 7: D. Daly, R. F. Stevens, M. C. Hutley, N. Davies, J. Meas. Sci. Technol. 1, 1990, pp. 759-766.
- 8: J. Schulze, W. Ehrfeld, H. Müller, A. Picard, Proc. SPIE Photonics West 1998, to be published

A fiber-optic tactile microsensor for detection of tip of a fiberscope

O. Tohyama, S. Maeda and H. Itoh

Central Research Laboratory, Mitsubishi Cable Industries, Ltd.

4-3, Ikejiri, Itami-City, Hyogo-Pref., 664-0027, Japan

SUMMARY

A fiber-optic tactile microsensor has been developed and estimated. The sensing principle is based on the detection of optical reflection intensity changes from a diaphragm located in front of an optical fiber. The sensors have been fabricated using silicon micromachining and laser ablation process. For the transmitting source and signal light, a multimode optical fiber 50/125 μm (core/clad) in diameter is used. The results show that easy and safe tactility measurements are possible in blood vessel. This paper describes the structure, fabrication process and performance of the sensor.

INTRODUCTION

Fiber-optic sensors have the advantages of very high resolution and accuracy, small geometry of the sensing element and immunity to electromagnetic interference. In contrast to electronic devices, fiber-optic sensors are potentially very well suited for biomedical applications [1]. In our previous work [2,3], we showed the design, fabrication process and basic performance of an intensity-modulated pressure microsensor. The sensors showed sufficient sensitivity and accuracy.

In the use in thin tubule such as blood vessels, it is very important to detect positions of tip of a fiberscope. If it touches the inner wall, it is necessary to retrace its steps for avoiding perforation. Tactile sensors are essential for fiberscopes [4]. A detailed account of the sensor design, fabrication procedure and testing results is provided.

STRUCTURE OF THE SENSOR

The design of the fiber-optic tactile microsensor is shown in Figure 1. The sensor consists of a diaphragm structure made of a silicon frame and gold/Chromium thin films, and polyurethane tube. For the transmitting source and signal light, a multimode optical fiber 50/125 μm (core/clad) in diameter has been used. The principle of sensing is modulation of the optical reflection intensity by deflection of the diaphragm. Polyurethane tube plays a role of external protection tube of a fiberscope. The wall thickness of the tube is 0.35 mm, and the outer diameter is 2.2 mm. Bosses are formed on the tip of the

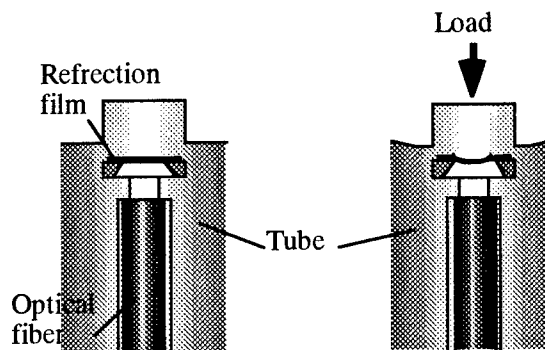


Figure 1: Structure of tactile sensor

polyurethane tube as feelers. The diaphragm structures and optical fibers are filled in outer wall of the polyurethane tube.

FABRICATION

For the diaphragm structures, n-type, (100) orientation, 2-inch silicon wafers with a resistivity of 5.6-7.4 Ωcm and a thickness of 100 μm were used. A silicon-dioxide layer of 0.65 μm was grown in wet oxygen. The gold/Chromium film is deposited by evaporation and is patterned by alignment lines. The wafer on the membrane with UV-curable resin is diced along the alignment lines to obtain individual diaphragm structures. The schematic diagram of laser ablation system is shown in Figure 2.

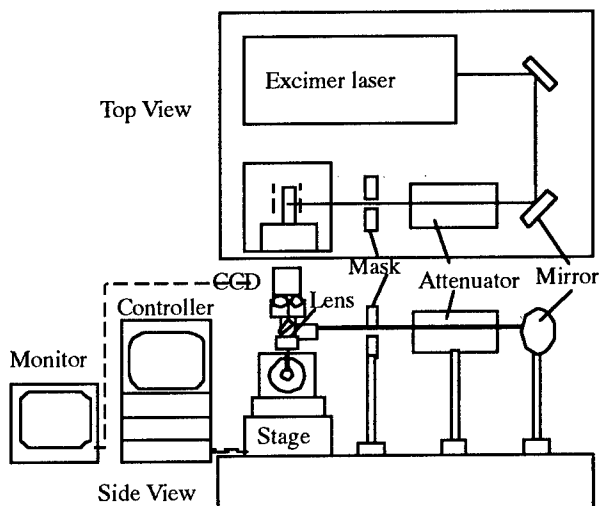


Figure 2: Schematic diagram of laser ablation system

Bosses are fabricated at the tip of the polyurethane tube. Slots for the diaphragm structures and optical fibers are fabricated on the outer wall of the polyurethane tube. All of them are formed by KrF excimer laser ablation ($\lambda = 248 \text{ nm}$). The width and height of the boss are both $200 \mu\text{m}$. The slot is $100 \mu\text{m}$ wide and $350 \mu\text{m}$ long. Finally, the diaphragm structures and optical fibers are inserted in the slots and fixed using UV-curable resin. Figure 3 shows SEM image of the tactile sensor built-in the polyurethane tube.

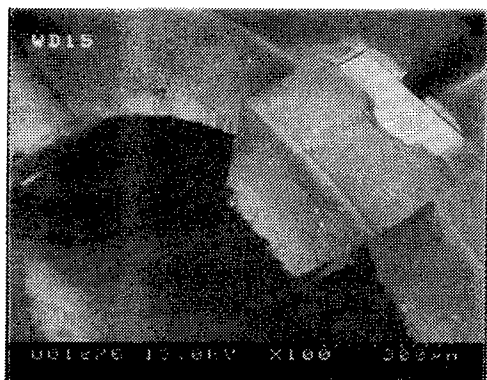


Figure 3: SEM image of the sensor

RESULTS

The optical fiber from the polyurethane tube is attached to a fiber-optic coupler (fused coupler, split ratio=1:1). The light from the source (LED, wave length: $1.31 \mu\text{m}$) is transmitted through the coupler to the sensing element. The light is reflected by the gold diaphragm in the side of the polyurethane tube. The reflected light is returned through the coupler and detected by an InGaAs photo diode. Experimental setup is shown in Figure 4.

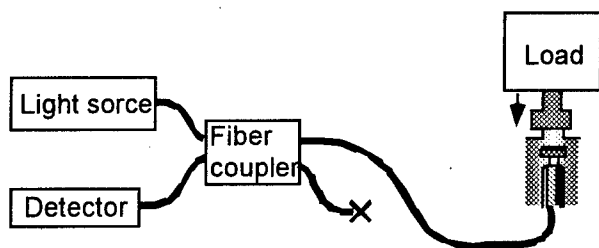


Figure 4: Schematic diagram of experimental setup

Load in the range 0-20 gf is applied to the sensor. Figure 5 shows the performance of the sensor for reflection intensity (triangle) and displacement of the tip of the boss (square) under different loads. This shows that reflection intensity and displacement varies in proportion to the loads. This figure shows that the average

sensitivity of the sensor is 0.9 nW/gf .

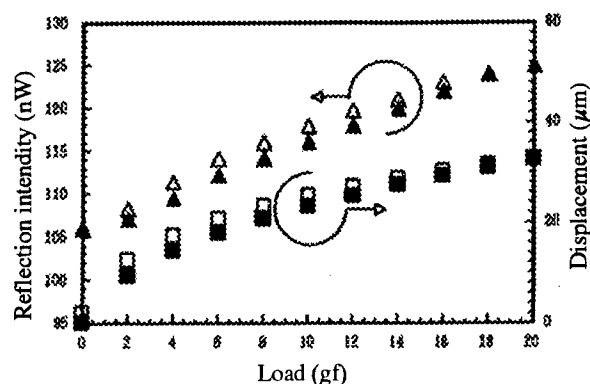


Figure 5: Relationship between load and reflection intensity and displacement

CONCLUSION

We have developed fiber-optic tactile microsenors. The results show that easy and safe tactility measurements are possible in narrow tubule such as blood vessel. We thus conclude that the fiber-optic tactile microsensor that we have developed can be applied to a wide range of medical applications such as minimally invasive surgery and microsurgery.

ACKNOWLEDGMENTS

A part of this work was performed by Mitsubishi Cable Industries, Ltd. under the management of the Micromachine Center as Industrial Science and Technology Frontier Program, "Research and Development of Micromachine Technology", of MITI supported by New Energy and Industrial Technology Development Organization.

REFERENCES

- [1] L. Tenerz, B. Hök and T. Engström, "0.5 mm Diameter Pressure Sensor for Biomedical Applications", Proc. Transducers'87, pp.312-315, June 1987
- [2] O. Tohyama, M. Kohashi, K. Yamamoto, H. Itoh, "A fiber-optic silicon pressure sensor for ultra-thin catheters", Sensors and Actuators, A54, pp. 622-625, 1996
- [3] O. Tohyama, M. Kohashi, M. Sugihara, H. Itoh, "A fiber-optic pressure microsensor for biomedical applications", Sensors and Actuators, A66, pp. 150-154, 1998
- [4] S. Maeda, K. Minami, M. Esashi, "Excimer laser induced CVD and its application to selective non-planar metallization", J. Micromech. Microeng., 5, pp.237-242, 1995

High Temperature Operation of Optically Resonant Microbeams

W.R. Herb, J.D. Zook, M.L. Wilson and C.J. Bassett
Honeywell Technology Center, 12001 Hwy. 55, Plymouth, MN 55441

I. Introduction.

Micromachined resonant microbeams are sensitive strain transducers that provide a basis for high performance temperature, pressure, strain, and acceleration sensors. Microbeams excited optically by an optothermal mechanism [1-3] or a photovoltaic mechanism[4-6] can provide the basis for fiber optic sensors which combine the advantages of silicon micro-fabrication with those of optical fiber communication. Work at Honeywell[4-6] is based on polysilicon microbeams integrated monolithically into single crystal silicon microstructures, sealed in high vacuum shell enclosures which enable high mechanical Q values at frequencies in the several 100kHz range. They can be driven by modulated light or can be self-resonant[5]. The vibration of the beam modulates the light reflected back into the fiber, which is then detected using a photo-detector. A network of 16 optically resonant microbeam temperature sensors driven by the same laser has been demonstrated[6].

Many potential applications for fiber optic based sensors involve harsh environments, including EMI, chemicals, and high temperature. Fiber optic sensors also have advantages for aerospace because of their light weight and EMI immunity. The highest previously reported operational temperature for a resonant microsensor is 150C in a sensor designed to go to 450C[2]. The present paper describes the high temperature operation of an optically resonant microbeam sensor at temperatures up to 520 C.

II. Device Fabrication and Packaging. The resonant microbeams are fabricated using

polysilicon as the structural material and low temperature oxide as the sacrificial layer, and require six masking steps. For the temperature sensor device discussed, two mask layers are used to form the cantilever paddles in the single crystal silicon substrate. A final mask is used to etch the round die alignment features using a deep RIE process. The completed temperature sensor is all silicon, with the exception of a thin silicon nitride anti-reflection coating. This structure yields a temperature sensor with a sensitivity of approximately 50 Hz/C. This sensitivity may be increased by sputtering another material on the cantilever paddle to increase the bimorph effect[6].

The completed wafers are tested at the wafer level, diced, and packaged. The present die are packaged with a single resonator aligned to a single multimode fiber at normal incidence. The fiber is automatically aligned to the center of the microbeam using the round alignment feature etched in the silicon die, which mates to a precision bore pyrex tube, as shown in Figure 1. This sub-assembly may be tested as is, or packaged further in a metal can or probe.

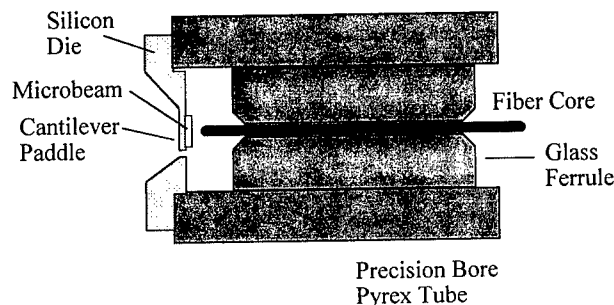


Figure 1. Partially packaged resonant microbeam temperature sensor. The silicon die fits into the precision bore pyrex tube with 5-10 μm clearance.

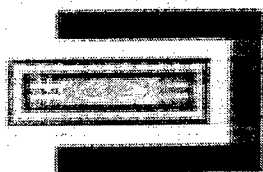


Figure 2. Optical micrograph of a resonant microbeam temperature sensor. The rectangle is the polysilicon resonator in its integral vacuum enclosure on the cantilever paddle. The dark space is the etch pit which separates the paddle from the rest of the chip.

III. Test Results.

The temperature sensor device was tested in a thermal well installed in a high temperature oven with a RTD temperature pickup. The sensor was driven with a 3mW 780 nm laser diode through a single multimode fiber and a commercial 2 x 2 splitter. About 1mW is incident on the chip. The modulated light reflected from the sensor was detected and fed to a spectrum analyzer and/or a gain/phase analyzer, enabling measurements such as those shown in Figures 3 and 4. The device maintained a reasonable signal level up to 450 C. Above 500 C, degradation of the signal was observed, with an apparent loss of Q, as shown in Figure 4. The drift rate of the sensor also increased markedly above 450 C, from a few hundred Hz/day to a few thousand Hz/day. As the temperature was lowered back below 450 C the signal level and Q returned, but with a frequency offset of several kHz.

Several operating regimes were observed over the temperature range tested. Between 360C and 420C the device was self-resonant, requiring no modulation of the laser to produce a strong modulated frequency peak. At other temperatures, the self-resonant behavior disappeared, and the sensor was interrogated by modulating the laser. The base frequency and temperature sensitivity showed no significant deviations from monotonic behavior in transitioning from the self-resonant to the driven mode.

After a number of days of operation at high temperature the polymer parts of the package including the cladding of the optical fiber had disintegrated, but alignment was maintained and the silicon chip was unaffected, except for the color of the anti-reflection coating, which presumably oxidized during the long time at high temperature.

IV. Conclusions.

An all-silicon, optically interrogated sensor has been demonstrated with potential for reliable operation at 450C. The operation of a simple temperature sensor is reported here, however the basic high temperature resonant strain gage technology may be extended to other applications, notably pressure sensing[2,4]. Challenges exist in further developing this sensor technology. The variation of the

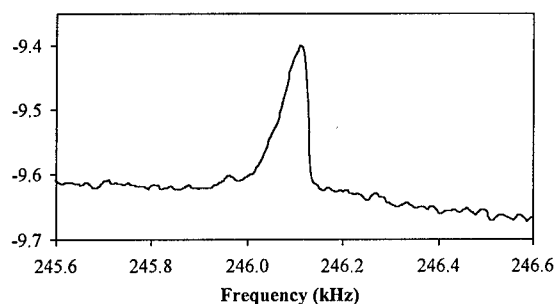


Figure 3: Measurement of the resonance peak 252 C. The device has a room temperature frequency of 255 kHz and a Q of about 10,000.

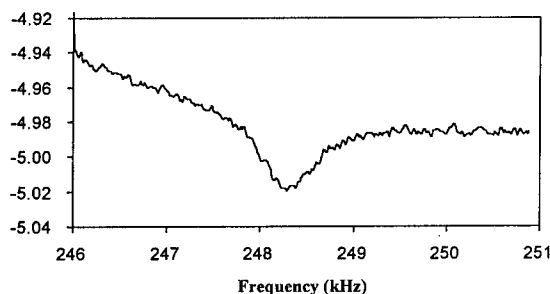


Figure 4: Measurement of the resonance peak at 522 C. The device Q has degraded to approximately 300 and the phase has changed sign with respect to the drive signal.

refractive index of silicon with temperature complicates the optical design of the

resonator. More detailed characterization of the sensors will be required to verify the drive mechanism and to determine the high temperature mechanical properties of silicon and achievable sensor stability. Packaging for high temperature operation will also require substantial work.

References

1. R.M.A. Fatah, et al, *Sensors and Actuators* **A33**, 229-236 (1992) and references therein.
2. D. Angelidis, et al, *Optical Engineering* **31**, 1638-1642 (1992).
3. A. V. Churenkov, *Sensors and Actuators* **A39**, 141-148 (1993).
4. D.W. Burns, et al, *Sensors and Actuators* **A48**, 179-186 (1995).
5. J.D. Zook, et al, *Sensors and Actuators* **A52**, 92-98 (1996).
6. M.W. Wilson, et al, *Proc. SPIE* **3007**, 92-99 (1997).

**Integrated micro-displacement sensor that can be incorporated
into mini 3-dimensional actuator stage**

Renshi Sawada, Eiji Higurashi, Takahiro Itoh, and Mieko Tsubamoto*

NTT Opto-electronics Laboratories

*NTT Advanced Technology Corporation

3-9-11 Midori-Cho, Musashino-Shi, Tokyo, 180-8585, Japan

Telephone: +80 422-59-2456

Fax: +80 422-59-2961

An integrated optical micro-displacement sensor has been developed that uses the beam diverging from a laser diode. It can measure the distance traveled relative to an external reflective mirror. The measurement resolution is as low as of the order of $0.01 \mu\text{m}$. It is 0.5 by 0.5mm . Three of these sensors can be incorporated into the 7-mm-cubic space of a 3-dimensional actuator stage to obtain the displacements in the x, y, and z directions.

As shown in Fig. 1, this sensor basically consists of a laser diode, monolithically fabricated photodiodes, and a fluorinated polyimide waveguide for converging the light beam. This is fundamentally the same composition as previously reported for a micro-encoder. After being reflected by the external mirror, the beam diverging from the etched mirror of the laser diode is detected by two photodiodes adjacent to the laser diode. The "inner" photodiode is the one nearer the waveguide, and the "outer" photodiode is the other one. The outer photodiode is used to calibrate the signal gain. The ratio of the gradients in the displacement-output voltage curves can then be made constant for both photodiodes, which eliminates the reflectivity effect of the external mirror. The divergence angle of the beam emerging from the waveguide is controlled by the curvature of the edge in the plane direction. Because this sensing principle is based on the divergence of a light beam emerging from a waveguide, alignment to the external mirror is easy compared to using a laser displacement sensor including Michelson interference.

The relationship between the displacement of the external mirror and the voltage output by the photodiodes is shown in Fig. 2. In the displacement-output curve there are two linear regions, one in the front region and one in the back region. In the vicinity of the sensor edge, there is linearity with a large gradient. Far from the edge, the noise is greater because the beam diverging perpendicular to the sensor-chip plane is picked up by the photodiode inside the chip. The relationship between the measurable range and the resolution is shown in Table 1. The resolution is determined by N_{FWHM}/G and by the linearity of the displacement-output voltage curve (N_{FWHM} is the full width at half maximum of the noise and G is the gradient of the displacement-output voltage curve). If a region with good linearity is chosen, the resolution is almost the same as N_{FWHM}/G . For a sensor with a long focus (Type A), the smallest resolution obtained is 10 nm with a range of $15 \mu\text{m}$.

A three-dimensional actuator stage consisting of a cubic stage with a hinged structure and of actuators with cantilevers for magnifying the piezoelectric displacements, into which three sensors are to be incorporated, is shown in Fig. 3. The signals fed back by the sensors complement the hysteresis of the piezoelectric actuator.

This integrated optical micro-displacement sensor actively uses the beam diverging from a laser diode and can be easily positioned, while the previously reported micro encoder can only be used under the condition of a constant gap relative to the grating scale, so the beam divergence is not as critical. Both sensors are suitable for incorporation into a micro-actuator, although their measuring directions differ.

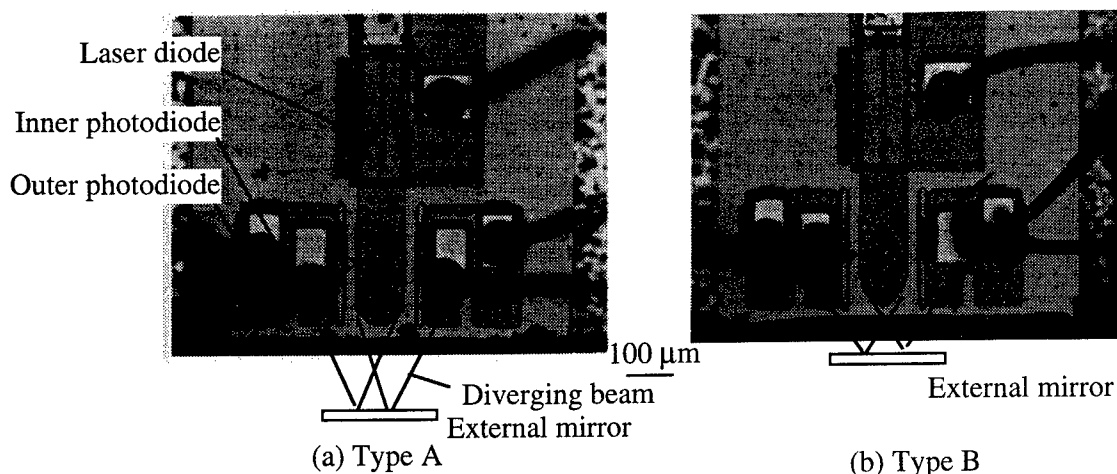


Fig. 1 Microphotographs of micro-laser displacement sensor consisting of a laser diode, monolithically fabricated photodiodes, and polyimide waveguides: Type A, long focus, and Type B, short focus.

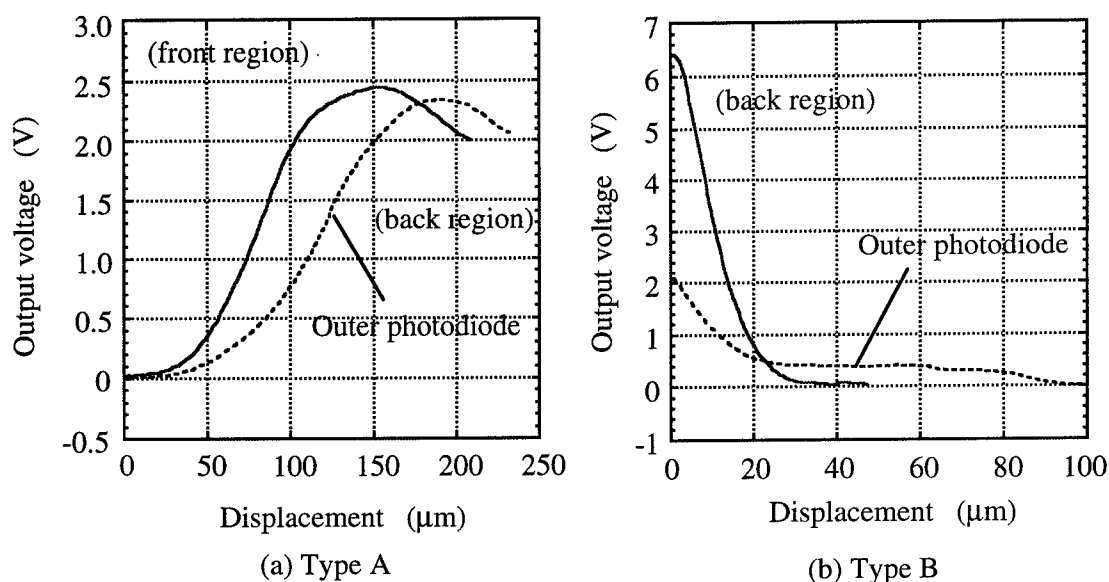


Fig. 2 Relationship between displacement of external mirror and voltage output by photodiodes.

Cantilever magnifying the piezoelectric displacement Region where sensors are to be installed

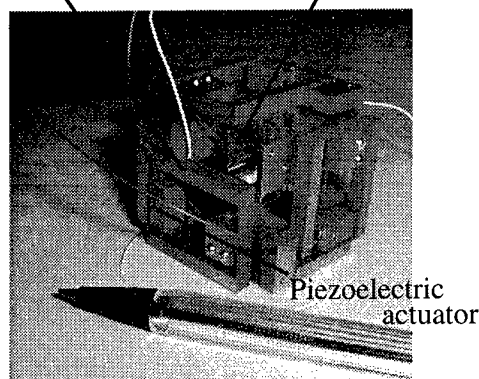


Table 1 Relationship between measurable range and resolution.

Type	Linear range	Resolution
A	19.5 μm	100 nm
B	13 μm	9 nm

Fig. 3 Three-dimensional actuator stage into which three sensors are to be incorporated.

TuB5

11:45am - 12:00noon

Micro-Mechanical Optoelectronic Switch and Amplifier (MIMOSA)

Richard Waters, Jim Patterson* and Bart Van Zeghbroeck

Department of Electrical Engineering and the Optoelectronic Computing Systems Center

University of Colorado at Boulder, Boulder, CO 80309-0525

watersrl@colorado.edu, (303) 492-0581

We report for the first time the monolithic integration of a micro-mechanical modulator and a p-n photodiode on a silicon substrate. Such a structure can be used as a wavelength tunable detector [1] and as a versatile Optoelectronic device. In addition, we also demonstrate that such a device combination yields a transistor-like element with positive and negative small-signal voltage gain.

The MIMOSA structure was fabricated on an n-type 10^{15} cm^{-3} phosphor doped (111) oriented silicon wafer. The wafer was oxidized in water vapor at 950 °C for 8 hours yielding a 0.97 μm thick thermal oxide. Wet etching in KOH was used to undercut the silicon dioxide structure shown in Fig.1a and Fig.1b. Figure 1a is a 3-D drawing of the MIMOSA showing the undercut oxide and relevant features of the device. The high selectivity between the (110) and (111) planes in KOH allowed the SiO_2 platform to be undercut while controlling the airgap distance in the (111) direction. Boron was then diffused into the silicon yielding a p-type layer underneath the platform. A 10 nm layer of gold was thermally evaporated onto the top surface of the silicon dioxide platform creating the upper mirror of a Fabry-Perot modulator. The air-silicon interface acts as the lower mirror. The light transmitted through the Fabry-Perot modulator is absorbed in the underlying p-n diode. The final MIMOSA structure consists of a 50 μm by 50 μm platform supported by 4 beams of length 65 μm and width 10 μm . An SEM Micrograph of the fabricated device is shown in Fig.1b. The structure shown has an oxide thickness of 0.63 μm , airgap distance of 1 μm , and p-n junction depth of 1 μm .

The MIMOSA was tested by applying 1 mW of optical power from an 830 nm semiconductor laser to the modulator. The modulation characteristic of the device is shown in Fig.2. The modulation curves were measured by increasing the voltage on the top mirror, V_c , while keeping the p-n junction at a constant reverse bias. The change in photocurrent with voltage is consistent with a quadratic displacement of the SiO_2 platform caused by a capacitive electrostatic force between the top mirror and the silicon below. The bottom of the platform makes contact to the silicon surface at 7.36 volts, thus causing the photocurrent to remain constant as the voltage is increased further. The photocurrent versus photodiode voltage was measured while applying stepped voltages to the top mirror yielding the transistor-like I-V characteristics shown in Fig. 3, 4. The device in Figure 4 is similar to the device depicted in Figures 2, 3, and 5 except exhibiting a higher on/off ratio of approximately 3:1. The transfer characteristics of the device, biased with a 35 μA current source, illustrate that the device possesses both positive and negative small signal voltage gain with a gain of 75 occurring at 6.9 volts. The complete transfer characteristic is shown in Fig. 5. with the bottom of the platform once again making contact to the underlying p-type region at 7.36 volts. A maximum small signal voltage gain of 500 has been obtained thus far for a similar device structure.

In summary, we have successfully fabricated a micro-mechanical modulator integrated together with a p-n photodiode on a silicon substrate. We demonstrated that the device possesses transistor-like characteristics as well as positive and negative small signal voltage amplification. An on/off ratio of 3:1 and a small signal voltage gain of 500 have been obtained.

[1] G.S. Li et. al., Proc. 55th DRC, paper IV.B.5, Fort Collins, CO, June 24,1997.

* Also with NASA, Langley Research Center, Hampton, VA, 23681-0001.

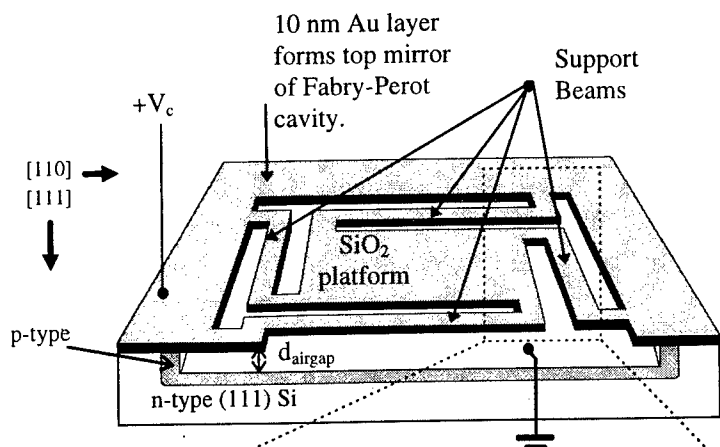


Fig. 1a. Structure of the completed device. Drawing is a 3-D schematic of the MIMOSA showing the relevant crystallographic directions and airgap distance, d_{airgap} . Also indicated on the drawing are the four supporting legs and the suspended SiO_2 platform.

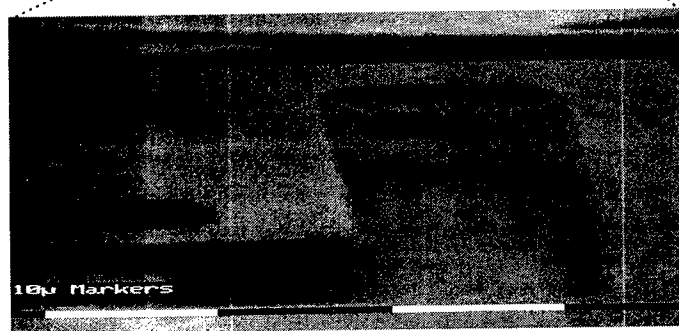


Fig 1b. SEM micrograph of the region indicated in Figure 1a. The SiO_2 platform is $50\text{ }\mu\text{m}$ by $50\text{ }\mu\text{m}$ and has a thickness of $0.63\text{ }\mu\text{m}$. The four supporting legs are $65\text{ }\mu\text{m}$ long and $10\text{ }\mu\text{m}$ wide. The airgap spacing is $1\text{ }\mu\text{m}$.

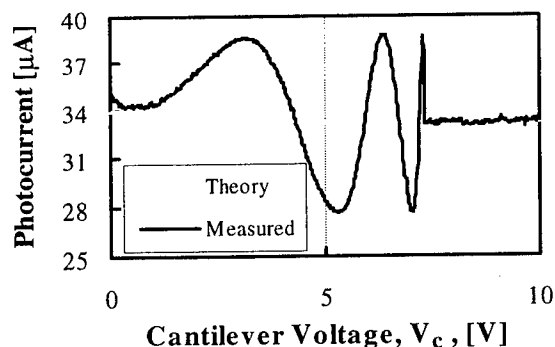


Fig 2. Photocurrent versus cantilever voltage at $V_{\text{pd}} = 5\text{ V}$.

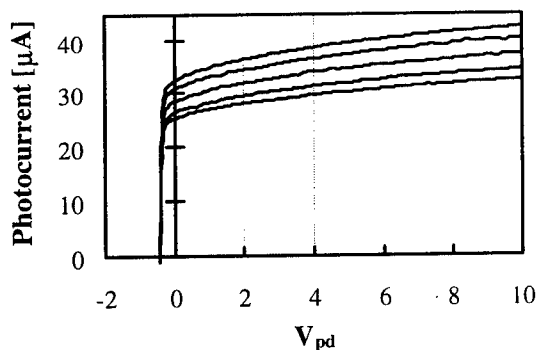


Fig 3. Photocurrent versus diode voltage at $V_c = 5.6$ (bottom curve), 5.75 , 5.9 , 6.05 , and 6.2 V (top curve).

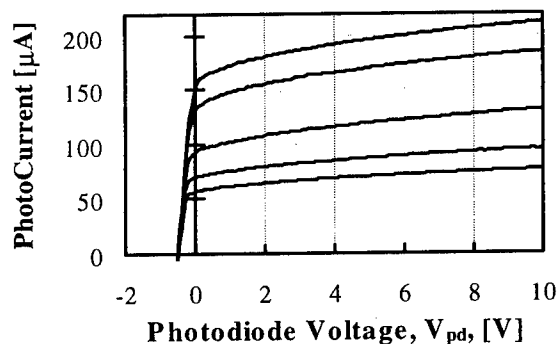


Fig 4. Photocurrent versus diode voltage at $V_c = 4.1$ (top curve), 4.35 , 4.6 , 4.85 , and 5.1 V (bottom curve).

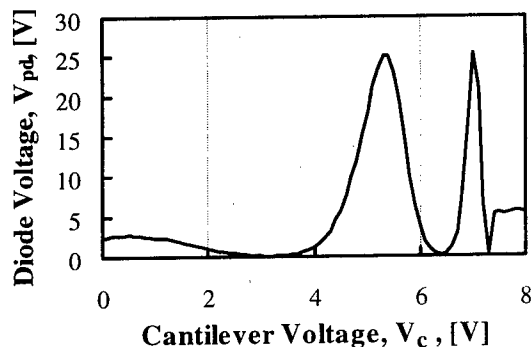


Fig 5. Transfer characteristics of the MIMOSA biased with a $35\text{ }\mu\text{A}$ current source. The voltage gain of the device is 75 at $V_c = 6.9\text{ V}$.

TuC1 (Invited)
1:30pm - 2:00pm

Integrated Optics for WDM

Alice E. White, John V. Gates, Allan J. Bruce, Mark A. Cappuzzo,
Louis T. Gomez, Charles H. Henry, Edward J. Laskowski, Christi K. Madsen,
Dirk J. Muehlner, Ron Scotti, and Joseph Shmlovich
Bell Laboratories, Lucent Technologies
Murray Hill, NJ 07974

ABSTRACT

It is clear that WDM has arrived, that the trend is to more and more wavelengths, and that integrated optical components are going to be critical to future system developments. The opportunities and challenges for these devices will be discussed.

The drive to higher and higher network capacity has come in part through deregulation, but also from demand for internet access, telecommuting, and broadband services. Historically, in order to meet that demand, the service providers used higher transmission rates, but now there is a clear trend toward WDM, which has some significant advantages. In the future, there will be more wavelengths, higher bit rates, and more powerful amplifiers. Moreover, systems will evolve from WDM transport to WDM networks as first fixed and then reconfigurable add/drop are incorporated. If the switching can be done in the optical layer, then it is possible to have true wavelength routing and a reconfigurable network. To implement this vision, we will need a large number of sophisticated optical components. Some of the opportunities for integrated optical components include: WDM sources, optical mux/demux, wavelength conversion, flatband filter response for concatenation, reconfigurable add/drops, optical cross-connects, and wavelength alignment of sources, routers, cross-connects and receivers. Some of the challenges include polarization independence, flat filter response for concatenation, and low cost manufacturing and packaging. Integrated optical devices fabricated using silicon optical bench (SiOB) technology are already having major impact in several of these areas.

As far as the devices mentioned above as challenges are concerned, there are several competing technologies for implementation. There are bulk-type devices (such as MEMs devices and thin film filters), fiber-type devices (such as fiber couplers) and planar-type devices (such as silicon optical bench or monolithic devices) that can provide some or all of the desired functionality. Planar integration has a number of advantages including compactness, which is particularly important when an invention leaves the lab and goes into the field where there is a limited amount of space on the board. When complex functions are integrated in a planar geometry, reduced cost is achieved with batch processing of wafers and fewer manual interconnections. Finally, fabricating optical circuits using photolithography allows design of components with numerous optical paths, such as the star coupler. The silicon wafer can be used as a platform to attach lasers and detectors as well—hence the name “silicon optical bench” for this technology. Silicon optical bench technology leverages off the silicon IC industry for low cost, high quality flat substrates as well as processing developments and equipment.

The waveguide grating router (WGR), which can be used as a passive multiplexer or demultiplexer for WDM systems, was first proposed around 1990 (for a review, see [1]). Since then, the router has undergone significant refinement. Eight and sixteen channel routers are commercially available, 40 channel routers are in the prototype stage and a research demonstration of a 64 channel router has

been published by NTT [2]. One important characteristic of a router is the flatness of the passband. This becomes an issue as routers are cascaded. At low channel counts, filters made using thin film dielectric stacks may have comparable performance with lower loss, but the loss in these serial devices increases roughly linearly with the number of wavelengths.

Since the primary cost in a silicon optical bench device is the packaging, particularly the fiber attachment, it is cost-effective to pack as many functions as possible onto a chip. With this goal in mind, we are developing the technologies to fabricate devices that incorporate thermo-optic (TO) switches and UV-induced Bragg gratings [3,4]. In combination with WGRs or gratings, TO switches can be used to create, for instance, reconfigurable add/drop demultiplexers and eventually, perhaps, an optical cross-connect. Currently, the competition here are lithium niobate and fiber grating devices.

One of the most exciting applications of silicon optical bench comes in the access arena, where the cost of the optics, both at the central office and at the living unit, is a barrier to fiber-to-the-home (FTTH) systems. Silicon optical bench packaging provides a path to a low cost transceiver to do the optics-to-electronics conversion in the optical network unit that would be on the side of a home in an FTTH system. A photograph of such a device is shown in Fig. 1. The optical components, including a coarse WDM splitter, 1.3 μ m PIN receiver, expanded beam laser and PIN monitor, as well as 1.55 μ m reversing element, are all integrated on a single chip [5]. At high volumes, such PLC-based subsystems are expected to be more cost-effective than micro-optic solutions. Eventually, these devices may be monolithically integrated in InP, but commercial realization of such a device is still in the future.

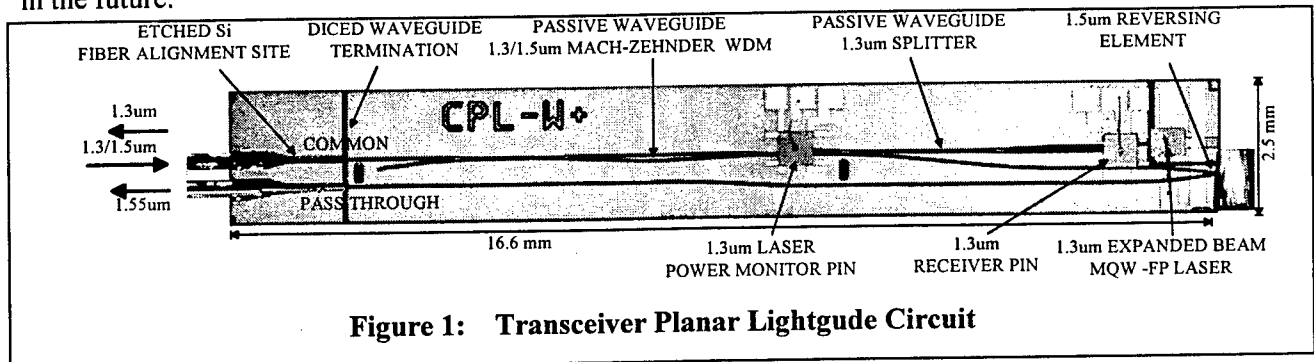


Figure 1: Transceiver Planar Lightguide Circuit

In summary, WDM has arrived. Long distance point-to-point WDM transmission systems are now being deployed. Next generation WDM networks will require photonic and opto-electronic integration with greater functionality *and* reduced cost. Manufacturability of these complex components is a critical issue that needs to be taken into consideration when weighing the alternatives.

References

- [1] Yuan P. Li and Charles H. Henry, "Silicon Optical Bench Waveguide Technology" in Optical Fiber Telecommunications vol. 111B (Academic Press: New York) p. 319 (1997).
- [2] Okamoto, *et al.*, Electron. Lett. **31**, p. 184 (1995).
- [3] Scotti, *et al.*, OFC '98 Technical Digest, p. 142 (1998).
- [4] Madsen, *et al.*, to be published in the Proceedings of the IPR '98 Conference.
- [5] Gates, *et al.*, to be published in the Proceedings of the 48th ECTC, Seattle, May 1998.

Microsystems for Three Axis Active Fiber Alignment

Robert L. Wood, Vijay R. Dhuler, John M. Haake*, Allen B. Cowen

MEMS Technology Application Center, MCNC
3021 Cornwallis Road, RTP, NC 27709
E-mail: rwood@mcnc.org

*Nuvonyx Inc.
3753 Pennridge Drive, Bridgeton, MO 63044

We report on development of novel Microsystems capable of three-axis active in-package fiber alignment with submicron tolerances. Existing procedures for aligning fiber optics and micro-optics are very labor and capital intensive. The packaging of individual single mode opto-electronic components currently dominates the photonic device product cost, limiting their implementation in the market place. Solutions for passive alignments with tolerances of few microns (not adequate for single mode coupling) have been demonstrated. Researchers^{1,2} have reported active alignment strategies that either are not fully integrated or do not provide alignment in three axes. Also, it is desirable to glue the devices in place once they are actively aligned, which has not been demonstrated before. Microsystems presented here are batch fabricated using a combination of silicon micromachining and LIGA. A novel actuation mechanism is used to produce the high force and displacement necessary to overcome friction, fiber bending moment, counter force springs, and wire bonds.

Three designs ³(Figs. 1-3) have been fabricated and tested. Each design provides a platform for holding the fiber using a V-Groove or a LIGA channel. The platform is moved with respect to a fixed reference provided either internally or externally to the silicon chip. In-plane thermal actuators either on the movable platform or on the fixed base move the platform and hence the fiber in two axes. A nickel-silicon thermal bimorph actuator lifts the platform out-of-plane. For design 1 the silicon platform is supported by four springs and a frame on two fixed mounts that are attached to an external base. In-plane actuators on the platform push against the frame and move the chip in two axes. Design 2 uses an external housing for reference, with in-plane actuators acting against counter force springs slide the stage in two axes. Design 3 represents the most integrated of the three designs and provides the reference on the fixed base. The platform is separated from the base by channels formed via bulk silicon etching, and is supported by four LIGA-defined springs. The fiber is attached to the platform using LIGA-defined channels. In-plane actuators on the fixed base push the platform in two axes. Designs 2 and 3 include the thermal bimorph to lift the platform out-of-plane. Devices presented here have not been fully optimized for size, and significant chip size reduction looks feasible. All designs proved capable of providing sufficient force and accuracy for submicron fiber alignment.

Fabrication of the fiber aligner begins with patterning of LPCVD silicon nitride layer on both sides of the wafer to define the movable stage. Micromachined layers are then patterned on the surface to form the thermal isolation structures and microheaters for the thermal actuators. A thick electroplated nickel layer is patterned using the LIGA technique. This step relies upon synchrotron-based deep X-ray lithography, provided by the Center for Advanced Microstructures and Devices (CAMD) at Louisiana State University (Baton Rouge, LA). Following LIGA patterning, the movable portions of the nickel structure are released via sacrificial etching. The silicon is then subjected to anisotropic etching to cut away the stage portion of the aligner chip. At this point, the stage is suspended by nickel springs defined in the LIGA layer and is responsive to positioning via the three microactuators.

Figures 4-5 show the measured performance of in plane actuation⁴. Out-of-plane actuation of the platforms have been measured to be over 100 μm at 0.4 W. Figure 6 shows the experimental setup and demonstration for two-axis alignment including oscilloscope display of actuation and detector signals. Figure 7 shows the mechanical frequency response for design 1. Operation of over 10 million actuation cycles without failure have been demonstrated. At present, design 3 has been successfully tested for three axis motion.

References:

1. Li Fan *et al.*, Transducers 97 Technical Digest, Vol. 1, p. 319.
2. R. Jebens, *et al.*, Sensors and Actuators, 20 1989, pp. 65-73.
3. Patenting in progress
4. J. Haake *et al.*, to appear in Photonics West 98.

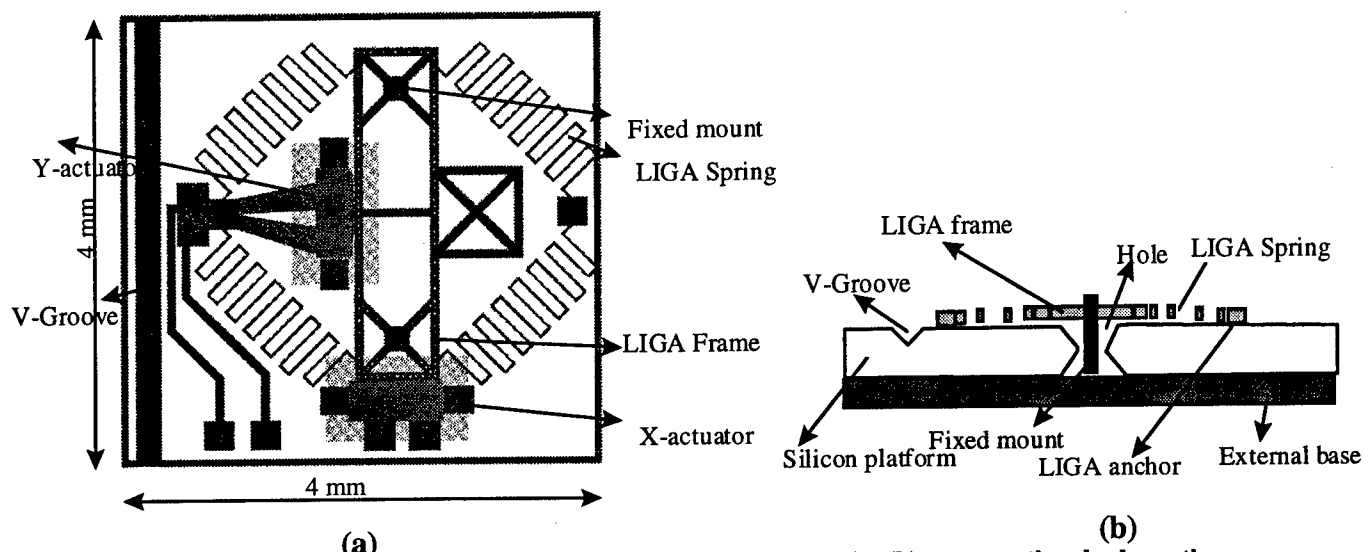


Figure 1. 2-axis In-package micro aligner (Design 1): (a) plan view schematic; (b) cross-sectional schematic

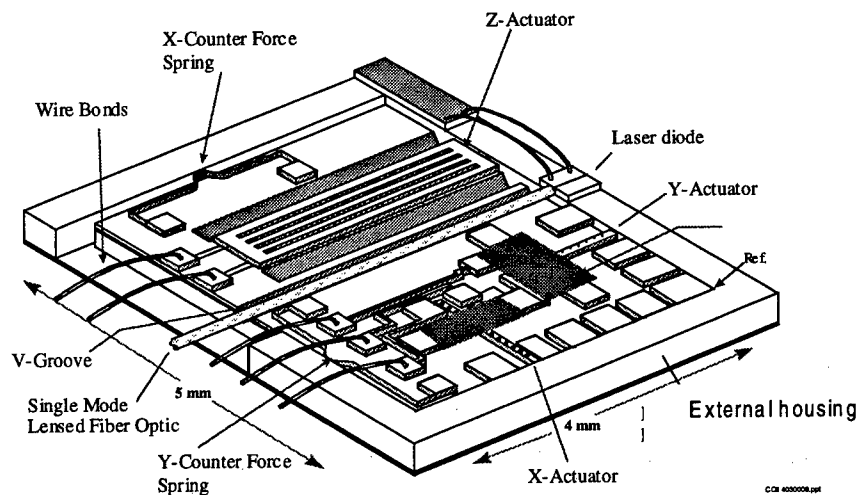


Figure 2. 3-axis In-package micro aligner (Design 2)

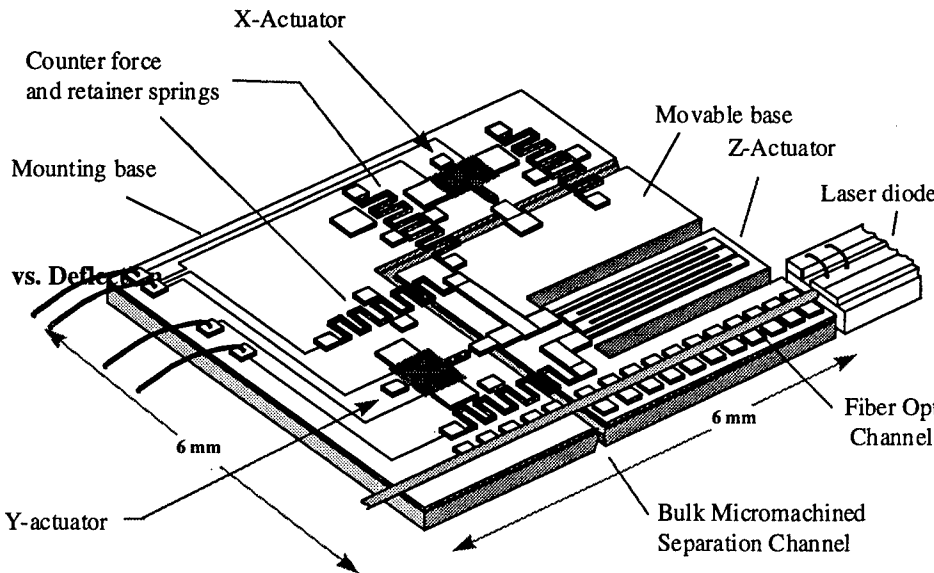


Figure 3. Mounted 3-axis in-package micro aligner (Design 3) actuation

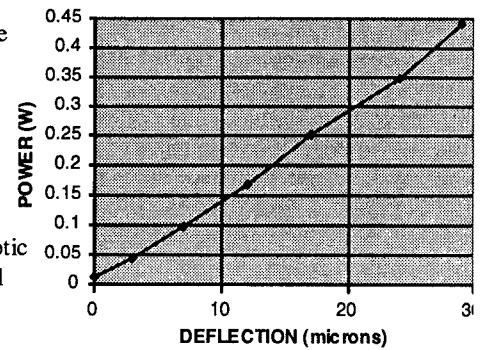


Figure 4. In-plane thermal

- * 240 micron Diameter Polyimide Coated fiberoptic
- * Fiber optic Length = 11mm
- * Forced measured at 5 μ m back deflection of actuator at each power level

- 3 dB @ 60 Hz

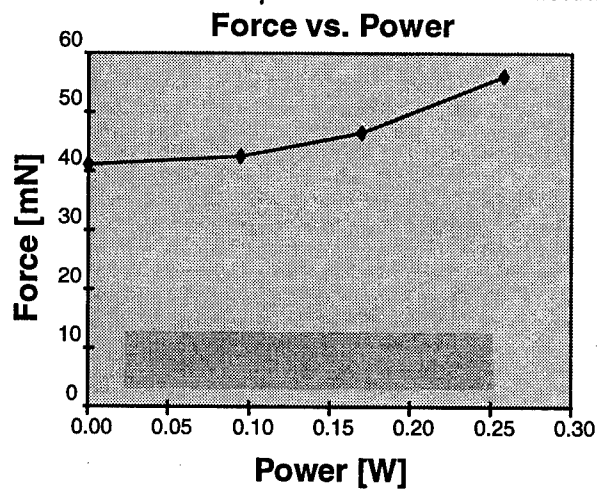


Figure 5. In-plane actuation: force versus power (design 1)

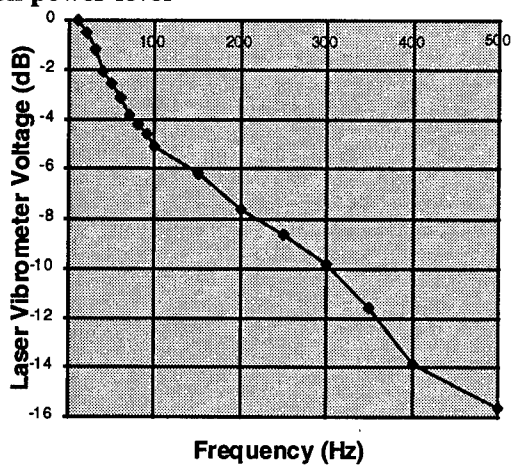


Figure 6. Mechanical frequency of in-plane actuation

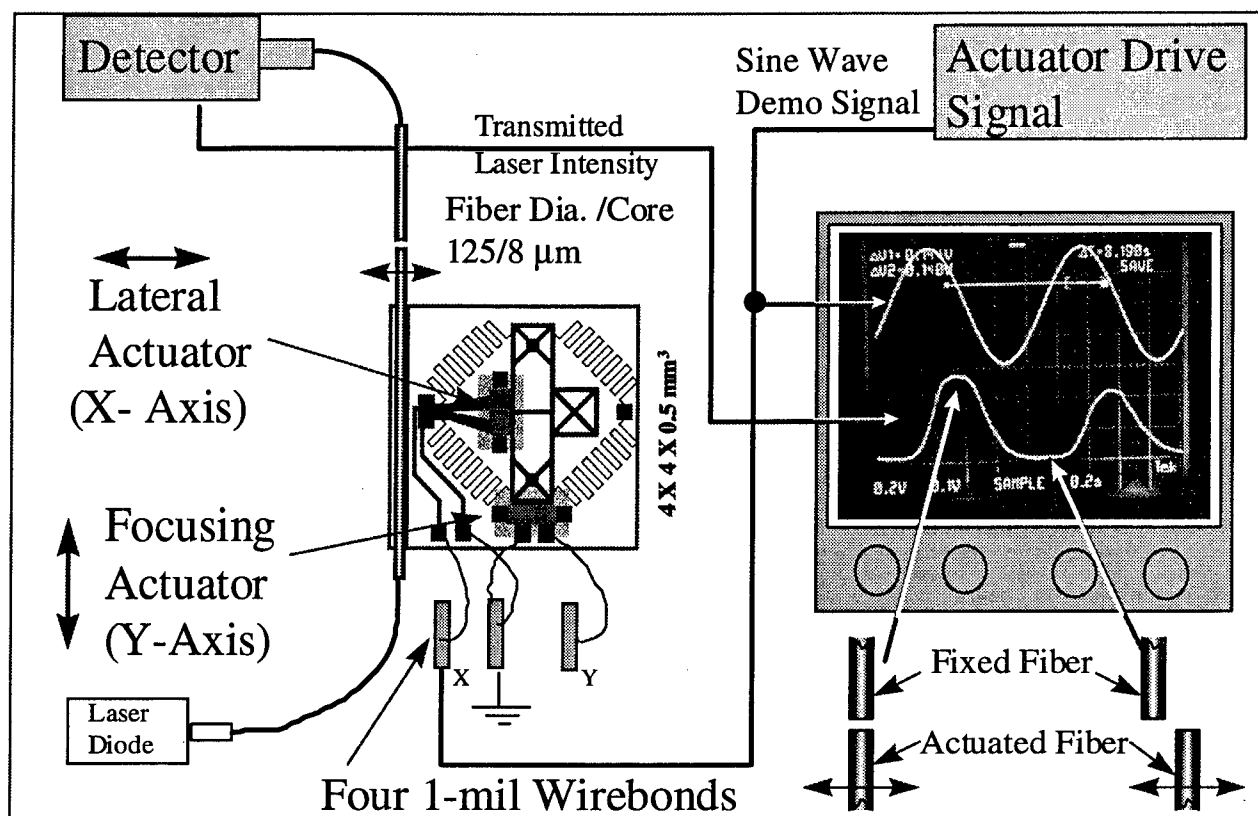


Figure 7. Two-Axis active fiber aligner experimental set-up and demonstration

TuC3
2:30pm - 2:45pm

A Micro Optical Bench for Alignment-Free Optical Coupling

Y. Aoki, T. Kato, J. R. Mizuno and K. Iga

Tokyo Institute of Technology, P&I Lab.

4259 Nagatsuta, Midori-ku, Yokohama, Japan 226-8503

1. Introduction

Optical fiber communication systems are becoming more important for parallel optical data transmission system because of their large data throughput and insensitivity for electromagnetic interference. In such system, arrayed components should be interconnected. But, the alignment of optical components takes a long time to obtain high coupling efficiency between optical components and makes the system costly.

For the realization of alignment free optical coupling, we proposed a "micro optical bench (MOB)"[1] using put-in microconnector [2].

In this study, A prototype was fabricated and we achieved the optical coupling loss of less than 3dB for single mode fibers.

2. Concept of MOB

An alignment concept of MOB is shown in Fig. 1. By only placing optical components on Si substrate and adjusting them to the V grooves, reference planes, and terrace, optical components are aligned at proper position. So, any precise alignment is not necessary in this concept.

The scheme of the proposed MOB is shown in Fig. 2. This module has the following advantages: (1) efficient optical coupling without precise alignment, (2) low return loss by using optical microconnector [2], (3) easy to extend to 2-dimensional array coupling using planar microlens (PML) and vertical cavity surface emitting laser (VCSEL), and (4) mass production capability due to simplicity of fabrication process.

3. Experimental Results

In this time, we fabricated a MOB for 4-channel coupling between PML and fiber array. The SEM photograph of the fabricated module is shown in Fig. 3. It shows that the PML is aligned along the referential planes and single mode fibers are aligned to each microlens.

For measuring the coupling loss of fabricated module, we used a collimated beam of a laser diode ($\lambda = 1.55\mu\text{m}$). The experimental result is shown in Fig.4. The optical coupling loss of less than 3dB and small fluctuation among channel as low as 1dB were achieved without any precise alignment. For multi mode fibers, the coupling loss of about 0.5dB was achieved.

4. Conclusion

We have fabricated micro optical bench (MOB) for realization of alignment free optical

coupling module. For single mode fibers, the coupling loss of less than 3dB for $\lambda = 1.55\mu\text{m}$ and channel uniformity of less than 1dB was achieved. For multi mode fibers, the coupling loss of about 0.5dB was achieved. In this study, we have demonstrated the feasibility of realizing alignment-free coupling using MOB scheme.

Acknowledgment

We would like to acknowledge Dr. M. Oikawa of Nippon Sheet Glass Co., Ltd. for helpful discussions. This study was supported by Grant-in-Aid for COE Research from the Ministry of Education, Science, Sports and Culture (# 07CE2003, "Ultra-parallel Optoelectronics").

Reference

- [1] Y. Aoki, T. Kato, J. R. Mizuno and K. Iga, MOC/GRIN '97, Technical Digest, K6
- [2] T. Kato, J. R. Mizuno and K. Iga, *IEICE Trans. on Electronics.*, Vol. E80 C, no.1, 1997

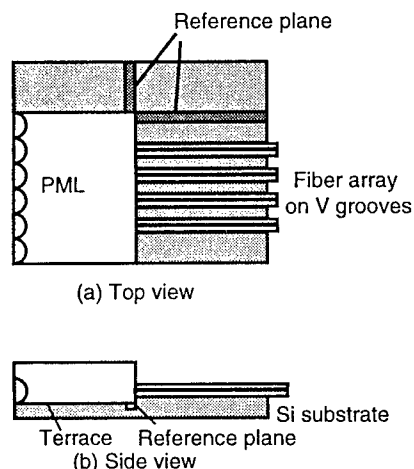


Fig. 1 An alignment concept of micro optical bench (MOB)

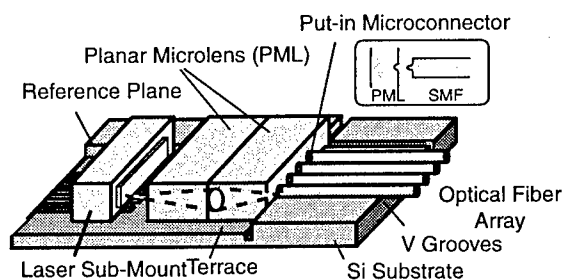


Fig. 2 The scheme of a proposed micro optical bench (MOB)

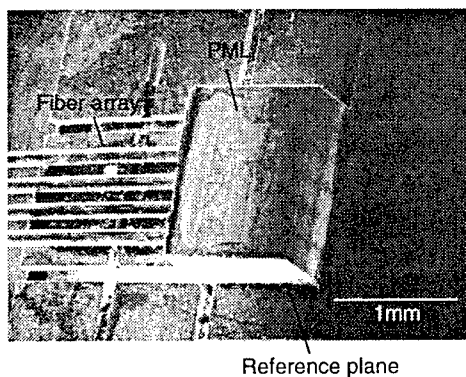


Fig. 3 A SEM image of a fabricated module

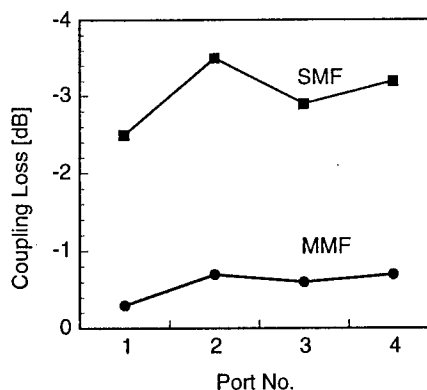


Fig. 4 The measured optical coupling loss

Full duplex 1.3/1.55 μm wavelength division multiplexing optical module using a planar lightwave circuit platform

Toshikazu Hashimoto, Takeshi Kurosaki, Masahiro Yanagisawa, Yuji Akahori, Yasuyuki Inoue, Yuichi Tohmori, Kazutoshi Kato, Yasufumi Yamada, and Kuniharu Kato

NTT Opto-electronics laboratories, 162, Shirakata, Tokai, Naka, Ibaraki, 319-11, Japan.

Introduction A full duplex optical module is a key device for 1.3/1.55 μm bidirectional wavelength division multiplexing (WDM) optical subscriber systems [1][2] and reducing its cost is particularly important. The most promising way to do this is hybrid integration with a planar lightwave circuit (PLC) platform, where a laser diode (LD) and a receiver photodiode (R-PD) are directly mounted on a compact PLC wafer board [3][4]. However, when this technology is applied to a full duplex optical module, the signal crosstalk between the LD and PD is a severe problem, because the LD is located near the PD on the platform. This paper describes a full duplex optical module configuration on a PLC platform that suppresses the signal crosstalk and the first demonstration of full duplex operation on a hybrid integrated optical module using a PLC platform operating at a speed of 156 Mbit/s.

Module configuration and crosstalk measurement

Figure 1 shows the configuration of the full duplex optical module. A 1.55 μm waveguide photodiode (WGPD)[5] as a receiver and a 1.3 μm spot size converter integrated laser diode (SS-LD)[6] as a transmitter are flip-chip-bonded on a PLC platform. A 1.3 μm WGPD as a monitor photodiode is also mounted behind the LD for automatic output power control. To suppress the optical crosstalk, we used a filter reflection type WDM circuit [7]. The LD and R-PD face each other and the WDM film is inserted into a thin slot between them. The WDM filter optically isolates the R-PD from the LD by reflecting uncoupled light from the LD as well as the 1.3 μm output signal. This reduces the optical crosstalk between them. This configuration also has the advantage of reducing the electrical crosstalk between them since it separates the LD and PD in a compact platform by deflecting the waveguide for the LD at the WDM filter.

In this configuration, the distance between the LD and the R-PD is an important factor. Therefore, we fabricated three types of optical modules having LD-PD distances of 6, 9 and 14 mm, and investigated the relationship between the distance and the optical and electrical crosstalk. Figure 2 shows the optical crosstalk against the LD-PD distance before and after WDM filter installation. The optical crosstalk was effectively suppressed by the WDM filter and was less than -40 dB when the LD-PD distance was more than 9 mm. Figure 3 shows the relationship between the electrical crosstalk and the LD-PD distance. When the LD-PD distance was more than 9 mm, the crosstalk was below -100 dB at a modulation speed of 130 MHz and was less than -80 dB at 600 MHz.

A rough estimation showed that the electrical crosstalk of -100 dB corresponds to an optical signal noise of -50 dBm at 0 dBm LD modulation. Using the optical and the electrical crosstalk values, we evaluated the total crosstalk to be less than -40 dBm in terms of optical signal noise at 0 dBm LD modulation when the LD-PD distance was more than 9 mm. This indicates that when a signal noise ratio of about more than 10 dB is required for a bit error rate of 10^{-10} [8], the module can receive a minimum signal power of about -30 dBm in full duplex operation at an operating speed of 130 MHz.

Module performance and conclusion

Based on these results, we fabricated an optical module with the LD and R-PD separated by 14 mm and housed it in a ceramic package as shown in Fig. 4. A pre-amplifier was also mounted on the package as a bare chip IC [9]. The signal lines from the R-PD were directly wire-bonded from pads on the PLC platform to the IC pads. The module characteristics are summarized in Table 1. The driving current for a 5 dBm CW output power, which corresponds to a peak power at 2 dBm output power modulation, was 43 mA. The responsivity and parasitic capacitance were measured before bonding to the pre-amplifier. They were 0.65 A/W and 0.7 pf respectively. The minimum sensitivity at a bit error rate of 10^{-10} was -35.9 dBm without LD operation (filled circle). Even when the LD was operated at 156 Mbit/s with 2 dBm average output power, sensitivity of -35.2 dBm was achieved (filled square). The power penalty due to the simultaneous LD operation was only 0.7 dB. This means that full duplex operation was successfully achieved in a compact optical module using a PLC platform.

These performance results confirm that the hybrid integration technology can provide a compact, low crosstalk, and cost effective optical module for optical subscriber systems.

References

- [1] C. A. Jones et al., Electron. Lett., vol. 31, no.25, pp. 2208-2210 (1995)
- [2] W. Metzger et al., Optical and Quantum Electronics, vol. 28, pp. 51-56 (1996)
- [3] Y. Yamada et al., Electron. Lett., vol. 29, no. 5, pp. 1888-1890 (1997)
- [4] N. Uchida et al., IEICE Trans. Electron., pp. 88-97 (1997)
- [5] K. Kato et al., Electron. Lett., vol. 32, no. 22, pp. 2078-2079 (1996)
- [6] H. Ohashi et al., ECOC '97, pp. 351-354 (1997)
- [7] Y. Inoue et al., Electron. Lett., vol. 32, no. 9, pp. 847-848 (1996)
- [8] R.G Smith et al., "Semiconductor devices for optical communication," Springer-Verlag, H. Kressel, Ed., Chapter 4 (1988)
- [9] M. Nakamura et al., Proc. of 8th Int. Workshop on Optical/Hybrid Access Networks, poster session, p.12 (1997)

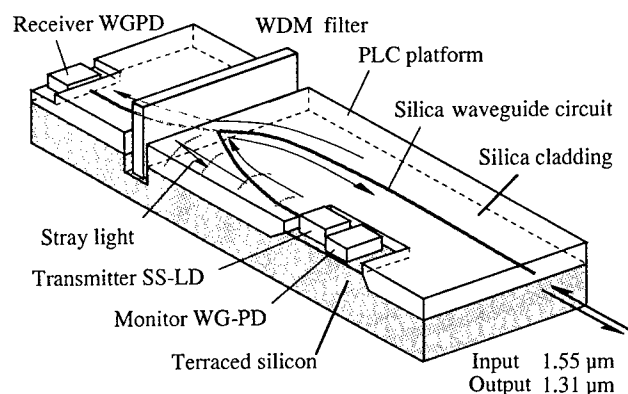


Fig. 1 Full duplex 1.3/1.55 μm WDM optical module configuration with PLC platform

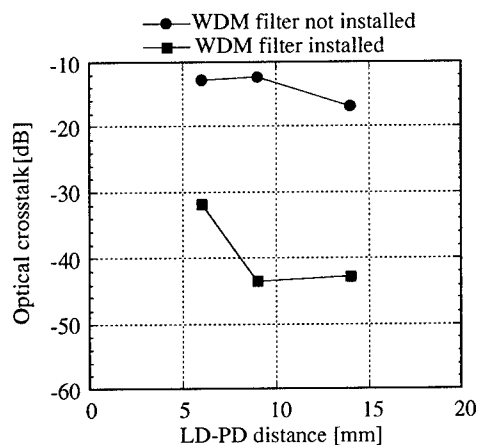


Fig. 2 Relationship between LD-PD distance and optical crosstalk

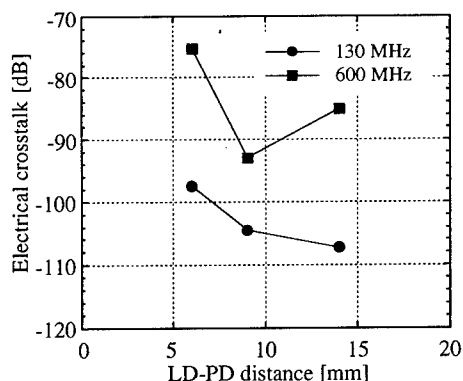


Fig. 3 Relationship between LD-PD distance and electrical crosstalk

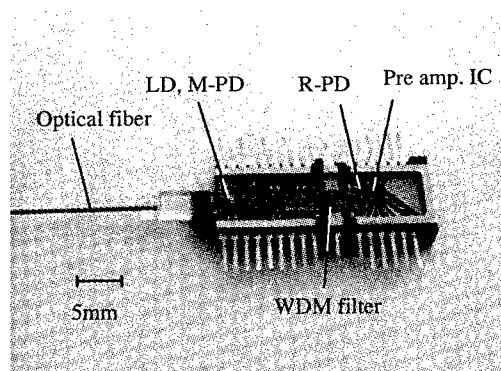


Fig. 4 Photograph of module housed in ceramic package with preamplifier IC

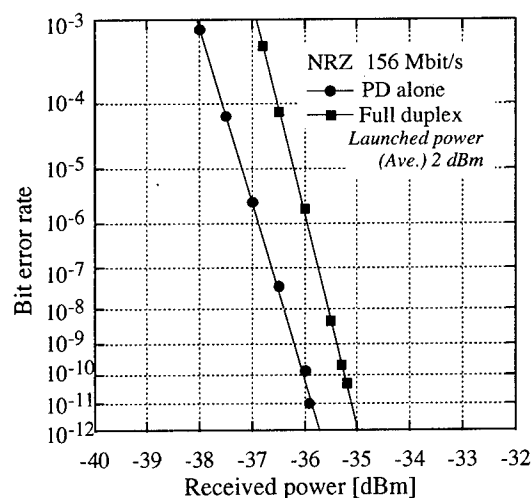


Fig. 5 Receiver performance

Optical module characteristics		
Transmitter	Operating wavelength	1.3 μm
	Threshold	7 mA
	LD driving current at 5 dBm CW output power	43 mA
Receiver	Operating wavelength	1.55 μm
	Responsivity (without pre amp. IC)	0.65 A/W
	Capacitance (without pre amp. IC)	0.7 pF
Optical crosstalk		-44 dB
Minimum sensitivity 156 Mbit/s BER = 10^{-10}	Launched power (Ave.)	-35.9 dBm
	+2 dBm	-35.2 dBm

Table 1 Module characteristics

OptoElectronic Multichip Modules Using MEMS Fabrication Techniques

Seungug Koh

University of Dayton, Department of Electrical and Computer Engineering
300 College Park, Kettering Lab, Dayton, OH 45469-0226

Danjin Wu

ITI, 42 East Rahn Road, Kettering, OH 45429

Mark Lantz

DoD, 9800 Savage Road, Fort G.G. Meade, MD 20755

1 Introduction

Information processing systems of today demand a balanced performance on data processing and data transmission. Efficient and reliable signal interconnects among processing units are as important as data processing capabilities of such systems. During past two decades, we have observed a very successful implementation of fiber-optic communication networks and microprocessor based computer systems. A hybrid module, i.e. optoelectronic multichip module (OE-MCM) can take advantage of enormous throughput of both microprocessor based computer systems and fiber-optic communication networks, once these systems are seamlessly integrated. In this paper OE-MCM has been proposed as an integrated hybrid system capable of supporting both electronic and photonic microsystems at a module level without showing any compatibility problems. Specifically this paper addresses design, fabrication, and packaging issues of optoelectronic multichip module (OE-MCM), which combines guided wave optoelectronic interconnects, MCM packaging, and micro-electro-mechanical systems (MEMS) fabrication techniques.

2 OptoElectronic Multichip Modules

Optoelectronic multichip modules (OE-MCMs) is a hybrid mixed-technology module, which can seamlessly integrate both optical interconnect networks and microprocessor based electronic processing systems. The proposed OE-MCM device structure is illustrated in Figure 1. OE-MCM integrates optical waveguides, multilayer electrical transmission lines, micromachined silicon mirrors, and flip-chip bonded photonic/electronic devices into a single structure.[1]

[2] The proposed OE-MCM structure suggest a Micro-Opto-Electro-Mechanical Systems (MOEMS) at the module level by utilizing electronic & photonic integrated circuits, multilayer metal interconnects, optical waveguides, and silicon mirrors at the micro scale. Using both sides of the MCM substrate in the proposed device configuration, multiple metal and optical waveguide layers can successfully be integrated for various types of metal or optical waveguide materials without causing any fabrication compatibility problems. The proposed input/output (I/O) coupling method utilizes innovative combinations of through-holes across OE-MCMs and micromachined silicon mirror arrays, which are fabricated by MEMS techniques[3] [4].

3 Prototype Fabrication and Characterization

The photonic integrated circuits for optical clock distribution network (OCDN) have been designed, fabricated and packaged along with a micromachined silicon mirror array wafer. There are various design parameters being considered: PIC sizes determined by the minimum bending radius rules, waveguide and coupling excess losses, and distribution of equivalent powers at the clock fanout nodes. From these design considerations, the single-mode, step-index, buried-type silica glass waveguide networks are designed by utilizing the H-tree network configurations and 3 dB Y-branching beam splitters. The Y-branching for 3 dB coupling has been selected due to its polarization and wavelength insensitive characteristics. The silica glass was choice of the material due to its low propagation losses and mature fabrication processes available. The minimum bending radius for the H-tree network was chosen to be 4 mm for the high-delta silica waveguide processes, where the delta is 0.7 %. The waveguide

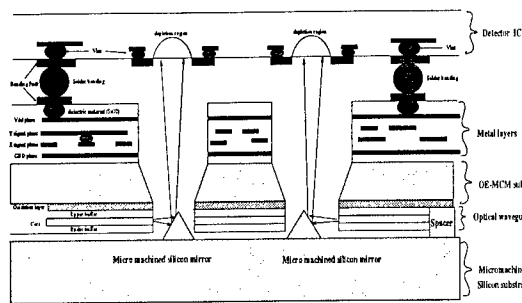


Figure 1: Device structures of the proposed Optoelectronic Multichip Modules for high-speed computer systems or communication networks.

cross-sectional dimensions are 6 by 6 micrometers and the I/O coupling sidewall has been designed to be 1.2 mm by 1.2 mm to accommodate the silicon mirror arrays. The four-fanout OCDN prototype consists of two modular components: optoelectronic signal interconnect modules and micromachined silicon mirror array modules. These two components are separately fabricated and then assembled using an interactive alignment method. Figure 2 illustrates the assembled prototype with He-Ne lasers output beams coming out of four fanout nodes. The clock signals are coupled into the OE-MCM module using an input single-mode fiber & fiber chip block.

The characterization of four fanout optoelectronic clock distribution networks shows average total insertion losses of 10.8 dB and 10.7 dB with uniformity 1.6 to 2.6 dB at wavelengths of 1310 nm and 1550 nm respectively. The uniformity is measured by taking the difference between the maximum and minimum signal losses at the fanout nodes. The total insertion losses include losses due to fiber-to-waveguide coupling, waveguide beam propagation, waveguide bending, Y-branching, and through-hole output coupling. The through-hole output coupling losses are influenced by mirror reflectivity and waveguide-to-mirror coupling efficiencies, which are determined by the mirror size and the separation between the waveguide end-facet and micromachined silicon mirror arrays.

4 Discussion

OE-MCM prototypes are developed and characterized using guided-wave optical interconnect, MCM packaging and MEMS fabrication technologies. The optical implementation of H-tree clock distribution

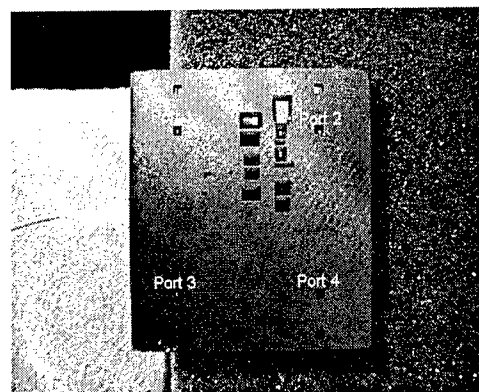


Figure 2: OE-MCM prototype showing the He-Ne laser beams at the four fanout nodes.

network on MCMs can support a very high-speed operation of future-generation digital systems as it improves system bandwidths, fanout capability, and power consumption of clock distribution networks. The proposed OE-MCM will find many important applications in the high-performance parallel processing computer systems, photonic ATMs, and GPS systems to name a few.

References

- [1] S. Koh, H.W. Cater and J.T. Boyd, "Synchronous global clock distribution on multichip modules using optical waveguides", *Optical Engineering* Vol. 33 No. 5, pp. 1587-1595, 1994
- [2] S. Koh, D. Sadler, and C.H. Ahn, "Optoelectronic Multichip Modules for High-Speed Computer Systems and Communication Networks", *Optical Engineering Special Issue on Micro-Opto-Electro-Mechanical Systems*, May 1997
- [3] K.E. Peterson, "Silicon as a Mechanical Material", *Proc. IEEE*, Vol. 70, No. 5, pp. 420-427, May 1982
- [4] T. A. Kwa, P. M. Sarro, W. V. D. Vlist, P. J. French, and R. F. Wolffenbuttel, "Fabrication of Extremely Smooth Mirror Surface in Silicon for Application in An Integrated Spectrometer", *Proc. 7th International Conference on Solid-State Sensors and Actuators*, pp. 242-245, 1993.

Tunable microcavity based on III-V semiconductor Micro-Opto-Electro-Mechanical Structures (MOEMS) with strong optical confinement

P. Viktorovitch^{a)}, J.-L. Leclercq^{a)}, X. Letartre^{a)}, T. Benyattou^{d)}

Staffan Greek^{b)}, Klas Hjort^{b)}, N. Chitica^{c)}, J. Daleiden^{c)}

^{a)}Ecole Centrale de Lyon, LEAME, BP 163, F-69131 Ecully Cedex, France

^{b)}Uppsala University, Dept. of Materials Science, Box 534, S-75121 Uppsala, Sweden

^{c)}Royal Institute of Technology, Dept. of Electronics, S-16440 Kista, Sweden

^{d)}INSA de Lyon, LPM, 20 Ave. Albert Einstein, F-69621 Villeurbanne Cedex, France

1. Introduction

Semiconductor microcavities have emerged as a major component for optical signal processing and light generation. The desired characteristics of these devices can be summarized as follows : 1) a high finesse, which means the combination of a wide free spectral range and of a high mode selectivity ; 2) a strong optical mode confinement for an efficient control of the electromagnetic field, which is required for example in thresholdless lasing operation ; 3) continuous and wide range tunability.

Most semiconductor microcavities fabricated to date have a planar configuration and consist in a vertical Fabry-Perot resonator ; the cavity is bounded by mirrors formed of thin-film multilayer stacks (Bragg reflectors), within which the electromagnetic field of the cavity extends over depths of the order of a few wavelengths, while they cannot prevent the photon to leak out of the cavity for oblique incidences. These undesired features result from the generally small index contrast achievable with the semiconductor layers which compose the Bragg reflectors. In this contribution, we present and discuss the properties of vertical micromachined InP-air gap based Fabry-Perot vertical microcavities. Owing to the high index contrast between air and InP, the above mentioned drawbacks of conventional semiconductor microcavities are considerably reduced ; in addition, large and continuous wavelength tunability can be attained via electromechanical vertical displacement of suspended InP layers.

In the next section we illustrate the potential of this class of microcavity in terms of selectivity and tunability with the report on a highly selective and widely tunable 1.55 μm InP/air-gap micromachined Fabry-Perot filter for Optical Communications, showing unreached performances to date. In the last section the field confinement provided by air-gap semiconductor Bragg mirror is discussed.

2. Highly selective and widely tunable 1.55 μm InP/air-gap micromachined Fabry-Perot filter

The key performances of optical filters requested by Optical Communications for Wavelength-Division-Multiplexing (WDM) systems are (i) a high wavelength selectivity, enabling the selection of neighboring channels 1.6 nm apart with a crosstalk ratio of 20 dB, (ii) a continuous wavelength tuning range of about 30 nm around 1.55 μm (compatible with the bandwidth of Erbium Doped Fiber Amplifier or EDFA), with no degradation of the selectivity.

We demonstrate the design and the fabrication of a vertical micromachined InP-air gap based Fabry-Perot filter, continuously tunable via electrostatic micromechanical actuation of the cavity air gap, which meets the WDM system requirements.

The proposed micromechanical approach offers number of material-related and technological advantages over other recently published micromechanical tunable Fabry-Perot : use of InP related materials allows for monolithic integration of the optical filter with active layers, for tunable and selective photodetection¹ and light emission operating at 1.55 μm and beyond (with strain active layers), paving the way to new applications for optical communications as well as for spectroscopic gas detection. Also InP/air gap Bragg reflectors (DBR) offer the desirable optical characteristics described in the introduction over their full semiconductor or dielectric counterparts. Finally the excellent material quality provided by epitaxial growth techniques (uniformity, reproducibility, tight control over mechanical properties and in particular over the in plane strain of the epilayers, very sharp interfaces,...) combined with the high precision attainable in micromachining due to the quasi infinite compositional etching selectivity of sacrificial layers, result in structures with accurately predictable optical properties, unlike solutions where suspended dielectric layers or oxide based DBR are employed².

Due to the high index contrast between the air and the InP quarter-wave layers, reflectivity as high as 99.9 % is achieved with only 2.5 pairs. All reflectors and cavity air gaps can be easily fabricated by selective micromachining of InGaAs sacrificial layers. Smooth optical graded non-sticking multi air gap InP paddle-shaped bridges were fabricated (fig 1) : the central (30x30 μm^2) platforms are suspended by two, 5 μm wide, arms. The maximum length of each arm was 55 μm .

The experimental reflectance spectrum of the unbiased filter shows a Full Width at Half Maximum (FWHM) of 0.8 nm. The determined FWHM is in fact controlled by the ultimate performances of the experimental set-up and the actual FWHM of the device is very closed to the targeted record 0.4 nm in the theoretical design³. The filter tuning spectra are shown in figure 2. Tuning was achieved over a wavelength range of 62 nm for an applied voltage of 14 V across the cavity air gap. The filter F.W.H.M. is kept below 1 nm over a tuning range of 40 nm.



Fig. 1 : SEM micrograph of a 140 μm paddle-shaped bridge.

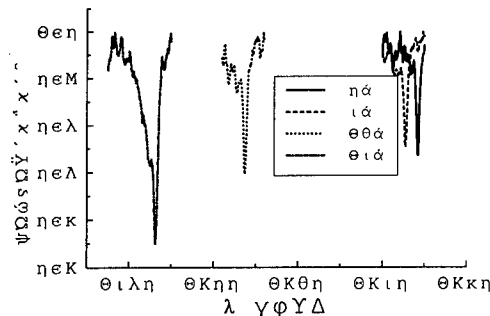


Fig. 2 : Tuning spectra of the filter.

3. Semiconductor-air gap Bragg reflector for the control of spontaneous emission

The control of spontaneous emission in semiconductor microcavities has emerged as a major issue in recent years, with considerable implications in the domain of optoelectronics. The ideal microcavity for lasing operation is expected to enhance the useful modes of the device and to inhibit the modes which cannot result in an efficient coupling with spontaneous emission. Among useless modes are those which cannot be prevented to leak out of the cavity. In conventional semiconductor vertical microcavities, Bragg reflectors are transparent to oblique incidence modes, due to their narrow stop band. It can be shown that TE modes which are produced by the emission of a planar quantum well are stopped for any incidence as soon as the index contrast of the Bragg pairs exceeds the ratio 2 : this means that the cone angle defined by the stop band is larger than the minimum angle of incidence which achieves total reflection of the light within the semiconductor cavity layer. This condition is achieved with air/semiconductor pair; it is also achieved, to a lesser extent, with $\text{AlOx}/\text{GaAlAs}$ system⁴. The remaining useless modes are guided in the cavity layer and can be coupled to a significant part of the spontaneous emission, thus resulting in a reduction of the control of the emission rate. One way to circumvent this difficulty lies in the use of a 2D Photonic Band Gap (PBG) formed in the cavity layer as illustrated in figure 3. The fabrication of such structures is under way in our groups.

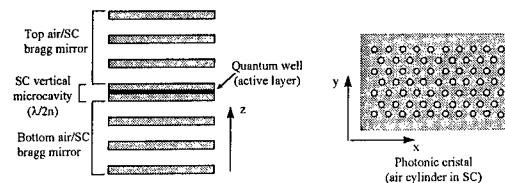


Figure 3 : Semiconductor/air gap vertical microcavity with a 2D PBG formed in the cavity layer.

This study is supported by the European ESPRIT-MOEMS project. The French Academic groups are part of the CRELYMO (Lyon Research Center in Micro-Opto-Electronics).

References

- [1] K. Hjort, S. Greek, R. Gupta, D. Pasquariello, N. Chitica, K. Streubel, C. Seassal, J.L. Leclercq, P. Viktorovitch, T. Benyattou, A. Dehe, J. Peerling, J. Pfeiffer, P. Meissner, R. Riemenschneider, H.L. Hartnagel, D.D. Mongardien and O. Sahlén: "Demands and solutions for an indium phosphide based micromechanically tunable WDM photodetector", *MOEMS 97 International conf. on optical MEMS and their applications*, Nara-Japan, 18-21 november 1997
- [2] M. S. Wu, G. S. Li, W. Yuen and C.J. Chang-Hasnain: "Widely tunable 1.5 μm micromechanical optical filter using $\text{AlOx}/\text{AlGaAs}$ DBR", *Electronics Letters*, vol. 33, No. 20, pp. 1702-1704, 1997
- [3] A. Spisser, R. Ledantec, C. Seassal, J.L. Leclercq, T. Benyattou, D. Rondi, R. Blondeau, G. Guillot and P. Viktorovitch: "Highly selective 1.55 μm InP/air-gap micromachined Fabry-Perot filter for optical communications", *Electronics Letters*, under press
- [4] I. Abram, I. Robert, and R. Kuszelewicz : « Spontaneous emission control in Semiconductor Microcavities with metallic or Bragg Mirrors », *IEEE Journal of Quantum Electronics*, vol. 34, No 1, pp. 71-76, 1998.

Electrostatically operated micromirrors for a Hadamard transform spectrometer

Torsten Diehl, Wolfgang Ehrfeld, Manfred Lacher and Thomas Zetterer

IMM Institut für Mikrotechnik Mainz GmbH, Carl-Zeiss-Str. 18-20
D-55129 Mainz, Germany

Abstract

The paper presents the development of a linear micromirror array which can be used as a switchable entrance mask for a double-array Hadamard transform spectrometer. In addition to the detector array the double-array spectrometer has a linear multi-slit array realised by independently switchable micromirrors at the entrance side. Two different switch positions of the electrostatically operated mirrors allow the reflection of light into or away from the spectrometer. With this arrangement (mirror array, concave grating and array detector) and the use of the Hadamard transform principle it is possible to increase the signal-to-noise ratio and the resolution of the system compared to conventional spectrometers of the same size.

In order to use a micromirror array as an entrance mask the dimensions of the switching elements must be similar to those of entrance slits and the mirror surface must have a high reflectivity in the desired spectral range. To obtain a high resolution a given pitch between the mirrors must be realised. Using thin film technology we developed a linear array with 18 tiltable mirrors. The mirrors consist of a multilayer system of aluminum and silicon nitride deposited on a structured sacrificial layer of polyimide. The aluminum has a comparatively high reflectivity in the UV/VIS region and the silicon nitride yields good mechanical properties for realising stress reduced mirrors and bending structures. After etching of the sacrificial layer, the mirrors can be switched electrostatically. The angle between on and off position is about 5 degrees. Low switching voltages in the range of 15 - 45 V can be realised.

1 Introduction

The intention of the project in which the linear micromirror array was realised is the development of a compact UV/VIS-spectrometer for space applications. The spectrometer should be light weight, small in dimension, have a high resolution and a high signal-to-noise ratio. In the last decade several miniaturised diode array spectrometers have been developed [1-4], whose performance was a compromise between small dimensions and resolution. To fulfil the above mentioned requirements regarding resolution and signal-to-noise ratio a spectrometer concept was developed which combines the advantages of a diode array spectrometer and a multi-slit (Hadamard transform) spectrometer.

The advantage of a diode array spectrometer in general is that it has no moving parts and with the array detector the whole spectrum can be recorded simultaneously (Fig. 1a). The disadvantage of a diode array spectrometer is that the

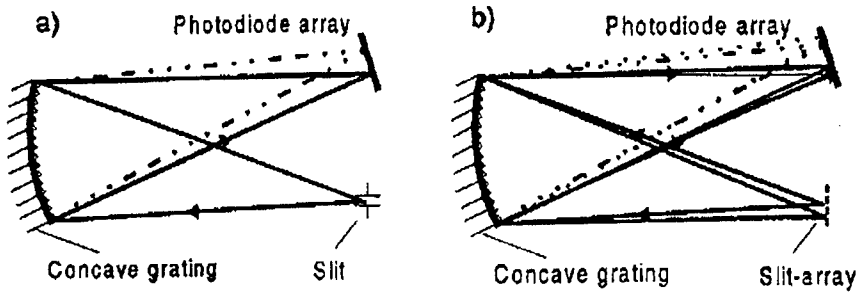


Figure 1: a) Diode array spectrometer and b) double-array Hadamard spectrometer

resolution is limited by the number of elements N of the detector array. The number of detector elements determine the number of wavelength dependent measurement points. To resolve a spectral line with a diode array spectrometer it is necessary to image the entrance slit onto a minimum of three detector elements lying next to each other. This statement is valid for the spectral resolution (Rayleigh criterion) and the determination of the wavelength accuracy (Fig. 2; sub pixel resolution [5]). If a wavelength region $\lambda_{\max} - \lambda_{\min}$ is imaged onto the detector array the maximum resolution of the spectrometer $\Delta\lambda$ can be calculated by

$$\Delta\lambda = \frac{\lambda_{\max} - \lambda_{\min}}{N} \cdot 3.$$

Compared to single slit spectrometers Hadamard spectrometers comprise a higher signal-to-noise ratio [6]. This advantage is obtained by having a mask with several slits in the entrance plane thus giving it a higher light throughput in contrast to a normal spectrometer. The spectral distribution of the light falling into this spectrometer can be calculated by the use of the Hadamard transformation [7]. To obtain the data the slits have to be opened and closed in a coded sequence.

The combination of these two types of spectrometers allows the fabrication of a compact spectrometer with an increased signal-to-noise ratio (Fig. 1b), called double-array Hadamard transform spectrometer. Furthermore, through realisation of a distinct distance between each slit the above mentioned limitation of the resolution of diode array spectrometers, which depends on the number of detector elements, can be overcome. For that, it is necessary that the images of the entrance slits for one wavelength fall on each detector element in another relative position (Fig. 3). The slits have to be arranged in a way that the pitch p between the slits is

$$p = \frac{i}{n} \cdot M \cdot b,$$

where M is the magnification and b is the pitch of the detector elements [8]. i represents an integer and n the number of entrance slits. If i is larger than n , which is the requirement for a physical distance between two slits and i is chosen so that i

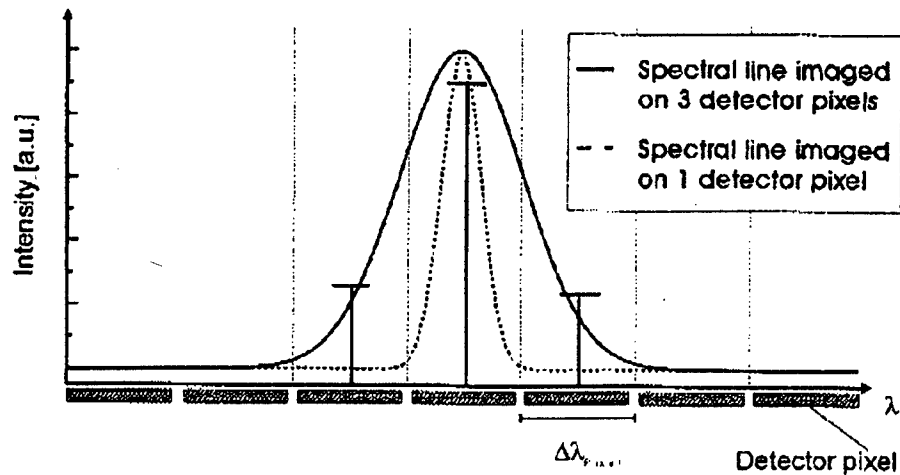


Figure 2: Two images of a spectral line on the detector of a normal array spectrometer. The wavelength of spectral line falling onto a minimum of three detector elements can be determined accurately by fitting. The wavelength of a line falling on one pixel can only be determined with the inaccuracy of a detector element $\Delta\lambda_{\text{Pixel}}$.

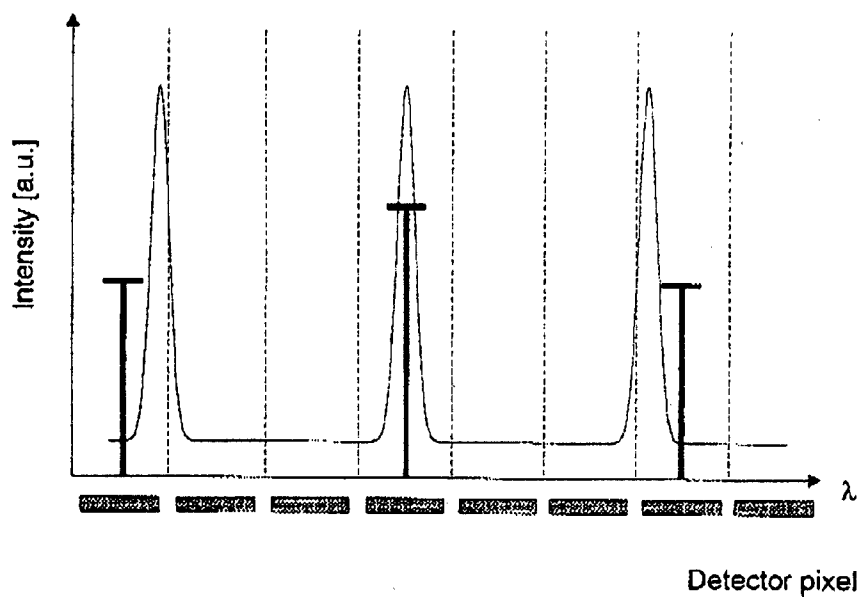


Figure 3: Image of the same spectral line on the detector coming from three entrance slits. Each line falls onto a detector element in another relative position so that the number of wavelength dependent measurement points is increased.

and n have no common divisor other than 1, then for each detector element $n-1$ additional measurement points are recorded. In other words, it is possible to shift a spectral line virtually in n steps over a detector element. With this arrangement the number of wavelength dependent measurement points can be increased which leads to a higher resolution.

In order to realise this Hadamard spectrometer a switchable entrance mask is required. For the optical considerations it is necessary that the slits of the mask lie close to each other with a defined distance between. These requirements can be fulfilled by a micromirror array where each mirror represents a slit. In one switching state the mirror reflects the light into the spectrometer and the mirror is imaged onto the detector, in the other state the mirror reflects the light away from the spectrometer.

Nowadays there are several developments of single micromirrors and micromirror arrays [9-10]. Especially the digital mirror device (DMD) of Texas Instruments [11-12] are well known. These mirrors normally have a square mirror surface with sizes ranging from $16 \times 16 \mu\text{m}^2$ up to $3 \times 3 \text{ mm}^2$ and static switching voltages between 10 V up to 1000 V. For the application of the micromirrors to function as entrance slits of a spectrometer, the dimensions of the mirrors are defined by optical considerations. We have realised an array of 18 tiltable micromirrors with a size of $30 \times 500 \mu\text{m}^2$ and a pitch of $52 \mu\text{m}$ [13].

A schematic presentation of a mirror is shown in figure 4. The mirror is switched electrostatically by a control electrode beneath the mirror and the mechanical movement is allowed by four bending arms positioned on one of the long sides of the mirror. The bending arm suspension of the mirrors precludes that the mirrors are totally dragged down to the control electrode. This would happen if a torsional suspension is used because of the length of the mirrors and the torsional arms.

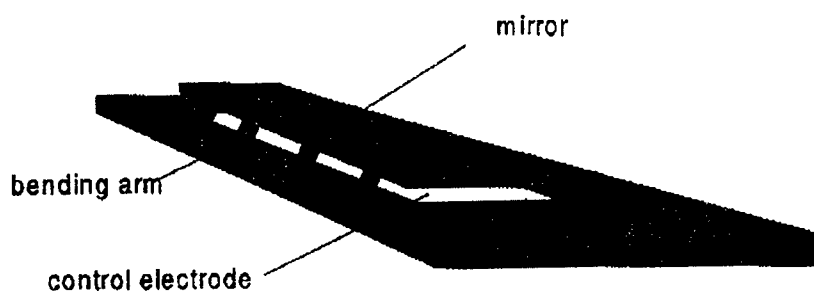


Figure 4: Schematic presentation of a mirror with bending arms

2 Fabrication

For the fabrication of the micromirrors thin film technology processes with seven masks are used (Fig 5). Thermally oxidised silicon wafers are used as substrates for the production of the mirrors. With the first two lithography steps the electrodes and contact pads are structured and then isolated with a PECVD-silicon dioxide layer. The third step is the deposition and structuring of the sacrificial layer. For the sacrificial layer a photostructurable polyimide is used. The polyimide precursor is deposited by spin coating. With normal UV-lithography the polyimide plateaus are formed on which the mirror surfaces are deposited later on. Polyimide acts as a negative resist. The irradiated regions of the precursor are pre-crosslinked, so that they are not soluble in the development process. The imidisation of the polyimide takes place in a curing step at temperatures up to 400°C. This heat-treatment results in a decrease of the layer thickness which has to be taken into account. Once the polyimide has been heated up to the cure temperature it is resistant against PVD- and CVD-processes carried out at lower temperature.

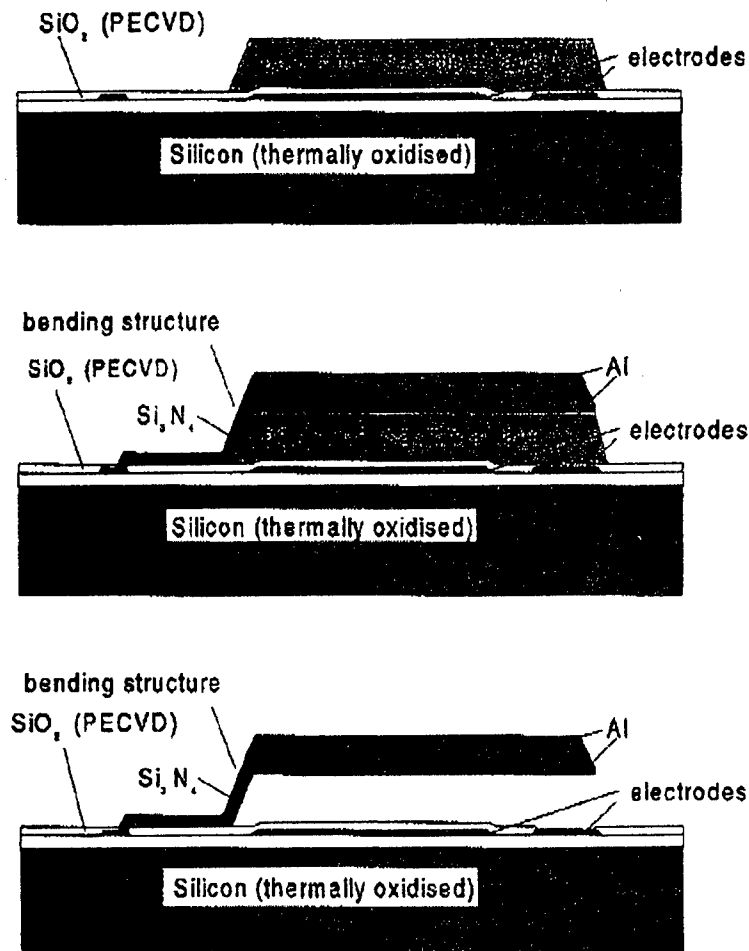


Figure 5: Steps of the micromirror production

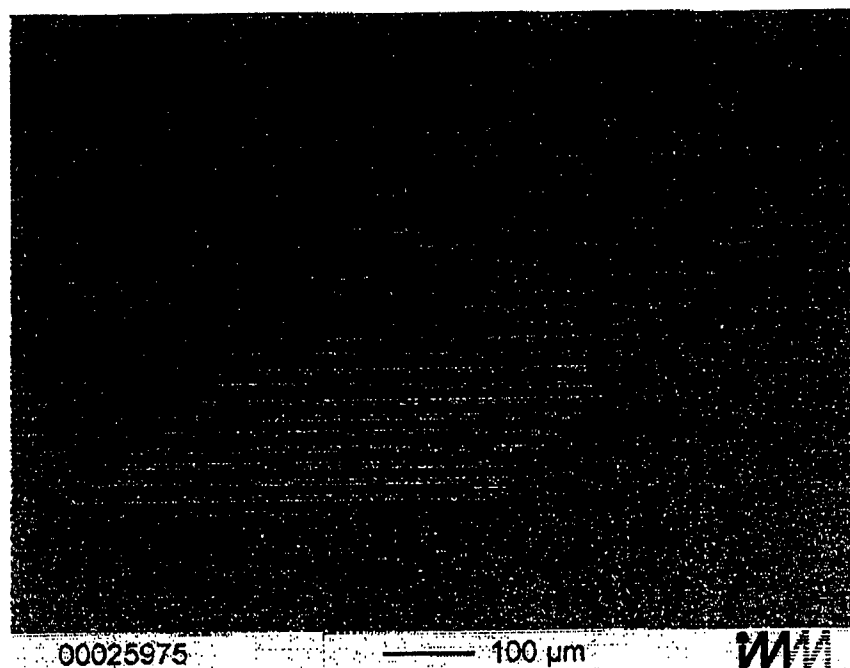


Figure 6: SEM-picture of the micromirror array

The following steps are the deposition of the different layers which form the mirror and the bending arms. The first layer of the mirror consists of aluminum which forms the counter electrode. Its mechanical properties are realised by two layers of silicon nitride. One layer of 300 nm thickness forms the bending arms, the other stress optimised silicon nitride layer is responsible for a flat mirror surface. The top layer of the mirror consists of aluminum which is responsible for a high reflectivity of the light in the UV/VIS region and the electrical contact to the counter electrode via the bending arms.

After dicing the mirror chips the sacrificial layer is removed. For that, the polyimide is ashed by an oxygen plasma. The advantage of dry etching processes is that sticking effects caused by capillary forces in stripping and rinsing liquids are avoided. In the last step the mirror chips are assembled in a standard IC-carrier and wire bonded.

3 Characterisation

The application of the mirrors as entrance slits of an array spectrometer requires that the size of each mirror is approximately the size of a detector element. The single mirror is 30 μm wide and 500 μm high. The layers of the mirrors are built upon a 3 μm thick sacrificial layer of polyimide. After removing the polyimide the mirrors (Fig. 6) are supported only by four bending arms and can be tilted by 5° from their equilibrium position (off position) to the on position by applying an electrical voltage. The optical properties of the mirrors depend on the quality of the mirror surfaces. For that, the surfaces have to be flat to reflect the light only in the desired direction. The

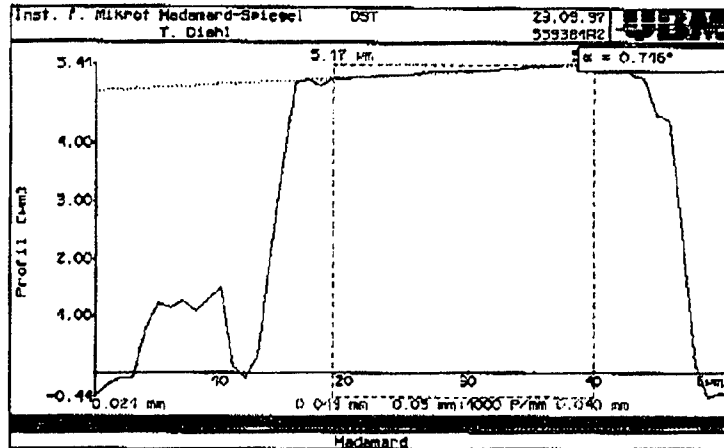


Figure 7: Tilt angle of a mirror in the equilibrium position

surface roughness must be low so that light scattering by the mirrors is minimised. The characterisation of the mirror surface is performed by white light interferometric measurements. After the optimisation of the intrinsic stress of the silicon nitride layer it was possible to produce mirrors with a rms surface roughness of less than 60 nm and a waviness of less than 0.35 μm measured in the direction of the length of the mirror. These values are sufficient because the mirrors are not used for deflecting a light beam, but only as an object point for projection.

Each mirror is suspended by four bending arms which are located along one side of the mirror. The bending arms consisting of a silicon nitride and aluminum layer are nearly perpendicular to the substrate surface. The cross section of each arm is $0.5 \times 5 \mu\text{m}^2$. To control the tilt of the mirrors in the equilibrium position the intrinsic stress of the silicon nitride and aluminum layers have to be optimised. Confocal surface scanning microscope (UBM) measurements (Fig. 7) show that a tilt as small as 0° - 1° can be reached.

Presently, the switching voltage for the micromirrors is in the region of 40 V. By reducing the thickness of the bending arms down to 300 nm in future fabrication processes the switching voltage may be reduced down to 15 V.

4 Measurements

The micromirror array was incorporated into a spectrometer system to act as a switchable entrance mask. In this tentative spectrometer set-up a commercial concave grating and a detector array with 1024 pixels were used. The optical imaging properties of this grating are designed for imaging a slit onto three detector elements and not to one detector element as an increase in resolution would require. Nevertheless, this set-up can be used to demonstrate that the number of wavelength dependent measurement points is increased.

Figure 8 shows an overlay of the recording of the 250 nm line of a mercury lamp where each mirror was separately turned to the on-position. As can be seen from the figure it was not possible to image each mirror onto a single detector element. The plot of the raw data in figure 8a shows relatively high background intensity, which

Optical modulator with independent control of attenuation and spectral tilt

K.W. Goossen, W.H. Knox, J.A. Walker and J.E. Ford

Lucent Technologies, Bell Laboratories

4B-519 Crawfords Corner Road, Holmdel, NJ 07733

Optical networks employing multiple wavelengths of light (Wavelength Division Multiplexed, or WDM networks) are becoming increasingly important commercially. Typically in WDM networks, especially for long-haul, Erbium-doped fiber amplifiers are used to replenish losses. This leads to a problem, since it is necessary that the various wavelength channels have similar power levels so that the same communication circuitry may be used, but as wavelengths are added or subtracted at various nodes in the network the gain spectrum of the amplifiers changes [1]. A device which equalizes the power in the channels would solve this problem. Such a device was presented in [2] that had independent control of the attenuation of any wavelength channel. However, the device in [2] had relatively complicated packaging compared to a simple modulator since it required wavelength demultiplexing and multiplexing and so may be more expensive. Also, in some cases it may not be necessary to have independent control of each channel, but simply provide a monotonic change in attenuation as the wavelength changes, i.e., a spectral attenuation tilt.

We describe here such a device based on the Mechanical Anti-Reflection Switch, or MARS modulator. The MARS modulator is a broad spectrum, high contrast reflection modulator based on the vertical movement of an optical membrane above a substrate [3]. The movement is via electric force on the membrane induced by a bias applied between the membrane and the substrate. This device has demonstrated digital

modulation in excess of several Mbit/sec [4]. Its use as a fast variable attenuator has been shown and an inexpensive package described [5].

The MARS modulator is basically a Fabry-Perot cavity with the air gap as the cavity and the substrate (typically silicon) air interface as the bottom mirror. As exemplified here, the membrane's structure may be complex to achieve a certain result but the finesse and hence broad wavelength range of the cavity remains fixed by the bottom mirror. The device does produce spectral tilt of the reflectivity at intermediate reflectivities, and if a particular tilt as a function of attenuation is required a single MARS device may suffice. To have independent control of attenuation and tilt two controls are necessary. To accomplish this one places two MARS modulators in series (Fig. 1). One modulator has positive spectral tilt and the other with negative spectral tilt (Fig. 2), and then tilt and attenuation can be independently controlled by adjusting the air gap of each modulator. In Fig. 2 we show MARS devices which have been redesigned for reduced insertion loss [6]. The device described by the solid lines is designed to move from air gaps between 10770 Å and 8080 Å, and the one described by the dashed lines from 14760 Å to 11700 Å. When placed in series these modulators produce various spectra as shown in Fig. 3, demonstrating independent control of tilt and attenuation.

It may be desirable that the attenuation

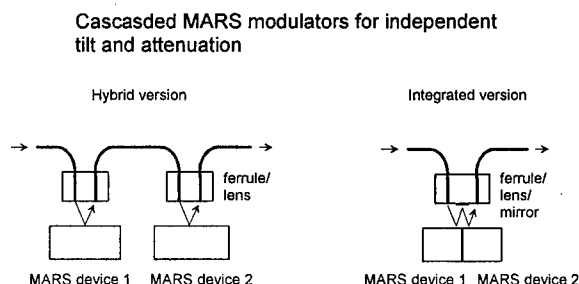


Fig. 1: Schematic of device which consists of two MARS modulators in series.

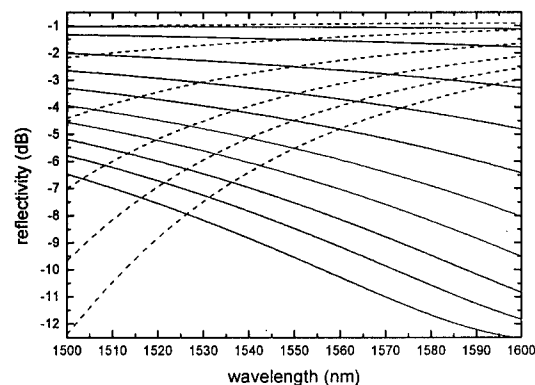


Fig. 2: Spectra of negative tilt (solid) and positive tilt (dashed) MARS modulators which compose tilting attenuator device.

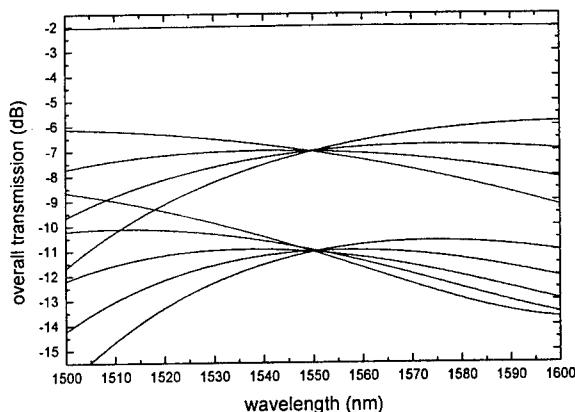


Fig. 3: Overall spectra of tilting attenuator composed of the MARS devices of Fig. 2.

tilt linearly in dB. There is no qualitative way of describing how this result is achieved since linear spectra in dB have no special meaning. But by taking the design of Fig. 2, which has a two-layer membrane whose top layer is SiNx and bottom layer is poly-Si, and plotting the 2nd derivative of the dB spectra as a function of these layer thicknesses, linearity may be achieved. This plot is shown in Fig. 4 as a contour plot. Shown is the plot for the positive tilt device. Curvature is minimized for top and bottom layer thicknesses of 2505 and 486 Å, respectively. Shown in Fig. 5 are the corresponding spectra, and Fig. 6 shows the spectra of the final device. Note that added loss has been incurred to obtain linearity.

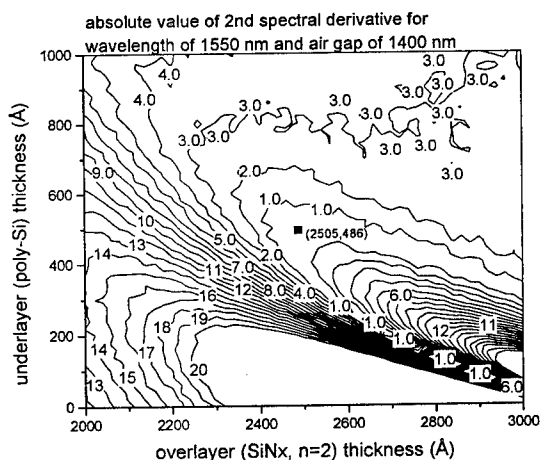


Fig. 4: Contour plot of curvature of spectra as a function of membrane layer thicknesses, showing optimum for linear spectra.

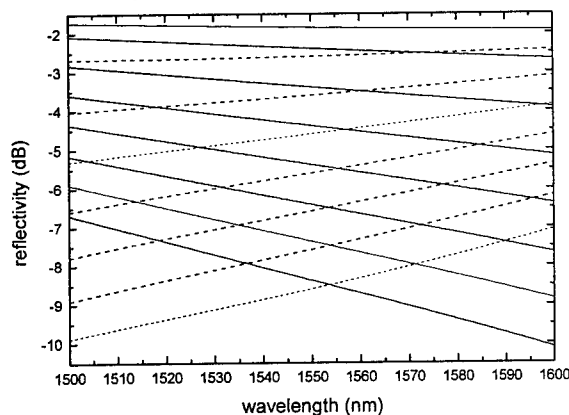


Fig. 5: Spectra of MARS modulators optimized for spectra linearity.

In conclusion, we have shown how by cascading two MARS modulators independent attenuation a spectral tilt equalization may be simply achieved.

REFERENCES

- [1] A. Chraplyvy, R. Tkach, K. Reichmann, P. Magil, and J. Nagel, *IEEE Phot. Tech. Lett.* **4**, 428 (1993).
- [2] J.E. Ford, J.A. Walker, M.C. Nuss, and D.A.B. Miller, *IEEE Summer Topical, Broadband Networks*, Keystone, Colorado (1997), p. 26.
- [3] K.W. Goossen, J.A. Walker, and S.C. Arney, *IEEE Phot. Tech. Lett.* **6**, 1119 (1994).
- [4] J.A. Walker, K.W. Goossen, S.C. Arney, N.J. Frigo, and P.P. Iannone, *J. Lightwave Tech.* **14**, 2382 (1996).
- [5] J.E. Ford, J.A. Walker, and K.W. Goossen, *SPIE vol. 3226, MEMS for Optical Processing III*, p. 86 (1997).
- [6] K.W. Goossen, submitted to *MEMS for Optical Processing IV*.

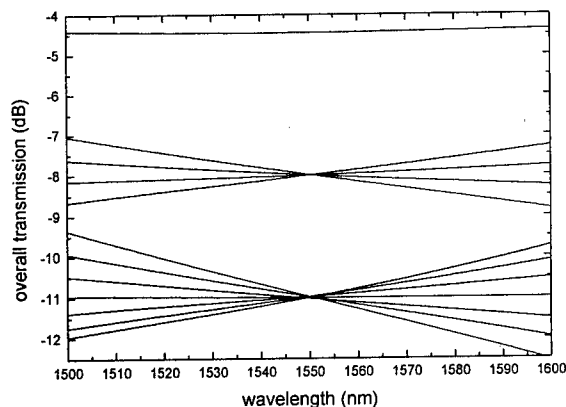


Fig. 6: Overall spectra of tilting attenuator composed of the MARS devices of Fig. 5.

Miniaturized Piezo Electric Chopper For Fiber Optical Multimode Applications Realized Using LIGA-Technology

T. v. Freyhold, H. Debéda, P. Krippner, J. Mohr, U. Wallrabe, and J. Wengelink

Forschungszentrum Karlsruhe
Institut für Mikrostrukturtechnik (IMT)
Postfach 3640; D-76021 Karlsruhe

Choppers are used in optical systems for the modulation of light. Their main application is to increase the signal-to-noise-ratio in the field of optical measurements. In the course of the miniaturization of optical systems, size and cost adapted choppers with high performance are desirable.

A miniaturized chopper for fiber optical multimode applications has been developed at the Institut für Mikrostrukturtechnik at Forschungszentrum Karlsruhe. Transmittance is modulated by a piezo electric driven shutter, moving in a gap between two multimode fibers. Figure 1 shows a schematical view of the miniaturized chopper.

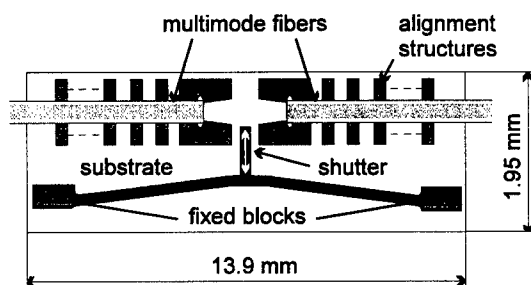


Fig. 1 Schematical view of the miniaturized piezo electric chopper.

The chopper is built up by nickel structures 175 μm in height on top of a piezo electric substrate and comprises the shutter mechanism and alignment structures for the input and output fibers.

For the fabrication of the chopper a new concept of LIGA-technology is used, permitting the integration of LIGA-microstructures on piezo electric substrates [1]. The use of batch processing and the passive alignment of the fibers results in an easy and low-cost production.

The shutter mechanism consists of a moveable beam, which connects two blocks fixed on the substrate. The shutter is located in the middle of the beam. Applying a voltage between the bottom and the top surface of the piezo electric substrate, the spacing between the two fixed blocks is reduced due to the contraction of the substrate and the beam is bent. The resulting displacement of the shutter, shown in figure 2, causes a decrease of the transmittance.

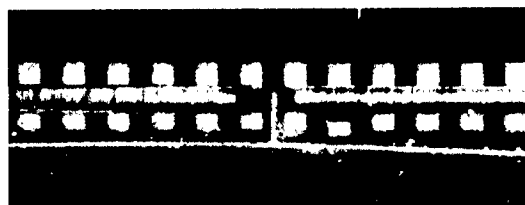


Fig. 2 Photograph of the miniaturized piezo electric chopper with an applied voltage of 1000 V.

The optical performance of the chopper is investigated by means of its static and dynamic behaviour. For the measurements, light from a diode laser module, emitting at a wavelength of 1290 nm, is coupled into the input fiber and detected at the output fiber with a Germanium photodiode.

Using multimode fibers with a core diameter of 105 μm and a cladding diameter of 125 μm , the insertion loss was measured to be 2.3 dB. The loss is mainly caused by the spacing of 200 μm between the two fibers. Applying a voltage, the transmittance can be varied within a range of 45 dB.

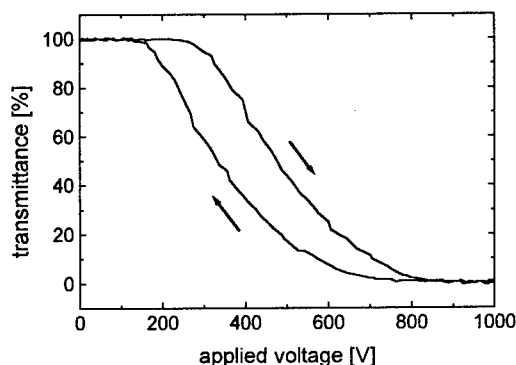


Fig. 3 Transmittance of the chopper as a function of the applied voltage (excluding the insertion loss).

Figure 3 shows the transmittance of the chopper as a function of the applied voltage. The hysteresis of the piezo electric ceramic causes a shift in the transmittance characteristics, which was measured to be about 150 V for increasing the applied

voltage from 0 V to 1000 V and decreasing to 0 V again.

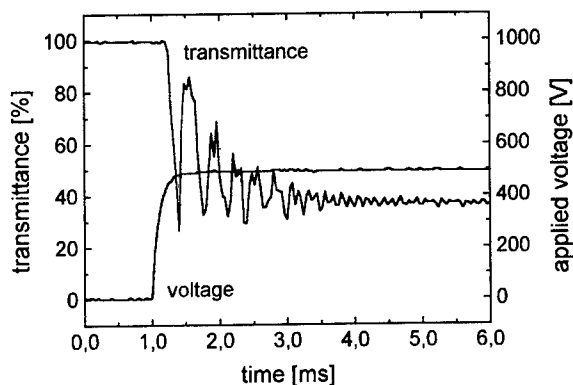


Fig. 4 Step response of the transmittance for a discrete change of the applied voltage from 0 V to 500 V.

The resonance characteristics of the shutter mechanism is observed by the step response of the beam. Figure 4 shows the transmittance for a discrete change of the applied voltage from 0 V to 500 V. The step response is mainly composed of two resonant vibrations with frequencies of about 3 kHz and 9 kHz. The initial amplitude and the attenuation of a single resonant vibration strongly depends on the mechanical stress of the beam. For a constant step of the applied voltage, increasing the stress, e.g. by applying an additional offset voltage to the substrate, decreases the initial amplitude and the fading time. This effect is stronger for the resonant vibration at 3 kHz than for that at 9 kHz.

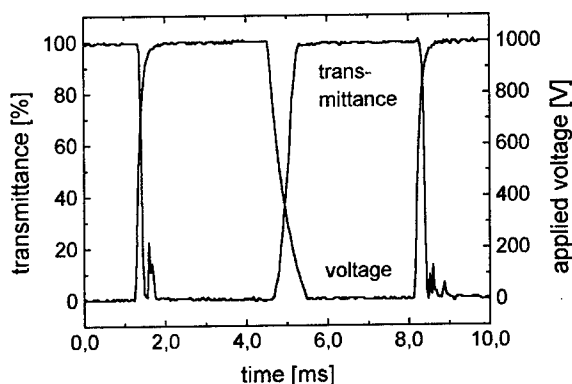


Fig. 5 Transmittance modulation for an applied square voltage of 1000 V at 145 Hz.

In figure 5 the transmittance modulation for an applied square voltage of 1000 V at 145 Hz is shown. The step response of the beam has only a slight influence on the modulation, because both rest positions of the shutter are located outside the light path of fiber-fiber coupling. Increasing the frequency leads to a more and more unstable vibration behavior of the shutter mechanism.

As mentioned above, the vibration behavior of the shutter mechanism can be stabilized by applying additional mechanical stress to the beam. However, for driving the shutter mechanism at high frequencies, the use of a harmonic voltage instead of a square voltage and an additional reduction of the voltage amplitude is necessary.

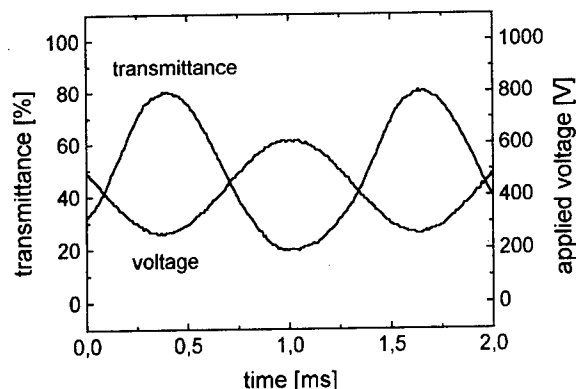


Fig. 6 Transmittance modulation for an applied harmonic voltage of 360 V at 800 Hz, added to an offset voltage of 260 V.

Figure 6 shows a harmonic transmittance modulation with a frequency of 800 Hz and a modulation depth of 60%, clearly demonstrating the stable behavior of the shutter mechanism. Further investigations indicate, that at the cost of modulation depth and loss a transmittance modulation with frequencies up to 2 kHz is possible.

Finally, it can be concluded, that the optical performance of this first type of miniaturized piezo electric chopper is promising. In a following design, the geometry of the shutter mechanism needs to be improved in order to minimize the step response of the beam. Decreasing the spacing between the two fibers, insertion loss can be reduced. Furthermore, the voltage needed for driving the shutter mechanism can be strongly reduced by using multilayer piezo electric substrates or substrates made by thick film technology.

References

- [1] H. Debéda, J. Mohr, C. Rembe, J. Schulz, U. Wallrabe, and J. Wengelin „Fully batch fabricated LIGA actuators integrated on piezoelectric ceramic substrates“. To be published at ACTUATORS '98, June 17-19, 1998, Bremen, Germany.

TuE1

5:30pm - 7:30pm

DIAMOND MICROSTRUCTURES FOR OPTICAL MEMS

H. Björkman, P. Rangsten, P. Hollman, and K. Hjort
Department of Materials Science, Uppsala University
Box 534, S-751 21 Uppsala, Sweden.
henrik.bjorkman@material.uu.se

Diamond is one of the most interesting materials under consideration for optical microelectromechanical systems (MEMS), [1, 2]. It is possible to make it both semiconducting or insulating. It is the hardest and stiffest and strongest material we know. It has the widest electromagnetic radiation transparency range of all materials known ranging from deep UV to far IR. Also, diamond shows the highest thermal conductivity of all known materials, about 5 times higher than copper. Combined with the possible insulating property this makes it an ideal heat sink for high effect semiconductor devices. Additionally, diamond has a very low friction coefficient and is extremely high wear [3,4]. The chemical inertness gives substantial benefits in microfluidic applications and when exposed to reactive gases.

Diamond is difficult to micromachine due to its hardness and chemical inertness. Therefore it is preferable to make use of diamond replication. The well developed area of silicon micromachining makes it possible to fabricate complicated structures that can be used as moulds for diamond. A microstructure technology for diamond replicas following the process flow scheme below is suggested, Fig. 1. Each step is described in more detail below:

Different silicon microstructures have been manufactured by standard bulk micromachining processes i.e. lithography, wet etching, and dry etching, to evaluate diamond replication. Both single sided and double sided anisotropic wet etching have been performed. The only etch stop technique used was time stop.

Polycrystalline diamond films were deposited on the surfaces of microstructured silicon wafers by HFCVD using a mixture of 150 sccm hydrogen and 1.5 sccm methane gas at substrate temperatures 850-900°C and chamber pressure 50 mbar. The substrate was pre-treated in an HF-dip (1:50) to remove oxides and with ultrasonic agitation with diamond seeds in ethanol to promote diamond nucleation

After the thick film deposition the top diamond surface is rough, with rms >1 µm. To thin the diamond film, hot iron plate thermo mechanical thinning was used [5], i.e. by just pressing an iron plate to the diamond. The diamond, still on the silicon substrate, was put in a vacuum chamber at 50 mbar and with reducing hydrogen atmosphere. The thinning rate was approximately 2 µm/hours cf. [5].

Following the deposition of diamond, the silicon mould had to be sacrificially etched away. Due to the good chemical resistance of diamond the most aggressive and fast etching solutions can be used. An isotropic etch was used consisting of 7:3 of HNO₃: HF, which etched through a 380 µm silicon wafer at 80°C in less than 10 minutes without stirring. Because of the violent reaction of the etch at 80°C all critical sacrificial etching, e.g. inside the diamond channels, was performed at room temperature.

All structured samples show low roughness and very good coverage. Diamond coverage at the convex corners of the of the silicon mould gives a radius of curvature not visible in our SEM. Still, there are problems with the nucleation density on larger flat surfaces on our samples. The roughness measured in an AFM on a flat diamond surface after sacrificial etching is rms 2 nm and 4 nm for 1•1 and 50•50 µm scanning areas, respectively. On the structured surfaces the nucleation density is substantially higher and the roughness consequently lower. For flat and convex corners the surface coverage and roughness are of high quality, enabling optical quality for, e.g. high performance optical applications with rms < λ/20.

Our diamond microstructure technology may be used for diverse applications. Figures 6 and 7 show demonstrators, which could be used for fluidic applications. With this technique it is possible to create well-defined capillary channels. Compared to the ordinary fused silica channels used in e.g. electrophoresis, diamond has as good transparency in the UV region, it is as inert and insulating, and it has the best thermal conductivity encountered - approximately 1000 times better than that of silica. Cooling systems for high power electronics or detectors needing low temperatures are other interesting alternatives for the fluidic application area. The silicon mould is sacrificially etched away, leaving channels with funnel shaped inlets and outlets.

The non-sticking and other tribological properties of diamond make it a good master material for polymer and metal replication. Using replication microstructures in polymers and metals could be fabricated cheaply, thus competing with other master materials such as nickel and copper. Polymer replication on diamond moulds has been tested, using polycarbonate (Makrofol®), Fig. 3. The polymers filled the diamond moulds well with low sticking.

Due to the electric insulating properties and good heat transfer capacity of diamond, it is suitable as heat transfer material for electronic devices. To demonstrate this, a microstructured carrier for lasers and optical fibres was made using dry etched silicon microstructures as master material followed by the HFCVD diamond deposition, Fig. 9.

- [1] K.E. Spear and J.P. Dismukes, Synthetic diamond: Emerging CVD science and technology, John Wiley & Sons, Inc., New York, 1994
- [2] V.S. Trava-Airoldi, E.J. Corat, E. Del Bosco and N.F. Leite, Surface and Coatings Technology 76-77 (1995) p. 797-802
- [3] P. Hollman, A. Alahelisten, M. Olsson and S. Hogmark, Thin Solid Films, 270 (1995) 137-142.
- [4] S. Hogmark, P. Hollman, A. Alahelisten and P. Hedenqvist, Wear (1996), p. 225-232
- [5] S. Jin, J.E. Graebner and T.H. Tiefel, Thinning and polishing of diamond films by diffusional reaction with metals, SPIE Vol. 1759 Diamond optics V (1992), p. 57

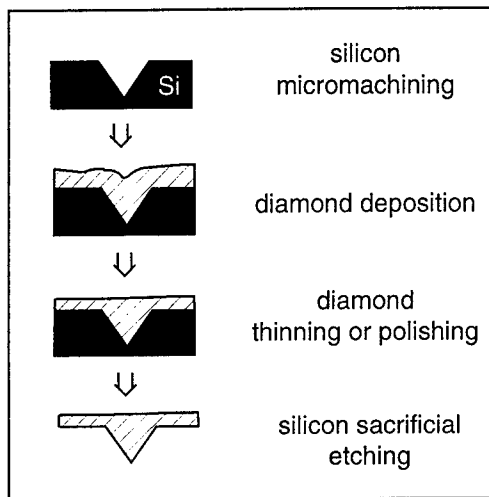


Fig. 1 A process flow scheme for the manufacturing of diamond replicas.



Fig. 2 Cross-section of capillary channels in diamond. The silicon mould is sacrificially etched away leaving channels with inlets and outlets.

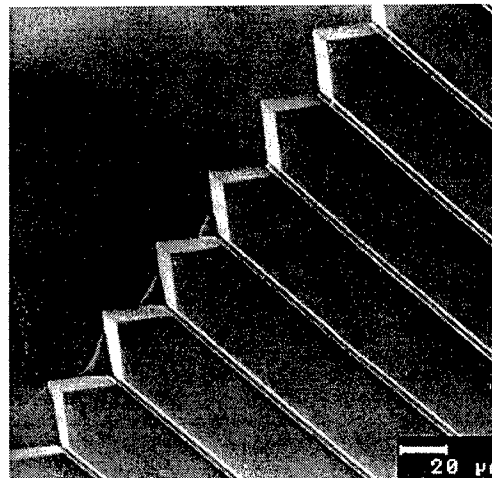


Fig. 3 Polycarbon replica from a diamond master.

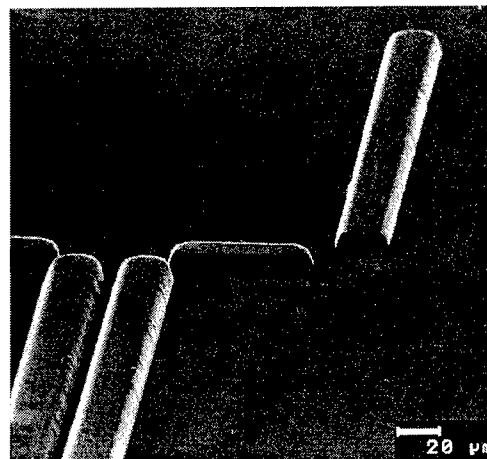


Fig. 4 A demonstrator structure for a carrier for passive alignment of a laser and an optical fibre.

Technique to Improve Flatness of MEM Backplanes

K. Seunarine and I. Underwood.

The University of Edinburgh, Department of Electrical Engineering, Edinburgh, EH9 3JL.
Scotland, United Kingdom.
Tel: +44(131)6505608
email: K.Seunarine@ee.ed.ac.uk

1. Introduction

All reflective optical devices fabricated on silicon require flat backplanes. Unfortunately the thermal processing, which is essential in the manufacture of such devices, causes the silicon die to become warped ($\sim 1\text{-}2\mu\text{m}$). Fig 1a. This backplane warping produces spurious phase modulation effects when the devices are used in coherent applications such as correlators, cross bar switches and dynamic holograms. Our investigations have been carried out on Liquid Crystal Over Silicon (LCOS) SLMs.

2. Backplane Flattening

Robust ECR-PECVD SiO_2N_x structures are patterned on a wafer scale to geometries small enough to be positioned between the pixel mirrors of the SLM ($\sim 3\mu\text{m}$). The SiO_2N_x is patterned using the "lift-off" process to prevent deterioration of the aluminum pixel mirrors.

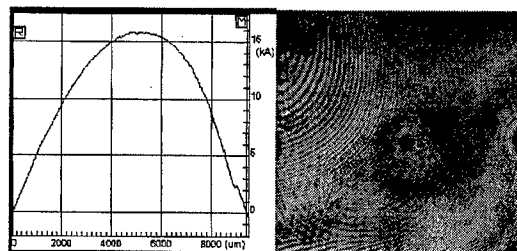


Figure 1. a. Surface profile of a warped backplane. b. Interferogram of one of the least flat backplanes produced. The fringe of interest is the large circular fringe, centre right.

When assembled under pressure the SiO_2N_x pillars, on the warped silicon die, are forced against an optical flat, pushing down on the backplane, forcing the backplane to conform to the flat, fig 2. The resulting backface deformation is then held in place by a thick layer of high viscosity UV curing

adhesive, sandwiched between the device and a transparent substrate. Excellent uniformities, and hence die flatness', are achieved (≤ 2 white light fringes, over 1cm^2) with this technique. Interferometer investigations, of these backplanes, are in agreement with our initial visual inspections. Fig. 1b. We have found that this method of cell assembly requires spacer pillars in both the device aperture and perimeter as opposed to just the perimeter.

3. Cell Gap Spacing

In addition to a flat backplane, FLCOS SLM's require an accurate cell gap spacing to define the liquid crystal layer thickness. This gap spacing is provided by our ECR-PECVD pillars. Although silica spacer particles are currently used to provide an adequate cell gap uniformity[1], they cannot be used in device flattening in the same way our ECR-PECVD pillars are used, as described above. The pressures required to flatten a warped backplane are on the order of 1-2 bar. At these pressures the silica spacer particles have been found to fracture along their long axes or become embedded in the soft aluminum mirrors. Any lateral motion of the cover glass, during cell assembly, also causes the particles to "tear" the aluminum mirrors, reducing their efficiency and even shorting them to neighboring pixels or the common ground ITO electrode on the cover glass.

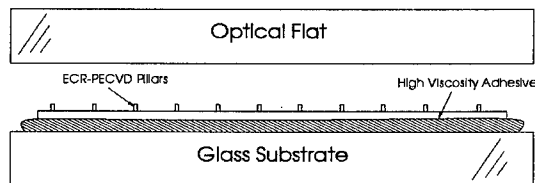


Figure 2. Backplane flattening.

4. Patterned Layer Characterization

The heights of the pillars are influenced by their dimensions and the thickness of the photoresist used in their patterning, fig 3. Our investigations have revealed that the length of the feature has an effect on its height only when the length is of a similar magnitude to the width.

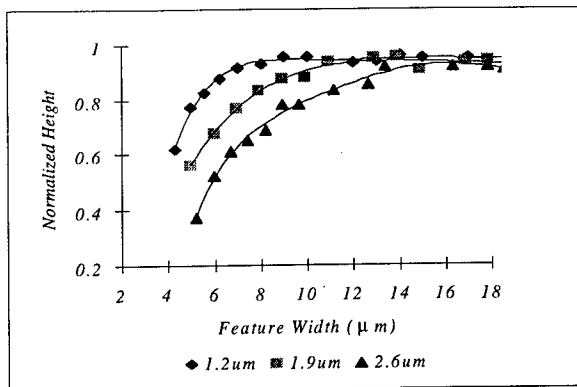


Figure 3. Effect of feature geometry and photoresist thickness (1.2, 1.9 and 2.6 μm) on pillar height.

It is clear from these results, fig 4, that the deposition rate, which must be known in order that the pillars can be deposited to high tolerances (from wafer to wafer), varies with the aspect ratio of the patterned photoresist layer.

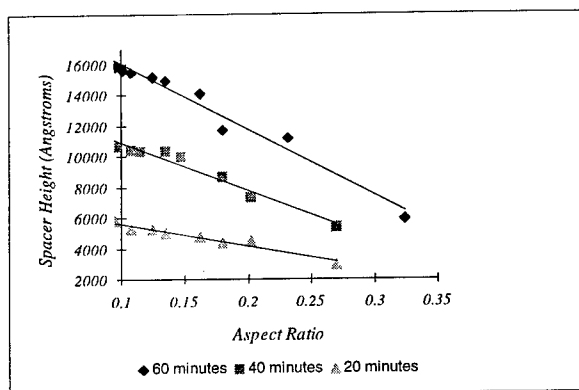


Figure 4. Feature height vs. Aspect ratio of the patterned photoresist layer for various deposition times.

5. ECR-PECVD Characterization

We have optimized the ECR-PECVD SiO_2N_x deposition process, using a statistical design of

experiments' approach[2], to produce the best thickness uniformity for the pillars/spacer layer. It is found that the most uniform depositions occur under a high N_2O flow rate and low microwave power. The SiH_4 is found to have no significant effect on the film uniformity, over the factor space examined. We have obtained SiO_2N_x uniformities of <1%, over a 3 inch wafer. This is better than that of commercially available spacer particles both on a die and wafer scale.

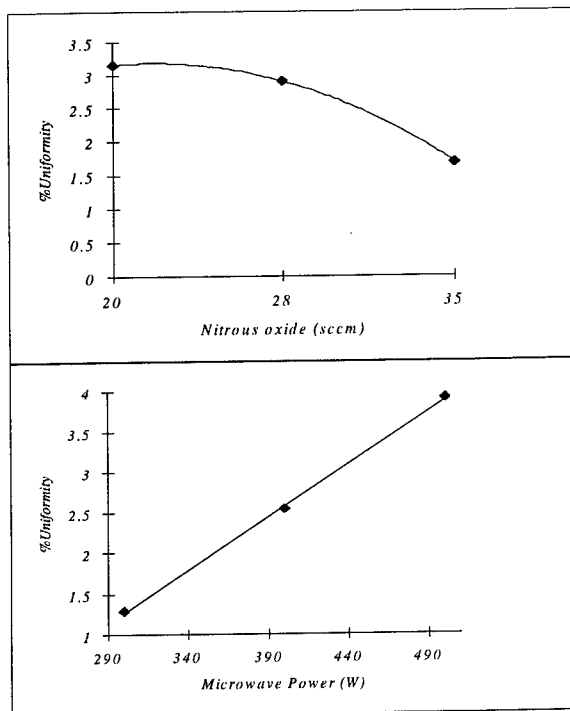


Figure 5. ECR-PECVD uniformity optimization (first order effects).

Acknowledgements

The spacer layers were printed and the ECR oxide deposited by J.T.M.Stevenson and D.D.Archibald respectively.

References

- [1] D. C. Burns et al. Optics Communications, 1995, vol.119, no.5-6, pp. 623-32.
- [2] G. Z. Yin et al. Solid State Technology, May 1987, pp.127-32.

TuE3
5:30pm - 7:30pm

Laser Opto-microactuators Rotated by Molecular Gas Dynamics Effects

Masahiro OTA, Tomohiko NAKAO and Moriyoshi SAKAMOTO
Department of Mechanical Engineering,
Graduate School of Engineering,
1-1, Mimami-Oosawa, Hachi-Oji, Tokyo 192-0397, Japan.
Tel. +81-426-77-2715, FAX. +81-426-77-2701
E-mail Address ota-masahiro@c.metro-u.ac.jp

ABSTRACT

Laser opto-microactuators are discussed in this study. The actuators rotate by the effects of molecular gas dynamics such as the forces by a thermal creep force and a radiometric force. The effects are induced by heating of the rotor surface of the actuators with a laser beam. It is elucidated that the maximum torque of the actuators occurs at the Knudsen number of about 0.2 and the maximum rotational rate of the actuators is at the Knudsen number of 0.5. The Knudsen number is defined as the ratio of the mean free path length of the gas in the chamber to the rotor blade length of the actuators in this paper.

1. Laser Opto-microactuators

The actuators are composed of a vacuum chamber, microrotor and laser power supply at the moment. The schematic drawing of the actuators is shown in Figure 1. In Figure 1, the device for measuring a rotational rate of the rotor is also shown. The microrotor has 4 blades each made of an aluminum plate with very thin thickness. The blade lengths of the rotor are 1 mm and 10 mm, respectively. The thickness of the blade is 0.1 millimeter; only one side surface of the blades is coated with carbon-black powder. The 4 blades are connected with a bearing like a cap made of a Pyrex glass. In this study an argon ion laser beam with 514.5 micron wave length is used for heating the rotor surface. The gas pressure in the vacuum chamber is reduced down to a certain pressure using a vacuum pump system. At the pressure the laser beam is irradiated to the rotor. The irradiation of the laser beam heats the carbon-black coated surfaces of the rotor. Immediately after the irradiation, the rotor begins to rotate.

2. Characteristics of Laser Opto-microactuators

The experimental results of the rotational rate of the rotor are shown in Figure 2. The vertical axis in Figure 2 is the rotational rate of the rotor by revolution per second. The horizontal axis is a Knudsen number. The Knudsen number is a non-dimensional parameter for molecular gas dynamics. The Knudsen number is defined as the ratio of the mean free path length of the gas in the chamber to the blade length of the rotor in this paper. Therefore, increasing the Knudsen number the gas pressure in the chamber decreases or the blade length of the rotor decreases. Because decreasing the gas pressure the mean free path length should increase. In the Knudsen number range from 0.05 to 5, the actuator can be rotated by the effects of molecular gas dynamics ⁽¹⁾⁽²⁾⁽³⁾ such as the force induced by a thermal creep force and a radiometric force.

The experimental results of a twisted torque of the rotor are shown in Figure 3. The rotor was suspended from a ceiling of the chamber by a Pyrex glass cylinder with a diameter 100 micron for measuring the twisted torque of the rotor with laser irradiation. The deviation angle of a reflected He-Ne laser beam from the rotor surface between laser irradiation and without irradiation was measured and then the twisted torque was evaluated by an elastic theory. It is elucidated that the maximum torque of the actuators occurs at the Knudsen number of about 0.2.

3. Conclusions

Laser opto-microactuators are proposed in this paper. In the Knudsen number range from 0.05 to 5, the actuators can be rotated by the effects of molecular gas dynamics such as a thermal creep force and a radiometric force. It is elucidated that the maximum torque of the actuators occurs at the Knudsen number of about 0.2. The maximum rotational rate of the actuators is achieved at the Knudsen number 0.5.

References

- (1) M. OTA and N. KAWATA, Driving force estimation of opto-microengines worked by rarefied gas dynamics effects, Proc. 3rd International Symp. Micro Machine and Human Science Nagoya, Japan, 1992, pp.35-43.
- (2) M.OTA and N. Kawata, [Direct simulation] of gas flows around rarefied gas dynamics engines, for a micro-machine, Proc. of 19th International Symp. On Rarefied Gas Dynamics, Oxford, 1994, pp.722-728.
- (3) M. OTA, M.ISHIGURO and M.SAKAMOTO, On Selective Optical Absorber Film for Rotor of Opto Microengine, Transport Phenomena in Material Processing and Manufacturing, ASME, HTD-Vol.336, ASME, 1996, pp.193-206.

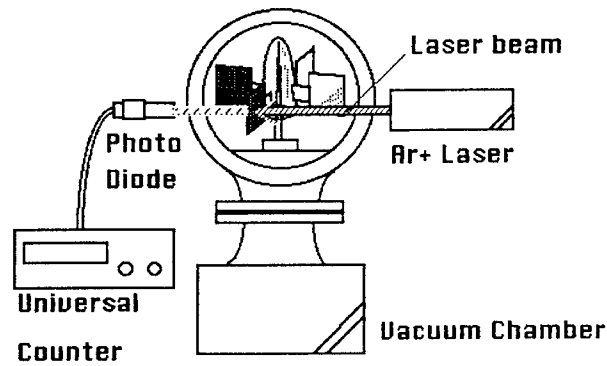


Figure 1 Schematic illustration of laser opto-microactuator

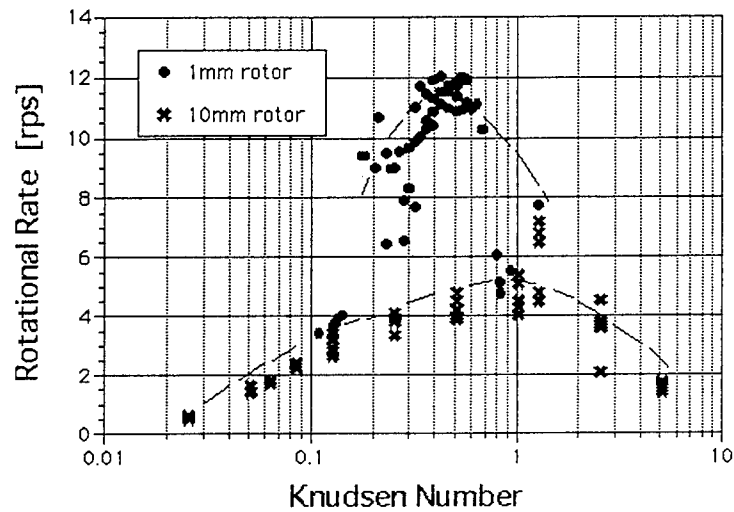


Figure 2 Effects of Knudsen number on rotational rate of laser opto-microactuator

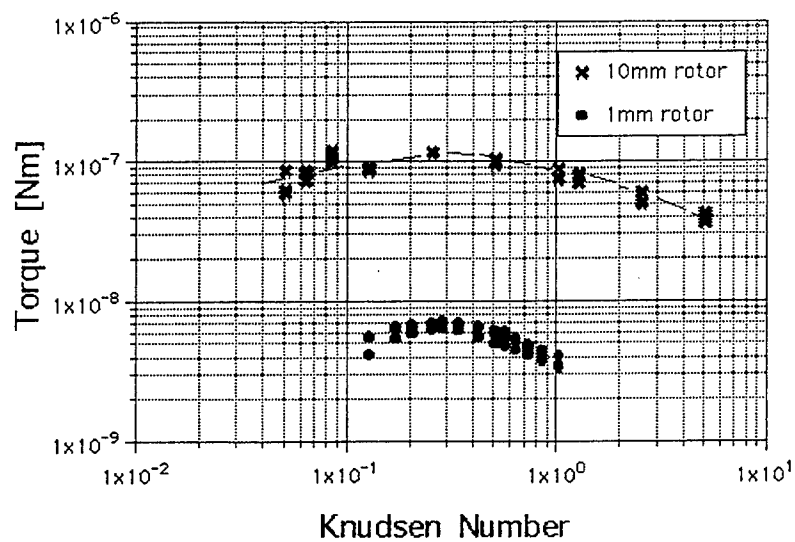


Figure 3 Effects of Knudsen number on twisted torque of laser opto-microactuator

TuE4

5:30pm - 7:30pm

Deflectable Micro-Mirror Arrays for Implementation of a Recirculating Folded Perfect Shuffle Processor

Alva E. Hare and F. R. Beyette Jr.

Department of Electrical & Computer
Engineering and Computer Science
University of Cincinnati,
P O Box 210030
Cincinnati OH, 45221-0030
Email: beyette@ececs.uc.edu

Abstract

An optical interconnect system based on deflectable micro-mirrors is discussed. The electrostatically actuated mirrors are surface micro-machined on a silicon substrate and positioned for implementation of an optical folded perfect shuffle. Design criteria and application to smart pixel systems are presented.

Key Words: deflectable micro-mirrors, Optical Interconnects, perfect shuffle, recirculating architectures, MEMS, MOEMS

Summary

Based on innovations from a wide variety of disciplines, smart pixel technology has progressed from individual optoelectronic devices to fully operational photonic information processing systems. Similarly Micro-Optical Electro-Mechanical Systems (MOEMS) have recently been proposed which utilize Micro Electro Mechanical Systems (MEMS) in the design of photonic systems. In this paper we present the design concepts of such a system.

Figure 1 shows an optical interconnect system which is controlled by four arrays of deflectable micro-mirrors. These mirrors are surface micro-machined on a silicon wafer which also holds the detectors and processing logic of an optoelectronic smart pixel system. Each mirror array has four individually addressable mirrors for a total of sixteen interconnection paths. The optical interconnect system is configured in a recirculating architecture by placing a fixed mirror parallel to the silicon wafer. The four mirror arrays are arranged such that a folded perfect shuffle interconnect system can be implemented by electronically connecting the smart pixel array to the mirror address electrodes. Finally a laser, which illuminates the deflectable micro-mirrors, is mounted above the wafer. For each interconnect path, light from the unmodulated laser is reflected off of the deflectable mirrors, up onto the fixed mirror, and back down to the wafer where it strikes the smart pixel detector array. Since the laser is not modulated, encoding of the optical data is performed by actuation, or tilting of the deflectable mirrors.

In a fully operational smart pixel system the input data could be loaded by illuminating the detector array with optical data in a bit serial fashion. After the input data is loaded, optoelectronic processing is performed by the smart pixel array. To complete the optoelectronic processing each pixel's output connection directs data (via a deflectable micro-mirror) through the shuffle network to the input of another smart pixel. Thus a recirculating architecture is realized. Clearly this smart pixel architecture is well suited for implementing recursive algorithms such as sorting. While our long range goal is to implement such a system, this paper will focus on the mirror design and evaluation of mirror arrays for a folded perfect shuffle interconnection.

Figure 1 also shows the design dimensions which are critical to implementing an optical folded perfect shuffle interconnection. The lateral shift of the beam is controlled by the micro-mirror angle of deflection, and the distance between the surface of the wafer and the fixed mirror. Figure 2 plots the micro-mirror deflection angle (θ) vs. the fixed mirror height (h) and the lateral separation (S) between the micro-mirror and corresponding detector. The separation, is given by $S = 2 h \cdot \tan(2\theta)$. When the mirror is actuated, it will bend until it touches the underlying micro-structures. Therefore, the deflection angle is limited by the micro-mirror's elevation above the substrate, and the size of the micro-mirror. If the micro-mirror is square, with a side of length L , and is elevated above the substrate a distance E . The mirror deflection angle is given by $\theta = \sin^{-1}(E/L)$. The surface micro-machining process used by MUMPs allows us to obtain an elevation E of either $0.75\mu\text{m}$ or $2.0\mu\text{m}$. Assuming $E = 2\mu\text{m}$, $L = 50\mu\text{m}$, and $S = 7500\mu\text{m}$, the fixed mirror height, h , is $\sim 3.5\text{ cm}$.

We have designed an evaluation system which will be fabricated by the Multi-User MEMS Process (MUMPS) facility. In addition to presenting the optical system suitable for implementing the perfect shuffle This paper will discuss the test results of that structure. Our paper will concentrate on the ability of the of a micro-mirror structure to perform an optical folded perfect shuffle. The experiment must address such concerns as interfacing the often high voltage/low power micro-machines with standard CMOS devices.

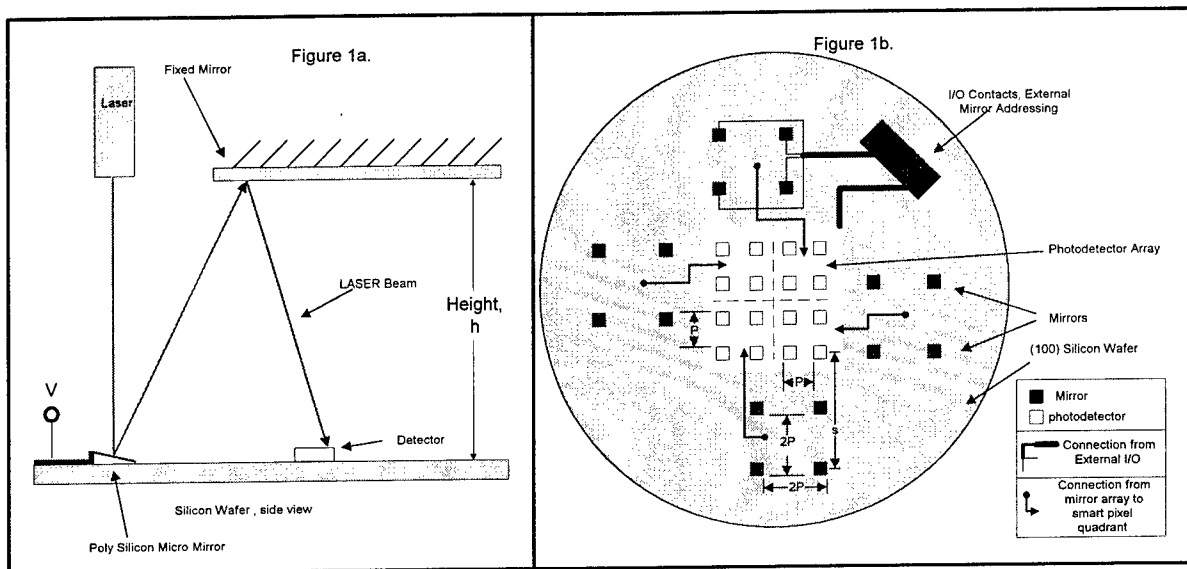


Figure 1a. Simplified side view of the interconnect system. Applying a voltage to the micro-mirrors surface causes the micro-mirror to tilt toward the wafer reflecting the laser light up onto a fixed mirror and back onto the smart pixel detector array.

Figure 1b. Top down view of the wafer depicting the mirrors and smart pixel array. The detector pitch (P) and detector-mirror separation (S) is used to determine the fixed mirror height (h). For clarity some electrical connections have been omitted.

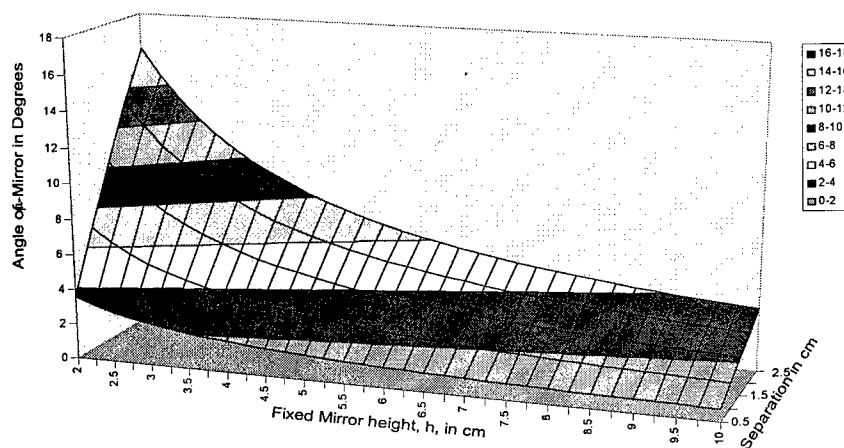


Figure 2. Relationship between angle of deflection (θ) vs. separation (S) and height of the fixed mirror (h).

TuE5
5:30pm - 7:30pm

ERBIUM-DOPED WAVEGUIDE DEVICES FOR WDM APPLICATIONS

Marco Federighi, Noor Othman and Fabrizio Di Pasquale

*Department of Electronic and Electrical Engineering, University College London
Torrington Place, London WC1E 7JE, England*

In recent years considerable advances have been made in the study of Er-doped waveguides for telecommunications applications. These devices have been developed to allow on-chip integration between active and passive components, and differ from their fiber-based counterparts (Er-Doped Fiber Amplifiers, or EDFAs) in their much smaller size (typically a few cm versus a few m). For these devices to be of any use, they must provide gains of the order of a few dB per cm, which can be achieved with Er concentrations of about 10^{20} ions/cm³, or about one order of magnitude higher than in fibers. In order to prevent Er ion pair formation, such high Er concentrations require low-temperature fabrication techniques and/or co-doping with Al or P oxides. Even so, the high dopant concentration leads to a significant increase in up-conversion and concentration quenching. One consequence of this is a maximum gain coefficient which, in the limit of very high doping, is independent of the Er concentration and cannot exceed 16 dB/cm. Another consequence is a much higher threshold pump power, increasing with the Er concentration^[1].

From the point of view of system applications, these features of highly doped Er have significant implications. With respect to EDFAs, waveguide-based amplifiers have the only advantage of a much smaller size and are thus only preferable to EDFAs if integration with other devices is required, and then only for gains of a few dBs. For this kind of applications, however, their only significant advantage over Semiconductor Laser Amplifiers (SLAs) is their better dynamic response - with the significant disadvantage of the need for optical pumping, made more difficult by the high threshold pump power particularly if waveguide arrays, star couplers or power splitters are considered. The fact that Er-doped waveguides have significantly lower gains than SLAs is also a drawback that effectively rules out use as straight amplifiers. In summary, Er-doped waveguides can only be useful in applications where the requirements are a good dynamic response and a few dBs of gain, and then only if they can be pumped efficiently by integratable laser diodes.

Experimental work on Er-doped waveguides has concentrated on single-channel amplifiers^[2] and on lasers. In the former case gains of several dBs have been demonstrated, but the high pump powers required (of the order of 100 mW) have recently suggested a lowering of the Er concentration in favor of a greater pump efficiency^[3]. Unexpectedly high gains have also been reported^[4], but these, if confirmed, can only be explained by a significant change in the Er cross-section due perhaps to increased mixing of the f levels with the s and d bands, as shown in Er-doped crystals.

In the case of waveguide lasers, sufficiently low thresholds have been achieved by using Er/Yb co-doped glass, with a typical Yb:Er ratio of 10:1. However, few attempts^[5,6] have been made to date either to assess the behavior of the same waveguides for applications other than lasers, or to optimise the Er concentration and the Yb:Er ratio. We have investigated both topics by using a theoretical model based on rate equations for Er and Yb, with the energy transfer from Yb to Er represented by a term $C_{tr}n_b n_1$ where n_b and n_1 are the populations of the excited level of Yb and the ground level of Er respectively. The transfer coefficient C_{tr} has been calculated by fitting experimental data to the Foster-Dexter model; cross-relaxation between neighboring Yb ions, which is important at high Yb concentration and cannot be represented directly in the rate equations, has been taken into account by multiplying

C_{tr} by a normalization factor $n_1/(n_1+n_a)$, where n_a is the population of the ground level of Yb.

Our results are shown in Figure 1 below. We have calculated the gain coefficient, in dB/cm, of bulk Silica doped with 2×10^{20} Er ions per cm^3 (or about 2.6 wt% Er) in three different configurations: an "ideal" (and unrealistic) material with no up-conversion, as a term for comparison; a material doped with Er alone; and a material co-doped with 2×10^{21} Yb ions per cm^3 (Yb:Er=10:1).

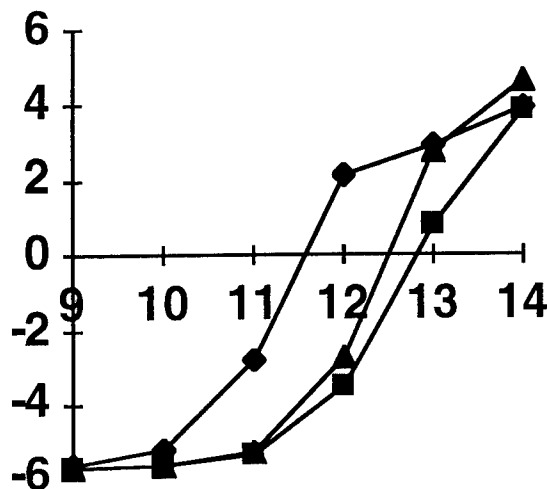


Figure 1: gain coefficient (in dB/cm) of Er-doped (triangles, without up-conversion; squares, with up-conversion) and Er/Yb co-doped (diamonds) Silica versus \log_{10} of pump photon density

As shown in the figure, the maximum gain is somewhat reduced as a result of up-conversion and, as expected, co-doping with Yb does not change this. Around the point of population inversion, however, the presence of Yb has a dramatic effect, reducing the pump power required for threshold well below the level that should be expected for the "ideal" material with no up-conversion. The improvement is very substantial, more than a factor 10 at this Er concentration. The actual power in mW depends on the material loss and on the waveguide design; for the devices reported in the literature, our calculations show a typical change from about 60 mW to about 10 when ten times as much Yb as Er is introduced. Increasing the Yb concentration even further does not bring any substantial improvement.

We can conclude that, if the limited gain of Er-doped waveguides makes them unsuitable as a replacement for EDFAs in straight amplifier roles, the very low threshold achievable with Yb co-doping allow their use in integrated configurations where gains of a few dB/cm are adequate, with the possibility of pumping several waveguides from a single 980 nm laser diode.

References:

- [1] M.Federighi et al., to be submitted to IEEE J. Quantum Electron.
- [2] J.Shmulovich et al., Electron. Lett.**28**: 1181 (1992)
- [3] R.N.Ghosh et al., IEEE Photon. Technol. Lett. **8**: 518 (1996)
- [4] P. Fournier et al., Electron. Lett. **33**: 293 (1997)
- [5] J.-M.P.Delavaux et al., IEEE Photonics Technol. Lett. **9**: 247 (1997)
- [6] D. Barbier et al., IEEE Photonics Technol. Lett. **9**: 315 (1997)

TuE6
5:30pm - 7:30pm

OPTICAL DESIGN OF MICRO-OPTICAL-ELECTRO-MECHANICAL SYSTEMS

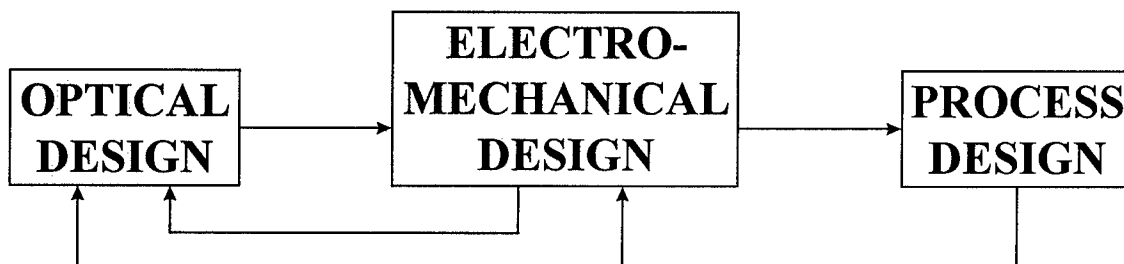
Steven J. Walker and David J. Nagel
Naval Research Laboratory
4555 Overlook Ave. SW
Washington DC 20375
steve.walker@nrl.navy.mil

Microsystems in general, including MOEMS, have four central phases in their life cycle: design, manufacture, testing and use. Each of these has sub-categories. For example, manufacturing must include attention to packaging, as well as the basic production of devices. Testing can include both partial electronic testing, maybe during manufacturing, as well as full operational testing after manufacturing. The use phase might require built-in testing and calibration, in addition to the fundamental operation.

This paper is concerned with the design phase of MOEMS. It should, in principle, include three sub-phases. While they can be considered and performed separately, these phases are interactive and should be performed iteratively. The first phase is *optical or functional design*. It involves choosing the geometry and optical characteristics (materials) for the MOEMS so that it will perform the desired function. This phase is the focus of the current paper and will be discussed at length below. The primary issue to be addressed is whether or not any of the commercially available optical design codes are useful for the design of MOEMS. If so, can they be used with the other codes needed to design MEMS?

The second process is the *electro-mechanical design* of the MOEMS device. This in itself involves iterative, detailed and self-consistent calculations of the electronics and the mechanics of the device. It requires consideration of many germane bulk characteristics of materials, such as stiffness, that are beyond the optical properties of their surfaces. There are a few companies which now offer design codes for MEMS in general. They include, to varying degrees, material parameters and physical characteristics, such as electrostatics, mechanics, thermal processes, fluidics, and others.

The third phase is *process design*. Here, the patterning, material deposition and etching steps, which must be done sequentially to produce the desired devices with the needed performance, are laid out in enough detail for the fabrication personnel to make the devices. While there are several codes for process design of integrated circuits, process design of MEMS is at a more primitive state. Some of the IC codes do apply, and there are codes for the orientation-dependent etching of silicon, for example. However, the development of process design codes for MEMS is an area rich with opportunity. This will be increasingly true as new materials are employed to develop new MEMS which perform better or are cheaper. For example, compound semiconductors and plastics will be used increasingly in MOEMS.



Returning to the optical design of MOEMS, there is reason for hope that the codes developed to design macroscopic optics might also be good for the design of optical MEMS. This is because the wavelengths of light in and near the optical region of the spectrum are still short compared with the lateral dimensions of MOEMS devices. The physical dimensions of MOEMS optics often fall in the range of 10 to 100 micrometers. In this region, diffraction effects due to the clear-aperture size may be negligible. Of, course for some MOEMS, smaller structures do bring diffraction effects into play. These might disqualify many of the commercial optical design codes from being useful for MOEMS design.

This study was initiated by using a compilation of optical design software companies which was published in a trade journal review article. Twenty-five firms were listed. Of these, 21 companies were contacted in order to learn details of their codes. 16 companies responded. The available material, much of it gotten by downloading trial codes over the internet, was examined to determine the characteristics of each code. These characteristics fall into two classes. The first involves the situations to which each of the codes applies, for example, refractive or reflective optics, or optical fibers. A major aspect for each involves how the surfaces being designed are input, modified and described. These solid model descriptions can have much in common with the descriptions which go into the electro-mechanical models. Such commonality could be important for the overall MOEMS design problem. The second class of descriptors for each code involves its size, cost and the required platforms and performance to get results in reasonable times. Some of the codes are relatively small so that they fit and run easily on ordinary personal computers. Others require work stations and much more extensive calculations.

Many simple optical codes, like AutoRay and Beam Four, will perform a basic analysis of optical designs. These codes typically use ray tracing, gaussian ray propagation, ABCD methods, or rotationally-symmetric propagation algorithms. More robust codes use non-sequential ray-tracing to accommodate non-symmetric optical elements. Codes, such as GLAD, use complex amplitude distribution functions to represent optical beams. These programs will be better suited to MOEMS designs because they handle diffraction effects more rigorously. Design software for MOEMS must have the capability to model diffractive optical components such as fresnel zone plates, binary lenses, and binary grating structures. Fiber optics and 3-D waveguides also play an important role in some MOEMS devices. Design codes, such as IFO_Gratings, do an excellent job of modeling waveguide structures, but will need to handle waveguides in conjunction with standard lenses to increase its utility. Many optical design programs, such as CODE V, have extensive catalogues of materials incorporated within the program. MOEMS devices will need a very different materials selection, and thus the ability to input custom materials parameters is mandatory. The usefulness of these optical codes will also depend on their ability to output standard file formats, such as IGES, DXF, and STEP, that can be used as input files for both design and fabrication software. Sixteen commercial optical CAD programs have been reviewed and assessed for their applicability to the design of MOEMS.

Proposal of human eye's crystalline lens-like variable focusing lens

Si-Hong Ahn and Yong-Kweon Kim

School of Electrical Engineering, Seoul National University

#301-1104, San 56-1, Shillim-dong, Kwanak-gu, Seoul 151-742, Korea

Tel: +82-2-888-5017, Fax: +82-2-873-9953, Email: equalize@chollian.net

1. The variable focusing lens

A novel variable focusing lens is proposed. The lens is composed of two glass diaphragms on both sides of silicon substrate, which has micro-channels on it for working fluid.

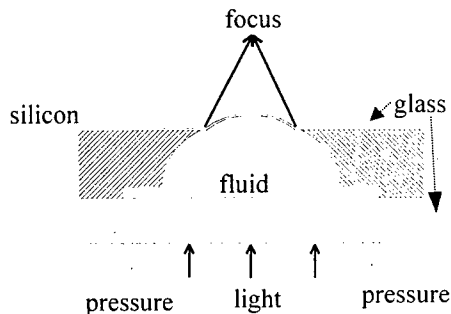


Figure 1. Variable focusing lens

The chamber between two glass diaphragms is filled with the working fluid. Refractive index matching fluid such as silicon oil can be used as working fluid, which is pumped into or out of the chamber through the microchannel. The curvature of the lens can be changed by the oil pressure, which is built by micropump outside. The change of curvature of the lens produces the focal plane shift. It works like *human eye's crystalline lens*. In addition, both convex lens and concave lens can be realized by control of oil pressure. Commercial micropump is used for the experiment of fabricated variable focusing lens. Designed diameter of the variable focusing lens is 10mm. Thickness of the glass diaphragm is 40 μ m. Mechanical characteristics (such as glass diaphragm deflection by the fluidic pressure) and optical characteristics (such as focal plane shift) of the variable focusing lens are calculated. The fabrication process for the lens is designed. The

variable focusing lens can apply to optical pickup, CCD camera and microscope etc.

2. Modeling of the lens

Since the glass diaphragm of the lens is a circular plate symmetric about the axis perpendicular through its center, the deflection should be also symmetric with the uniform pressure. In all points equally distant from the center of the plate whose radius is a , the deflections will be the same. Then the deflection can be considered in one diametral section through the axis of symmetry. If we take the origin of the coordinates O at the center of the undeflected plate and denote the radial distance of points from the center by r , the deflection in the downward direction w can be obtained from the differential equation of equilibrium [1].

$$\frac{d^3 w}{dr^3} + \frac{1}{r} \cdot \frac{d^2 w}{dr^2} - \frac{1}{r^2} \cdot \frac{dw}{dr} = \frac{Q}{D} \quad (1).$$

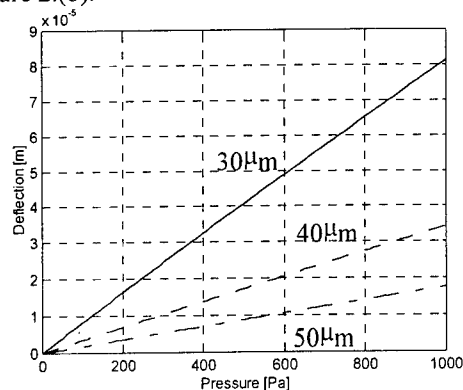
In equation (1), Q is the shearing force per unit length and D is the flexural rigidity determined by the modulus of elasticity of the material and Poisson's ratio. In the case of the lens whose curvature is changed by the fluidic pressure P , the shearing force Q can be replaced by P . Differential equation (1) can be solved as equation (2) with the boundary conditions that the slope of the deflection surface in the radial direction should be zero at $r=0$ and $r=a$, and that the deflection w is zero at $r=a$ [2].

$$w = \frac{P}{64D} \cdot (a^2 - r^2)^2 \quad [\text{m}] \quad (2),$$

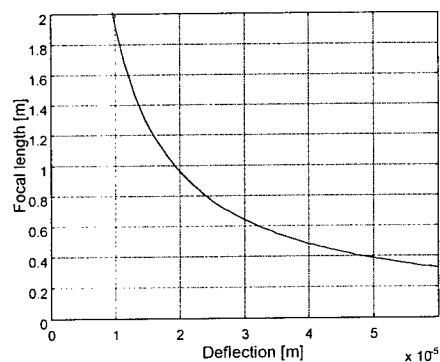
$$f = \frac{32D}{(n-1) \cdot P \cdot a^2} \quad [\text{m}] \quad (3).$$

With the solution (2) the focal length of the lens, f , can be obtained as a function of pressure P ,

which is shown in equation (3). In figure 2.(a), deflection vs. pressure is plotted for the lens which has a glass diaphragm thick to $30\mu\text{m}$, $40\mu\text{m}$, $50\mu\text{m}$ and whose diameter is fixed to 10mm . Deflection vs. focal length is plotted in figure 2.(b).



(a) Deflection vs. pressure



(b) Deflection vs. focal length

Figure 2. Modeling results

3. Design of fabrication process

Figure 3 shows the fabrication process of variable focusing lens. The opening for the lens is patterned on silicon-nitride layer and silicon-oxide layer (figure 3.(a)). The chamber is formed by isotropic etching of silicon in buffered $\text{HNO}_3\text{-HF}$ (figure 3.(b)). #7740 glass is bonded to silicon substrate by anodic bonding after removal of silicon-nitride layer and silicon-oxide layer (figure 3.(c)). Bonded glass is thinned to the designed thickness, $40\mu\text{m}$ (figure 3.(d)). Glass surface is mechanically polished after chemical thinning. Metal is deposited (figure 3.(e)) and etched with pattern (figure 3.(f)). Microchannel is

formed by reactive ion etching (figure 3.(g)). Finally glass substrate with the inlet and outlet is bonded to the other side of silicon substrate (figure 3.(h)).

The fabrication of the variable focusing lens is in process. The mechanical and optical characteristics of the lens will be measured and reported.

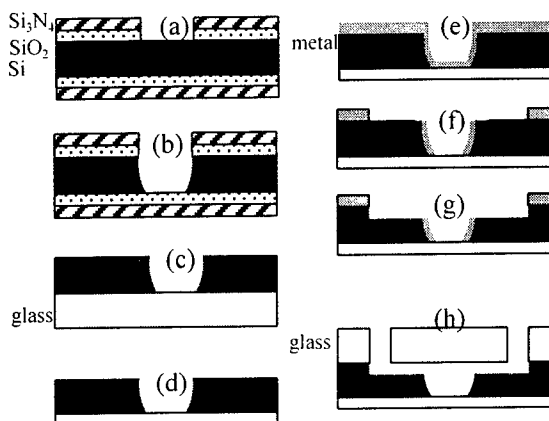


Figure 3. Fabrication process

Acknowledgment

This research was supported by Ministry of Science and Technology under National Research Program.

References

- [1] S.P. Timoshenko, THEORY OF PLATES AND SHELLS, McGraw-Hill, 1959
- [2] R.Schellin, G.Hess, C.Thielemann, D. Trost and J.Wacker, 'Measurement of the mechanical behavior of micromachined silicon and silicon nitride membranes for microphones, pressure sensors and gas flow meters', Sensors and Actuators, Vol.A 41-42, pp287-292, 1994

A novel approach to corner compensation of multistep Si(100) terraced structure for microlens

C.K. Chung, C.C. Lee and C.Y. Wu

Microsystems Laboratory, Industrial Technology Research Institute,
Chutung, Hsinchu 310, Taiwan, R.O.C.

SUMMARY

The multistep microlens with same step height are the important components in the optical microelectromechanical system (MEMS), especially Si(100) microlens for the infrared (IR) imager to condense IR radiation into the detector module and increase its responsibility. We have demonstrated the multistep Si(100) terraced structure for microlens by one photo mask and KOH anisotropic etching [1]. It simplifies the conventional process, in which m masks are necessary for 2^m -step microlens, along with no misalignment problem of the masks. A key issue in KOH anisotropic etching is to avoid the undercutting of convex corner. Offereins et al. had reported many different designs for corner compensation in aqueous KOH solution [2]. To achieve nearly perfect square corners, the modified geometrical layout had been studied by some researchers [3, 4]. But, only two-level terraced structures were presented. No compensation design for multi-level terraced structures is reported until now. It is of thus a need to provide a method for corner compensation of multistep Si(100) structure.

Fig. 1 shows the schematic diagram of the multi-level Si(100) terraced structures prepared by one photo mask and KOH anisotropic etching. The terrace formation mechanism can be explained by the sequences of V-grooves formation in the intervals $[a_n]$ of the masked areas $[b_n]$, underetching and breakthrough of the masked areas, and terrace planarization. The terrace planarization and corner formation start from the highest level (or depth), then followed by lower level terraces and finished at the first level terrace. Because the convex corner undercutting results from the faster etching rate in $\{411\}$ planes than in $\{100\}$ planes [2], the different level terrace corners should have a buffer region to keep good square corner during the etching process. Our mask layout with the grid buffer region is shown in Fig. 2. The dark region represents the open areas, $[a_n]$, to etching solution with fixed dimension at $5\ \mu\text{m}$. The clear region represents the masked areas, $[b_n]$, of silicon nitride film with dimensions varied from 2 to $4\ \mu\text{m}$. The grid buffer regions play an important role in compromising the etching rate of convex corners at different levels to get good square corners as shown in Fig. 3.

References

- [1] C.K. Chung, Y.T. Li, C.C. Lee, T.S. Lee and C.Y. Wu, "Multistep Si(100) terraced structure by one photo mask for microlens", Transaction of IEE of Japan (submitted).
- [2] H.L. Offereins, H. Sandmaier, K. Maruscryk, K. Kuhl and A. Plettner, "Compensating Corner Undercutting of (100) Silicon in KOH", Sensors and Materials, vol. 3, (1992) 127-144.
- [3] Q. Zhang, L. Liu and Z. Li, "A new approach to convex corner compensation for anisotropic etching of (100) Si in KOH", Sensors and Actuators, vol. A56, (1996) 251-254.

- [4] P. Enoksson, "New structure for corner compensation in KOH anisotropic etching", J. Micromech. Microeng. Vol. 7 (1997) 141-144.

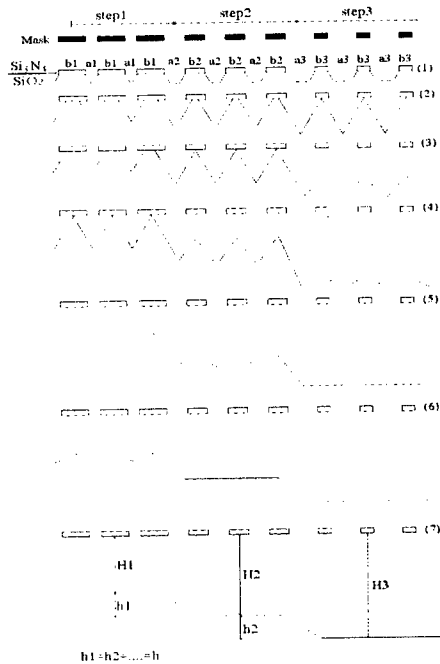


Fig. 1 The schematic diagram of the multi-level Si(100) terraced structures prepared by one photo mask and KOH anisotropic etching.

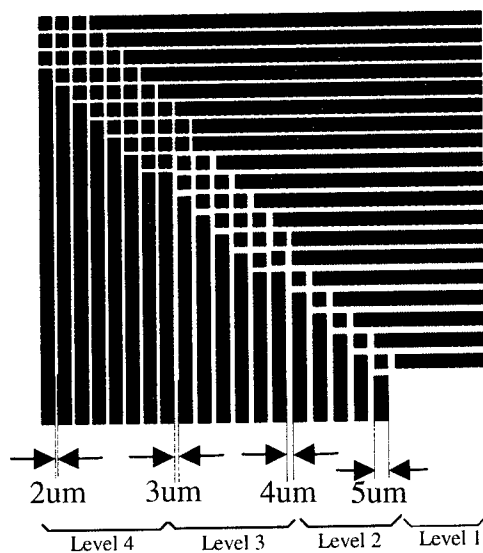


Fig. 2 The mask layout with grid buffer regions for the multistep terraced structures.

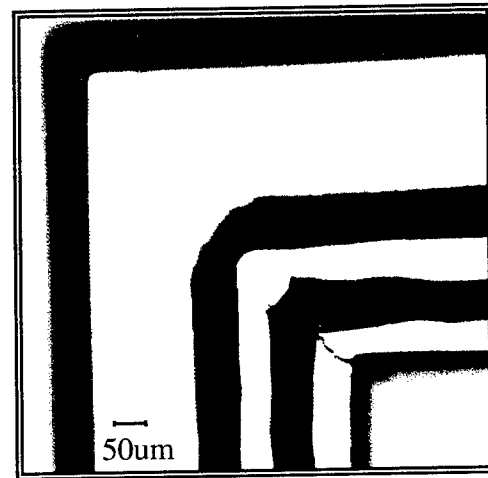


Fig. 3 The 4-level Si(100) terraced structure with good square corners by one photo mask and KOH anisotropic etching.

Optical MEMS

Wednesday, 22 July 1998

WA: Adaptive Optics/SLMs

WB: Displays & Scanners

Wednesday Papers Not Available

WB1 Surface-Micromachined Micro-Scanning Display,
Kam Lau, University of California, Berkeley, CA

WA1 (Invited)
8:30am - 9:00am

MOEMS FOR ADAPTIVE OPTICS

John H. Comtois

Air Force Research Laboratory
Space Vehicles Directorate
3550 Aberdeen Avenue SE
Kirtland AFB, NM 87117-5776
Voice: (505) 846-9753
Fax: (505) 846-2290
comtoisj@plk.af.mil

Natalie Clark

Air Force Research Laboratory
Space Vehicles Directorate
3550 Aberdeen Avenue SE
Kirtland AFB, NM 87117-5776
Voice: (505) 846-9969
Fax: (505) 846-5815
clarkn@plk.af.mil

M. Adrian Michalick

Air Force Research Laboratory
Space Vehicles Directorate
3550 Aberdeen Avenue SE
Kirtland AFB, NM 87117-5776
Voice: (505) 846-4955
Fax: (505) 846-5815
michalia@plk.af.mil

William Cowan

Air Force Institute of Technology
Department of Electrical Engineering
2950 P Street
Wright-Patterson AFB, OH 45433-7765
Voice: (937) 255-3636
Fax: (937) 255-2176
wcowan@afit.af.mil

SUMMARY

This paper presents an overview of research and development programs at the Air Force Research Laboratory, Space Vehicles Directorate (AFRL/VS) in Micro-opto-electro-mechanical Systems (MOEMS) for adaptive optics. Adaptive optic systems typically consist of a wavefront phase sensor, focusing optics, a spatial light modulator (SLM) for correcting phase errors, imaging sensors, and the control and processing electronics. These systems have a simple purpose: they improve image quality by reducing the phase aberrations introduced when the wavefront travels through turbulent atmosphere or aberrations introduced by the optical system itself. As will be shown, aberration correction and controllable focus can also enable new system functions.

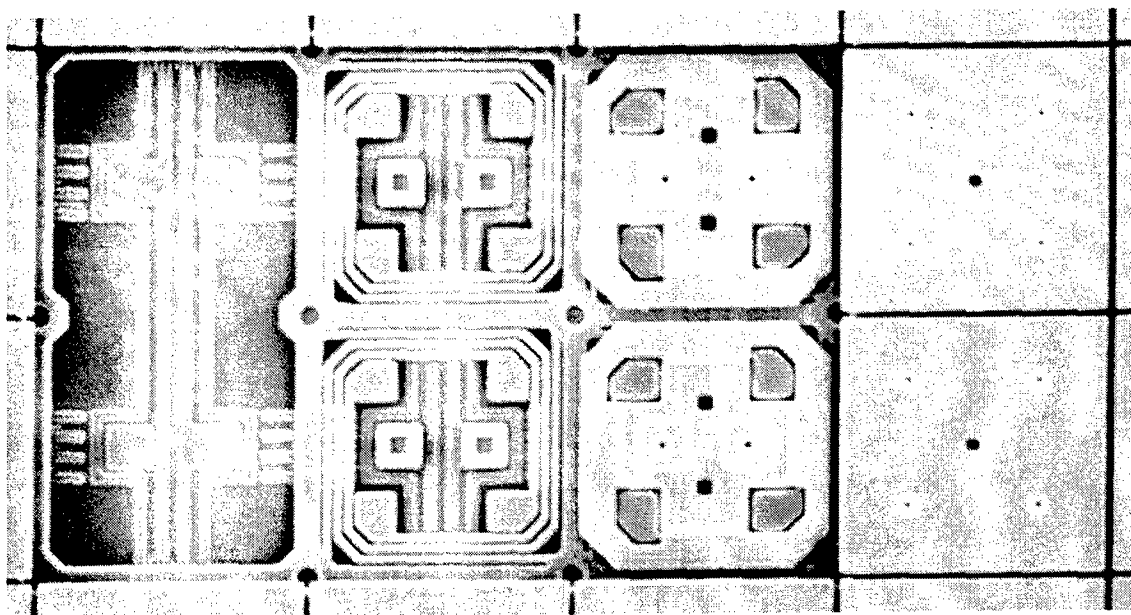
Adaptive optic systems are a growing area of interest because advanced technologies are now becoming available to make these systems lightweight, low power, and compact. In short, they are becoming practical for space, missile, and man-portable applications. The technologies that are making this possible include highly integrated low power electronics, and new processing architectures for error sensing and control, flexible high density packaging, and especially MOEMS. The latter technology is the crucial element for size and power reduction of the deformable element of the adaptive optic system.

Comparisons are made between current macro-optical aberration correction systems and the micro-mirror based systems currently under development. These comparisons show how micro-mirrors are the crucial enabling technology for compacting these systems down to a size where their use in space can be contemplated. As an example of a space application, a proposed star tracker system is used as an example of a complete micro-optical system that employs not only a micromirror based SLM, but also a novel wavefront sensor, analog processing electronics, and new sensor electronics. This system is the subject of ongoing research for the Defense Advanced Research Projects Agency (DARPA).

Research on surface-micromachined polycrystalline silicon micromirrors will be reported, including work on several fabrication technologies for piston micromirrors and also for highly advanced micromirrors with tilting as well as piston motion. Details of the fabrication processes will be discussed, along with design tradeoffs. Design techniques for both individual micromirrors and arrays of micromirrors will be detailed for both the most advanced of these

processes, the Sandia Ultra-planar Multi-level MEMS Technology (SUMMiT) process, and for the most widely available process, the Multi-User MEMS Process (MUMPS), offered commercially by the Microelectronics Corporation of North Carolina (MCNC). Figure 1 shows how the SUMMiT process can be used to create a state-of-the-art piston micromirror device.

Results of characterization testing and device modeling will be presented to show the advantages of each of the various design approaches. The characterization testing results will summarize the effectiveness of the different design approaches. Modeling results will delineate the advantages of different array sizes, as well as the effect of having tilt as well as piston motion, which promises to greatly reduce the number of deformable elements needed for a given percentage of error correction.



Address Wiring Four Thin Springs Lower Electrode Planarized Mirror

Figure 1. SEM micrograph of an advanced micromirror showing the how the four available polycrystalline silicon layers of the SUMMiT process are used. Mirrors are 50 microns square.

ACKNOWLEDGMENTS

Portions of this work are supported by the Defense Advanced Research Projects Agency (DARPA). The portion of this work done at Sandia National Labs was supported by the U.S. Dept. of Energy contract DE-AC04-94AL85000. Sandia is a multiprogram laboratory operated by Sandia Corporation, a Lockheed Martin Company, for the U.S. Dept. of Energy. Some of this work is also being carried out under a Small Business Innovative Research phase two contract to AFRL/VS by SY Technologies, Inc.

Technology and applications of micromachined membrane deformable mirrors.

G.Vdovin, P.M. Sarro, S. Middelhoek

Laboratory of Electronic Instrumentation, Delft University of Technology,
Mekelweg 4 2628 CD Delft, The Netherlands

We report on technology and applications of micromachined membrane deformable mirrors (MMDM) [1, 2]. MMDM – see Fig. 1 – is formed by a thin flexible membrane, coated with a reflective material and stretched over the electrostatic actuator structure. The membrane can be locally deflected by applying voltages to the electrostatic actuators, these local deflections can be superimposed to form the necessary optical figure.

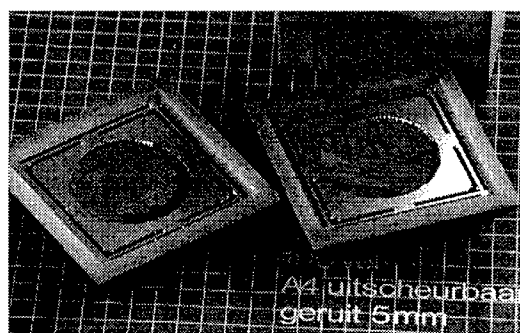


Figure 1: Micromachined adaptive mirror with 25-mm clear aperture, the membrane on the left device is removed making visible the hexagonal arrangement of 53 electrostatic actuators.

Micromachining has greatly simplified the fabrication, allowing for serial production of MMDMs in the price range of 10 ... 100 US\$ per control channel on a very careful estimation. In spite of their simplicity, PCB-based mirrors (see Fig. 1) have good optical quality, which is demonstrated by interferograms shown in Fig 2.

The dynamics of MMDM temporal response depends on the membrane resonant frequency and the air damping. Usually the air damping defines cut-off frequency in the range 50 ... 1000Hz [2], which is much lower than the resonant frequency of the membrane (2...15kHz). The damping depends on the ambient gas pressure and the distance between the membrane and the electrode structure. Perforation of the actuator structure, facilitating air flow under the membrane, increases the cutoff frequency by reducing the air damping. The typical oscillogram of the mirror response (15-mm 37-channel

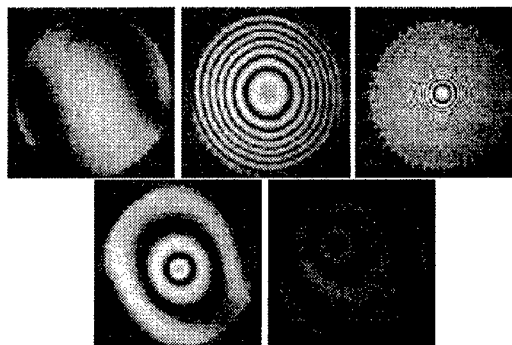


Figure 2: The initial optical figure of MMDM, the response to bias voltage of 125V, response to bias voltage of 255V (top left to right); response to 255V applied to the first actuator and to 19-th actuator (bottom left to right).

MMDM) is shown in Fig. 3.

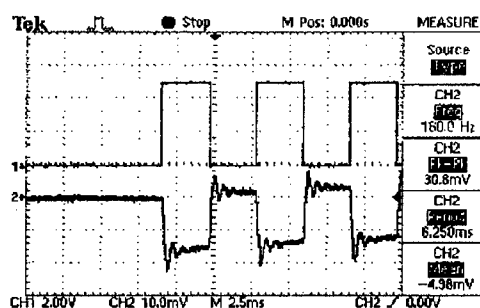


Figure 3: MMDM response (bottom curve) to a meander input signal (top curve). The amplitude of mirror deformation corresponds to an optical power of $\sim 1\text{dp}$.

As the tilt correction ability is of special interest in many applications, we have conducted special investigation on the tilt correction performance using 10-mm 19-ch MMDM. We have realized a simple projection scanner by rapidly steering the beam (500 pixels per second) between the image points (see Fig. 4). MMDMs have negligible hysteresis, permitting for quick and precise one-step program control of the surface shape. We also have

obtained good optical quality when the system was calibrated to scan through an aberration.



Figure 4: Examples of a diffraction-limited focal spot scanning, demonstrating the tilt correction performance. These images were obtained by scanning 6-mm laser beam using 19-ch MMDM with 1cm clear aperture.

Correction performance (15mm-diameter 37-ch MMDM with actuator-to-actuator spacing of 1.75mm) for low-order optical aberrations described by Zernike terms is illustrated in Fig. 5. As we could expect, the device provides good correction for defocus (4-th term), tilt (2 and 3 terms) and astigmatism (5 and 6 terms). In general the correction performance is better for axi-symmetrical terms. The typical correction performance for a randomly introduced aberration is illustrated in Fig. 6.

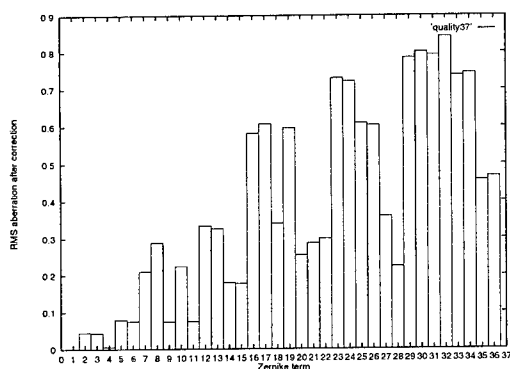


Figure 5: Quality of correction for first 36 Zernike modes for 15-mm MMDM controlled by 37 actuators inside 10mm light aperture.

In our experiments RMS errors of low-order aberrations, randomly introduced into the measurement arm have been reduced from a level of 6...16rad to a level of 0.8...1.0rad by optimization-based correction using micromachined adaptive mirror.

We have also implemented modal optimization in terms of Zernike polynomials, which improved the convergence of the control procedure but did not change the ultimate optical quality.

Applications of MMDM technology include:

- Laser beam shaping including intracavity and extracavity laser adaptive optics.
- Correction of the aberrations of human eye including retinal imaging and visual acuity correction.

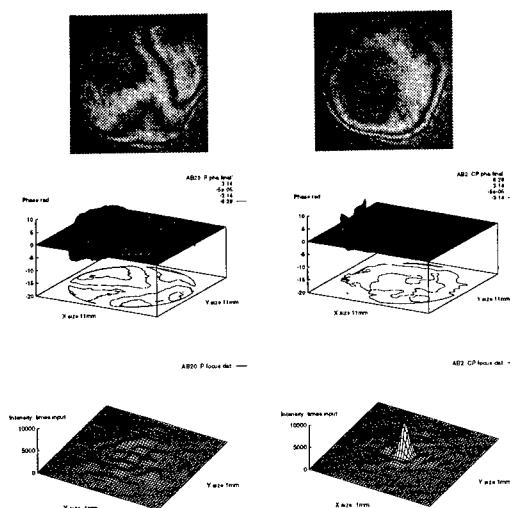


Figure 6: 10-mm aberrated beam before (left) and after (right) correction using a 15-mm 37-ch MMDM. Top to bottom: interferogram, reconstructed phase, far-field intensity. The RMS deviation from the reference sphere was reduced from 8.6rad (left) to 0.95rad (right) as a result of the optimization performed.

- Quick correctors of defocus in imaging optical systems.
- Laser microscopy, including laser scanning and confocal microscopy.
- Astronomical adaptive optics.
- Correction for atmospheric laser beam propagation including laser communication systems.

The research on MMDM and applications is currently supported by the Long-term ESPRIT project on Micro-Optical Silicon Systems (MOSIS), European Space Agency (research project on Adaptive Optics Technology) and Dutch Technical Foundation (imaging applications of MMDM).

References

- [1] L.M. Miller, M.L. Argonin, R.K. Bartman, W.J. Kaiser, T.W. Kenny, R.L. Norton, E.C. Vote, Fabrication and characterization of micromachined deformable mirror for adaptive optics applications, in Proc. SPIE **1954**, 421-430 (1993)
- [2] G.V. Vdovin and P.M. Sarro, "Flexible mirror micromachined in silicon", Applied Optics **34**, 2968-2972 (1995)
- [3] M.C. Roggemann, B. Welsh, Imaging through turbulence, CRC Press, 1996.

Design and Fabrication of 10×10 Micro SLM Array for Phase and Amplitude Modulation

Seok-Whan Chung and Yong-Kweon Kim

School of Electrical Engineering, Seoul National University
 #301-1104, San 56-1, Shillim-dong, Kwanak-gu, Seoul 151-742, Korea
 Tel: +82-2-888-5017, Fax: +82-2-873-9953, E-mail: elanjsh@plaza1.snu.ac.kr

INTRODUCTION

In this paper, a micro spatial light modulator (SLM) for phase and amplitude modulation of incident light is designed and fabricated using surface micromachining technology. In the fields of adaptive optics and pattern recognition system, SLM is used to modulate the phase and amplitude of incident light in order to correct aberration in an optical system through active control of mirror array[1,2]. In this paper, AI micro SLM, which can modulate phase or amplitude of an incident light simultaneously, is designed and fabricated. In order to maximize the fill factor, hidden spring structure is used and in order to lower driving voltage, double crab leg type spring is used.

STRUCTURE

Figure 1 shows the schematic view of a designed micro SLM which is composed of a mirror plate, upper electrode, five support posts, and bottom electrode. The spring structures are composed of four double crab leg springs for phase modulation and two torsional spring for amplitude modulation. The micro SLM is actuated by electrostatic force generated by electric potential applied between upper electrode and bottom electrode.

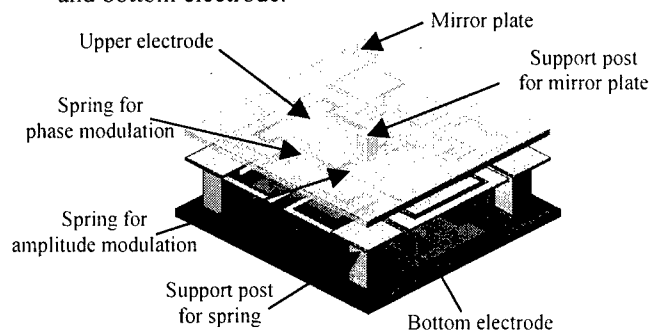
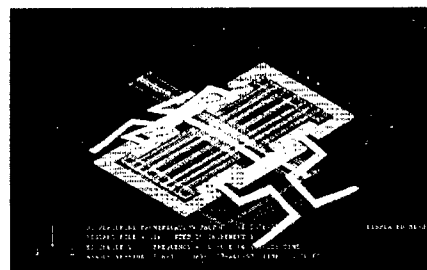


Fig. 1. Schematic view of a designed micro SLM

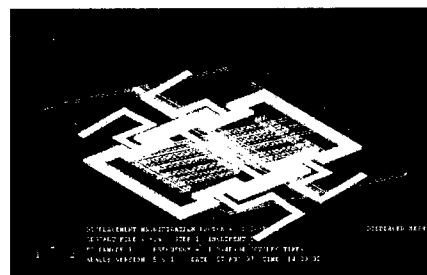
SIMULATION

Some electromechanical characteristics of the designed micro SLM are analyzed with the

calculated spring constant and simulated with FEM simulation program (ABAQUS). In the case of phase modulation, the calculated resonance frequency is about 25.7 kHz and the FEM result is about 25 kHz and in the case of amplitude modulation, the calculated resonance frequency is about 15.5 kHz and the FEM result is about 12.7 kHz. The errors between analytical results and the results of FEM simulation of both cases are 2.8% and 22% respectively. Figure 2 shows the results of FEM simulation.



Phase modulation



Amplitude modulation

Fig. 2. Results of FEM simulation

FABRICATION

The fabrication steps of micro SLM are divided into two main steps. First is the electrode forming step and second is the mirror plate forming step. Bottom electrode forming step, 1st sacrificial layer forming step, and upper electrode forming step are included in the electrode forming step and 2nd sacrificial layer forming step, mirror

plate forming step, and sacrificial layer removal step are included in mirror plate forming step. Figure 3 shows the fabrication sequence of the designed micro SLM. In the fabrication of micro SLM, sputtered aluminum is used as the material of electrodes, spring structures, and mirror plate and thick photoresists (such as AZ 4562 and AZ 4533) are used as the material of 1st and 2nd sacrificial layers. All thick photoresists are dry-etched by reactive ion etching (RIE) system [3,4].

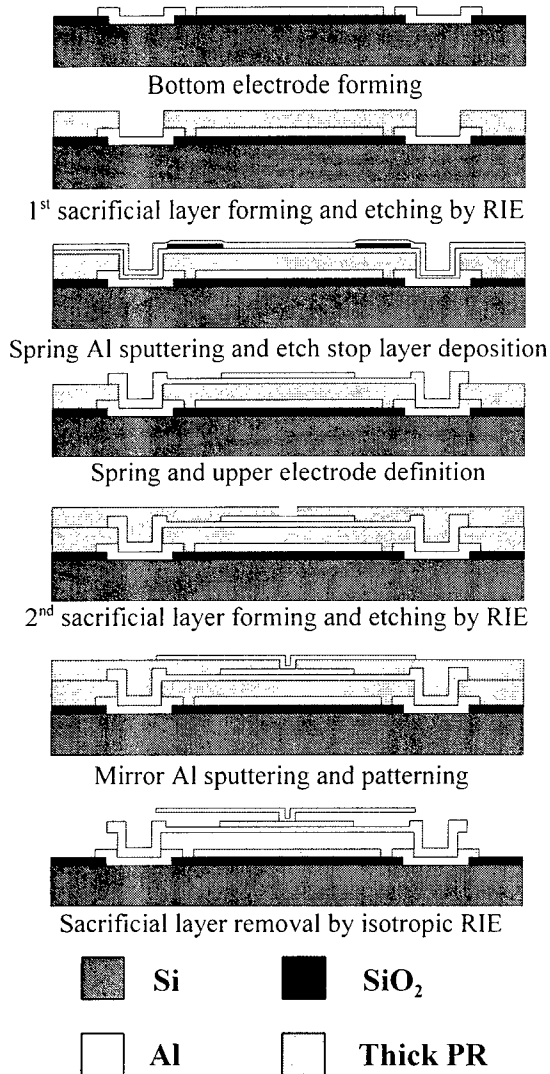


Fig. 3. Fabrication process of micro SLM

RESULTS

10×10 micro SLM array is designed and fabricated using surface micromachining technology. Figure 4 is the SEM photograph of fabricated micro SLM array.

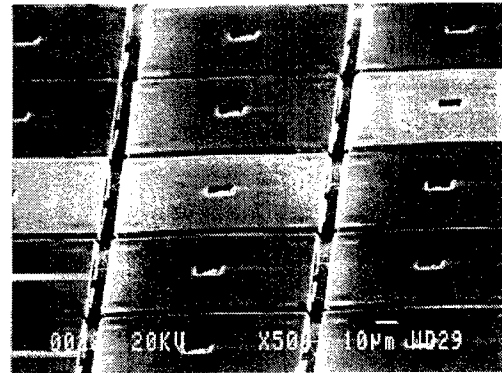


Fig. 4. SEM photograph of fabricated micro SLM

The shapes of the support posts for spring structure and upper electrode are reflected on the surface of mirror plate but the surface uniformity of mirror plate is good. And support posts are fabricated very rigidly by Al sputtering.

[Reference]

1. J.E. Pearson, S.Hansen, "Experimental studies of a deformable mirror adaptive optical system," J. Opt. Soc., 1997
2. M. Yellin, R. P. Grosso, "The membrane mirror as an adaptive optical element," J. Opt. Soc., 1997
3. S.W.Chung, J.W.Shin, Y.K.Kim, and B.S.Han, "Design and Fabrication of Micro Mirror Supported by Electroplated Nickel Posts", Sensors and Actuators A Physical, vol.54 pp.464-467, 1996.
4. S.W.Chung, J.W.Shin, Y.K.Kim, H.S.Kim, E.H.Lee, B.G.Choi, and S.J.Ahn, "Characteristics Measurements of the Fabricated 100×110 µm² Micro Mirror", IEEE/LEOS Summer Topical Meetings "Optical MEMs and their Applications", pp.3-4, 1996.

A proposal of vertical spring as a mechanical element for MEMS and fabrication of vertical spring using simple shadow evaporation process

Jong-Woo Shin, Yong-Kweon Kim, Hyung-Jae Shin*

School of Electrical Engineering, Seoul National University
#301-1104, San 56-1, Shillim-dong, Kwanak-gu, Seoul, 151-742, Korea
Tel: +82-2-888-5017, Fax: +82-2-873-9953, Email: hinge@plaza1.snu.ac.kr

*Core Technology Research Center, Samsung Electronics

I. Introduction

Surface micromachining technologies are mainly based on the advanced semiconductor integrated circuit fabrication technology. Accordingly, almost all the surface micromachined structures are planar 2-dimensional structures. In the surface micromachined sensors and actuators, mechanical spring elements such as torsional hinges^[1], flexures^[2] and cantilever beams^[3] are co-planar with the structural moving elements. Co-planar spring elements cost some area in the device to increase the chip size. Compared with those conventional structures, the vertical spring proposed in this paper lies underneath the structural layer costing no additional device area as shown in Fig. 1. In this paper, we propose the vertical spring as a mechanical element in micromachines. And we fabricate the vertical spring with a simple shadow evaporation process, which requires no other mask than the mask required for anchor formation. Finally, to demonstrate the usefulness of vertical spring as a mechanical element, we adopt the vertical spring in the micromirror array in which the fill-factor is an important parameter for performance of the device.

II. Fabrication of vertical springs

The vertical springs are fabricated using shadow evaporation process, which requires only one mask to define spring shape. A trench-hole with trapezoidal cross-section is formed in the sacrificial layer, and the spring metal layer is evapo-rated with some incident angle. The sidewalls of trench-hole are used as shadow mask except for the sidewall on which the spring metal is deposited. To optimize the shadow evaporation process, we examined the influence of trench hole shape, incident angle(20, 30, 40 degrees), evaporation thickness on the fabricated spring shape. As a result, we concluded that the most important parameter to define spring shape was the shape of trench-hole cross-section(Fig. 2). To obtain a flat plate

spring, the angle between the spring deposited sidewall and the shadow mask sidewall must be acute.

III. Application of vertical spring to micro mirror array

We applied the vertical spring to micromirror array in which the fill-factor is very important for device performance. Compared with the hidden-hinge micromirror of Texas Instruments^[4], micromirror array with vertical spring can be fabricated with simple fabrication process without additional sacrificial layer. The fabricated micromirror array with vertical spring can be seen in Fig. 3(a, b). The micromirror is square shape(50 μm one side), and the 2-dimensional array has a high fill-factor of about 88% hiding vertical spring underneath. In Fig. 3(c), we can see the fabricated flat vertical plate springs

In the experiments^[5] over the fabricated micromirror array, about 8 volts of downward threshold voltage (collapse voltage), and response time of 17 μs was measured. In the lifetime measurement, the vertical spring operated successfully without any mechanical problems such as fatigue or breakage over 200 million cycles of actuation.

IV. Conclusion

We proposed a vertical spring as a mechanical element for effective use of device area in micromachines. The experiments over shadow evaporation process showed that the shape of trench-hole cross-section is the most important parameter for a flat vertical spring fabrication. To demonstrate the usefulness of vertical spring, we adopted the vertical spring to micromirror array, and the fabricated micromirror operated successfully over 200 million cycles without any mechanical problems.

Acknowledgement

This research was supported by the Ministry of Science and Technology and the Ministry of Industry

and Energy under Micromachine Technology Development Program.

References

- [1] J. M. Younse, "Mirrors on a Chip", *IEEE Spectrum*(Nov. 1993), pp. 27-31.
- [2] Tsen-Hwang Lin, "Implementation and characterization of a flexure beam micromechanical spatial light modulator", *Optical Engineering*, Vol. 33, No. 11(1994), pp. 3643-3648.
- [3] W. C. Tang et al., "Laterally Driven Polysilicon Resonant Microstructures", *Sensors and*

Actuators, Vol. 20(1989), pp. 25-32.

- [4] L. J. Hornbeck, "Current Status of Digital Micromirror Device(DMD) for Projection Television Applications", *International Electron Devices Tech. Digest*(1993), pp. 381-384.
- [5] J. W. Shin et al., "Design and Fabrication of Micromirror Array Supported by Vertical Springs", *Digest of Transducers '97*(1997), pp. 201-204.

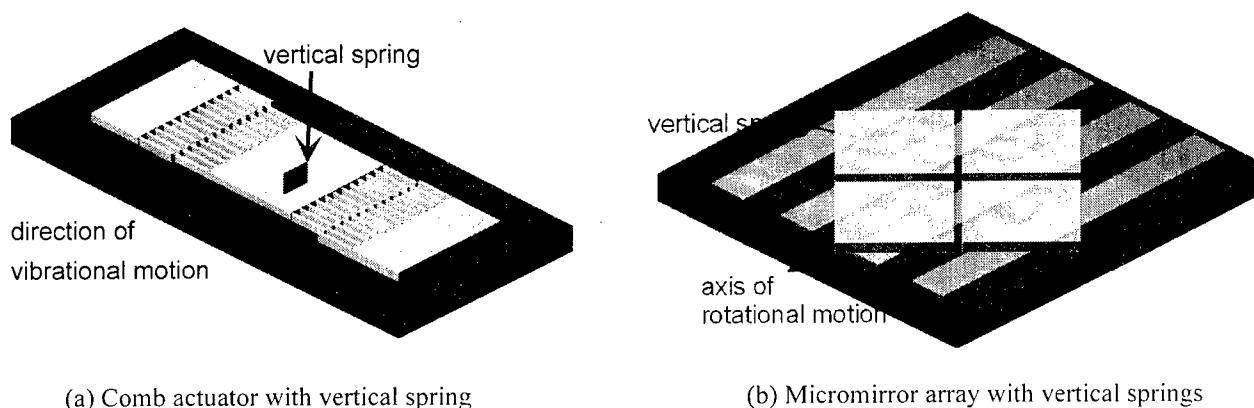


Fig. 1 Micromachines with vertical springs underneath the structural layer

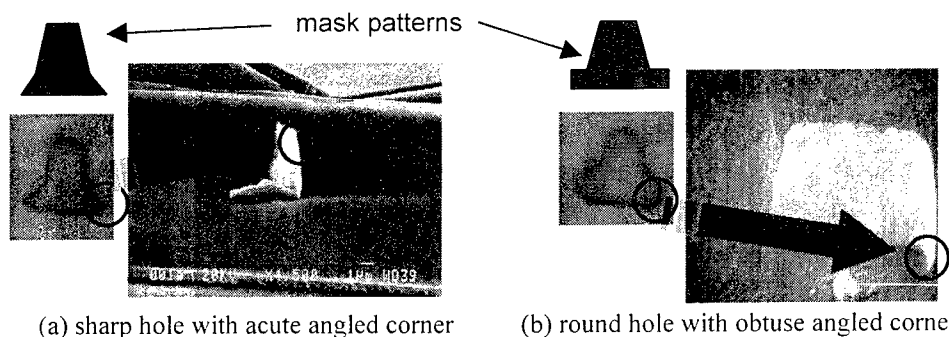


Fig. 2 Vertical spring fabrication result

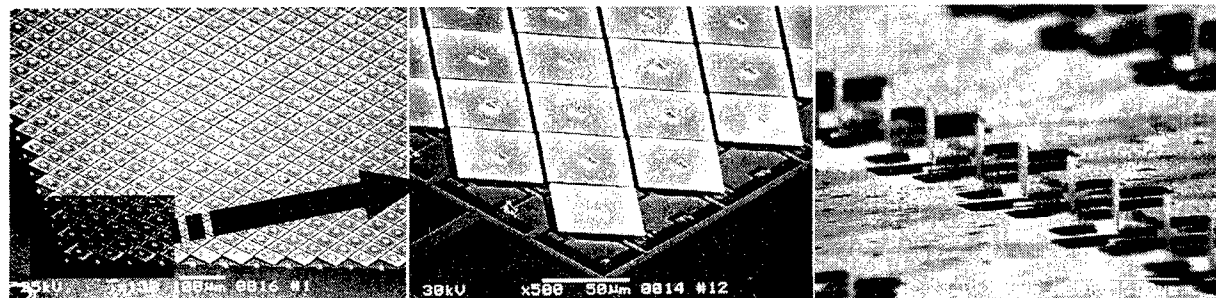


Fig. 3 SEM micrographs of fabricated micromirror array with vertical springs

WB2

11:00am - 11:15am

CMOS friendly MEMS manufacturing process.

Jim Hunter, Mike Bruner and Josef Berger
Silicon Light Machines
385 Moffett Park Drive, Suite 115
Sunnyvale, CA 94089-1208

Phone: 408 541-4949, fax: 408 541-1244

Abstract.

This paper describes a novel approach to manufacturing technology of Optical MEMS devices. The devices are manufactured at a local foundry using fully CMOS compatible front-end processes complemented by unique release and seal processing steps performed at SLM. The paper will cover the process flow, technological challenges and process control issues related to this unique approach.

Summary.

SLM is developing large area HD projection displays based on a MEMS based light modulator. The modulator is an electrically actuated phase grating consisting of a one-dimensional array of aluminum coated silicon nitride ribbons.

The one-dimensional array of ribbons forms a borderless array of pixels, which create an image in the following way. In the off state the ribbons are in their rest position, forming a reflective surface. In this case all the light is returned back to the source and no image is formed on the screen. When the ribbons are actuated, they are deflected by electrostatic force forming a phase grating. The light energy is then directed into diffraction orders and by using a Schlieren-type optical system an image is formed. One of the unique properties of this type of light modulator is speed. Since this device is fast enough, the two-dimensional image is formed on the screen by scanning a line. This type of simple, small area light modulator offers several unique advantages. First is its inherent simplicity. The light modulation is accomplished by a very small deflection of thin silicon nitride beams. This enables very high reliability as well as high power handling capability. Second, it is inexpensive because of its small area. The one-dimensional array can then be easily combined with peripheral drive CMOS circuitry creating a compact, fully integrated light valve.

The problem for a small start-up such as SLM is where to find a resource capable of manufacturing a MEMS device in volume. SLM devised a novel process flow that uses a fully MOS compatible, generic front-end CMOS process to form the MEMS structure, including the sacrificial layer, nitride ribbons and overlaying aluminum electrode. Such wafers are produced in a CMOS foundry.

The MEMS specific processing steps, etching of the sacrificial layer and the subsequent seal step are performed in a small, dedicated fab at SLM. The resulting wafers are fully passivated, capable of being diced and packaged using standard processes. In this way, SLM obtained a reliable and cost effective manufacturing capability for minimum investment.

The SLM light valve is an optical device and this fact presents a new and unique challenge to the process engineer. The device has to achieve a high level of efficiency and uniformity, which challenges the process technology in new ways. Areas such as film thickness and stress control, particularly for the ribbon material and sacrificial layer, are critical. It is not only important to control overall film stress, but careful attention must be paid to stress gradients within films. Gradients can lead to unwanted film curling after release. As well, special attention to film morphology is crucial and the needs for film smoothness go beyond the typical concerns of building CMOS circuitry.

The next challenge is integration of the MEMS part of the process with the CMOS circuitry. The challenge is finding a sacrificial layer etch which doesn't attack any of the materials commonly used in CMOS. This was accomplished by using poly-silicon as the sacrificial layer and XeF_2 etch. The STS fully automated, modular plasma etcher was modified to include a XeF_2 sublimation chamber. The end result was a robust release process that could be performed as the very last step. The robustness of the process relies on the extremely high selectivities that are maintained during the etch. By being able to perform the release after all other processes are complete, the need to send wafers back to the foundry was eliminated which allows for a much more streamlined process as well as avoiding any processing after release when the device is most sensitive to contamination.

The paper will describe the novel process architecture, technological challenges imposed by the optical, mechanical and electrical nature of the device and data illustrating the process control issues related to this unique approach.

Paper Title : Thin-Film Actuated Mirror Spatial Light Valve For High-Brightness Projection Displays.

At the present time, there is no projection display device that can transmit enough light to the screen for the display of electronic images at normal room light condition with high brightness and high contrast. Thin Film Actuated Mirror Array (TFAMA) is a breakthrough reflective type light modulator that uses micromachined thin-film piezoelectric actuators in conjunction with microscopic mirrors. In this paper, the operation, design, fabrication, and performance of TFAMA device are described for high-brightness projection display systems.

As shown in Fig. 1, a TFAMA module consists of the active matrix, where the image signal voltages are applied, the cantilever-type piezoelectric actuators, and the reflection mirrors, on top of the actuators. In order to use the TFAMA module as a display device, the variation of the tilting angle of the individual mirror pixel need to be expressed as the change in light intensity of the corresponding point on the projected screen. Figure 2 shows the light modulation principle of TFAMA. When there is no tilting of mirror pixels, no light goes out through the light stop. When the mirror pixels are fully tilted, full light goes out to the screen. By controlling the tilting angle of the mirror pixel according to the signal voltage applied to the corresponding actuator, 256 steps of gray levels in between the brightest and the darkest can be generated on the screen.

Currently, one TFAMA module with VGA(640 \times 480) resolution(>300,000 mirror pixels with 100 μ m \times 100 μ m size) is fabricated on a 4-inch silicon wafer. The cantilever-type actuators are fabricated using micromachining and thin film manufacturing process. As shown in Fig. 3, It has a simple configuration of the supporting layer (SiN_x), the bottom electrode (Pt/Ta) layer, the piezoelectric layer (PZT), and the top electrode (Pt) layer. A hidden actuator structure is designed to maximize the fill factor and a double sacrificial layer process is introduced to achieve this.

The micromachined thin film piezoelectric actuators show promising characteristics such as linear actuation with respect to the applied signal voltages up to 10V (Fig. 4), fast response time of microseconds order, and enough life time of more than 1 \times 10⁹ cycles. The high fill factor more than 94% along with the unique analogue light modulation makes it possible to achieve the brightest light valve(>2000 lumen with 270W source lamp) with simple image processing circuitry. Projectors and Projection TVs with TFAMA modules will soon be on the market and be a good example of commercialized MEMS products.

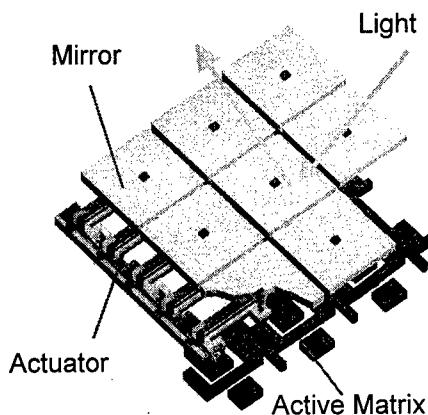


Fig. 1. Schematic diagram of thin-film actuated mirror array module

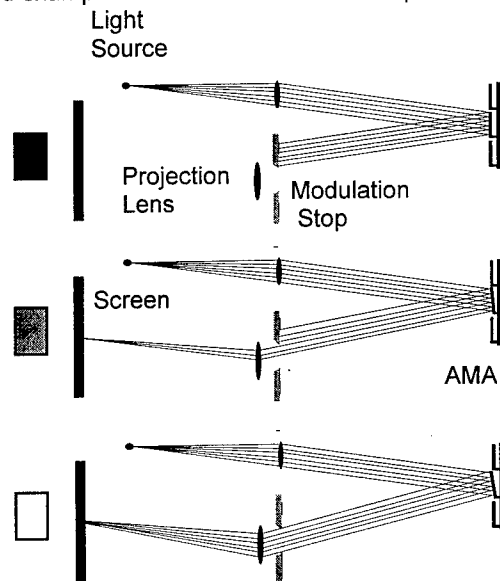
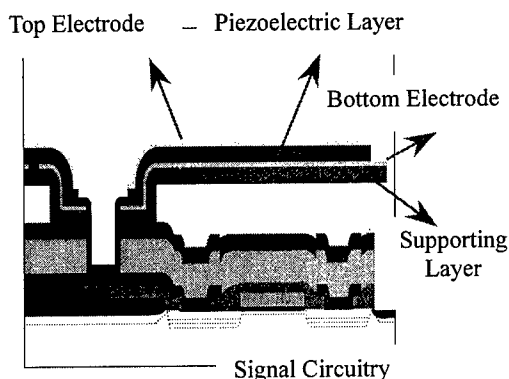
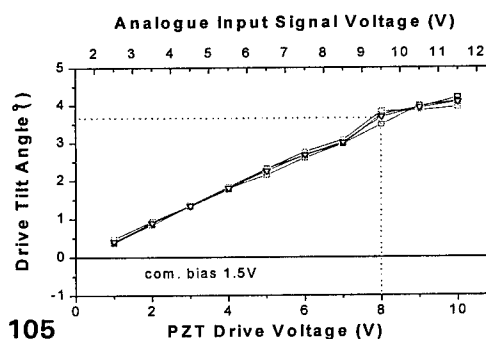


Fig. 2. Light modulation principle of TFAMA display system



Two-Dimensional Optical Scanner with Large Angular Rotation Realized by Self-Assembled Micro-Elevator

Li Fan and Ming C. Wu

Tel: 310-825-6859, Fax 310-825-6954, Email: wu@ee.ucla.edu

Department of Electrical Engineering, University of California at Los Angeles (UCLA)
66-147D Engineering IV Building, Los Angeles, CA 90095-1594, USA

Two-dimensional (2D) optical scanners with large-area mirrors and large angular rotation are of great interest for applications in display, printing, optical scanning and sensing, optical data storage, and free-space optical links between satellites. The Micro-Electro-Mechanical System (MEMS) technology is very attractive to reduce the size, weight, and complexity of the optical scanners. Several bulk- [1,2] and surface-micromachined [3,4] 2D scanners have been reported. To achieve large angular rotation for large-area micromirrors, the mirrors need to be suspended high above the substrate. This requires the use of complicated processing steps such as thick sacrificial materials or wafer bonding with bulk-micromachined structures.

Previously, we reported a novel micromechanical structure called Micro-Elevator by Self-Assembly (MESA) [5] that can raise the surface-micromachined plates to several hundred micrometers above the wafer surface. In this paper, we report a novel 2D scanner realized by the MESA technology. Large optical deflection angles ($> \pm 14^\circ$) have been achieved for large-area mirrors $400 \times 400 \mu\text{m}^2$ without employing thick sacrificial layers.

The schematic structure of the MESA-based 2D scanner is shown in Fig. 1. The micromirror is attached to a pair of suspended frames through two sets of orthogonal torsion beams. It can be rotated around two axes by applying electrostatic force between the mirror and the quadrant electrodes on the substrate. The outer frame is connected to four side-support plates by microhinges. By pushing the four microactuator plates inwards simultaneously, the center plate can be raised above the substrate. Its height can be controlled by programming the in-plane microactuators connected to the MESA. Figure 2 shows the scanning electron micrograph (SEM) of the 2D scanner. It is fabricated by the standard three-layer polysilicon surface-micromachined process offered by MCNC [6]. The micromirror used in this experiment has an area of $400 \mu\text{m} \times 400 \mu\text{m}$. Previously, micromirrors as large as $5 \text{ mm} \times 5 \text{ mm}$ have been successfully suspended by the MESA structure. By applying bias to electrode 1 and 2, the mirror is rotated around the Y-axis, as shown in Fig. 2(a). If the bias is switched to electrode 2 and 3, the mirror is rotated around the X-axis as shown in Fig. 2(b). Independent scanning around two axes has been verified. The performance of the 2D scanner is characterized by shining a HeNe laser beam on the micromirror. Figure 3 shows the far-field patterns of the steered optical beams. The optical deflection angle versus applied voltage is shown in Fig. 4. A maximum deflection angle of $\pm 14^\circ$ has been achieved. A pull-in voltage of 70 V is measured at 14° scan angle. The voltage can be reduced by employing thinner torsion beams. The resonant frequency of the scanner is measured to be 1.5 kHz.

In summary, a novel 2D scanner with large mirror area and large angular rotation has been proposed and demonstrated. The mirror is supported by the surface-micromachined micro-elevators by self-assembly (MESA). Maximum optical deflection angles of $\pm 14^\circ$ and a resonant frequency of 1.5 kHz have been achieved.

Reference:

- [1] D. L. Dickensheets, G. S. Kino, "Microfabricated biaxial electrostatic torsional scanning mirror", *Proceeding of SPIE*, vol. 3009, pp. 141-5, 1997.
- [2] K.E. Petersen, "Silicon Torsional Scanning Mirror," *IBM J. Res. Dev.* vol. 24, p.631.
- [3] L. J. Hornbeck, "Projection displays and MEMS: Timely convergence for a bright future," *Proceedings of SPIE*, vol. 2639, pp. 2, 1995.
- [4] V.R.Dhuler, M. Walters, R. Mahadevan, A. B. Cowen and K. W. Markus, "A novel two axis actuator for high speed large angular rotation", *Proceedings of Transducers*, pp. 327-330, 1997.
- [5] L. Fan, M. C. Wu, K. D. Choquette and M. H. Crawford, " Self-assembled microactuated XYZ stages for optical scanning and alignment," *Proceedings of Transducers*, pp. 319-322, 1997.
- [6] MEMS Technology Applications Center at Microelectronics Center at North Carolina (MCNC), Research Triangle Park, North Carolina.

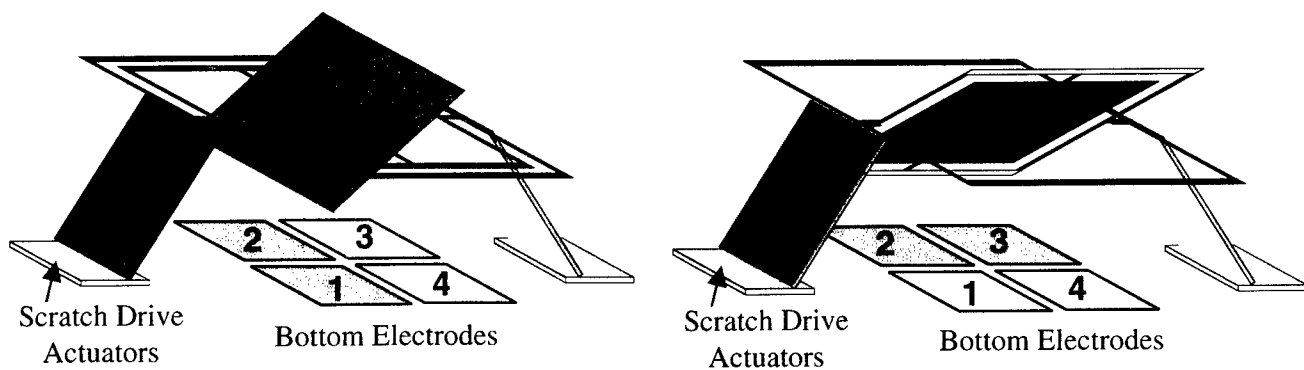


Figure 1: The schematic structure of the MESA-based 2D scanner.

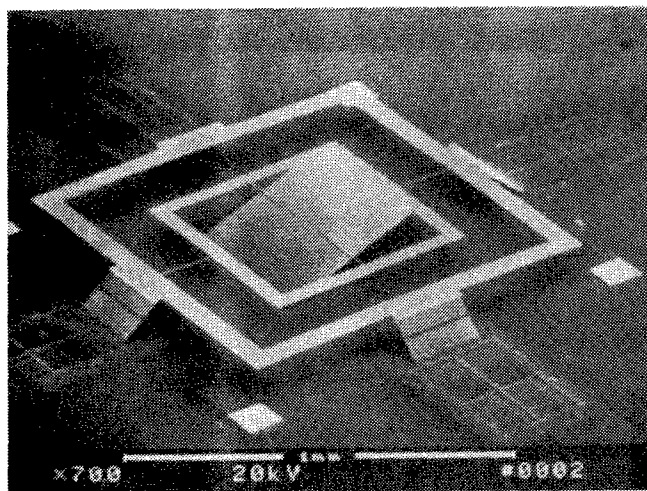


Figure 2(a): The mirror is rotated around the Y-axis

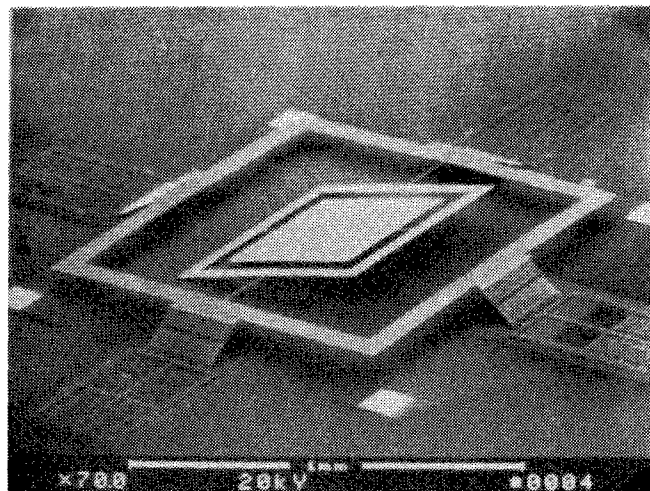


Figure 2(b): The mirror is rotated around the X-axis

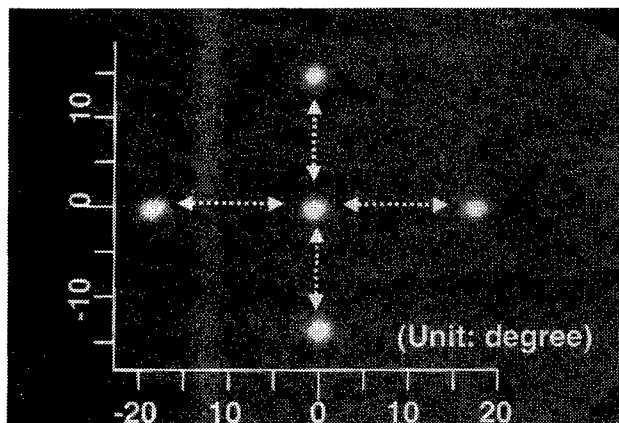


Figure 3: Far field patterns of the steered optical beam.

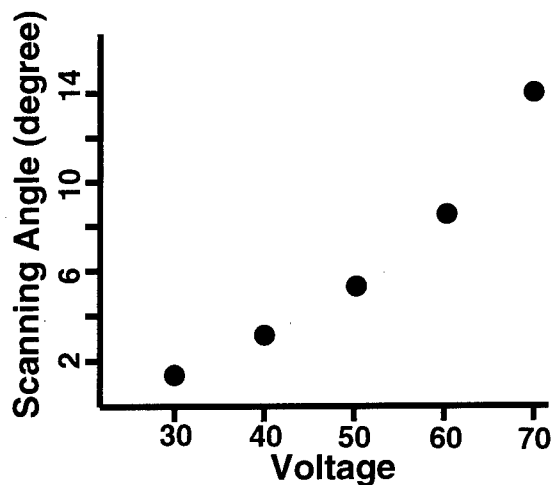


Figure 4: The optical deflection angle versus applied voltage.

Micromachined Mirrors in a Raster Scanning Display System

Paul Hagelin, Kimberly Cornett, and Olav Solgaard

Department of Electrical and Computer Engineering, University of California, Davis

This paper describes a 2-D raster scanning system incorporating two surface-micromachined mirrors fabricated on separate chips: a fast mirror for horizontal and a slow mirror for vertical scanning (Figure 1). The mirrors are tilted out-of-plane on polysilicon hinges and are connected to their supporting frames with torsional polysilicon beams (Figure 3). The tilt-up mirror design accommodates large mirror areas and allows integration of optical components on the same chip. Prior work on tilt-up micromirrors by Kiang et. al. [1-2] has demonstrated the feasibility of resonant mirrors for 1-D barcode scanning. The raster scanning mirrors are nearly circular, measuring 565 μm along the scan axis and 500 μm along the perpendicular axis. The mirror surfaces are linked to comb drive actuators, and both have a resonant frequency of 4.54 kHz (Figure 2). The measured optical scan angle of the fast mirror is 5.3 degrees when operated at resonance, driven with a 116 Vpp sine wave and zero DC offset. The scan axis of the fast mirror is oriented perpendicular to the slow mirror. The slow mirror is identical to the fast mirror, except bi-directional comb drives allow it to be driven in opposing directions. Triangular voltage waveforms at 167 Vpp rotate the mirror, deflecting the optical beam through 5.7 degrees. The slow mirror governs the image refresh rate.

The mirrors in this scanning system exhibit convex curvature, resulting from stress gradients in the polysilicon film. Differences in curvature were found between identical devices on separate chips. Such anomalies are likely due to variations in the fabrication process. The horizontal and vertical axes of the mirrors also exhibit slightly different curvature. The fast and slow mirrors have focal lengths of -1.2 cm and -1.9 cm respectively.

A 5 mW HeNe laser operating in the red (633 nm) is the light source for the raster scanner. The light first passes through an acousto-optic (AO) modulator followed by a spatial filter and a mechanical shutter. A 50.2 mm and a 100 mm focal-length lens correct for curvature in both mirrors. The optics form a virtual 6.02-micron waist 7.5 mm behind the fast mirror, with a $1/e^2$ beam radius of 250 μm at the mirror. Two 62.9 mm focal-length lenses between the mirrors image the fast mirror onto the slow mirror. These lenses could also be used to correct for mirror curvature. In the Fourier plane of the 30cm output lens, the $1/e^2$ optical beam radius is 360 μm on the vertical axis and 410 μm on the horizontal axis. Without optical curvature compensation, the spot would have been 1,716 times greater in area. Preliminary data suggests that the spot size does not change appreciably as the mirror rotates.

Several raster patterns were photographed to demonstrate the 2-D scanning ability of the system (Figure 4). Speckle is observed when the raster-scanned image is projected onto a screen. The speckle in the figures was eliminated by projecting the light directly onto film in the camera. Raster images are made by modulating the light with the AO crystal. A 3 cm horizontal by 2.8 cm vertical raster scan is present in the Fourier plane of the 30 cm output lens. By rule of thumb [3], spacing between scan lines is the full-width-half-maximum of the intensity of the optical field. In accordance with this principle, the 2-D scanning resolution is 62x66 pixels, which is supported by experimental evidence. Figure 4b shows 88 light and dark horizontal lines, and Figure 4f shows 60 light and dark vertical lines. Vertical line contrast is limited by the performance of the AO modulator. Horizontal resolution is determined by the number of lines that the fast mirror can scan during the refresh period of the slow mirror. An image containing the characters "UCD" (Figure 4e) was generated by driving the fast mirror at 4.6 kHz and the slow mirror at 11.5 Hz. Mechanical instability of the fast mirror causes overlap of scan lines, distorting the image and requiring a 2X reduction in slow mirror frequency. The slow mirror also exhibits mechanical instability. The effect of mechanical inaccuracies are avoided by selectively switching the light off. The light was switched off by the AO modulator during the right-to-left half-cycle of the fast mirror scan and the bottom-to-top half-cycle of the slow mirror scan. Optical scan angles of up to 11 degrees have been demonstrated on both mirrors, with a corresponding decrease in scan repeatability.

This experiment has demonstrated raster-scanned images generated by a surface-micromachined mirror system. The mechanical stability of the optical scan limits the refresh rate and resolution in the current design. Continuing research is aimed at extending the resolution to VGA quality by further refining the mechanical design and increasing the scan angle.

References

1. M-H Kiang, O. Solgaard, K.Y. Lau, R.S. Muller, "Electrostatic Combdrive-Actuated Micromirrors for Laser-beam Scanning and Positioning", *Journal of Microelectromechanical Systems*, March 1998, vol. 7, no. 1. p. 27-37.
2. M-H Kiang, O. Solgaard, R.S. Muller, K.Y. Lau, "Micromachined Polysilicon Microscanners for Barcode Readers", *IEEE Photonics Technology Letters*, vol. 8, no. 12, pp. 1707-1709, December 1996.
3. J. Hagerman, "Optimum spot size for raster-scanned monochrome CRT displays", *Journal of the SID*, vol. 1, no. 3, 1993. pp. 367-369.

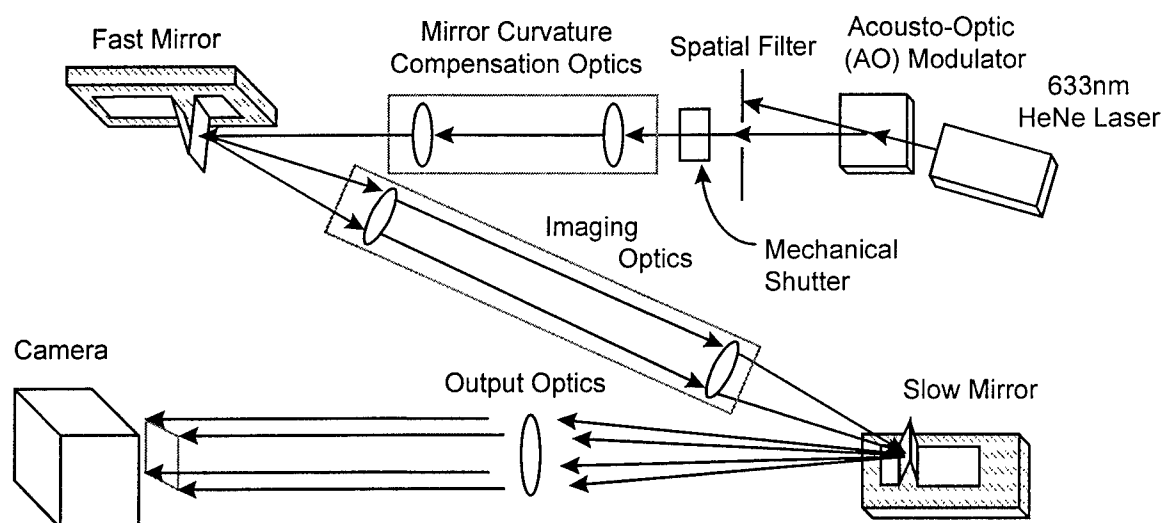


Figure 1. Experimental setup for orthogonal raster scanner

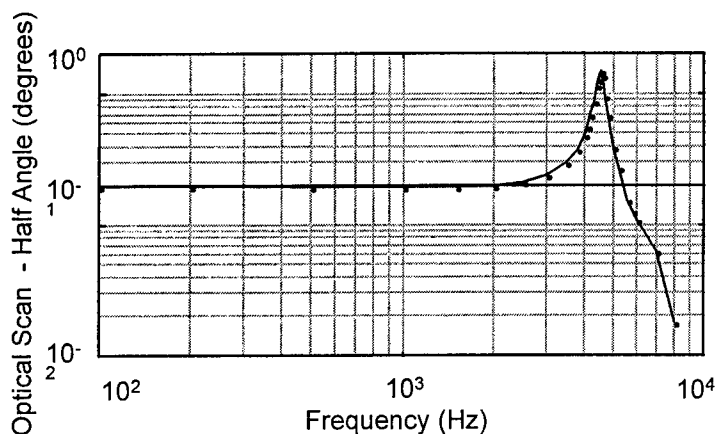


Figure 2. Small-signal freq. response of slow mirror

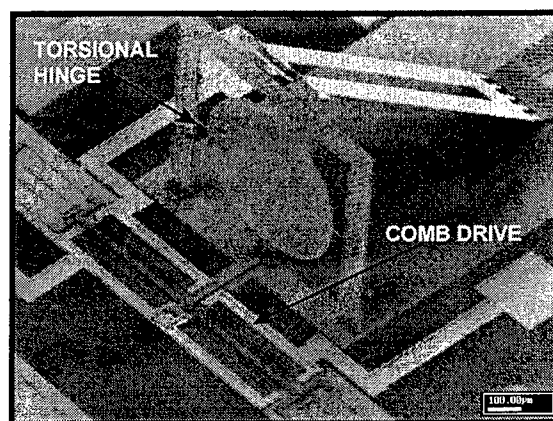


Figure 3. SEM image of slow mirror - vertical scan

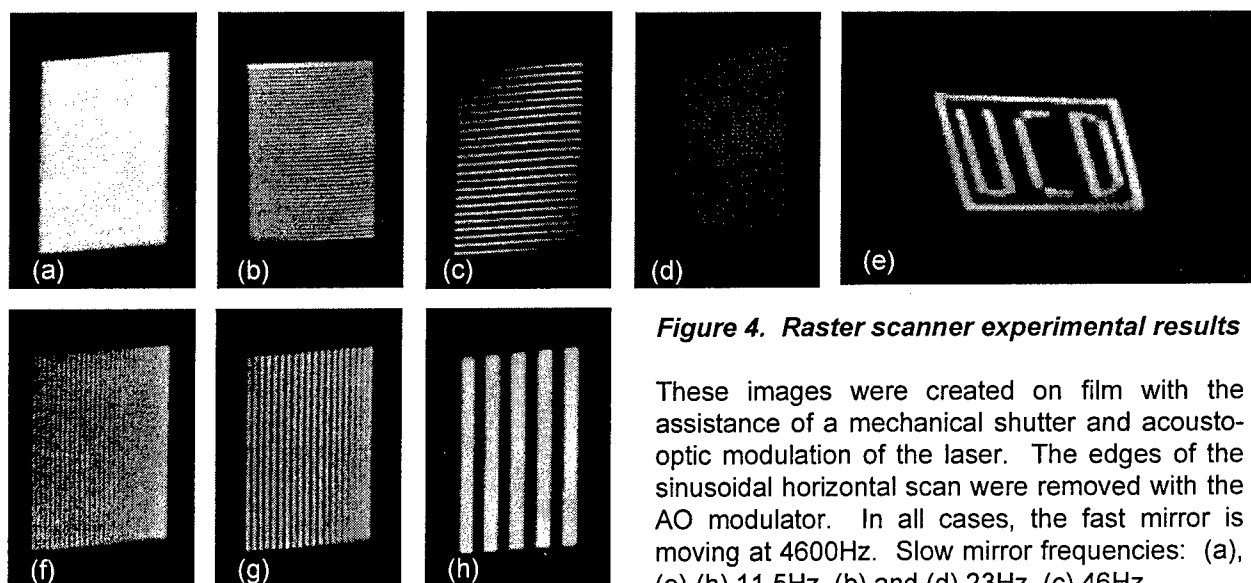


Figure 4. Raster scanner experimental results

These images were created on film with the assistance of a mechanical shutter and acousto-optic modulation of the laser. The edges of the sinusoidal horizontal scan were removed with the AO modulator. In all cases, the fast mirror is moving at 4600Hz. Slow mirror frequencies: (a), (e)-(h) 11.5Hz, (b) and (d) 23Hz, (c) 46Hz.

AUTHOR INDEX

Ahn, S.-H.	TuE7	Gomez, L. T.	TuC1	Leclercq, J.-L.	TuD1
Akahori, Y.	TuC4	Goosen, K. W.	TuD3	Lee, C. C.	TuE8
Aoki, Y.	TuC3	Greek, S.	MB2, TuD1	Letarte, X.	TuD1
Bassett, C. J.	TuB3	Gundlach, A. M.	MB4	Lo, Y.-H.	MC4
Baukens, V.	MB5	Haake, J. M.	TuC2	Madsen, C. K.	TuC1
Benyattou, T.	TuD1	Hagelin, P.	WB5	Maeda, S.	TuB2
Berger, J.	WB2	Hare, A. E.	TuE4	Marxer, C.	MD1
Beyette Jr. F. R.	TuE4	Hashimoto, T.	TuC4	McCormick, F. B.	MA2
Björkman, H.	TuE1	Henry, C. H.	TuC1	Michalicek, M. A.	WA1
Blum, O.	MA1	Herb, W. R.	TuB3	Middelhoeck, S.	WA2
Bruce, A. J.	TuC1	Hermanne, A.	MB5	Min, Y.-H.	MB3
Bruner, M.	WB2	Herzig, H. P.	MD2	Mita, M.	MD4
Calton, D. W.	MB4	Higurashi, E.	TuB4	Miyauchi, D.	MD4
Cappuzzo, M. A.	TuC1	Hjort, K.	MB2, TuD1, TuE1	Mizuno, J. R.	TuC3
Chitica, N.	TuD1	Hoffman, M.	MD3	Mohr, J.	TuD4
Chung, C. K.	TuE8	Hollman, P.	TuE1	Muehlner, D. J.	TuC1
Chung, S.-W.	WA3	Hossfeld, J.	TuA3	Nagel, D.	TuE6
Clark, N.	WA1	Hunter, J.	WB2	Nakao, T.	TuE3
Comett, K.	WB5	Hwang, K.-H.	WB3	Neumeier, M.	TuA3
Comtois, J. H.	WA1	Iga, K.	TuC3	Ota, M.	TuE3
Cowan, W.	WA1	Inoue, Y.	TuC4	Othman, N.	TuE5
Cowen, A. B.	TuC2	Itoh, H.	TuB2	Ottevaere, H.	MB5
Daleiden, J.	TuD1	Itoh, T.	TuB4	Patterson, J.	TuB5
Davis, C. Q.	MB1	Kato, K.	TuC4	Peter, Y.-A.	MD2
De Rooij, N. F.	MD1	Kato, T.	TuC3	Picard, A.	TuA3
Debéda, H.	TuD4	Kato, K.	TuC4	Pu, C.	MC4
Dhuler, V. R.	TuC2	Kim, Y.-	MB3, TuE7, WA3, WA4	Rangsten, P.	TuE1
Di Pasquale, F.	TuE5	Kino, G. S.	TuB1	Rodgers, M. S.	MA1
Diehl, T.	TuD2	Knox, W. H.	TuD3	Rossi, M.	TuA1
Edwall, G.	MA3	Kopka, P.	MD3	Sakamoto, M.	TuE3
Ehrfeld, W.	TuA3, TuD2	Krippner, P.	TuD4	Sarro, P. M.	WA2
Fan, L.	WB4	Kufner, M.	MB5	Sawada, R.	TuB4
Federighi, M.	TuE5	Kufner, S.	MB5	Schiff, H.	TuA1
Ford, J. E.	TuD3	Kurosaki, T.	TuC4	Schulze, J.	TuA3
Freeman, D.	MB1	Lacher, M.	TuD2	Scotti, R.	TuC1
Freyhold, T. v.	TuD4	Laor, H.	MC2	Seunarine, K.	TuE2
Fujita, H.	MC1, MC3, MD4	Laskowski, E. J.	TuC1	Shin, H.-J.	WA4
Gates, J. V.	TuC1	Lau, K.	WB1	Shin, J.-W.	WA4

AUTHOR INDEX

Shmulovich, J.	TuC1	Zetterer, T.	TuD2
Shul, R. J.	MA1	Zhu, Z.	MC4
Sniegowski, J. J.	MA1	Zook, J. D.	TuB3
Söchtig, J.	TuA1		
Solgaard, O.	WB5		
Stevenson, J. T. M.	MB4		
Sullivan, B.	TuA2		
Sullivan, C. T.	MA1		
Thienpont, H.	MB5		
Tohmori, Y.	TuC4		
Tohyama, O.	TuB2		
Toshiyoshi, H.	MC1, MC3, MD4		
Tsubamoto, M.	TuB4		
Tuteleers, P.	MB5		
Underwood, I.	MB4, TuE2		
Van Zeghbroeck, B.	TuB5		
Vass, D. G.	MB4		
Vdovin, G.	WA2		
Verennicoff, I.	MB5		
Verschaffelt, G.	MB5		
Viktorovitch, P.	TuD1		
Voges, E.	MD3		
Vynck, P.	MB5		
Walker, J. A.	TuD3		
Walker, S.	TuE6		
Wallrabe, U.	TuD4		
Warren, M. E.	MA1		
Waters, R.	TuB5		
Weber, L.	TuA3		
Wengelink, J.	TuD4		
Westenhöfer, S.	TuA1		
White, A. E.	TuC1		
Wilson, M. L.	TuB3		
Wood, R. L.	TuC2		
Wu, C. Y.	TuE8		
Wu, M. C.	WB4		
Yamada, Y.	TuC4		
Yanagisawa, M.	TuC4		

**IEEE/LEOS
Summer Topical Meeting**

22 – 24 July 1998

**Organic Optics and
Optoelectronics**

**Monterey Plaza Hotel
Monterey, CA**

**IEEE Catalog Number: 98TH8369
ISBN: 0-7803-4953-9**

The papers in this book make up the digest of the 1998 IEEE/LEOS Summer Topical Meetings. They reflect the author's opinions and are published as presented and without change in the interest of timely dissemination. Their inclusion in this publication does not necessarily constitute endorsement by the editors, the Institute of Electrical and Electronics Engineers, Inc.

Copyright and Reprint Permission: Abstracting is permitted with credit to the source. Libraries are permitted to photocopy beyond the limit of U.S. copyright law for private use of patrons those articles in this volume that carry a code at the bottom of the first page, provided per-copy fee indicated in the code is paid through Copyright Clearance Center, 222 Rosewood Drive, Danvers, MA 01923. For other copying, reprint or republication permission, write to IEEE Copyrights Manager, IEEE Operations Center, 445 Hoes Lane, PO Box 1331, Piscataway, NJ 08855-1331.

© 1998 by the Institute of Electrical and Electronics Engineers, Inc. All rights reserved.

IEEE Catalog Number: 98TH8369

ISBN: 0-7803-4953-9 Softbound Edition
0-7803-4954-10 Microfiche Edition

ISSN: 1099-4742

Library of Congress:

Additional copies can be ordered from:

IEEE Service Center
445 Hoes Lane
P.O. Box 1331
Piscataway, NJ 08855-1331
Tel: (732) 981-1393
Fax: (732) 981-9667

Organic Optics & Optoelectronics

Co-Chairs:

Nasser Peyghambarian, University of Arizona, Tucson, AZ
Andre Persoons, Katholieke Universiteit Leuven, Leuven, BELGIUM

Program Committee:

Christoph Brauchle, University of Munich, Munich, GERMANY
Jean Luc Bredas, Service de Chimie des Matériaux Nouveaux, BELGIUM
Larry Dalton, University of Southern California, Los Angeles, CA
Harold Fetterman, University of California, Los Angeles, CA
Steve Forrest, Princeton University, Princeton, NJ
Richard Friend, Cavendish Laboratory, Cambridge, UK
Tony Garito, University of Pennsylvania, Philadelphia, PA
Francis Garnier, Laboratoire des Matériaux Moléculaires, Thiais, FRANCE
Attilio Golemme, Università della Calabria, Rende, ITALY
Georges Hadziannou, University of Groningen, Groningen, THE NETHERLANDS
I.C. Khoo, Pennsylvania State University, University Park, PA
Bernard Kippelen, University of Arizona, Tucson, AZ
Charles Lee, Air Force Office of Scientific Research/NC, Bolling AFB, CO
Louis Lome, Department of Defense, Arlington, VA
Hachiro Nakanishi, Tohoku University, Sendai City, JAPAN
Seong-Han Park, Yonsei University, Seoul, KOREA
Hiroyuki Sasabe, The Institute of Physical & Chemical Research, Saitama, JAPAN
Keizuki Sasaki, Keio University, Yokohama, JAPAN
William Steier, University of Southern California, Los Angeles, CA
George Stegeman, University of Central Florida, Orlando, FL
Mostafa A. H. Talukder, Office of Naval Research, Asian Office, Tokyo JAPAN
Kenneth J. Wynne, Office of Naval Research, Arlington, VA

TABLE OF CONTENTS

Wednesday, 22 July 1998

Session WA: NLO Polymers

WA1	Processing Assisted Self Assembly of Nonlinear Optical Polymers.....	3
WA2	New Molecular for EO Polymers.....	N/A
WA3	Polymers for Second-Order Nonlinear Optical Applications.....	5
WA4	Nonlinear Optical Relaxation Times from Incoherent and Coherent Second-Harmonic Generation.....	7

Session WB: Polymeric High Speed Modulators

WB1	High Speed Organic Electro-Optic Modulators	9
WB2	Evaluation of Some New Polymer Systems.....	N/A
WB3	The Role of Intermolecular Electrostatic Interactions in Defining Electro-Optic Activity for Poled Polymeric Materials.....	N/A

Thursday, 23 July 1998

Session ThA: Plastic Fibers

ThA1	Polymer Optical Fibers	13
ThA2	Studies of Plastic Optical Fibers	15
ThA3	Scattering Loss in Plastic Optical Fiber	17

Session ThB: Organic LEDs and Passive Devices

ThB1	Photorefractive and Electroluminescent Organics	19
ThB2	Organic Electro-Luminescence.....	N/A
ThB3	Passive Polymeric EO Devices.....	21

Session ThC: Photopolymers for Data Storage

ThC1	Holographic Data Storage Using Photo Polymers	N/A
ThC2	Organic Photorefractive Materials.....	N/A
ThC3	Thermally Stimulated Current and Electro-Optic Responses in Photorefractive Polymers	

Session ThD: Plastic Transistors

ThD1	Plastic Transistors	N/A
ThD2	Plastic Electronics: Materials and Devices.....	N/A

TABLE OF CONTENTS

Friday, 24 July 1998

Session FA: Organic Nonlinear Optics

FA1	Theoretical Design of Mechanisms for Enhanced Two-Photon Absorption in Organic Chromophores	N/A
FA2	Access to New X3 Materials	N/A
FA3	High Electric Field Poling of Polymers	N/A

Session FB: Polymeric High Speed Modulators II

FB1	Design and Fabrication of Low Vp Polymer Modulators	N/A
FB2	Applications of Polymer Modulators to Commercial Systems	N/A
FB3	New Directions in Polymer Modulators for Interconnectors	N/A

Session FC:

FC1	Polymeric EO Modulators Based on Chiral Structures	27
FC2	Improved Coupling Efficiency using Δn -Controlled Polymer Waveguides with Two-Dimensional Spot-Size Transformation	29
FC3	Three Dimensional Integration of Polymer Electro-Optic Modulators.....	31
FC5	High-Frequency Demodulation of Multiphoton Fluorescence for Hyper-Rayleigh Scattering in Solution	33

Session FD: Polymeric Waveguide Devices

FD1	Polymeric Optical Waveguides	35
FD2	All-Optical Parallel Processing by Photoinduced Complex Refractive Index Changes in Guided Wave Geometry Containing Organic Dye	37
FD3	Organic Microcrystals for Linear and Nonlinear Optics	39

Organic Optics & Optoelectronics

Wednesday, 22 July 1998

WA: NLO Polymers

WB: Polymeric High Speed Modulators

Wednesday Papers Not Available

- WA2 New Molecular for EO Polymers, *Seth Marder, California Institute of Technology, Pasadena, CA*
- WB2 Evaluation of Some new Polymer Systems, *S. Ermer, Lockheed Martin, Palo Alto, CA*
- WB3 The Role of Intermolecular Electrostatic Interactions in Defining Electro-Optic Activity For Poled Polymeric Materials, *Larry R. Dalton, University of Southern California, Los Angeles, CA*

WA1 (Invited)
1:30pm - 2:00pm

PROCESSING ASSISTED SELF ASSEMBLY OF NONLINEAR OPTICAL POLYMERS

M. J. Roberts, J. D. Stenger-Smith, P. Zarras, G. A. Lindsay, R. A. Hollins, A. P. Chafin, and R. Y. Yee

United States Department of the Navy, Naval Air Weapons Center Weapons Division, Materials and Chemistry Branch, Code 4B2200D, 1 Administration Circle, China Lake, CA 93555

Kenneth J. Wynne

Physical Sciences S&T Division 331, Office of Naval Research, 800 North Quincy Street, Arlington, VA 22217-5660

This presentation explores a number of polymer architectures with the objective of *intrinsically* polar polymer films for applications such as electro-optic switches and signal modulators for high bandwidth data processing.¹ The goal of this work is to offer an alternative to the poled polymer approach in order to avoid high temperature processing and high electric fields. This paper reports progress toward achieving this goal.² One approach to obtain polar bilayers utilizes a syndioregic mainchain NLO polymer topology in which hydrophilic and lipophilic bridging groups are located on alternating bridging sites between the chromophores in order to bring about polar self-ordering at an air-water interface. This architecture has been used to prepare polar films and the ability to fabricate a modulator using a processing assisted self organized thin film has been demonstrated. Unfortunately, the use of lipophilic interactions alone leads to minimal thermal stability.

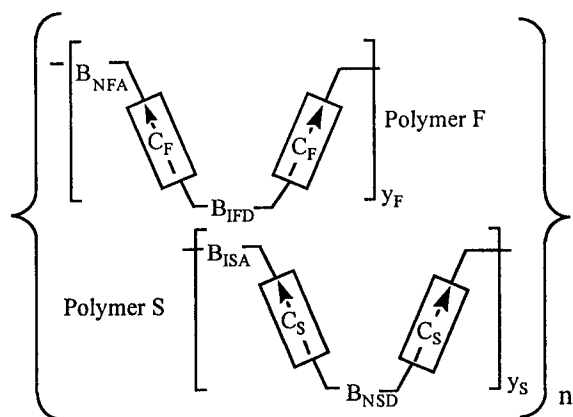


Figure 1. Structural concept for intrinsically polar pairwise deposited films.

A new approach to producing thermally stable polar films utilizing polyionomers is now underway. This approach uses Langmuir Blodgett processing with a floating layer (Polymer F) and a soluble layer (Polymer S) which are deposited in a pairwise manner. The electron accepting end of the chromophore in Polymer F is connected to neutral (N) bridging unit, and its electron donating end is connected to an ionic (I) bridging unit while the converse is true for Polymer S. A linear increase of absorption with the number of bilayers indicates the films have a

uniformity in thickness. Quadratic increase in SHG intensity as a function of the number of bilayers indicates polar alignment.

Another promising approach for the preparation of polar films utilizes alternating polyelectrolyte deposition (APD) in aqueous solutions at ambient temperature.³ The process comprises alternately dipping a substrate into aqueous solutions of a polycation and a polyanion to build up a multilayer film.

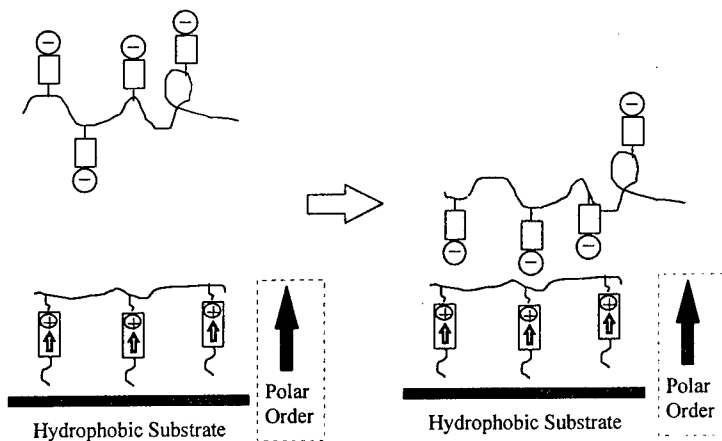


Figure 2. Polar bilayer fabrication utilizing Alternating Polymer Deposition (APD).

We have extended the APD approach using polyepichlorohydrin substituted with stilbazolium side-chain chromophore as the cationic NLOP with an inactive polyanion, polystyrene sulfonate, as represented schematically in Figure 2. Uniform layer to layer deposition is observed as evidenced by a linear increase of UV-Visible absorbance up to 48 bilayers. Quadratic dependence of SHG increases up to 24 bilayers but then begins to level off and does not increase above the value obtained for the 32 bilayer film. Thus, bilayers continue to be deposited, but polar order is lost past about 32 bilayers. The cause of the change from polar ordered bilayers to isotropic bilayers is under investigation.

Acknowledgment: The authors thank the Office of Naval Research for partial support.

References

- ¹ *Polymers for Second-Order Nonlinear Optics*, G. A. Lindsay and K. D. Singer, Eds., Am. Chem. Soc. Adv. Chem. Ser. 601, Washington, D.C., 1995.
- ² G. A. Lindsay, K. J. Wynne, W. Herman, A. Chafin, R. Hollins, J. Stenger-Smith, J. Hoover, J. Cline, J. Roberts. J. Nonlinear Optics, Sec. B, 15, 139, 1996.
- ³ X. Wang, S. Balasubramanian, L. Li, X. Jiang, D. J. Sandman, M. F. Rubner, J. Kumar, S. K. Tripathy, *Macromol. Rapid Commun.*, 18, 451, 1997.

POLYMERS FOR SECOND-ORDER NONLINEAR OPTICAL
APPLICATIONS.

C. Samyn^a, K. Van den Broeck^a, M. Van Beylen^a, T. Verbiest^b, A. Persoons^b

^a Laboratory of Macromolecular and Physical Organic Chemistry, University of Leuven, Celestijnenlaan 200F ,B-3001 Leuven, Belgium

^b Laboratory of Chemical and Biological Dynamics and Center for Research on Molecular Electronics and Photonics, University of Leuven, Celestijnenlaan 200D ,B-3001 Leuven, Belgium

The aim of our investigation is the development of new polymeric materials with nonlinear optical properties which are comparable or even better than the existing organic salts such as LiNbO₃, KDP etc.

Nonlinear optical (NLO) polymers which show large second-order NLO properties and which show long-term stability, low optical loss and good processibility to fabricate thin films and fibers are of considerable interest in the development of new materials used for frequency doubling applications and for their use in optical communication. In contrast to polymeric films doped with dyes which suffer from limited solubility in the host polymer matrix and gradually loss of orientation over a short period, films fabricated from polymers in which NLO-phores are covalently bound to the polymeric backbone, have an enhanced density of NLO-phores and may exhibit therefore higher nonlinear susceptibilities. Copolymers of chromophore substituted methacrylate and MMA, with systematically varied concentration of the chromophore were synthesized. Several series of different donor- π -conjugated-acceptor systems were introduced.

From the copolymers, thin films were obtained by spin coating, then poled in order to transform them into their noncentrosymmetric structure. The second harmonic coefficients and related susceptibilities, expressing the frequency doubling intensities were evaluated by second harmonic generation measurements at 1064 nm of fundamental wavelength. $\chi^{(2)}$ values as high as $324 \cdot 10^{-9}$ esu could be achieved. Some of this copolymers show reasonable to high stability for their frequency doubling effect in function of time.

By the incorporation of heterocyclic rings in the chromophore system, enhanced nonlinear optical activities were obtained, this because of the lower delocalization energy of thiophene and furan compared to benzene.

Introduction of an additional donor- or acceptor group in the chromophore system does mostly not result in a cooperative effect with higher NLO-intensities.

Long term stability of the NLO-response is a major objective in the search for new polymeric materials with these properties. As high stability is connected with T_g (glass transition temperature) and as the highest T_g we obtained for the functionalized copolymethacrylates was not higher than 140°C , several of this copolymer combinations can only be applied at rather low temperature so to keep the NLO-activity loss at a minimum. Some new high T_g side chain copolymers based on azo chromophore functionalized poly(maleimide-4-phenyl styrene)s have therefore been synthesized. T_g 's up to 219°C could be obtained, the $\chi_{zzz}^{(2)}$ values vary from 258 to $606 \cdot 10^{-9}$ esu

The stability which was verified at 125°C is extremely high for this type of copolymers, 90 to 64% of remaining NLO-intensity could be achieved after 1,000 h of heating and this values seems to stabilize in function of time. These polymers are therefore a major contribution in the search for polymeric systems with improved stability of their second-order nonlinear optical properties and their use in frequency doubling materials for waveguide constructions.

Nonlinear optical relaxation times
from incoherent and coherent second-harmonic generation

Koen Clays, Geert Olbrechts, and André Persoons,
Laboratory of Chemical and Biological Dynamics, Center for Research in Molecular
Electronics and Photonics, Department of Chemistry, University of Leuven,
Celestijnenlaan 200D, B-3001 Leuven, Belgium
tel.: 321-6327508, fax: 321-6327982
e-mail: koen@lcbdiris.fys.kuleuven.ac.be

SUMMARY:

Incoherent second-order nonlinear optical scattering, also known as hyper-Rayleigh scattering (HRS)[1], has become widely accepted as an experimental technique for the determination of the molecular second-order nonlinear optical polarizability (first hyperpolarizability). The generic laser type used for this experiment is a high-power Q-switched nanosecond pulse laser,[2] due to the low quantum efficiency of the HRS process. A femtosecond version of HRS has been developed.[3] This has led to the implementation of high-frequency demodulation techniques for the multi-photon fluorescence contribution in hyper-Rayleigh scattering.

Apart from the opportunity offered by femtosecond incoherent scattering for molecular characterization, relating to the temporal resolution offered by a shorter pulse, another possibility is offered through the high peak power available from a moderate energy content in such a short pulse.[3] It is now possible to measure incoherent hyper-Rayleigh scattering from solid samples. This allows us to probe the orientational correlation between individual chromophores in a bulk arrangement. An attractive format for nonlinear optics is a thin film waveguide. We have used femtosecond pulses (10 nanoJoule energy, but 100 kilowatt peak power in a 100 femtosecond pulse) to study the spatial orientational correlation length between chromophores as a function of poling and relaxation in a polymer matrix. The positive influence of the degree of poling is clearly evidenced as an increase in the orientational correlation length between the chromophores.[4] Due to temporal relaxation in the polymer film, the correlation length decreases after the poling.[5] The relaxation time, retrieved from this incoherent

scattering experiment, has been compared with the relaxation time from coherent second-harmonic generation.[6] The difference in relaxation time has now been rationalized in terms of translational diffusion of the local free volume in the polymer matrix and the rotational diffusion of the chromophores in this free volume. This rationalization is based on the ratio of the relaxation times, that is related to the ratio of the characteristic length in the two types of experiment. For the incoherent scattering experiment, the only characteristic length is the wavelength (800 nm for a Titanium-sapphire laser), while for coherent second-harmonic generation, the relevant length is the coherence length (10 μm for polymethylmethacrylate at this wavelength). The ratio of the relaxation times (0.006) equals the square of the ratio the characteristic lengths. This points unequivocally to translational diffusion, governed by the relation between diffusion length x , time interval t and translational diffusion coefficient D , $\langle x^2 \rangle = 2Dt$. However, due to symmetry requirements for second-order effects, a rotational relaxation needs to be invoked at the molecular level. The combination can be understood as the molecular reorientation in the free volume, that exhibits translation diffusion with diffusion coefficient D that is, of course, independent of measurement technique. What is specific for the experiment, is the characteristic length of the experiment, leading to different relaxation times.

This opportunity for second-order nonlinear femtosecond incoherent scattering is on the level of the bulk arrangement of chromophores. The correlation experiments provides guidelines for the optimal arrangement of chromophores, and for techniques to provide for this arrangement.

References:

- [1] K. Clays and A. Persoons, Phys. Rev. Lett. 66 (1991) 2980.
- [2] K. Clays and A. Persoons, Rev. Sci. Instrum. 63 (1992) 3285.
- [3] K. Clays and A. Persoons, Rev. Sci. Instrum. 65 (1994) 2190.
- [4] G. Olbrechts, E.J.H. Put, K. Clays, A. Persoons and N. Matsuda, Chem. Phys. Lett. 253 (1996) 135.
- [5] N. Matsuda, G. Olbrechts, E.J.H. Put, K. Clays and A. Persoons, Appl. Phys. Lett. 69 (1996) 4145.
- [6] G. Olbrechts, E.J.H. Put, D. Van Steenwinckel, K. Clays, A. Persoons, C. Samyn and N. Matsuda, J. Opt. Soc. Am. B 15 (1998) 369.

HIGH SPEED ORGANIC ELECTRO-OPTIC MODULATORS

H. Fetterman, D. Chen, A. Udupa, D. Bhattachaya, B. Tsap
University of California, Los Angeles 90024

S. Lee, A. Chen, J. Chen, W. Steier, L. Dalton
University of Southern California 90089

Ultra-high speed electro-optic modulators have been fabricated and tested with integrated electrode transitions for W-band (75-110 GHz) operation. These devices use new polymer systems that are low loss, stable and have electro-optic coefficients exceeding that of LiNbO_3 .

Recently we have fabricated and tested modulators that have worked as high as 113 GHz. These were prototype devices, based upon DR19 were contacted using high frequency coplanar probes. In this paper we have extended these measurements to integrated optical modulators which directly couple to W-band waveguide. Further, we have fabricated these devices from a new class of chromophores that have been designed to have a shape that reduces dipole-dipole pairing. This leads to structures that have large loading densities and relatively high electro-optic coefficients. In particular, this paper reports results with APII and FTC materials.

The materials that we have been working with have also been developed with an additional emphasis on high thermal stability and low optical loss. These typically are about 1 dB/cm and are only slightly higher in going from 1.3 to 1.5 μm . The r_{33} for these materials range up to 55 pm/volt with V_π as low as 4.5 volts.

The basic structures are shown in Fig. 1. Note that it is very straightforward to make arrays of modulators with polymer materials.

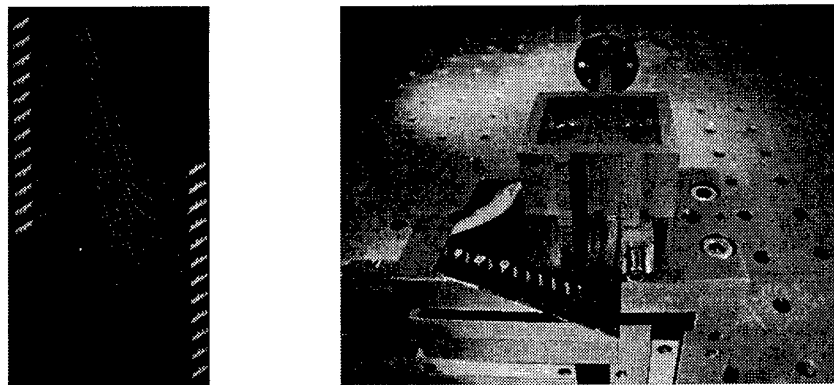


Fig.1: Photograph of Integrated W-band Modulator (a) before insertion and (b) after insertion into rectangular waveguide.

In going to high frequencies, which must connect to waveguide, silicon substrates cannot be used because of their high microwave losses. Instead, we have used mylar substates which are inserted directly into the microwave guides with fin-line transitions. The typical response of this system at high frequency is indicated in Fig. 2. A Gunn diode is used as the 94 GHz driving source. The polymer used in this case was APII, which was the first of the next generation polymers we have used.

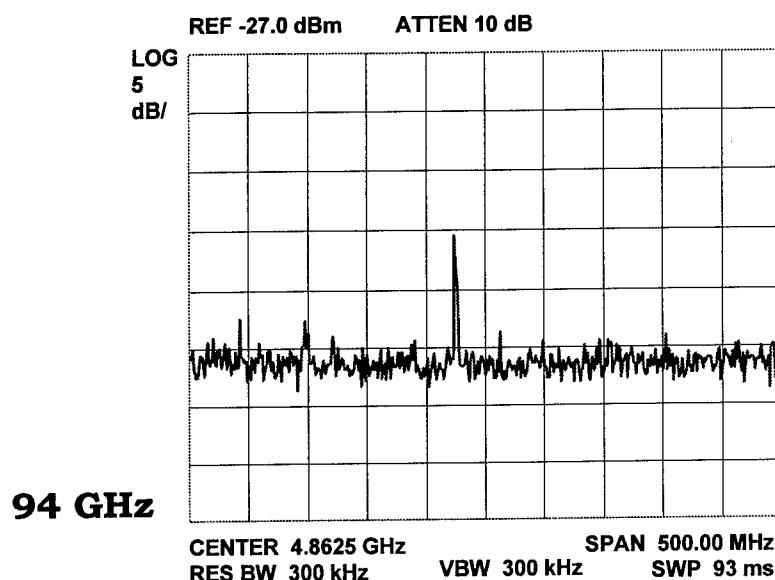


Fig. 2: Spectrum analyzer trace of modulation signal at 94 GHz downconverted to an IF of 4.8625 GHz by optical heterodyne technique.

We have also measured another extremely high nonlinear material, FTC and have made Mach Zehnder devices that operate below 5 volts. In measuring the frequency response up to 40 GHz we found several resonances as shown in Fig. 3. These are a function of our electrode design and are now being addressed to extend this material to higher frequencies while still maintaining the favorable low voltage capability.

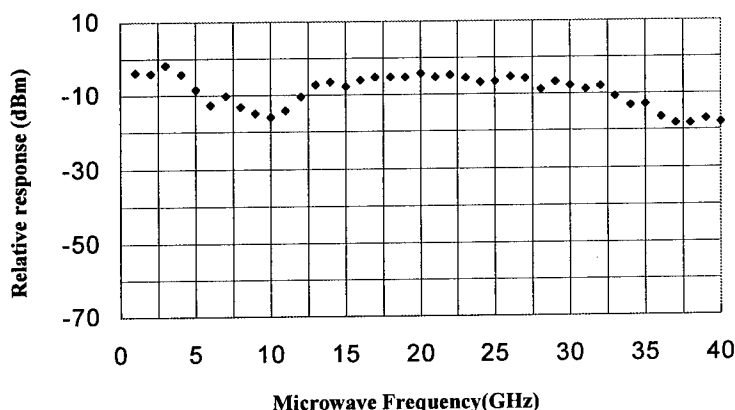


Fig. 3: Relative Response of FTC modulator to 40 GHz with a $V_{\pi} = 4.5$ V.

Organic Optics & Optoelectronics

Thursday, 23 July 1998

ThA: Plastic Fibers

ThB: Organic LEDs and Passive Devices

ThC: Photopolymers for Data Storage

ThD: Plastic Transistors

Thursday Papers Not Available

- ThB2 Organic Electro-Luminescence,
*Georges Hadziannou, University of Groningen,
Groningen, The Netherlands*
- ThC1 Holographic Data Storage Using Photo
Polymers, *K. Curtis, Lucent Technologies,
Bell Laboratories, Holmdel, NJ*
- ThC2 Organic Photorefractive Materials,
*Klaus Meerholz, University of Munich, Munich,
Germany*
- ThD1 Plastic Transistors, *Francis Garnier, Lab des
Materiaux Moleculaires, Thiais, France*
- ThD2 Plastic Electronics: Materials and Devices,
*Zhenan Bao, Lucent Technologies, Bell
Laboratories, Murray Hill, NJ*

Polymer Optical Fibers

Yasuhiro Koike, Takaaki Ishigure, Masataka Sato, and Eisuke Nihei
Faculty of Science and Technology, Keio University
Kanagawa Academy of Science and Technology
3-14-1, Hiyoshi, Kohoku-ku, Yokohama 223-0061 JAPAN
Phone: +81-45-563-1141 ext. 3454
Fax: +81-45-562-7373
e-mail: koike@applc.keio.ac.jp

Abstract

The progress of the GI polymer optical fiber (GI POF) for high-speed telecommunication is reviewed. Gigabit data transmission for several hundred meters from visible to 1.3- μm wavelength was experimentally enabled by the low-loss perfluorinated (PF) polymer base GI POF. We describe an improvement in the thermal stability and long-term reliability of the GI POF.

Introduction

Increasing speed in data communications and the trend to networks with distributed computing require high data throughput even for the physical layer of network. Growing research interests are focused on the optical access network systems. The electrical lines generally used in the access arena cannot cover the required bit rate in the multimedia society. However, the single mode silica fiber that is already utilized in the trunk area is not a necessarily suitable media for such short distance network, because the small core diameter of the single mode fiber requires accurately designed optical devices such as the ferrule in the connector, which increases the total system cost.

A large-core, high-bandwidth, and low-loss GI polymer optical fiber (POF) we have proposed is one of the ideal candidates to overcome such fiber distributing and connecting problems. Recently, we succeeded in preparing the low-loss perfluorinated (PF) polymer base GI POF from visible to 1.5- μm wavelength¹. In this paper, we describe the current status of the GI POF for high speed data communications

Thermal stability of GI POF

Thermal stability and the long-term reliability is one of the main problems in the POF. Since the refractive-index distribution of the GI POF is formed by the concentration distribution of the dopant, diffusion and migration of the dopant in the POF degrade the refractive index profile. Furthermore, the stability particularly in the attenuation under high humidity is an important issue. In this paper, we describe the stability of the PMMA base GI POF under high temperature and high humidity atmosphere.

In order to clarify the thermal stability of the GI POF, we selected several kinds of dopant. It was confirmed that stability of the refractive index profile was dependent on the glass transition temperature (T_g) of the core of the POF, and that by selecting the suitable dopant, higher T_g of the core than 85 °C can be maintained, and thermally stable GI POF in which no index profile degradation was observed even at 85 °C was obtained. Since the bandwidth of the GI POF is measured by the pulse broadening through the POF, the degradation of the output waveform stability was investigated. The measurement result of the thermal stability in bandwidth is shown in Fig. 1. It is noted that the output waveform from 100 m GI POF is maintained through 6000 hours aging at 85 °C.

It was confirmed that the attenuation increment of the GI POF under high temperature and high humidity atmosphere strongly depended on the used dopant. PMMA, which is the typical polymer material for the commercially available POF, can usually absorb approximately 2 wt. % of water at maximum. However, little attenuation increase is observed in the commercially available PMMA core SI POF under high humidity. Since the absorbed water molecule is not forming cluster, no excess scattering loss is caused by absorbed water molecules.

On the other hand, the core material of the GI POF involving the aromatic compound as the dopant absorbs less amount of water than PMMA. However, slightly absorbed water molecule in the core of the GI POF makes cluster structure easily even though the absorbed water concentration is lower than 1 wt. %. Critical water concentration in the core to form the cluster causing the excess scattering loss is dependent on the miscibility in PMMA-dopant-water. Therefore, it is important to select a suitable dopant to obtain the thermally stable GI POF not only in bandwidth but attenuation.

Stability of the attenuation of the GI POF under high temperature and high humidity (70 °C, 95 % R.H.) is shown in Fig. 2. It should be noted that remarkable attenuation increase was observed in BEN (benzyl benzoate), which is previously

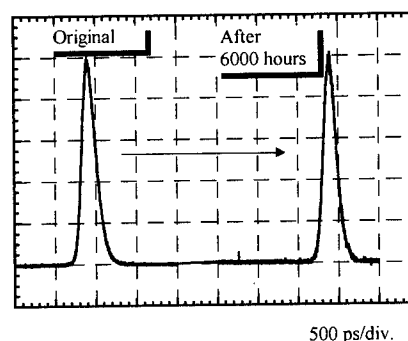


Fig. 1 Thermal stability in bandwidth of PMMA base GI POF through 85 °C aging. Fiber length is 100 m. Wavelength is 0.65 μm .

used dopant, doped GI POF. On the other hand, highly stable GI POF under high humidity atmosphere was successfully obtained by selecting the suitable dopant (Type A) in which low attenuation is maintained through 400 hours aging.

Bandwidth achieved by POF

We have proposed a low-loss perfluorinated (PF) polymer base GI POF even at the near infrared region. Experimentally, less than 40 dB/km at 1.3- μ m wavelength was obtained, and we theoretically estimated that the attenuation limit of the PF polymer base POF is approximately 0.3 dB/km.

The low-loss PF polymer base GI POF allows extending the POF link length to more than 500 m or more. In order to realize the gigabit POF network, investigation of the relation between the dispersion property and refractive index profile becomes the key issue.

The dispersion property of the GI POF was theoretically calculated with using WKB method in which modal, material, and profile dispersions were taken into consideration. The refractive index profile of the GI POF was approximated by a power-law form described by eq. (1). These power-law approximation enables to obtain the analytical solutions of the wave equation derived from the Maxwell's equation.

$$n(r) = n_1 \left[1 - 2\Delta \left(\frac{r}{a} \right)^g \right]^{1/2} \quad 0 \leq r \leq a \quad (1)$$

$$\Delta = \frac{n_1 - n_2}{n_1} \quad (2)$$

where n_1 and n_2 are the refractive indices of the center axis and the cladding, respectively, and a is the core radius. where n_1 and n_2 are the refractive indices of the center axis and the cladding, respectively, and a is the core radius. The parameter g called index exponent determines the index profile.

It is noted that, the optimum index exponent value is located around $g=2.3$ in the case of the PMMA base GI POF because of the large profile dispersion. Since the optical window of the attenuation is located around 0.65- μ m wavelength, the large material dispersion limits the bandwidth to approximately 3 GHz even if the index profile is optimized. A good agreement was observed in the theoretical estimation and experimentally measured values. On the other hand, more than 5 GHz can be achieved by the PF polymer base GI POF at the same wavelength because of the low material dispersion.

Furthermore, the low absorption loss of the PF polymer base GI POF enables to use near infrared region as the signal wavelength². Use of near infrared light source has the great advantage in the material dispersion. As shown in Fig.3, the low material dispersion at 1.3 μ m enables 80 GHz which is higher than that of SiO₂-GeO₂ multimode fiber.

Conclusion

Recent prospect of the GI POF for high-speed data transmission was reviewed. PF polymer has many advantages: low attenuation, low material dispersion, no flammability, etc. It was clarified that the PF polymer base GI POF enables 10 Gb/s 1km POF link. Furthermore, thermal stability of the GI POF has been an important issue, and it is improved by investigating the dopant material. We believe that use of the PF polymer for the GI POF opens the way for great advantage in the new fiber network infrastructure.

References

1. Y. Koike and T. Ishigure, Proc. of ECOC'97, vol. 1, 59 (1997)
2. Y. Koike, E. Nihei, and T. Ishigure, Proc. of OECC'97, 64 (1996)

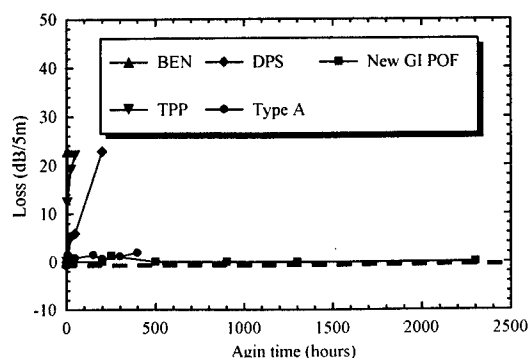


Fig. 2 Stability in attenuation of the PMMA base GI POF under 70°C, 95 %R. H.

TPP, DPS and Type A are the name of dopant

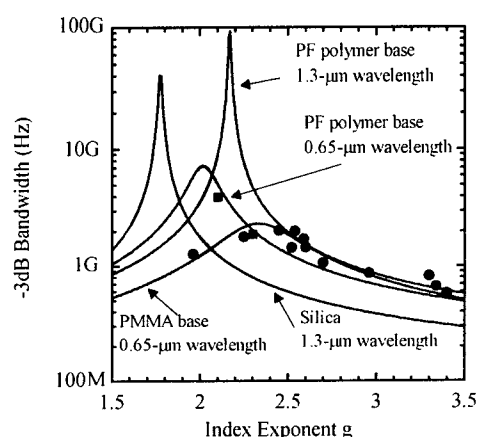


Fig.3 Relation between the index exponent g and the bandwidth of 100 m GI POF.

●: Experimental values of PMMA base GI POF at 0.65- μ m
■: Experimental values of PF polymer

Studies of Plastic Optical Fibers

J. Wang, R. Gao, Y. Cai, R. F. Shi, and A. F. Garito

Department of Physics and Astronomy; University of Pennsylvania; Philadelphia, PA 19104 USA

High speed fiber optic networks increasingly require high performance fiber links in short distance (~ 100 m) applications such as local area networks (LANs), data links, and multi-node bus networks. Current high performance short distance fiber links are multimode, graded refractive index (GI), glass optical fibers (GOF). Primarily because of its attractive ductile properties and light weight, multimode plastic optical fiber (POF) is also being considered, especially for short (< 50 m) quick-connect applications

In recent studies of POF, ^{1,2} we and co-workers discovered that strong mode coupling largely determines the measured bandwidth performance in POF, especially in GI POF. We observed in both SI POF and GI POF the square root-like fiber length dependence of optical pulse broadening and far-field radiation patterns characteristic of strong mode coupling. A key observation in our GI POF study that led to these findings was the measured refractive index profile which is found to be not uniform and parabola-like, but composed of two widely differing regions. Consequently, the overall GI POF index profile significantly under compensates by nearly an order of magnitude (inter)modal dispersion, which mainly limits bandwidth.

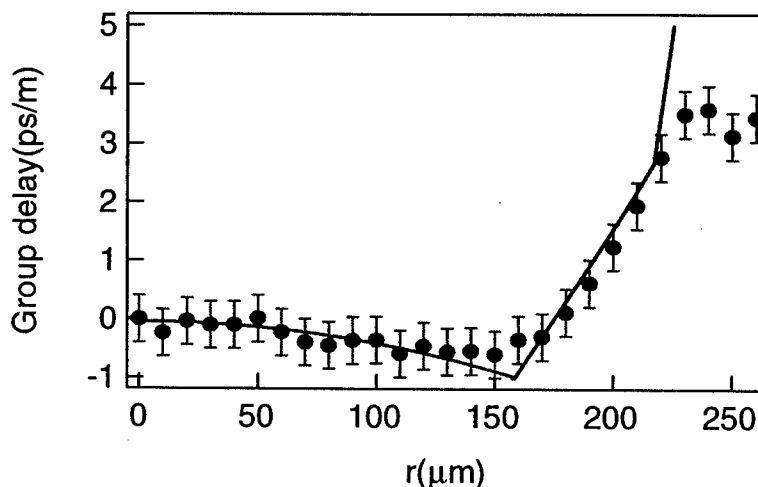


Figure 1. Differential mode delay profile of GI POF: exp. (dots) and calc. (solid).

Differential mode delay (DMD) measurements are highly sensitive to relatively small feature sizes in the index profile that are more difficult to observe in direct determinations of index profiles such as the near field refracted ray and transverse interferometric methods used in our earlier study. DMD measures the time delays of small guided mode groups launched down the fiber from specific radial positions at the fiber input end.

The GI POF samples of standard dimensions were fabricated by inter-facial gel polymerization of a mixture consisting of poly(methyl methacrylate) (PMMA) and benzyl benzoate to yield a numerical aperture of 0.25 for each fiber.

Figure 2 is the DMD as a function of fiber radial position for a typical GI POF sample. In addition to the clear symmetry, the important features of the DMD profile are the two major optical regions of differing slopes, joining near $160 \mu\text{m}$. The central core region extends approximately over $0 < r < 160 \mu\text{m}$, maintaining a negative slope with

increased fiber radial position. Thus, the outer modes travel faster than the inner modes, indicating that the refractive index profile in this region over compensates modal dispersion. The second major region is the core-cladding region extending approximately

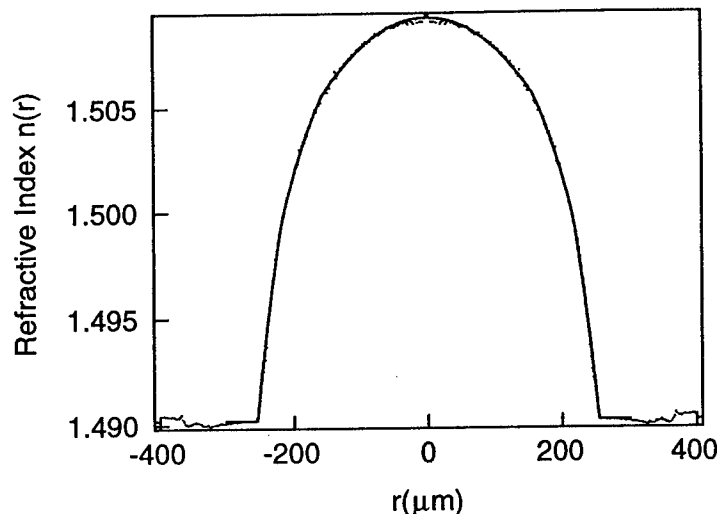


Figure 2. Refractive index profile of GI POF: exp. (dots) and calc. (solid).

over $160 \mu\text{m} < r < 250 \mu\text{m}$, with a positive slope. Thus, the index profile undercompensates modal dispersion. The measured DMD profile is in good agreement with our earlier observations of the refractive index profile of GI POF, namely that the directly measured refractive index profile contains two broad optically distinct regions joined near $160 \mu\text{m}$.

The results demonstrate the high sensitivity of DMD measurements to make prominent detailed features in the GI POF index profile previously unresolvable. Further, the DMD results enable the index profile, $n(r)$, to be analyzed in terms of alpha- (α) profiles with higher precision than previously possible using a dual polynomial. In the procedure, the different profile sections are fit with different α -values in the following expression

$$n(r) = n_f \sqrt{1 - 2\Delta \left(\frac{r}{a_i}\right)^{\alpha_i}}$$

where both n_f (n_c), the refractive index at the core center (cladding) is fixed in the fitting process, $\Delta = (n_f^2 - n_c^2) / 2n_f^2$ and i denotes each profile section.. Figure 2 demonstrates the good comparison between the measured and calculated index profiles. The central part of the index profile is nearly parabola-like with an α -value of 2.06. In contrast, the core/cladding region connects steeply to the cladding, reminiscent of low bandwidth multi-mode step index fiber with step-like α -values greater than 3. The differences between the multiple α -profile and the earlier reported dual polynomial fit¹ are barely noticeable. Both yield an under compensated bandwidth consistent with our previous calculations and analysis.

References

- ¹R. F. Shi, C. Koeppen, G. Jiang, J. Wang, and A. F. Garito, *Appl. Phys. Lett.* **71** 3625 (1997).
- ²G. Jiang, R. F. Shi, and A. F. Garito, *IEEE Photonics Tech. Lett.* **9**, 1128 (1997).

ThA3 (Invited)
9:30am - 10:00am

SCATTERING LOSS IN PLASTIC OPTICAL FIBER

*Whitney R. White, Pierre Wiltzius, and Michael Dueser, Bell Laboratories, Lucent Technologies,
Murray Hill, NJ 07974*

Introduction

In recent years, dramatic loss reduction has been achieved in plastic optical fiber (POF) by use of perfluorinated polymers as a matrix material. In fibers based on poly-perfluorobutenylvinylether (PBVE) losses as low as 50 dB/km have been reported¹. While losses have been steadily improving, the ultimate potential for PBVE, and perfluorinated materials in general, remains unclear. Since the scope for possible POF applications depends greatly on loss, it is important to establish lower bounds for loss in prospective plastic fibers. Toward this end, we have performed light scattering measurements of fundamental loss mechanisms in PBVE as well as blends of PBVE and a low molecular weight dopant. In order to measure scattering intensities in the absence of stress birefringence, we have performed our measurements primarily at temperatures above the samples' glass transition temperatures. Since the fluctuations responsible for scattering become frozen in at the glass transition, room temperature values should be well approximated by those measured just above this point.

Experimental

We prepared both polymer and blend samples by evaporation from filtered dilute solution. Since the dopant had a vapor pressure of a few torr under these conditions, we confirmed the final composition of the blend sample with thermal gravimetric analysis. To measure light scattering losses, we allow a vertically polarized beam from a 100 mW Argon ion laser ($\lambda = 488$ nm) to pass through a 2cm diameter sealed cuvette containing the sample, and we measure the polarization resolved scattered light intensity with a cooled photomultiplier tube.

Measurements of undoped PBVE reveal only Rayleigh scattering in both the polarized (V_V) and depolarized orientation, and Fig. 1 shows the temperature dependence of both scattering components. Below the glass transition temperature (108 C), the V_V scattering intensity approaches $8 \times 10^{-6} \text{ cm}^{-1}$, in agreement with previous measurements². Nihei et al have considered² this scattering component in detail, and have shown it to be consistent with the value expected from thermodynamic fluctuations of density. As the temperature increases, the magnitude of this scattering component also increases, presumably due to increasing isothermal compressibility of the polymer. The H_V scattering is approximately independent of temperature, at $2.1 \times 10^{-6} \text{ cm}^{-1}$. Presumably, this depolarized scattering results from local orientational ordering of the polymer chains, with a very short orientational correlation length. (The orientational correlations also contribute slightly to the V_V scattering, since we expect $V_V = V_V^{\text{iso}} + 4/3 H_V$, where V_V^{iso} is the polarized scattering due to isotropic sources such as density fluctuations) Since stress birefringence becomes important in the vicinity of the glass transition, we may not measure this component below 110 C. However, since the sample densifies slightly at the glass transition, the value reported above should be viewed as a lower limit for the depolarized scattering intensity in the glassy state at room temperature. Taking both of the measured scattering intensities together, we expect these contributions to result in total attenuation (for unpolarized light) of $\alpha = 10\pi \log(e) (8/3 V_V^{\text{iso}} + 80/9 H_V) = 5 \text{ dB/km}$ at 850 nm, assuming the λ^{-4} wavelength dependence associated with Rayleigh scatterers. This value is significantly higher than the 2 dB/km expected² for density fluctuations alone.

As shown in Fig. 2, addition of 10 wt. % dopant considerably increases the V_V scattering intensity in PBVE, without significantly changing the H_V scattering intensity. The scattering intensities shown in Fig. 2 are independent of the thermal history of the sample, and are measured above the glass transition temperature of the mixture. Thus, the increased scattering does not arise from phase separation, since

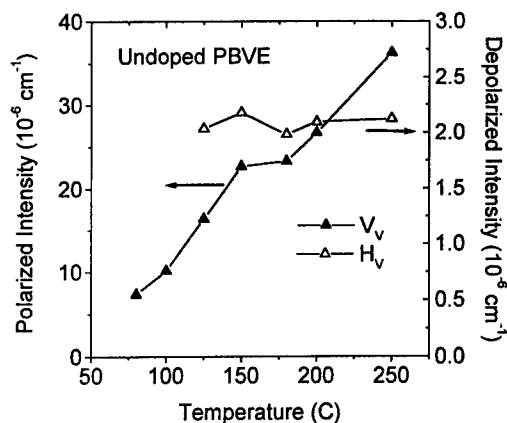


Fig. 1

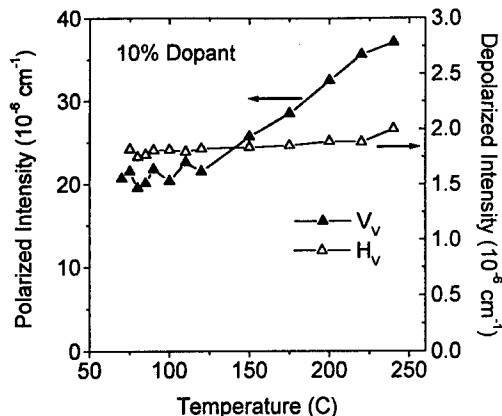


Fig. 2

there should be no limit to domain growth in the melt. With dynamic light scattering, we have measured speckle pattern correlation times of order 100 seconds in this sample at 75 C, decreasing smoothly to approximately 0.1 seconds at 110 C. Since this blend is extraordinarily viscous in this temperature range ($\eta \sim 10^6$ poise at 110 C), it appears that the excess scattering results from thermodynamically excited nonuniformities of the dopant concentration, since only objects of molecular dimension could exhibit the high diffusivities implied by these correlation times. At room temperature, these concentration fluctuations will be frozen in, resulting in additional loss of ~ 5 dB/km in this mixture at 850 nm. While the magnitude of the loss associated with concentration fluctuations will clearly depend on the choice of dopant, it might be expected to be significant in fluoropolymer/dopant systems, since there is no opportunity for attractive interactions between the two species. Only entropy acts to overcome the repulsive Van der Waals interactions between the polymer and the more polarizable dopant. By contrast, in many protonated systems hydrogen bonding provides an attractive interaction, thereby decreasing the magnitude of concentration fluctuations.

Conclusion

In this paper, we have investigated lower limits for scattering loss in plastic optical fibers produced from PBVE. Even in the undoped polymer, frozen-in variations of density and orientation cause Rayleigh scattering, resulting in a minimum attenuation at 850 nm of ~ 5 dB/km. Upon addition of dopant, this minimum attenuation increases to 10 dB/km. Since all of these scattering mechanisms (as well as any extrinsic scattering) introduce coupling between the various modes of a multimode plastic fiber, it is conceivable that scattering will positively impact the fiber bandwidth by reduction of modal dispersion. Indeed, convincing evidence of mode mixing in POF has recently been reported³ by Jiang et al. With differential mode delay measurements, we are currently examining the role of scattering in mode mixing.

Acknowledgements

The authors gratefully acknowledge H. Bair for thermal gravimetric analysis.

References

- [1] H. Murofushi, Proceedings of the Fifth International Conference on Plastic Fibers and Applications, Paris, France, October 22-24, 1996.
- [2] E. Nihei, T. Ishigure, N. Tanio, and Y. Koike, IEICE Trans. Electron, v. E80-C, p.117, 1997.
- [3] G. Jiang, R. F. Shi, and A. F. Garito, IEEE Photonics Technology Letters, v. 9, p.1128, 1997.

ThB1 (Invited)
10:30am - 11:00am

Photorefractive and Electroluminescent Organics

Bernard Kippelen
Optical Sciences Center, The University of Arizona, Tucson, AZ 85721
kippelen@u.arizona.edu

The tailoring of organic molecules and polymers has enabled the recent development of multifunctional materials such as photorefractive polymers and organic electroluminescent materials. Recent advances show that photorefractive polymers keep their promises as optically active media for optical storage, processing, and imaging technologies. First-generation highly efficient materials [1] had several drawbacks including a shelf lifetime of a few months at room temperature, and the need for a high applied field to fully take advantage of the high dynamic range. Recently, we did overcome the shelf-stability problem by developing thermodynamically stable guest/host polymer composites. Stability was achieved in several steps: (i) shelf lifetime could be improved by two orders of magnitude in a PVK- (polyvinylcarbazole) based polymer composite doped with isomeric mixtures of chromophores and with no loss of dynamic range [2]; (ii) further stability improvement was obtained in polymers doped with a modified polyene chromophore (DHADC-MPN) that was designed to combine good solubility, high dipole moment, and large polarizability anisotropy, leading to improved dynamic range and stability simultaneously [3]; (iii) finally the substitution of the nearly apolar PVK matrix with the more polar matrix of poly(methyl methacrylate-co-tricyclodecyl methacrylate-co-N-cyclohexyl maleimide-co-benzyl methacrylate) (PTCB) led to stable materials with higher performance [4]. In current PTCB-based materials, total diffraction is observed at 633 nm at fields $E = 28 \text{ V}/\mu\text{m}$ and net gain coefficients $\Gamma > 200 \text{ cm}^{-1}$ at $E = 50 \text{ V}/\mu\text{m}$ (to be compared with $E = 60 \text{ V}/\mu\text{m}$ and $E = 90 \text{ V}/\mu\text{m}$, respectively, in the 1994 polymers). In these polymers the dopant chromophore DHADC-MPN provides several functionalities such as charge transport and refractive index change.

Furthermore, by using (2,4,7-trinitro-9-fluorenylidene)malonitrile (TNFDM) as a sensitizer, the spectral sensitivity of previous materials (633-690 nm) could be extended to the near infra-red (830 nm). Current polymer composites of DHADC-MPN:PVK:ECZ:TNFDM exhibit a diffraction efficiency of $\eta = 74\%$ at a field of $E = 59 \text{ V}/\mu\text{m}$ at 830 nm [3]. These photorefractive polymer composites with high dynamic range and near infra-red sensitivity offer new opportunities. Of particular importance is their compatibility with GaAs semiconductor laser diodes and commercial solid-state fs lasers such as Ti:sapphire lasers. Because of their spectral compatibility with the transparency window of biological tissues (700-900 nm), they are promising real-time holographic recording materials for imaging through scattering media. Recently, we demonstrated [3,5] reconstruction of an image through a solution with an effective optical density of 4 using a Ti:Sapphire laser in pulsed and in continuous low-coherence operation using holographic-time gating in the photorefractive polymer as the technique to filter out scattered light.

Recently, we also developed high-resolution photorefractive polymer-dispersed liquid crystals [6] that lead to high diffraction efficiency at lower applied fields compared with photorefractive polymers. The diffraction efficiency reaches 100% internally for 105- μm -thick samples at a field of $8 \text{ V}/\mu\text{m}$. Net optical gain and diffraction efficiencies of 56% are demonstrated in 53 μm -thick devices (see Fig. 1).

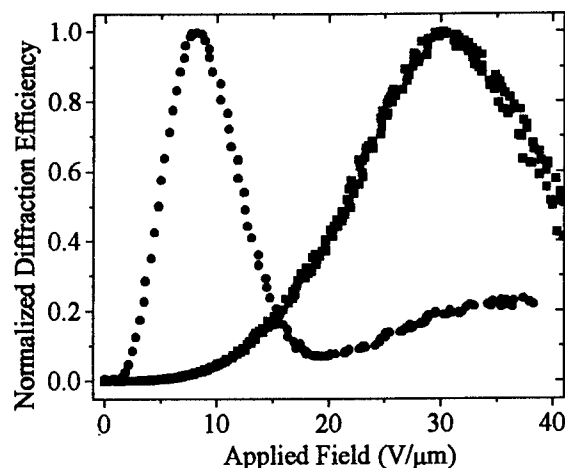


Figure 1: Normalized diffraction efficiency versus applied field measured in 105 μm -thick samples of the polymer-dispersed liquid crystal TL202:PMMA:ECZ:TNFDM (circles) and the photorefractive polymer DHADC-MPN:PVK:ECZ:TNF from Ref. 3.

Conjugated polymers and organic molecules combine transport and light-emitting properties that enable their use in electroluminescent devices for display applications. In this field, we have made the following advances: (i) fabricated and characterized ultra-bright electroluminescent devices using LiF/Al, and alloys of Al and LiF cathodes [7]; (ii) studied the optical gain properties of the conjugated polymer BEH:PPV and the origin of the spectrally narrow emission observed in these polymers above threshold for stimulated emission; (iii) demonstrated several optically pumped laser structures using a conjugated polymer in devices where feedback was provided in different ways [8,9].

This work was supported by AFOSR, ONR through the MURI Center for Advanced Multifunctional Nonlinear Optical Polymers and Molecular assemblies (CAMP) and by NSF.

- [1] K. Meerholz, B. L. Volodin, Sandalphon, B. Kippelen and N. Peyghambarian, *Nature (London)* **371**, 497 (1994).
- [2] E. Hendrickx, B. L. Volodin, D. D. Steele, J. L. Maldonado Rivera, J. F. Wang, B. Kippelen, N. Peyghambarian, *Appl. Phys. Lett.* **71**, 1159 (1997).
- [3] B. Kippelen, S. R. Marder, E. Hendrickx, J. L. Maldonado, G. Guillemet, B. L. Volodin, D. D. Steele, Y. Enami, Sandalphon, Y. J. Yao, J. F. Wang, H. Röckel, L. Erskine, and N. Peyghambarian, *Science* **279**, 54 (1998).
- [4] E. Hendrickx, J. Herlocker, J. L. Maldonado, S. R. Marder, B. Kippelen, A. Persoons and N. Peyghambarian, to appear in *Appl. Phys. Lett.* (1997).
- [5] D. D. Steele, B. L. Volodin, O. Savina, B. Kippelen, N. Peyghambarian, H. Röckel, S. R. Marder, *Opt. Lett.* **23**, 153-155 (1997).
- [6] Golemme, B. L. Volodin, B. Kippelen, N. Peyghambarian, *Opt. Lett.* **22**, 1226 (1997).
- [7] G. E. Jabbour, Y. Kawabe, S. E. Shaheen, J. F. Wang, M. M. Morrell, B. Kippelen, N. Peyghambarian, *Appl. Phys. Lett.* **71**, 1 (1997).
- [8] Schülzgen, Ch. Spiegelberg, M. M. Morrell, S. B. Mendes, B. Kippelen, N. Peyghambarian, M. F. Nabor, E. A. Mash, P. M. Allemand, *Appl. Phys. Lett.* **72**, 269 (1998).
- [9] Y. Kawabe, Ch. Spiegelberg, A. Schülzgen, M. F. Nabor, E. A. Mash, P. M. Allemand, M. Kuwata-Gonokami, K. Takeda, B. Kippelen, and Peyghambarian, *Appl. Phys. Lett.* **72**, 141-143 (1998).

PASSIVE POLYMERIC EO DEVICES

T.C. KOWALCZYK, L-Y LIU, H.S. LACKRITZ
Gemfire Corporation, Palo Alto, CA 94303

ABSTRACT

Initial experiments of a passive polymeric TE-to-TM polarization converter that utilizes laterally offset upper and lower poling electrodes to induce a 45° optical axis in the core of a nonlinear optical polymer waveguide are reported. By optimizing the device length, we have demonstrated polarization conversion efficiencies greater than 95% in devices as short as 240 μm with negligible insertion loss.

INTRODUCTION

Polymers are seeing increasing use in passive and active waveguiding applications for integrated optics technology. Polymeric devices have advantages because of their ease of manufacture, low cost, and compatibility with other processing needs and components. Nonlinear optical polymers have already been demonstrated as efficient modulators, couplers, and frequency converters [1,2]. More recently, polymeric polarization converters and rotators have been proposed and demonstrated [3,4]. Unlike their inorganic counterpart, polymeric polarization converters can operate in both active and passive modes. In particular, passive polarization converters for simplifying packaging requirements. In this case, an integrated polarization converter simplifies attachment of a laser diode (primarily TE polarized output) to an electro-optic waveguide device that requires TM polarization. The devices are passive in the sense that applied voltage is unnecessary for device operation after poling.

The polarization converter described in this study is shown in figure 1. The essential elements of the polymer wave-plate are its birefringence, optic axis orientation, and length. In polymer polarization converters, the orientation of the optical axis in the waveguide is determined by the poling electrode geometry (lateral offset). In the case of a polymer half wave-plate, the optical axis is oriented at a 45° angle with respect to the input polarization state. The resulting output polarization state is then rotated by 90° , producing an orthogonal polarization state compared to that of the input light.

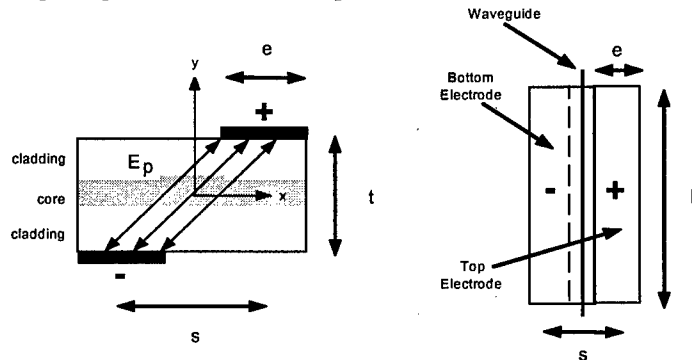


Figure 1. Cross-sectional (left) and top view (right) of the polymer half-wave plate TE-TM polarization converter showing device fabrication parameters e , t , s , L , and E_p . (electrode width, polymer stack thickness, lateral offset, length, and poling field, respectively).

Unlike active polarization conversion methods, the polymer half wave-plate requires a phase-mismatch between the propagating modes. The amount of phase mis-match determines the correct device length for polarization conversion. For a half-wave plate the phase between the fast and slow axis must be a multiple of π . The minimum propagation length for polarization conversion is then defined as the beat length, $L_B = \lambda / 2 \Delta n$. In typical poled polymers the induced birefringence can be as high ($\Delta n = 0.02$) so that the beat length and corresponding electrode length require precise fabrication. However this also provides a means for adjusting the beat length during processing, so that the index difference is small ($\Delta n \sim 0.005$). In this case the beat length is longer and the conversion efficiency does not critically depend on electrode fabrication tolerances. Equations 1 and 2 to determine the device's sensitivity to fabrication parameters.

EXPERIMENT

Samples were placed on a 3-axis high precision translation stage while a 6.0 μm core pig-tailed IR laser was butt-coupled to the waveguides containing the polarization converters of various lengths. The

polarization extinction ratio of the laser was greater than 100:1 with typical throughput powers of 1.0 mW. A microscope objective collected light output from the device and passed it through a linear polarizer. For each waveguide containing a polarization converter, power was measured for each polarization state and the ratio of TM component divided by the sum of TE and TM components was recorded as the conversion efficiency. The conversion efficiencies were then plotted as a function of device length (see figure 2.).

RESULTS

Figure 2. shows the conversion efficiency of devices poled under a field of 100 V/ μm plotted as a function of device length and fit to a theoretical curve containing adjustable parameters for the birefringence and poling field angle. A reasonably qualitative agreement between theory and experiment was obtained using $\Delta n = .0075$ and an electric field poling direction of 45°. These parameters were in agreement with electric field angles predicted from static field calculations.

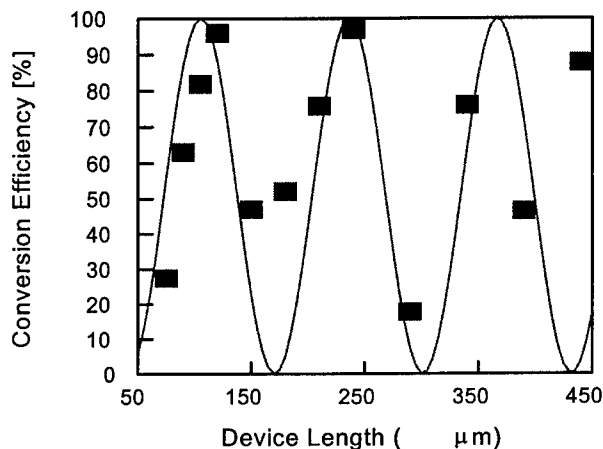


Figure 2. Polarization conversion efficiency data plotted as a function of device length illustrating the agreement between theory (solid) and experiment (points) using a birefringence value of 0.007 and an electric field poling angle of 45 degrees.

As figure 2 shows, there are conversion efficiencies (data points) that are not on the theoretical curve. These differences may be attributed to local poling field variations. It is also interesting to note that the birefringence obtained from fitting ($\Delta n = .0007$) was in agreement with the poling induced index change predicted by the oriented gas model [5,6]. The largest conversion efficiency we measured was 96% and 97% with device lengths of 120 μm and 240 μm , respectively.

CONCLUSIONS

We have demonstrated a passive polymeric polarization conversion efficiency of 97% with a 240 μm device length while maintaining low insertion losses. Our experimental results were consistent with theoretical predictions allowing us to correlate processing variables (poling field and device length) with device performance.

ACKNOWLEDGEMENTS

This work was funded by DARPA under contract DAAH01-96-C-R218.

REFERENCES

1. D. Chen, H.R. Fetterman, A. Chen, W.H. Steier, and L. R. Dalton, *Appl. Phys. Lett.* **70**, (1997).
2. T.A. Tumolillo and P.R. Ashley, *Appl. Phys. Lett.* **62**, pp.3068-3070 (1993).
3. W-Y Hwang, J-J Kim, T. Zyung, M-C Oh, S-Y Shin, *IEEE J. Quantum Electron.* **QE-32**, pp.1054-1062 (1996).
4. M-C Oh, S-Y Shin, W-Y Hwang, J-J Kim, *Appl. Phys. Lett.* **67**, pp. 1821-1823 (1995).
5. K.D. Singer, M.G. Kuzyk, and J.E. Sohn, *J. Opt. Soc. Am. B* **4**, 968 (1987).
6. C.C. Teng, M.A. Mortazavi, and G.K. Boudoughian, *Appl. Phys. Lett.* **66**, 667 (1995).

ThC3
2:30pm - 2:45pm

Thermally stimulated current and electro-optic responses in photorefractive polymers

Tetsuya Aoyama^{a, b}, Tatsuo Wada^{b, c}, Ya-Dong Zhang^c, Yuji Moritsuki^b, Yuriko Yonechi^b,
Hiroyuki Sasabe^{b, c}, Keisuke Sasaki^d, and Yasuhiro Koike^a

^a Department of Material Sciences, Faculty of Science and Technology, Keio University
3-14-1 Hiyoshi, Kohoku-ku, Yokohama 223-8522, Japan

^b Frontier Research Program, ^c CREST (Core Research for Evolutional Science and Technology), JST,
The Institute of Physical and Chemical Research (RIKEN)
2-1 Hirosawa, Wako, Saitama 351-0198, JAPAN

^d Chitose Institute of Science and Technology,
758-65 Bibi, Chitose, Hokkaido 066-0012, JAPAN

Recently organic photorefractive materials have attracted a lot of attention both from the point of view of fundamental science and practical applications. Most of the reported photorefractive polymers consist of multi-components: a carrier transporting agent, an electro-optic (EO) chromophore and a photosensitizer for photocarrier generation. Although these multi-component polymeric systems have film-forming properties and large index change,¹ they are not stable material systems.² There is a principal limitation of the maximum concentration of chromophores due to the phase separation or crystallization. In order to improve physical properties of multi-component polymeric systems, our group has developed monolithic photorefractive polymers. A monolithic photorefractive polymer (Figure 1) containing a carbazole moiety with two acceptor groups in the main chain and an additional EO chromophore in the side chain has been synthesized by Knoevenagel polycondensation.³ The glass transition temperature (T_g) of the polymer was found to be 87°C by the differential scanning calorimetric (DSC) analysis. Relaxation behavior of multifunctional polymers is of fundamental interest for development of photorefractive devices. In this paper, we describe the depolarization of photorefractive polymers by means of thermally stimulated current (TSC) and electro-optic responses.

The film was prepared by spin-coating from a chloroform solution onto an ITO substrate, and dried overnight at 50°C under vacuum. A layer of gold electrode (1.2cm² area for TSC measurements) was evaporated onto the film surface under high vacuum. Contact poling was performed to align dipole moments at 90°C slightly above T_g . For TSC measurements, the poled polymer samples were heated at a constant heating rate of 3°C/min. The resulting depolarization current was measured using a Keithley 6512 electrometer. The EO response of the poled photorefractive polymer was measured with the reflection method^{4, 5} at a wavelength of 532nm (frequency doubled Nd: YAG laser) and 633nm (He-Ne laser). The EO coefficients were measured as a function of the poling electric field. We also measured EO response as a function of temperature by heating the poled sample at a rate of 3°C/min.

Figure 2 shows the TSC curves of the poled photorefractive polymer. We observed two different processes labeled α and ρ . An α relaxation peak was observed around the T_g . TSC increased with the poling electric field. These results are explained by the

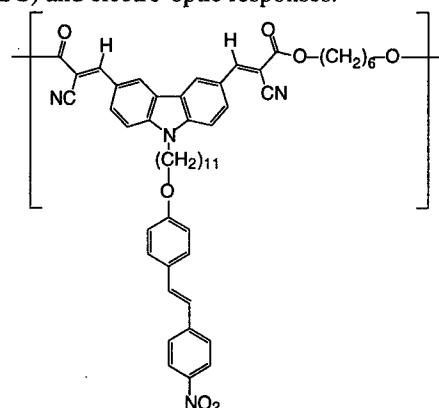


Figure 1. Chemical structure of photorefractive polymer.

relaxation of the electric field-induced polar orientation. The ρ peak located above 110°C in Fig. 2 is associated with the motion of the space charges induced during the poling process.

Figure 3 shows the EO coefficients r_{33} at a wavelength of 532nm as a function of the poling electric field. The EO responses linearly increased with the poling electric field. This result shows noncentrosymmetric alignment was achieved and the multifunctional polymer has the electro-optic activity.

Figure 4 shows the temperature dependence of the EO response at a wavelength of 633nm. The sample was poled with an electric field of $40\text{V}/\mu\text{m}$. The EO signal decreased with heating the sample. The decay behavior of EO signal coincided with the α relaxation peak near the T_g . This result suggests that the α peak is caused by the depolarization of the nonlinear optical chromophores.

In summary, depolarization of a photorefractive polymer containing acceptor-substituted carbazole with multifunctionality was measured by TSC and EO responses as a function of temperature. TSC and EO responses showed similar depolarization behavior. The combination of these experiments can give important information to study the depolarization dynamics of photorefractive polymers.

REFERENCES

- 1 K. Meerholz, B. L. Volodin, Sandalphon, B. Kippelen and N. Peyghambarian, *Nature* **371**, 497, (1994).
- 2 C. Poga, D. M. Burland, T. Hanemann, Y. Jia, C. R. Moylan, J. J. Stankus, R. J. Twieg and W. E. Moerner, *Proc. SPIE* **2526**, 82, (1995).
- 3 Y. Zhang, T. Wada, T. Aoyama, L. Wang and H. Sasabe, *Mol. Cryst. Liq. Cryst.*, **295**, 51, (1997).
- 4 C. C. Teng and H. T. Man, *Appl. Phys. Lett.* **56**, 1734, (1990).
- 5 J. S. Schildkraut, *Appl. Opt.* **29**, 2839, (1990).

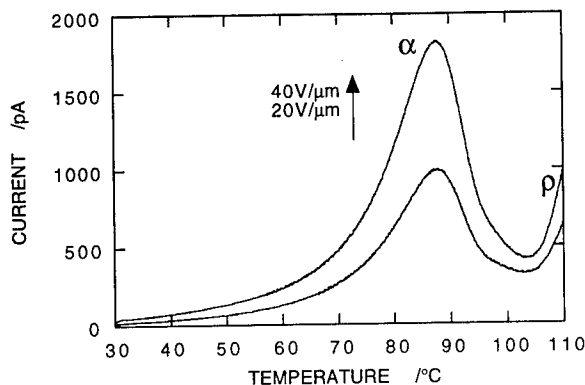


Figure 2. TSC current of the photorefractive polymer at a heating rate $3^\circ\text{C}/\text{min}$.

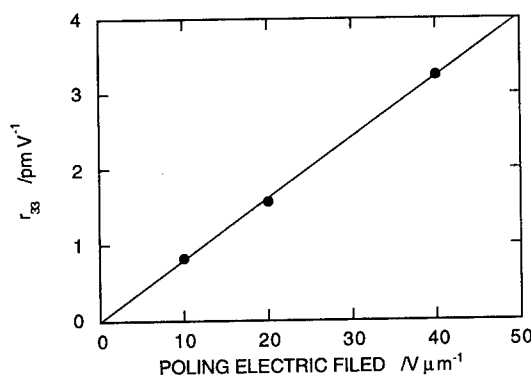


Figure 3. Poling electric field dependence of EO coefficients at a wavelength of 532nm.

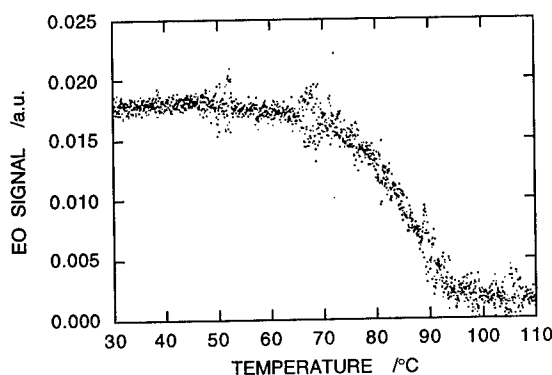


Figure 4. EO signal of the photorefractive polymer poled with a field strength of $40\text{V}/\mu\text{m}$ at a wavelength of 633nm as a function of temperature.

Organic Optics & Optoelectronics

Friday, 24 July 1998

FA: Organic Nonlinear Optics

FB: Polymeric High Speed Modulators II

FC: EO Polymers

FD: Polymeric Waveguide Devices

Friday Papers Not Available

- FA1 Theoretical Design of Mechanisms for Enhanced Two-Photon Absorption in Organic Chromophores, Jean Luc Bredas, Universite de Mons – Hainaut, Mons, Belgium
- FA2 Access to New X3 Materials, K. A. Ostoja Starzewski, Katholieke Universiteit, Leuven, Belgium
- FA3 High Electric Field Poling of Polymers, Manfred Eich, University of Hamburg-Harburg, Hamburg, Germany
- FB1 Design and Fabrication of low v_p Polymer Modulators, Sang-Shin Lee, University of California, Los Angeles, CA
- FB2 Applications of Polymer Modulators to Commercial Systems, Y. Shi, TACAN Corporation, Carlsbad, CA
- FB3 New Directions in Polymer Modulators for Interconnectors, R. Chen, University of Texas, Austin, TX

Polymeric EO modulators based on chiral structures

M. Kauranen, A. Persoons, D. Beljonne*, Z. Shuai*, and J. L. Brédas*

*Research Center on Molecular Electronics and Photonics, University of Leuven
and University of Mons*, B-3001 Heverlee, Belgium, Tel.: +32-16-327508, Fax:
+32-16-327982*

Second-order nonlinear processes are electric-dipole-forbidden in centrosymmetric materials. For organic materials, noncentrosymmetry is relatively easy to achieve on the molecular level. However, for macroscopic noncentrosymmetry, such materials need to be poled. This results in a thermodynamically unstable material whose nonlinearity tends to relax with time. Isotropic materials are usually also neglected as second-order materials. However, isotropic chiral materials are noncentrosymmetric and possess a nonvanishing second-order response, as shown by sum-frequency generation.^{1,2}

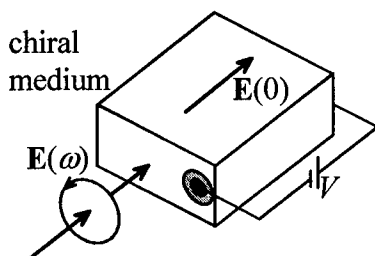


Figure 1. Geometry for the electro-optic effect in chiral isotropic media.

We show that isotropic chiral materials possess also an electro-optic response. In isotropic media, the second-order polarization^{1,2} leading to the electro-optic effect is

$$\mathbf{P}(\omega) = \chi(\omega, \omega, 0) \mathbf{E}(\omega) \times \mathbf{E}(0) . \quad (1)$$

The effective susceptibility is

$$\chi = \frac{N}{6} (\beta_{123} + \beta_{231} + \beta_{312} - \beta_{132} - \beta_{321} - \beta_{213}) , \quad (2)$$

where the subscripts refer to the molecular frame and N is the number density. The relevant components of the hyperpolarizability tensor β vanish for achiral molecules. In addition, the susceptibility reverses sign between the left- and right-hand enantiomers (mirror-image forms) of a chiral molecule and vanishes for their racemic (50/50) mixture.

In linear optics, chiral media have circular eigenpolarizations. Eq. (1) implies that for a transverse nonlinear source, the longitudinal configuration (Fig. 1) must be used. The left- (+) and right- (-) hand circular eigenpolarizations are maintained and the nonlinear source is

$$P_{\pm}(\omega) = \pm i \chi E(0) E_{\pm}(\omega) . \quad (3)$$

The response reverses sign when any of the following quantities is reversed: 1) the static field, 2) the circular polarization, 3) the enantiomer of the molecule.

The imaginary unit as an overall factor in Eq. (3) implies that, contrary to traditional electro-optic materials, phase (absorption) modulation in chiral media is due to the imaginary (real) part of the susceptibility. Hence, there is no fundamental connection between the real part of the susceptibility and phase modulation in second-order nonlinear optics.

When material damping is neglected, the hyperpolarizability β possesses full permutation symmetry and the electro-optic susceptibility χ vanishes.³ On the other hand, damping makes χ nonvanishing. A density-matrix-based expression for χ contains terms that are always nonvanishing in the presence of damping and terms that are nonvanishing only in the presence of dephasing. These dephasing-induced terms are similar to those known in third order⁴ and they vanish in a purely lifetime-broadened material. In addition, these terms contain resonances between two unpopulated intermediate excited states (Fig. 2). Our results also suggest that such resonances could lead to gain for the optical field.

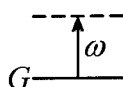
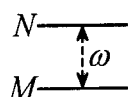


Figure 2. A dephasing-induced resonance.

Under a wide range of conditions, the susceptibility is of the form

$$\chi = iS\chi_0, \quad (4)$$

where χ_0 is the second-order susceptibility for a process that does not rely on damping (e.g., sum-frequency generation^{1,2}). The scaling constant S is essentially the ratio between the damping rate and the frequency (or detuning) that characterize the interaction. For completely nonresonant interactions, χ is imaginary and, similar to traditional electro-optic materials, only phase modulation is possible. For dephasing-induced resonances, the scaling constant is imaginary and of the order unity. We estimate that the nonresonant susceptibility of recently developed chiral media with strong optical activity could be comparable to that of KDP (10^{-9} esu). An estimate of the same magnitude is obtained for more traditional chiral media and dephasing-induced resonances. These estimates have also been confirmed by quantum-chemical calculations for a model helicene molecule.⁵

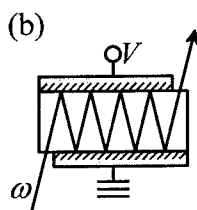
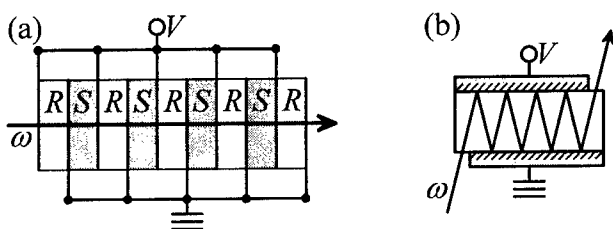


Figure 3. Thin-film configurations that can reduce the required voltage. *R* and *S* are the enantiomers of the material.

The electro-optic effect is longitudinal with net response proportional to applied voltage. However, the device configurations based on thin polymer films (Fig. 3) can reduce the required voltage. In Fig. 3(a), both the enantiomer and the direction of electric field are reversed in successive segments. In Fig. 3(b), each

reflection reverses the circular polarization and the direction of electric field (with respect to direction of propagation). In both cases, the net effect builds up across the whole device.

1. J. A. Giordmaine, *Phys. Rev.* **138**, A1599 (1965).
2. P. M. Rentzepis, J. A. Giordmaine, and K. W. Wecht, *Phys. Rev. Lett.* **16**, 792 (1966).
3. H. F. Hameka, *Chem. Phys. Lett.* **7**, 157 (1970).
4. N. Bloembergen, H. Lotem, and R. T. Lynch, Jr., *Indian J. Pure Appl. Phys.* **16**, 151 (1978).
5. D. Beljonne, Z. Shuai, J. L. Brédas, M. Kauranen, T. Verbiest, and A. Persoons, *J. Chem. Phys.* **108**, 1301 (1998).

Improved coupling efficiency using Δn -controlled polymer waveguides with two-dimensional spot-size transformation

Ryoji Inaba, Miwa Kato, and Haruo Akahoshi
Hitachi Research Laboratory, Hitachi, Ltd.

7-1-1, Omika-cho, Hitachi, Ibaraki 319-1292, Japan

Tel: 81-294-52-7528 Fax: 81-294-52-7634 e-mail: inaba@hrl.hitachi.co.jp

I. Introduction

Two-dimensional spot-size transformation in waveguides is essential in order to realize high coupling efficiency in a connection of guided-wave components of different spot-sizes without using lens elements which make optical devices complicated and expensive. Whereas lateral tapering of the spot-size can be readily achieved by tapering the width of the waveguide mask, tapering of the vertical dimension is more difficult to realize. Various methods for two-dimensional spot-size transformation have been proposed so far, but their fabrication processes are not straightforward or they have other drawbacks. One of the approaches to achieve tapered horn structures in a quartz waveguide is to diffuse dopants in the waveguide thermally by postbaking it in an optimum temperature gradient [1]. It is difficult, however, to find the suitable temperature gradient which transforms the spot-size as desired.

In this work, a new type of polymer waveguide for two-dimensional spot-size transformation is described. For this waveguide, while the core cross section in the waveguide is uniform, the Δn is properly controlled along the direction of propagation such that the penetration of guided light beyond the core-cladding interface is controlled and spot-size is expanded two dimensionally at one end of the waveguide. In order to fabricate such a Δn -controlled waveguide, a waveguide-writing method [2] using an electron beam for fluorinated polyimide is utilized. The merit of this approach is that the spot-size is easily transformed as designed and it is controlled in the restricted small area in a lightwave circuit. This results from the fact that the extent of the refractive index increase in a fluorinated polyimide induced by electron beam irradiation depends on the dose of the electron beam. Therefore, we can easily obtain Δn -controlled waveguides by controlling the electron dose along the direction of propagation.

We fabricate a Δn -controlled waveguide which expands the spot-size as much as twice, and we confirm there is improved coupling efficiency in a connection of two guided-wave components which have different spot-sizes by using the Δn -controlled waveguide.

II. Experimental

A solution of polyamic acid, which was a precursor of the fluorinated polyimide, was spin-coated on a silicon wafer, and baked at 350 °C to convert the polyamic acid into polyimide. A scanning electron microscope was used as an electron beam source. The direction of the electron beam was fixed, and a computer-controlled translation stage on which the polyimide film was placed was moved such that lines were written by the electron beam and the irradiated part was converted to the waveguide core. Refractive index of the core was controlled along the waveguide axis by holding the electron beam current constant and tuning the driving speed of the stage properly. The diameter and energy of the electron beam were tuned properly so that depth and width of the core obtained were both 4 μm . After the electron beam exposure, the precursor polyamic acid solution was spin-coated on the first polyimide layer and baked in the same way as for the first layer to form the second polyimide layer.

III. Results and Discussions

Fig. 1 plots observed spot-size for Δn -constant waveguides with 4- μm core diameter against the dose of the electron beam irradiated when making the waveguides. As the dose increases, the guiding beam is more tightly confined and the spot size becomes smaller. When the electron dose is larger than 8.3 mC/cm^2 , the guiding beam results in multi-mode propagation. The spot-size of an optical fiber with

8- μm core diameter is also shown as the chain line. Fig. 1 provides the guideline when designing electron dose distribution along the direction of propagation in fabrication of spot-size transforming waveguides. Fig. 1 implies, for example, that the spot-size is expanded from 2.7 μm to $\approx 5 \mu\text{m}$ by tuning the irradiated electron dose from 6.25 mC/cm^2 to 1.0 mC/cm^2 along the direction of propagation.

The Δn -controlled, spot-size transforming waveguides were fabricated where the core diameter was $\approx 4 \mu\text{m}$ and the spot-size at $\lambda = 1.3 \mu\text{m}$ was expanded from 2.7 μm to approximately 5 μm . Lengths of Δn -controlled area along the direction of propagation were varied from 1 to 4 mm. Based on the results described in Fig. 1, electron dose of 6.25 mC/cm^2 was irradiated at the input end of each waveguide in order to adjust the spot size to 2.7 μm while the electron dose of 1.0 mC/cm^2 was irradiated at the output end in order to adjust the spot size to $\approx 5 \mu\text{m}$. A high- Δn waveguide was also made where the spot size was 2.7 μm and kept uniform along the direction of propagation. The length of each waveguide is 5 mm. The spot-sizes of the waveguides are listed in Table I. We confirm that the spot-size is expanded two-dimensionally through the Δn -controlled waveguides.

In a Δn -controlled area, the electron dose was designed to decrease along the direction of propagation in proportional to the square root of the waveguide coordinate as:

$$\text{Electron dose} = 6.25 \text{ mC}/\text{cm}^2 - (6.25 \text{ mC}/\text{cm}^2 - 1.0 \text{ mC}/\text{cm}^2) \times (X/L)^\omega \quad (\omega = 0.5)$$

where L is a length of the Δn -controlled area and X is a coordinate along the direction of propagation in the Δn -controlled area. It was confirmed in simulations based on the beam propagation method (BPM) that radiation loss accompanied by spot-size transformation was minimized by adjusting ω between 0.25 and 0.75. If $\omega = 0.5$, the radiation loss accompanied by spot-size transformation was calculated to be 0.08 dB, 0.06 dB, and 0.06 dB for $L = 0.5, 1$, and 4 mm, respectively.

Table I also lists the throughput loss in connections of the waveguides and an optical fiber with 8- μm core diameter. The loss is 3.7 dB for high- Δn waveguide, and is about 2.1 dB for the Δn -controlled waveguides. The efficiency is improved by ≈ 1.6 dB by using the Δn -controlled waveguides. Estimated loss arising from spot-size mismatch is also listed in Table I. Most of the throughput loss for Δn -controlled waveguides is due to reflection loss at the facets and propagation loss in the waveguides. The loss for the Δn -controlled waveguides is independent of length of the Δn -controlled area as is indicated by the BPM calculation.

Throughput loss was also measured for connections of a laser diode and an optical fiber with or without insertion of the Δn -controlled waveguides between them. The loss is 11.5 dB in the direct connection of the laser diode and the optical fiber, and is 7.0-7.4 dB in connections with Δn -controlled waveguides. It is confirmed that insertion of Δn -controlled waveguides reduces the coupling loss by ≈ 4.5 dB.

Table I.

Waveguide	spot-size / μm		Throughput loss / dB	spot-size mismatch loss / dB
	lateral	vertical		
high- Δn	2.77	2.62	3.67	≈ 1.6
Δn -controlled	5.37	5.45	2.08	≈ 0

REFERENCES

- [1] M. Yanagisawa, et al. *IEEE Photon. Technol. Lett.*, vol. 4, pp. 433-435, 1993.
- [2] Y. Y. Maruo, et al. *Appl. Opt.*, vol. 34, pp. 1047-1052, 1995

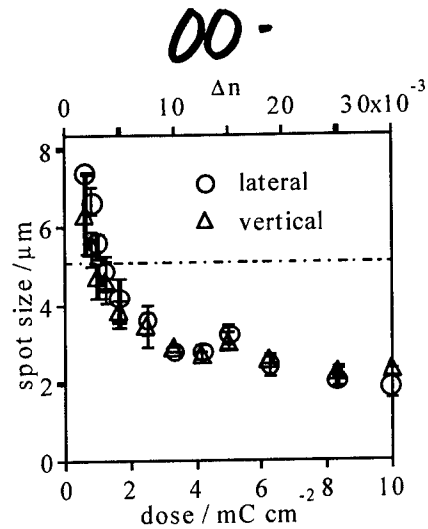


Fig.1 spot-size vs. dose

Three Dimensional Integration of Polymer Electro-Optic Modulators

Sean M. Garner, Vadim Chuyanov, Sang-Shin Lee, Araz Yacoubian, Antao Chen, and
William H. Steier

Department of Electrical Engineering - Electrophysics
University of Southern California, Los Angeles, CA 90089-0483

Fang Wang, Albert S. Ren, Mingqian He, and Larry R. Dalton

Department of Chemistry
University of Southern California, Los Angeles, CA 90089-1062

Present and future integrated switching networks require the ability to fabricate high density optical waveguide structures. Large scale 1x128 fan-outs^[1] have demonstrated this fabrication ability. These structures equally distribute power from a single input fiber to 128 output waveguides. This, however, creates routing difficulties when trying to interconnect non-adjacent waveguides due to the crossover-losses that occur. Also, this requires considerable substrate area to insure no coupling between adjacent waveguides. The required area increases further when considering the Y-branches used in typical integrated Mach-Zehnder modulators. A need exists for low loss, high density active integrated optical circuits.

Three dimensional integrated optics solves this problem. It offers discrete levels of active and passive integrated optic elements interconnected by appropriate vertical waveguide junctions. Figure 1 compares standard 2-D and 3-D integrated optics. Vertical separation of about 10 μ m and separate driving electrodes insure both optical and electrical isolation of the distinct vertically integrated layers. This design greatly increases the integration density and reduces the routing difficulty because the extra vertical layers enable routing of waveguides around obstacles. By vertically integrating waveguide devices into a 3-D structure, the interconnection density of integrated optics becomes comparable to that of free-space holographic interconnects.^[2]

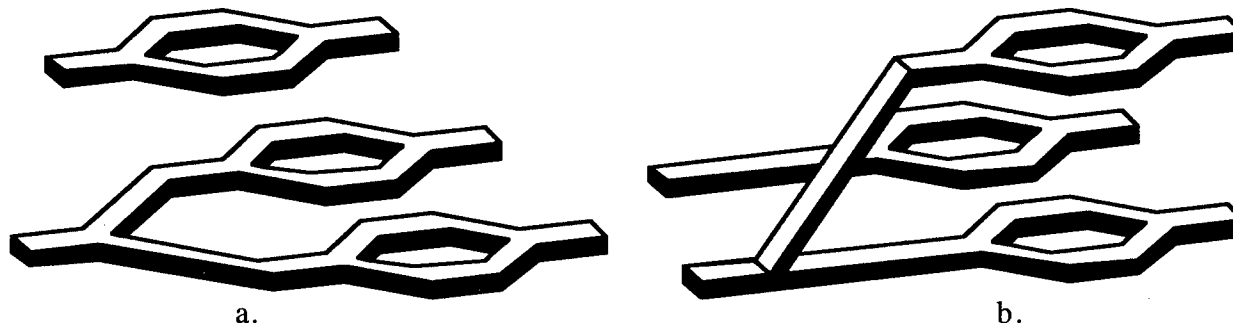


Figure 1: Integrated Optics: a). Two dimensional integration, b). Three dimensional integration

Building active three dimensionally integrated optical structures places strict demands on the material properties including the refractive index control and processing flexibility. Electro-optic polymers meet these demands. First of all, variation of the chromophore loading density precisely tunes the refractive index. Second, they offer excellent adhesion to virtually any substrate. Finally, fabrication procedures of shadow reactive ion etching^[3], offset lithography^[4], and gray scale lithography^[5] enable constructing polymers into true three dimensional architectures. We will show how these qualities of electro-optic polymers make them ideal for three dimensionally integrated active structures.

Preliminary demonstrations hint at the vast potential of 3-D integrated electro-optic polymer devices. Initial attempts of vertically integrating polymer devices have included demonstrations of multi-level Mach-Zehnder modulators^[6] and vertical directional coupler switches^[7]. These active elements allow signal modulation on multiple vertical layers. Recently we have demonstrated vertical power splitters^[8] and vertical polarization splitters^[4]. These necessary passive elements allow low-loss interconnections between isolated optical layers and demonstrate the design complexity achievable with optical polymers. Figure 2 shows the high integration density obtained

from a 3-D 1x4 splitter. We will present the first attempts at integrating both of these active and passive elements to create a fully functional three dimensionally integrated optical structure.

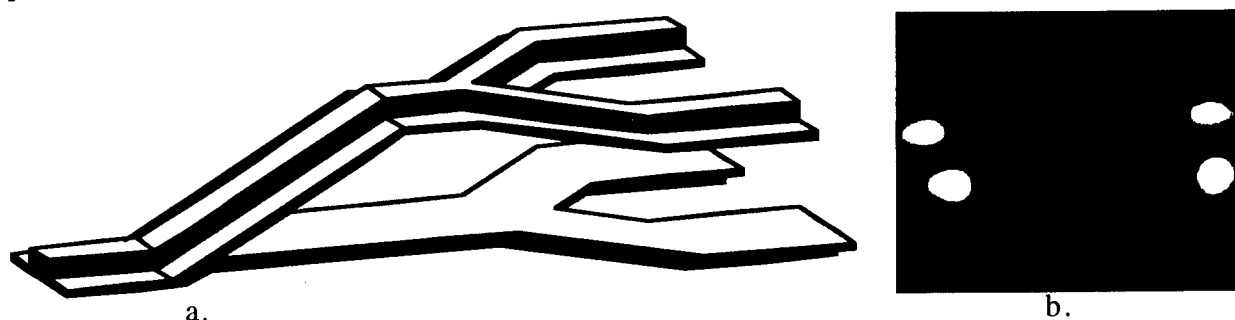


Figure 2: Three dimensional 1x4 splitter: a). Waveguide structure b). Optical output pattern

The proposed structure (Figure 3) consists of a vertical power splitter that divides the fiber coupled optical input among the vertical layers. Modulators on each layer share a common intermediate ground plane which provides electrical isolation. We will present preliminary beam propagation simulation, fabrication, and experimental results including the required drive voltages, crosstalk, and insertion losses of the individual modulators.

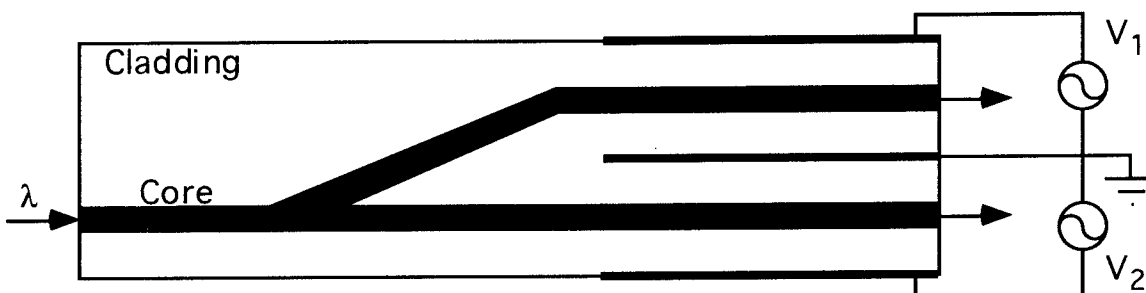


Figure 3: Cross section of vertically integrated active devices

With the ability to support both active modulators on multiple vertical layers and low-loss passive vertical waveguide interconnects, electro-optic polymers enable practical three dimensional integrated optics. Vertically integrated active elements create a high density of functional optical interconnects, and passive vertical structures allow the flexibility to create novel three dimensional architectures. By incorporating both active and passive elements, these fully functional integrated structures provide the routing capabilities previously found only in holographic interconnects.

References:

- [1] H. Takahashi, K. Okamoto, and Y. Ohmori, *IEEE Photon. Technol. Lett.*, vol. 5, pp.58-60, 1993.
- [2] L.J. Camp, R. Sharma, and M.R. Feldman, *Appl. Opt.*, vol. 33, pp. 6168-6180, 1994.
- [3] A. Chen, F.I. Marti-Carrera, S. Garner, V. Chuyanov, and W.H. Steier, in *Organic Thin Films for Photonic Applications*, vol. 14, OSA Technical Digest Series (Optical Society of America, Washington DC, 1997), pp. 152-154.
- [4] S. Garner, V. Chuyanov, A. Chen, S.S. Lee, W.H. Steier, and L.R. Dalton, in *Integrated Optic Devices II*, Giancarlo C. Righini, S. Iraj Najafi, Bahram Jalali, Editors, Proceedings of SPIE, vol.3278, pp. 259-267 (1998).
- [5] T.J. Suleski and D.C. O'Shea, *Appl. Opt.*, vol. 34, pp. 7507-7517, 1995.
- [6] T.A. Tumolillo, Jr. and P.R. Ashley, *Appl. Phys. Lett.*, vol. 62, pp. 3068-3070, 1993.
- [7] M. Hikita, Y. Shuto, M. Amano, R. Yoshimura, S. Tomaru, and H. Kozawaguchi, *Appl. Phys. Lett.*, vol. 63, pp. 1161-1163, 1993.
- [8] S. Garner, V. Chuyanov, S.S. Lee, A. Chen, A. Yacoubian, W.H. Steier, and L.R. Dalton, *IEEE LEOS Annual Meeting Proc.*, vol. 1, pp. 264-265, 1997.

High-frequency demodulation of multiphoton fluorescence for hyper-Rayleigh scattering in solution

Geert Olbrechts, Tom Munters, Koen Clays, and André Persoons,
Laboratory of Chemical and Biological Dynamics, Center for Research in Molecular
Electronics and Photonics, Department of Chemistry, University of Leuven,
Celestijnenlaan 200D, B-3001 Leuven, Belgium
tel.: 321-6327171, fax: 321-6327982
e-mail: geerto@lcbsdiris.fys.kuleuven.ac.be

SUMMARY:

Incoherent second-order nonlinear optical scattering, also known as hyper-Rayleigh scattering (HRS)[1, 2], has become widely accepted as an experimental technique for the determination of the molecular second-order nonlinear optical polarizability (first hyperpolarizability) β . HRS has provided a wealth of information on the tensor properties of the hyperpolarizability of molecules of all types of symmetry. It has proven indispensable for the experimental verification of the octopolar paradigm in second-order nonlinear optics.[3] In this field of molecular characterization by incoherent second-order nonlinear light scattering, the multiphoton fluorescence contribution to the hyper-Rayleigh scattering signal has become recognized as an experimental problem.[4] A number of very large hyperpolarizabilities have been suspected to be caused by fluorescence contribution to the incoherently scattered second-harmonic intensity. A very elegant solution to this problem had been proposed based on the temporal difference between the immediate scattering and the time-delayed fluorescence.[5] Only the photons detected in an early and narrow time window are regarded as due to scattering. We now demonstrate a novel technique in the frequency-domain for the suppression of the multiphoton fluorescence contribution in hyper-Rayleigh scattering experiments.[6] The technique takes advantages of the demodulation and the phase-shift in the frequency-domain of the time-delayed (multi-photon) fluorescence in the time-domain. For this technique, we use the improved temporal resolution offered by the femtosecond pulse versus the nanosecond pulse. We demonstrate the effectiveness of the demodulation of the fluorescence at high modulation frequencies of the fundamental laser beam by determining the molecular second-order nonlinear polarizability for a reference molecule under fluorescent conditions. The value that was obtained for the β of crystal-violet in

methanol with 9,10-diphenylanthracene added as a centrosymmetric fluorophore ($338 \pm 80 \times 10^{-30}$ esu), compares very well with the values that were previously obtained.[2] The frequency-dependence of the retrieved value shows both the overestimation at DC and low modulation frequencies and the convergence towards the fluorescence-free value at high modulation frequencies.

A number of well-known donor-acceptor molecules, *e.g.*, *para*-nitroaniline, 4-methoxy-4'-nitrostilbene and 4-dimethylamino-4'-nitrostilbene, have been revisited. Depending on the chromophore, the solvent, and the wavelength, the presence or absence of fluorescence contributions to the first hyperpolarizability value could be indiscernible demonstrated.

The suppression of multiphoton fluorescence, induced by inclusion in a host to enhance the nonlinear optical properties, has also been demonstrated. The scaling of the hyperpolarizability with the number of chromophores in mono-, bi- and terchromophoric model compounds has been derived only after multiphoton fluorescence suppression in the highly symmetric terchromophoric compound.

The possibility of complete suppression of all fluorescence, based on phase-sensitive measurement in quadrature with the fluorescence, is also proposed.

By adding the high-frequency demodulation for suppression of the multiphoton fluorescence contribution in hyper-Rayleigh scattering, we have further improved this experimentally simple, yet widely applicable technique, to be capable of measuring the first hyperpolarizability of fluorescent molecules also. Therefore, femtosecond incoherent second-order nonlinear scattering has become an invaluable tool for the experimental verification of the engineering guidelines in molecular second-order nonlinear optics.

References:

- [1] K. Clays and A. Persoons, Phys. Rev. Lett. 66 (1991) 2980.
- [2] K. Clays and A. Persoons, Rev. Sci. Instrum. 65 (1994) 2190.
- [3] T. Verbiest, K. Clays, C. Samyn, J. Wolff, D. Reinhoudt and A. Persoons, J. Am. Chem. Soc. 116 (1994) 9320.
- [4] M.C. Flipse, R. de Jonge, R.H. Woudenberg, A.W. Marsman, C.A. van Walree and L.W. Jenneskens, Chem. Phys. Lett. 245 (1995) 297.
- [5] O.F.J. Noordman and N.F. van Hulst, Chem. Phys. Lett. 253 (1996) 145.
- [6] G. Olbrechts, R. Strobbe, K. Clays and A. Persoons, Rev. Sci. Instrum., accepted for publication (1998).

Polymeric Optical Waveguides

Saburo Imamura

NTT Opto-electronics Laboratories, Tokai, Ibaraki, 319-1193 Japan

1. Polymeric waveguide characteristics

Polymer materials offer a number of interesting features for the fabrication of optical waveguides when compared with other materials such as silica glass. Silica glass has a low optical loss of below 0.01 dB/cm as well as high thermal stability. Organic polymers, by contrast, have attracted a lot of attention due to their ease of fabrication and structural flexibility. These are important factors with regard to their use as packaging and optical interconnects. In addition, the thermo-optic (TO) coefficient of polymers is an order of magnitude larger than that of silica glass and some non-aromatic polymers have very low birefringence. These are desirable characteristics in terms of their application to such optical integrated devices as TO switches. Polymeric waveguide applications are therefore divided into two categories. The first comprises optical packaging and interconnects and the second, optical integrated devices. Nevertheless, polymeric materials have certain disadvantages. An optical waveguide must retain its optical and physical properties under a variety of environmental conditions including high temperature and high humidity. However, polymer materials do not have sufficient reliability and thermal stability except for polyimide and the like. To solve these problems, we have worked to develop new materials, processes and packaging.

2. Polymer materials

In order to realize buried polymeric waveguides, we developed three polymer materials, deuterated polyfluoromethacrylate (PFMA)¹⁾, UV cured epoxy resin²⁾ and deuterated polysiloxane³⁾. PFMA has very low loss at shorter wavelengths to 1.3 μm and very low birefringence. UV cured resin and deuterated polysiloxane have high thermal stability. We used UV cured epoxy resin as the core material for multimode waveguides at shorter wavelengths. The UV cured epoxy resins also have some other merits. (1) Their refractive indices can be easily controlled in the 1.48 - 1.60 region with a 0.001 order of accuracy by mixing several resins together. (2) They have high thermal stability because they have a high glass transition temperature of over 200 °C. (3) They are photocurable. Patterning and replication for device fabrication can be carried out with a simple process. We used deuterated polysiloxane as the core material for single-mode waveguides at longer wavelengths. The deuteration of substituents and polysiloxane backbones gave this polymer low loss at 1.55 μm and good environmental stability. The propagation loss was below 0.5 dB/cm. The refractive index of the polymer film changed less than 0.1% after being stored for over 1000 hrs at 120 °C. We examined the environmental stability of the waveguides at 90% RH and 75 °C and observed no change in the insertion loss over 1000 hrs. This indicates that polysiloxane waveguides offer long term stability in humid conditions.

The polymers have certain characteristics and advantages which make them suitable for optical device applications.

3. Polymeric waveguides for optical telecommunication devices

We have successfully fabricated polymeric waveguide films for optical interconnects and packaging, and a TO switch for the wavelength division multiplexing (WDM) optical network by using polymers we have developed.

Polymer waveguide film for optical interconnection and optical packaging⁷⁷

We focused on inter-module level optical interconnections for which waveguides need a low propagation loss and high flexibility and fabricated flexible single-mode and multimode polymer waveguide films.

We used UV cured resin for the cladding of the multimode waveguides to achieve good flexibility and mechanical strength. The relative index difference between the core and cladding was set at 1.0 % to reduce the bending loss. Moreover, we fabricated flexible polymer waveguide films with MT-compatible plugs for practical use. We also applied the polymer waveguide film to parallel optical interconnection. We used waveguide film with a 45 degree mirror as a 90 degree out-of-plane optical deflector. This is required in order to facilitate optical connection between an optical waveguide and a surface emitting laser (or a surface sensitive photodiode) or between optical layers on a board and a backplane.

Thermo-optic (TO) switch and arrayed waveguide grating (AWG) multiplexers in WDM optical network

Space division photonic switches based on the TO effect are becoming increasingly important in optical path cross-connections and for protection switching. This is because they theoretically offer the advantages of a high extinction ratio, large operating tolerance, polarization independent operation and low switching power. We used thermosetting deuterated polysiloxane with a large TO coefficient, high thermal stability, a low optical loss at 1.55 μm and low birefringence⁵⁾. With an applied power of 130 mW, the transmission port insertion loss was lower than 2.5 dB and the extinction ratio exceeded 30 dB. The switching time was 6 ms. Proper operation was demonstrated even at 80 $^{\circ}\text{C}$. We fabricated arrayed waveguide grating (AWG) multiplexers using PFMA⁶⁾. The spectra near the peak wavelength are almost identical for both polarizations, which indicates that this multiplexer can achieve polarization insensitive operation without any birefringence compensation due to PFMA's very low birefringence. We also fabricated AWG multiplexers using deuterated polysiloxane⁷⁾. They operated with a 0.8 nm spacing around 1.55 μm and an insertion loss in the 9-13 dB range, a crosstalk of <-20dB, and a polarization-dependent wavelength shift of 0.35 nm. The transmission peak wavelength was tunable over 10 nm with a temperature change of 55 $^{\circ}\text{C}$.

References

- 1) R. Yoshimura et al., Electron. Lett., 1997, 30(12), pp. 959-960.
- 2) S. Tomaru et al., Technical Digest of Organic Thin Films for Photonic Application, 1997, pp. 220-223.
- 3) M. Usui et al., IEEE J. Lightwave Technol., 1996, 14, pp. 2338.
- 4) M. Hikita et al., Proc. of ECOC'97, 1997, pp. 285-289.
- 5) T. Watanabe et al., Jpn. J. Appl. Phys., 1997, 36, Pt. 2, No. 12B, L1674.
- 6) Y. Hida et al., Electron. Lett., 1994, 30(12), pp. 959-960.
- 7) T. Watanabe et al., Electron. Lett., 1998, 33(18), pp. 1517-1518.

Acknowledgments : The author thanks his many colleagues at NTT Laboratories who have contributed useful discussions on polymeric waveguide devices. He also thanks Drs. H. Kozawaguchi, H. Hiratsuka, K. Sugii and T. Izawa for their encouragement.

All-optical parallel processing by photoinduced complex refractive index changes in guided wave geometry containing organic dye

Toshihiko Nagamura

Crystalline Films Laboratory, Research Institute of Electronics, Department of Electronic Materials Science, Graduate School of Electronic Science and Technology, Shizuoka University, 3-5-1 Johoku, Hamamatsu 432-8011, Japan

All optical data processing has recently attracted much interest especially in the fields of spatial light modulation and optical data storage. Several optically addressed spatial light modulators (SLM) have been proposed. There are limits in time responses and spatial resolution in practical SLMs based on liquid crystal and photoconductive materials.

In order to construct molecular photonics system we have been studying ultrafast, picosecond (ps) - femtosecond (fs), colour changes and highly sensitive detection of steady and transient absorption changes by the optical waveguide method. We recently proposed and demonstrated a novel all-optical light modulation and optical switching by the use of reversible changes of a complex refractive index upon photoexcitation in a guided mode geometry composed of silver and polymer thin films containing organic dyes as schematically shown in Fig. 1.¹⁻³

In addition to the surface plasmon resonance, we can observe very sharp dips depending on the thickness of a polymer film in an incident angle dependence of reflectance as shown in Fig. 1. An incident angle of a probe beam was set at a value corresponding to the minimum reflection due to the guided wave mode. Pulsed laser excitation causes changes of absorption spectrum of the polymer films due to the excited state formation, photochromism, and other photoreaction. The increase of the imaginary part results in the increase of reflection from a, to b or c in Fig. 1. According to the Kramers-Kronig relationship the real part also changes, which results in the shift of the minimum. So we can select appropriate wavelength

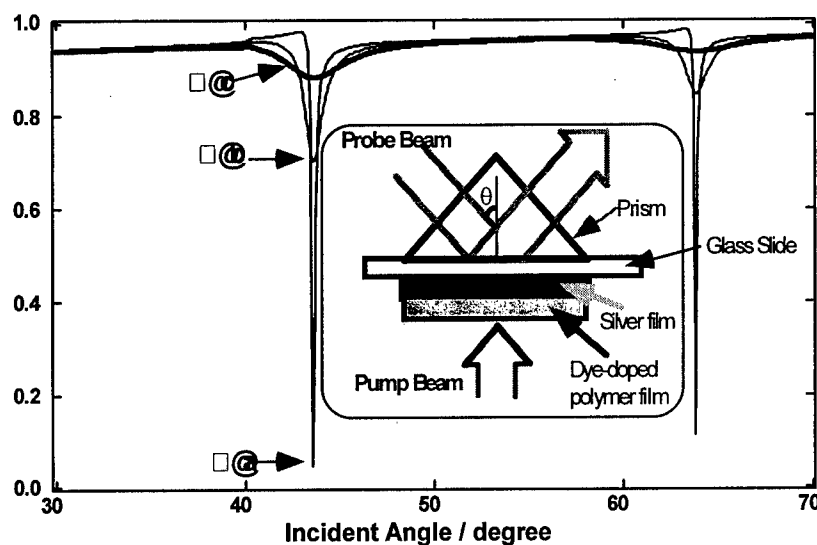


Fig. 1 Schematic representation of novel all-optical parallel processing in guided wave geometry.

for all-optical light modulation or self-holding optical switch in this geometry. The response time and spatial resolution of this system are expected to be much

superior than practically used SLMs based on liquid crystals, since it depends on photoexcitation or photoreaction of molecules.

We used water-soluble Cu- or Zn-phthalocyanines (CuPcS, ZnPcS) dispersed in poly(vinylalcohol) for demonstration of such parallel processing. Transient absorption due to the excited triplet state formation was observed for both polymer films in the region from about 400 to 600 nm upon excitation at 355 nm or 670 nm by ns laser. The lifetime depended on the structure of phthalocyanines and the microenvironment. Fig. 2 shows the repeated changes of reflected light intensity at 543 nm observed at the minimum incident angle (ca. 42.6°) for CuPcS/PVA film (738 nm). A fast and highly reversible modulation of green light was demonstrated. The rise time is less than the time resolution of the system (< 20 ns) and the fall time is about 3.5 μ s for CuPcS/PVA film. The fall time was found to be affected by several factors such as the lifetime of the excited triplet state, the thickness of polymer films and the incident angle. No responses were observed at wavelengths where no transient absorption was observed, which clearly excluded the possibility of pure thermal refractive index changes.

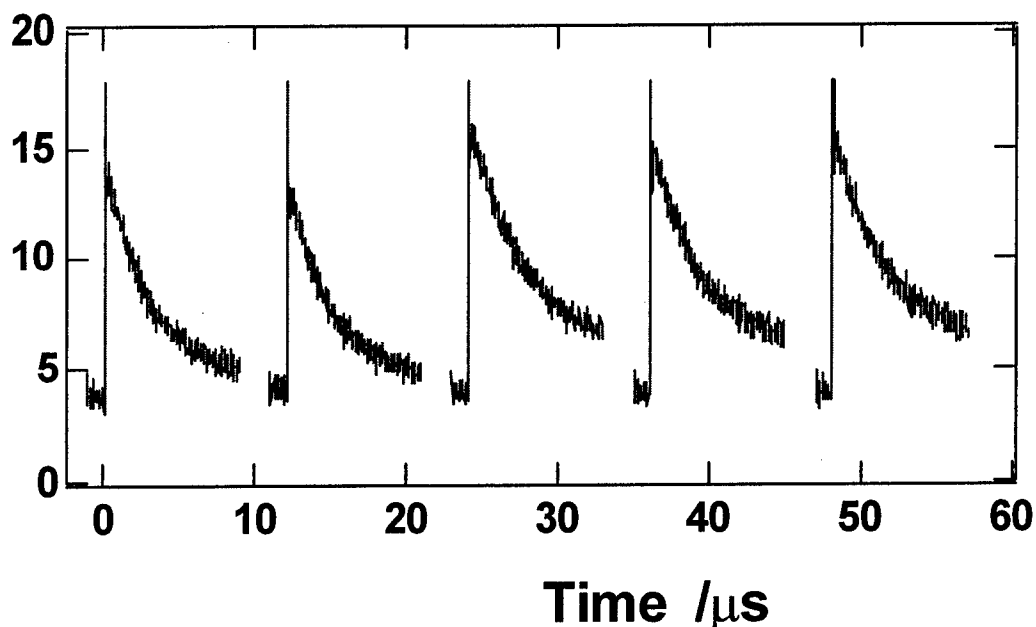


Fig. 2 Changes of reflected light intensity at 543 nm during repeated excitation of CuPcS in PVA film with a ns laser at 670 nm.

By the use of photochromic dyes dispersed in poly(styrene) in a similar guided wave geometry, we have also achieved ultrafast wide range all-optical self-holding switch. We succeeded to write or erase a two dimensional image by the similar device in less than 20 ns which is limited by the ns pulsed laser. Both ON and OFF states were held without applied powers. By appropriately combining these optically addressed reflection-type devices, we can make, in principle, all-optical parallel data processing with the time response of less than picosecond and the spatial resolution of molecules.

References

- 1) T. Nagamura and T. Hamada, *Appl. Phys. Lett.*, 69, 1191 (1996).
- 2) K. Sasaki and T. Nagamura, *Appl. Phys. Lett.*, 71, 434 (1997).
- 3) K. Sasaki and T. Nagamura, *J. Appl. Phys.*, 83, 2894 (1998).

FD3 (Invited)
4:30pm - 5:00pm

Organic Microcrystals for Linear and Nonlinear Optics

Hachiro Nakanishi

Institute for Chemical Reaction Science, Tohoku University,

2-1-1, Katahira, Aoba-ku, Sendai 980-8577, Japan

Tel:81-22-217-5643 Fax:81-22-217-5645 E-mail:hnakanis@icrs.tohoku.ac.jp

SUMMARY

Crystalline materials always provide us the best performance. This is also the case of organic optical materials. Their device fabrication, however, is one of the big issues. Recently we have demonstrated that organic microcrystals can easily be prepared by reprecipitation method from the solution in its nonsolvent(1,2), and the resulting dispersion, not only the liquid dispersion but also the polymer-embedded dispersion, gives materials having optical quality acceptable for device performance evaluation(3,4). In addition, some peculiar size-dependant properties for organic microcrystals compared with semiconductors or metals have also been found(5,6). Much recent progress in our studies will be introduced.

One of the remaining issues of these dispersion was to increase contribution from crystalline portion. To solve the issue, we have studied the so-called layer-by-layer deposition technique(7,8). The sample used was an aqueous dispersion of microcrystals of polydiacetylene, say poly-(1,6-di(N-carbazolyl)-2,4-hexadiyne) (poly-DCHD), which was obtained by solid-state polymerization of the monomer microcrystal dispersion. Since the poly-DCHD microcrystals in water were charged up negatively, a polycation, i.e. poly-(diallyl ammonium chloride) (PDAC) was chosen for electrostatic attachment of the microcrystals onto substrate. Typical experimental procedure was as follows. First, PDAC monolayer was deposited onto the microscope glass slides by simply immersing them into PDAC aqueous solution. These PDAC-deposited glass slides were then immersed into the poly-DCHD microcrystals aqueous dispersion. Thorough rinsing in water was carried out during each process to remove any nonspecific binding, and these processes were, if necessary, repeated several times. After the deposition was completed, the samples were dried and subjected to the characterization of UV-VIS-absorption spectroscopy, SEM observation and so on. It turned out that the layer-by-layer deposition of poly-DCHD microcrystals into a thin film, from almost completely isolated dispersion to very dense

dispersion which was impossible to attain by conventional spin-coating, is possible by this method(9). In extension, any desired patterned and super-latticed structures as well might be at hand for sophisticated optics.

Next, if molecules with fairly large dipole moment crystallize in non-centrosymmetric crystal structure, its microcrystals should have huge dipole moment, far greater than that of chained chromophers (10), and therefore the microcrystals dispersed in non-polar liquid must easily respond orientationally to a very weak electric field. To confirm this idea, we have prepared microcrystals of ionic chromophers such as dimethylamino-, methoxy, and hydroxy-stilbazonium tosylate (DAST, MOST, and HOST, respectively), for which fairly large dipoles and non-centrosymmetric crystal structures had already been confirmed. Among these DAST microcrystals gave considerably stable dispersion in decahydro-naphthalene. And, it was shown that absorption strength of DAST microcrystals, ca. 500nm in size, varies linearly with surprisingly weak DC electric field of upto 200V/cm. Though there are lots to be tackled, the present demonstration may open up a new field of functional materials of a liquid-and-crystals (L&C), in addition to the well-known liquid crystal (LC).

These are the collaborative studies with Prof. S. Tripathy's and Dr. H. Matsuda's groups.

References

- 1) H.Kasai et al., Jpn.J.Appl.Phys.**31**,L1132 (1992)
- 2) H.Katagi et al., *ibid.***35**,L1364 (1996)
- 3) T.Yanagawa et al., Optics Communs**137**,103 (1997)
- 4) H.Matsuda et al., SPIE Proc.**2998**,241(1997)
- 5) H.Katagai et al., J. Macromol. Sci.**A34**,2013 (1997)
- 6) H.Kasai et al., Jpn.J.Appl.Phys.**34**, L221(1996)
- 7) G.Decher,Science**277**,1232 (1997)
- 8) X.Wang et al., Macromol.Rapid Commun.**18**,451(1997)
- 9) S.Tripathy et al., Jpn.J.Appl.Phys.**37**,L343 (1998)
- 10) X.M.Duan et al., Jpn.J.Appl.Phys.**34**, L1161(1995)

AUTHOR INDEX

Adameck, M.	FA3	Katz, H. E.	ThD2	Tsap, B.	WB1
Akahoshi, H.	FC2	Kauranen, M.	FC1	Udupa, A.	WB1,FB1
Aoyama, T.	ThC3	Kippelen, B.	ThB1	Van Beylen, M.	WA3
Bao, Z.	ThD2	Koike, Y.	ThA1,ThC3	Van den Broeck, K.	WA3
Beljonne, D.	FC1	Kowalczyk, T. C.	ThB3	Verbiest, T.	WA3
Bhattachaya, D.	WB1	Lackritz, H. S.	ThB3	Wada, T.	ThC3
Blum, R.	FA3	Lee, S.- S.	WB1,FB1,FC3	Wang, F.	FB1,FC3
Bredas, J. L.	FC1	Lindsay, G. A.	WA1	Wang, J.	ThA2
Cai, Y.	ThA2	Liu, L.Y.	ThB3	White, W. R.	ThA3
Chafin, A. P.	WA1	Lovinger, A. J.	ThD2	Wiltzius, P.	ThA3
Chen, A.	WB1,FC3	Luc Bredas, J.	FA1	Wynne, K. J.	WA1
Chen, D.	WB1	Marder, S.	WA2	Yacoubian, A.	FC3
Chen, J.	WB1	Meerholz, K.	ThC2	Yee, R. Y.	WA1
Chen, R.	FB3	Moritsuki, Y.	ThC3	Yonechi, Y.	ThC3
Chuyanov, V.	FB1,FC3	Munters, T.	FC5	Zarras, P.	WA1
Clays, K.	WA4,FC5	Nagamura, T.	FD2	Zhang, H.	FB1
Curtis, K.	ThC1	Nakanishi, H.	FD3	Zhang, Y.-D.	ThC3
Dalton, L. R.	WB1,	Nihei, E.	ThA1		
	WB3,FB1,FC3	Ohar, I.	ThC1		
Dodabalapour, A.	ThD2	Olbechts, G.	WA4,FC5		
Dueser, M.	ThA3	Ostoj Starzewski, K. A.	FA2		
Eich, M.	FA3	Persoons, A.	FA2		
Elken, T.	FA3		WA3,WA4,FC1,FC5		
Ermer, S.	WB2	Raju, V. R.	ThD2		
Fetterman, H. R.	FB1	Ren, A. S.	FC3		
Fetterman, H.	WB1	Ren, A.	FB1		
Gao, R.	ThA2	Roberts, M. J.	WA1		
Garito, A. F.	ThA2	Rogers, J. A.	ThD2		
Garner, S. M.	FC3	Samyn, C.	WA3		
Garner, S.	FB1	Sasabe, H.	ThC3		
Garnier, F.	ThD1	Sasaki, K.	ThC3		
Hadziannou, G.	ThB2	Sato, M.	ThA1		
He, M.	FC3	Shi, R. F.	ThA2		
Hollins, R. A.	WA1	Shi, Y.	FB2		
Imamura, S.	FD1	Shuai, Z.	FC1		
Inaba, R.	FC2	Steier, W. H.	WB1,FB1,FC3		
Ishigure, T.	ThA1	Stenger-Smith, J. D.	WA1		
Kato, M.	FC2	Tackx, P.	FA2		

IEEE/LEOS
Summer Topical Meeting

22 – 24 July 1998

Smart Pixels

Monterey Plaza Hotel
Monterey, CA

IEEE Catalog Number: 98TH8369
ISBN: 0-7803-4953-9

The papers in this book make up the digest of the 1998 IEEE/LEOS Summer Topical Meetings. They reflect the author's opinions and are published as presented and without change in the interest of timely dissemination. Their inclusion in this publication does not necessarily constitute endorsement by the editors, the Institute of Electrical and Electronics Engineers, Inc.

Copyright and Reprint Permission: Abstracting is permitted with credit to the source. Libraries are permitted to photocopy beyond the limit of U.S. copyright law for private use of patrons those articles in this volume that carry a code at the bottom of the first page, provided per-copy fee indicated in the code is paid through Copyright Clearance Center, 222 Rosewood Drive, Danvers, MA 01923. For other copying, reprint or republication permission, write to IEEE Copyrights Manager, IEEE Operations Center, 445 Hoes Lane, PO Box 1331, Piscataway, NJ 08855-1331.

© 1998 by the Institute of Electrical and Electronics Engineers, Inc. All rights reserved.

IEEE Catalog Number: 98TH8369

ISBN:	0-7803-4953-9	Softbound Edition
	0-7803-4954-9	Microfiche Edition

ISSN: 1099-4742

Library of Congress:

Additional copies can be ordered from:

IEEE Service Center
445 Hoes Lane
P.O. Box 1331
Piscataway, NJ 08855-1331
Tel: (732) 981-1393
Fax: (732) 981-9667

Smart Pixels

General Chair:

Nan Marie Jokerst, *Georgia Institute of Technology, Atlanta, GA*

Program Chair:

Rick McCormick, *Call/Recall, San Diego, CA*

Program Committee:

Joseph Ford, *Lucent Technologies Bell Laboratories, Holmdel, NJ*

Masatoshi Ishikawa, *University of Tokyo, Tokyo, JAPAN*

Kenichi Kasahara, *NEC Corporation, Ibaraki, JAPAN*

Philippe Marchand, *University of California San Diego, La Jolla, CA*

Timothy Pinkston, *University of Southern California, Los Angeles, CA*

David Plant, *McGill University, Montreal, CANADA*

Hugo Thienpont, *Vrije Universiteit Brussel, Brussels, BELGIUM*

Ian Underwood, *University of Edinburgh, Scotland, UK*

TABLE OF CONTENTS

Wednesday, 22 July 1998

Session WA: Devices and Integration Technologies

WA1	VCSEL/MSM Detector Smart Pixel Arrays.....	3
WA2	Fabrication of 12 x 12 Matrix-Addressed 780 nm Oxide-Confined VCSEL Arrays.....	5
WA3	Monolithically Integrated Surface and Substrate Emitting Vertical Cavity Surface Emitting Lasers for Smart Pixels.....	7
WA4	New Materials for 1.3 μ m VCSEL Smart Pixels.....	9
WA5	Novel Technique for Monolithic Integration of Microlensed Resonant Detectors and Vertical Cavity Lasers.....	11
WA6	Feasibility of Tera-bps Smart Pixel Arrays Using Monolithic Emitter-Based Optoelectronic VLSI Circuits.....	13
WA7	Flip-chip Bonded MQW Modulator Operating at ECL Voltage Levels.....	15
WA8	Temperature Dependence of QCSE Device Characteristics and Performance.....	17

Thursday, 23 July 1998

Session ThA: Circuits and Interconnections I

ThA1	Solving the Interconnect Bottleneck Optoelectronic FPGAs	21
ThA2	1 Gb/s Single-Beam Smart-Pixel Receiver/Transmitter Realized in Hybrid MQW-CMOS OE-VLSI Technology	23
ThA3	Automated Design of ICs with Area-Distributed I/O Pads	25
ThA4	3D Stacked Si CMOS VLSI Smart Pixels Using Through-Si Optoelectronic Interconnections	27
ThA5	1 Gb/s CMOS Optical Receiver with Integrated Detector Operating at 850 nm.....	29

Session ThB: Circuits and Interconnections II

ThB1	CMOS Circuits for Switching and Processing.....	N/A
ThB2	Mixed Signal Circuits VLSI Smart Pixels.....	N/A
ThB3	Second-Generation CMOS-SEED Smart Pixel Implementation of the Error Diffusion Neutral Network.....	31
ThB4	Smart Pixel with Four-Level Amplitude or Phase Modulation	33

TABLE OF CONTENTS

Session ThC: Architectures and Applications

ThC1	CMOS DSP and Microprocessor Cores Using Optoelectronic VLSI	N/A
ThC2	A Dynamically Reconfigurable Token-Based Optical Backplane	35
ThC3	CMOS Based Optoelectronic Smart Pixel Array for Accessing Optical Page-Oriented Memories	37
ThC4	The Constraints on Feedforward Neural System Design Using Smart Pixels	39
ThC5	A System Architecture for use with Free Space Optical Interconnects in a 3D Stacked Processor Environment	41

Friday, 24 July 1998

Session FA: Optics and Packaging

FA1	Fiber Optic Packaging of Surface-Normal Device Arrays	45
FA2	Integrated Micro-Optical Systems	N/A
FA3	Multi-channel Optical Coupling Between VCSEL Arrays and Multimode Optical Fibers for a 40-Channel Parallel Optical Interconnection Module	47

Session FB: Systems and Demonstrations I

FB1	Evolution in the Technology and Applications of Smart Pixel Devices	N/A
FB2	Optoelectronic-VLSI Smart Pixels for Data Networking	N/A
FB3	4 x 4 ATM Crossbar using N ⁴ Global FSOI	49
FB4	Networking with Free Space Optical Data Packets Using Carrier-Sense Multiple-Access with Collision Detection (CSMA/CD) Protocol	51

Session FC: Systems and Demonstrations II

FC1	Optoelectronic Computer-Aided Design	53
FC2	Optoelectronic Multichip Modules Using MEMS Fabrication	N/A
FC3	High Speed, Smart Focal Plane Processing Using Integrated Photodetectors and Si CMOS VLSI Sigma Delta Analog to Digital Converters	55
FC4	A High Resolution, High Frame-Rate Spatial Light Modulators	57
FC5	VLSI Development of Smart-Pixel ICs: A Hybrid DSP Core and a Multi-Threaded Programmable DSP	59

Smart Pixels

Wednesday, 22 July 1998

WA: Devices and Integration Technologies

VCSEL/MSM Detector Smart Pixel Arrays

M. K. Hibbs-Brenner, Y. Liu, R. Morgan and J. Lehman
Honeywell Technology Center
3660 Technology Drive
Minneapolis, MN 55418
(612) 951-7719
E-mail: Hibbs-Brenner_Mary@htc.honeywell.com

A smart pixel module consisting of two-dimensional arrays of electronic logic elements, drive and receive electronics, optical sources, optical detectors, and lenses for conditioning the optical beams, provides the building block for 3D optically interconnected systems. In order to justify the development of a new technology such as smart pixels, one needs to provide a capability significantly beyond that projected for chop scale packages, for instance, which implies optical device array sizes of thousands of devices. In addition, the integration of optoelectronic devices and optical components must be done very cost effectively, which implies monolithic or heterogeneous integration techniques.

Honeywell's approach to heterogeneous smart pixel integration is illustrated in Figure 1. This approach allows for the attachment of VCSELs, MSM photodetectors, and refractive or diffractive passive optical elements to a CMOS substrate containing both logic elements and drive/receive circuitry. To date, Honeywell has demonstrated low power VCSELs with good yield, as well as monolithic integration of VCSELs and photodetectors.

Some of the requirements for the optoelectronic devices used in smart pixels include uniformity of output power versus current, since monitoring each device is not possible, high yield and low power dissipation, since array sizes on the order of 1000 are expected, and a data rate which matches the capability of the underlying I.C. technology. In the case of CMOS, state-of-the-art is currently around 1 Gbps, but may be expected to rise to 2.5 Gbps within the next five years.

Figure 2 illustrates the performance and uniformity of a 12 element array of VCSELs fabricated with the oxide aperture approach for current confinement. These devices are consistent with the requirement that they be driven by 3.3V CMOS, and with a 50% duty cycle each will dissipate an average of approximately 2.5mW. Yield and uniformity across a full 3" wafer are illustrated by Figure 3. While not every device on the wafer was tested, based upon the sample taken, a yield of approximately 99.7 is estimated. The eye diagram of a VCSEL driven at a current of 3mA is given in Figure 4, illustrating a wide open eye diagram at 1.25 Gbps.

The next step in heterogeneous integration is to combine VCSELs and photodetectors in a monolithic structure which can subsequently be attached to CMOS electronics. Figure 5 illustrates a 2D integrated array of 32 proton implanted VCSELs and 32 MSM photodetectors fabricated with coplanar contacts.

We wish to acknowledge DARPA and ONR for support of the work reported here, and the excellent technical assistance of R. Walterson, E. Kalweit, S. Bounnak, T. Marta, and B. Koch.

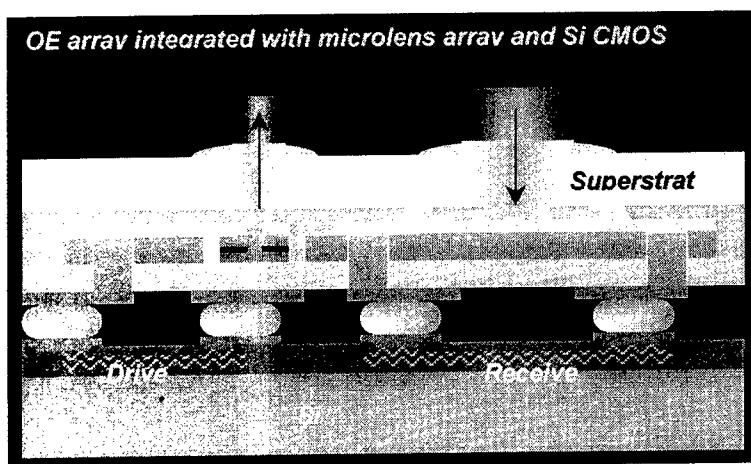


Figure 1: Honeywell's smart pixel module heterogeneous integration approach

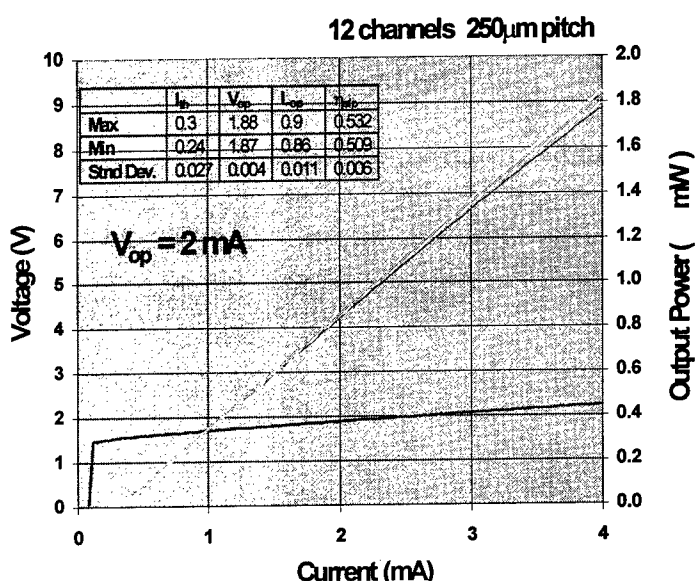
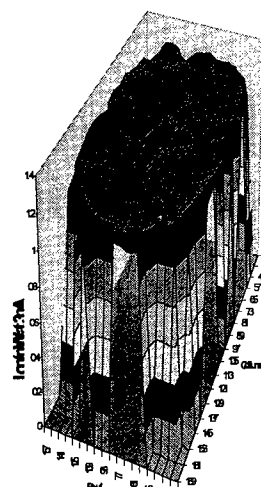


Figure 2: Voltage and output power versus drive current for a 12 element oxide aperture VCSEL array.

Uniformity & Yield of 3"-dia MOVPE-Grown Planar Oxide-Confined VCSEL Wafer



- HTC Wafer Growth/Process
- High Wafer Yield (99.7%est.)
- High Uniformity
- Utilizes In-House Commercially-Available MOVPE Chamber
- Material growth compatible with HI-Micro-Switch VCSEL Production

Figure 3: Uniformity and yield of 3" diameter MOVPE-grown oxide aperture VCSEL wafer

5 μ m-dia VCSEL : $I_{th} = 0.25 \text{ mA}$; $I_{hi} = 3 \text{ mA}$
No system filter: BW of receiver = 1.7 GHz

1.25Gb/s NRZ Eye for $I_b = I_{th}$

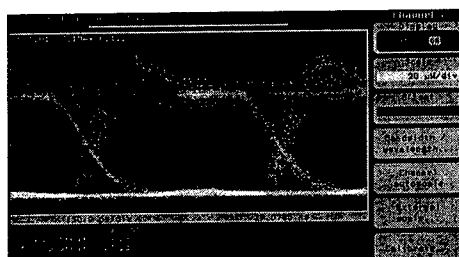


Figure 4: High Speed properties of oxide VCSELs

2D
VCSEL/
MEM
Array
OEICs
chip

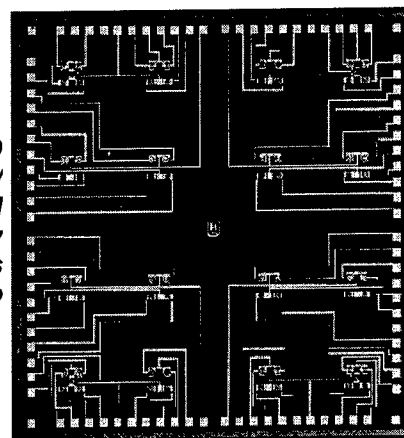


Figure 5: Photograph of a monolithically integrated 32 element VCSEL and 32 element MSM array

Fabrication of 12 X 12 Matrix-Addressed 780nm Oxide-Confined VCSEL Arrays.

Hideo Nakayama, Takeshi Nakamura, Jun Sakurai, Nobuaki Ueki, Hiromi Otoma

Yasuaki Miyamoto, Masateru Yamamoto, Ryoji Ishii, Masahiro Yoshikawa and Mario Fuse

Optical Devices Laboratory, Fuji Xerox, 2274 Hongoh Ebina, Kanagawa, Japan

Phone: 462-38-3111, E-mail: nakayama@crl.fujixerox.co.jp

Large scale integration of VCSELs and their addressing is a key technology which opens up other new VCSEL applications like smart pixels and print heads than optical interconnections. Matrix addressed VCSEL arrays can be most promising in integrating a large number ($> 8 \times 8$) of VCSELs in higher density to make a chip size smaller. Here we describe the fabrication process of 12×12 matrix-addressed oxide-confined VCSEL arrays and their characteristics. Complete planarization enabled p(top) and n(bottom) electrode to be successfully formed across DBR layers whose total thickness is $10 \mu\text{m}$. As a result, high yield and good uniformity in device performance was achieved.

Each VCSEL consists of n and p- semiconductor DBR and 3QW active region, which are all $\text{Al}_x\text{Ga}_{1-x}\text{As}$. $22 \mu\text{m}$ diameter post structure is made by dry-etching and then kept in wet-oxidizing environment to form $4 \mu\text{m}$ oxide aperture. Uniformity of oxide aperture size is $\pm 0.2 \mu\text{m}$ in the area of $11 \times 19\text{mm}$ as shown in fig.1, and the variation in the actual device area is less than $0.1 \mu\text{m}$, which caused excellent device uniformity. To make n contacts, n^+GaAs layer was grown underneath n-DBR, and gold electrode was patterned on this n^+ layer after post etching down to n^+GaAs layer. After n-electrode formation, isolation trenches are made by etching n^+GaAs layer. Since the pitch of the each VCSELs is $42 \mu\text{m}$ corresponding to pixel pitch required for print head application, width of n-electrode and isolation trench is both $5 \mu\text{m}$ and formed $5 \mu\text{m}$ aside from post structure. Thick photoresist was used to form these patterns. Figure 2 shows SEM photograph of these structures.

For planarization of airposts, thick polyimide was coated and mechanically polished. Figure 3 shows cross-sectional view of the device. It is seen that the polyimide film buried $10 \mu\text{m}$ depth trenches between post structures resulting in totally flat surface leveling to top of VCSELs. Therefore, p-electrode can run on flat surface without any breaks, which would lead to high yield process even in very large scale integration.

Figure 4 shows I-L and I-V characteristics of 12×12 individual VCSELs. Uniformity of I_{th} in the whole array is about $\pm 12\%$, and becomes about 5% if the peripheral pixels are excluded as can be seen in fig.5. Low I_{th} 's in the peripheral pixels are due to smaller aperture size. The smaller aperture size is due to smaller post size originated from loading effect of dry etching, which can be solved by optimizing etching conditions. Accordingly, we can expect uniform VCSEL array with high yield in large scale VCSEL integration where oxidation uniformity would only be a limiting factor. Table 1 summarizes the characteristics of matrix-addressed 780nm oxide-confined VCSEL array.

- 1) M.Orenstein, A.C.Von Lehmen, C.Chang-Hasnain, N.G.Stoffel, J.P.Harbison and L.T.Florez, Electron.Lett.27,437 (1991)
- 2) R.A.Morgan, G.D.Guth, C.Zimmer, R.E.Leibenguth, M.W.Focht, J.M.Freund, K.G.Glogovsky, T.Mullally, F.F.Judd and M.T.Asom, IEEE Photon.Technol.Lett. 6, 913 (1994)

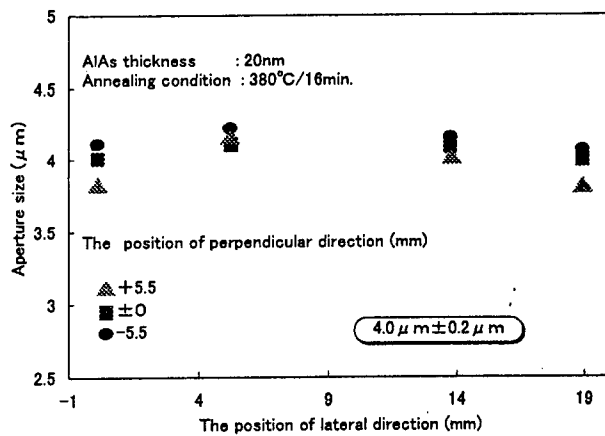


Fig.2 Scanning electron micrograph of air posts and isolation trenches structure.

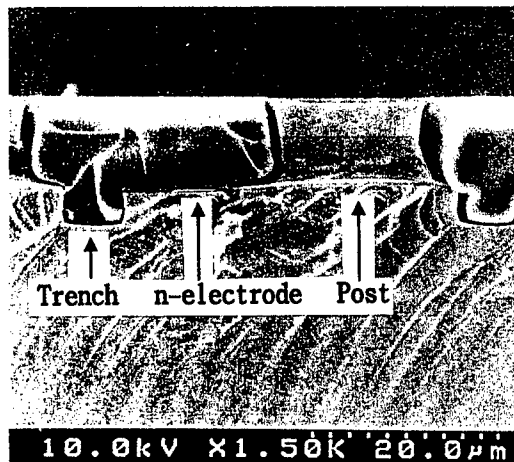


Fig.3 Cross-sectional SEM micrograph of the matrix-addressed VCSEL Array.

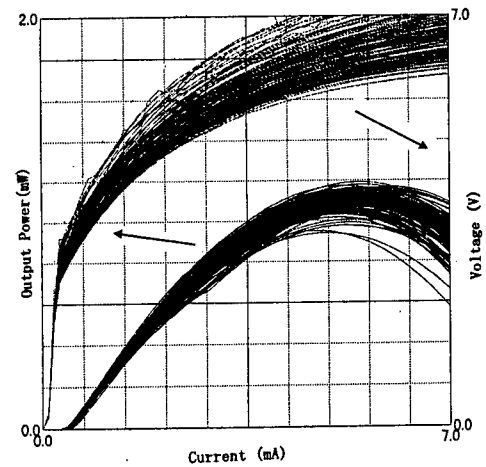


Fig.4 I-L and I-V characteristics of 12x12 matrix-addressed VCSEL Array.

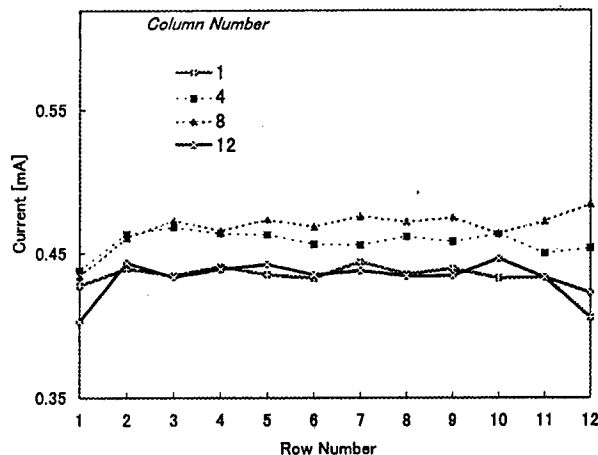


Fig.5 The threshold current distribution of 12x12 matrix-addressed VCSELs.

	Min.	Avr.	Max.
I _{th} (mA)	0.40	0.46	0.52
V _{th} (V)	2.68	2.99	3.57
S _d (W/A)	0.33	0.38	0.42
Power(mW) @3.5mA	0.82	0.91	0.99
λ (nm)	781.52	782.06	782.36

Table 1 Characteristics of 12x12 matrix-addressed VCSEL Array.

WA3

2:45pm - 3:00pm

Monolithically integrated surface and substrate emitting vertical cavity surface emitting lasers for smart pixels

Aaron E. Bond, P. Daniel Dapkus

University of Southern California, University Park Campus, PHE 504-MC0271
Los Angeles CA 90089-0271, bond@scf.usc.edu, dapkus@mizar.usc.edu

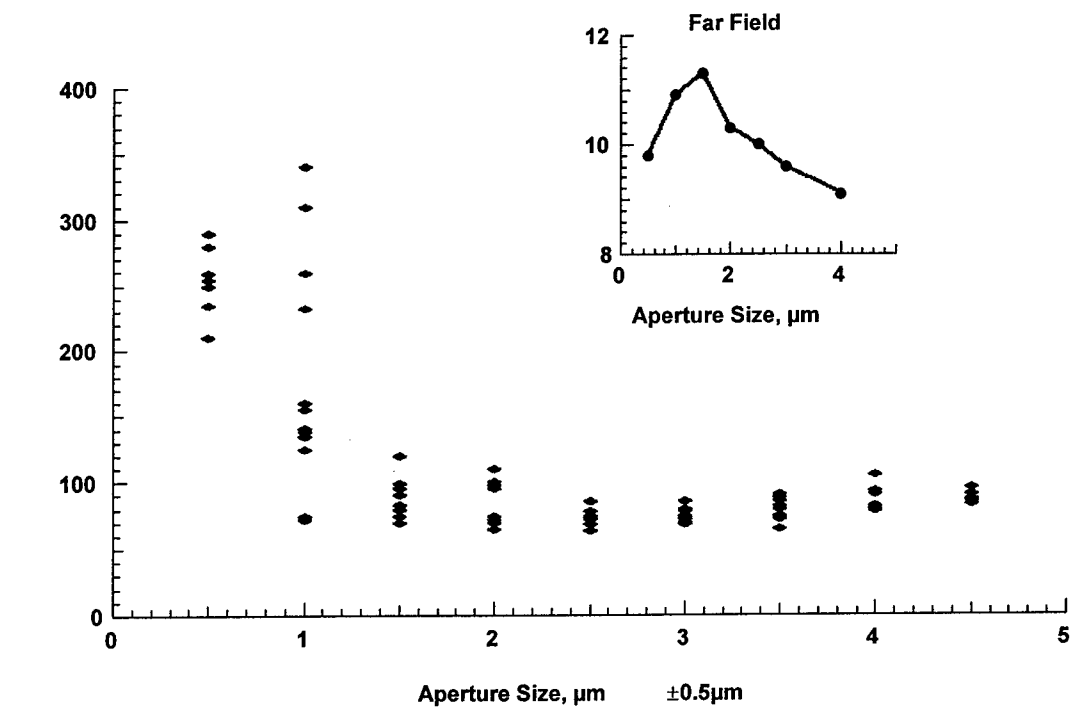
The oxidation of AlAs [1] to form AlO_x has enabled the fabrication of very high performance vertical cavity surface emitting lasers (VCSEL's)[2,3]. AlO_x is used as an insulator to confine current flow to very small dimensions, create an index step for lateral mode confinement, and to effect extremely high contrast distributed Bragg reflectors (DBR's)[4].

Oxidation of AlO_x is a selective process over GaAs in an epitaxial stack, and can also be spatially selective over a wafer by defining predetermined areas of a wafer to be exposed to the oxidation process. Using the spatial selectivity of the oxidation we have fabricated monolithically integrated surface and substrate emitting VCSEL's side by side on a single epitaxial wafer separated by only 125 μm . This technology will allow the fabrication of high density arrays of smart pixels with dual communication capabilities in a free space optical system.

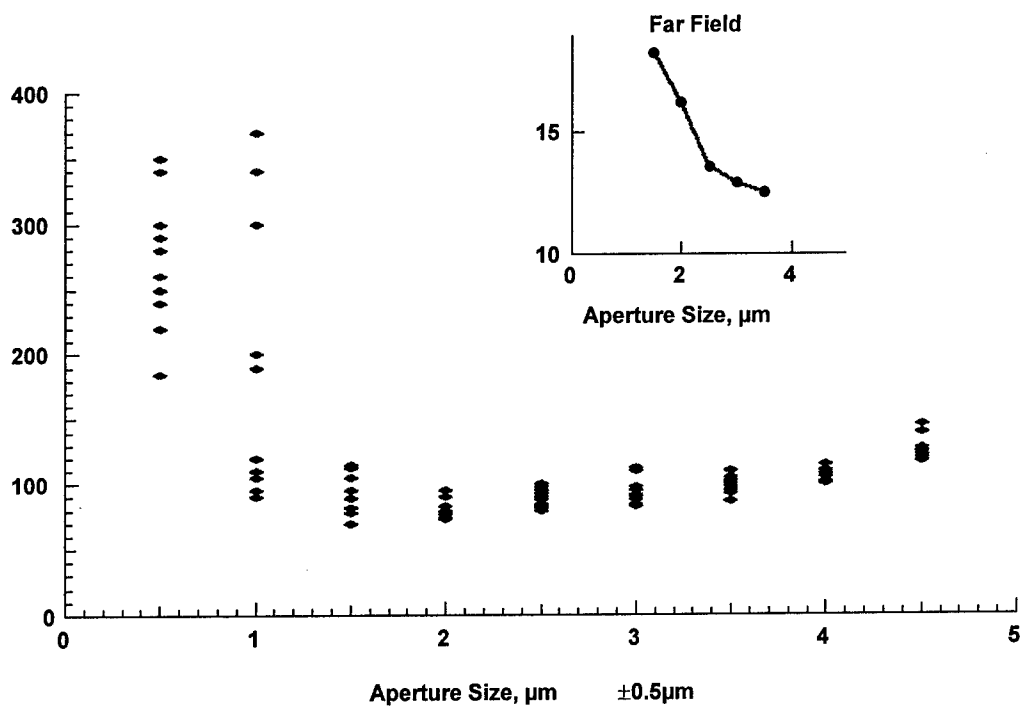
The top and bottom emitting VCSEL's we will present both show high performance. Figure 1a, 1b show typical threshold current dependencies as a function of AlO_x aperture width for surface and substrate emitting VCSEL's respectively. The far field full width at half maximum power (FWHM) is shown in the inset for the two devices. The threshold current for both devices is well below 100 μA . Surface emitting devices had threshold currents as low as 65 μA , and substrate emitting devices had thresholds as low as 75 μA . Slope efficiencies for both types of devices were 19-20%.

Using spatially selective oxidation VCSEL's, MESFET's, and detectors can all be integrated in a compact high performance smart pixel.

1. Dallesasse, J. M., Holonyak, N. Jr., Sugg, A.R., Richard, T. A., and El-Zein, N.: "Hydrolyzation oxidation of $\text{Al}_x\text{Ga}_{1-x}\text{As-AlAs-GaAs}$ quantum well heterostructures and superlattices", *Appl. Phys. Lett.*, 1990, **57**, (26), pp. 2844-2846
2. Huffaker, D.L., Deppe, D. G., and Kumar, K.: "Native-oxide defined ring contact for low threshold vertical-cavity lasers", *Appl. Phys. Lett.*, 1994, **65**, (1), pp. 97-99
3. Yang, G. M., MacDougall, M. H., Dapkus, P. D.: "Ultralow threshold current vertical-cavity surface-emitting lasers obtained with selective oxidation", *Electron. Lett.*, 1995, **31**, pp. 886-888
4. MacDougall, M. H., Zhao, H., Dapkus, P. D., Ziari, M., and Steier, W. H.: "Wide-bandwidth distributed Bragg reflectors using oxide/GaAs multilayers," *Electron. Lett.*, 1994, **30**, pp.1147-1149



a) Surface Emitting Device



b) Substrate Emitting Device

Figure 1: Typical threshold current vs. aperture width and FWHM for surface and substrate emitting VCSEL's.

New Materials for 1.3- μ m VCSEL Smart Pixels

Shigeo Sugou, Takayoshi Anan, Kenichi Nishi, Takashi Yoshikawa,
Hideaki Saito, and Kenichi Kasahara

Optical Interconnection NEC Laboratory, RWCP *

* RWCP; Real World Computing Partnership

34 Miyukigaoka, Tsukuba, Ibaraki 305-8501, Japan

Optical interconnections are in high demand for connecting the nodes of parallel and distributed processor systems because using high-speed and high-capacity electric interconnections introduces problems such as a short connection distance, electro-magnetic interference (EMI), and too many signal numbers. One way to develop an optical interconnection smart pixel is to use a CMOS-LSI with flip-chipped optical devices. Figure 1 shows an image of a future LSI with optical pinouts in our project. A smart pixel can be developed using CMOS-LSI with optical interface function blocks, such as codecs, mux/demux blocks, synchronous buffers, and driver/amplifiers. Function blocks should be prepared as intellectual property (IP). This is because by introducing optical functions as IP, the LSI designer can easily treat optical pinouts as one of the methods that reduce the pin bottleneck problem.

Current trends in CMOS point to a design rule, clock frequency, and voltage of 0.15 μ m, 1.4 GHz, and 1.5 V, respectively, by 2001. If this is the case, a maximum bandwidth over 100 Gbps, and an operation voltage less than 1.5V will be required for optical devices. A connection distance over 1 km will also be better for LAN applications. One of candidate for operation at 100Gbps and 1.5 V is to use 1.3- μ m vertical cavity surface emitting lasers (VCSELs) pixels with a single mode fiber (SMF) array. However, producing 1.3- μ m VCSEL pixels is problematic. One of the major problems is the lack of a distributed Bragg reflector (DBR) mirror with high-contrast refractive indexes, high thermal conductivity, and full wafer process treatment. Various approaches to solving this using wafer fusion¹⁾ and AlGaAsSb DBR²⁾ have been proposed. Recently, new material systems that can be grown on GaAs and emitted at 1.3 μ m have been attracting great interest³⁾. This is because they can be combined with conventional VCSEL techniques, such as the AlAs/GaAs DBR mirror and oxide current confinement. Here, we report on our approach using new GaAs-based materials (GaAsSb/GaAs and InAs- quantum dots (QDs)) emitting at 1.3- μ m.

Figure 2 shows the room temperature photoluminescence (PL) spectrum from the 12-nm-thick GaAs_{0.7}Sb_{0.3}/GaAs quantum well (QW). The peak is positioned at 1.27 μ m, indicating that 1.3- μ m lasers can be developed by using this QW. PL from a GaAsSb QW with a higher Sb content showed a peak wavelength of 1.322 μ m. No misfit dislocations due to lattice relaxation were observed. The threshold current density and lasing wavelength for a single quantum well broad area laser were 3 kA/cm² and 1.22 μ m, respectively. Although the lasing occurred at a shorter wavelength, this shift can be avoided by increasing the number of QWs.

Another 1.3- μ m emitting material on GaAs is QDs. There have been reports on 1.3- μ m PL from InGaAs-QDs on GaAs but higher density and sharper PL properties are still required for 1.3- μ m lasing^{4,5)}. This is because these properties are important to prevent lasing at the shorter wavelength due to state filling in the QDs discrete quantum levels. Figure 3 shows the room-temperature PL spectra of conventional InAs-QDs and new InGaAs-capped InAs-QDs. Insets show schematic cross sections of these QDs. In the InGaAs-capped QD structure, a InGaAs cap-layer was introduced to reduce the QD

compressive strain that enlarges the bandgap energy. A 1.3- μm PL with high peak intensity and sharp PL (FWHM:29meV) compatible to QWs was obtained.

In summary, our approaches to developing 1.3- μm VCSELs are introduced. The two new materials, Sb QWs and InGaAs-capped InAs QDs, are found to be candidates for the active layers of VCSELs on GaAs substrates. These new GaAs-based materials will be key in making 1.3- μm VCSEL pixels and in enlarging the capacity of optical interconnections.

References

- [1] Y. Qian, Z.H. Zhu, Y.H. Lo, D.L. Huffaker, D.G. Deppe, H.Q. Hou, B.E. Hammons, and W. Lin, IEEE LEOS summer Topical Meetings, TuB2, pp. 45-46, 1997
- [2] G. Almuneau, F. Genty, L. Chusseau, S. Gaillard, and N. Bertru, IEEE LEOS summer Topical Meetings, TuA5, pp.41-42, 1997
- [3] S. Sato et al. In the proceedings of CLEO/Pacific Rim 97, PD2.6.
- [4] R. Mirin, J. Ibbetson, K. Nishi, A. Gossard, and J. Bowers, Appl. Phys. Lett., Vol. 67, pp. 3795-3797, 1995.
- [5] K. Mukai, N. Ohtsuka, M. Sugawara, and S. Yamazaki, Jpn. J. Appl. Phys., Vol. 33, pp. L1710, 1994

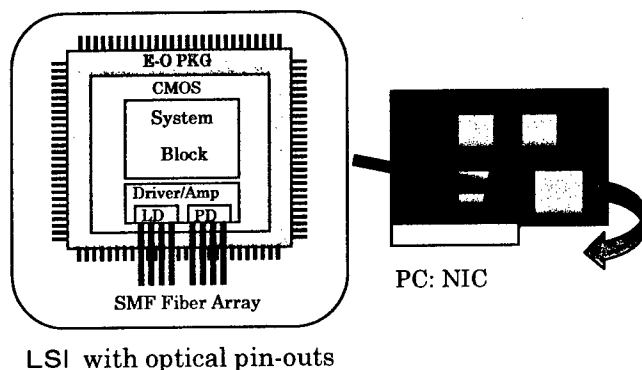


Fig.1 Image of future LSI with optical pinouts. If the optical interface block is prepared as intellectual property, it will be easier for a designer to develop optical interconnections.

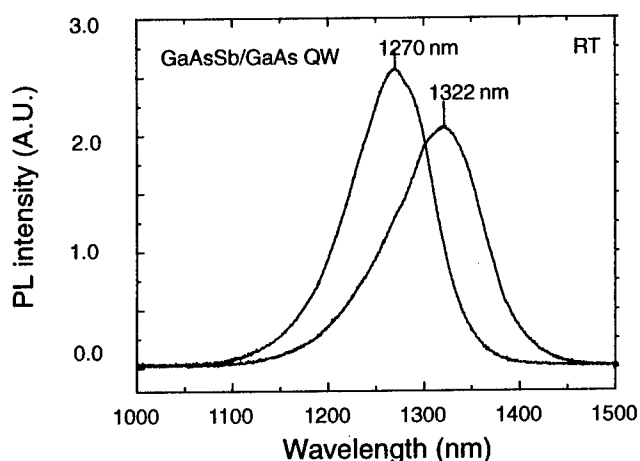


Fig. 2. Room temperature PL spectrum from GaAsSb QW. Over 1.3- μm PL was observed for GaAsSb($x=0.32$) QW.

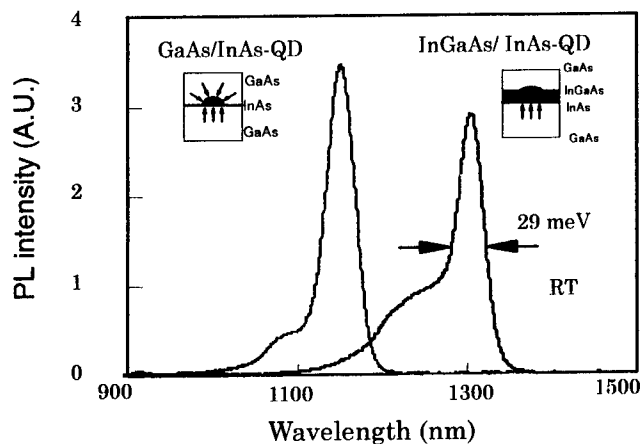


Fig. 3 Room temperature PL spectrum from InAs-QDs

Novel Technique for Monolithic Integration of Microlensed Resonant Detectors and Vertical Cavity Lasers

D. A. Louderback, O. Sjölund, E. R. Hegblom, J. Ko, and L. A. Coldren
ECE Department
University of California
Santa Barbara, CA 93106
6500dl@ucsbuxa.ucsb.edu

Abstract

We demonstrate a novel design that allows fabrication of through-the-substrate input/output photodetectors and vertical-cavity lasers with integrated microlenses from a single epitaxial growth by selective oxidation of the bottom mirror.

Free-space optical interconnects have received considerable interest for their potential to relieve bottlenecks associated with electrical board-to-board and chip-to-chip interconnects. Recent developments in VCLs have created devices with low threshold currents, high wallplug efficiencies, and large modulation bandwidths [1,2]. In addition, two-dimensional arrays of VCLs can be easily fabricated, and for the bottom-emitting geometry, they are compatible with flip-chip bonding without the need for substrate removal. In this case, monolithic microlenses [3] can also be integrated to greatly simplify or eliminate external optics. For two-way communication, each board must have detectors as well as VCLs operating at the same wavelength.

We present a new technique for monolithically integrating VCLs and detectors on a single epitaxial growth structure that are compatible with integrated microlenses and flip-chip bonding [4]. The structure contains VCLs and resonant-cavity photodetectors that have their bottom (input/output) mirror reflectivities individually designed and implemented by post growth selective oxidation of some of the mirror periods to convert the detector structure into a VCL structure. To achieve a reasonably broad optical bandwidth for the detector, its input mirror reflectivity must be significantly lower than that of the VCL's output mirror. With the proper choice of input mirror reflectivity, the detector can have both a reasonably large optical bandwidth and adequate absorption. The input mirror reflectivity for the detector was chosen to be $\sim 85\%$, whereas the VCL output mirror had a reflectivity of $\sim 99.3\%$.

The required difference in bottom mirror reflectivities is obtained by adding a few special AlGaAs layers in the VCL's bottom mirror. These layers are designed to be oxidized to form layers of Al_xO_y with a refractive index of ~ 1.57 . Therefore, they are detuned when not oxidized and thus do not affect the reflectivity of the detectors. Because of the large index difference only a few periods of the oxidized mirror are needed [5]. A schematic of the epitaxial structure, designed to be resonant at 990 nm, is shown in Figure 1. The right side of the figure shows the structure when used as a detector, or as grown. The left side shows the structure when converted into a VCL by the oxidation of the bottom mirror. The device structure was grown by solid source molecular beam epitaxy. The 1λ cavity contains three 80 \AA $\text{In}_{0.2}\text{Ga}_{0.8}\text{As}$ quantum wells. The mirror layers that were oxidized consisted of $\text{Al}_{0.98}\text{Ga}_{0.02}\text{As}$, while the other mirror periods consisted of $\text{Al}_{0.9}\text{Ga}_{0.1}\text{As}$ and GaAs layers that will not significantly oxidize.

The detectors were characterized using a Ti/Sapphire laser as the optical input, and the photocurrent was measured using a HP 4145 parameter analyzer. The responsivity versus wavelength characteristics at 1 V reverse bias are shown in Figure 2a for a $50\text{ }\mu\text{m}$ diameter detector adjacent to one of the VCLs shown below. The peak responsivity is $\sim 0.30\text{ A/W}$, corresponding to an absorption, or quantum efficiency, of 39% . The optical bandwidth, measured as the full width at half maximum (FWHM) of the responsivity, was found to be 5.1 nm . Other detectors from the same material exhibited responsivities as high as 0.46 A/W and optical bandwidths of 5.9 nm .

Figure 2b shows the output power versus current characteristics of several VCLs. The lasers have threshold currents as low as $174\text{ }\mu\text{A}$ and differential efficiencies as high as 60% . The smallest VCLs had mode suppression ratios of $\sim 38\text{ dB}$ at bias currents of 13 times threshold. The emission wavelength was approximately the same as that of the peak detector responsivity. These results show the potential for monolithically integrating high-performance, individually-designed vertical-cavity lasers and resonant-cavity photodetectors that are compatible with flip-chip bonding and monolithic microlenses for bi-directional free-space optical communication applications.

ACKNOWLEDGEMENT

This work was supported by AFOSR and DARPA via HOTC and the Free-Space Optical Interconnect Initiative.

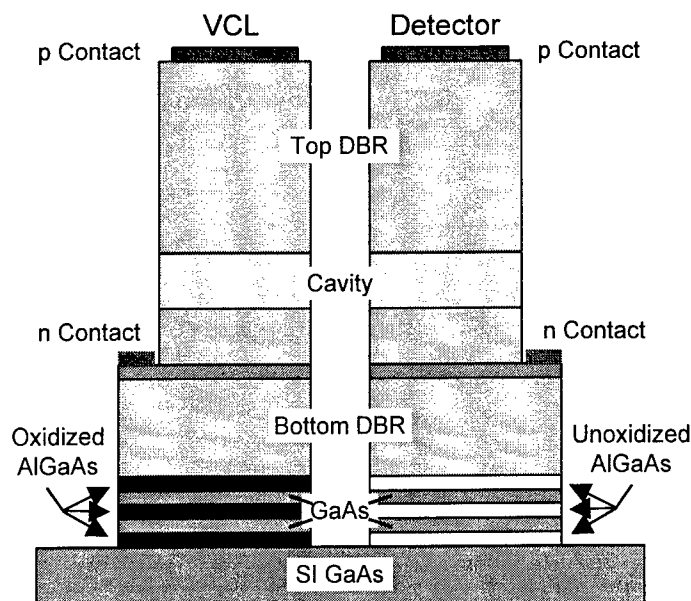


Figure 1 Schematic of the device structure showing the VCL (left) and detector (right).

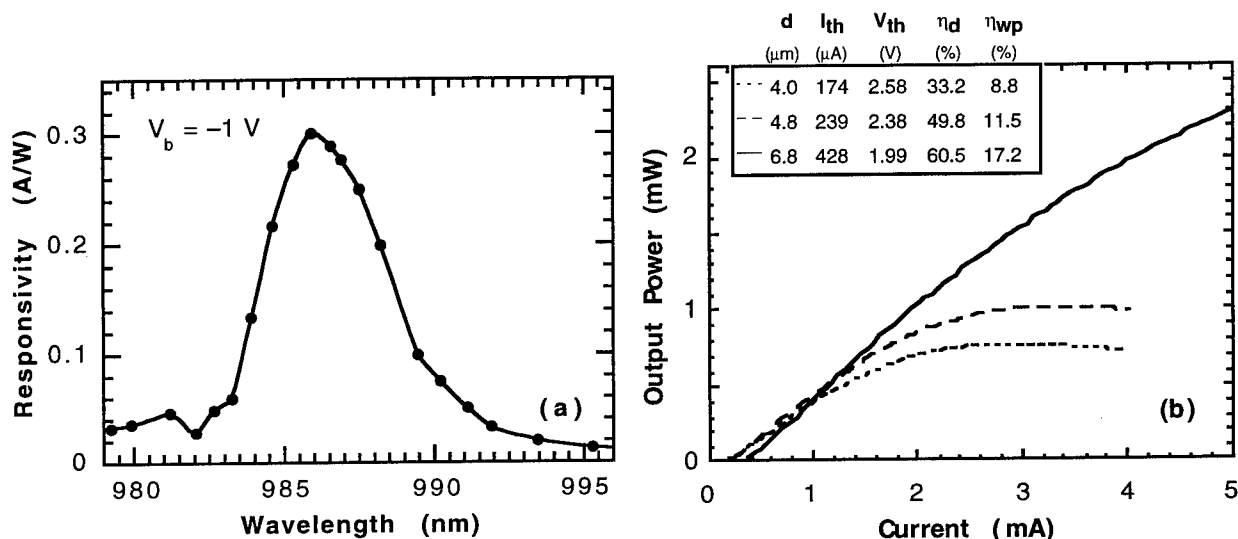


Figure 2 (a) Detector spectrum and (b) L-I characteristics of different size VCLs.

REFERENCES

- [1] K. L. Lear, K. D. Choquette, R. P. Schneider, Jr., S. P. Kilcoyne, and K. M. Geib, "Selectively oxidized vertical cavity surface emitting lasers with 50% power conversion efficiency," *Electron. Lett.*, 1995, **31**, pp. 208-209.
- [2] B. J. Thibeault, K. Bertilsson, E. R. Hegblom, E. M. Strzelecka, P. D. Floyd, and L. A. Coldren, "High-speed characteristics of low-optical loss oxide-apertured vertical-cavity lasers," *IEEE Photon. Technol. Lett.*, 1997, **9**, pp. 11-13.
- [3] E. M. Strzelecka, D. A. Louderback, B. J. Thibeault, G. B. Thompson, K. Bertilsson, and L. A. Coldren, "Parallel free-space optical interconnect based on arrays of vertical cavity lasers and detectors with monolithic microlenses," *Appl. Opt.*, to be published.
- [4] O. Sjölund, D. A. Louderback, E. R. Hegblom, J. Ko, and L. A. Coldren, "Novel integration of vertical cavity lasers and resonant photodetectors," 1998, submitted.
- [5] M. H. MacDougall, H. Zhao, P. D. Dapkus, M. Ziari, and W. H. Steier, "Wide-bandwidth distributed Bragg reflectors using oxide/GaAs multilayers," *Electron. Lett.*, 1994, **30**, pp. 1147-1148.

Feasibility of Tera-bps Smart Pixel Arrays Using Monolithic Emitter-based Optoelectronic VLSI Circuits

J. F. Ahadian^a, P. T. Vaidyanathan^b, S. G. Patterson^a, Y. Royter^a, D. Mull^c,
G. S. Petrich^a, W. D. Goodhue^d, S. Prasad^b, L. A. Kolodziejski^a, and C. G. Fonstad, Jr.^a

^aDepartment of Electrical Engineering and Computer Science, Massachusetts Institute of Technology,
Cambridge, MA 02139; 617-253-5165, 617-258-6640 (Fax), joeah@oevlsi.mit.edu

^bDepartment of Electrical and Computer Engineering, Northeastern University, Boston, MA 02115

^cLincoln Laboratory, Lexington, MA 02173

^dDepartment of Physics and Applied Physics, University of Massachusetts Lowell, Lowell MA 01854

A technology which brings together optoelectronic devices with VLSI electronics has long been sought as part of the drive to incorporate optical interconnects into high speed computing and communication systems. Such a technology will have a dramatic impact if it is able to provide an information processing capacity in excess of 1 tera-bit/s per cm^2 of die area. The Epitaxy-on-Electronics (EoE) optoelectronic integration technology meets this goal. EoE begins with a commercial, economical GaAs VLSI process and monolithically integrates heterostructure devices such as emitters, detectors, or modulators to produce complex and manufacturable optoelectronic integrated circuits (OEICs). The opportunity to design and receive prototype LED-based EoE OEICs was recently made available to nine research groups as part of the OPTOCHIP research foundry project (Figure 1(a)) [1]. The various OPTOCHIP designs include free-space, guided-wave, and sensor applications of emitter-based OEICs. An example of a 6×11 , 4444 pixels/cm^2 EoE smart pixel array is given in Figure 1(b) [2]; the specific OPTOCHIP demonstrations, such as this, will be detailed elsewhere by their designers. The present paper explores EoE's short-term potential to produce 1 tera-bit/s/ cm^2 smart pixel arrays. The issues of pixel density, processing complexity, electronic and optoelectronic bandwidth, and thermal management will be addressed in detail, along with the technical and economic advantages of using GaAs VLSI electronics rather than CMOS. Specific examples of OPTOCHIP designs and of a canonical smart-pixel demonstration circuit will be presented.

A complete description of the Epitaxy-on-Electronics process appears elsewhere [3]. EoE uses conventional MBE growth and fabrication to produce optoelectronic devices within arbitrarily sized and placed openings in the dielectric stack of commercially fabricated, fully-metallized GaAs VLSI integrated circuits. The commercial electronics platform features enhancement and depletion mode MESFETs and four Al-based metallization levels, in addition to metal-semiconductor-metal (MSM) and optically-sensitive FET (OPFET) photodetectors. A close up look at an integrated LED is given in Figure 2. Integrated LEDs have been produced with a power efficiency of $0.3 \pm 0.1\%$ and an external differential quantum efficiency near their theoretical limit of 1%. These LEDs emit at a wavelength of $873 \pm 1 \text{ nm}$ with a Lambertian angular distribution and have a measured bandwidth of 30 MHz. The limited efficiency, directionality, and speed of these devices is adequate for initial demonstrations. Work is currently under way to integrate surface emitting lasers.

The information density of a smart pixel array is the product of the pixel density and the bit-rate of the individual pixels. From a system-level perspective, the pixel density and speed must be optimally chosen in light of the complexity of the resulting optical system, the difficulty of the electronic design, the extent of processing required within the pixels, and the packaging expense associated with managing the OEICs thermal environment. Consider a 1 cm^2 die containing 100 pixels operating at 10 Gb/s each, 1,000 pixels operating at 1 Gb/s each, and 10,000 pixels operating at 100 Mb/s. The first choice leads to very difficult electronics design while the last choice, though readily possible in CMOS, leads to very difficult optical system design. On the other hand, the choice of 1000 pixels/cm^2 operating at 1 Gb/s each minimizes optical system complexity and may be implemented in GaAs VLSI electronics. As for the power dissipation and pixel complexity, it is observed that commercial GaAs VLSI devices dissipating up to 20 W/cm^2 are comfortably packaged in thermally enhanced plastic ball-grid arrays [4]. If the power dissipation of the 1 cm^2 die is limited to 20 W, each of the 1,000 pixels may dissipate 20 mW. For a pixel containing one emitter and one detector, this 20 mW may be distributed as 5 mW for the emitter+driver, 5 mW for the receiver, and 10 mW for

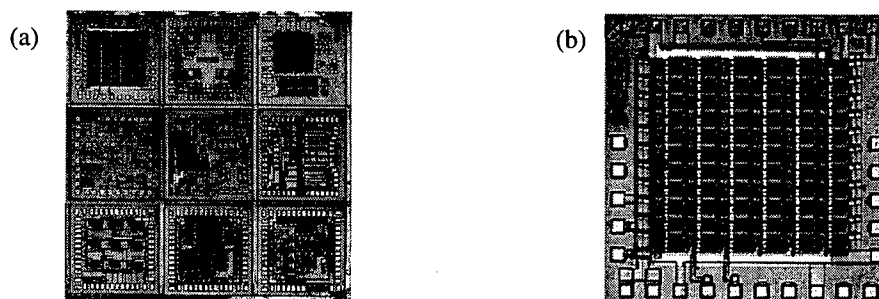


Figure 1: VLSI OEIC chips. (a) The OPTOCHIP master die is composed of nine $2 \text{ mm} \times 2 \text{ mm}$ OEICs. (b) Close up of a 6×11 , 4444 pixels/cm^2 optical neural-network OEIC; each pixel consists of one LED, two OPFET photodetectors, and a 20-transistor processing circuit [CIT].

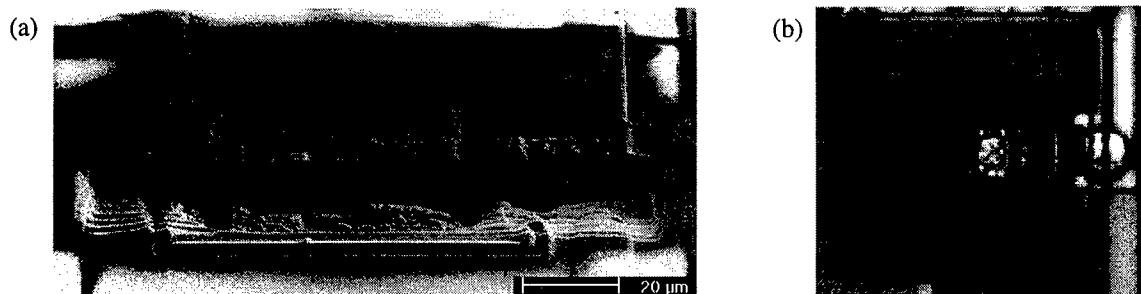


Figure 2: Integrated LED. (a) SEM of FIBE cross-section [6]. (b) Microscope photograph.

the processing electronics. Using direct coupled FET logic (DCFL) electronics capable of 1 Gb/s operation, the 10 mW budget allows for a 40-gate processing circuit. This level of complexity qualifies the smart-pixel as “smart” [5].

Figure 3 describes a demonstration smart pixel designed according to the above pixel density guidelines. The cell is 300 x 300 μm, allowing 1,000 such pixels to be arrayed on a 1 cm² die. It contains one LED and its associated drive electronics, one OPFET-based receiver, and well over 40 gates. In this circuit, the output of an internally-loaded, 63-stage ring oscillator is divided by a series of seven D-flip-flops. The output of one of the final two flip-flops is selected by a multiplexer on the basis of the optical input and applied to an LED driver (Figure 4(a)). The integrated LED thus oscillates at 476 KHz in the absence of optical input, and at 943 KHz when an optical input is applied. The electronics were intentionally slowed to these frequencies in order to simplify characterization. Internally, however, the electronics are operating at very high speeds: a gate delay of 130 ps was determined for the heavily loaded ring oscillator in this pixel. The gate delay measured on a 23-stage ring oscillator with a fanout of one was 67±2 ps. The electrical and optical outputs of the smart pixel are shown in Figure 4(b).

The performance of the current LED-based EoE OEICs is sufficient to implement a realistic demonstration of an optical interconnect system. However, the LEDs and OPFETs are not adequate to reach the tera-bit/s/cm² performance level. Nevertheless, various OPTOCHIP designs, and the canonical smart pixel detailed above, clearly show that the EoE technology is well matched to the system requirement of high performance optical interconnect applications. The integration of vertical-cavity and/or in-plane surface emitting lasers, now under development, and the use of MSM photodetectors, a standard element in other OPTOCHIP cells, will overcome the current limitations and allow EoE to be used to its full potential.

- [1] J. F. Ahadian, *et. al.*, CLEO'98, San Francisco, CA, 3-8 May 1998, CThG1.
- [2] This OPTOCHIP array was designed by J. P. Drolet, *et. al.*, California Institute of Technology.
- [3] J. F. Ahadian, *et. al.* *IEEE Journal of Quantum Electronics*, Accepted for publication.
- [4] Jim Mikkelsen, Vitesse Semiconductor Corporation, Personal communication.
- [5] T. M. Pinkston, *et. al.* *Applied Optics*, Vol. 36, No. 20, p. 4871, 1997.
- [6] FIBE conducted by K. Edinger and J. Melngailis, Laboratory for Ion Beam Research and Application, University of Maryland.

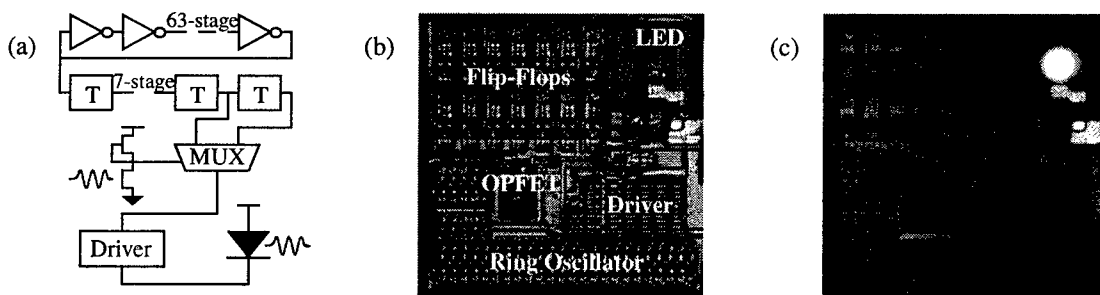


Figure 3: 1 Tb/s/cm² demonstration smart pixel. (a) Functional block diagram. (b) Microscope photograph of fabricated smart pixel. (c) Smart pixel in operation showing LED emission.

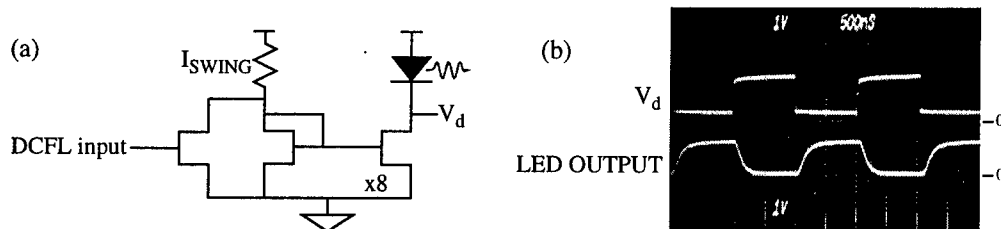


Figure 4: Characterization of demonstration smart pixel. (a) Circuit diagram of LED driver circuit. (b) Scope trace showing electrical driving voltage (top) and optical LED output (bottom) as measured by an external optical receiver (response time is limited by the receiver).

Flip-chip bonded MQW modulator operating at ECL voltage levels

K.W. Goossen, J.E. Cunningham and W.Y. Jan

Lucent Technologies, Bell Laboratories

4B-519 Crawfords Corner Road, Holmdel, NJ 07733

Currently there is much interest in extending local area network data speeds to multi-GHz levels while maintaining low transceiver cost. One approach to doing this is to use optoelectronic integration to VLSI electronics to both reduce electrical parasitics and alleviate assembly costs. The techniques demonstrated for producing arrays of smart *pixels* for parallel optical interconnection to computing chips could be applied to producing arrays of transceiver chips in a single step, as has essentially been demonstrated in the Lucent/George Mason Optoelectronic/VLSI foundry,¹ where flip-chip bonding followed by substrate removal,^{2,3} allows subsequent dicing into individual chips.

A LAN transceiver module typically consists of several chips, however. These are the

serialization/deserialization (serdes) chip, which multiplexes and demultiplexes between the high-speed optical fiber signal and the lower speed electrical line signals, the laser driver chip, laser, photodetector, and receiver chip. Compressing all of these into a single chip, let alone several of them into a flip-chip bondable die, seems a daunting task. Eliminating the need for any of these chips would help greatly.

The laser driver chip is necessary since the output of the serdes chip is a low voltage (typically ± 1 volt) ecl level differential signal. For example, the Vitesse VSC8071 10 Gbit/sec multiplexer chip produces a ± 800 mV output into 50 ohms, and perhaps larger levels into high impedance.⁴ Even if the serdes output can provide sufficient current, a laser needs a dc offset placed on it. The minimum voltage threshold of a 850 nm VCSEL (the only standard wavelengths for LAN's are 790-860 nm and 1.3 μ m) the authors found was 1.6 volt.^{5,6} A bias-tee could be used for this function, but microwave bias-tee's can add substantially to the final cost of the transceiver, and it is not clear if an integrated version can be produced anyway. Therefore typically a driver chip is used instead to convert the low voltage signal to that necessary to drive a laser.⁷

Whereas it is fundamental that a laser needs > 1 volt dc offset to operate, no such restriction applies to a modulator. We demonstrate here a multiple quantum well (MQW) surface-normal modulator that produces a contrast of 1.75:1 with ± 1 volt drive, and 2.04:1 with ± 1.6 volt. This device is not based on Fabry-Perot effects, and so does not require critical layer thickness control, although higher contrast Fabry-Perot devices are being pursued by the authors.

Our p-i(MQW)-n modulator uses asymmetric coupled quantum wells, which have previously been demonstrated in non-flip chip bonded, transmission modulators to have large absorption changes at low electric fields.⁸ It is necessary to work at low fields since the intrinsic region must be large enough to provide sufficient light absorption for high contrast, and additionally to produce low capacitance in the device. For a 50 ohm series resistance in the signal path, the maximum signal frequency of the device is given by $f = 50000h/d^2$, where h is the thickness of the

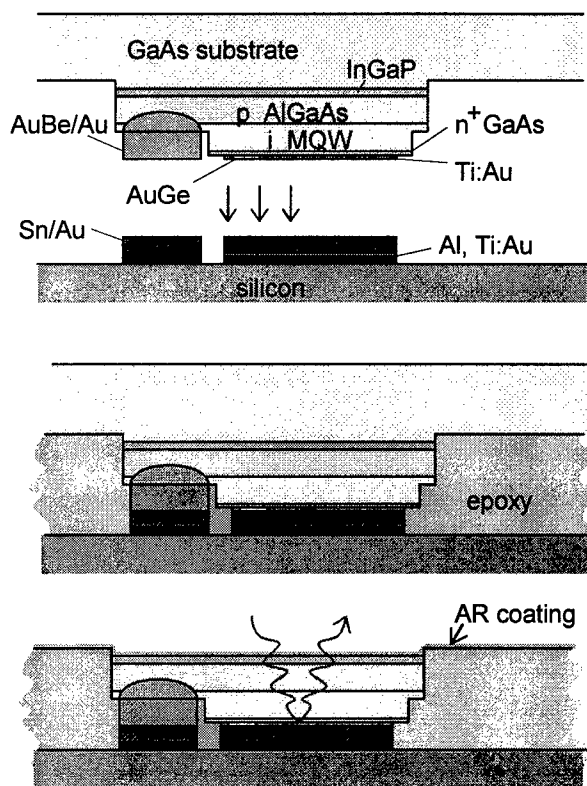


Fig. 1: Technique of flip-chip bonding followed by substrate removal for optoelectronic/VLSI integration.

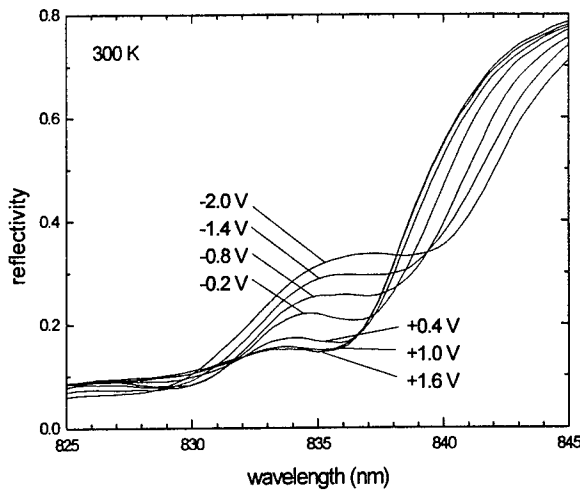


Fig. 2: Spectra of our flip-chip bonded, low voltage, low capacitance p-i(MQW)-n reflection modulator utilizing asymmetric coupled quantum wells.

intrinsic region and d is the diameter of the (circular area) modulator (in microns). An inexpensive fiber-optic coupler for reading out the state of a modulator has been demonstrated,⁹ capable of resolving an optical window of diameter of 70 microns. Therefore for a maximum frequency of 10 GHz, the intrinsic region must be greater than 1 micron thick. Therefore our device consists of 60 coupled GaAs quantum wells of 63 Å and 58

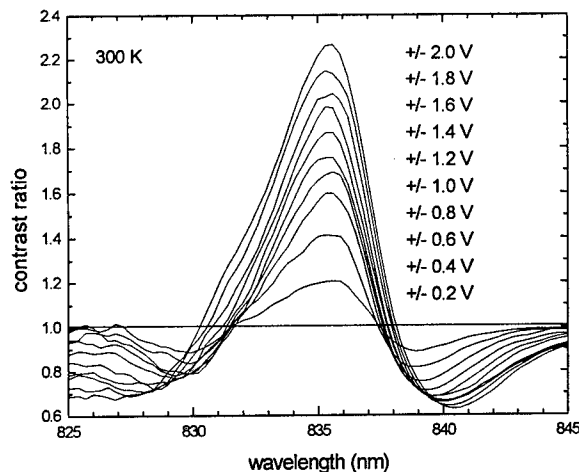


Fig. 2: Contrast ratio spectra of our modulator at differential eel voltage levels.

Å separated by a 14 Å $\text{Al}_{0.2}\text{GaAs}$ barrier, with each pair separated by a 35 Å $\text{Al}_{0.2}\text{GaAs}$ barrier. This provides the large electroabsorption of coupled quantum wells slightly offset from zero field.⁸ Since the modulator is anticipated to be large area, it should not suffer saturation due to high intensity.

Shown in Fig. 2 are the spectra of the device at different biases. Note that there is little change for forward biases greater than 1 volt, but should it be necessary to apply a differential signal, forward biases up to 2 volts do not produce appreciable forward current or light output. In Fig. 3 the contrast for differential signals up to ± 2 volt are shown. At ± 1.6 volt, the minimum voltage threshold for a 850 nm VCSEL the authors found, the contrast is 2:1

In conclusion, we have noted that VCSEL's at 850 nm, the only LAN standard wavelength where VCSEL's have been shown to operate, have thresholds greater than 1.6 volt, so that if it is desirable to operate circuits at lower absolute voltage levels, VCSEL's may not be used. However, we have demonstrated a modulator that has a contrast of 2:1 at a differential drive of ± 1.6 volt.

REFERENCES

- [1] A.V. Krishnamoorthy and K.W. Goossen, *Int. J. Optoelectron.* **11**, 181 (1997).
- [2] K.W. Goossen, J.E. Cunningham, and W.Y. Jan, *IEEE Phot. Tech. Lett.* **5**, 776 (1993).
- [3] K.W. Goossen, J.A. Walker, L.A. D'Asaro, S. Hui, B. Tseng, R. Leibenguth, D. Kossives, D. Bacon, D. Dahringer, L.M.F. Chirovsky, A.L. Lentine, and D.A.B. Miller, *IEEE Phot. Tech. Lett.* **7**, 360 (1995).
- [4] Vitesse VSC8071 data sheet.
- [5] M. Grabherr, R. Jager, R. Michalzik, B. Weigl, G. Reiner, and K.J. Ebeling, *IEEE Phot. Tech. Lett.* **9**, 1304 (1997).
- [6] C-K. Lin, M.H. MacDougall, A.E. Bond, and P.D. Dapkus, *Proc. 1997 LEOS Annual Meet.*, p. 348.
- [7] Hewlett-Packard HFBR-5305 data sheet.
- [8] K.W. Goossen, J.E. Cunningham, D.A.B. Miller, W.Y. Jan, A.L. Lentine, A.M. Fox, and N.K. Ailawadi, *Proc. 1991 OSA Quantum Optoelectronics*, p. 26.
- [9] J.E. Ford, J.A. Walker, and K.W. Goossen, *Proc. SPIE MEMS 1997*, vol. 3226, p. 86.

Temperature Dependence of QCSE Device Characteristics and Performance

M.B. Venditti, D.N. Kabal, M.H. Ayliffe, D.V. Plant, F.A.P. Tooley¹,
E. Richard², J. Currie², and A.J. SpringThorpe³

Department of Electrical and Computer Engineering, McGill University, Montréal, Canada

¹Department of Physics, Heriot Watt University, Edinburgh, UK.

²Laboratoire LISA, École Polytechnique, Montréal, Canada

³Nortel Technology, Advanced Components Division, Ottawa, Canada

I. Introduction

Multiple quantum well (MQW) devices based on the quantum-confined Stark effect (QCSE) occupy a prominent place in the development of smart pixel technologies. The devices are typically p-i(MQW)-n diodes which can perform the function of a modulator or detector. The devices may be operated in reflection mode, where reflecting mirror layers are grown atop the device, which is then flip-chip bonded onto a silicon CMOS chip. For GaAs/AlGaAs devices operating near 850 nm, substrate removal is a necessary final step in the hybridization process. [1]

Active control of the die temperature results in it becoming a free operating parameter. It will be shown that, through active control of device temperature, MQW devices can be operated efficiently over wide ranges in operating parameters.

Analysis was performed on data obtained from MQW device samples consisting of 90 Å GaAs wells and 35 Å AlGaAs (40% Al mole ratio) barriers. The devices have 60 wells, for an active region thickness of 0.75 µm. Absorption spectra were measured before the reflecting mirror layers had been grown and before flip chip bonding. The data were taken as a function of reverse bias, wavelength, and temperature, and then used to calculate derived MQW device characteristics for the case of a flip-chipped device with reflecting mirror layers.

II. Characteristics of QCSE Devices

The main characteristic in the absorption spectra of a MQW device is the exciton absorption peak. The strength of the peak is denoted as α_{MQW} . The wavelength position of the peak is denoted as λ_0 at zero-bias, and λ_p at an arbitrary bias. λ_0 and λ_p are dependent on the band-gap energy of the well material, and thus shift to longer wavelengths with increasing temperature. For the MQW samples, the measured shift was 0.241 nm/K, which is in close agreement with [3].

The QCSE [2] is a means by which efficient, high-speed modulation of λ_p can be achieved. The applica-

tion of an electric field perpendicular to the quantum well layers results in a shift of λ_p to longer wavelengths. Associated with the wavelength shift of the QCSE is a reduction in α_{MQW} , both of which are approximately quadratic with applied field.

III. Principles of Operation of QCSE Devices

QCSE Reflection Modulators

The normal method of operation for a QCSE reflection modulator is $\lambda_0 < \lambda_{op}$, where λ_{op} is the device operating wavelength, taken as 852 nm for the analysis in this paper. Modulation in the intensity of a reference optical beam is achieved by shifting λ_p toward λ_{op} to achieve low reflectivity, and by shifting λ_p away from λ_{op} to achieve high reflectivity. Shifting is usually achieved by utilizing the QCSE, but can also be achieved by changing the operating temperature of the device.

With $\lambda_0 < \lambda_{op}$, a pre-bias voltage, V_{pb} , corresponds to the high reflectivity state, and a high reverse-bias, $V_{pb} + V_{sw}$, corresponds to the low reflectivity state. V_{sw} is the voltage swing provided by the drive electronics, which is taken as 5 V for the analysis in this paper.

The figure of merit for a QCSE modulator is its change in reflectivity from the low state to the high state [3]:

$$\eta_{\text{modulator}} = \Delta R = R(V_{pb}) - R(V_{pb} + V_{sw}) \quad (1)$$

The efficiency of a MQW modulator depends greatly on the relative positions of λ_0 and λ_{op} . Following [4], we define $\delta\lambda = \lambda_{op} - \lambda_0$. Furthermore, we define $\Delta\lambda$ as the wavelength shift that is achieved when a reverse bias of $V_{pb} + V_{sw}$ is applied. For efficient operation of the modulator, one requires $\delta\lambda \approx \Delta\lambda$. This can be achieved by changing the parameters of the usually by adjusting V_{pb} . However, it is not always advantageous to do so. For example, if $\delta\lambda \gg \Delta\lambda$, a large increase in V_{pb} may be required, and the resulting reduction in α_{MQW} may overcome the benefits of operating in the $\delta\lambda \approx \Delta\lambda$ regime. If $\delta\lambda \ll \Delta\lambda$, a significant reduction in V_{pb} may be required, which may be incompatible with

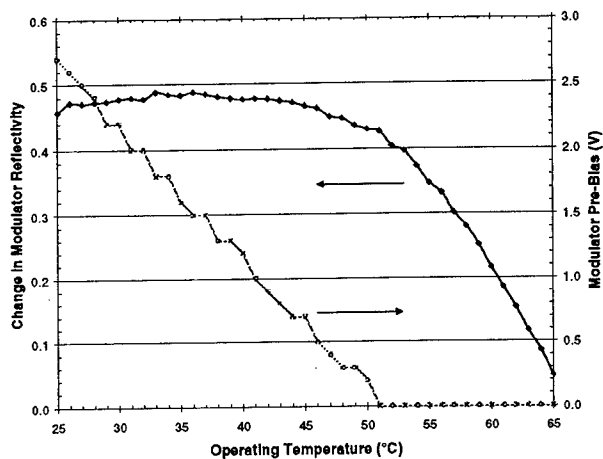


Figure 1 – Optimal ΔR versus T_{op}

the requirement that V_{pb} be positive. Under either of these circumstances, the alternative to modifying V_{pb} is to modify the operating temperature, T_{op} .

Figure 1 shows the optimal ΔR (with the corresponding optimal V_{pb}) plotted versus T_{op} . At 51°C, the optimal V_{pb} becomes 0, and the efficiency of the modulator decreases rapidly with increasing T_{op} . At the low end of the temperature axis, the efficiency begins to slowly decrease, indicating that the reduction in α_{MQW} due to the large V_{pb} is starting to dominate.

QCSE Detectors

As for QCSE modulators, QCSE detectors are typically designed such that $\lambda_o < \lambda_{op}$. The objective of the detector is to convert incident optical power into photocurrent as efficiently as possible, so the figure of merit for a detector is simply quantum efficiency [3]. To optimize quantum efficiency requires $\lambda_p \approx \lambda_{op}$. This can be achieved by the application of a reverse bias voltage, V_{det} , utilizing the QCSE. However, the reduction in α_{MQW} will reduce the gain in efficiency. As an alternative, T_{op} can be increased, which has no effect on α_{MQW} . This reduces the dependence on the QCSE

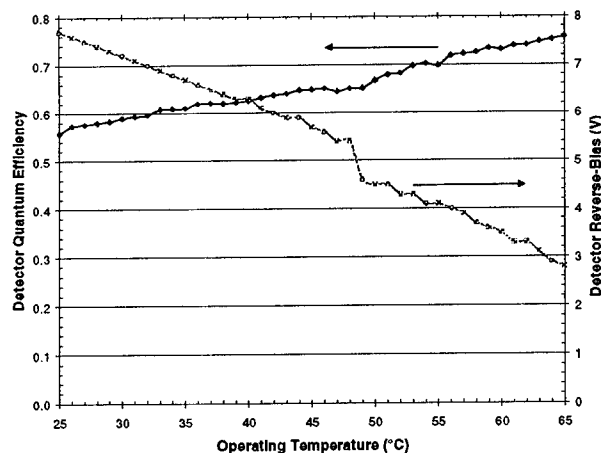


Figure 2 – Optimal $\eta_{detector}$ versus T_{op}

to achieve the required shift in λ_p , which increases efficiency. It is apparent that the detector will be more efficient at higher operating temperatures, provided that λ_o is not shifted past λ_{op} . Figure 2 plots the optimal detector efficiency (with the corresponding optimal V_{det}) versus T_{op} . The efficiency of the detector increases monotonically over the entire range of the temperature axis.

Systems using both QCSE Modulators and Detectors

For a QCSE modulator-detector combination, the overall figure of merit can be taken as the product of the individual figures of merit: [3]

$$\eta_{combined} = \eta_{modulator} \times \eta_{detector} \quad (2)$$

In combination, the parameters V_{pb} and V_{det} can be selected to optimize the combined efficiency for a given T_{op} , which is common to both devices. Based on the previous sections it is clear that, for modulators and detectors utilizing the same structure, the temperature ranges corresponding to highest efficiency for the modulator and detector will not be the same.

A plot of combined efficiency versus T_{op} is a point-wise multiplication of figures 1 and 2, and the general characteristics will be dominated by the modulator over the displayed temperature range. The optimal operating parameters for the system fall within the range:

$$\begin{array}{lll} T: & 35^\circ\text{C} & \text{to } 45^\circ\text{C} \\ V_{pb}: & 0.8\text{ V} & \text{to } 1.6\text{ V} \\ V_{det}: & 5.7\text{ V} & \text{to } 6.8\text{ V} \end{array}$$

Within the ranges specified above, the combined efficiency can be kept near 0.30.

IV. References

- [1] A.L. Lentine et. al., "High-Speed Optoelectronic VLSI Switching Chip with > 4000 Optical I/O Based on Flip-Chip Bonding of MQW Modulators and Detectors to Silicon CMOS", *IEEE J. Select. Topics Quantum Electron.*, vol. 2, no. 1, p. 77, 1996.
- [2] D.A.B. Miller et. al., "Electric Field Dependence of Optical Absorption near the Bandgap of Quantum-Well Structures", *Phys. Rev.*, vol. B32, pp. 1043-1060, 1985.
- [3] D.T. Neilson, "Optimization and Tolerance Analysis of QCSE Modulators and Detectors", *IEEE J. Quantum Electron.*, vol. 33, no. 7, p. 1094, 1997.
- [4] G.D. Boyd et. al., "Wavelength Optimization of Quantum-Well Modulators in Smart Pixels", *Appl. Opt.*, vol. 34, no. 2, p. 323, 1995.

Smart Pixels

Thursday, 23 July 1998

ThA: Circuits and Interconnections I
ThB: Circuits and Interconnections II
ThC: Architectures and Applications

Thursday Papers Not Available

- ThB1 CMOS Circuits for Switching and Processing,
H. Scott Hinton, Colorado Univesity, Boulder, CO
- ThB2 Mixed Signal Circuits VLSI Smart Pixels,
*Martin Brooke, Georgia Institute of Technology,
Atlanta, GA*
- ThC1 CMOS DSP and Microprocessor Cores Using
Optoelectronic VLSI, *Fouad Kiamelev,
University of North Carolina, Chapel Hill, NC*

Solving the interconnect bottleneck Optoelectronic FPGAs

Jan M. Van Campenhout*
Department of Electronics and Information Systems
University of Gent
Sint-Pietersnieuwstraat 41
B-9000 Gent, Belgium
Email jvc@elis.rug.ac.be

The term 'smart-pixel architectures' usually refers to systems that consist of optically connected electronic planes, having a regular two-dimensional structure, and in which the electronics form a high-performance array processing structure. In this paper, we use the term 'smart-pixel interconnect' to designate an optical interconnect that consists of a massive number of light sources or detectors placed on a two-dimensional grid, that interconnect to a similar array located on the surface of a neighboring chip. We do not imply any dedicated nature of the underlying electronics.

Such smart-pixel interconnects are being considered as a possible way to solve or alleviate the rapidly worsening interconnect problems of VLSI. These problems are caused by the decreasing feature sizes, leading to the deep sub-micron integration technology with $0.1\ \mu\text{m}$ feature sizes expected around 2006. The major problems anticipated are the steep increase of pin numbers required to connect these highly complex chips (40 million transistors per cm^2 for auto-layout Asics [1]) with their surroundings, and the relative shift of device speed versus interconnect speed due to scaling—interconnect becoming markedly slower than the gates interconnected. Smart-pixel interconnects, due to their area-I/O nature, offer far greater connectivity potential than bond wire perimeter I/O. And optical high-density inter-chip interconnect is demonstrably better on many counts than electrical interconnect, even at relatively short distances [2, 3].

In well-designed simple circuits, wire lengths have a sharply decreasing distribution, that is, long wires are far less numerous than short ones. It is known that fast and complex circuits, in particular those of the 'random logic' sea-of-gates variety, have distributions that level off less rapidly, leading to a greater proportion of long wires on-chip, and to more pins for inter-chip interconnect.

Short wires are predominant at the lowest hierarchical systems levels—the so-called gate or logic levels. The latency of the interconnect at those levels is assumed to be small or negligible, and usually all latency is attributed to the gates rather than to the interconnect. The clock frequency driving synchronous circuits (the vast majority) critically depends on the worst-case combinatorial delay between flip-flops.

As a consequence of the relationship between wire length, wire count and hierarchical level, the introduction of a massive number of optical area I/O interconnects almost unavoidably results in a large fraction of them emerging at the logic circuit level. At that level, optical links are considered as mere replacements of the existing passive electrical, galvanic interconnects. Such a replacement is meaningful, provided that the properties of the optical interconnects are sufficiently similar (or better) than those of the electrical interconnects they replace. However, for the short-

*The following text presents results of the Interuniversity Attraction Poles Program IUAP IV-13, initiated by the Belgian State, Prime Minister's Service, Science Policy Office.

distance logic-level interconnects (which form the great majority of all interconnects in traditionally designed VLSI-circuits), this requirement is mostly violated. In their current state, optical interconnects are *not* superior to the short-distance on-chip electrical interconnects in VLSI systems; in particular both the required on-chip area and the resulting latency of the optical interconnect are worse than that of short-range metal-1 interconnects. The blind replacement of a large number of these interconnects by optical ones will therefore not be a meaningful use of optical interconnects.

Of course, this pitfall can be avoided or circumvented by designing architectures in such a way that (massive) optical interconnects emerge at higher levels in the system's hierarchy, where their beneficial properties are more prominent than their harmful ones. Typical examples of such architectures are optically interconnected computer systems (system-level interconnect), highly parallel processor-memory interconnects (at the Processor/Memory/Switch PMS-level), or inside special architectures such as the firehose architectures ([4], R/T-level interconnect). In these particular uses of optical interconnects for instance, latency hiding techniques ensure that the link-level latency of the optical interconnect is relatively unimportant, and does not detract from the advantages of high bandwidth and massive parallelism with its associated low packet-level latency.

So one might rightfully ask whether there is any meaningful use at all of massive gate-level optical interconnects in general circuits. It turns out that a very interesting perspective is created by the special class of general-purpose components called *programmable logic*. This economically important component class, in particular the sub-class of field programmable gate arrays (FPGAs), is typically used to implement designs at the logic or gate level. FPGAs are typically used as a substitute for custom chips to implement random logic in relatively small or quickly changing product series. Other applications are multi-FPGA rapid-prototyping environments for VLSI design, or re-configurable coprocessor structures in general purpose computing environments.

Due to their programmability, FPGAs are slower, and can only harbor circuits of lower complexity than custom integrated circuits. Furthermore, complex designs typically require several interconnected FPGAs for their realization; a lack of interconnect capacity, either intra-FPGA or inter-FPGA is a well known bottleneck in such applications. These facts, and the additional property that the internal structure of FPGAs is geometrically very regular, appear to blend very well with the properties of smart-pixel like optical interconnects.

The presentation will address in more detail the properties of (multi-)FPGA circuits that make them into ideal candidates to benefit from smart-pixel optical interconnects. Some research work going on in this field at the University of Gent [5] will be presented.

References

- [1] SIA semiconductor Industry Association, 1997, *The National Technology Roadmap for Semiconductors*.
- [2] Miller, D., and Ozaktas, H., 1997, Limit to the bit-rate capacity of electrical interconnects from the aspect ratio of the system architecture, *Journal of Parallel and Distributed Computing*, 4, pp. 42—52.
- [3] Yayla, G., Marchand, P., and Esener, S., 1997, Energy and speed analysis of digital electrical and free-space optical interconnections, *Optical Interconnections and Parallel Processing: The Interface*, edited by A. Ferreira and P. Berthome (Kluwer, to appear).
- [4] Krisnamoorthy, A., and Miller, D., 1997, Firehose architecture for free-space optically interconnected VLSI circuits, *Journal of Parallel and Distributed Computing*, 41, pp. 109—114.
- [5] Depreitere, J., Van Marck, H., and Van Campenhout, J., 1997, A quantitative analysis of the benefits of the use of area-I/O pads in FPGAs, *Microprocessors and Microsystems*, 21, pp. 89—97.

1 Gb/s Single-Beam Smart-Pixel Receiver/Transmitter Realized in Hybrid MQW-CMOS OE-VLSI Technology

T. K. Woodward, A. V. Krishnamoorthy, K. W. Goossen, J. A. Walker, B. T. Tseng, J. E. Cunningham, R. E. Leibenguth, W. Y. Jan

Bell Laboratories, Lucent Technologies, Holmdel, NJ 07733

Smart pixel systems are enabled by high-speed, low-power, physically compact receivers. Using an optoelectronic-VLSI technology capable of low-parasitic flip-chip integration between GaAs multiple-quantum well (MQW) modulator/detectors and CMOS electronics,¹ we have previously described CMOS receivers intended for these applications, as well a performance metric that includes the criteria of sensitivity, area, and power consumption.² To date, 1 Gb/s performance in a single-beam photo-receiver of this type has not been reported, while such performance has been available for some time in two-beam receivers. This is due to the difficulties associated with realizing single-beam, dc-coupled photoreceivers with simple feedback elements. Single-beam receivers are particularly desirable for certain applications, particularly those based on fiber transport, such as local area networks (LAN). Here, we describe operation to 1 Gb/s of two types of dc-coupled single-beam photo-receiver, enabled by higher-performance 0.35 micron linewidth CMOS technology.

a diode-connected p-FET stabilizes, broadens, reduces, and offsets its gain.³ The geometry of all three gain stages (their W/L ratios) are identical (2:1 P:N sizing was used), thereby providing improved matching across process variations. The operating characteristics of the receivers are determined exclusively by the supply bias, the gate voltage and geometry of the feedback FET, and the geometry of the diode-loading FET in the second stage. The interaction between feedback FET Q8 and gain-broadening FET Q5 is critical.

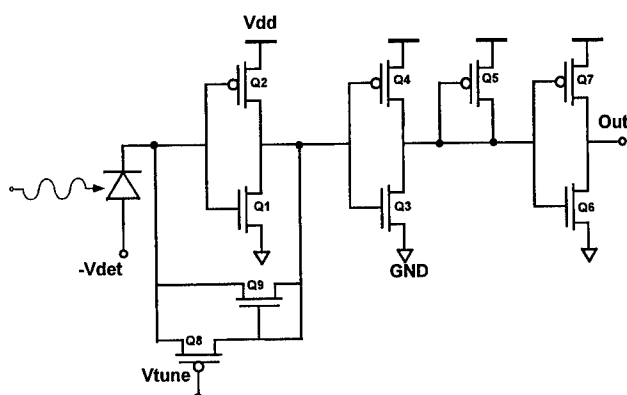


Figure 1: Schematic of basic receiver design. Q1, Q3 and Q6 all equal size. Q2, Q4, Q7 all equal size.

A schematic of a basic receiver of this type is shown in Fig. 1. Note the first two stages of the receiver are intended to provide analog gain for the photo-diode signal, while the final is intended as an asynchronous decision circuit. Cascaded inverters following the final stage drive a pair of MQW modulators used to communicate signals off-chip via interrogation by an external 850 nm readout laser. To improve stability, transimpedance feedback is employed only about the first stage, while shunt feedback of the output to Vdd in the second stage with

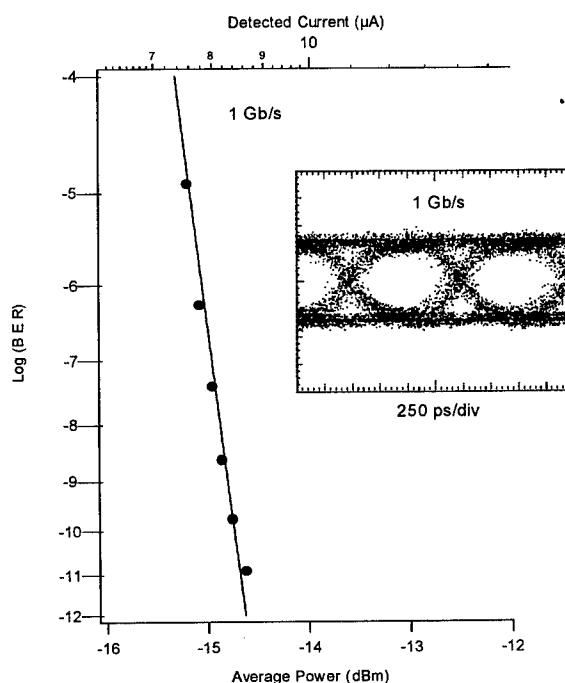


Fig. 2. BER and eye-diagram at 1 Gb/s for Fig. 1 receiver.

The bit error rate (BER) and eye pattern of a receiver of the type shown in Fig. 1 is shown in Fig. 2. The bias conditions were $V_{dd} = 3.6$, $V_{det} = -5.2$, and $V_{tune} = -1.750$ V. The average detected current required is also shown. At the indicated detector bias, responsivity was about 0.25 A/W, which is roughly a factor of two reduced from that typically obtained in our MQW devices. When biased to higher voltages, a responsivity of 0.5 A/W could be obtained, but receiver operation was degraded, possibly due to excess leakage. This is supported by our observation

that the receiver worked with reduced photocurrent as detector bias was dropped.

At a supply voltage of 3.3 V, designs of the type shown operated to 800 Mb/s. To obtain 1 Gb/s operation, it was necessary to increase the supply voltage to 3.6 V, which we believe is necessary to create the proper interaction between the first two stages of the receiver. At 3.6 V, an exemplary version of such a receiver draws 2 mA of current, leading to a power consumption of roughly 7 mW. At 3.3 V, dissipation decreases to about 5 mW. Subsequent designs along these lines have operated to 1 Gb/s with reduced supply voltages.⁴

A variation on the design in which the photo-detector is returned to a positive supply has also been realized and operated to 1 Gb/s, albeit with somewhat degraded sensitivity (24 micro-amps input current, or -10.2 dBm). In such a design, the diode-connected feedback element Q5 is now a n-type FET connected between second stage output and ground. If needed, the final stage decision circuit may be made with different W/L ratios from the first two. In either design, the diode-connected clamping FET connected in parallel with the feedback resistor is there for dynamic-range enhancement as described elsewhere,⁵ although it appears that this element has limited utility in receivers with a second analog gain stage.

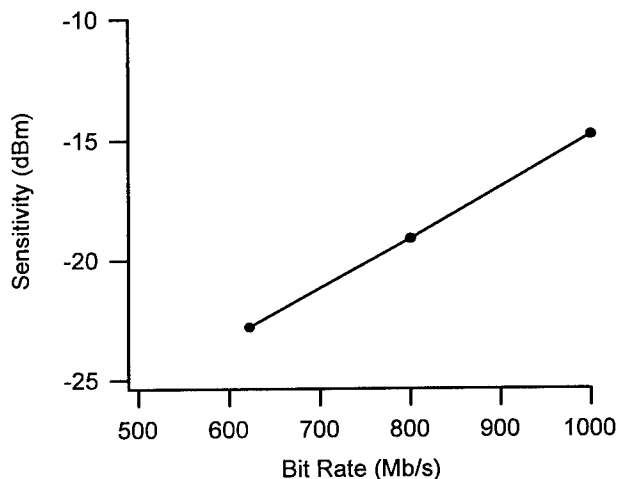


Fig. 3. Sensitivity vs. bit-rate for the receiver of Fig. 1.

The sensitivity vs. bit-rate between 622 Mb/s and 1 Gb/s for the receiver from Fig. 1 are shown in Fig. 3. The layout area consumed by the circuit is 253 square microns. For an OE/VLSI application, one wishes to minimize the $SPA^{1/2}$ product, where S is sensitivity (dBm), P is power dissipation (dBm), and $A^{1/2}$ is the square root of the layout area (in dBum).² This is shown in Fig. 4, along with our previous best reported values for these data rates from a two-beam 0.8 micron CMOS receiver.² We find the reported receiver to be at least 10 dB better at all rates. However, it should be noted that the dynamic range of this receiver is quite low, in contrast to the large values typically obtained from two-beam receivers.

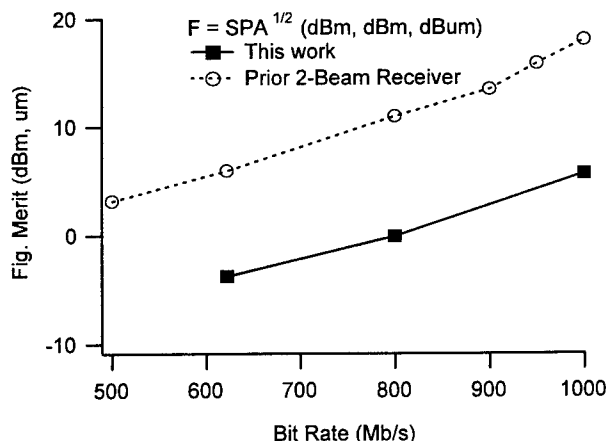


Fig. 4. Figure of merit comparison between this work and prior 2-beam receiver made in 0.8 micron CMOS.

In conclusion, we present the first operation of an OE/VLSI compatible single-beam receiver-transmitter pair operating to 1 Gb/s. The circuits were realized in 0.35 micron CMOS and hybridized via a flip-chip bonding technique to an array of 850 nm MQW modulator/detectors.

Lucent Technologies' 0.35 micron production CMOS was used for this work, and the authors are pleased to acknowledge D. Inglis for his help in accessing the technology.

¹ K. W. Goossen, J. A. Walker, L. A. D'Asaro, S. P. Hui, B. Tseng, R. E. Leibenguth, D. Kossives, D. D. Bacon, D. Dahringer, L. M. F. Chirovsky, A. L. Lentine, D. A. B. Miller, "GaAs MQW Modulators integrated with Silicon CMOS", IEEE Phot. Tech. Lett. V. 7 pp. 360-362, 1995.

² T. K. Woodward, A. V. Krishnamoorthy, A. L. Lentine, L. M. F. Chirovsky, "Optical Receivers for Optoelectronic VLSI", IEEE J. Spec. Topics in Quant. Electr. V. 2 no. 1, pp. 106-116, 1996.

³ G. Williams, "Lightwave Receivers" in Topics in Lightwave Systems Tingye Li, ed. (Academic Press, 1991) pp. 79-148. ISBN: 0-12-447302-4.

⁴ T. K. Woodward, A. V. Krishnamoorthy, "1 Gb/s CMOS Photo-Receiver with Integrated Detector Operating at 850 nm", submitted to Electr. Lett.

⁵ A. V. Krishnamoorthy, A. L. Lentine, K. W. Goossen, J. A. Walker, T. K. Woodward, J. E. Ford, G. F. Aplin, L. A. D'Asaro, S. P. Hui, B. Tseng, R. Leibenguth, D. Kossives, D. Dahringer, L. M. F. Chirovsky, D. A. B. Miller, "3-D Integration of MQW Modulators over active submicron CMOS circuits: 375 Mb/s Transimpedance Receiver-Transmitter Circuit" IEEE Phot. Tech. Lett., v.7 pp. 1288-1290, 1995.

Automated Design of ICs with Area-Distributed I/O Pads

Richard Rozier, Ray Farbarik*, Fouad Kiamilev, Jeremy Ekman, Premanand Chandramani,
Ashok Krishnamoorthy**, and Richard Oettel*

University of North Carolina at Charlotte 9201 University City Blvd., Charlotte, NC 28223

*Duet Technologies

**Bell Labs, Lucent Technologies

1 Introduction

Recent developments in the silicon CMOS integrated circuit (IC) industry have focused heavily on packaging and interconnect technology. A large amount of research has been done to develop free-space optical interconnects (FSOI) -- ICs that have light producing and detecting devices attached to them. These devices establish data communication using light refractive, diffractive, or reflective optics [1]. Designs with up to 2000 I/Os are being produced [2]. In addition, designs with area-pad I/Os have higher performance since the chip-to-chip connection is made through optical devices [3]. Thus, the trend for future implementations of digital IC systems is to use ICs with area-pad I/Os.

VLSI CAD tools have evolved also. Several CAD tool suites offer extensive CMOS transistor layout and analysis programs. However, the software has not completely kept up with the advances in packaging technology. Very few CAD tools possess the ability to place and route area-distributed I/O signals. One of these exceptions is Duet Technologies' CAD tools "Epoch" and "Eggo". Epoch performs traditional CMOS transistor placement, routing, and analysis, and Eggo places the area pads and routes the signals.

In this paper, we present a methodology that incorporates Epoch and Eggo into the IC design flow for area-pad implementation. This method includes creation of an area-pad package description, inclusion of a cell library, building an HDL description netlist of the design that includes area-pads, and execution of the place and route tools.

2 Procedure

The procedure begins with creation of a package file for integration with Epoch. Area pads are generally placed in a gridded manner. A package description file enables the designer to specify the exact location of each pad. From this file, the positioning and layout of the pads will then be read by the physical design tools.

Cell libraries need to be included in the design of the chip. Often, custom circuits are built to provide additional functionality to the present library of cells. Specifically, the input and output buffers for the area pads need to be designed and incorporated into the library offering. Also, the actual area pad is merely a square of metal (usually in the top layer of metal) with a glass cut over it. It can be drawn to any size depending on the requirements of the interconnect method. These special circuits tend to be updated as the technology advances.

Using our methodology, these special circuits need to be brought into the Epoch environment using "cell importation." Once assimilated into the database, the physicals can be used by any of the Epoch operations, namely automatic placement and routing to other components. The area pad physical is created in a manual-layout CAD tool and then converted to GDSII data format. After the library part has been imported, as described in Epoch's User Manual [4], it can then be instantiated in the HDL netlist, just like any other component. This procedure has to be followed for both input area pads and output area pads.

The library import capability allows invaluable flexibility. The importer can also utilize special power rails to optoelectronic devices which might enable the area pad router to be more efficient. Optoelectronic devices typically require two pads -- one for power (Vdd) and one for the signal. When they are placed in a grid, as shown in Figure 2, all the power pads appear in the same row. Therefore, power can be routed by shorting all the power pads together with one power rail. The easiest way to do that is to create two different area pad components -- one normal signal pad and one pad that has a power rail included. This is shown in Figure 18. Since the power rails in an optoelectronic area pad design are a fixed piece of geometry, it is better to create them as a single, long strip of area power ports. This would in turn reduce the number of signals that the area-pad router needs to route.

IC designers create the designs of their chips using many different methods. One manner is to describe the design using a HDL description. Using our methodology for area pad designs, this HDL description may be in the structural form of either a Verilog or a VHDL netlist. Each area pad needs to be declared and included as a component. The key to including area pads in the HDL netlist is the attributes declared with each pad. These attributes describe the type and number of the pad. One drawback to this approach is that each pad needs two attributes in addition to the instantiating. Therefore, each pad requires at least four lines of HDL code. Area pad designs could have from 400 to 1,000

pads, leading to between 1,600 and 4,000 lines of HDL code. It would not be practical to type in 4,000 lines of code (especially without error). As a result, a custom-designed Perl or C-language program might be needed to generate the voluminously repetitive lines of VHDL code.

The physical design tools for area pad designs need to operate at two levels: the main circuitry of the design (also called the "core") and at the area pad level of hierarchy. These two areas are separate, yet interdependent, of one another. Using our methodology, the main components of the software operation are the Epoch executables and Eggo router. Epoch include programs to perform hierarchical placement, routing, and buffer sizing. Epoch completes the physical design of all levels within the subblocks. Afterwards, Eggo places the area pads and routes them to the rest of the design.

3 Results

To test the methodology presented in this paper, we applied it to the design of a DSP circuit that performs a multiply-accumulate (MAC) function, like so: $d = a * b + c$. The circuit contains approximately 21,000 transistors, and has 400 area pads with 44 perimeter pads. Layout was performed in Hewlett-Packard's HP14B 0.5 μ m, 3.3V ruleset. The circuit was fabricated on Bell Labs' 1997 CMOS-MQW foundry. To illustrate the improvement with the new methodology, we compare it with previously used approaches. In Figure 1 is a snapshot (metal 3 only) of an SRAM designed with a manual layout technique. In Figure 2 is a snapshot (metal 3 only) of the MAC designed using Epoch and Eggo. For the SRAM, we found that the average wiring length from pad to buffer was 400 μ m. Using Eggo, that length dramatically shortened to 100 μ m. Shorter wiring length in VLSI will increase the maximum operating frequency of a circuit, since for sub-micron designs the majority of the timing delay from gate to gate is in the interconnect. In addition, placing the buffer close to its associated pad will help prevent corruption of the signal between the detector and its receiver. Finally, our new methodology provides an effective means to automating the layout process and shortening the design cycle while maintaining high performance in IC operation.

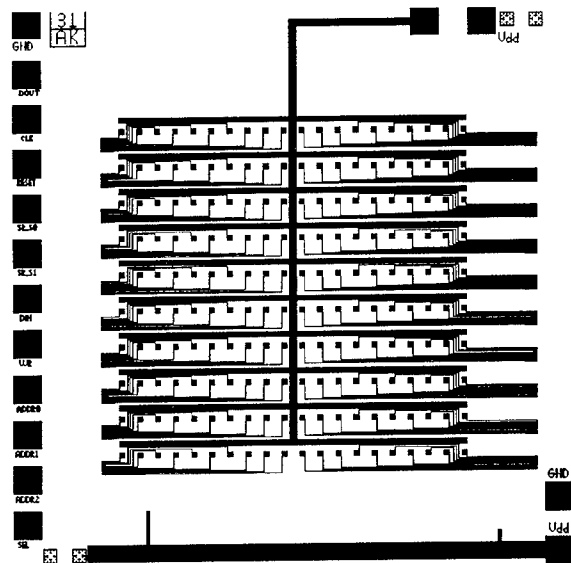


FIGURE 1. Layout of an SRAM using manual layout methods (M3 only)

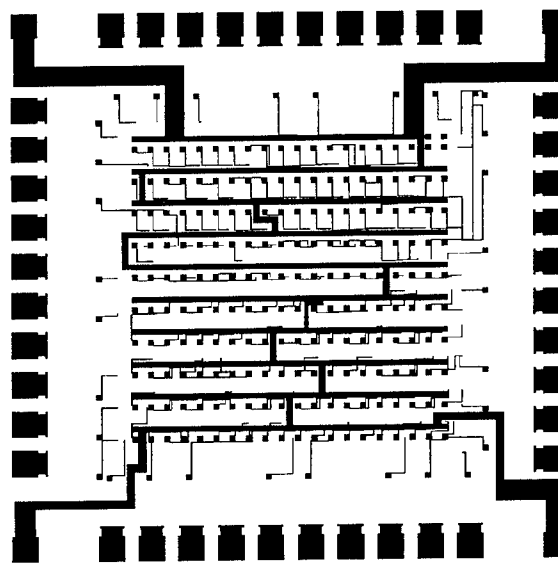


FIGURE 2. Layout of a MAC using automated layout methods (M3 only)

References

- [1] MPPOI'96, *Proceedings of the Third International Conference on Massively Parallel Processing using Optical Interconnects*, IEEE Computer Society, Gottlieb, A., Li, Y., Schenfeld, E., editors, Los Alamitos, CA, Oct. 27-29, 1996.
- [2] A. V. Krishnamoorthy, et al, "The AMOEBA Chip: An Optoelectronic Switch for Microprocessor Networking Using Dense-WDM", *Proceedings of MPPOI 1996*, IEEE Computer Society, Gottlieb, A., Li, Y., Schenfeld, E., editors, Los Alamitos, CA, Oct. 27-29, 1996, pp. 94-100.
- [3] T. K. Woodward, et al, "1Gb/s two-beam transimpedance smart pixel receivers made from hybrid GaAs MQW modulators bonded to 0.8 μ m silicon CMOS", *IEEE Photonics Technology Letters*, vol. 8 no. 3, March, 1996, pp. 422-424.
- [4] *Epoch User's Manual*, Duet Technologies Corporation, Bellevue, WA, 1997, pp. 5-1 - 5-113.

ThA4
9:30am - 9:45am

3D Stacked Si CMOS VLSI Smart Pixels Using Through-Si Optoelectronic Interconnections

Steven W. Bond, Sungyong Jung, Olivier Vendier, Martin A. Brooke, Nan M. Jokerst
School of Electrical and Computer Engineering
Microelectronics Research Center & NSF Packaging Research Center
Georgia Institute of Technology; Atlanta, GA 30332-0269
Tel. 404-894-9918 Fax. 404-894-0222
Email: sbond@azalea.mirc.gatech.edu

A fundamental limitation of smart pixel systems is the interconnection of the pixels to a high level of Si signal processing circuitry. Often, the limited Si area under or surrounding each pixel is insufficient for a high level of Si CMOS VLSI signal processing. Interconnection to more Si circuitry could enable a higher level of signal processing associated with each pixel. However, interconnection of more than two vertically stacked layers of functional Si CMOS signal processing circuitry with vertical optical interconnections has never before been demonstrated. This is essentially an interconnection problem, which is a limitation that also plagues electronic systems [1]. Three dimensionally interconnected systems with vertical optical interconnections can offer solutions to these fundamental electrical interconnection limitations. For example, one such limitation, latency, plagues even highly advanced electrical interconnection technologies such as MCM and HDI interconnection substrates [2]. Architectures in which a critical data path can be routed in three dimensions (to circuit layers above or below) can minimize the path length, and, since the signal is transmitted near the speed of light, the delay usually associated with long electrical interconnections can be reduced. Further, although MCMs enable a high level of electrical interconnection, they are not scalable with increasing interconnection densities and system size [3]. Thus, enabling 3D smart systems using vertical optical interconnections can have profound effects upon electronic and smart pixel signal processing systems. One example of a smart pixel system that utilizes a 3D through-Si vertical optical interconnection for processing of image data from a focal plane array is shown in Figure 1 [4,5].

This paper reports the first demonstration of a three layer, 3D vertically optically interconnected Si smart pixel system. Three layers of standard foundry Si CMOS VLSI circuits, each integrated with long wavelength thin film emitters and detectors (to which the Si is transparent), have been stacked to realize a three dimensional system with optical interconnections between the layers. Each circuit operates both electrically and optically, and optical communication between the three layers has been demonstrated up to speeds of 1 Mbps.

Each hybrid smart pixel Si CMOS VLSI integrated circuit contains analog components designed for implementation in any digital Si CMOS process. Each circuit contains a transmitter capable of DC and AC modulation currents up to 120 mA, a receiver operating in an open loop mode with current gain of 243, and a clocked comparator for data regeneration to digital levels. Hybrid integration of thin film InP/InGaAsP/InP LEDs ($\lambda=1.3\mu\text{m}$) and InAlAs/InGaAs/InAlAs MSM photodetectors was used to create the smart pixel integrated optoelectronic circuit (OEIC) [6,7]. Each of the three OEICs in the stacked system was assembled with silicon support pieces to provide mechanical support during wire bonding of the 3D system. The individual layers were aligned using an IR backplane alignment feature of a Karl Suss mask aligner. After all three layers were assembled and attached using an UV and heat curing epoxy, the system was packaged into a 144 pin ceramic pin grid array. Figure 2 shows a photomicrograph of the packaged system.

To demonstrate the vertical optical interconnections in the 3D smart pixel three layer Si CMOS circuit stack, the integrated transmitter and receiver circuits were tested. The vertical communications link between the middle and top layer operated at 1 Mbps with bit error rates of 1×10^{-9} with a PRBS of 2^7-1 . An infinite persistence receiver eye diagram at 1 Mbps for this channel is shown in Figure 3. The bottom to middle chip channel suffered from decoupling problems in the test network, and functioned at speeds up to 100 kHz. Although the bottom optical communication channel did not operate with low noise, the clean operation of the top channel indicates that, with adequate off-chip decoupling in the bottom channel, that the system will produce high quality operation in both of the vertical optical communication channels.

We have presented the first demonstration of an optically interconnected three dimensional smart pixel system connecting three stacked layers of Si CMOS VLSI circuitry. We have demonstrated vertical optical communication between three CMOS circuit layers with operation speeds up to 1 Mbps. This system demonstrates the viability of implementing optical interconnections for scalable 3D interconnection systems for ultra-smart pixel applications.

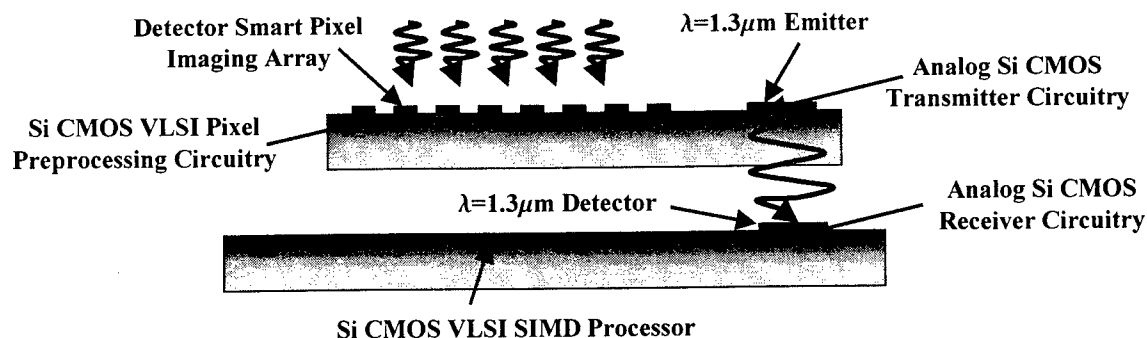


Figure 1: Smart Pixel Focal Plane array with VLSI Processing and Through-Si Interconnection

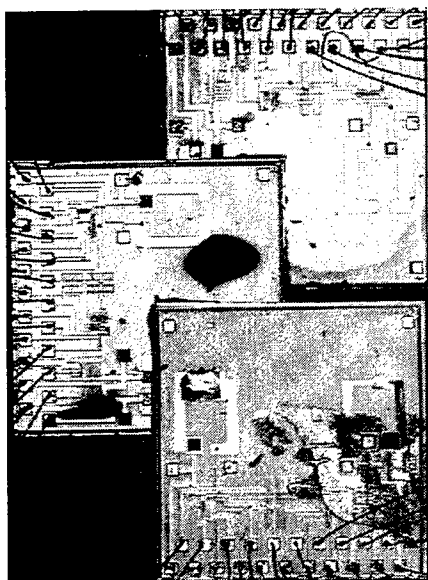


Figure 2: Photograph of the tested three-layer stack with layers focused individually.

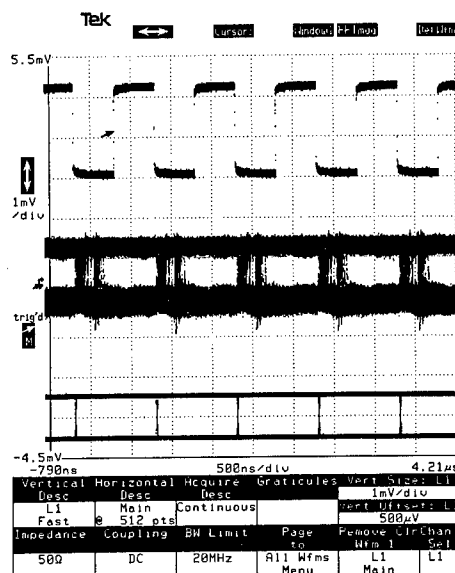


Figure 3: 1Mbps Infinite persistence eye diagram from the output of the top-chip receiver.

- 1 J.D. Meindl, "Gigascale integration: Is the sky the limit?" *Circuits and Devices*, pp.19-32, November 1996.
- 2 N. Awaya, Y. Arita, H. Inokawa, T. Kobayashi, "Copper interconnection technology for silicon large scale integrated circuits," *NTT R&D*, vol. 45, no. 4, pp. 373-378, 1996.
- 3 R. Senthinathan, J.L. Prince, and A.C. Cangellaris, "Module frequency and noise budget limitations/tradeoffs in multi-chip modules as a function of CMOS chips integration," *Thirteenth IEEE/CHMT International Electron. Manuf.*, Baltimore, MD, pp. 348-352, Sept., 1992.
- 4 H.H. Cat, A. Gentile, J.C. Eble, Myunghee Lee; O. Vendier, Young Joong Joo; D.S. Wills, M. Brooke, N.M. Jokerst, A. Brown, "SIMPil: an OE integrated SIMD architecture for focal plane processing applications," *Proceedings of the 3rd Intern. Conf. on Massively Parallel Processing Using Optical Interconnections*, pp.44-52, 1996.
- 5 YoungJoong Joo, S. Fike, Kee Shik Chung, M. Brooke, N.M. Jokerst, D.S. Wills, J. Goodman, S. Hinton, T. Pinkston, E. Schenfeld, "Application of massively parallel processors to real time processing of high speed images," *Proceedings of the 4th Intern. Conf. on Massively Parallel Processing Using Optical Interconnections*, pp.96-100, 1997.
- 6 O. Vendier, M. Lee, N.M. Jokerst, M.A. Brooke, R.P. Leavitt, "Integrated 200 Mbit/s receiver: silicon CMOS transimpedance amplifier with a thin film InGaAs photodetector", *CLEO '96, Conference on Lasers and Electro-Optics*, Anaheim, CA, Vol.9. pp.402-3, 1996.
- 7 S.W. Bond, M. Lee, J.J. Chang, O. Vendier, Z. Hou, M. Brooke, N.M. Jokerst, and R.P. Leavitt, "An Integrated 155 Mbps Digital Transmitter Using a 1.3μm Wavelength Thin Film LED," *9th Annual Conference of Lasers and Electrooptics Society*, vol. 1, pp.342-3, November, 1996.

1 Gb/s CMOS Optical Receiver with Integrated Detector Operating at 850 nm

T. K. Woodward, A. V. Krishnamoorthy

Lucent Technologies, Bell Laboratories, Holmdel, NJ 07733

As the performance of complementary metal oxide silicon (CMOS) integrated circuits improves, the interest in using it for applications in optical communications has risen, particularly for cost-sensitive applications such as optical interconnect and local area networks (LAN). For these applications, operation at wavelengths near 850 nm is of interest, because of the ready availability of optical sources, with rapidly increasing demands on the data rates. The use of high-volume, low-cost production CMOS processes for such applications is naturally desirable. Here we describe the first (to our knowledge) 1 Gb/s operation of a fully integrated CMOS optical receiver made in a standard production 0.35 micron linewidth CMOS process at a wavelength of 850 nm.

Several workers have identified the slow response times of integrated CMOS photo-detectors as the major obstacle to high-speed fully-integrated Silicon-based receivers.^{1,2,3} Kuchta, et al. have employed the buried collector of a BiCMOS process to screen bulk-generated carriers arising from long absorption depths in Si at 850 nm to make a detector that sacrifices responsivity for speed. Here, we use a similar concept based on the n-well of a standard CMOS process, holding it to a fixed potential while intra-well p-diffusions define the active contact of the detector.³ This terminal is connected to the input of a CMOS multi-stage receiver similar in design philosophy to previously described smart-pixel receivers.⁴

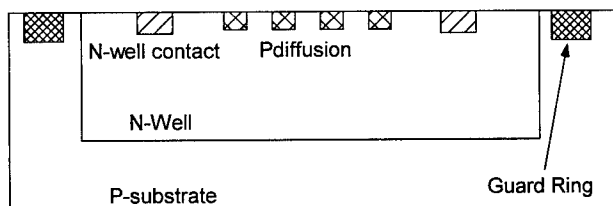


Fig. 1 Cross-section of detector structure. Guard ring is grounded, N-well is tied to detector bias (positive), and p-diffusion is connected to amplifier.

A cutaway sketch of our detector structure is shown in Fig. 1. The n-well region in which the detector was made measures 16.54 x 16.54 micron, and is surrounded by a grounded p⁺ guard ring. Inside the n-well an interdigitated network of p-diffusion fingers forms the active terminal of the detector. The n-well is tied to the detector bias and is intended to screen the active terminal from the slowly-responding bulk-generated carriers.

0-7803-4953-9/98\$10.00©1998 IEEE

The photo-receiver circuit is shown in Fig. 2, and consists of three stages. The first stage (Q1-Q2 in Fig. 2) is an inverter-based transimpedance stage, using a p-type FET as the feedback element. The gate voltage of this FET can be adjusted for optimum performance at a given bit rate and optical power. The second stage (Q3-Q4) is identical in size (W/L ratio) to the first, with a diode-connected n-FET load (Q5) added to reduce, broaden, and stabilize the gain and switching threshold of this stage.⁵ The final stage is a high-gain inverter acting as an asynchronous decision circuit, again identical in geometry to the first two stages. The interaction between Q5 and Q8 is key to the operation of the circuit, defining respectively the first stage transimpedance and the switching offset between the analog gain stages and the decision circuit necessary to permit single-beam dc-coupled operation.

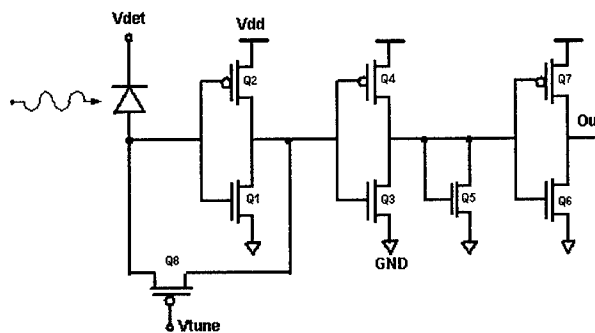


Fig. 2 Schematic of receiver circuit. All transistor gate lengths are 0.35 micron. Gate widths of Q1, Q3, and Q6 are equal, as are widths of Q2, Q4, and Q7. Output is digital logic level.

Following the preamplifier are digital logic elements designed to generate zero-skew differential output signals, as described by Weste, et al.⁶ These complementary digital signals are then applied to a source-follower-based off-chip driver circuit (Fig. 3). The entire circuit was fabricated in Lucent Technologies' 0.35 micron production CMOS process (non-silicided) and wire bonded into in a ceramic pin-grid-array, housed for testing in a standard PC-board test fixture. Testing was done with directly modulated 850 nm lasers. Operation was measured to 1.25 Gb/s, with preamplifier supply voltages ranging from 1.8 to 3.3 V. Best sensitivity was obtained at a supply bias of about 2.3 V, which we attribute to interaction between the stages of the receiver. As optical power is reduced, the switching offset of the second stage must be adjusted, which can be accomplished by reducing the supply voltage. This permits reduction of the first stage transimpedance gain, thereby maintaining high

bandwidth operation. Reduced supply furthermore drops the off-chip drive voltage to roughly 40 mV, resulting in cleaner off-chip signaling, vs. about 125 mV at $V_{dd}=3.3$ V.

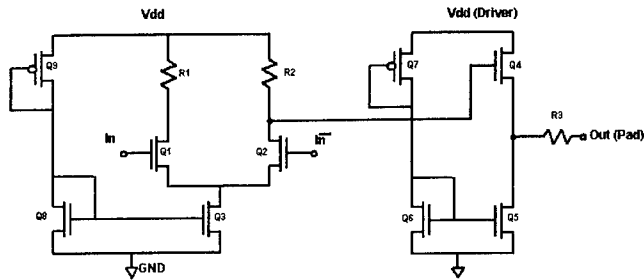


Figure 3 Off-chip driver schematic. Inputs are full logic-level signals generated by digital elements following the preamplifier.

The off-chip signal was amplified and low-pass filtered to 933 MHz prior to taking the bit error-rate and eye pattern data shown in Fig. 4. A bit error rate (BER) of 1×10^{-9} is obtained at an average optical input power of -6.3 dBm. The bias conditions for such operation were $V_{dd} = 2.2$, $V_{dd}(\text{driver}) = 3.2$, $V_{tune} = -0.86$, $V_{det} = 10$ V. Under these conditions while operating at 1 Gb/s, the current drawn from supply for two complete receivers including everything except the follower of Fig. 3 was 1.26 mA, suggesting a single receiver dissipation of less than 1.5 mW. At $V_{dd}=3.3$ V static dissipation increases to about 6 mW/receiver. The minimum BER obtainable at 1.25 Gb/s was 1×10^{-8} . The sensitivity of the receiver improves somewhat at lower bit rates, with a BER of 1×10^{-9} requiring an average input power of -8.6 dBm at 622 Mb/s, and -14 dBm at 155 Mb/s. The relatively high input optical powers required for these measurements can be attributed to the low responsivity of the shallow n-well detection region. Most of the carriers collected by the n-well originate in the substrate, with test diodes showing a responsivity at 850 nm of about 0.25 A/W. However, far fewer carriers are collected to the p-diffusion/n-well active diode, which exhibits a voltage dependent responsivity of between about 0.01 A/W and about 0.04 A/W near junction breakdown (≈ 10 V).

While the relatively high levels of average power required to operate these receivers may appear daunting, it should be noted that in many LAN and interconnect applications, optical power is not in short supply.

In summary, we present the first operation of a fully-integrated optical receiver made entirely within a standard production CMOS process, operating to 1 Gb/s at a wavelength of 850 nm. Our results bode well for the use of standard CMOS processes in new optoelectronic applications.

We are pleased to acknowledge the technical assistance of J. Salata and D. Inglis of Lucent Technologies.

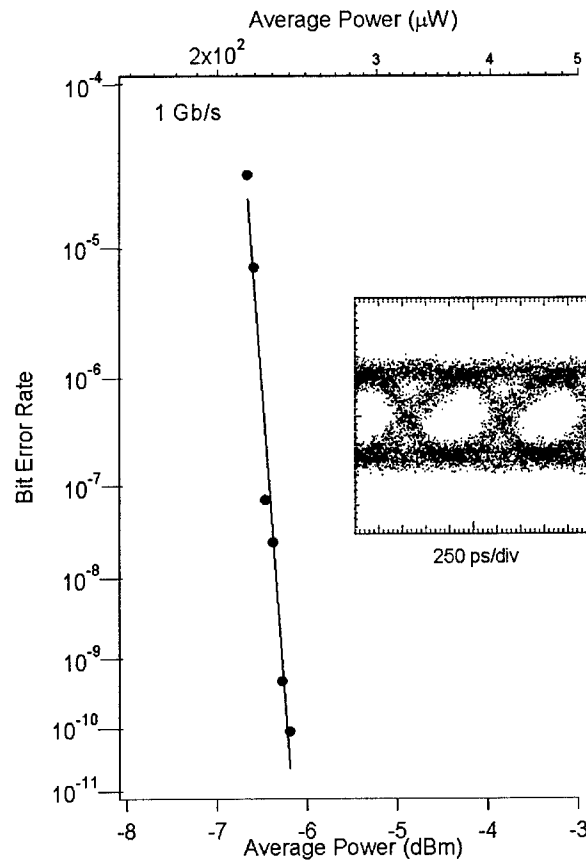


Figure 4 Bit Error Rate characteristics at 1 Gb/s and 850 nm from the receiver circuit. Inset: eye diagram obtained at 10 s persistence on sampling oscilloscope at a BER of 1×10^{-9} .

¹ D. M. Kuchta, H. A. Ainspan, F. J. Canora, R. P. Scheider, Jr. "Performance of fiber-optic data links using 670-nm cw VCSELS and a monolithic Si photodetector and CMOS preamplifier", IBM J. Res. Develop. v. 30, pp. 63-72, 1995.

² H. H. Kim, R. G. Swartz, Y. Ota, T. K. Woodward, M. D. Feuer, W. L. Wilson, "Prospects for Silicon Monolithic Opto-Electronics with Polymer Light-Emitting Diodes", Journal of Lightwave Technology, v. 12, pp. 2114-2121, 1994.

³ Philippe Lalanne, Jean-Claude Rodier, "CMOS photodiodes based on vertical p-n-p junctions", Workshop on Optics and Computer Science, Proceedings of the 11th International Parallel Processing Symposium, Geneva, Switzerland, April 1-5 1997

⁴ T. K. Woodward, A. V. Krishnamoorthy, A. L. Lentine, L. M. F. Chirovsky, "Optical Receivers for Optoelectronic VLSI", IEEE J. Special Topics in Quant. Electr., v. 2, pp. 106-116, 1996.

⁵ G. Williams, "Lightwave Receivers" in Topics in Lightwave Systems Tingye Li, ed. (Academic Press, 1991) pp. 79-148. ISBN: 0-12-447302-4.

⁶ Neil H. E. Weste and Kamran Eshraghian, Principles of CMOS VLSI Design (Addison Wesley, New York, 1993) ISBN 0-201-53376-6.

Second-Generation CMOS-SEED Smart Pixel Implementation of the Error Diffusion Neural Network

B. L. Shoop, R. W. Sadowski, G. P. Dudevoir, D. A. Hall, A. H. Sayles, and E. K. Ressler
Photonics Research Center and Department of Electrical Engineering and Computer Science
MADN-PRC, United States Military Academy, West Point, New York 10996
shoop@exmail.usma.edu

Smart pixel technology, which integrates optics and electronics technologies, provides the ability to realize novel signal processing architectures and functionality previously considered too difficult with a single technology. Smart pixel arrays provide the designer additional degrees of freedom by integrating electronic circuits, optoelectronic devices, and refractive, reflective, and diffractive optical components into a single compact architecture. These architectures simultaneously leverage the programmability and increased functionality of integrated electronic circuitry and the parallelism and high-speed switching of arrays of optoelectronic devices. Recently, we have investigated the application of smart pixel technology to the problem of a massively parallel, analog neural network for the purpose of achieving a specific image processing function known as digital image halftoning. Here, the input to the neural network is a high-resolution gray-scale image and the resulting output image is strictly binary. For optimum performance, this specific neural architecture requires symmetric, full-rank connectivity across the entire image in the form of an error diffusion filter. This massive interconnect requirement cannot be achieved with a purely electronic implementation. Smart pixel technology provides a means of implementing this massively parallel architecture while simultaneously enabling other signal processing features previously considered intractable.

In contrast to the majority of current smart pixel research, the research results reported here result from a mixed signal, analog and digital, application of smart pixel technology. The optoelectronic circuitry for a 5×5 error diffusion neural network was implemented in $0.5\mu\text{m}$ silicon CMOS technology and required the functionality of one-bit quantization, subtraction, neuron-to-neuron weighting and interconnection, and optical input and output. Figure 1 shows the circuitry associated with a single neuron of this error diffusion neural network implemented using CMOS-SEED smart pixel technology. Here, the one-bit quantizer is implemented using a wide-range transconductance amplifier operated in the subthreshold regime. The slope of this sigmoidal function was carefully designed by matching MOSFET transistors to meet the convergence criteria and the nonlinear dynamics of the error diffusion neural network.

Figure 2(a) shows the input-output relationship of the wide-range transconductance amplifier as well as the error signal that results from the input and output of the quantizer.

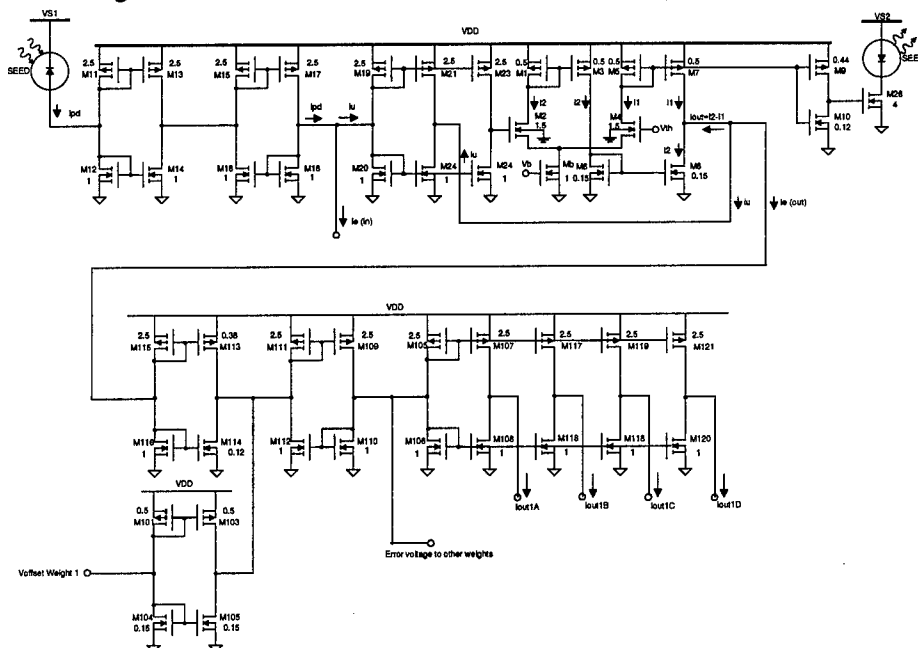


Figure 1. Circuit diagram of a single neuron and a single error weight of a 5×5 error diffusion neural network based on a CMOS-SEED-type smart pixel architecture.

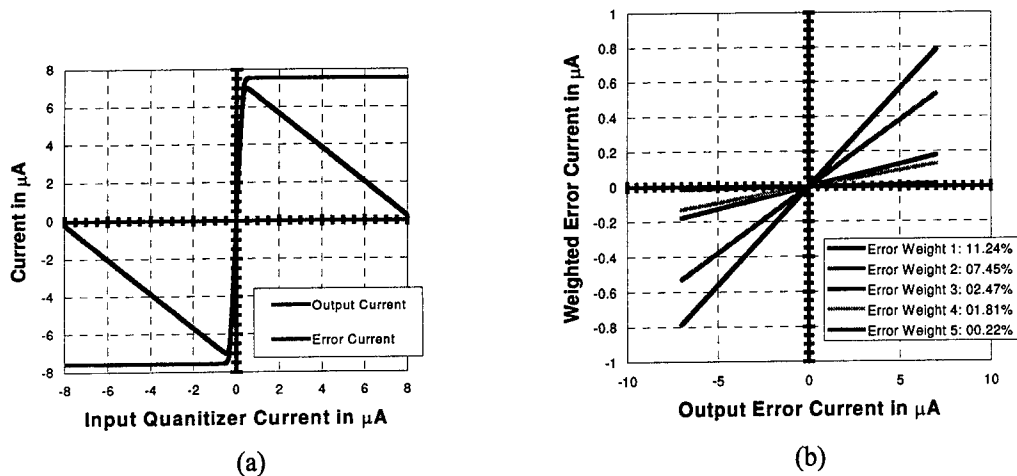


Figure 2. (a) Quantization and error relationship for the wide-range transconductance amplifier, and (b) Modeled linearity performance of the error weighting circuitry.

All state variables in this circuit are represented as currents and therefore the subtraction functionality was implemented using current summation techniques at specified nodes. For proof-of-concept demonstration only, the error weighting and distribution circuitry for the 5×5 array was implemented in silicon circuitry by designing and matching the width-to-length ratios of both the individual and stage-to-stage MOSFET transistors. Bi-directional error currents were implemented to provide the circuitry and the network with fully-symmetric performance. Figure 2(b) shows the linearity of each of the five unique interconnect weights over the entire operating range of the circuit. Optical input and output to each neuron was implemented using SEED multiple quantum well (MQW) modulators. The input MQW is reverse-biased and functions as an optical detector while the output optical binary signal is produced using a forward biased MQW which provides photoemission through electroluminescence.

The central neuron of the smart pixel array consists of approximately 160 transistors while the complete 5×5 array accounts for over 3600 transistors. The central neuron is interconnected to the surrounding 24 neurons in the 5×5 array using a fixed interconnect and weighting scheme. SPICE simulations of each of the functional components as well as the complete 5×5 nonlinear dynamical neural network were performed using transistor parameters extracted from a previous $0.5 \mu\text{m}$ MOSIS foundry run and have verified both functional operation as well as overall network performance. The quantization functionality was verified and resulted in a signum function with a slope of 14 while the linearity of each of the error weights was within 2% of the design specifications. Figure 3 shows the SPICE simulation for the performance of the complete 5×5 array to a linear input signal. As the input signal is linearly increased over the input dynamic range, the number of neurons in the on-state goes from zero to 25, representing the analog input level at any given time interval as the ratio of the number of neurons in the on-state to those in the off-state. The simulations also predict individual neuron switching speeds of less than $1 \mu\text{s}$ demonstrating the capability for real-time digital image halftoning.

Acknowledgments. This research was supported by the Army Research Office, the National Reconnaissance Office and the Defense Advanced Research Projects Agency through the Consortium for Optical and Optoelectronic Technology in Computing (CO-OP)

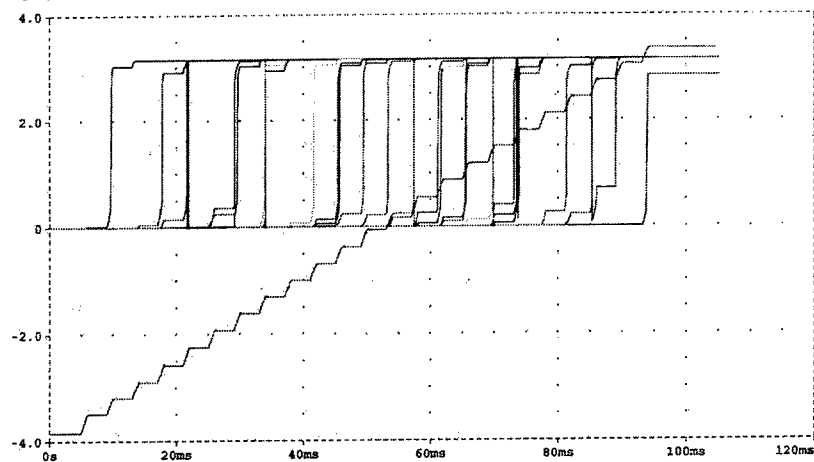


Figure 3. Dynamic performance characterization of the 5×5 error diffusion neural network to a stepped linear input.

Smart pixel with four-level amplitude or phase modulation

J.A. Breslin, J.K. Low and I. Underwood

The University of Edinburgh Department of Electronics and Electrical Engineering
The Kings Buildings Mayfield Road Edinburgh EH9 3JL UK
Tel +44 131 650 5652 fax +44 131 650 6554 email i.underwood@ee.ed.ac.uk

Introduction

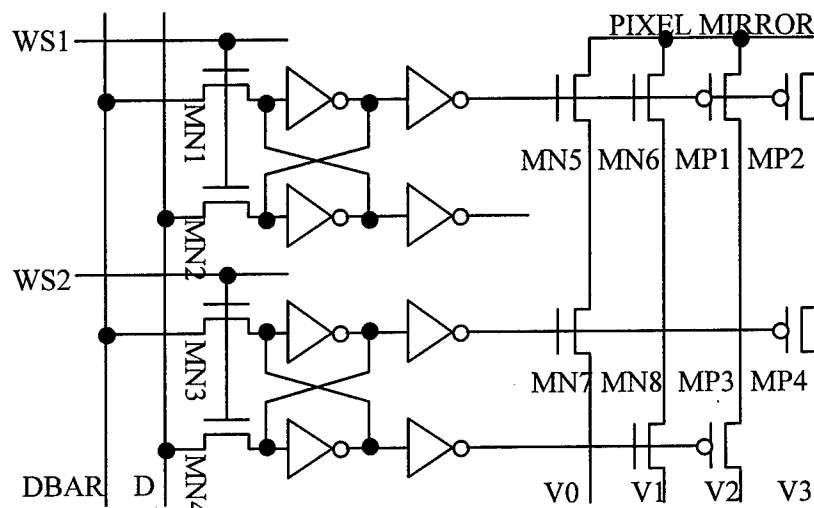
The hybrid technology which utilizes a CMOS silicon active backplane to drive a thin layer of (nominally) binary-switching Ferroelectric Liquid Crystal (FLC) in order to produce a reflective Spatial Light Modulator (SLM) is now relatively mature [1]. The most commonly used pixel design uses only one active device - a MOS transistor configured as a digital switch to a storage capacitor. While suitable for most applications, leakage current from the pixel leading to a loss of voltage from the capacitor and a consequent perturbation of the state of the FLC is of concern [2] in coherent applications, e.g., when used as a programmable binary-phase holographic element. The use of static memory in the pixel has been demonstrated to alleviate the above problem [3].

In order to improve on the optical efficiency of a phase hologram produced by a binary SLM it is necessary to both (a) drive either multiple voltage levels or a continuously variable analog voltage into the pixel, and (b) utilize a fast switching analog-capable L.C. configuration. A single transistor can act as an analog switch but with the perturbation risk described above present.

In this paper we give an initial description of a pixel which allows one of four levels of (highly stable) voltage to be driven onto the pixel mirror thus allowing four levels of phase to be generated. This provides the advantages static memory drive with those of four level phase modulation, albeit at the expense of circuit complexity.

Pixel Circuit

Figure 1 shows a schematic diagram of the pixel circuit. The active circuitry comprises two main parts - a static digital two bit memory and a number of MOS pass transistors.



As well as the conventional $V_3 = V_{dd}$ and $V_0 = 0V$ rails, an additional two voltage rails - V_1 and V_2 - are supplied to the pixel - V_1 at a nominal $V_{dd}/3$, V_2 at a nominal $2V_{dd}/3$. In practice, the intermediate voltages can be adjusted to compensate for nonlinearity in the response of the L.C..

The operation of the pixel is straightforward. The two bit word stored in the pixel memory determines which of the four voltage rails is shorted to the pixel mirror via the pass transistors as illustrated in Table 1.

Memory	Transistors ON	V mirror
0 0	MN5, MN6, MN7	$V_0 (= 0V)$
0 1	MN5, MN6, MN8	V_1
1 0	MP1, MP2, MP3	V_2
1 1	MP1, MP2, MP4	$V_3 (= V_{dd})$

Table 1 Routing of voltage to mirror as a function of word stored in memory

Implementation and initial optical characterization

An array of 4×4 of pixels has been implemented on a test chip. Due to an interconnect fault only one row of 4 pixels is addressable. Figure 2 shows a pattern programmed onto that row. Three of the four possible modulation states are visible. (The optics was configured to give amplitude modulation.)

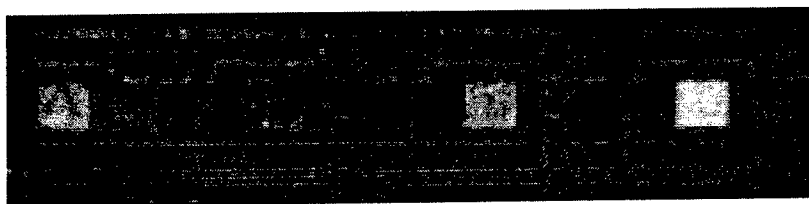


Figure 2 Four pixels showing amplitude modulation on the test chip

Conclusions

FLC/VLSI SLMs offer a means of implementing programmable holograms. The pixel described here offers advantages over those previously used and has the potential to be implemented in a large array.

Acknowledgments

The authors acknowledge the COOP scheme through which the test chip was supplied and Boulder Nonlinear Systems which carried out the FLC cell fabrication and filling; the company also supplied. JAB is sponsored by the UK EPSRC and CRL Smectic Technology.

References

- [1] I. Underwood "Liquid crystal over silicon spatial light modulators - principles, practice and prospects", OSA TOPS Vol. 14, pp76-88, 1997
- [2] J.Gourlay et al, "Real-time binary phase holograms on reflective ferroelectric liquid crystal spatial light modulators", Appl. Opt. Vol 33, pp8251-4, 1994
- [3] A.J. Stevens, "Experimental investigation of free-space optical routing systems using static and dynamic binary holographic elements", Ph.D. Thesis, The University of Edinburgh, 1995

A Dynamically Reconfigurable Token-based Optical Backplane

Brian E. Angliss and H. Scott Hinton, University of Colorado, Boulder, CO, 80509-0425, USA
Fax #: (303) 492-2758 Phone #: (303) 492-4452
email: angliss@schof.colorado.edu

1. Introduction

This paper presents a two-dimensional (2D) token-based dynamically reconfigurable smart pixel array (DRSPA) for intelligent optical backplanes. The DRSPA has the ability to reconfigure both the location and the size of the backplane optical communication channels (between 8, 16, 24, and 32 bits), dynamically enhancing the backplane throughput under light backplane load. This functionality is realized through the use of a 2D token, a 4 clock cycle backplane header, and a distributed control environment. Finally, the DRSPA is an extension of the *HyperPlane* backplane architecture, which allows it to implement any K-dimensional network architecture¹.

2: DRSPA Fundamentals

The initial *HyperPlane* backplane implementations were capable of address recognition, and data injection, regeneration, and extraction¹. The buffered *HyperPlane* smart pixel array (BHSPA) was then developed to include on-chip *KnockOut* output queuing with priority-based cell overwrite when the output queue was full². A weakness of the BHSPA is that once the injection and extraction channels are initialized, their configuration is static until the backplane is shut down and reinitialized. The DRSPA overcomes this weakness through the use of a 2D token which enables reconfiguration of the optical connections in real time. The number of injecting OCCs is adjusted dynamically to improve backplane throughput when the backplane is lightly loaded, and the 2D token enables blocked data to be temporarily queued when the backplane is highly loaded. This is accomplished through distributed control, with each DRSPA responsible for its section of the backplane, instead of requiring a fast and complex centralized routing processor to control the backplane. The DRSPA also implements a "plug-and-play" optical backplane. Since there is no centralized backplane controller, each DRSPA is intelligent enough to reset itself, determine the number of nodes connected to the backplane, and to choose a DRSPA to complete the remaining initialization steps prior to normal operation.

Figure 1 illustrates the circulation of the 2D token, backplane header, and ATM cell around the

backplane from the perspective of a single DRSPA. Each array octet is a 4 x 8 array of data arriving sequentially at the DRSPA.

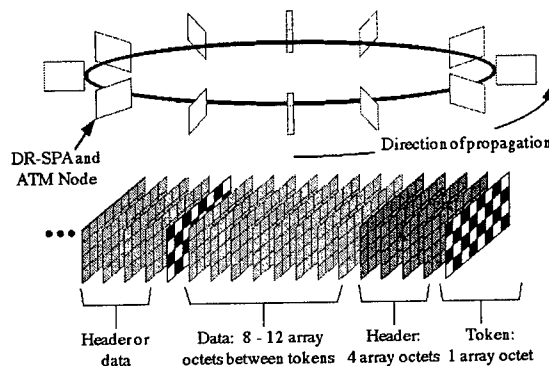


Figure 1: 12 DRSPA *HyperPlane* architecture.

In Figure 1, the first 2D token contains active header bits, thus the next four clock cycles are a backplane header rather than cell data. The next 8 clock cycles contain data. 12 clock cycles later, the token has circulated around the backplane and it returns to the DRSPA. The next four clock cycles may be either header or cell data, depending on the status of the header bit in the returning token.

Under low load, many unused backplane OCCs are available for cell injection. The DRSPA initially injects 8-bit wide cells, but if the backplane is lightly loaded, the DRSPA dynamically increases the number of injecting OCCs, injecting cells that are 16, 24, or 32 bits wide. This reduces the time required to transmit an ATM cell from 57 clock cycles (53 clock cycles for the ATM cell and 4 clock cycles for the backplane header) for an 8-bit wide cell to only 18 clock cycles for a 32-bit wide cell.

As the backplane load increases, the DRSPA dynamically reduces the width of injected ATM cells, freeing backplane resources for cell injection by other backplane nodes and reducing the cell loss probability. In addition, the DRSPA includes a transparent queue (XQ) which temporarily stores blocked cells until the backplane resources required for cell reinjection are available. The use of the transparent queue further reduces the cell loss probability and enables the extraction of low priority cells off the backplane and the injection of high priority cells in their place.

The ATM node injects and extracts 8-bit wide cells from the DRSPA. Because the cells may be injected by the DRSPA onto the backplane on multiple 8-bit wide OCCs (16, 24, or 32 bits wide), the destination DRSPA reconstructs the arriving data into the original 8-bit wide ATM cell. The information required for this function is part of the 4-clock cycle backplane header. This header is appended to the ATM cell and includes the destination address for address recognition as well as the OCC addresses required for cell reconstruction.

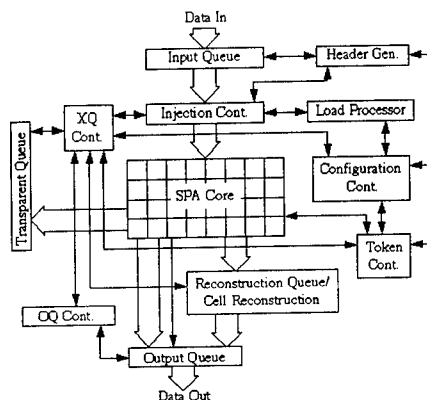


Figure 2: DRSPA block diagram.

The two main controllers responsible for the functionality of the DRSPA have been modeled and verified in VHDL. The token controller has a critical path of approximately 96 gate delays while the configuration controller has a critical path of approximately 54 gate delays. Using the .35 μm fabrication technology available from MOSIS³, the maximum operating clock rates are 67 MHz and 119 MHz, respectively. Using these maximum data rates produces an aggregate throughput of 2.1 Gb/s if the DRSPA is token controller limited and 3.8 Gb/s if it is configuration controller limited. Because the clock rate used for normal operation can be higher than the clock used for initialization, utilizing the 119 MHz clock rate is possible. Finally, neither controller has been optimized using VLSI, so the actual operating clock rates following optimization will be higher than those calculated above.

An approximation of the DRSPA's complexity can be calculated from the number of transistors per smart pixel. The token and configuration controllers contain approximately 12000 transistors apiece. If we assume a minimum of 7 ATM cells worth of queuing on the DRSPA itself (including input, output, reconstruction, and transparent queues), then the queues will contain at least 25000 transistors. Initial designs of the reconstruction logic required

approximately 4000 transistors, and the remaining DRSPA control logic will require at least 20000 transistors. This produces a minimum of 73000 transistors, or approximately 2300 transistors per smart pixel.

3: Token/Configuration Controllers

The token controller generates the 2D tokens, controls the initialization sequence, and resets, reinitializes, or shuts down the backplane. While the DRSPA implements a distributed control environment during normal operation, a single DRSPA, the master controller, controls the initialization sequence. The token controller generates and recognizes the various 2D tokens, and it distinguishes them from cell data by tracking their location on the backplane. Finally, the token controller resets, reinitializes, and shuts down the backplane following reception the command token associated with those backplane operations.

The configuration controller reconfigures the backplane's optical connections. If the local load is higher than the average backplane load and there are OCCs available for cell injection, then the configuration controller allocates additional OCCs to injecting data. If the local load is lower than the average backplane load, then the controller allocates fewer OCCs for cell injection. If the controller allocates fewer OCCs for cell injection than there are available, then backplane load is reduced by activating the OCCs with the lowest load first. Finally, the configuration controller decides when to extract blocked backplane cells into the transparent queue and when to declare blocked cells lost.

4: Conclusions

The functions of the DRSPA, including the 2D tokens and backplane header as well as the token and configuration controllers, have been introduced. This paper will discuss the completed VHDL simulation of the token and configuration controllers

5: References

1. H. S. Hinton and T. H. Szymanski, "Intelligent Optical Backplanes," *MPPOI'95*, San Antonio, Texas, October 23-24, 1995.
2. K. E. Devenport et. al., "Architecture and Implementation: A Buffered ATM HyperPlane Smart Pixel Array," *OSA Spring Topical Meeting on Optics in Computing*, Lake Tahoe, Nevada, March 18-21, 1997.
3. The MOSIS Service, "MOSIS IC Vendor's Processes," <http://www.mosis.org/vendors.html>, March 1998.

CMOS Based Optoelectronic Smart Pixel Array for Accessing Optical Page-Oriented Memories

Chris Kanyuck, Mark Slutz, and F. R. Beyette Jr.

Department of Electrical & Computer Engineering
and Computer Science

University of Cincinnati

PO Box 210030

Cincinnati, OH 45221-0030 USA

Email: beyette@ececs.uc.edu

Abstract

A smart pixel array suitable for accessing page-oriented optical memories is presented. In addition to optical/electrical data conversion, this smart pixel array reduces the high data rate input to a low data rate output compatible with conventional electronics.

Key Words: smart pixel, CMOS optoelectronics, optoelectronic systems, database processing

1. Introduction

Optical memories are soon expected to provide the terabyte secondary storage capacities required by many large database systems.² Unfortunately, increasing storage capacity only accentuates the memory/processor bottleneck associated with conventional electronic information processing hardware. While optical storage devices are expected to minimize this restriction by exploiting the massive parallelism of optics, the predicted page oriented optical data rates of a few hundred Mbits/read cycle,³ are not compatible with electronic read cycles which are limited by word oriented memory and processing operations. With a data access rate ~5 orders of magnitude faster than electronic I/O optical, page-oriented reading leads to a significant I/O bottleneck that will limit the incorporation of high density optical storage devices into conventional information processing systems.

For database applications, the concept of an optoelectronic database filter has been proposed as a possible solution to this I/O bottleneck.⁴ An optoelectronic database filter serves as an interface between page oriented optical storage devices and an electronic host computer. In addition to providing the necessary optical/electrical data conversion, this smart pixel based subsystem is capable of executing relational database queries involving both the selection and/or the projection functions. These database operations can be used to identify the data that satisfies a user defined database query. By outputting only the data that matches a query, the optoelectronic database filter is capable of reducing the high data rate optical signal to a low data rate electronic signal that is compatible with conventional electronic database management systems.

Recently, a first generation system was used to demonstrate the feasibility of a database filter.⁵ However, the practicality of this first generation system was limited by: 1) a immature smart pixel device technology and 2) a complex system architecture which required the alignment of 8 optical paths. While the filter presented here utilizes similar information processing concepts, this paper presents a complete redesign of the filter. In addition to major modifications in the selection and projection circuitry, this filter design provides a buffer to hold valid data waiting to be transferred into the electronic host.

2. Motivation for Enhancing the Database Filter Functionality

Optimization of system performance suggests that simplification of the optical system will improve system reliability. Further, the incorporation of conventional electronics (where possible) will improve device reliability while reducing both fabrication time and cost. With these thoughts in mind, the redesigned database filter utilizes CMOS optoelectronic circuits to address the following objectives. First, by incorporating a data buffer into the filter design, it is possible to eliminate the optoelectronic RAM used in the previous database filter design. This allows the electronic host to access data directly without having to first scan an entire page for memory locations that contain valid data. Further, by implementing the buffer with an asynchronous queue, it is possible to separate timing issues in the filter from the timing constraints of a host computer's read cycle. Thus, assuming the database query hit ratio does not overwhelm the asynchronous queue capacity, the optical storage access rate is truly independent of the host computer's read cycle time.

The second objective of this redesigned filter is to further reduce the optical system complexity. This issue raises the primary question; where does the use of optical interconnections improve performance of the filter? Since the filter is required to interface with a page oriented optical storage system, an optical interconnections is still needed for the input data. In fact, this is a useful interconnect since it provides a high bandwidth connection for transferring large volumes of data from optical secondary storage into the filter. In contrast, the control signals, which were input optically in the first generation design, are all low volume signals that only change when a new query is issued by the host computer. Further, these signals are generated in electronic form by the host computer and must be converted to optical signals if optical control is to be used. In this application, converting the control signals from electrical to optical format and transmitting via a high bandwidth optical channel represents a potentially unnecessary use of optical interconnection.

Figure 1 shows an overall system level description of the single smart pixel array used in this system. Entering from the top, optical page oriented data is input to the system. Each pixel in the system contains a photoreceiver that converts the optical data signal to an electronic logic level. Following the optical-to-electrical conversion, each pixel uses a combinatorial logic circuit to perform a bitwise selection function. The results from each bitwise selection are summed along each record to determine if the record matches the query. Matching records are input to the top of an asynchronous queue which accepts page oriented input at the top and uses a tree structure to pass only matching records down to a single output record. Attached to the asynchronous queue output is an array of AND gates that implement a projection operation prior to the filter passing data to the host computer.

To date each of the components required to implement the redesigned filter has been designed and fabricated using the MOSIS fabrication service. Along with a detailed description of each component of the optoelectronic CMOS smart pixel array, this paper will present experimental verification of the filter functionality and evaluate the overall filter performance in terms of input page rate, filter throughput, and maximum acceptable hit ratio. In addition, the paper will discuss the technological barriers associated with building a very large (~ 100 Mbits per input page) filter for use with page-oriented memory devices expected in the near future.

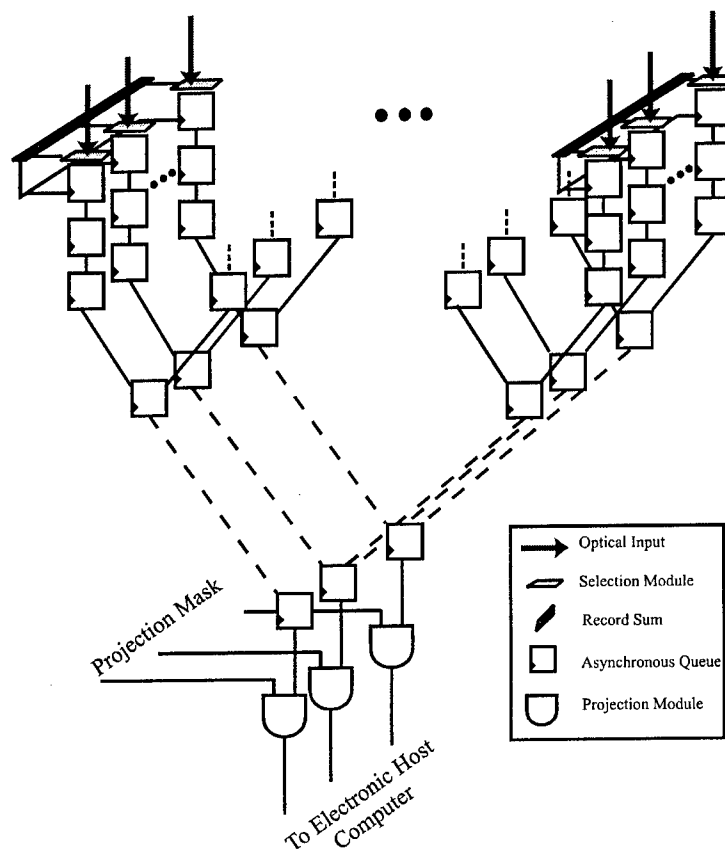


Figure 1. Functional overview of the single chip optoelectronic database filter.

3. References

- ². P. A. Mitkas and L. J. Irakliotis, "Three-Dimensional Optical Storage for Database Processing", *Optical Memory and Neural Networks*, Vol. 3, No. 2, pp. 217-229, 1994.
- ³. S. Hunter, F. Kiamilev, S. Esener, D. A. Parthenopoulos, and P. M. Rentzepis, "Potentials of two-photon based 3-D optical memories for high performance computing", *Applied Optics*, Vol. 29, No. 14, pp. 2058-2066, May, 1990.
- ⁴. P. A. Mitkas, L. J. Irakliotis, F. R. Beyette Jr., S. A. Feld, and C. W. Wilmsen, "Optoelectronic data filter for selection and projection", *Applied Optics*, Vol. 33, No. 8, pp. 1345-1353, March, 1994.
- ⁵. R. D. Snyder, S. A. Feld, P. J. Stanko, E. M. Hayes, G. Y. Robinson, C. W. Wilmsen, K. M. Geib, and K. D. Choquette, "Database Filter: Optoelectronic design and Implementation", accepted for publication *Applied Optics*.

The constraints on feedforward neural system design using smart pixels

W.M.D. Bradley and R.J. Mears

Cambridge University Engineering Department
Cambridge, CB2 1PZ, United Kingdom

Tel: +44-1223-332600 Fax: +44-1223-332662 e-mail: wmdb100@cam.ac.uk

Abstract: Smart pixels give a means of realising massively parallel optical processing, but there are always a number of trade-offs that need to be made so that the system becomes viable. In this paper, we take a look at two optical neural network architectures under development, both of which incorporate *in situ* learning. The design constraints, and the requirements on the underlying theory that make them possible are briefly considered.

Introduction

When designing an optical processing system, there is a desire to take full advantage of the benefits that the use of optics can give us, but weighed against complexity on the optical bench, we often have to perform a portion of the work in the electronic domain.

The special constraints imposed when signals are processed and carried in the optical domain often mean that we also have to rethink the underlying mathematics of the operations we are trying to perform; at the very least, we have to be very careful about the algorithms that we select.

There is clearly an interdependent relationship between the optical and electronic phases of the design. In this paper, we briefly describe the optoelectronic structures required for two feedforward neural network designs, both of which incorporate on board learning, but which get around the particular problems associated with the optics in different ways.

Feedforward architecture

Feedforward network architectures, apart from being widely used in electronic neural networks, are particularly suited to the application of optics. The complex interconnections required mean that optical systems can offer a significant advantage when it comes to scaling the network up.

There are four basic operations that are important in such networks:

1. Non-linear thresholding
2. Weight storage and update
3. Signal fan-out and multiplication
4. Fan in and summation

The first two are most likely best done electronically, but (3) and (4) are candidates for optical processing. The multiplication is done after the fan-out stage; the thresholding is done before (and also after the subsequent

fan-in). This points towards two separate pixel planes, interconnected optically

Thus in both the schemes described here, the neural (thresholding) and synaptic (weight storage and update) devices are on separate planes. They are implemented as liquid crystal on silicon spatial light modulators, although the transmitters in the second circuit's neurons could easily be VCSELs.

Constraints on system design

The main issue that impedes neural network design is that of signal polarity. Electronic networks can deal with this fairly easily, but unlike electrical currents, optical signals are very obviously unidirectional. This places certain conditions on how the signal is represented. A common solution is to split the signal into positive and negative components – this clearly complicates both the optical and electronic components of the system.

Alternatively, the signal can be biased into the positive range, but apart from making the system critically dependent on obtaining the right biases across all the circuits, this also precludes the use of fast optical weight multiplication on the pixels' liquid crystal modulation pads.

If we are to keep the system simple (this is, after all the aim), then we must accept the constraint that the signals, as well as the weights, must be kept positive.

Unfortunately most learning techniques rely on positive and negative values to operate. In general, feedforward networks can be defined using positive input signals, but the weights that they are multiplied by are generally to be regarded as bipolar. Thus we require new network designs and update rules to accommodate the special needs of an optical implementation.

The other main constraint is the system's resistance to noise and irregularities. Fortunately neural systems are typically resilient to this kind of interference, as the discrepancies are 'learned out' during training; in fact the noise can contribute to the generalised learning ability of

the network (although in the recall phase it is still undesirable).

SASLM* - single layer network

The first system employs Iterative Delta Learning (IDL), which is not an idealised learning method, but is quite effective in single layer networks where thresholded binary inputs and outputs are expected. The device is designed to be used as an associative memory, and operates by comparing a target pattern with the current (initially random) output pattern, and updating the weights by a small amount with each pattern presentation.

Because the target patterns are binary, the constraints on the learning ability are loosened somewhat. This enables a solution to be found with a reasonable probability when using positive weights. The system is also noise resistant due to the thresholding of all signals.

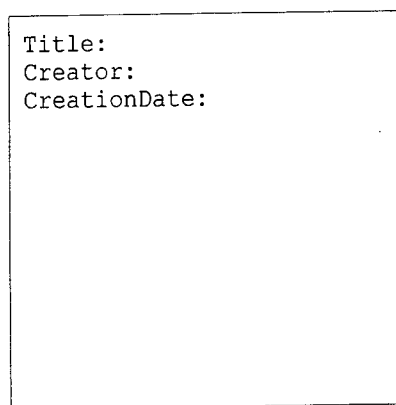


Figure 1 - the SASLM synaptic pixel layout

AMONN† - multilayer network

The second architecture implements a form of what is perhaps the most well known and the most commonly used learning algorithms. Backpropagation is frequently used because of its relative simplicity for hardware purposes and for its ability to teach multilayer networks.

Multilayer nonlinear networks are often considered to have greater power, can solve more (if not all) presented problems, and can be made by cascading much simpler networks in series. The major drawback, as far as optical implementations are concerned, is the requirement that weight multiplication be done with positive and negative values.

AMONN uses a specially adapted version of backpropagation learning, combined with a mixture of excitatory and inhibitory thresholding devices. This not only enables solutions to be found in the search space during learning, but allows the learning rule to be simplified so that the synaptic devices are relatively easy to implement. The learning rule is fairly resilient to

irregularities in the devices and the illumination during training (although accurate analogue circuitry is required to ensure faithful reproduction in the recall phase).

An extra degree of complexity comes in due to the feedback path necessary for learning. However, there is a high degree of symmetry in the feedforward and feedback paths, and the operations that the pixels perform, as well as their layout, are designed so that many of the optical components do not have to be duplicated.

Because AMONN has its basis in Backpropagation, the learning rule analytically homes in on a minimum error state for the given training set, which is a necessary condition for continuous (rather than hard thresholded) signals.

Outlines of the functions of the neural and synaptic devices are shown in Figure 2. Note that both have a photodiode/LC pixel pair for each pathway. One multiplier and a thresholding/derivative circuit is needed in the neuron. All that is needed to implement on board learning is a capacitive stored weight and two multipliers.

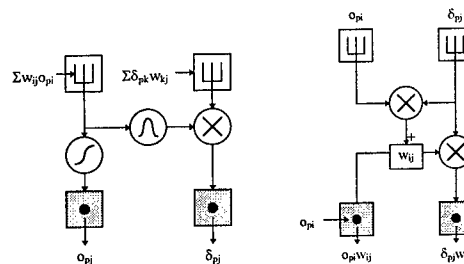


Figure 2 - AMONN neural (left) and synaptic devices

Conclusions

By tailoring learning algorithms it is possible to simplify the optical components of the neural networks significantly without sacrificing the advantages that make the use of optics worthwhile.

References

- [1] W.M.D.Bradley, R.J.Mears, "Backpropagation learning using positive weights for multilayer optoelectronic neural networks", Proceedings of the IEEE Lasers and Electro-Optics Society, 1996, Vol. 1, pp. 294-295

SASLM was fabricated under the EPSRC/DTI LINK programme 'Smart Advanced Spatial Light Modulator'. The authors are grateful to CRL for their part in the assembly of the device.

* Smart Advanced Spatial Light Modulator

† Analogue Multilayer Optoelectronic Neural Network

A System Architecture for use with Free Space Optical Interconnects in a 3D Stacked Processor Environment.

J. Rorie¹, P. Marchand², P. Chandramani¹, J. Ekman¹, F. Kiamilev¹, F. Zane², V. Ozguz³, S.C. Esener²

¹Department of Electrical Engineering, UNCC, Charlotte NC 28223

²Department of Electrical-Computer Engineering, UCSD, La Jolla CA 92093

³Irvine Sensors Corp., Costa Mesa, CA 92626

Introduction

In the near future, technological growth in computer development will encompass areas where there is a requirement of high data throughput to achieve useful operation. Many applications in these areas, which include real-time and adaptive signal processing systems, are the key benchmarks for performance evaluation of new technologies. These applications present the new challenges for the next decade of computation.

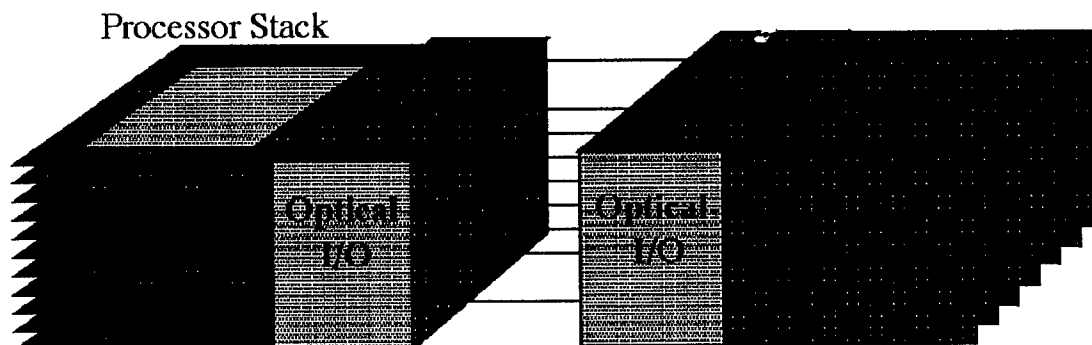
Analysis of these applications has shown that they, like most complex systems, can benefit from parallel processing. However, current VLSI technology supports these highly parallel operations only through large transistor counts. Additionally, parallel systems require an even greater increase in routing between functional units. It is in this area where planar VLSI technology becomes inefficient.

Stacking technology is an approach by which separate VLSI dies are stacked vertically to form a three dimensional logic unit. By using the vertical dimension, the designer can build highly parallel systems in a uniform manner. Each parallel functional unit can be designed in a planar fashion and can be expanded through stacking to meet computational needs. However, this new technology presents fundamental problems in the area of routing.

Since components are no longer located local to a single die, some novel approach must be taken to allow communication between planes. For signals between chips in the same stack, this global routing can be performed by adding traces on the edges of the die stack. But high speed datapaths between different stacks require a more robust solution. Current planar technologies implement high speed datapaths through the use of electrical planes to isolate external signals. Unfortunately, this approach is not feasible in the stacked processor technology.

There exists a technology suited for dealing the unique constraints of the 3 dimensional stacked processor environment; Free Space Optical Interconnects. This technology uses VCSEL's, Vertical Cavity Surface Emitting Lasers, as a communications medium. FSOI has been proven to work in a two dimensional matrix format that would be optimal for communications between stacks. By use of an optical approach, the problems associated with the coupling effects of electrical connections carrying high speed signals are eliminated.

Figure 1: Block Diagram for the 3D OESP System



Architecture

The 3D OptoElectronic Stacked Processor project [1] contains a number of different goals, one of which consists of the development of a custom system architecture for computation in a multi-stack environment. This

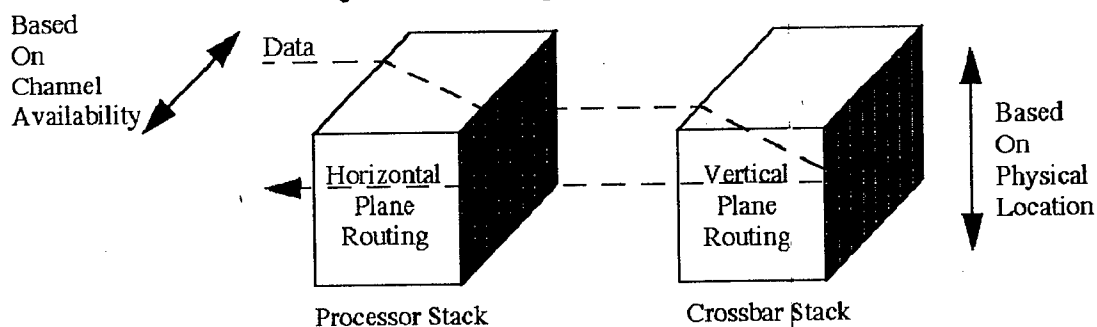
architecture should support the calculation of two dimensional FFT's and other signal processing functions using free space optical interconnects for communication between planes and stacks. Major architectural points are the development of reliable high speed serial bus and an inter-processor communication protocol to operate upon it. This protocol must account for the unique requirements of the free space optical interconnects while maximizing the bandwidth available.

An additional goal is to use this project as a test bed for developing a general purpose reliable optical link. This link could be directly targeted for use in future projects without additional cost due associated with design adaptation. Development will be accomplished through the design a of robust full duplex communication architecture centered around the two dimensional VCSEL array. This architecture should be self sufficient, requiring no external logic for implementation. The 3D OESP system uses a centralized Tri-State databus [2] for communications through a die. By using a centralized approach, routing area is reduced saving time and equalizing propagation delay. Since all components connected to the bus operate independently of each other, some mechanism required for orderly communication. The Bus Arbitration Unit performs this task.

The Bus Arbitration Unit is the interface between the processors local to the die and the optical interconnects. It is the central authority for communications along the central databus. The BAU receives interrupt signals from interrupt controller indicating a processor attempting to transmit. The priority of a request is determined relative to other requests that may be pending. In the current configuration, a request from the Optical Interconnects overrides an processor requests. Since each of the processors is general purpose, it will be the job of the Interrupt Controller provide the required logic to facilitate transfers between the processor, optical interconnects and the data bus. Its job is to queue data from the processor and route it to its respective destination. It provides the special purpose handshake logic that, in conjunction with the BAU, allows orderly sequential access to the data bus.

The Free Space Optical Transceiver performs the first of a two stage routing operation. As shown in Figure 2, first stage routing is performed on the horizontal plane. This routing is based on channel availability. determines the appropriate serial channel to route the information on the data bus. This is determined by the horizontal decode logic. This module keeps track of the state of all serial channels and routes information to the current open channel. By tracking this selection, the FSOT can optimize transmission speed by routing data to currently unused planes on the destination stack. This system is just one of the many configurations possible with this architecture. With the advent of stacked processor technology, the development of VLSI systems enters, quite literally, a new dimension. The possibilities in parallel processing are just being explored. By merging this with FSOI, the maximum level of performance can be achieved.

Figure 2: Two Stage Routing Diagram



References

- [1] S. Esener, P. Marchand, *3D Optoelectronic Stacked Processors: Design and Analysis*, to be presented at Optical Computing Meeting, Bruges, Belgium (June 1998).
- [2] B. A. Wilkinson *Computer Architecture Design and Performance*, Second Edition, Prentice Hall, 1996

Smart Pixels

Friday, 24 July 1998

FA: Optics and Packaging

FB: Systems and Demonstrations I

FC: Systems and Demonstrations II

Friday Papers Not Available

- FA2 Integrated Micro-Optical Systems,
Michael R. Feldman, Digital Optics Corporation,
Charlotte, NC
- FB1 Evolution in the Technology and Applications of
Smart Pixel Devices, Ravi Athale, George Mason
University, Fairfax, VA
- FB2 Optoelectronic-VLSI Smart Pixels for Data
Networking, Ashok Krishnamoorthy, Lucent
Technologies, Bell Laboratories, Holmdel, NJ
- FC2 Optoelectronic Multichip Modules Using MEMS
Fabrication

Fiber Optic Packaging of Surface Normal Device Arrays

Joseph Ford

Bell Laboratories, Lucent Technologies

jeford@lucent.com - 101 Crawfords Corner Road, Room 4B-411, Holmdel, NJ 07733

Lithographic fabrication technology originally developed for manufacturing electronic integrated circuits is now being applied to create a variety of surface-normal operation optical devices, including the opto-electronic detector and transmitter arrays (multiple quantum well modulators, light emitting diodes, and vertical cavity surface-emitting lasers) which have been extensively investigated for smart pixel applications in data processing. Lithographic fabrication is also being applied to construct arrays of micron-scale mechanical devices called MEMS, for micro-electro-mechanical systems, which can be used to modulate or deflect optical signals. Both Opto-Electronic and MEMS devices can be closely integrated with silicon VLSI electronics to provide local signal processing and control. The resulting devices have potential use in a wide range of optical application areas.

Fiber optic telecommunication networks, in the public long-haul and metropolitan networks as well as in local (campus) data networks, provides an "opportunity-rich environment" for optical components and systems. In other words, providing the increase in transmission and switching bandwidth necessary to accommodate the exponential growth in network traffic will continue to spur rapid technological development. High-bandwidth data transmission over appreciable distances must be carried over single mode fiber, which means a characteristic 1 micron lateral alignment tolerance. The application of any of these surface-normal device arrays then becomes an exercise in opto-mechanical packaging.

Low-cost passive alignment techniques have been successfully applied to single fiber and 1-D fiber arrays using preferentially-etched silicon alignment features such as V-groove arrays [K. Petersen, "Silicon as a Mechanical Material," IEEE Proc. 70(5), p.420-457, May 1982]. Unfortunately, such techniques do not extend to constructing and aligning 2-D fiber arrays. However, telecommunications systems use wavelength division multiplexing to increase transmission capacity. This provides a new opportunity for array packaging.

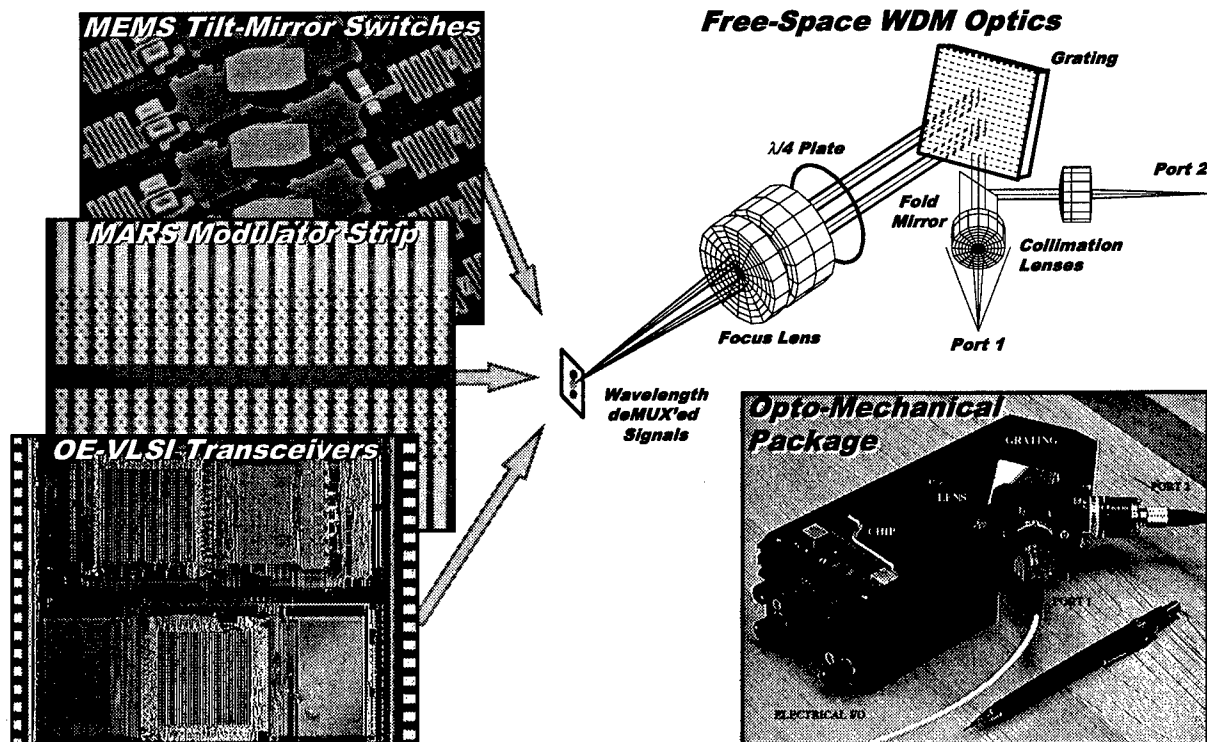


Figure 1 - A suite of fiber components using different surface-normal devices in a free-space WDM platform.

If a single fiber is imaged through a planar diffraction grating, a WDM input signal creates a column of spots distributed according to wavelength. A row of fibers, oriented appropriately relative to the grating angle, can create a 2-D array of spots. If the reflected optical signals are recombined into a row of fibers, then the need for a 2-D fiber array is eliminated. This concept can form the basis for a variety of optical components, depending on the device used. Figure 1 shows the wavelength multiplexing optical system for imaging light from single mode fibers on and off the device plane, along with the resulting optomechanical package. This package can be used to host different opto-electronic and opto-mechanical devices for a wide variety of applications.

With multiple quantum well detectors and modulators integrated with VLSI silicon, high-speed data signals can be detected and transmitted over 850 nm light. Using a short pulse laser to generate a train of broad spectrum pulses, filtered through an etalon to define data wavelengths at 0.5 nm pitch, data was transmitted and detected on 24 channels. [J. E. Ford, A. V. Krishnamoorthy, S. Tsuda, W. H. Knox, M. C. Nuss and D. A. B. Miller, *IEEE/LEOS 1996 Summer Topical Meeting on Smart Pixels*, pp.97-98, 1996]. The transceiver used a single input and output fiber. Multiple transceivers can be interconnected through a OE-VLSI switch which uses an array of 16 input and 16 output fibers using the same basic design.

The MARS (mechanical anti-reflection switch) device is another modulator based on a completely different effect; essentially, it is a low-finesse Fabry-Perot etalon with an electrostatically controlled gap. A mechanically continuous modulator strip with 32 discrete electrodes was used to make a continuous 1 mm long by 40 micron wide variable reflectivity mirror. This device, operated over a 24 nm range centered at 1550 nm, provides active equalization for WDM telecommunications systems to compensate for dynamic changes in amplifier gain and channel loss [J. E. Ford and J. A. Walker, "Dynamic spectral power equalization using micro-opto-mechanics," to be published in *Photonics Technology Letters*].

Micro-mechanical tilt-mirror arrays, extensively developed by Texas Instruments for display applications, can also perform optical switching. In particular, an array of tilt-mirrors placed at the demultiplexed wavelength plane can switch the individual wavelength signals from being transmitted from port 1 to port 2, or back-reflected to port 1. Placing this switch between optical circulators creates a 4-port wavelength add/drop switch, where each individual wavelength of a WDM data stream is either passed or dropped (and where new data can be added to re-use any dropped wavelength channel). A 16 channel add/drop switch was demonstrated using mirrors fabricated through MCNC's multi-user MEMS foundry [J. E. Ford, J. A. Walker, V. Aksyuk and D. J. Bishop, Postdeadline paper PD2.3, IEEE LEOS 1997 Annual Meeting].

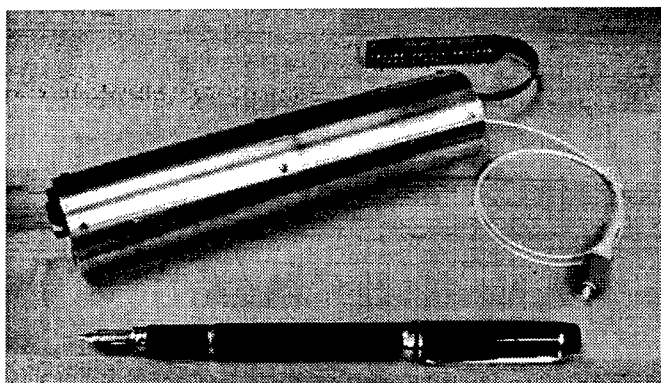


Figure 2 - "Tube" WDM multiplexing package; smaller, simpler, and easier to align.

The WDM package of Figure 1 allows 16 separate position adjustments on the optical components. This is convenient for laboratory use but impractical for manufacture and long-term stability. Figure 2 shows the next generation WDM package, retaining most of the original versatility while cutting the alignment to 4 orthogonal degrees of freedom (tip, tilt, rotation and focus). The design consists of: a device mount holding the fiber (or fiber array), the device (possibly including planar micro-optics), and a flextape electrical connection; a single collimation/focus lens; a quarter wave plate to cancel polarization dependent loss; and a planar Littrow grating. This package is intended to serve as a platform for a wide range of fiber-optic WDM components.

This work is a collaboration with many Bell Labs researchers, including Ashok Krishnamoorthy, Jim Walker, Keith Goossen, David Bishop and Vladimir Aksyuk. Their contributions are gratefully acknowledged.

Multi-channel optical coupling between VCSEL arrays and multimode optical fibers for a 40-channel parallel optical interconnection module

Akira Ohki, Mitsuo Usui, Nobuo Sato, Nobuaki Matsuura, Kohsuke Katsura, and Yasuhiro Ando

NTT Opto-electronics Laboratories
3-9-11, Midori-cho, Musashino-shi, Tokyo 180, Japan
TEL:+81 422 59 4079 FAX:+81 422 59 2593
email: ohki@ilab.ntt.co.jp

1. Introduction

Parallel inter-board optical interconnection technology (ParaBIT)^{1,2)} is a promising candidate for a large capacity board-to-board interconnection in next-generation information systems, such as Tb/s-class ATM switching systems and parallel computer systems. We are now focusing on developing a prototype front-end ParaBIT module with capacity of up to 28 Gb/s and 40 data channels. In the prototype ParaBIT module, some new assembly techniques have been developed to provide efficient and uniform multi-channel optical coupling between VCSEL/PD arrays and multimode optical fibers. In this paper, we describe the characteristics of these newly developed assembly techniques.

2. Packaging structure of prototype ParaBIT module

Figure 1 schematically shows packaging structure of the prototype ParaBIT module. The module has 40 data channels and can carry 32-bit wide data without multiplexer and demultiplexer. Unifying the packaging structures of transmitter (Tx) and receiver (Rx) modules, the Tx module has four 10-channel VCSEL arrays on p-type GaAs substrate³⁾ as optical signal sources and the Rx module has four 10-channel GaAs pin PD arrays as photodetectors. Simple electronic circuits with a fixed-decision-level Rx IC and an APC-less Tx IC are used. Although these features of ICs are effective at reducing the cost, power consumption and packaging size, they restrict on the permissible variation of the incident optical signal intensities among 5-channels of PDs which are connected with the same Rx IC. This variation is mainly caused by the variations in the optical properties of VCSELs in 10-channel array (ΔL_V) and in optical coupling between each optical fiber and VCSEL (ΔL_C). Taking into account the ΔL_V and yield of 10-channel VCSEL arrays, ΔL_C should be restricted to less than 1.5 dB to obtain the adequate module performance.

3. Multi-channel optical coupling in prototype ParaBIT module

Figure 2 schematically show details of the optical coupling structure in the Tx module. The optical coupling structure consists of a 10-channel VCSEL array chip, 20-channel BF connector and optical coupling component which consists of a 20-channel polymeric optical waveguides with 45° mirrors⁴⁾ and 20-channel BF connector interface. The BF connector can be joined by direct physical contact with short fibers in the BF connector interface which is fixed at the end of the waveguide film. The buckling forces of the bare fiber themselves secure physical contact. This BF connector does not need a ferrule or spring, unlike conventional physical contact connectors, and has high optical coupling efficiency with insertion loss at the connecting point of less than 0.1 dB. Of course the variation in the insertion loss between each channel of BF connector is much lower than 0.1 dB⁵⁾. Therefore ΔL_C is caused by the variations in the

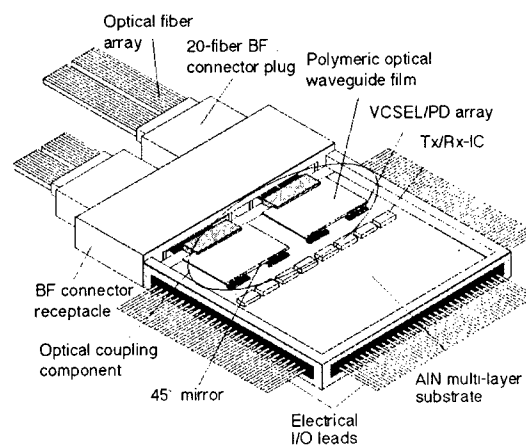


Fig.1 Packaging structure of prototype ParaBIT

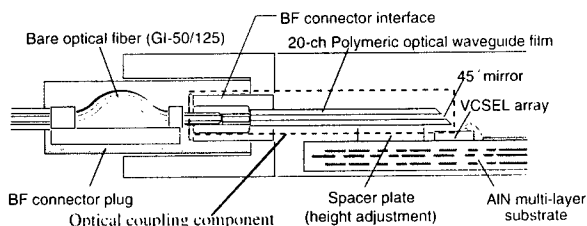


Fig. 2 Optical coupling structure of prototype ParaBIT

propagation loss of each optical coupling component channel, which include a loss at the 45° mirror, and in the insertion loss of each waveguide channel due to the position errors of VCSEL array chips (ΔD).

We measured the propagation loss of each optical coupling component channel. The result is shown in figure 3. The typical average propagation loss of the optical coupling components was 2.3 dB. The variations among the channels were within 1 dB (average value ± 0.5 dB). Because of the 1 dB variation among the channels of optical coupling component, the variation in the insertion loss of waveguide film due to ΔD must be less than 0.5 dB to achieve the ΔL_c of less than 1.5 dB. The variation in the insertion loss of waveguide film caused by ΔD was measured and plotted in figure 4. The variation in the insertion loss increases as ΔD increases and exceeds 0.5 dB when ΔD is more than $\pm 6 \mu\text{m}$. In addition, VCSEL arrays are likely to be degraded by thermal stress during step-by-step alignment and soldering of four VCSEL array chips, so we have developed a new diebonding technique which is called TMB⁶⁾ (transferred multichip bonding technique). The main features of TMB are the simultaneous and accurate bonding of four VCSEL array chips. In regard to simultaneity, TAB remarkably reduce the time for which the VCSEL arrays are kept at high temperature and thus should reduce the thermal damage to them. The maximum position errors of the four VCSEL chips bonded simultaneously by TAB are plotted in figure 5 as a histogram. We can see from this histogram that the chip position errors less than $\pm 6 \mu\text{m}$ is achieved with the probability of nearly 100 %. This result also indicates that the ΔL_c less than 1.5 dB is achieved with high reliability.

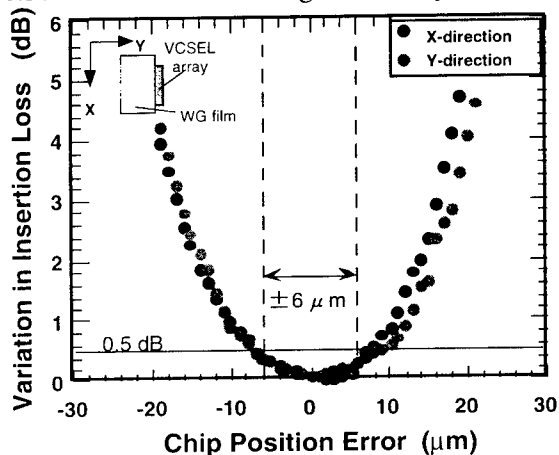


Fig. 4 Variation in insertion loss due to ΔD

4. Conclusion

We have successfully developed some new assembly techniques for the prototype ParaBIT module to provide the efficient and uniform multi-channel optical coupling between VCSEL/PD arrays and multimode optical fibers. The modules which were assembled by using these techniques satisfied the restriction on the optical coupling variation of 1.5 dB.

Acknowledgments

We would like to thank Takaaki Ohsaki, Toshiaki Kagawa, Makoto Hikita, and Saburo Imamura of NTT Opto-electronics Laboratories.

References

- (1) Y. Ando, in Proc. 1997 LEOS 10th Annual Meeting, San Fransisco, vol. 1, pp. 126-127, (1997).
- (2) M. Usui et al., in Proc. 1997 LEOS 10th Annual Meeting, San Fransisco, vol. 1, pp. 51-52, (1997).
- (3) Y. Kohama et al., Electron. Lett., vol. 33, No. 14, pp. 1240-1242, (1997)
- (4) M. Hikita et al., in Proc. IOOC/ECOC'97, Edinburgh, UK, vol. 2, pp. 285-288, (1997)
- (5) M. Usui et al., in Proc. 2nd IEMT/IMC Symposium, Omiya, Japan, pp. 127-131, (1998)
- (6) A. Ohki et al., in Proc. 2nd IEMT/IMC Symposium, Omiya, Japan, pp. 123-126, (1998)

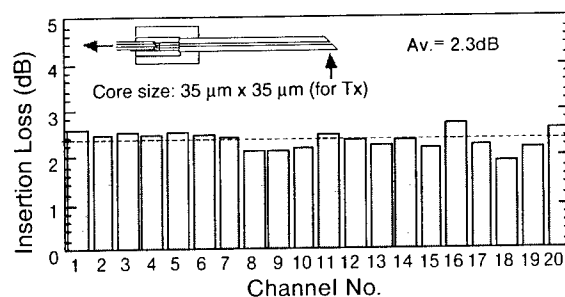


Fig. 3 Insertion loss of optical coupling component

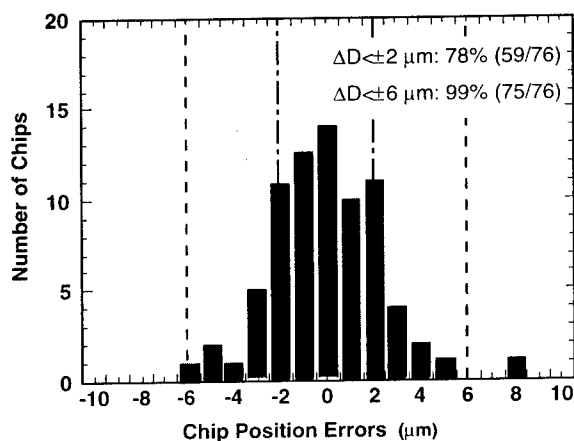


Fig. 5 Histogram of chip position errors

4 x 4 ATM Crossbar using N^4 Global FSOI

Christine M. Travers, John M. Hessenbruch, Jongwoo Kim, Richard V. Stone and Peter S. Guilfoyle

OptiComp Corporation
P.O. Box 10779, Zephyr Cove, NV, 89448
Phone: 702-588-4716, FAX: 702-588-1348
connect@opticom.com
http://www.opticom.com

1. INTRODUCTION

The integration of optoelectronic devices with conventional electronics will ultimately enable free space optical interconnects (FSOI) for high speed switching applications. Specifically, the development of smart pixels allows compact integration of optics and electronics for use in various systems and applications. OptiComp has integrated these smart pixel arrays into a high performance optoelectronic computing (HPOC) module which is composed of an array of 850 nm VCSELs, laser drivers, diffractive optical interconnect elements (DOIEs), detectors, and receivers¹. The HPOC module was used to implement a 4 x 4 crossbar switch for ATM by exploiting global (N^4) FSOI.

2. CROSSBAR ELEMENTS AND CONFIGURATION

The design of the crossbar is demonstrated with the schematic shown in Figure 1. The switch is operated by first applying the 2-bit destination address to the inputs of the crossbar. The delayed packet signal is inverted and then broadcast across all possible output detectors of the first stage. The DOIE routes only the light from the signal to the desired output detector, passing none of the light from the address lines. All other non-selected detectors receive continuous light from the routed address lines. The first stage DANE output is detected, amplified, negated, and optically emitted to the corresponding 4-input NOR gate detectors of the second stage. Thus, a high speed ATM data packet can be routed without decoding any further than the ATM virtual circuit address which is transformed into the appropriate optical interconnections when it is received by the decode/control logic lines.

The basic configuration of an HPOC module is shown in Figure 2. For the purposes of demonstration, the first stage of the crossbar was integrated on an optics bench (Figure 2b). The VCSEL array was aligned with a lenslet array which illuminated the DOIE. The DOIE directed the interconnects through a Fourier lens and then into the detectors. The VCSELs used in the 4 x 4 crossbar switch were 850 nm GaAs/AlGaAs epitaxial structures with threshold currents from 4-8 mA and single mode operation near threshold. The DOIE used in the HPOC module was programmed by using a computer generated hologram to implement the wide fan-in/wide fan-out architecture required for the 4 x 4 crossbar². The DOIE was fabricated on a quartz substrate using e-beam lithography to generate the phase patterns in a layer of polymethyl methacrylate (PMMA).

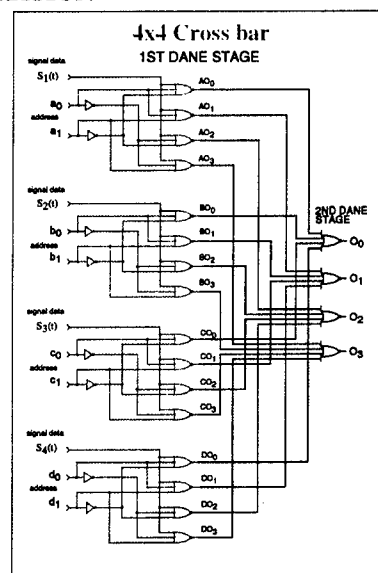


Figure 1: 4 x 4 crossbar switch.

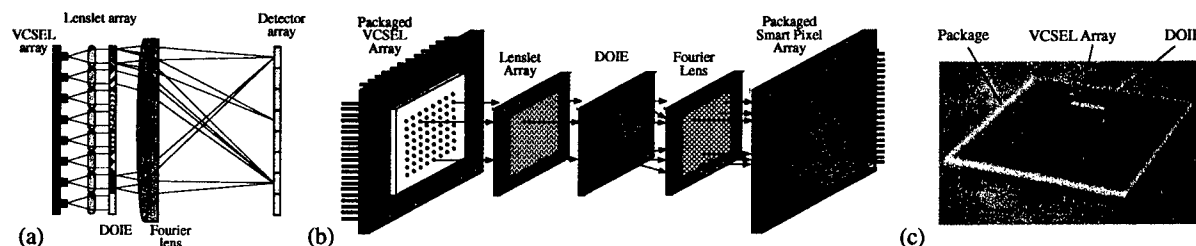


Figure 2: First stage HPOC module demonstration setup: (a) theoretical, (b) experimental, and (c) actual.

3. CROSSBAR IMPLEMENTATION

The interconnect patterns for a 4 x 4 crossbar are shown in Figure 3. The required phase maps generated for the hologram of a 4 x 4 crossbar are shown in Figure 4. The phase maps of the first stage are more complicated than those of the second stage. Each set of four NOR gates in the first stage of the crossbar has one row in the DOIE pattern.

In that row, the NOR gate set has one signal line and four address lines (where two address lines are represented in complementary notation). If any of the address lines are illuminated in the same path as the signal line, then no signal will pass for that address selection in the first stage. For the crossbar switch to function without conflicts, each signal input must be routed to a different column in the second stage which is set by an external circuit. All the signals from one column of the second VCSEL array are routed to one detector with only a single signal illuminating the detector at a time.

The output results of the top row for the first stage of the crossbar are presented in Figure 5. The data presented in each case is the light incident on the first stage of detectors produced by single VCSEL illumination of the optics array from each position on the top row for the first VCSEL array. Figures 5a, b, d, and e, are the address lines. Figure 5c is the signal line for the first set of 3-input NOR gates. The 2-D plots show that the data is distinguishable from any noise. The isometric plots clearly indicate the dynamic range of the address and data signals. With an 8-bit camera, the peaks can be easily resolved demonstrating the signal strength is in excess of 255:1 over the noise floor. In some of the figures, a zero order spot is slightly visible in addition to the signals. Any stray noise from this spot is negligible because it is positioned in the center of the array, such that it will not illuminate any active detectors.

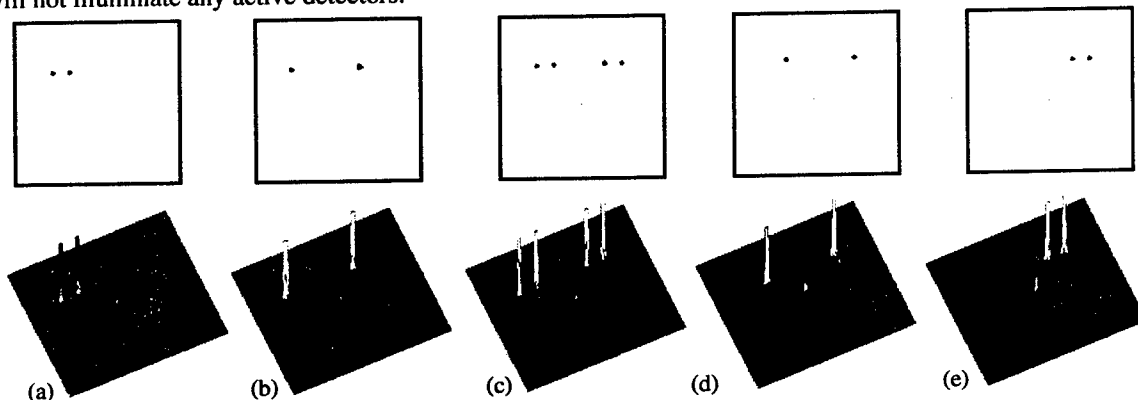


Figure 5: Imaged output from the first row of the hologram where the top figure is the 2-D view and the bottom is the isometric plot.

4. CONCLUSIONS

This crossbar implementation has demonstrated the usefulness of smart pixels in ATM switch applications. When smart pixels are utilized in conjunction with DOIEs, the global FSOI provided by the HPOC module enables the construction of a variety of functions including adders, multipliers, and large switches, demonstrating that optoelectronic smart pixel devices can be effectively utilized.

5. ACKNOWLEDGMENTS

OptiComp Corporation would like to acknowledge the following supporters of this program: Dr. Robert Leheny of the Defense Advanced Research Projects Agency (DARPA), Mr. Lou Lome of the Ballistic Missile Defense Organization (BMDO), Mr. Robert Kaminski of Rome Laboratory, Mr. Scott Spence of the Naval Surface Warfare Center (NSWC), and Mr. Max McCurry and Mr. Esam Gad of the U.S. Army Space and Strategic Defence Command (SSDC).

6. REFERENCES

1. P. S. Guilfoyle et al., "Low power optoelectronic modules for high performance switching applications," *IEEE Aerospace Proceedings*, pp. 211-234, 1997.
2. P. S. Guilfoyle et al., "Optimization of diffractive optical interconnect elements for high performance optoelectronic computing modules," *Proc. of SPIE: Optoelectronics and Interconnects IV*, Vol. 3005, pp. 87-98, 1997.

Networking with Free Space Optical Data Packets Using Carrier-Sense Multiple-Access with Collision Detection (CSMA/CD) Protocol

Jen-Ming Wu, C.B. Kuznia, Chih-Hao Chen, Bogdan Hoanca and A.A. Sawchuk

Signal and Image Processing Institute; University of Southern California

3740 McClintock Avenue; Los Angeles, CA 90089-2564

Tel: (213) 740-4143 Fax: (213) 740-4651 email: jwu@biron.usc.edu

1. TRANSPAR Network Introduction

We have developed a smart pixel networking scheme for distributing three-dimensional optical data packets among nodes. The system has a large array of parallel channels operating at on-chip clock rates, allowing for a potential throughput of > 1 Tb/s between VLSI chips [1]. The use of parallel data packets results in lower latency because each parallel packet spends less time on the network as compared to serial methods. Each network node implements a modified Carrier-Sense Multiple-Access with Collision Detection (CSMA/CD) media access protocol derived from the Ethernet standard and is extended to operate over ring networks that pass spatially parallel packets.

To demonstrate this novel networking concept, we created an optoelectronic VLSI chip TRANslucent Smart Pixel Array (TRANSPAR). The TRANSPAR chip is being fabricated through the DARPA/GMU/CO-OP foundry program using the Lucent Technologies OE/VLSI process [2]. This foundry offers flip-chip bonding of 2-D arrays of MQW modulators and detectors (that operate as free space optical data ports) onto 0.5 micron CMOS circuitry. The TRANSPAR chip contains a 5×8 array of identically replicated smart pixels in a 2×2 mm² chip. Each smart pixel contains digital circuitry (550 transistors/pixel), a one-bit optical transmitter and a one-bit optical receiver. A TRANSPAR network contains multiple copies of the TRANSPAR chip, with each chip acting a network node. TRANSPAR nodes are inter-linked by a two-dimensional array of free space optical channels as shown in Fig. 1.

The TRANSPAR transfers data between nodes using 3-D packets of bits called optical parallel data packets (OPDPs). An OPDP consists of multiple 2-D arrays of bits transmitted from optical I/O ports by smart pixels over several clock cycles. The OPDP contains a data payload, source and destination address information and an optical clock channel. When transferring an OPDP, the transmitters of a source node are synchronously linked to the receivers of a destination node using the optical clock channel. This allows TRANSPAR nodes to perform high-speed data transfers between nodes having independent (and widely varying) clock rates. The source and destination address fields are spatially encoded in the OPDP for parallel packet recognition. Because TRANSPAR processes packet header information in parallel, no packet buffering is required at any node.

2. CSMA/CD Networking with OPDPs

The TRANSPAR nodes are physically arranged as a ring network shown in Fig. 2. The TRANSPAR nodes have distributed control of the network, with attached host processors performing uploading/downloading of packets to/from the nodes.

Once transmitted from a source TRANSPAR node, an OPDP travels through the entire ring, optically propagating in free space between nodes and electrically propagating on the VLSI plane within nodes. All TRANSPAR nodes detect the OPDP and compare its destination address with their own

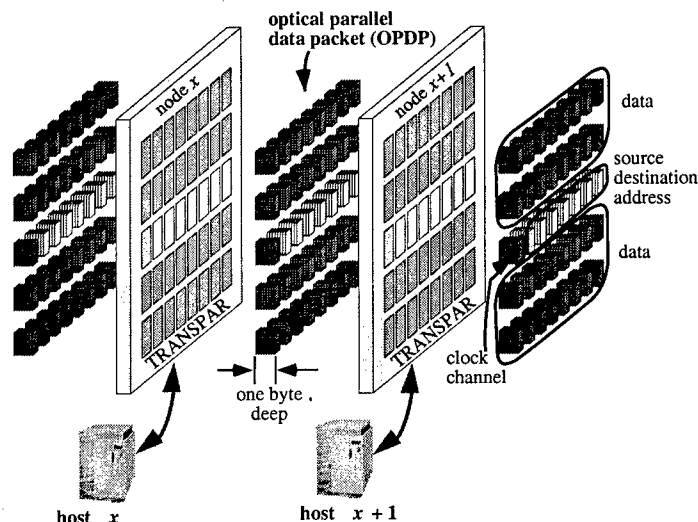


Figure 1: TRANSPAR nodes communicate using 3-D Optical Parallel Data Packets (OPDPs). An OPDP contains payload data, packet source/destination address, and a data clock channel for synchronous transfer.

address, downloading on a match. The latency per node (including both the propagation time through the node and the optical propagation between nodes) in a typical physical system is less than 2 ns.

TRANSPAR has been designed and simulated to have a target on-chip clock rate of 200 MHz. Since the optical data channels are formed directly between the internal (or core) circuitry on communicating nodes, the data transfer rate is comparable to the on-chip clock rate. This contrasts with traditional computing architectures that use a much lower off-chip clock rate for data transfer between chips or boards.

Figure 3 shows the optical network interface circuitry within a smart pixel PE. This circuit contains an optical receiver (Rx), optical transmitter (Tx), and an 8-bit FIFO buffer for downloading OPDPs. The 5×8 array of smart pixels form an OPDP that is 5×8 bits in spatial dimension by 8 bits deep in the temporal dimension. Thus, TRANSPAR forms a $5 \times 8 \times 8$ OPDP by having all smart pixels transmit data over eight clock cycles. Scaling this prototype to standard CMOS chip sizes

creates OPDPs containing 4 Kbytes (64×64 array size) of data with a network throughput of over 800 Gb/s.

When a node is not adding an OPDP onto the network, all of its smart pixels are in *transparent* mode. In transparent mode, any signal entering the Rx passes *directly* on to the Tx, incurring only a few gate delays (~ 1 ns). When adding an OPDP onto the network, the PE is in *opaque* mode. Signals entering the Rx are blocked while the Tx transmits the OPDP onto the network. The transmitted packet travels through all other TRANSPARs almost instantaneously, since they are transparent. The smart pixels dedicated to destination address recognition determine if there is an address match and, if so, signal all smart pixels on the chip to download the OPDP. When downloading, a dedicated optical clock smart pixel detects the optical clock, supplied in the OPDP, and broadcasts the signal electronically to all PEs for synchronous transfer into their 8-bit FIFO buffers.

When a source node wants to add an OPDP onto the network, it 'senses' the network for inactivity. There is a chance that two or more TRANSPAR nodes will detect an idle network at nearly the same moment and upload OPDPs that will cause contention (or a *collision*, in Ethernet terms). Each node contains circuitry to detect such a collision and reset the network.

3. Conclusions and Acknowledgments

The TRANSPAR chips are being assembled into a packaged optoelectronic system. We will present additional details of its protocol and operational parameters. This work was supported by the Integrated Media Systems Center, a National Science Foundation Engineering Research Center, with additional support from the Annenberg Center for Communication at the University of Southern California and the California Trade and Commerce Agency. It was also supported by the Joint Services Electronics Program through the Air Force Office of Scientific Research.

4. References

- [1] D. A. B. Miller and H. Ozaktas, "Limit to the Bit-Rate Capacity of Electrical Interconnects from the Aspect Ratio of the System Architecture," *J. Parallel and Dist. Computing, Special Issue on Optical Interconnects*, vol. 41, pp. 42-52, 1997.
- [2] K. W. Goossen, et. al., "GaAs MQW modulators integrated with silicon CMOS," *IEEE Photon. Technol. Lett.*, vol. 7, pp. 360-362, 1995.

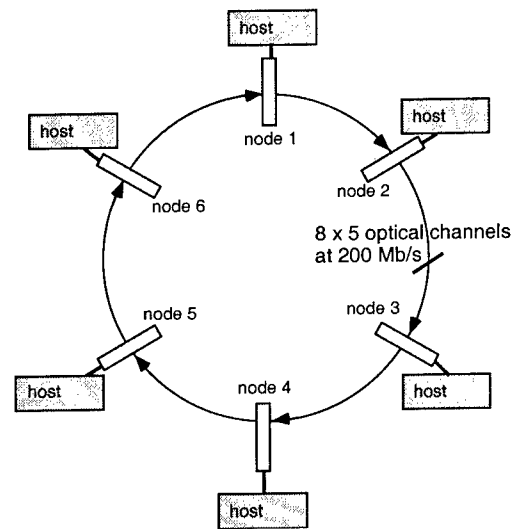


Figure 2: A TRANSPAR node interfaces a host machine to a ring network. OPDPs travel unidirectionally through the ring from source to destination nodes.

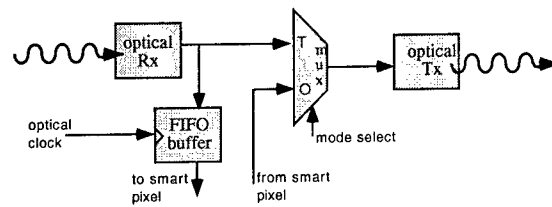


Figure 3: Smart pixel receiver (Rx) and transmitter (Tx) pair. In transparent mode, detected signal is passed through to the transmitter. In opaque mode, signals from the smart pixel are transmitted. The transparent mode of the smart pixel array allows OPDPs to propagate quickly through all nodes in the TRANSPAR ring.

OPTOELECTRONIC COMPUTER-AIDED DESIGN
(Invited)

J. Morikuni[†], P. Mena, A. Harton, and K. Wyatt
Motorola
Applied Simulation and Modeling Research
1303 E. Algonquin Road, Annex 2
Schaumburg, IL 60196
[†]ajm035@email.mot.com

The success of the modern silicon electronics industry can be attributed, in part, to the availability of advanced modeling and simulation computer-aided design (CAD) tools. Without such tools, it would be impossible to design multi-million-transistor VLSI integrated circuits, printed circuit boards (PCBs) and multichip modules (MCMs), or the myriad of other technologies that comprise modern electronic products. This modeling and simulation infrastructure is crucial for product design; without these tools, multiple design and fabrication iterations are required in order to optimize design and system parameters, a process which severely impacts cycle time and end-product cost.

Because the field of optoelectronics has not yet reached the same level of product proliferation as the electronics industry, a corresponding CAD infrastructure does not yet exist for the modeling and simulation of optoelectronic devices, circuits, and systems. It would be inaccurate, however, to state that no such commercial tools exist; indeed, tools have existed for quite some time at the device level for the detailed design of individual device structures such as laser diodes and photodetectors. These approaches typically involve the discretization of relevant equations from semiconductor physics into space and time and their subsequent spatio-temporal solution by finite-difference or finite-element methods. At higher levels, tools are also available to perform detailed optical component (e.g., lens) and system design; typically, these tools employ ray tracing methods. Optoelectronic design tools have also emerged recently to address the simulation of fiber-optic systems. The rate of CAD tool development and commercialization in recent years has been quite encouraging and is clearly a response to the needs of optoelectronic product designers. There is still, however, much CAD development work to be done before optoelectronic design can be accomplished in as seamless a manner as electronic design.

One area that has not been addressed in great detail is the modeling and simulation requirements of optoelectronic subsystem and component design. The design of a laser-based transmitter is a good example. While elaborate tools exist for the detailed design of laser diodes, the nature of their spatio-temporal solution algorithms can result in simulation times on the order of hours. On the other hand, for the electronic portions of the transmitter, there are many well-accepted compact transistor models as well as several industry-standard SPICE-like simulators that are used for circuit design. Simulation of electronic circuits using these models and tools can be accomplished in seconds or minutes. Since the majority of effort for optical transmitter design lies in the design of the drive circuit, responsibility for the design of the transmitter, as a whole, is often assigned to a circuit designer who may or may not have any background or expertise in optoelectronic devices. Thus, it is critical for the circuit designer to have access to models for optoelectronic devices that have been implemented in standard electronic simulation tools that the designer is familiar with. When such tools do not exist, the circuit designer traditionally attempts to model only the electrical properties of the laser, such as its equivalent input impedance or parasitics, but takes no steps to model the optical properties [1]. While this approach will facilitate the design of a driver circuit that provides the correct amount of bias current and signal modulation current, it is inadequate to predict optical or optoelectronic properties such as relaxation oscillations, turn-on delay, or optical phenomena related to carrier distribution and spatial hole burning. The approach often results in a working laser driver *circuit* but a non-functioning transmitter *subsystem*. Measurements are taken and designs are then iterated until the transmitter as a whole performs according to specification. Since the transmitter contains hundreds or thousands of transistors but only one laser, this process, while painful, is often

tolerated. However, the situation is exacerbated when it is necessary to design more complex systems such as those which utilize laser arrays [2] and those which are achieved through advanced optoelectronic integration methods (e.g. smart pixels). Although several researchers have addressed the circuit-level modeling of optoelectronic devices in the literature [3], commercial CAD companies have only begun to adopt such models into their software packages. The situation is much worse when advanced optoelectronic devices, such as VCSELs, are required; in this case, no commercial tools exist.

A well-accepted model for laser diode operation is the rate-equation formulation:

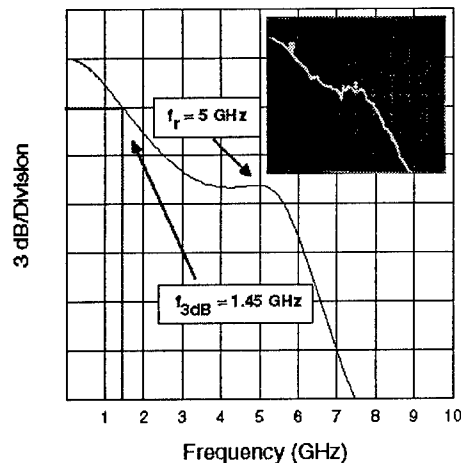
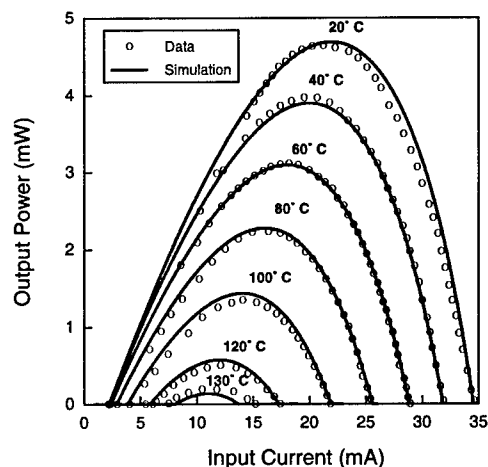
$$\frac{dN}{dt} = \frac{I}{q} - \frac{N}{\tau_n} - G_o(N - N_o) \quad \frac{dS}{dt} = \beta \frac{N}{\tau_n} + G_o(N - N_o) - \frac{S}{\tau_s}$$

In these equations, N and S are the electron and photon populations respectively; τ_n and τ_s are the electron and photon lifetimes, respectively; I is the injected current; q is the electronic charge, β is the spontaneous emission coupling coefficient, N_o is the electron transparency population and G_o is the gain coefficient. Typical commercial implementations of circuit-level laser diode models rely on variants of this formulation. While these equations have been used to varying degrees of success to model edge-emitting laser diodes, without augmentation, they are unable to model advanced laser structures, such as VCSELs. This is a critical situation since VCSEL-based products are already in production today.

Depicted below are two simulations; the light-current characteristics of one VCSEL and the AC characteristics of another. These VCSEL simulations are the results of a research program in our laboratories to develop optoelectronic models using standard circuit simulation tools that are well-embraced by the electronics community. Similar efforts are underway to develop models for other components necessary to simulate optoelectronic and optical interconnect systems. As stated previously, many optoelectronic device models and theories do exist; however, it has been our experience that their impact on product development is maximized when they are implemented into tools already in use by product designers.

REFERENCES

- [1] J. J. Morikuni and S. M. Kang, *Computer-Aided Design of Optoelectronic Integrated Circuits and Systems*. Upper Saddle River, NJ: Prentice Hall, 1997.
- [2] L. J. Norton, F. Carney, N. Choi, C. K. Y. Chun, R. K. Denton Jr., D. Diaz, J. Knapp, M. Meyering, C. Ngo, S. Planer, G. Raskin, E. Reyes, J. Sauvageau, D. B. Schwartz, S. G. Shook, J. Yoder, and Y. Wen, "OPTOBUS I: A production parallel fiber optical interconnect," *IEEE Electronic Components and Technology Conference*, pp. 204-209, 1997.
- [3] R. S. Tucker, "Large-signal circuit model for simulation of injection-laser modulation dynamics," *IEE Proceedings*, vol. 128, pt. I, no. 5, pp. 180-184, 1981.



High Speed, Smart Focal Plane Processing Using Integrated Photodetectors and Si CMOS VLSI Sigma Delta Analog to Digital Converters

YoungJoong Joo, Suzanne Fike, Mikkel Thomas, Kee Shik Chung, Martin Brooke, Nan M. Jokerst, D. Scott Wills
School of Electrical and Computer Engineering
Georgia Institute of Technology
Atlanta, Georgia 30332

High speed imaging applications such as combustion, transMach fluid flow, and aerooptic sensing require a high frame rate image acquisition system with frame rates in excess of 100 kfps (frames per second). Currently, imaging systems implemented using charge-coupled device (CCD) technology with off-chip analog to digital data converters are limited to continuous frame rates of approximately 1 kfps [1]. Analog data transfer bottlenecks, which are limited by signal to noise ratios and the requirement for fast ADCs, are the cause of this low frame rate limitation and the lack of scalability of these imaging systems. Smart pixel imaging systems which implement low speed direct digital ADC at the pixel level translate this data transfer problem to that of parallel digital links, which can be realized with through-Si vertical optical data links [2], which can be used to realize fully scalable smart pixel imaging systems.

This paper reports the first demonstration of a high frame rate smart pixel imaging system which uses an ADC per pixel in an 8x8 integrated detector array. The smart pixel architecture of this system enables frame rates up to 100 kfps operating in continuous imaging mode. This integrated imaging system has been implemented in digital Si CMOS VLSI, and, to realize scalability, has been integrated with an emitter driver circuit for through-Si vertical optical communication down to a second layer of dedicated Si image processing circuitry [3][4].

There are three main building blocks used to realize this smart pixel image acquisition system. The first building block is the integrated photodetector array. Two implementations have been demonstrated herein: Si CMOS and thin film hybrid integrated GaAs-based PiN detector arrays. Figure 1 is a schematic illustration of the smart pixel imaging system, and Figure 2 is a photomicrograph of the integrated GaAs-based 8x8 photodetector array directly on top of the ADC array. This implementation realizes higher fill factor than the monomaterial Si detector array. The second smart pixel system building block is the ADC. Due to the small Si area available underneath each pixel, a compact ADC with high speed and large dynamic range is necessary. A current input sigma delta ADC has been used in the demonstrated system. A sigma-delta ADC is a good candidate for this imaging application because it is immune to component mismatch, and through subsequent digital filtering of the ADC output signals, a tradeoff between dynamic range and frame rate can be achieved. In addition, the digital filtering can remove high frequency noise from the image data, which is impossible with CCD imagers operating at the same frame rate, resulting in an improved signal to noise ratio for the ADC-based system. The final system building block is the ADC readout system. By locating an ADC at each pixel, the readout noise associated with the analog transfer of charge in CCD arrays has been eliminated. The integration of an emitter driver enables a fully parallel, scalable transfer of data down through the Si circuit using a vertical optical link to a second layer of digital processing hardware. Maintaining this fully parallel data link enables the scalable realization of 100 kfps smart pixel imaging systems since each 8x8 array in a larger, tiled system can be associated with a vertical readout link.

The Si and GaAs-based imaging array smart pixel circuits have been fabricated and successfully tested, and the Si imaging array has been extensively tested. Each of the sigma delta ADCs is clocked at 15.6kHz, resulting in a frame rate of 976 fps. The output data is captured using a digital acquisition card in a Pentium-class computer. This test configuration, shown in Figure 3a, is the primary limitation of the measured frame rate. Figure 3b shows the image data displayed on a video screen, which cannot display the measured frame rate. Simulated results indicate a frame rate capability in excess of 100 kfps. To measure this performance, a faster test facility is necessary.

In conclusion, this paper reports the first demonstration of a high frame rate smart pixel imaging system using an ADC per pixel in an 8x8 integrated detector array. This integrated imaging system has been implemented in digital Si CMOS VLSI, and has measured operation of 976 fps, with a projected frame rate of 100 kfps.

8 X 8 focal plane array:
detectors and ADCs

Emitter driver

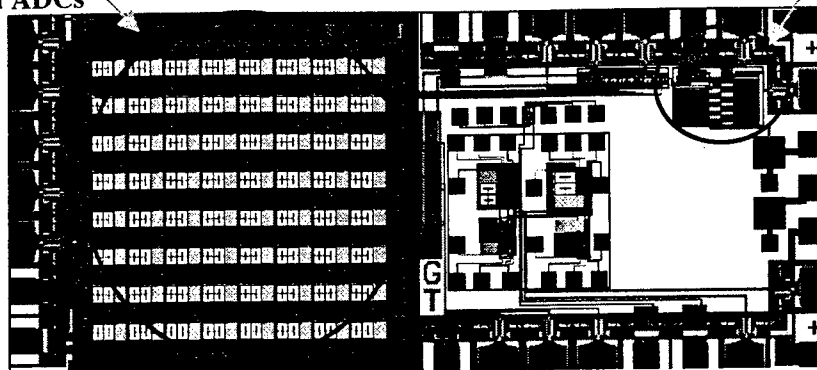


Figure 1. Si CMOS VLSI smart pixel imaging array.

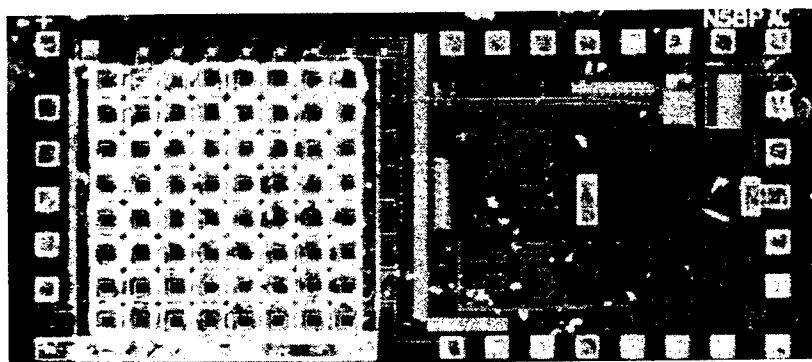


Figure 2. Photomicrograph of hybrid integrated GaAs-based detectors directly on top of sigma delta ADCs to form integrated smart pixel imaging array.

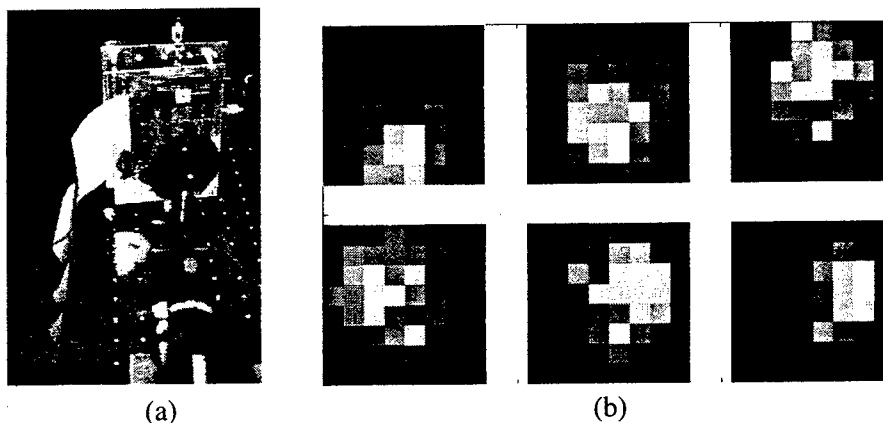


Figure 3. Test setup with low speed test results

1. Bojan T. Turko, Georgia J. Yates, Nicholas S. King, " Processing of multiport CCD video signals at very high frame rates," Proc. SPIE Int. Soc. Opt Eng., vol. 2549, pp. 11-15, 1995.
2. Steven W. Bond, Sungyong Jung, Olivier Vendier, Martin A. Brooke, Nan M. Jokerst, "3D stacked Si CMOS VLSI smart pixels using through-Si Optoelectronic interconnections," IEEE/LEOS summer tropical meetins, 1998.
3. Huy H. Cat, Antonio Gentile, John C. EbleMyunghye Lee, Olivier Vendier, Young Joong Joo, Scott D. Wills, Martin Brooke, Nan Marie Jokerst, and April S. Brown, "SIMPil: An OE Integrated SIMD Architecture for Focal Plane Processing Applications," MPPOI, pp. 44-52, Oct. 1996.
4. YoungJoong Joo, S., Fike, Kee Shik Chung, Martin A. , Brooke, Nan M. Jokerst, Scott Wills, " Application of Massively Parallel Processors to Real Time Processing of High Speed Images," MPPOI, pp.96-100, 1997.

A high resolution, high frame-rate spatial light modulator

I. Underwood, D.G. Vass, W.J. Hossack,

M.W.G. Snook, S. Nath and I.D. Rankin

The University of Edinburgh Department of Physics and Astronomy

(* Department of Electronics and Electrical Engineering)

The Kings Buildings Mayfield Road Edinburgh EH9 3JL UK

tel +44 131 650 5652 fax +44 131 650 6554 email i.underwood@ee.ed.ac.uk

M.R. Worboys, M.S. Griffith and S.N. Radcliffe

GEC Marconi Research Centre West Hanningfield Road Great Baddow

Chelmsford CM2 8HN Essex UK

D. MacIntosh, J. Harkness and B. Mitchel

Admit Design Systems Ltd Scottish Software Partner Centre

South Queensferry West Lothian EH30 9TG UK

G. Rickard and J. Harris

Swindon Silicon Systems Ltd Radnor Street Swindon Wiltshire SN1 3PR UK

Introduction

We describe a Ferroelectric Liquid Crystal (FLC) Spatial Light Modulator (SLM) which is electronically addressed via a VLSI CMOS silicon backplane. Designed specifically for use in a miniature colour display system, the device nevertheless exhibits a specification which is suitable for many non-display applications.

SLM Specification

A summary specification of the (non-display characteristics of the) SLM is given in Table 1

Characteristic	Value
Pixel count	1024 x 768
Pixel pitch (um)	12
Mirror size (um)	9 - 11
Fill factor (%)	~70 to >80 (depending on process spec)
Frame rate (kHz)	2.5 (1.2, dc balanced)
Modulation	binary amplitude or phase
Contrast ratio	100:1

Table 1 Summary SLM specification

SLM Design

The backplane was fabricated on a 0.7 μ m, 5V CMOS process. The SLM pixels are of the single transistor (DRAM) type. They are addressed row-at-a-time via a 64 bit wide data bus. An interface accepts PAL and RGB data input.

Wafer fabrication and planarization

The conventional part of the wafer fabrication was carried out by Alcatel-Mietec. Subsequent to delivery of the wafers a post-processing planarization technique was applied in order to improve the flatness and fill factor of the pixel mirrors. This has resulted in a fill factor of around 70% for the first batch of SLMs. We expect to boost this to >80% in future batches.

SLM Assembly

SLMs have been assembled with a nominal cell gap of 2.4 μ m and filled with Chisso CS 1031 FLC. They are mounted on a small, lightweight custom-designed Multi Chip Module (MCM).

Optical Characterization

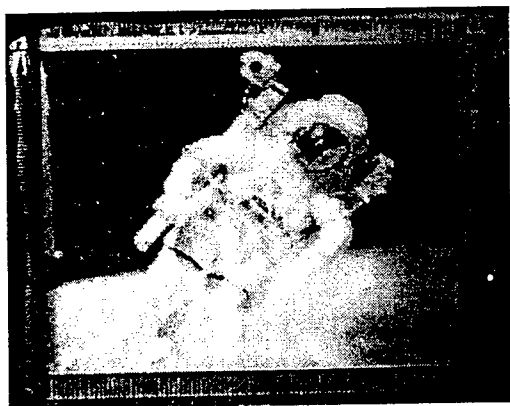


Figure 1 Monochrome reproduction of colour image on SLM

Due to a scarcity of early devices, progress on optical characterization for SLM applications has been slow. Effort has thus far been concentrated on planarizing more wafers and on characterization for displays.

Figure 1 shows a monochrome reproduction of a 16-bit colour image displayed on the full 1024x768 pixels of the SLM. The actual size of the image diagonal is approximately 15mm.

Acknowledgments

The SLM was designed and fabricated as part of the SLIMDIS project, partly funded under the LINK Photonics scheme by the Department of Trade and Industry and the Engineering and Physical Sciences Research Council of the U.K.

References

- [1] SLIMDIS descriptive document, GEC Marconi, 1996
- [2] DG Vass et al, "A high resolution, full colour, head mounted ferroelectric liquid crystal over silicon display", Ferroelectrics, in print.

VLSI Development of Smart-Pixel ICs: A Hybrid DSP Core and a Multi-threaded Programmable DSP

J. Ekman, P. Chandramani, R. Rozier, F. Kiamilev, J. Rorie
Dept. of Electrical Engineering - UNCC, Charlotte, NC 28223

F. Zane, P. Marchand, S Esener
Dept. of Electrical/Computer Engineering - UCSD, La Jolla, CA 92093

Introduction:

Development of digital ICs with the capability to interface with optical devices to yield high-speed/high-bandwidth communication between chips has been underway. Presented here are two ICs which target this development. The first, fabricated with Hewlett-Packard's 14B half-micron process as a part of the 1997 Bell Labs/Lucent Technology CMOS-MQW foundry is a DSP core whose layout is shown in Figure 1. The second is a prototype design of the multi-threaded programmable DSP engine that will be a part of the 3-D OESP Consortium demonstrator system. The aim of the consortium is to develop dense packaging of DSPs with low power consumption and high-speed operation through use of free-space optical interconnect and realized with 3-D stacking of ICs.

DSP-Core Chip:

An early generation IC was designed to test and demonstrate the multiply-add structure that is common to many DSP algorithms. The DSP-core chip is a hybrid design which is compatible with both MQW modulators and VCSELs. One-hundred and twenty area-distributed I/O pads and eighteen perimeter pads provide electrical contacts for sixty MQW modulators which are flip-chip bonded to the surface of the die and eighteen VCSEL inputs. Analog receiver and driver arrays allow the digital core circuitry to communicate with these optical devices. Input to the chip can come optically via the modulators or electrically through perimeter pads. Both modulator and VCSEL driver outputs are active simultaneously. In addition, scan chains at the input and the output of the multiplier allow isolation of the hardware components as a test feature. The inputs are two 10-bit data words which are inputs to a 10x10 high-speed multiplier and a 20-bit data word which joins the multiplier output as the second input to an ALU. Perimeter pads also serve to control the ALU operation and provide clock and clear signals. To maintain signal integrity of the analog signals to and from the optical devices, receiver and driver arrays were placed as close as possible to the pads with which they communicate. Also, to reduce noise in the ground plane due to the digital circuitry switching, separate power and ground connections were included for the modulator receivers and for the VCSEL drivers.

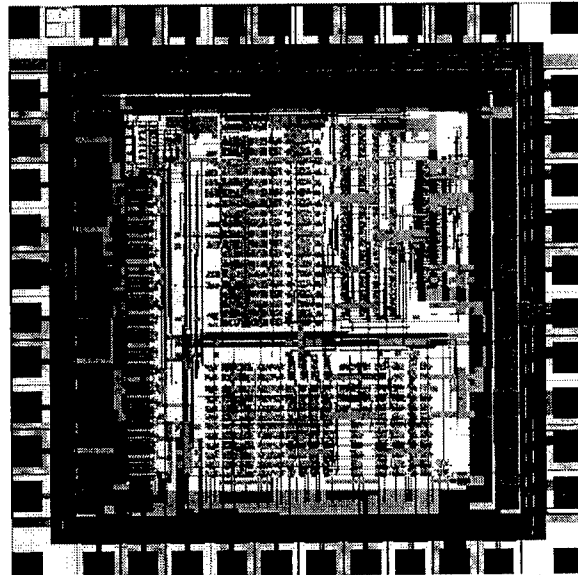


Figure 1: DSP-Core Chip layout

Multi-threaded Programmable DSP Chip:

The purpose of the second chip is to provide a prototype of the processor that will be a part of the multi-processor multi-chip 3-D OESP demonstrator system. This chip design extends upon the DSP core above to provide more flexibility and functionality.

The architecture for this chip, shown in Figure 2, is motivated by the desire to match the processor performance to the access time of the static RAM included with the processor. To achieve this, the separable nature of algorithms such as FFT and DCT was exploited. Multiple parts of the problem can be stored in separate RAMs and "threaded" through the processor so as to allow the RAM appropriate recovery time between accesses. The processor hardware

consists of four 24x12-bit multipliers and six add/subtract units. Precision through the processor is maintained by keeping all 36 bits from the multipliers and increasing the size of the add/subtract units in subsequent stages. The first two stages (multipliers and two adders) provide for complex multiplication. The third stage has programmable interconnect that allows for many different algorithms to be mapped into this hardware. Two of the four adder units in the third stage can be configured as accumulators which allows for complex multiply-accumulates to be performed.

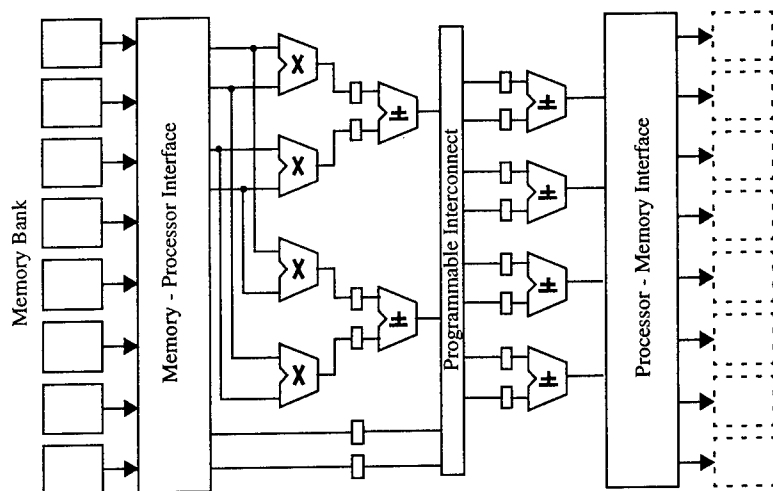


Figure 2: Prototype chip architecture

Eight separate SRAMs make up the memory bank. Only one bank of memory is included. The second memory bank shown in Figure 2 represents writing data back into the same bank from which it was taken. This RAM architecture was chosen based on the need to provide and receive two data points to and from the processor at each cycle in configurations such as the radix-2 butterfly and the need to have two clock cycles per RAM access.

Key to the high-performance operation of this design are the interface units between the processor and memory which provide data to the processor and write processed data back to memory with the appropriate timing. In general, data is taken from the

RAMs four points at a time and stored in a register bank. Likewise another register bank stores data until it is written back to the RAMs four points at a time. This scheme allows the RAM to be accessed at every possible cycle (read or write) while maintaining the processor at full speed.

A bottleneck in current DSP systems lies in performing corner turns in two-dimensional calculations due to limited I/O bandwidth. The 3-D OESP demonstrator system will accelerate this process by allowing each of the 64 processors operating on the data in parallel to communicate with each other optically. A communication protocol and a system architecture based on this is also being developed [1]. To take advantage of the future high-bandwidth communication, large data ports will be supplied to send data out of each processor. Furthermore, four such processors will be on each IC in order to fill the 16x16 array of Giga-hertz optical channels. Therefore, the design of this chip also takes into consideration the need to operate the processors in parallel by minimizing the need to provide different control signals to different processors.

One of the goals of the prototype chip is to test the processor operation and develop state machines that will provide the best performance. For this reason, full external control of this chip is provided. In addition, scan chains allow for separate testing of the memory and processor. This prototype processor is going to be fabricated using Hewlett-Packard's 0.35 μ m-four metal-layer process. It has a total memory capacity of 49 kilo-bits and integrates just over half a million transistors. The die size is roughly 5x5 mm and will be packaged in a 108-pin PGA package.

Reference:

1. J. Rorie, P. Marchand, F. Kiamilev, P. Chandramani, J. Ekman, S. C. Esener, "A System Architecture for use with Free Space Optical Interconnects in a 3D Stacked Processor Environment".

Effort sponsored by the Defense Advanced Research Projects Agency (DARPA) and Air Force Research Laboratory under agreement number F30602-97-2-0122. The US government is authorized to reproduce and distribute reprints for governmental purposes notwithstanding any copyright annotation thereon.

AUTHOR INDEX

Ahadian, J. F.	WA6	Hessenbruch, J. M.	FB3	Nakayama, H.	WA2
Anan, T.	WA4	Hibbs-Brenner, M. K.	WA1	Nath, S.	FC4
Ando, Y.	FA3	Hinton, H. S.	ThB1,ThC2	Nishi, K.	WA4
Angliss, B. E.	ThC2	Hoanca, B.	FB4	Oettel, R.	ThA3
Athale, R.	FB1	Hossack, W. J.	FC4	Ohki, A.	FA3
Ayliffe, M. H.	WA8	Ishii, R.	WA2	Otoma, H.	WA2
Beyette, Jr., F. R.	ThC3	Jan, W. Y.	WA7,ThA2	Ozguz, V.	ThC5
Bond, A. E.	WA3	Jokerst, N. M.	ThA4,FC3	Patterson, S. G.	WA6
Bond, S. W.	ThA4	Joo, Y. J.	FC3	Petrich, G. S.	WA6
Bradley, W. M. D.	ThC4	Jung, S.	ThA4	Plant, D. V.	WA8
Breslin, J. A.	ThB4	Kabal, D. N.	WA8	Prasad, S.	WA6
Brooke, M. A.	ThA4	Kanyuck, C.	ThC3	Radcliffe, S. N.	FC4
Brooke, M.	ThB2, FC3	Kasahara, K.	WA4	Rankin, I. D.	FC4
Chandramani, P.	ThA3,ThC5,FC5	Katsura, K.	FA3	Ressler, E. K.	ThB3
Chen, C. H.	FB4	Kiamilev, F.	ThA3,	Richard, E.	WA8
Chung, K. S.	FC3		ThC1,ThC5,FC5	Rickard, G.	FC4
Coldren, L. A.	WA5	Kim, J.	FB3	Rorie, J.	ThC5, FC5
Cunningham, J. E.	WA7,ThA2	Ko, J.	WA5	Royster, Y.	WA6
Currie, J.	WA8	Kolodziejewski, L. A.	WA6	Rozier, R.	ThA3,FC5
Dapkus, P. D.	WA3	Krishnamoorthy, A. V.	ThA2	Sadowski, R. W.	ThB3
Dudevoir, G. P.	ThB3		ThA3,ThA5,FB2	Saito, H.	WA4
Ekman, J.	ThA3,ThC5,FC5	Kuznia, C.B.	FB4	Sakurai, T.	WA2
Esener, S. C.	ThC5,FC5	Lehman, J.	WA1	Sato, N.	FA3
Farbarik, R.	ThA3	Leibenguth, R. E.	ThA2	Sawchuk, A. A.	FB4
Feldman, M. R.	FA2	Liu, Y.	WA1	Sayles, A. H.	ThB3
Fike, S.	FC3	Louderback, D. A.	WA5	Shoop, B. L.	ThB3
Fonstad, Jr., C. G.	WA6	Low, J. K.	ThB4	Sjölund, O.	WA5
Ford, J. E.	FA1	MacIntosh, D.	FC4	Slutz, M.	ThC3
Fuse, M.	WA2	Marchand, P.	ThC5,FC5	Snook, M. W. G.	FC4
Goodhue, W. D.	WA6	Matsuura, N.	FA3	SpringThorpe, A. J.	WA8
Goosen, K. W.	WA7,ThA2	Mears, R. J.	ThC4	Stone, R. V.	FB3
Griffith, M. S.	FC4	Mena, P.	FC1	Sugou, S.	WA4
Guilfoyle, P. S.	FB3	Mitchell, B.	FC4	Thomas, M.	FC3
Hall, D. A.	ThB3	Miyamoto, Y.	WA2	Tooley, F. A. P.	WA8
Harkness, J.	FC4	Morgan, R.	WA1	Travers, C. M.	FB3
Harris, J.	FC4	Morikuni, J.	FC1	Tseng, B. T.	ThA2
Harton, A.	FC1	Mull, D.	WA6	Ueki, N.	WA2
Hegblom, E. R.	WA5	Nakamura, T.	WA2	Underwood, I.	ThB4,FC4

AUTHOR INDEX

Usui, M.	FA3
Vaidyanathan, P. T.	WA6
Van Campenhout, J. M.	WA8,ThA1
Vass, D. G.	FC4
Vendier, O.	ThA4
Venditti, M. B.	WA8
Walker, J. A.	ThA2
Wills, D. S.	FC3
Woodward, T. K.	ThA2,ThA5
Worboys, M. R.	FC4
Wu, J. M.	FB4
Wyatt, K.	FC1
Yamamoto, M.	WA2
Yoshikawa, M.	WA2
Yoshikawa, T.	WA4
Zane, F.	ThC5,FC5